UNIVERSITY OF ALBERTA

Diagenetic Evolution of the Slave Point Formation, Clarke Lake, British Columbia, Canada

by

Jeffrey Scott Lonnee

©

A thesis submitted to the Faculty of Graduate Studies and Research in partial fulfillment of the requirements for the degree of Doctor of Philosophy

Department of Earth and Atmospheric Sciences

Edmonton, Alberta
Fall 2005

Library and
Archives Canada

Published Heritage
Branch

395 Wellington Street
Ottawa ON K1A 0N4
Canada

Bibliothèque et
Archives Canada

Direction du
Patrimoine de l'édition

395, rue Wellington
Ottawa ON K1A 0N4
Canada

0-494-08684-X

Your file Votre référence
ISBN:
Our file Notre reterence
ISBN:

NOTICE:
The author has granted a non-exclusive license allowing Library and Archives Canada to reproduce, publish, archive, preserve, conserve, communicate to the public by telecommunication or on the Internet, loan, distribute and sell theses worldwide, for commercial or non-commercial purposes, in microform, paper, electronic and/or any other formats.

The author retains copyright ownership and moral rights in this thesis. Neither the thesis nor substantial extracts from it may be printed or otherwise reproduced without the author's permission.

AVIS:
L'auteur a accordé une licence non exclusive permettant à la Bibliothèque et Archives Canada de reproduire, publier, archiver, sauvegarder, conserver, transmettre au public par télécommunication ou par l'Internet, prêter, distribuer et vendre des thèses partout dans le monde, à des fins commerciales ou autres, sur support microforme, papier, électronique et/ou autres formats.

L'auteur conserve la propriété du droit d'auteur et des droits moraux qui protège cette thèse. Ni la thèse ni des extraits substantiels de celle-ci ne doivent être imprimés ou autrement reproduits sans son autorisation.

In compliance with the Canadian Privacy Act some supporting forms may have been removed from this thesis.

While these forms may be included in the document page count, their removal does not represent any loss of content from the thesis.

Conformément à la loi canadienne sur la protection de la vie privée, quelques formulaires secondaires ont été enlevés de cette thèse.

Bien que ces formulaires aient inclus dans la pagination, il n'y aura aucun contenu manquant.

Canada

"...they display numerous cavities lined with
small rhombic crystals which have the luster and
the slight convexity of the faces which indicate pearl spar..."

Déodat de Dolomieu, 1791
Describing the occurrence of saddle dolomite

ABSTRACT

The Clarke Lake gas field in British Columbia, Canada, is hosted in pervasively dolomitized Middle Devonian carbonates of the Slave Point Formation. The Clarke Lake Field consists mostly of pervasive matrix dolomite and some saddle dolomite. Some of the saddle dolomite is replacive, some is cement, and both are associated with dissolution porosity and recrystallized matrix dolomite. A rigorous petrographic and geochemical examination of the reservoir dolomites was conducted, as well as consideration of the size and shape of the dolomitized rock body.

Pervasive matrix dolomitization was accomplished by long-distance migration of halite-saturated brines during the Late Devonian to Mississippian. Fluid inclusion homogenization temperatures suggest 150°C (uncorrected) to 190°C (corrected) at the time of matrix dolomitization. The replacive and cement saddle dolomites, as well as the associated dissolution and recrystallized matrix dolomites, at Clarke Lake are hydrothermal alteration products of the matrix dolomites, and formed from the invasion of a hydrothermal gypsum-saturated brine during periods of extremely high heat flow and regional plate-margin tectonics in the Late Devonian to Mississippian. Fluid inclusion temperatures suggest hydrothermal alteration occurred between 230°C (uncorrected) and 267°C (corrected), which are significantly higher than the maximum temperature of about 190°C attained by the Slave Point Formation during burial. The sources of the halite- and gypsum-saturated brines are Middle Devonian evaporite depositional environments roughly 200 km south and/or east of Clarke Lake, near the PRA.

The present chemistry of the formation waters in the Slave Point Formation is the result of mixing between the previously entrained halite- and gypsum-saturated brines

and meteoric water. This meteoric water end-member entered the basin through recharge in the Rocky Mountains to the west and was driven by topography. Isotopic compositions and ionic hydrochemistry suggest the meteoric water end-member was involved in water-rock interaction predominantly with the Proterozoic Muskwa Formation along its migration pathway. The migration pathways of the meteoric water, in combination with the overall geometry of the Slave Point Formation platform margin, are important for both trap development and preventing the previously emplaced hydrocarbons from being flushed through the active migration of formation waters in the Devonian. This observation may prove critical in the exploration for hydrocarbon accumulations in the Middle Devonian across northeastern British Columbia.

ACKNOWLEDGEMENTS

This thesis was financially supported by the Natural Sciences and Engineering Research Council (NSERC) of Canada and the Alexander von Humboldt Foundation (AvH) through operating grants to Hans G. Machel (University of Alberta). Funding to JL was provided by the University of Alberta through Province of Alberta Graduate Fellowships, a Province of Alberta Dissertation Fellowship, and a Petro-Canada Graduate Research Award. Additional support for this study, both financially and logistically, was provided by Petro-Canada Oil & Gas Limited.

I am honoured that Hans Machel accepted me to come to Edmonton and work with someone of his professional stature, and I am extremely grateful for his support and friendship over the past 6 years. I would also like to thank Doug Gardner, formerly of Petro-Canada, for providing me the opportunity to work on such a complex reservoir, and Martin Teitz, Petro-Canada, for his continued interest and support upon Doug's departure from Petro-Canada. I would also like to thank Karlis Muehlenbachs, Ben Rostron, Sarah Gleeson, and Jeremy Richards for providing their expertise when required, and the staff at the British Columbia Ministry of Energy and Mines Core Warehouse in Charlie Lake for assistance with core examination. Discussions with Rob Creaser, Pat Cavell, Eric Mountjoy, Dave Morrow, Jack Wendte, Ron Burwash, and Joe Tóth significantly improved this thesis. Some samples for this study were generously provided by Gerry Ross and Lavern Stasiuk from the Geological Survey of Canada (Calgary), and Ron Burwash from the University of Alberta.

A warm thanks to Ross Keilly, Markus Loegering, Alex MacNeil, Hilary Corlett, Michael Hearn, Randy Rice, and others in the department who made living in Edmonton enjoyable, even in the dead of winter. Most of all, I would like to thank my family for their love, support, patience and encouragement throughout my academic career.

TABLE OF CONTENTS

CHAPTER 1: GENERAL INTRODUCTION

1.1 Rationale 1
1.2 Study area 2
1.3 Geologic framework 4
    1.3.1 Paleogeography 4
    1.3.2 Structure 5
    1.3.3 Basement architecture and heat flow 11
1.4 Previous studies 18
1.5 Objectives 20

CHAPTER 2: STRATIGRAPHIC EVOLUTION OF THE SLAVE POINT FORMATION

2.1 Introduction 22
2.2 Methods 22
2.3 Stratigraphy 23
    2.3.1 Regional overview 23
    2.3.2 Beaverhill Lake and Woodbend groups in the study area 28
        Watt Mountain Formation 28
        Slave Point Formation 29
        Waterways Formation 30
        Otter Park Formation 32
        Muskwa Formation 33
2.4 Reference logs 34
2.5 Cross-sections 37
    2.5.1 Cross-section D-D' 37
    2.5.2 Cross-section E-E' 39
    2.5.3 Cross-section F-F' 41
    2.5.4 Cross-section G-G' 43

CHAPTER 3: DEPOSITIONAL FACIES IN THE SLAVE POINT FORMATION

3.1 Introduction 46
3.2 Methods 46
3.3 Facies in the Slave Point Formation 48
    3.3.1 General 48
    3.3.2 Previous studies 49
    3.3.3 Facies zone If 54
    3.3.4 Facies zone IIf 54
    3.3.5 Facies zone IIIf 57
    3.3.6 Facies zone IVf 57
    3.3.7 Facies zone IV/V 60
    3.3.8 Facies zone V 60
    3.3.9 Facies zone IVb 60
    3.3.10 Facies zone IIIb 67
    3.3.11 Facies zone IIb 67
    3.3.12 Facies zone Ib 70
    3.3.13 Patch reef facies 70
3.4 Facies distribution at Clarke Lake 73

CHAPTER 4: PETROGRAPHIC EVIDENCE FOR THE DIAGENETIC EVOLUTION OF THE SLAVE POINT FORMATION

4.1 Introduction 77
4.2 Methods 77
4.3 Diagenetic evolution 78
    4.3.1 Near-surface diagenesis 80
        Micrite envelopes 81
        Internal sediment 81
        Radial fibrous calcite 81

Drusy calcite 81
4.3.2 Shallow burial diagenesis 86
Fracture I 86
Blocky calcite I 86
Syntaxial calcite 86
Stylolite I 86
Fine crystalline brown dolomite 91
4.3.3 Intermediate burial diagenesis 91
Grey matrix dolomite 91
Replacive chert 97
Fracture II 97
Hydrothermal alteration 97
Stylolite II 109
4.3.4 Deep burial diagenesis 109
Fracture III 109
Shear and authigenic clay minerals 109
Vertical stylolite 120
Base-metal sulphide minerals 120
Liquid hydrocarbon 120
Quartz and barite 123
Microfractures and thermal cracking 123
Fracture IV 128
Blocky calcite II 128
4.4 Depositional facies control on diagenesis 128
4.4.1 Facies zone If 131
4.4.2 Facies zone IIf 131
4.4.3 Facies zone IIIf 134
4.4.4 Facies zone IVf 137
4.4.5 Facies zone IV/V 137
4.4.6 Facies zone V 140
4.4.7 Facies zone IVb 140

4.4.8 Facies zone IIIb 143
4.4.9 Facies zone IIb 143
4.4.10 Facies zone Ib 144
4.4.11 Patch reef facies 144
4.5 Spatial distribution of dolomite 147
4.6 Genetic implications of petrographic observations 151
4.6.1 Near-surface diagenesis 151
4.6.2 Shallow burial diagenesis 152
4.6.3 Intermediate burial diagenesis 154
4.6.4 Deep burial diagenesis 158

CHAPTER 5: GEOCHEMICAL EVIDENCE FOR THE DIAGENETIC EVOLUTION OF THE SLAVE POINT FORMATION

5.1 Introduction 161
5.2 Methods 161
5.3 Geochemical results and discussion 164
5.3.1 Stable isotopes 164
Results 166
Discussion 170
5.3.2 Strontium isotopes 179
Results 180
Discussion 181
Strontium source rocks 188
Laser ablation MC-ICP-MS 188
5.3.3 Trace elements 192
Results 193
Discussion 195
Microprobe analysis 202
5.3.4 Fluid inclusions 206
Introduction 208

Petrography 209
Microthermometry results 213
Microthermometry discussion 218
Leachates 223
5.3.5 Rare earth elements 235
Introduction 235
Results 237
Discussion 240
5.4 Burial and thermal history 246
5.4.1 Proof of hydrothermal activity 247
5.4.2 Burial curve and timing of hydrothermal activity 248
5.4.3 P-T conditions during dolomite formation 252
5.5 Dolomite timing 256
5.6 Dolomite models 262
5.7 Hydrological interpretation for dolomite formation 263

CHAPTER 6: ORIGIN AND EVOLUTION OF FORMATION WATERS IN THE SLAVE POINT FORMATION

6.1 Introduction 269
6.2 Hydrostratigraphy 269
6.3 Regional hydrogeology 273
6.4 Methods 275
6.5 Geochemical results and discussion 277
6.5.1 Stable isotopes 277
Results 281
Discussion 282
6.5.2 Strontium isotopes 285
Results 287
Discussion 287
6.5.3 Ionic hydrochemistry 294
Results 297

Discussion 298

6.5.4 Geochemical modeling 314

Results 315

Discussion 315

6.6 Fluid flow at Clarke Lake 325

CHAPTER 7: SYNOPSIS

7.1 Restatement of objectives 331

7.2 Diagenetic evolution of the Slave Point Formation 332

7.2.1 Stage I – Middle Devonian 332

7.2.2 Stage II – Middle to Late Devonian 338

7.2.3 Stage III – Late Devonian 339

7.2.4 Stage IV – Late Devonian to Early Mississippian .. 342

7.2.5 Stage V – Mississippian to Early Jurassic 347

7.2.6 Stage VI – Late Cretaceous to Recent 351

7.3 Contributions to original knowledge 352

7.4 Implications and future work 354

CHAPTER 8: REFERENCES 356

APPENDIX I: Core locations 396

APPENDIX II: Formation tops 398

APPENDIX III: Petrographic and geochemical samples 402

APPENDIX IV: Isotope results 411

APPENDIX V: Trace element results 414

APPENDIX VI: Fluid inclusion microthermometry results 419

APPENDIX VII: Fluid inclusion crush-leach results 423

APPENDIX VIII: Laser ablation ICP-MS results 425

APPENDIX IX: Strontium source rock results 427

APPENDIX X: Formation water chemistry 429

APPENDIX XI: List of publications and abstracts 432

LIST OF TABLES

CHAPTER 5:

Table 5.1 Carbon and oxygen stable isotope results by phase 167

Table 5.2 $^{87}Sr/^{86}Sr$ results by phase 181

Table 5.3 Stepwise non-carbonate dissolution procedure 189

Table 5.4 Trace element results by phase from neutron activation analysis 194

Table 5.5 Fluid inclusion microthermometry results by phase 207

Table 5.6 Fluid inclusion microthermometry and concentrations of the solutes in the fluid inclusion fluids 230

Table 5.7 Rare Earth Element results by phase from neutron activation analysis 236

Table 5.8 Vitrinite reflectance values from the Clarke Lake area 248

CHAPTER 6:

Table 6.1 Chemical composition of seawater 295

Table 6.2 Partial pressure and saturation index of carbon dioxide 316

Table 6.3 Formation fluid-mineral equilibria 317

CHAPTER 7:

Table 7.1 Diagenetic fluid stages in the Middle Devonian Slave Point Formation at Clarke Lake 335

Table 7.2 Hydrothermal alteration petrographic and geochemical characteristics in the Slave Point Formation 344

LIST OF FIGURES

CHAPTER 1:

Figure 1.1 Location map of the Clarke Lake study area 2

Figure 1.2 Middle Devonian paleogeographic reconstruction of the Euramerica continent 4

Figure 1.3 Paleogeographic reconstruction of the Middle to Late Devonian Beaverhill Lake Group 6

Figure 1.4 Regional tectonic map of the Canadian Cordillera 7

Figure 1.5 Major structural elements of the Western Canada Sedimentary Basin during the Late Devonian 9

Figure 1.6 Cross-section A-A' showing the present-day structural style of the northern Rocky Mountains 12

Figure 1.7 Tectonic domains for the basement of the Western Canada Sedimentary Basin 13

Figure 1.8 Cross-section B-B" showing the interpreted present-day Cordilleran-North American craton transition 15

Figure 1.9 Magnetic intensity map of northeastern British Columbia 16

Figure 1.10 Distribution of the integral geothermal gradient in the Western Canada Sedimentary Basin 17

CHAPTER 2:

Figure 2.1 Stratigraphic column for the Middle and Upper Devonian of northeastern British Columbia 23

Figure 2.2 Cross-section C-C' demonstrating the regional Devonian stratigraphy of northeastern British Columbia 25

Figure 2.3 Middle to Late Devonian sea-level curve 27

Figure 2.4 Typical wireline log signals 35

Figure 2.5 Map of cross-section lines D-D' through G-G' 37

Figure 2.6 Cross-section D-D' 38

Figure 2.7 Cross-section E-E' 40

Figure 2.8 Cross-section F-F' 42

Figure 2.9 Cross-section G-G' 44

CHAPTER 3:

Figure 3.1 Core locations and abbreviations 47

Figure 3.2 Carbonate classification 48

Figure 3.3 Facies model for Middle to Late Devonian reef carbonates ... 50

Figure 3.4 Schematic representation of the facies distribution in the Middle Devonian Slave Point Formation 74

CHAPTER 4:

Figure 4.1 Paragenetic sequence for the Middle Devonian Slave Point Formation at Clarke Lake 79

Figure 4.2 Dolomite textural classification 94

Figure 4.3 Schematic representation of dolomitization and subsequent hydrothermal alteration 111

Figure 4.4 Crossplot of permeability versus porosity according to facies for limestone and dolostone 130

Figure 4.5 Map of the spatial distribution of pervasive dolomite with cross-section lines H-H' and I-I' 148

Figure 4.6 Cross-section H-H' showing the stratigraphic and structural nature of dolomite distribution 149

Figure 4.7 Cross-section I-I' showing the stratigraphic and structural nature of dolomite distribution 150

CHAPTER 5:

Figure 5.1 Crossplots of carbon and oxygen stable isotope results 169

Figure 5.2 Plot of equilibrium isotope fractionation between dolomite and Middle Devonian seawater 175

Figure 5.3 Plot of equilibrium isotope fractionation between dolomite and meteoric water 176

Figure 5.4 Plot of equilibrium isotope fractionation between dolomite and highly evaporated Middle Devonian seawater 178

Figure 5.5 ^{87}Sr/^{86}Sr results from carbonate phases in the Slave Point Formation 183

Figure 5.6 Secular variation of marine carbonate $^{87}Sr/^{86}Sr$ during the Phanerozoic 184

Figure 5.7 Spatial distribution of $^{87}Sr/^{86}Sr$ values from saddle dolomite samples in the Clarke Lake field 185

Figure 5.8 Crossplot of $^{87}Sr/^{86}Sr$ versus $\delta^{18}O$ from all carbonate phases in the Slave Point Formation 190

Figure 5.9 Laser ablation ICP-MS strontium isotope results 191

Figure 5.10 Crossplots of trace element concentration for matrix and saddle dolomites 197

Figure 5.11 Crossplot of Fe and Mn concentration for matrix and saddle dolomites 201

Figure 5.12 Electron microprobe trace element results 204

Figure 5.13 Crossplot of fluid inclusion microthermometry results from matrix and saddle dolomites 215

Figure 5.14 Crossplot of fluid inclusion microthermometry results from non-dolomite mineral phases 217

Figure 5.15 Calculated dolomite-forming fluid compositions using equilibrium isotope fractionation 220

Figure 5.16 Fluid inclusion electrolyte chemistry 226

Figure 5.17 Crossplot of $^{87}Sr/^{86}Sr$ and Cl/Br results from dolomites and calcite cements 228

Figure 5.18 Crossplot of Cl and Br concentrations from fluid inclusions 231

Figure 5.19 Crossplots of absolute concentrations of fluid inclusion fluids 234

Figure 5.20 Crossplot of K and Al concentrations for all analyzed calcite and dolomite phases 238

Figure 5.21 Rare earth element plots for calcite components 239

Figure 5.22 Rare earth element plots for matrix dolomites 241

Figure 5.23 Rare earth element plots for saddle dolomites 242

Figure 5.24 Rare earth element patterns as a result of hydrothermal alteration of the Slave Point Formation 245

Figure 5.25 Fluid inclusion homogenization temperatures versus mean random vitrinite reflectance 249

Figure 5.26 Burial and thermal history of the Slave Point Formation 250

Figure 5.27 Calculated geothermal gradient in the Slave Point Formation 252

Figure 5.28 Pressure-Temperature plot showing the cooling path of an imaginary fluid inclusion 253

Figure 5.29 Pressure-Temperature plot showing the modelled fluid inclusion isochores 254

Figure 5.30 Tectonics and metallogeny during the Devonian-Mississippian 258

Figure 5.31 2D seismic line across the Slave Point platform margin 260

Figure 5.32 Summary of current dolomitization models 265

Figure 5.33 Hydrological interpretation of dolomite formation at Clarke Lake 267

CHAPTER 6:

Figure 6.1 Paleogeography of the Middle to Late Devonian Beaverhill Lake Group 270

Figure 6.2 General lithology and hydrostratigraphy of the Paleozoic succession of northeastern British Columbia 271

Figure 6.3 Distributions of hydraulic head and formation water salinity in the Beaverhill Lake aquifer 274

Figure 6.4 Stable isotope composition of formation waters from the Slave Point Formation 279

Figure 6.5 Plot of equilibrium isotope fractionation between carbonates and Clarke Lake formation waters 286

Figure 6.6 Crossplot of formation water ^{87}Sr/^{86}Sr versus Sr concentration 288

Figure 6.7 Distribution of ^{87}Sr/^{86}Sr values in formations waters 290

Figure 6.8 Crossplots of the isotopic composition of formation waters in the Slave Point Formation 293

Figure 6.9 Crossplot of Cl and Br concentrations 296

Figure 6.10 Crossplots of the Na and K versus Br results 301

Figure 6.11 Ratio crossplots of formation waters 305

Figure 6.12 Crossplots of the Mg and Ca versus Br results 308

Figure 6.13 Crossplots of Ca and Mg in formation waters 310

Figure 6.14 Crossplot of Ca excess versus Na deficit 313

Figure 6.15 Dolomite stability calculated from formation fluid-mineral equilibria 319

Figure 6.16 Equilibrium activity diagrams illustrating the effects of water-rock interaction on formation fluids 322

Figure 6.17 Cross-section A-A' showing the regional strontium source rock distribution in northeastern British Columbia 327

Figure 6.18 Schematic showing the present-day fluid flow in the Slave Point Formation at Clarke Lake 329

CHAPTER 7:

Figure 7.1 Paragenetic sequence showing diagenetic fluid stages and porosity evolution 334

Figure 7.2 Schematic showing the evolution of fluid flow patterns from the Devonian to the present 337

Figure 7.3 Slave Point hydrothermal alteration 'model' 346

LIST OF PLATES

CHAPTER 3:

Plate 3.1 Facies zones If to IIIf 56

Plate 3.2 Facies zone IVf 59

Plate 3.3 Facies zone IV/V 62

Plate 3.4 Facies zone V 64

Plate 3.5 Facies zone IVb 66

Plate 3.6 Facies zones IIIb to Ib 69

Plate 3.7 Patch reef facies 72

CHAPTER 4:

Plate 4.1 Near-surface I 83

Plate 4.2 Near-surface II 85

Plate 4.3 Shallow burial I 88

Plate 4.4 Shallow burial II 90

Plate 4.5 Shallow burial III 93

Plate 4.6 Intermediate burial I 96

Plate 4.7 Intermediate burial II 99

Plate 4.8 Intermediate burial III 101

Plate 4.9 Intermediate burial IV 103

Plate 4.10 Intermediate burial V 106

Plate 4.11 Intermediate burial VI 108

Plate 4.12 Intermediate burial VII 115

Plate 4.13 Deep burial I 117

Plate 4.14 Deep burial II 119

Plate 4.15 Deep burial III 122

Plate 4.16 Deep burial IV 125

Plate 4.17 Deep burial V 127

Plate 4.18 Facies control I 133
Plate 4.19 Facies control II 136
Plate 4.20 Facies control III 139
Plate 4.21 Facies control IV 142
Plate 4.22 Facies control V 146

CHAPTER 5:

Plate 5.1 Fluid inclusions 212

CHAPTER 1

GENERAL INTRODUCTION

1.1 Rationale

The Devonian system in western Canada is best known for the occurrence of extensive carbonate platforms, banks, and reefs. These carbonates have been the subject of extensive research and debate over the last 60 years because they contain vast quantities of hydrocarbons, hence, are of obvious economic importance. The Devonian carbonate system accounts for approximately sixty per cent of recoverable conventional crude oil and one-quarter of conventional gas reserves in western Canada (Reinson et al., 1993). Additionally, the Devonian in western Canada is host to giant unconventional, i.e., heavy oil and bitumen, petroleum reserves (Hay, 1994), and world-class base metal sulphide deposits. Furthermore, many of the subsurface Devonian reservoir carbonates are conveniently exposed in the Main and Front Ranges of the Rocky Mountains, aiding in the development of regional-scale outcrop to reservoir diagenetic models. As a result, the carbonates of the Devonian of western Canada have become a 'natural laboratory' for understanding the conditions and mechanisms of dolomite formation elsewhere (e.g., Machel and Mountjoy, 1986).

The Middle Devonian Slave Point Formation of northeastern British Columbia, Canada, hosts intervals of dolostone on the order of hundreds of metres that were encountered in subsurface drill cores. These rocks were selected from a location called Clarke Lake, to serve as a case study to investigate the origin and formation of dolomite for the following reasons:

(1) The Slave Point Formation at Clarke Lake has petrographic characteristics that are dissimilar from most pervasive dolomite reservoirs in the Devonian of western Canada, in that, it contains large volumes of coarse-crystalline saddle dolomite (Amthor et al., 1993; Mountjoy and Amthor, 1994; Machel et al., 1996; Wendte et al., 1998; Mountjoy et al., 1999; Machel, 2004).

(2) The Slave Point Formation has been extensively drilled in the study area (Figure 1.1), providing the opportunity to investigate in detail the spatial relationships between depositional facies, tectonic structures, and dolomite formation at a field-scale level, which can then be compared to previously published reservoir studies

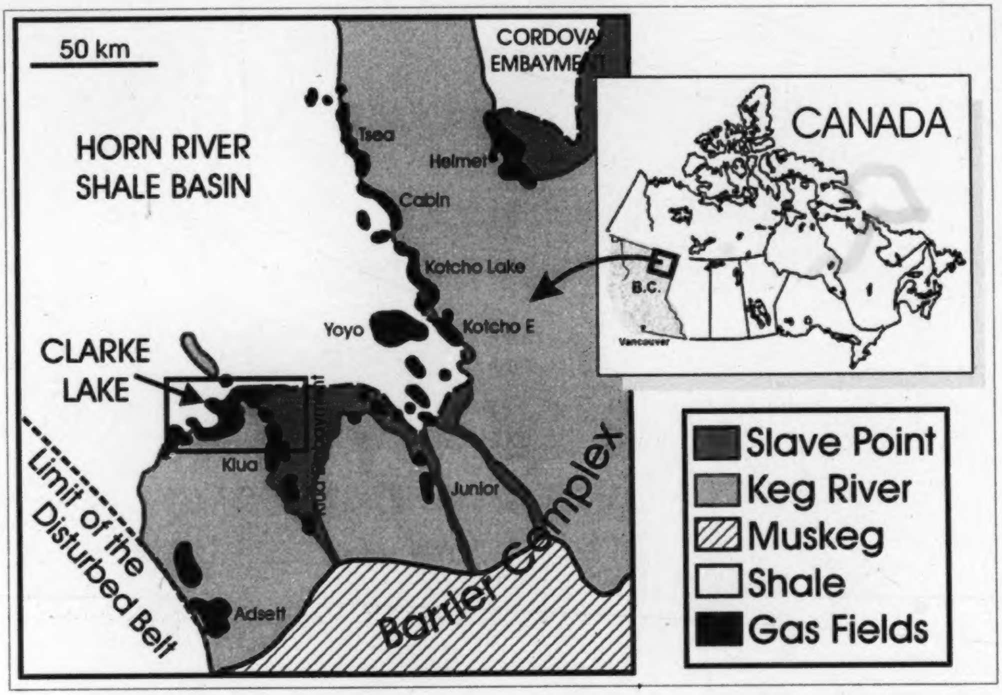
50 km
CORDOVA EMBAYMENT
HORN RIVER SHALE BASIN
Tsea
Helmet
Cabin
Kotcho Lake
Kotcho E
Yoyo
CLARKE LAKE
Klua
Junior
Adsett
Limit of the Disturbed Belt
Barrier Complex
CANADA
B.C.
Vancouver
Slave Point
Keg River
Muskeg
Shale
Gas Fields

Figure 1.1 Location map of the Clarke Lake study area in relation to the distribution of Middle Devonian units in the northern part of the Western Canada Sedimentary Basin. The box represents the area shown in greater detail in Figure 2.5. Modified after Reimer and Tearc (1992).

on a regional-scale (Morrow et al., 1986; 1990; Qing and Mountjoy, 1992; 1994a; 1994b; 1994c; Morrow and Aulstead, 1995). Available materials include original core descriptions (Davies, 1999), complete geophysical log data, and extensive seismic surveys.

(3) The Slave Point Formation, specifically its dolomitization, has not been studied with modern, sophisticated methods in northeastern British Columbia. As a result, the cause and manner of dolomite formation are poorly known and highly speculative, and no reliable models exist that may be used to improve exploration success.

1.2 Study area

The area of interest is the Clarke Lake gas field of northeastern British Columbia. This field is located roughly 15 kilometres south of the town of Fort Nelson, approximately 1000 km north of the city of Vancouver, British Columbia (Figure 1.1). The study area encompasses all of National Topographic Series (NTS) map sheets 94J/9 and 10, as well as the southern third of sheets 94J/15 and 16. In this area, the top of the Slave Point Formation is currently at depths of around 2000 metres, and dips gently to the southwest towards the Rocky Mountain disturbed belt, approximately 50 km away.

Discovered in the winter of 1957 (Gray and Kassube, 1963), Clarke Lake has produced in excess of 1.6 Tcf of sweet gas. It is therefore one of the largest Devonian gas fields discovered in western Canada. Discovery of the Clarke Lake gas field led to further exploration in northeastern British Columbia during the late 1950's and 1960's. Today, the majority of the producing fields in this region are located along the perimeter of the Middle Devonian Presqu'ile Barrier (Figure 1.1; 'Barrier Complex'). Production in these fields is from dolostones in the Middle Devonian Slave Point and Keg River formations. Relatively recent figures suggest that the Presqu'ile Barrier is host to natural gas reserves of 124 843 x 10^6 m^3 (4.4 Tcf) (Reinson et al., 1993).

The largest gas pool in the Clarke Lake field is the Slave Point A. Cumulative gas production from this pool to date totals 1.40 Tcf with estimates of 2.21 Tcf original gas in-place (OGIP). Smaller pools within the Clarke Lake Slave Point have reserve estimates of less than 50 Bcf. Within the Klua field at the southern end of the study area (Figure 1.1), the Slave Point B, D, and E pools have produced approximately 62 Bcf of dry gas to date from total reserve estimates of greater than 200 Bcf. All other Slave Point pools, including those at Hoffard to the east and Milo to the west, have limited production capabilities, with individual reserve estimates of <80 Bcf OGIP. According to Reinson et al. (1993), remaining probable potential in-place volume for all Slave Point pools located along the Presqu'ile Barrier is 1.15 Tcf, with the largest undiscovered pool measuring approximately 40 Bcf. To put this in perspective, the Clarke Lake Slave Point A pool contains the equivalent of approximately 367 million barrels of oil equivalent (MMboe), which approaches the cut-off for classification as a giant oil field (i.e., 500 MMboe), while the largest undiscovered pool would contain approximately 6.7 MMboe. In terms of volume of initial gas in-place, the Clarke Lake field is the largest producer from the Beaverhill Lake Group, however, these volumes pale in comparison to the largest carbonate-hosted oil field in Canada, the Devonian (Beaverhill Lake) Swan Hills field that contains initial in-place volumes of 2.4 billion barrels (Bbbl) (Viau, 1988).

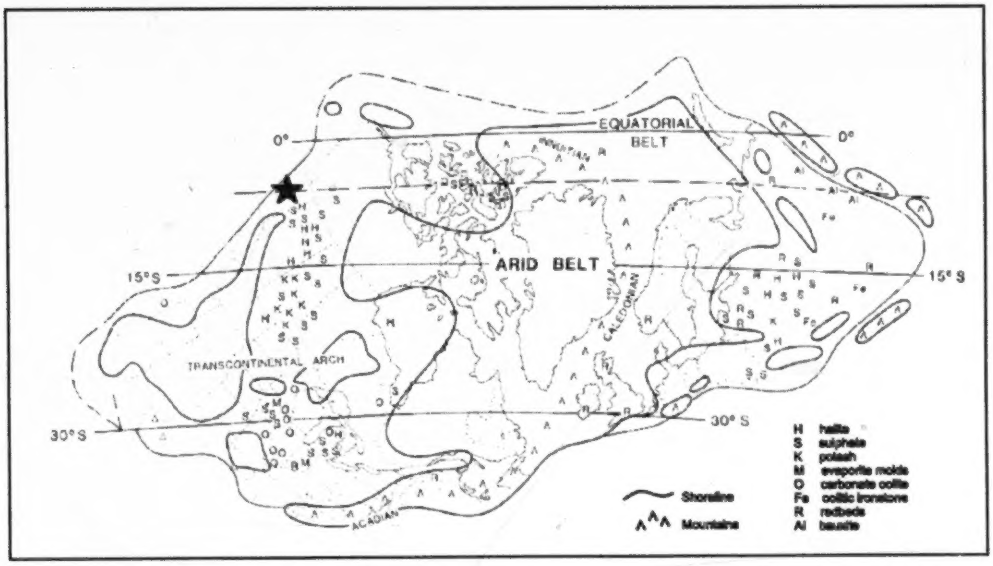
EQUATORIAL BELT
0°
0°
ARID BELT
15° S
15° S
30° S
30° S
TRANSCONTINENTAL ARCH
CALEDONIAN
ACADIAN
Shoreline
Mountains
H halite
S sulphate
K potash
M evaporite molds
O carbonate oolite
Fe oolitic ironstone
R redbeds
Al bauxite

Figure 1.2 Middle Devonian paleogeographic reconstruction of the Euramerica continent. The approximate location of the Clarke Lake field is represented by the black star. Modified after Witzke and Heckel (1988).

1.3 Geologic Framework

1.3.1 Paleogeography

During the Middle Devonian, the Clarke Lake area was situated along the western margin of the Euramerica (Laurussia) continent (Figure 1.2). The Euramerica continent was formed during the Late Silurian when the North American-Greenland and the European cratons collided (Ziegler, 1988). The Caledonian Fold Belt represents the suture between the two continents. Based on paleogeographic reconstructions by Witzke and Heckel (1988), northeastern British Columbia was located approximately 5° south of the paleoequator, in what would be considered the present-day humid climate belt (Figure 1.2). Therefore, the climate during the Middle Devonian was much warmer than today. Also, a shallow epicontinental sea covered much of western Canada during this period. These conditions led to the development of extensive Middle Devonian evaporite deposits, including halite, potash, and gypsum, in the arid belt farther to the south in Alberta and Saskatchewan (Figure 1.2 – H, K, S).

During the late Middle Devonian, the epicontinental seas expanded and a transcontinental seaway breached through ancestral North America, connecting present-day Saskatchewan (Williston Basin) with the northern United States. Northeastern British

Columbia and Alberta were still located within a belt favorable to carbonate deposition. During this time, thick shallow water carbonates of the Keg River Formation (Elk Point Group) were deposited, forming an east-west barrier to open-marine circulation, now called the Presqu'ile Barrier or Barrier Complex (Figure 1.1). This barrier restricted seawater circulation, resulting in extensive evaporite formation in present-day central and eastern Alberta preserved as the Prairie and Muskeg formations. During the late Givetian to early Frasnian, the Euramerica continent moved farther north, placing Alberta and British Columbia closer to the equator, and subsequently moving the evaporite depocentre farther to the south and east into present-day Saskatchewan and the northern United States. Also during this period, relative sea-level rose across western Canada, terminating much of the reef growth along the Presqu'ile Barrier, and thick shallow water carbonates of the Beaverhill Lake Group were deposited (Figure 1.3). Across northeastern British Columbia, these carbonates belong to the Slave Point Formation, and include small, laterally discontinuous, patch reefs that developed along structural highs coincident with the underlying Elk Point Presqu'ile Barrier bank margin. Farther to the south, in western and central Alberta, reefal and bank carbonates of the Swan Hills Formation were deposited (Figure 1.3). Meanwhile, deeper sections of the basin were filled with argillaceous carbonates of the Waterways Formation (Figure 1.3). Yet farther south, shallow marine to intertidal carbonates and evaporites of the Souris River Formation were deposited in present-day Saskatchewan (Figure 1.3). To the north of the Middle Devonian barrier complex, deep marine shales of the Horn River Group were deposited, with the main clastic input being the exposed Canadian Shield to the north and northeast (Figure 1.3). As Euramerica moved farther to the north during the Late Devonian, evaporite deposition shifted south and east from today's central Alberta to Saskatchewan, Montana and North Dakota. In addition to relative plate motion, continued marine transgression during deposition of the Late Devonian Woodbend and Winterburn groups pushed reef formation farther south and east into central Alberta, while much of northeastern British Columbia was covered with a thick package of shale, i.e., Muskwa and Fort Simpson formations.

1.3.2 Structure

The Western Canada Sedimentary Basin (Figure 1.4) is the name given to the southwesterly thickening wedge of sedimentary units that originate from a zero-edge

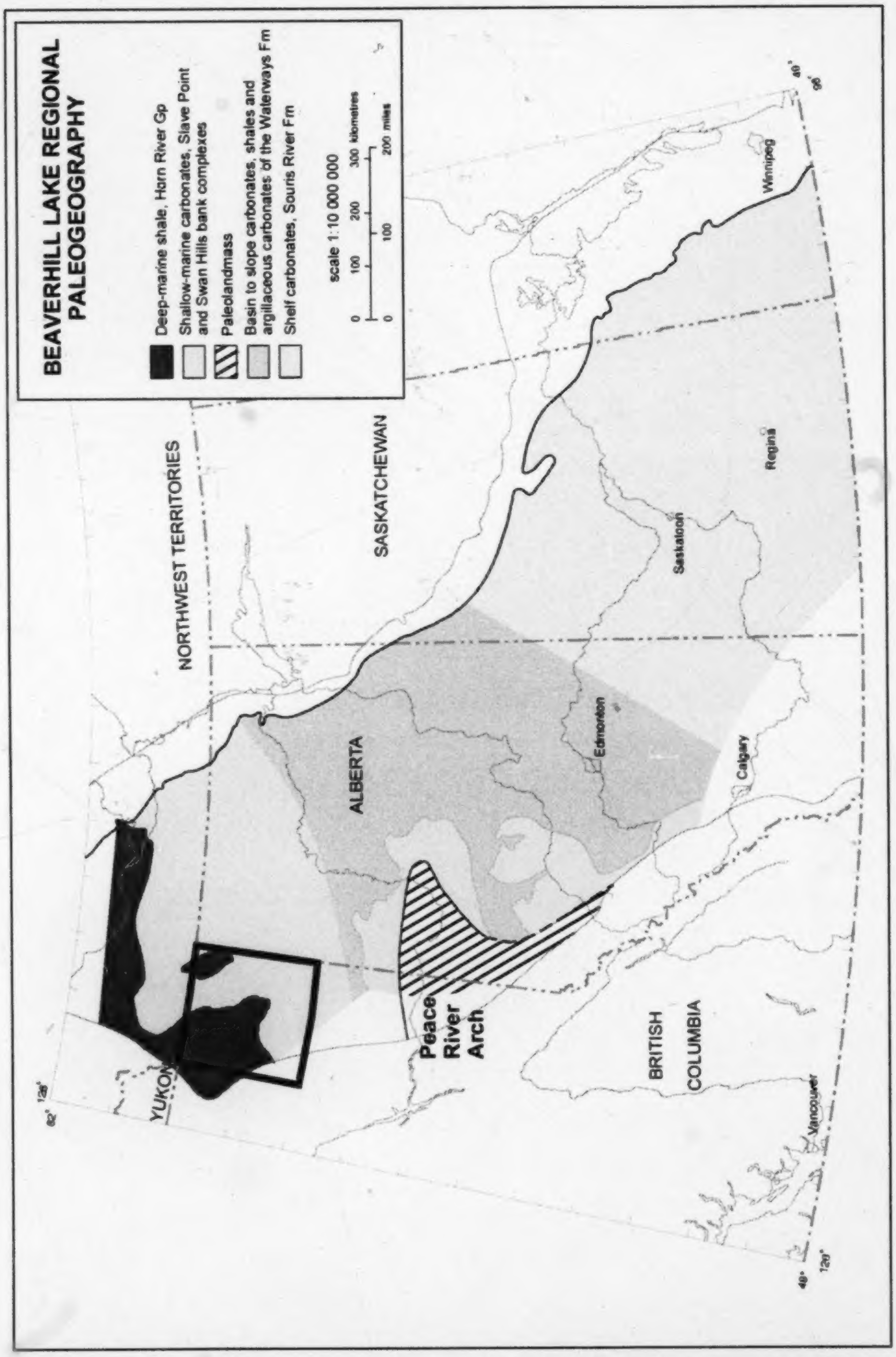
BEAVERHILL LAKE REGIONAL PALEOGEOGRAPHY
■ Deep-marine shale, Horn River Gp
☐ Shallow-marine carbonates, Slave Point and Swan Hills bank complexes
▨ Paleolandmass
▨ Basin to slope carbonates, shales and argillaceous carbonates of the Waterways Fm
☐ Shelf carbonates, Souris River Fm
scale 1:10 000 000
0 100 200 300 kilometres
0 100 200 miles
NORTHWEST TERRITORIES
SASKATCHEWAN
ALBERTA
BRITISH COLUMBIA
YUKON
Peace River Arch
Edmonton
Calgary
Saskatoon
Regina
Winnipeg
Vancouver
60°
128°
49°
120°
96°

Figure 1.3 Paleogeographic reconstruction of the Middle to Late Devonian (late Givetian-early Frasnian) Beaverhill Lake Group of the Western Canada Sedimentary Basin. The box outlines the area shown in Figure 1.1. Modified after Oldale and Munday (1994).

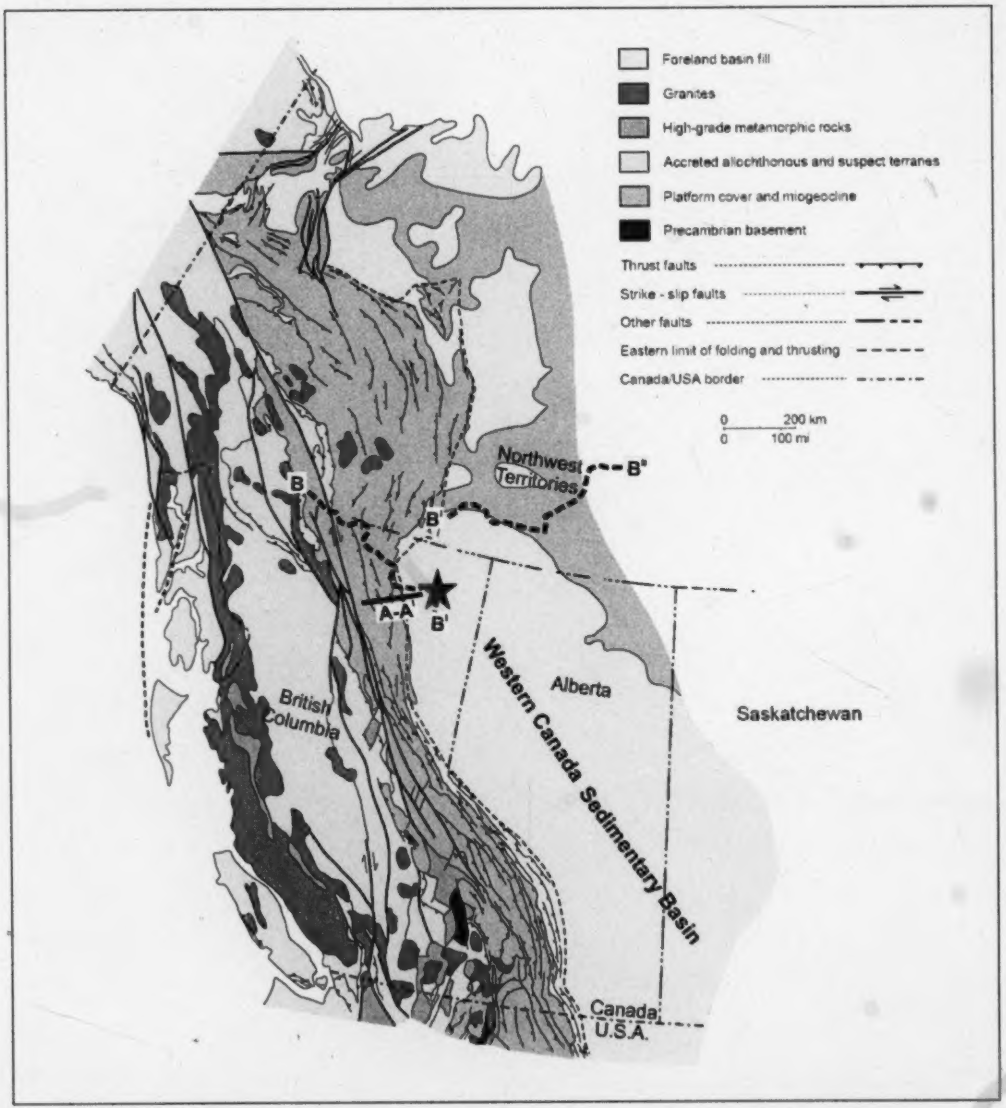
Foreland basin fill
Granites
High-grade metamorphic rocks
Accreted allochthonous and suspect terranes
Platform cover and miogeocline
Precambrian basement
Thrust faults
Strike - slip faults
Other faults
Eastern limit of folding and thrusting
Canada/USA border
0
200 km
0
100 mi
Northwest Territories
B"
B
B'
A-A'
B'
British Columbia
Alberta
Saskatchewan
Western Canada Sedimentary Basin
Canada
U.S.A.

Figure 1.4 Regional tectonic map of the Canadian Cordillera showing locations of structure sections A-A' and B-B" in Figures 1.6 and 1.8. The location of the Clarke Lake field is represented by the black star. Modified after Price (1994).

along the exposed margin of the Canadian Shield, i.e., Precambrian crystalline rocks, in Manitoba and Saskatchewan to a thickness of greater than 6 kilometres near the Cordilleran foreland thrust belt (Ricketts, 1989). The limits of the Western Canada Sedimentary Basin originally extended much farther than at present prior to the effects of either erosion or tectonic deformation. Today, the Tathlina High (Figure 1.5), in the southern reaches of the Northwest Territories, delimits the Western Canada Sedimentary Basin to the north, while the southern boundary extends into the northern United States, i.e., South Dakota and Montana. The western limit of the Western Canada Sedimentary Basin is defined today by exposed, deformed sediments that are coincident with the eastern limit of allochthonous terranes in British Columbia, usually located near the boundary between the Omineca and the Intermontane belts of the Cordillera (Figure 1.4 – platform cover and miogeocline) (Wright et al., 1994).

The Western Canada Sedimentary Basin is commonly subdivided into two sub-basins: the Alberta Basin, a northwest-trending trough in front of the Cordilleran fold and thrust belt; and, the Williston Basin, an intracratonic basin that is centred in North Dakota and extends into southeastern Saskatchewan and southwestern Manitoba. These two sub-basins of the Western Canada Sedimentary Basin are separated by a broad northeast-trending positive element, the Bow Island Arch (Figure 1.5). Other major geological elements that directly or indirectly influenced the deposition of Middle to Late Devonian carbonates include: the Rimbey Arc; the Peace River - Athabasca Arch; the West Alberta Ridge; the Tathlina High; the Fort Nelson Uplift; and the Meadow Lake Escarpment (Figure 1.5) (Switzer et al., 1994). All of these elements were topographic highs that restricted Devonian marine incursion to the west (Burrowes and Krouse, 1987), and most likely controlled the location of several Devonian carbonate buildups (Mountjoy, 1980; Moore, 1988). These carbonate buildups, in turn, controlled the deposition of the clastic basin-fill units.

The Peace River Arch, a positive Precambrian granitic basement landmass, was especially significant for the study area and surrounding region because it influenced subsidence and sedimentation patterns during the Devonian (Figures 1.5). The Peace River Arch originated in the early Paleozoic as an uplift over an incipient rift that extended from the western edge of the passive continental margin (Cant, 1988). During the Middle Devonian, crustal tension created fault-bounded horsts and grabens that were subsequently the centres for the development of reef carbonates (O'Connell et al., 1990). During

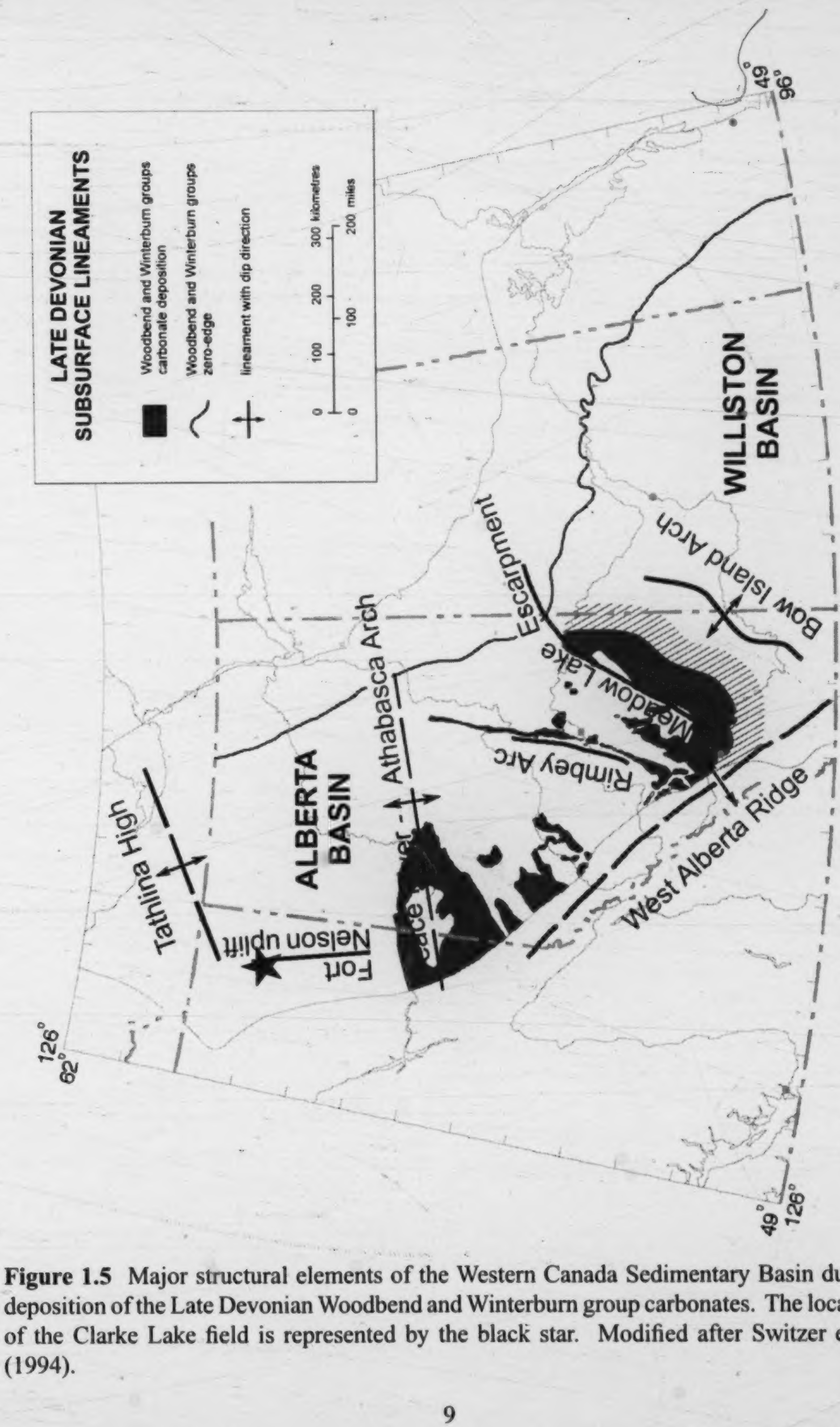
LATE DEVONIAN SUBSURFACE LINEAMENTS
Woodbend and Winterburn groups carbonate deposition
Woodbend and Winterburn groups zero-edge
lineament with dip direction
0 100 200 300 kilometres
0 100 200 miles
49° 96°
126° 62°
49° 126°
Tathlina High
Fort Nelson uplift
ALBERTA BASIN
ace
er - Athabasca Arch
Rimbey Arc
Meadow Lake Escarpment
West Alberta Ridge
Bow Island Arch
WILLISTON BASIN

Figure 1.5 Major structural elements of the Western Canada Sedimentary Basin during deposition of the Late Devonian Woodbend and Winterburn group carbonates. The location of the Clarke Lake field is represented by the black star. Modified after Switzer et al. (1994).

deposition of the Slave Point Formation, the Peace River Arch was a structural high, while the surrounding basin was subsiding slowly (Keith, 1990). The Peace River Arch then subsided and eventually disappeared as a topographic feature in the Mississippian, when it was covered by marine sediments just like the surrounding area (Burrowes and Krouse, 1987).

The West Alberta Ridge (Figures 1.5), another positive structure that consists primarily of eroded lower Paleozoic sequences, was mostly covered by the end of the Middle Devonian, but it still had an effect on Late Devonian carbonate deposition, although at a diminished level (Switzer et al., 1994).

The Tathlina High, located in the Northwest Territories, is comprised of Precambrian granite (Figure 1.5). This positive structural feature was completely buried by the end of the Middle Devonian Elk Point Group. However, this feature continued to influence Late Devonian carbonate deposition in the area. The Tathlina High, and similarly, the Fort Nelson uplift, remained submarine topographic highs against which basin-fill shales downlapped and thinned (Switzer et al., 1994).

The Meadow Lake escarpment, located northeast of the Bow Island Arch, is a major pre-Devonian erosional and structural feature (Figure 1.5). It is well known for its effect on mid-Devonian sedimentation, and also appears to have influenced many of the depositional changes in Upper Devonian strata (Switzer et al., 1994). These effects include a control on the position of both the southern bank edge of Beaverhill Lake Group and the Leduc shelf edge in southern Alberta (Switzer et al., 1994).

The structural development of the Western Canada Sedimentary Basin during the Phanerozoic is closely related to the tectonic evolution of the Canadian Cordillera. The development of the basin was governed by several tectonic phases. These include, but are not limited to: a rift and passive margin phase during the Precambrian and Cambrian; an extensional phase during the Late Devonian – Mississippian; and, foreland basin phases during both the Jurassic to Early Cretaceous and Late Cretaceous to Paleocene. The latter phases significantly influenced the size, depth, accommodation space, subsidence, and uplift of the Western Canada Sedimentary Basin.

The tectonic history outboard from the proto-Pacific margin during the middle and late Paleozoic was complex and may have involved compressional as well as extensional events (Richards, 1989). Within the Western Canada Sedimentary Basin, extension dominated, as evidenced by widespread block faulting in the Peace River Embayment and Liard Basin areas to the north.

Compressive regimes were initiated during the Middle Jurassic through the Eocene. In general, the lithological character of the deformed stratigraphic sequences largely controlled the structural style of the resulting fold and thrust belt. South of the Peace River Arch, thick, competent carbonate and/or sandstone successions favoured the development of thick thrust sheets. Meanwhile, north of the Peace River Arch, less competent interlayered shale and sandstone, or shale and carbonate successions, favoured the formation of folds. As a result, large-amplitude box and chevron folds in upper Paleozoic and Mesozoic strata characterize the foothills in northeastern British Columbia (Figure 1.6). These folds formed above a regional detachment within the Upper Devonian and Mississippian shale succession, while carbonates of Middle Devonian age and older remained essentially undeformed (Wright et al., 1994). For distances up to 200 km east of the foothills belt, included within the position of the present-day Clarke Lake field, low-amplitude folds developed in upper Paleozoic to Lower Cretaceous strata beneath nearly flat-lying Upper Cretaceous sandstone and shale (Wright et al., 1994).

1.3.3 Basement architecture and heat flow

The Precambrian crystalline basement of the Western Canada Sedimentary Basin is extremely complex, including as many as twenty domains of distinct age or mineralogy (Figure 1.7). The boundaries between the basement domains are based principally on the interpretation of public domain aeromagnetic data; hence, the subdivision of the Precambrian basement is actually a representation of distinct geophysical domains. In addition, distinct basement domains can be recognized through the U-Pb geochronology of basement drill cores (Ross, 1990).

Major aeromagnetic highs in the subsurface are interpreted as magmatic belts that are the extensions of known magmatic rocks from the exposed Canadian Shield. They are Proterozoic magmatic rocks that form the magmatic welds between formerly separate crustal fragments (Hoffman, 1989). The interpretation of regionally extensive aeromagnetic lows can be ambiguous. For example, depending on the ratio of induced to remanent magnetism, even magnetite-bearing rocks can produce a negative aeromagnetic signal (Ross et al., 1994). In some cases, negative aeromagnetic anomalies in the Canadian

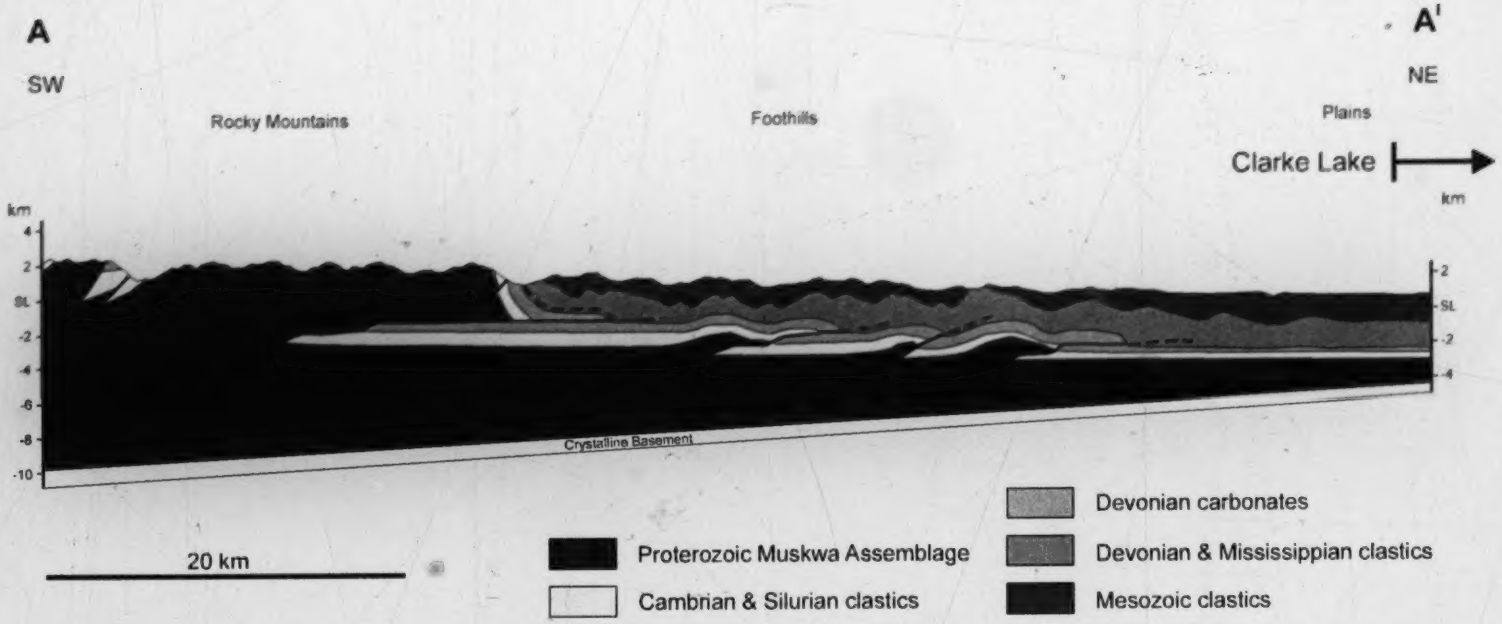
A
SW
A'
NE
Rocky Mountains
Foothills
Plains
Clarke Lake
km
4
2
SL
-2
-4
-6
-8
-10
km
2
SL
-2
-4
Crystalline Basement
20 km
Proterozoic Muskwa Assemblage
Cambrian & Silurian clastics
Devonian carbonates
Devonian & Mississippian clastics
Mesozoic clastics

Figure 1.6 Cross-section A-A' showing the present-day structural style of the northern Rocky Mountains and the deformed belt of the Western Canada Sedimentary Basin. The location of cross-section A-A' is shown on Figure 1.4. The western edge of the Clarke Lake study area is present near the eastern limit of the cross-section. Modified after Gabrielse and Taylor (1982)

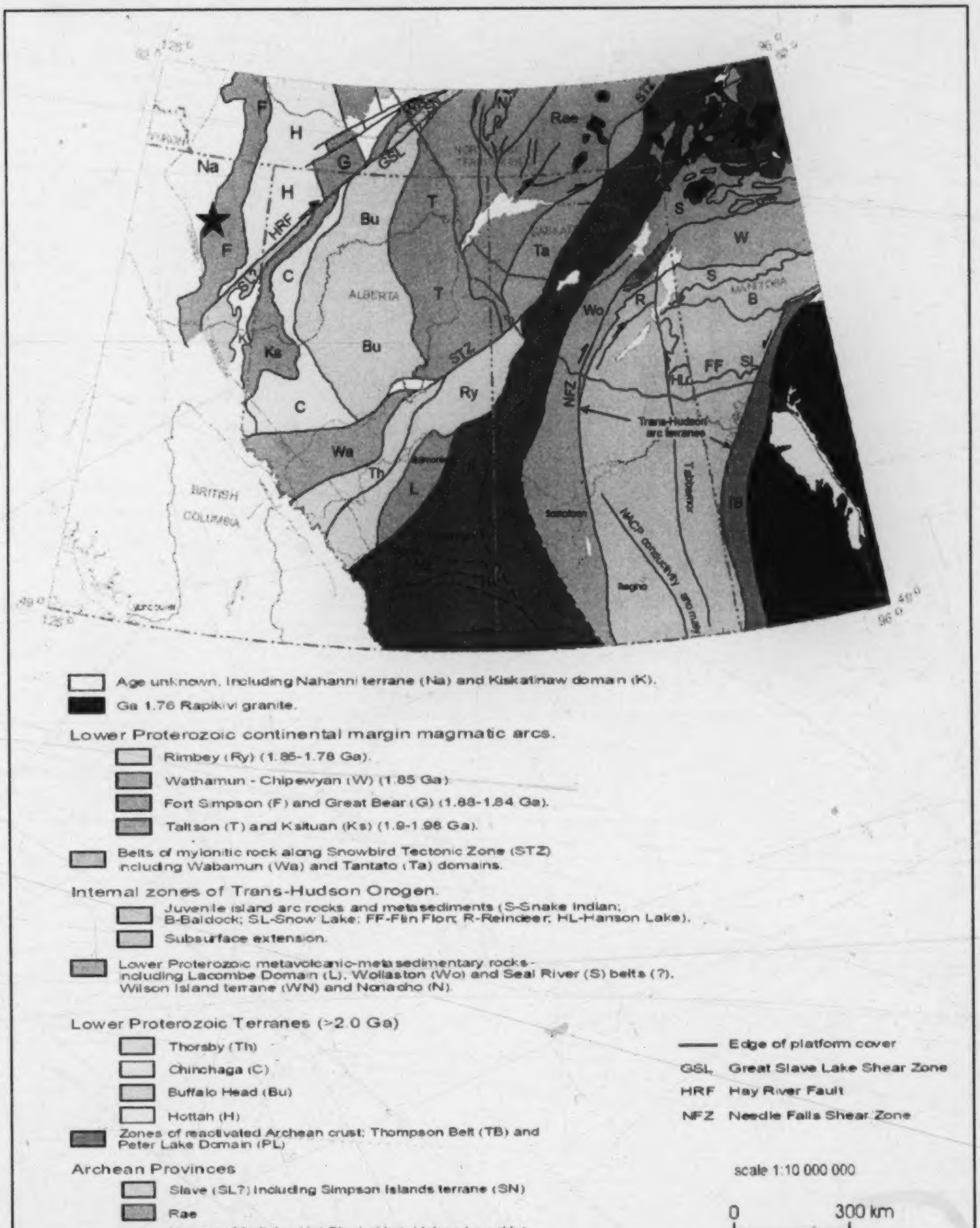
125°
60°
96°
60°
F
H
Na
H
G
GSL
HRF
Bu
T
C
ALBERTA
T
Ks
Bu
STZ
C
Ry
Wa
Th
L
BRITISH COLUMBIA
Rae
STZ
S
W
Ta
S
MANITOBA
B
R
Wo
FF
SL
HL
NFZ
Trans-Hudson arc terranes
Tabbernor
TB
Saskatoon
NACP conductivity anomaly
Regina
49°
125°
49°
96°
Age unknown, including Nahanni terrane (Na) and Kiskatinaw domain (K).
Ga 1.76 Rapikivi granite.
Lower Proterozoic continental margin magmatic arcs.
Rimbey (Ry) (1.85-1.78 Ga).
Wathamun - Chipewyan (W) (1.85 Ga).
Fort Simpson (F) and Great Bear (G) (1.88-1.84 Ga).
Taltson (T) and Ksituan (Ks) (1.9-1.98 Ga).
Belts of mylonitic rock along Snowbird Tectonic Zone (STZ) including Wabamun (Wa) and Tantato (Ta) domains.
Internal zones of Trans-Hudson Orogen.
Juvenile island arc rocks and metasediments (S-Snake Indian; B-Baldock; SL-Snow Lake; FF-Flin Flon; R-Reindeer; HL-Hanson Lake).
Subsurface extension.
Lower Proterozoic metavolcanic-metasedimentary rocks - including Lacombe Domain (L), Wollaston (Wo) and Seal River (S) belts (?), Wilson Island terrane (WN) and Nonacho (N).
Lower Proterozoic Terranes (>2.0 Ga)
Thorsby (Th)
Chinchaga (C)
Buffalo Head (Bu)
Hottah (H)
Zones of reactivated Archean crust: Thompson Belt (TB) and Peter Lake Domain (PL)
Archean Provinces
Slave (SL?) including Simpson Islands terrane (SN)
Rae
Hearne : Medicine Hat Block (Hm); Vulcan Low (Hv); Matzhiwin High (Hz); Eyehill High (He); Loverna Block (Hl); Mudjatik Domain (Hj).
Superior
Edge of platform cover
GSL Great Slave Lake Shear Zone
HRF Hay River Fault
NFZ Needle Falls Shear Zone
scale 1:10 000 000
0 300 km
0 200 mi

Figure 1.7 Tectonic domains for the basement of the Western Canada Sedimentary Basin, based largely on interpretation of potential field data and U-Pb geochronology of selected samples of basement. The location of the Clarke Lake field is represented by the black star. Modified from Hoffman (1989).

Shield correspond to regions underlain by peraluminous plutonic rocks (Ross et al., 1994). Regional metamorphism, which produces phase changes that transform Fe-oxides into Fe-silicates and/or oxidation of magnetite to hematite, may also account for regional aeromagnetic lows (Robinson et al., 1985).

The structure of the basement domains across northeastern British Columbia was examined as part of the national Lithoprobe Slave-Northern Cordillera Lithospheric Evolution (SNorCLE) seismic refraction transect during the summer of 1997. Seismic data from this transect provided the basis for generation of tectonic models for the evolution of the craton-Cordillera transition (Figure 1.8). During the Early Proterozoic, the Fort Simpson and Nahanni domains collided with the ancestral margin of North America, called the Hottah Terrane (Cook et al., 1999). Following this collisional event, the western edge of cratonic North America developed into a west-facing ramped rifted margin that bordered the paleo-Pacific ocean. This ramp margin was overlain by a 10 to 15 km thick package of passive margin Neo-Proterozoic and Paleozoic sediments of the Fort Simpson Basin, i.e., the Muskwa Assemblage. During the Mesosoic compressional events that formed the Cordillera, this passive margin sequence was folded, detached from the basement, and thrust upward onto the edge of ancestral North America to form the present-day Foreland Belt (Gabrielse et al., 1992). Farther to the west, the Omineca Belt was uplifted and metamorphosed during the compressional events that formed the Foreland Belt.

The Clarke Lake field straddles one of the major basement domain boundaries (Figures 1.8 and 1.9). The west side of the field overlies the Nahanni Terrane: characterized by a negative aeromagnetic anomaly, while the east side overlies the Fort Simpson Terrane: a positive aeromagnetic anomaly. This terrane boundary appears to control the geometry of the Slave Point platform margin, and it also defines the sub-orthogonal lineament/fault pattern across much of northeastern British Columbia (Figure 1.9). This has potentially important implications with respect to both deposition and subsequent diagenesis of the Slave Point Formation in the study area. Firstly, these lineaments/faults may have created structural highs during the Middle Devonian; hence, potential loci for carbonate deposition. Secondly, these subsurface lineaments/faults may have been used as conduits for diagenetic fluid flow later on.

The geothermal regime in a sedimentary basin is determined by the magnitude and interaction of various heat sources and transfer mechanisms by which the heat is transported

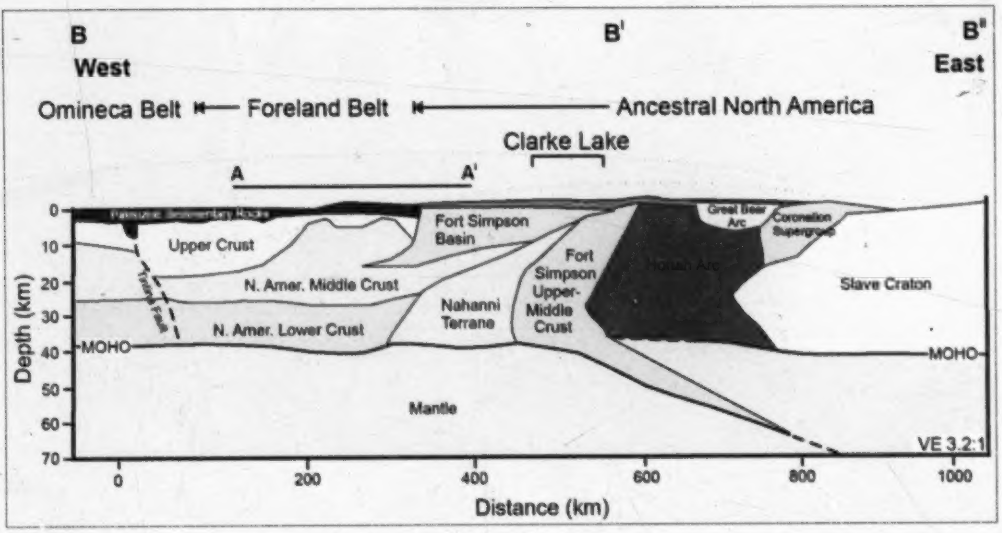
B
West
B'
B"
East
Omineca Belt
Foreland Belt
Ancestral North America
Clarke Lake
A
A'
Paleozoic Sedimentary Rocks
Upper Crust
Fort Simpson Basin
Fort Simpson Upper-Middle Crust
Hottah Arc
Great Bear Arc
Coronation Supergroup
Slave Craton
N. Amer. Middle Crust
N. Amer. Lower Crust
Nahanni Terrane
Tintina Fault
MOHO
MOHO
Mantle
VE 3.2:1
Depth (km)
0
10
20
30
40
50
60
70
0
200
400
600
800
1000
Distance (km)

Figure 1.8 Cross-section B-B" showing the interpreted present-day Cordilleran-North American craton transition. The location of cross-section B-B" is shown on Figure 1.4. The Clarke Lake field straddles the boundary between the Nahanni and Fort Simpson terranes. Cross-section line A-A' represents the rough position of the structural section shown in Figure 1.6. Modified after Welford et al. (2001).

to the surface. The two main sources of heat are that which flows upward from the mantle, and that which is generated internally in the crust by the decay of radioactive isotopes. The main mechanisms of heat transfer are convection by moving fluids, and conduction (Bachu and Burwash, 1994), while the transport of heat can be dominated by conduction or by convection. In a basin dominated by heat conduction, the geothermal regime is controlled basically by the distribution of heat sources and the thermal conductivity of rocks. In a convection-dominated basin, the main controlling factors are the fluxes and the directions of fluid movement.

The main characteristic of the geothermal regime in the Western Canada Sedimentary Basin is a progressive northerly increase in heat flow and geothermal gradient. In the south, i.e., the Williston Basin, the average geothermal gradient is less than 20°C/km (Figure 1.10). In the central part of the Alberta Basin, that is, bounded by the Bow Island Arch in the south and the Peace River Arch to the north, the average geothermal gradient is between 20 and 30°C/km (Figure 1.10). However, in the northern reaches of the Alberta Basin, including the Clarke Lake area, the average geothermal gradient is as high as 45 to 50°C/km (Figure 1.10). The high geothermal gradients in northeast British Columbia, northwest Alberta

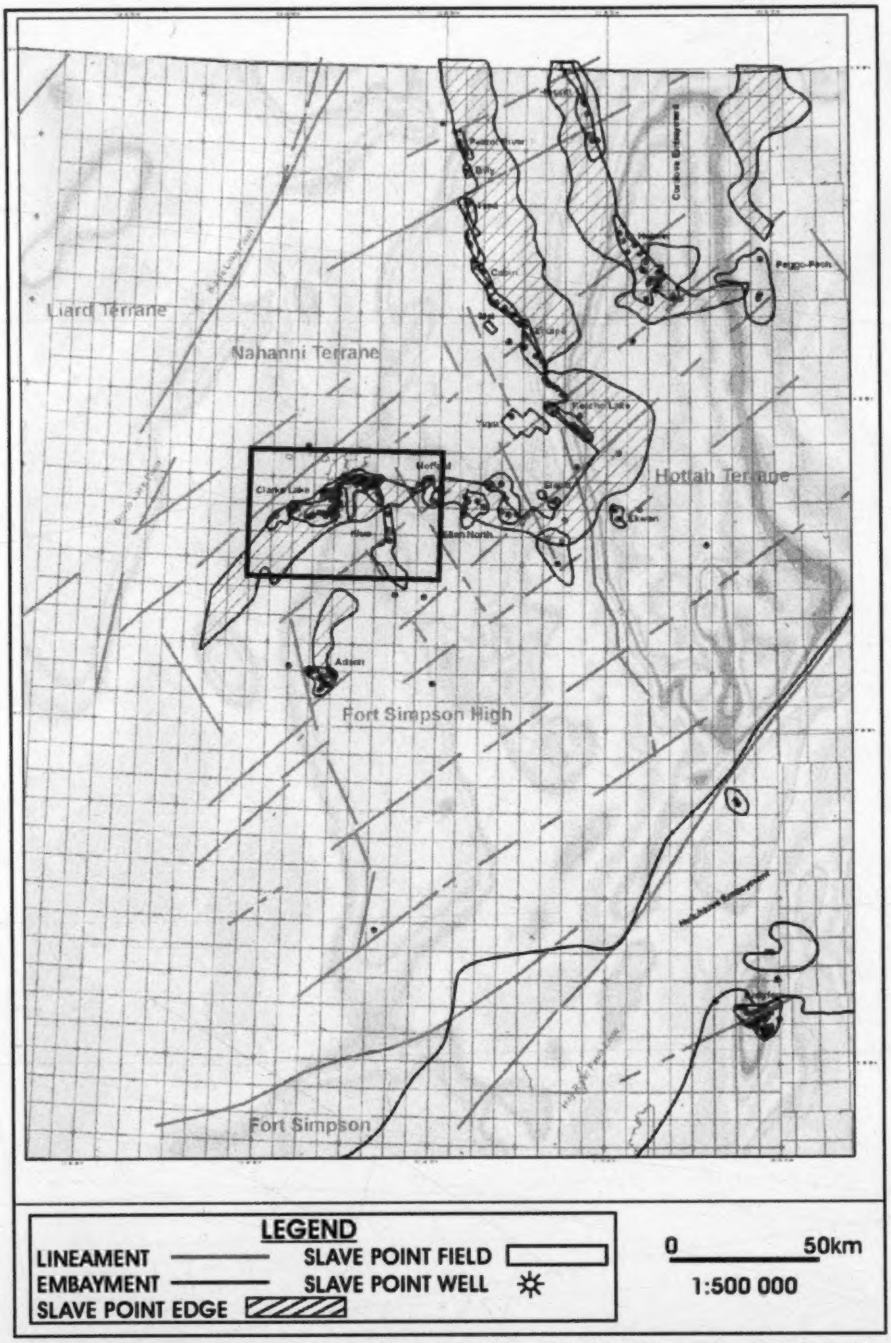
Liard Terrane
Nahanni Terrane
Hottah Terrane
Fort Simpson High
Fort Simpson
Clarke Lake
Adsett
LEGEND
LINEAMENT
EMBAYMENT
SLAVE POINT EDGE
SLAVE POINT FIELD
SLAVE POINT WELL
0
50km
1:500 000

Figure 1.9 Magnetic intensity map of northeastern British Columbia showing the position of major basement terrane boundaries and lineaments. The Clarke Lake study area (black box) straddles the boundary between the Nahanni and Fort Simpson terranes. Total field magnetic intensity of 0 is represented in magenta; 1400 in red. Modified after Petrel Robertson (2003).

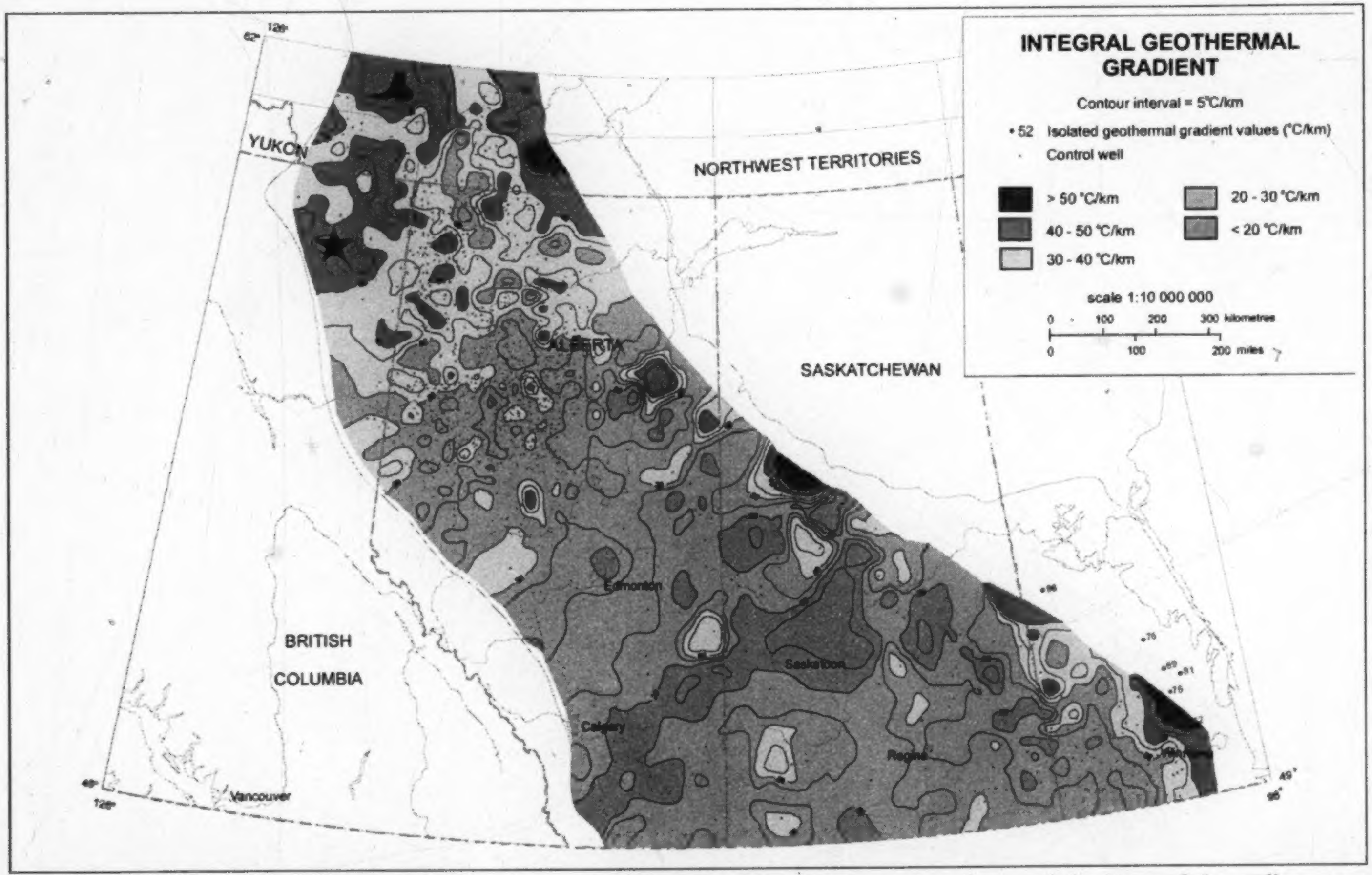
INTEGRAL GEOTHERMAL GRADIENT
Contour interval = 5°C/km
• 52 Isolated geothermal gradient values (°C/km)
· Control well
> 50 °C/km
40 - 50 °C/km
30 - 40 °C/km
20 - 30 °C/km
< 20 °C/km
scale 1:10 000 000
0 100 200 300 kilometres
0 100 200 miles
YUKON
NORTHWEST TERRITORIES
ALBERTA
SASKATCHEWAN
BRITISH COLUMBIA
Edmonton
Saskatoon
Calgary
Regina
Vancouver
62°
128°
49°
128°
49°
96°

Figure 1.10 Distribution of the integral geothermal gradient (between the ground surface and the base of the sedimentary column) in the Western Canada Sedimentary Basin. The location of the Clarke Lake field is represented by the black star. Modified after Bachu and Burwash (1994).

and adjacent Northwest Territories correspond to high radiogenic heat generation in the southern extension of the Great Bear Magmatic Arc (Bachu and Burwash, 1994). The low geothermal gradients in the Williston Basin correspond to low radiogenic heat generation in Archean rocks (Bachu and Burwash, 1994). Small-scale geothermal variations across the Western Canada Sedimentary Basin generally correlate to high radiogenic heat production from basement rocks (Bachu and Burwash, 1994).

1.4 Previous studies

Prior to this study, there was very little published work detailing either the petrographic or geochemical evolution of the Slave Point Formation in northeastern British Columbia, and almost nothing was published from the Clarke Lake field. Nevertheless, the few studies on Clarke Lake and those on the Slave Point Formation provide some constraints for the present study.

Gray and Kassube (1963) were the first to publish petrographic and stratigraphic information from the Clarke Lake field following an examination of the original wildcat exploration wells. This study concentrated on stratigraphic and facies correlations across the field, and, only in passing, referenced the occurrence of coarse-crystalline white dolomite. Nothing more was published on the Clarke Lake field until 1984, when Opalinski provided both a facies and a diagenetic interpretation for the Slave Point Formation. Opalinski (1984) suggested that the depositional facies from the platform interior are directly analogous to carbonate mud banks that are currently forming in Florida. As well, based on petrographic and seismic data, he (ibid.) suggested a common origin for both the Slave Point and Keg River saddle dolomites, interpreting that they formed as a result of upward fluid migration along faults. Phipps (1989) published a short paper on a seismic exploration model for the Slave Point Formation at Clarke Lake. He (ibid.) suggested using seismic to define the Slave Point platform edge: a favorable position for locating coarse-crystalline dolomite. This interpretation was based on the argument that the dolomite was formed as a result of seawater-meteoric water mixing, i.e., Dorag dolomitization model, during subaerial exposure. By the 1990's, it was becoming clear that massive dolostones do not form as a result of seawater-meteoric mixing (Machel and Mountjoy, 1986; Machel et al., 1991). Reimer and Teare (1992) proposed, based on petrographic and seismic evidence, that the coarse-crystalline saddle dolomites in the Slave Point Formation were the product of thermochemical sulphate reduction and the invasion of hot, i.e, hydrothermal fluids. Shortly thereafter, Hutton (1994) similarly proposed that the intrusion of hydrothermal fluids into the Slave Point Formation degraded organic matter, recrystallized matrix dolomites, and generated saddle dolomite cements. Finally, the most recent work prior to this study being undertaken is that of Davies (1999). This report provides a thorough facies examination of all cores penetrating the Slave Point Formation at Clarke Lake. However, Davies (1999) did not examine many of the diagenetic, or any of the geochemical characteristics of the Slave Point Formation, which are the focus of the study presented in this thesis.

Several studies have been conducted on other Slave Point Formation reservoirs in Alberta and British Columbia. These include: petrographic and geochemical studies of the Dawson field, which fringes the Peace River Arch in Alberta (Dunham et al., 1983; Keilly, 2005); detailed petrographic and stratigraphic studies of the Golden and Evi fields of northern Alberta (Gosselin et al., 1989); an examination of facies and stratrigraphic relationships in the Gift Lake field of northern Alberta (Tooth and Davies, 1989); a detailed characterization of facies and dolomite occurrences in the Hamburg field of northwest Alberta (Al-Aasm and Clarke, 2004); a stratigraphic examination and facies interpretation in the Cranberry field of northwestern Alberta (Sack, 2000); a comprehensive examination of burial and thermal history, dolomite fluid inclusion chemistry, and overall stratigraphic relationships in the Cordova Embayment region of northeastern British Columbia (Morrow et al., 2002); a core and outcrop study of the dolomites in the Middle Devonian of northeastern British Columbia (Nadjiwon et al., 2001); a compilation of petrographic and geochemical data from Slave Point Formation reservoirs across British Columbia, Yukon Territory, and Northwest Territories (Davies, 2004); and, a petrographic and seismic study of the giant Ladyfern gas field of northeastern British Columbia (Boreen and Davies, 2004). All of these studies are used to varying degrees in this thesis during the evaluation of the Slave Point Formation at Clarke Lake.

There has been extensive work published on dolomite and other diagenetic minerals in the Presqu'ile Barrier from British Columbia to Pine Point in the Northwest Territories. Most of these works tend to deal with the whole Presqu'ile Barrier rather than with specific fields, but nevertheless, are integrated into the interpretations forwarded in this thesis for the Slave Point Formation at Clarke Lake. These regional studies include: a characterization of subsurface fluid flow during dolomite formation (Qing and Mountjoy, 1992); the detailed petrographic and geochemical examination of coarse-crystalline dolomites (Qing and Mountjoy, 1994a; 1994b); an examination of rare earth element trends during diagenesis (Qing and Mountjoy, 1994c); and, a petrographic and geochemical discussion on the formation of early, fine-crystalline dolomites (Qing, 1998). Extensive studies have also been conducted on the Middle Devonian Nahanni Formation (Manetoe dolomite), host of the Liard gas reserves (Morrow et al., 1986; Morrow and Aulstead, 1995); and the Middle Devonian Keg River Formation, host of the Rainbow oil and gas reserves (Aulstead and Spencer, 1985). The so-called 'Presqu'ile' dolomite; white coarse-crystalline dolomite of the Slave Point and Keg River formations within the Presqu'ile Barrier, is also the host to the world class Mississippi Valley-type (MVT) Pb-Zn mineralization at Pine Point, NWT. Considering the economic potential of the Pine Point deposit, numerous techniques have been applied in order to resolve the genesis of the deposit. These included Rb-Sr ages on sphalerite (Nakai et al., 1993); Pb-Pb isotope ages on galena (Nelson et al., 2002); petrographic analysis and paragenetic reconstruction (Krebs and Macqueen, 1984); geochemical analysis (Qing and Mountjoy, 1994a; 1994b; Coniglio et al., 2005); and, paleomagnetic dating of gangue minerals (Symons et al., 1993).

1.5 Objectives

The major objective of this thesis is to elucidate the spatial distribution, origin, and timing of dolomite formation in the Slave Point Formation at Clarke Lake, British Columbia, using petrographic and geochemical methods. In particular, the scientific objectives are:

(1) to determine the primary controls dolomite distribution by investigating the relationships between stratigraphy, depositional facies, other diagenetic phases, and tectonic structures;

(2) to determine the controls on porosity distribution using the relationships between dolomite formation and original depositional facies, and tectonic structures;

(3) to determine the temperatures, compositions, and flow directions of the diagenetic fluids using stable and radiogenic isotopes, trace and rare earth element data, fluid inclusion microthermometry and crush-leach data, and the modeled burial and thermal history of the Slave Point Formation;

(4) to determine the relative timing of hydrocarbon migration by integrating both petrographic, and burial and thermal history data; and,

(5) to determine the relationship between the present formation fluids and dolomite formation using stable and radiogenic isotopes, and geochemical data.

The major applied (industrial) objective from this research is to provide a proper reservoir characterization in order to enhance production performance, and to address water production problems in the Clarke Lake field, and in similar dolostone reservoirs elsewhere along the Slave Point platform margin.

In Chapter 2, the stratigraphic nomenclature is defined, and the stratigraphic and structural controls on Slave Point platform formation are discussed. Chapter 3 identifies the locations of the studied wells, presents the depositional facies that comprise the Slave Point Formation at Clarke Lake, and a schematic representation of the facies distribution during the Middle Devonian. Chapter 4 provides a detailed petrographic description of all diagenetic phases and processes, discusses the controls on porosity distribution and the spatial distribution of dolomite, and presents petrographic evidence for the evolution of hydrothermal alteration textures using only petrography. Chapter 5 presents and discusses the extensive geochemical dataset for the dolomites and select other diagenetic phases, and provides a hydrological interpretation for dolomite formation at Clarke Lake. Chapter 6 presents the present-day hydrogeological framework, results and discussions pertaining to the formation water stable and radiogenic isotopes, trace element data, fluid-mineral interactions, and fluid flow patterns at Clarke Lake. Chapter 7 integrates all previously discussed observations and interpretations into a synopsis of the diagenetic evolution of the Slave Point Formation.

CHAPTER 2

STRATIGRAPHIC AND STRUCTURAL EVOLUTION OF THE SLAVE POINT FORMATION

2.1 Introduction

The overall stratigraphic evolution of the Slave Point Formation has been well documented by numerous researchers. However, in the area surrounding the Clarke Lake field, the stratigraphic evolution is relatively poorly documented. Therefore, the major objectives of Chapter 2 are to: 1) define the local stratigraphic nomenclature and, 2) identify the stratigraphic and structural controls on the formation of the Slave Point platform margin. These objectives were fulfilled by identifying locally correlative log markers using a comprehensive database of wireline logs, and using these log markers to generate representative stratigraphic and structural cross-sections. These results provide the framework for interpretation of facies distribution presented in Chapter 3.

2.2 Methods

Electric wireline logs were the principal source of information on formation tops, formation thickness, and lithology. Rasterized wireline logs were provided courtesy of AccuLogs™ by IHS Energy. Logs from 173 subsurface wells penetrating the Slave Point Formation around Clarke Lake were available for interpretation (see Appendix II for the list of formation tops and sequence boundaries). This data was then used to construct stratigraphic and structural cross-sections, and isopach and structure maps to establish the geometry of the Slave Point Formation.

The stratigraphic nomenclature in the Clarke Lake area is shown in Figure 2.1. Stratigraphic cross-sections were constructed using the top of the Muskwa Formation as a datum because it is a regionally recognizable marker throughout the study area. Previous studies have utilized alternative datums to construct cross-sections, including the base of the Muskwa Formation (Davies, 1999); the top of the Slave Point Formation (Williams, 1981); a shale marker within the lower Slave Point Formation (Sack, 2000); the top of the Watt Mountain Formation (Oldale and Munday, 1994); and, the top of the Chinchaga Formation (Oldale and Munday, 1994). Of all these alternative datums, only the base of the Muskwa Formation provides the same data resolution that is available for the top of

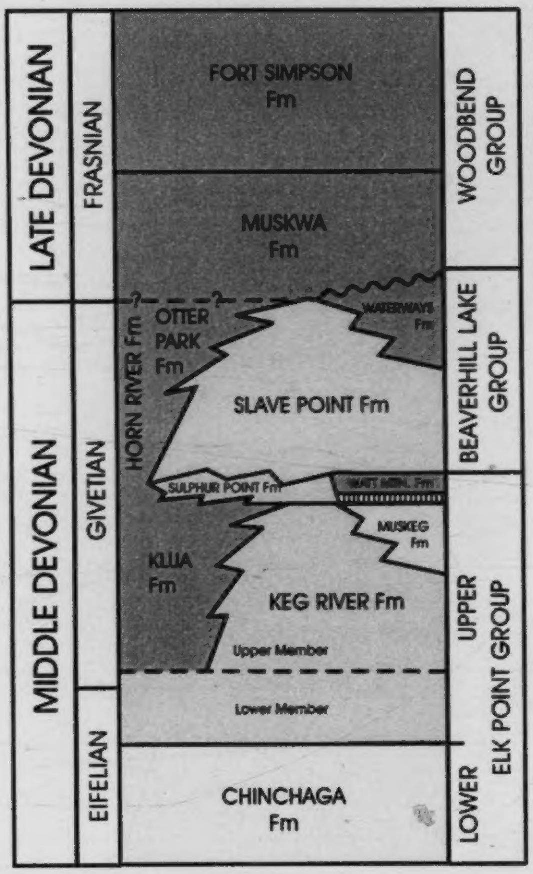
LATE DEVONIAN
MIDDLE DEVONIAN
FRASNIAN
GIVETIAN
EIFELIAN
FORT SIMPSON Fm
MUSKWA Fm
HORN RIVER Fm
OTTER PARK Fm
WATERWAYS Fm
SLAVE POINT Fm
SULPHUR POINT Fm
WATT MTN. Fm
MUSKEG Fm
KLUA Fm
KEG RIVER Fm
Upper Member
Lower Member
CHINCHAGA Fm
WOODBEND GROUP
BEAVERHILL LAKE GROUP
UPPER
ELK POINT GROUP
LOWER

Figure 2.1 Stratigraphic column for the Middle and Upper Devonian of northeastern British Columbia. The column is not drawn to scale. Green shaded units represent shale; pink shaded units represent evaporites; blue shaded units represent carbonates. See Figure 2.2 for further explanation. Modified after Meijer Drees (1994), and Oldale and Munday (1994).

the Muskwa Formation. This is due to the fact that the majority of wells in and around the Clarke Lake field only penetrate the top 10's of metres of the Slave Point Formation. However, the base of the Muskwa was not used as a datum in this study because of an ambiguity surrounding the nature of this contact (see below).

Structural cross-sections were constructed along lines analogous to the stratigraphic cross-sections. Present-day sea-level was used as the structural datum. Wells were not projected onto the cross-section line. As a result, the structural offset may be exaggerated by a few metres.

2.3 Stratigraphy

2.3.1 Regional overview

Most of the current stratigraphic nomenclature (Figure 2.1) and correlations between outcrop and subsurface strata from northeastern British Columbia and the southern

Northwest Territories are based on the early work of Law (1955), Belyea and Norris (1962), Gray and Kassube (1963), Norris (1965), Griffin (1965; 1967), and Belyea (1971). These works were followed by more detailed regional studies by Williams (1981; 1984), Meijer Drees (1994), and Oldale and Munday (1994).

The Devonian strata of northeastern British Columbia are dominated by a thick succession of platform carbonates that pass to basinal shales to the north and west. The earliest Phanerozoic sediments to be preserved in northeastern British Columbia are Cambrian quartzose sandstones that are only found in a few of the deeper wells. These sandstones were likely the product of the erosion of Archean and Proterozoic basement rocks followed by deposition in paleo-lows (Figure 2.2).

A marine low-stand during the lower Middle Devonian (Johnson et al., 1985) resulted the formation of the continental redbeds across portions of northern Alberta and British Columbia (Figure 2.2). A subsequent marine transgression (Johnson et al., 1985) invaded these continental basins and the fossiliferous carbonates of the Ernestina Lake Formation were deposited. Increased basin restriction led to the deposition of the Cold Lake salt (Meijer Drees, 1994) (Figure 2.2).

Continued marine transgression (Johnson et al., 1985: Figure 2.3) that overstepped the Cold Lake evaporite basin resulted in the formation of the Chinchaga Formation, which consists primarily of anhydritic dolomite, although, closer to the Peace River Arch, coarse clastics become dominant (Figure 2.2). Towards the northwest, the Chinchaga thickens and is representative of a platformal to reefal carbonate depositional environments in its upper parts (Figure 2.2).

Widespread marine transgression during the Middle Devonian (Johnson et al., 1985) is represented by the relatively deep-water carbonates of the lower Keg River Formation (Figures 2.1 and 2.3). This unit is characterized by variably dolomitized stromatoporoidal limestones. The lower Keg River is interpreted to have formed as a platform, and is the foundation for subsequent Middle Devonian reef growth (Figure 2.2).

The subsequent Middle Devonian carbonate package includes the upper Keg River Formation, the Sulphur Point Formation, and the Slave Point Formation, and form the Presqu'ile Barrier, the margin of which is shown in Figures 1.1 and 2.2. Physiographically, the Presqu'ile Barrier is an elongate reef complex about 400 kilometres long, with a width ranging from 20 to 100 km. This barrier extends from outcrop at the eastern edge of the basin

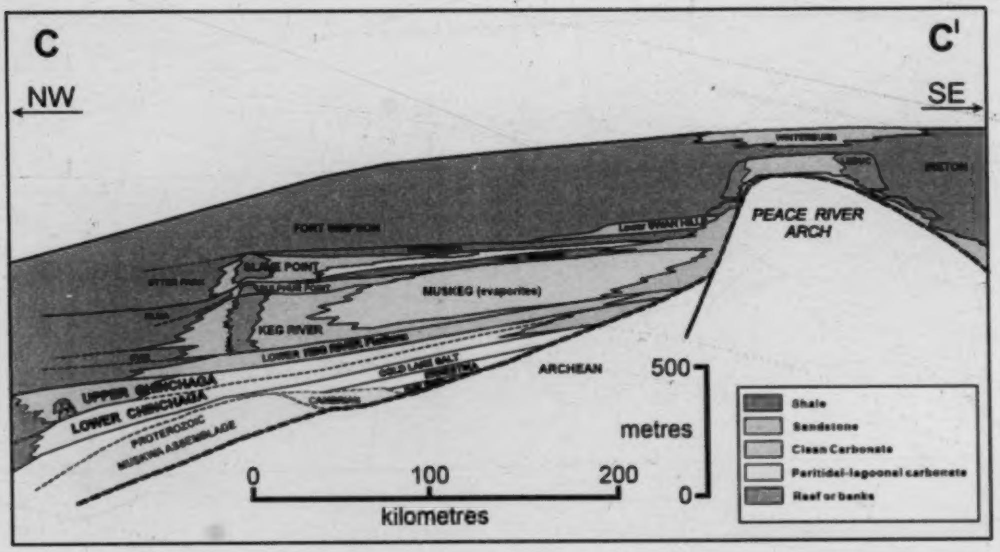
C
C'
NW
SE
WATERWAYS
IRETON
PEACE RIVER ARCH
FORT SIMPSON
Lower SWAN HILLS
SLAVE POINT
OTTER PARK
SULPHUR POINT
MUSKEG (evaporites)
KEG RIVER
LOWER KEG RIVER Platform
COLD LAKE SALT
ARCHEAN
UPPER CHINCHAGA
LOWER CHINCHAGA
CAMBRIAN
PROTEROZOIC
MUSKWA ASSEMBLAGE
500
metres
0
0
100
200
kilometres
Shale
Sandstone
Clean Carbonate
Peritidal-lagoonal carbonate
Reef or banks

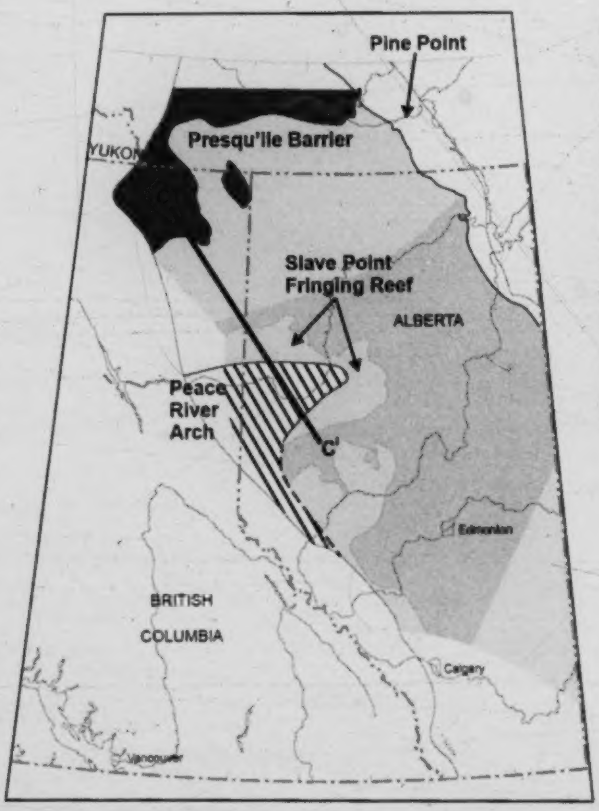
Pine Point
Presqu'ile Barrier
YUKON
Slave Point Fringing Reef
ALBERTA
Peace River Arch
C'
Edmonton
BRITISH COLUMBIA
Calgary
Vancouver

Figure 2.2 (Top) Schematic regional stratigraphic cross-section C-C' during the Late Devonian from northwestern Alberta to northeastern British Columbia. Modified after Petrel Robertson (2003). (Left) Position of cross-section line C-C' in relation to the paleogeographic distribution of the Middle to Late Devonian Beaverhill Lake Group. See Figure 1.3 for further explanation. Modified after Oldale and Munday (1994).

near Pine Point, Northwest Territories, into the subsurface of British Columbia at depths of around 2500 metres (Figure 2.2). The maximum thickness of the Presqu'ile Barrier is about 200 m in the Pine Point area, but thins to less than 50 m in regions overlying basement highs, such as the Tathlina Arch. The Presqu'ile Barrier restricted seawater circulation in the central and southern parts of the Western Canada Sedimentary Basin during the Middle Devonian. This led to evaporite and carbonate deposition south of the barrier in the Elk Point Basin in what is now largely Alberta and Saskatchewan, while deeper water, normal-marine sediments were deposited north of the barrier.

The Presqu'ile Barrier consists of two stacked carbonate reef barrier complexes. The lower barrier developed within the upper Keg River Formation, while Muskeg Formation evaporites fill regional depressions and sub-basins behind this barrier to the south and east (Figure 2.2). Shales of the Klua Formation fill various embayments along the northern and western edges of the barrier in the Cordova and Klua embayments (Figure 1.1). Numerous so-called pinnacle reefs of upper Keg River age occur within these shale embayments and immediately in front of the barrier (e.g., Yoyo), which are also exploration targets. The upper part of the overall barrier is the Slave Point Formation immediately overlying the Sulphur Point and Watt Mountain formations (Figure 2.2). Its northwestern limit more-or-less coincides with the Keg River barrier below, except in the shale embayments where the Slave Point progrades out to the edge of the shale clinoform. To the south, the Slave Point Formation forms fringing reef complexes around the emergent Peace River Arch (Figure 2.2). Depressions near the top of the Slave Point Formation are filled by shales of the Otter Park Member near the barrier margin, or by argillaceous limestones of the Waterways Formation behind the barrier (Figure 2.2).

A major Late Devonian marine transgression (Johnson et al., 1985: Figure 2.3) terminated carbonate deposition across much of northeastern British Columbia and northwestern Alberta, except around the still emergent Peace River Arch (Figure 2.2). Over most of the region thick packages of terrigenous clastic material of the Fort Simpson Formation were deposited (Figure 2.2).

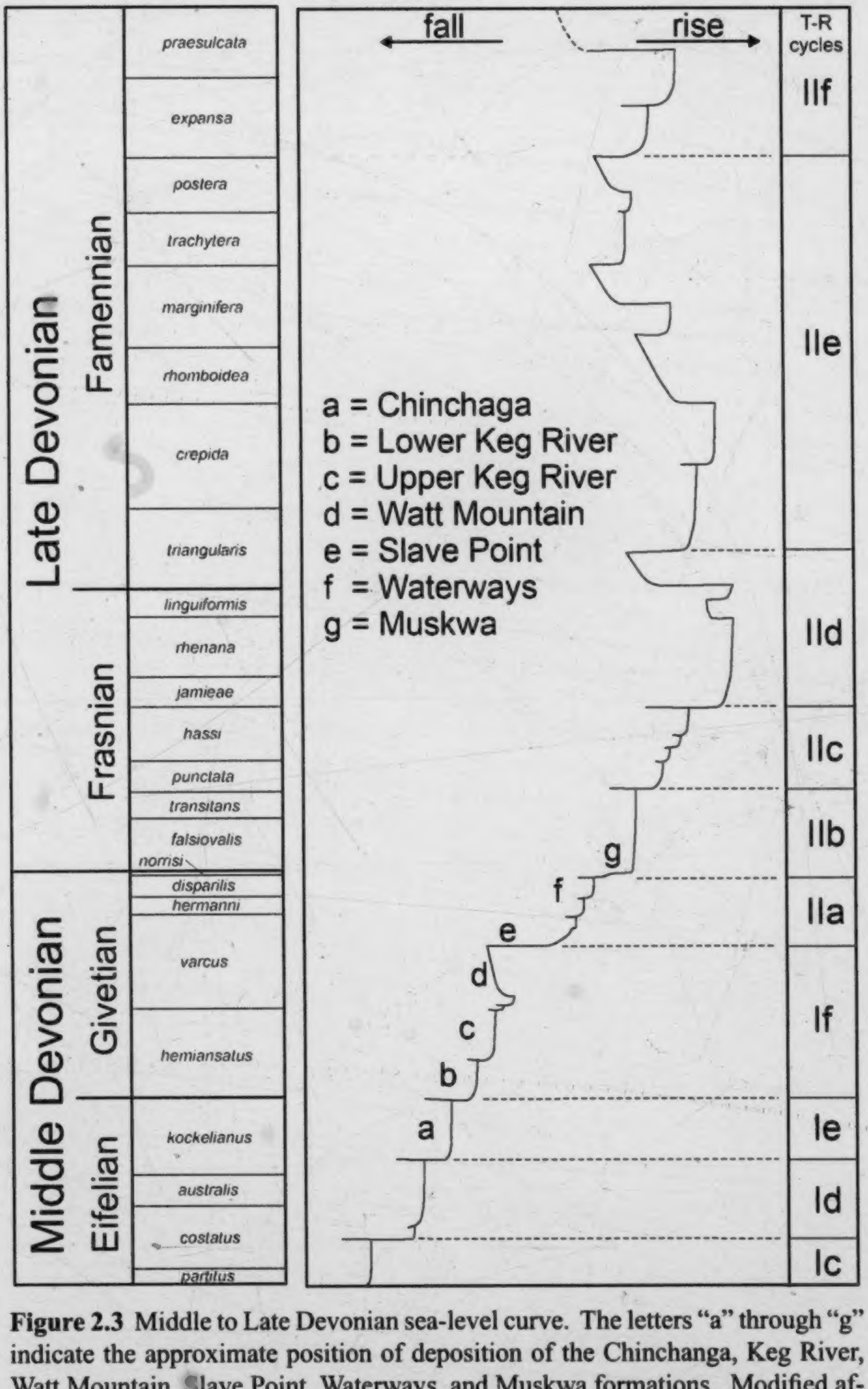

Figure 2.3 Middle to Late Devonian sea-level curve. The letters "a" through "g" indicate the approximate position of deposition of the Chinchanga, Keg River, Watt Mountain, Slave Point, Waterways, and Muskwa formations. Modified after Johnson et al. (1985). Conodont zones after Joachimski et al. (2004).

2.3.2 Beaverhill Lake and Woodbend groups in the study area

Watt Mountain Formation

The Watt Mountain Formation was proposed by Law (1955) and later re-defined by Belyea and Norris (1962) to the subsurface equivalent of the Amco shale: a thin, dark greenish-grey shale and argillaceous limestone overlying the porous dolomite beds at Pine Point, Northwest Territories (Campbell, 1950). The type section of the Watt Mountain Formation is located in northwestern Alberta, in the Steen River 2-22-117-5W6 well, where it is characterized largely by brecciated limestones with a thickness of less than 30 metres. Elsewhere, the formation is comprised of green, pyritic shales, arkosic sandstones, or minor amounts of anhydrite. The top of the formation is placed at the base of the limestones and dolomites of the Slave Point Formation.

The Watt Mountain Formation has historically been included within the Elk Point Group (Figure 2.1). However, Meijer Drees (1988) and Williams (1984) document the presence of a major unconformity at the base of the Watt Mountain Formation and suggest that it represents an erosional event and/or transgressive deposit. As a result, the Watt Mountain Formation may represent the base of the Beaverhill Lake Group (Campbell, 1992).

The Watt Mountain Formation in northern Alberta has been found to contain the remains of fresh- and brackish-water algae, primitive fish, and primitive plants (Kramers and Lerbekmo, 1967), as well as Givetian ostracodes in an area south of Great Slave Lake, Northwest Territories (Skall, 1975). This information in conjunction with both the lithologic character and the high radioactivity of the Watt Mountain Formation, as well as the unconformable contact with the underlying Elk Point Group carbonates, suggest deposition following a major marine regression and period of emergence.

Deposition of the Watt Mountain Formation, as well as the other units of interest in the study area, can be correlated to eustatic sea level curves, such as that shown in Figure 2.3. Accordingly, the Watt Mountain Formation is part of a transgressive systems tract (TST) in late Givetian time, i.e., post-mid *varcus* time (Figure 2.3), that introduced sediments eroded from highlands into the Presqu'ile Barrier under moist climatic conditions (Meijer Drees, 1994). Closer to the barrier margin, such as at Clarke Lake, reef growth continued unabated and prograded seaward to form the Sulphur Point Formation (Meijer Drees, 1988) (Figure 2.2).

Slave Point Formation

The Slave Point Formation was first described by Cameron (1918) based on a two-foot thick unit of grey, thin-bedded, fine to medium-grained limestones outcropping on the west shores of Great Slave Lake, Northwest Territories. Subsequent work by Cameron (1922) identified thick successions of limestone overlying the Presqu'ile dolomite, i.e., Middle Devonian strata containing abundant coarse-crystalline dolomite, and underlying the Upper Devonian shales along the north shore of Great Slave Lake, for which he formally proposed the name Slave Point Formation. Campbell (1950) defined the Slave Point Formation from subsurface cores drilled along the south shore of Great Slave Lake at Pine Point. The Slave Point Formation defined by Campbell (1950) included in its lower part the Amco shales, i.e., the present-day Watt Mountain Formation. Deeper in the subsurface of northern Alberta, Hunt (1954) in his examination of the Steen River 2-22-117-5W6 well, proposed the name Territories Formation for this package of sediments. However, Law (1955) recognized the similarity of the beds proposed by Campbell (1950) to the beds in the Steen River well. Law (1955) described the Slave Point Formation in the type Steen River well as a brown to light grey, cryptocrystalline, chalky and slightly dolomitic limestone that contains brachiopods, ostracodes, stromatoporoids, corals, and algae. He (ibid.) also redefined the Slave Point Formation to exclude the Amco shales. This nomenclature is accepted to this day.

The Slave Point Formation extends from the edge of the Presqu'ile Barrier in northeastern British Columbia and the southern Northwest Territories, southward into central Alberta and the regions immediately adjacent to the Peace River Arch (Figure 2.2). In northern and central Alberta, the Slave Point Formation acts as platform for younger reef growth of the Swan Hills Formation (Jansa and Fischbuch, 1974). To the south and east in Saskatchewan, the Slave Point Formation is known as the Dawson Bay Formation. The Slave Point Formation is at its thickest in northeastern British Columbia and northwestern Alberta, ranging anywhere from 60 metres to almost 200 metres (Oldale and Munday, 1994). Towards the south, the Slave Point Formation progressively thins to a zero-edge where in onlaps the Peace River Arch (Oldale and Munday, 1994) (Figure 2.2). North of the barrier margin, the Slave Point Formation rapidly thins to zero and is likely represented in the basinal areas by the shales of the Otter Park Formation (Figure 2.2). Across northern British Columbia and Alberta, Slave Point deposition was aggradational to backstepping in style, and resulted in the development of a wide carbonate platform termed the Hay River Bank, the edge of which was roughly coincident with the underlying margin of the Presqu'ile Barrier (Oldale and Munday, 1994). However, due to the historical and pervasive use of the term Presqu'ile barrier to describe the entire package of Middle Devonian reef growth along the platform margin, the term Hay River Bank is not used in this study.

Outside of the Clarke Lake region, the Slave Point Formation consists primarily of limestones, and only zones bordering the platform margin and isolated platform interior patch reefs show any development of dolomite. On the other hand, the barrier platform margin is extensively dolomitized in much of the region. Furthermore, many authors have suggested that the platform margin of the Slave Point Formation developed as a continuous shoal-type wave-resistant reef or rimmed platform (e.g. SB Geological Associates, 1988; Davies, 1999). However, there is evidence to suggest that the margin was discontinuous and channels penetrated far into the platform interior (see Chapter 3). Along the edges of these channels and embayments, reef-building organisms such as stromatoporoids and corals would have flourished.

Regarding global sea level fluctuations, the Slave Point Formation was deposited during the transgressive phase of the Beaverhill Lake Group (Oldale and Munday, 1994). This was a period of relative sea-level rise that commenced with the deposition of the base of the Watt Mountain Formation and continued through deposition of the open-marine carbonates of the Slave Point Formation during late *varcus* time (Figure 2.3). Deposition of the Slave Point Formation continued until such time that relative sea-level rise outpaced reef growth, drowning the reef-building organisms and filling topographic depressions with argillaceous carbonates of the Waterways Formation during post late-*varcus* time (Figure 2.3).

Waterways Formation

The name Waterways Formation was first proposed by Warren (1933) for a package of rocks in the Fort McMurray area of northeastern Alberta that lie unconformably below the Lower Cretaceous and above the Devonian evaporites. Subsequently, Crickmay (1957) subdivided the Waterways Formation into the Firebag, Calmut, Christina, Moberly, and Midred members, in ascending order. Norris (1963) recognized these same five members in the Bear Biltmore #1 7-11-87-17W4 well, which is now used as the standard reference section. In northeastern British Columbia south of the Presqu'ile Barrier margin, the name Waterways Formation is used for the dark-brown, brachiopod-rich, argillaceous limestones, which was termed the Beaverhill Lake Formation by Griffin (1965). The Beaverhill Lake Formation was originally defined by the Geological Staff of Imperial Oil Limited (1950) in the Anglo-Canadian Beaverhill Lake #2 11-11-50-17W4 well in central Alberta. However, the name Waterways Formation takes precedence, and the Beaverhill Lake Formation has been dropped from the lexicon of the Western Canada Sedimentary Basin (Oldale and Munday, 1994).

The stratigraphic relation between the Slave Point Formation and the Waterways Formation is controversial. Most studies have concluded that the two formations are the result of distinct, non-contemporaneous sedimentary events. This includes the works of Sheasby (1971), and Wendte and Stoakes (1982), who indicate that the two formations exhibit an onlap relationhip in the Swan Hills buildups of west-central Alberta. Conversely, Tooth and Davies (1989) and Gosselin et al. (1989) document the presence of a submarine hardground separating reefal carbonates of the transgressive phase from the Waterways Formation along the Peace River Arch. Alternatively, Jansa and Fischbuch (1974), Meijer Drees (1986), and Keith (1990), proposed that the Waterways Formation was contemporaneous with Slave Point deposition. In the Clarke Lake area, there is no core available to classify the contact between the two formations. However, Griffin (1967) proposed that tectonic movements allowed for continued deposition of the Slave Point Formation, while the Waterways Formation was being deposited to the east and south. He (ibid.) believed that these tectonic conditions provided the framework for full build-up of the Slave Point at the Presqu'ile Barrier margin, and hence, favours contemporaneous deposition of the Waterways Formation.

Compared to the basin-fill successions in the later Woodbend and Winterburn groups, the Waterways Formation is dominantly composed of fine-grained carbonate that lacks any significant clay to shale content. Stoakes (1992) speculated that the difference in lithology is primarily a function of both the shallow bathymetry during Waterways deposition combined with the large areas of the basin succession that existed as shallow, carbonate-dominated banks that shed material into the adjacent basin. Hence, sediments of the regressive Waterways Formation were sourced on the platform on the east side of the basin, and were shed into the basin to form westerly-dipping clinoforms (Campbell, 1992).

These clinoforms thin in a westward direction, and are absent along the Presqu'ile barrier margin, such as at Clarke Lake, but thicken locally within the Klua embayment (see later sections).

The Waterways Formation probably represents a regressive phase as a result of deposition during a relative sea-level fall or decreasing rate of relative sea-level rise (Oldale and Munday, 1994). In much of Alberta, the Waterways Formation exhibits a basinward progradation of the Slave Point platform margin facies, suggesting that the rate of sediment accumulation was greater than the accommodation space, producing a relative sea-level fall (Oldale and Munday, 1994). In terms of global sea level, however, the time of Waterways deposition coincided with a decreasing rate in an overall relative sea level rise during *hermanni* and *disparilis* times (Figure 2.3).

Otter Park Formation

The Otter Park Member of the Horn River Formation was formally proposed by Gray and Kassube (1963) to represent a 165 metre section of dark grey calcareous shale north of the Presqu'ile Barrier margin in the Western Natural et al. Fort Nelson a-95-J/94-J-10 well. Gray and Kassube (1963) linked the lower part of the Otter Park Member with the Klua Shale (Figure 2.1), implying that the Otter Park is time-equivalent to both the Slave Point and the upper Keg River Formation (Figure 2.1). Similar stratigraphic confusion reigned when Griffin (1967) suggested that the Sulphur Point Formation prograded to overlie tongues of the Otter Park shale. Using the stratigraphic nomenclature defined by Meijer Drees (1994), the name Horn River Formation was dropped, and both the Otter Park and Klua shales were raised to formation status. As defined by Meijer Drees (1994), the Otter Park Formation consists of only the dark-grey to green, calcareous shale that lies adjacent to, and may be correlative with, the Slave Point and Sulphur Point formations. Therefore, the Otter Park shales are those that lie above the upper Keg River-equivalent Klua Formation, are situated basinward and adjacent to the Presqu'ile Barrier margin, and are below the Muskwa Formation (Figure 2.1).

The Otter Park Formation currently has total organic carbon (TOC) contents of up to 4.43% in northeastern British Columbia, which likely consist of predominantly of kerogen types II and II-I (Fowler et al., 2001). Based on this data, Fowler et al. (2001) suggested that the Otter Park Formation was a very good source rock, and may have sourced much of the hydrocarbons that currently reside in the Middle Devonian reservoirs of northeastern British Columbia.

Muskwa Formation

The Muskwa Member of the Horn River Formation is the lowest lithologic unit of the Upper Devonian Woodbend Group in the study area, and was formally proposed by Gray and Kassube (1963) to represent a 37 metre section of black bituminous in the Western Natural et al. Fort Nelson a-95-J/94-J-10 well. The Muskwa was raised to formation status by Griffin (1965) and separated from the Horn River Formation. The Muskwa Formation provides an excellent regional stratigraphic marker due to its increasing downward natural radioactivity, culminating in a strong gamma-ray deflection at the base of the Muskwa Formation, and its regional extent. In front of the Presqu'ile Barrier margin, the Muskwa Formation is indistinguishable from the surrounding shales of the Otter Park and Fort Simpson formations (Figure 2.1).

According to Griffin (1965), the base of the Muskwa Formation represented a significant unconformity because it rested directly on the Slave Point and Waterways formations. The petrographic evidence, however, for an unconformity is equivocal.

The Muskwa Formation is considered to be the source rock for most of the conventional hydrocarbon accumulations found in the Upper Devonian reservoirs of Alberta (Allan and Creaney, 1991). According to Fowler et al. (2001), the Muskwa Formation currently has a maximum TOC content of > 2%, despite being thermally overmature in northeastern British Columbia. Also, kerogen is likely of Type II, similar to the time-equivalent Duvernay Formation in Alberta (Fowler et al., 2001). Based on these results, Fowler et al. (2001) suggest that the Muskwa Formation may be the source of much, if not most, Middle Devonian oil and gas in the study area.

The Muskwa Formation is time-equivalent to the Duvernay Formation of the Woodbend Group in Alberta (Switzer et al., 1994). Deposition of the Muskwa Formation and the remainder of the thick, Late Devonian shale package in northeastern British Columbia signalled a profound depositional change in the basin. The increased influx of terrigenous clastic materials prevented the formation of carbonate platforms, and thus, the potential for reef growth. Rather, the lowermost Woodbend time represents a period of accumulation and preservation of organic carbon, reflecting a major change in the stratification and oxygenation of basinal waters during the maximum transgressive stage of the Woodbend (Switzer et al., 1994), equivalent to global sea level rise and relatively high still stand during *falsiovalis* time (Figure 2.3).

2.4 Reference logs

The reference, or 'type', logs used to identify the wireline log responses from select Middle and Late Devonian formation and sequence boundaries are shown in Figure 2.4. The wireline log markers shown in these diagrams were used for all stratigraphic correlations assembled for this study.

The majority of the formation tops shown in Figure 2.4 do not differ significantly from those used by other authors (Williams, 1981; Oldale and Munday, 1994; Davies, 1999), with the exception of the top of the Muskwa Formation (Lonnee, 2001). The stratigraphic relationships characterized by the former studies are flawed for two reasons. Firstly, these studies show a large degree of inconsistency in the markers used to define to the top of the Muskwa Formation; and, secondly, these previously defined log markers are not recognizable across much of northeastern British Columbia. For this study, a consistent and regionally correlative wireline log marker was identified to represent the top of the Muskwa Formation: the Muskwa Formation was picked where the gamma-ray (GR) log shows a marked increase following a roughly 15-60 API decrease at the base of the Fort Simpson shale. This marker, informally called the JL-marker in Figure 2.4, also corresponds to a slight increase of approximately 10 µs/m on the sonic log (AC). This AC log deflection can also be correlated with a deflection in the deep induction log across much of the area. These wireline log deflections are most likely the result of a subtle change in the lithology between the bituminous Muskwa Formation and the overlying shales of the Fort Simpson Formation.

The base of the Muskwa Formation is represented by a sharp deflection in both GR and AC logs, regardless of the underlying formation, i.e., Otter Park, Waterways, or Slave Point. From the top of the Muskwa to its base, the GR log shows a gradual increase, peaking around 150 API. The base of the Muskwa also shows a sharp negative deflection on the AC log. This conspicuous marker has been interpreted by other researchers to represent a maximum flooding surface that is correlatable across much of northeastern British Columbia.

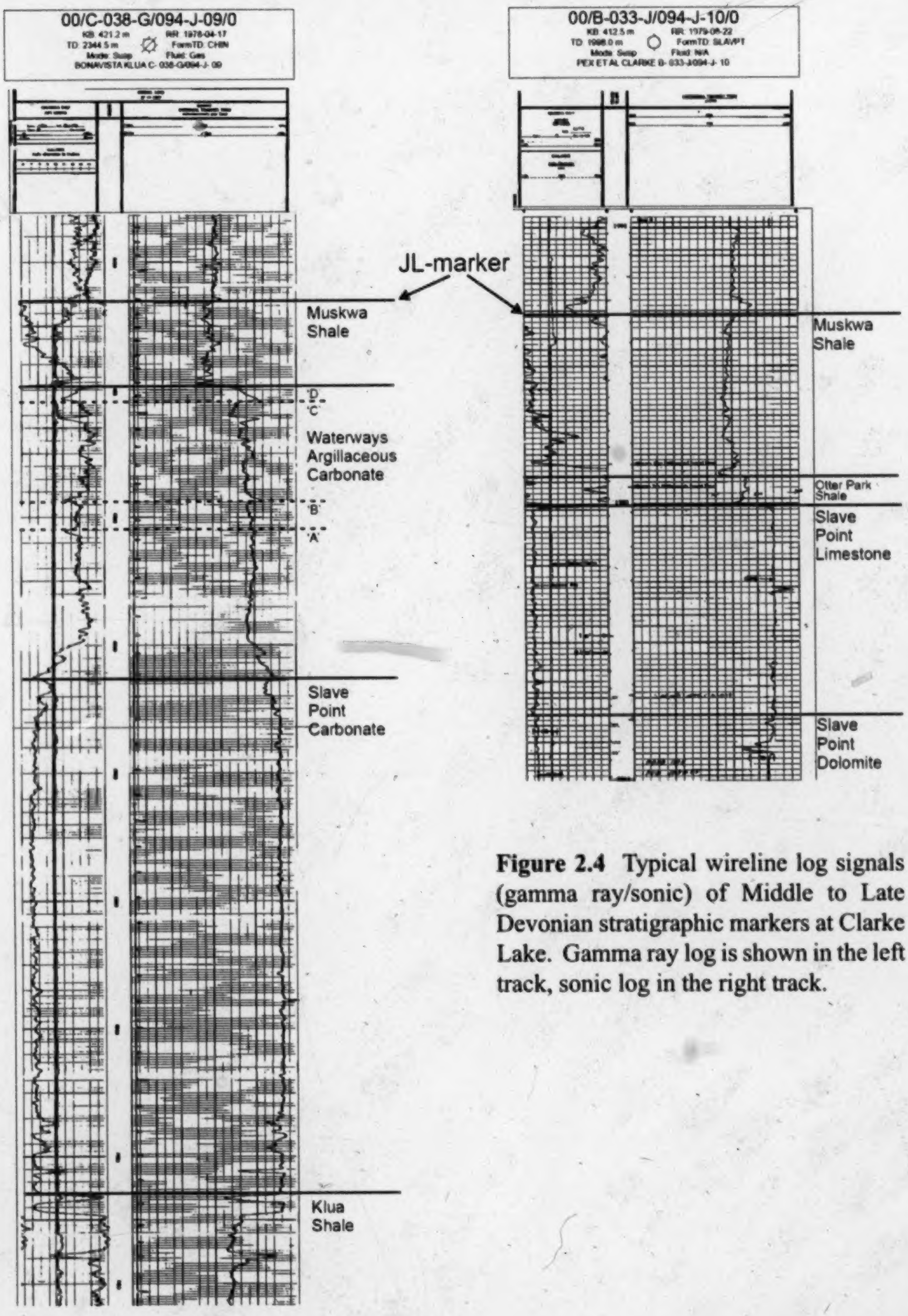

Figure 2.4 Typical wireline log signals (gamma ray/sonic) of Middle to Late Devonian stratigraphic markers at Clarke Lake. Gamma ray log is shown in the left track, sonic log in the right track.

The Otter Park Formation is characterized by slightly lower radioactivity compared to the overlying Muskwa Formation. In general, the GR log alone is not sufficient for identification of the Otter Park Formation. The AC log response in this formation is much lower than the Muskwa Formation, approximately 60 to 80 μs/m, and significantly higher than the underlying Slave Point Formation, at 160 μs/m. Nowhere across the Clarke Lake field, and surrounding area, does the Otter Park Formation occur in the same wells as those containing the Waterways Formation.

The top of the Waterways Formation is easily identified on wireline logs since it always occurs beneath the highly radioactive Muskwa Formation. Hence, the rapid decrease in the GR log is sufficient for identification of this marker. Overall, the Waterways Formation exhibits a consistent blocky pattern in both GR and AC logs, except near the underlying contact with the Slave Point Formation. At the base of the Waterways Formation, there is a gentle decrease in both GR and AC logs from highs of roughly 120 API and 230 μs/m to 30 API and 180 μs/m, respectively. This broad zone may represent a gradual facies change from platform to basin during mid-Slave Point deposition. Within this package of argillaceous limestones, 4 markers were defined in an attempt to further evaluate the evolution of the Waterways Formation. These markers, A through D, do not necessarily represent typical 4th order shallowing-upward cycles, i.e., sea level fluctuations; rather, their boundaries were defined based on the occurrence of consistent GR and AC log markers in the Clarke Lake study area (dashed in Figure 2.4).

The top of the Slave Point Formation is marked by the first occurrence of 'clean' carbonate below the Muskwa Formation, Otter Park Formation, or Waterways Formation. The Slave Point Formation displays relatively constant GR and AC responses, roughly 15-30 API and 160-180 μs/m, respectively. Lithologic identification, i.e., limestone or dolostone, is based on either a small increase in the AC log response due to increased porosity associated with dolomite, or through the use of neutron-density and photo-electric (pe) logs. The base of the Slave Point Formation is absent in most wireline logs from Clarke Lake; however, in deeper wells, it is represented by the contact with either the underlying shales of the Watt Mountain or Klua formations, or the carbonates of the Sulphur Point Formation.

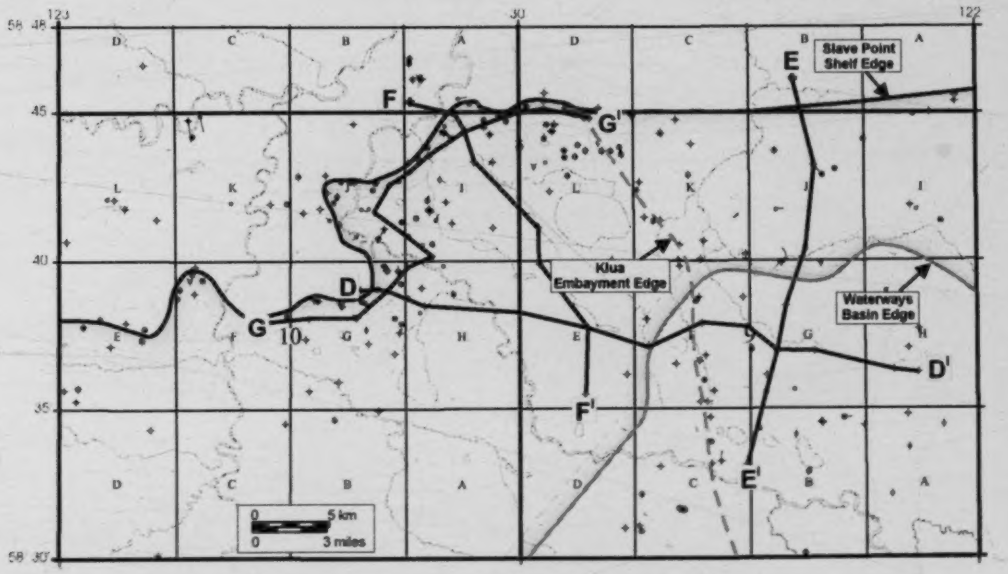
58 48
123
30
122
45
40
35
58 30
D
C
B
A
D
C
B
A
L
K
J
I
L
K
J
I
E
F
G
H
E
F
G
H
D
C
B
A
D
C
B
A
F
G'
E
Slave Point Shelf Edge
Klua Embayment Edge
Waterways Basin Edge
D
G
10
9
D'
F'
E'
0
5 km
0
3 miles

Figure 2.5 Locations of stratigraphic and structural cross-section lines D-D' through G-G' shown in Figures 2.6 through 2.9. Box is study area as shown in Figure 1.1.

2.5 Cross-sections

Four stratigraphic and structural cross-section lines were prepared for this study, which demonstrate the stratigraphic evolution of the Slave Point and adjacent formations. The placement of faults and their relative motion are based solely on the correlations *between* wells. The locations of the cross-sections are shown in Figure 2.5.

2.5.1 Cross-section D-D'

Cross-section D-D' roughly parallels depositional strike from the west side of the Clarke Lake field to the far east side of the study area (Figure 2.5). Stratigraphically, the west side of the cross-section starts basinward of the Slave Point platform margin (Figure 2.6). At this position, a thick package of Otter Park Formation shale was deposited on top of a thin carbonate unit that may be equivalent to the lowermost Slave Point Formation. Moving eastward, the top of the Slave Point Formation occurs at progressively higher levels (Figure 2.6). However, there is no evidence for significant relief on this surface, as might be expected if the Slave Point margin was a continuous, wave-resistant reef complex. Rather, a noticeable depression at the top of the Slave Point can be found around well c-70-E (Figure 2.6). This depression was subsequently filled by a thicker than normal

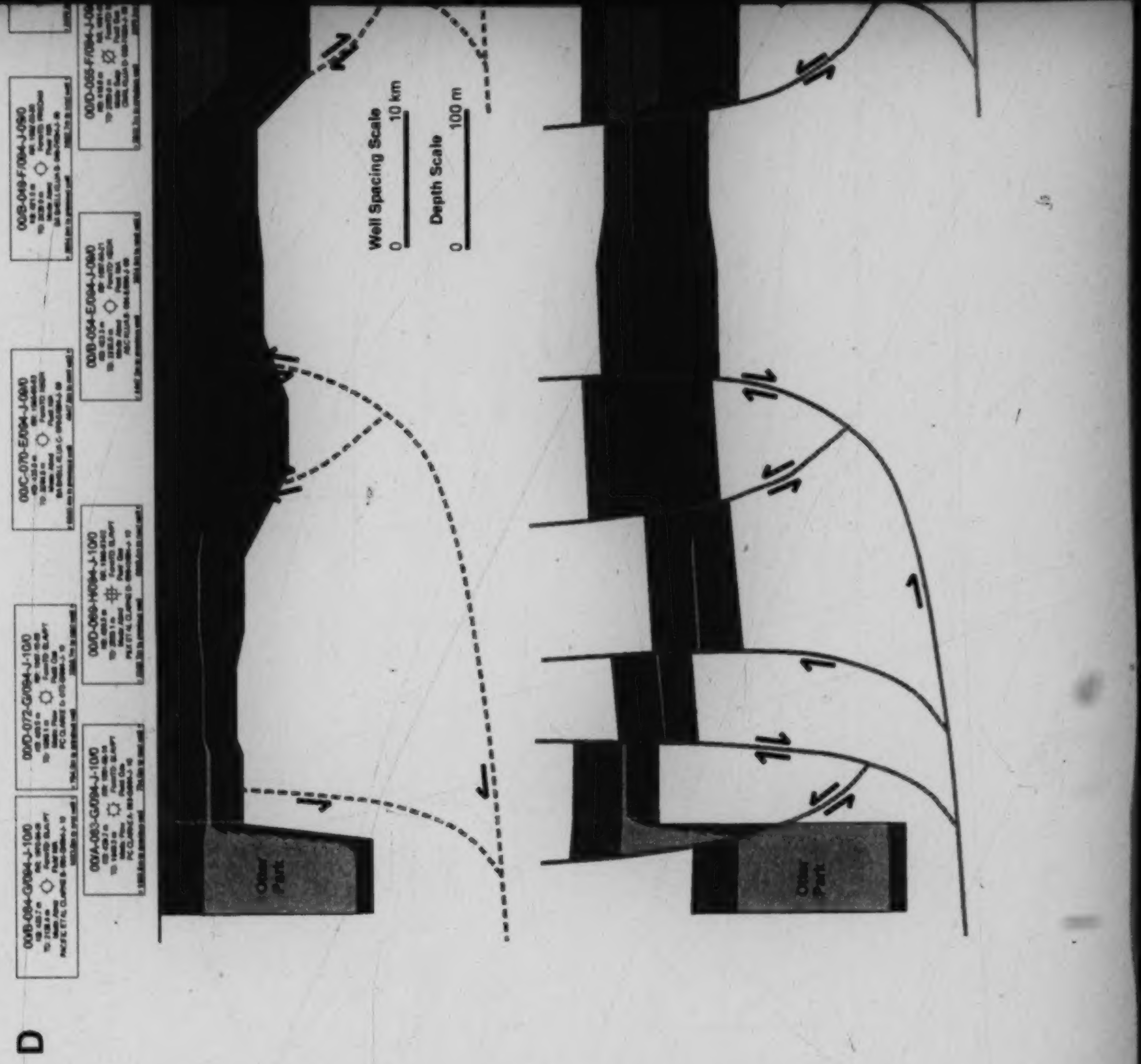
D
00/B-084-G/094-J-10/0
00/A-083-G/094-J-10/0
00/D-072-G/094-J-10/0
00/D-069-H/094-J-10/0
00/C-070-E/094-J-09/0
00/B-054-E/094-J-09/0
00/B-049-F/094-J-09/0
00/D-055-F/094-J-09
Otter Park
Well Spacing Scale
0
10 km
Depth Scale
0
100 m
Otter Park

Figure 2.6 Stratigraphic (top) and structural (bottom) cross-sections D-D'. The top of the Muskwa Formation was used as a datum in the stratigraphic section, sea level as the datum in the structural section.

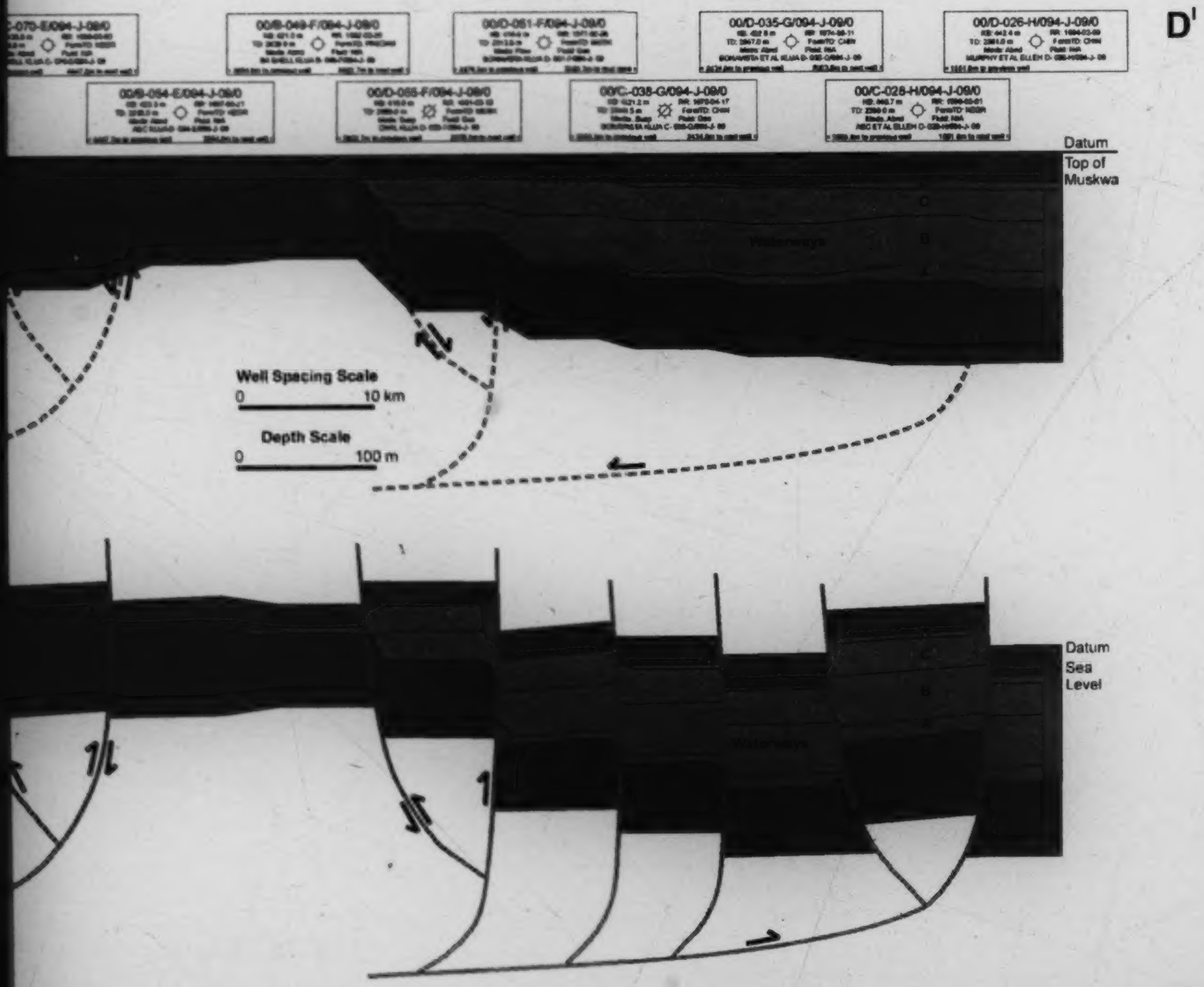
D'
C-070-E/094-J-09/0
00/B-049-F/094-J-09/0
00/D-061-F/094-J-09/0
00/D-035-G/094-J-09/0
00/D-026-H/094-J-09/0
00/B-094-E/094-J-09/0
00/D-055-F/094-J-09/0
00/C-038-G/094-J-09/0
00/C-028-H/094-J-09/0
Datum
Top of Muskwa
C
B
A
Waterways
Well Spacing Scale
0
10 km
Depth Scale
0
100 m
Datum
Sea Level
C
B
A
Waterways

succession of Muskwa shale. This depositional depression may have been fault bounded, or may be representative of, deep-water lagoons and/or channels of the platform interior. Farther to the east, the top of the Slave Point Formation abruptly rises to a maximum height around well b-49-F (Figure 2.6). This point marks the western boundary of an interior basin completely filled with argillaceous carbonates of the Waterways Formation. At this location, reefs probably developed in the Slave Point Formation presumably as a discontinuous, wave-resistant structure. The evidence for reef development can also be seen in wells d-51-F and c-38-G, where it appears that the Slave Point Formations retreated westward at stratigraphically higher levels below the Waterways Formation, which becomes progressively thicker (Figure 2.6). The westward movement of this Slave Point edge westward may have been due in part to a substantial increase in sea level and/or basin subsidence, or due to movement of bounding faults.

Drawn as a structural cross-section, D-D' shows that the present-day configuration around Clarke Lake is fairly complex (Figure 2.6). The most noticeable characteristic is that the area is divided into a number of fault blocks that assume a horst-and-graben structure. As a result, there is some structural inversion of depositional lows into structural highs, such as seen around well c-70-E. On seismic, this location may appear as a promising exploration target based on the elevation; however, the original deeper-water facies from this location are poor reservoir rocks (see Chapter 3). Similarly, the Slave Point platform margin near well a-83-G is currently situated in a structurally high position that may be interpreted to represent a continuous reef margin due to the relief. But this conclusion cannot be drawn when examining the stratigraphic section (compare top and bottom in Figure 2.6). In the Waterways basin, all the various 'backstepping' original Slave Point margins appear to be fault-bounded (Figure 2.6).

2.5.2 Cross-section E-E'

Cross-section E-E' is at a right-angle to section D-D' along the east side of the study area (Figure 2.5). E-E' parallels the depositional dip from the center of the Waterways basin in the south to the Horn River shale basin to the north. Stratigraphically, the north end of the cross-section is basinward of the Slave Point platform margin (Figures 2.5 and 2.7). Similar to section D-D', at this position, a thick package of Otter Park Formation shale was deposited. The extreme slope of the Slave Point Formation at the platform

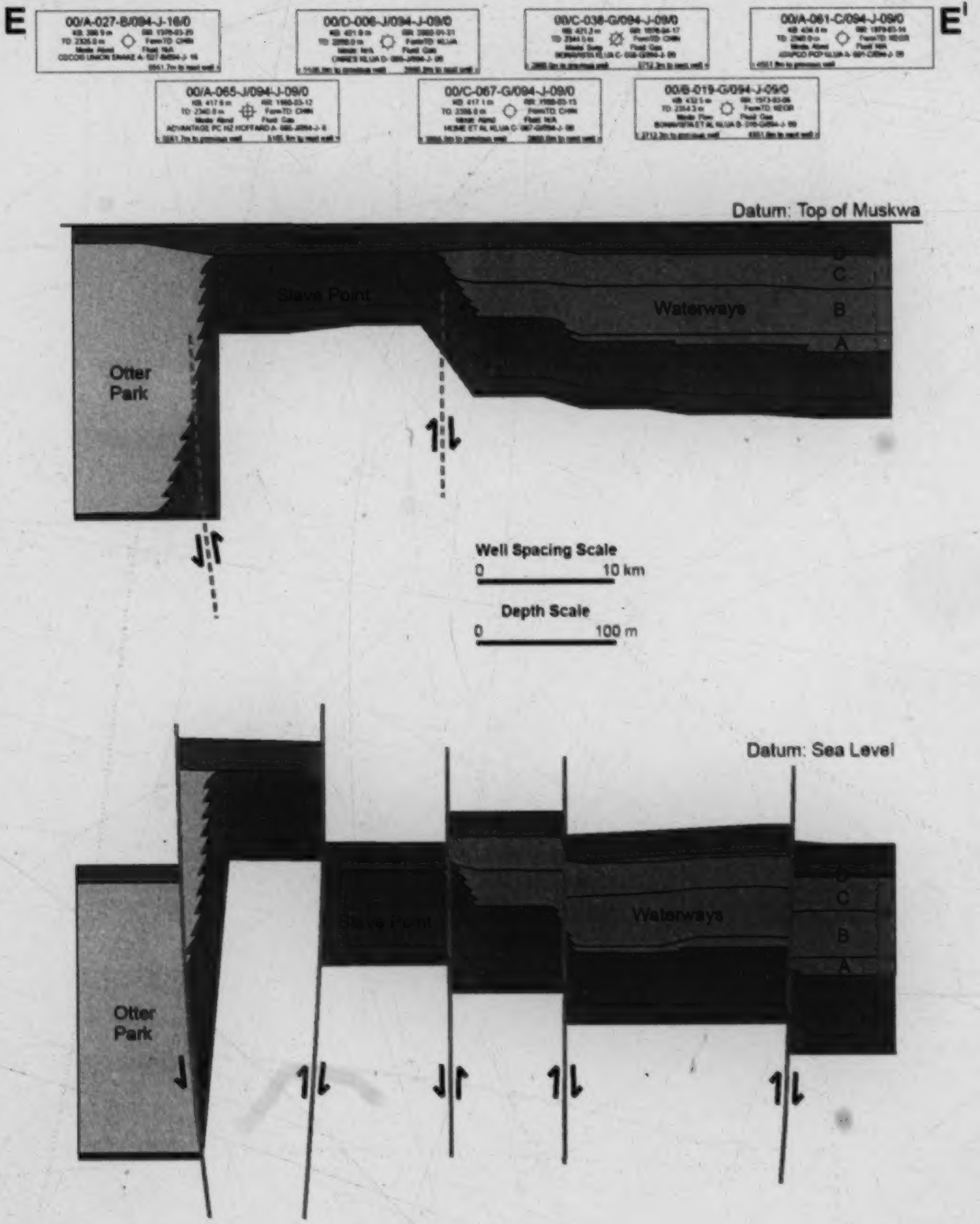
E
00/A-027-B/094-J-16/0
00/A-065-J/094-J-09/0
00/D-006-J/094-J-09/0
00/C-067-G/094-J-09/0
00/C-038-G/094-J-09/0
00/B-019-G/094-J-09/0
00/A-061-C/094-J-09/0
E'
Datum: Top of Muskwa
Slave Point
Waterways
D
C
B
A
Otter Park
Well Spacing Scale
0
10 km
Depth Scale
0
100 m
Datum: Sea Level
Slave Point
Waterways
D
C
B
A
Otter Park

Figure 2.7 Stratigraphic (top) and structural (bottom) cross-sections E-E'. The top of the Muskwa Formation was used as a datum in the stratigraphic section, sea level as the datum in the structural section.

margin may point toward an initial structural control (Figure 2.7). Moving south, the top of the Slave Point Formation occurs at roughly the same level until reaching the north edge of the Waterways basin. Compared to the west side of the Clarke Lake field (section D-D'), in section E-E' there is no evidence for the deposition of Otter Park shale on top of the Slave Point Formation (Figure 2.7). This suggests that the Slave Point along the east side of the study area was at an overall higher elevation. Along the northern edge of the Waterways basin, there is evidence for Slave Point back-stepping between wells c-67-G and d-6-J (Figure 2.7). The proposed reasons for the movement of the Slave Point Formation have been outlined in section 2.5.1.

The structural cross-section E-E' is dominated by the movement of the Slave Point Formation at the northern platform margin into a high present-day structural elevation (Figure 2.7). As was previously discussed, the present structural configuration can lead to the misinterpretation of the original depositional conditions, i.e., facies and bathymetry. To the south in the Waterways basin, structure forms several potential traps in fault blocks, but to a lesser degree from that exhibited in Figure 2.6.

2.5.3 Cross-section F-F'

Cross-section F-F' is also a depositional dip section that crosses sections D-D' at roughly right angles near the centre of the study area (Figure 2.5). At this position, the stratigraphic cross-section shows the development of a thick package of Otter Park Formation shale that onlaps/covers the Slave Point Formation (Figure 2.8). Near wells c-96-I and c-85-I, a thick tongue of Otter Park shale overlies the Slave Point Formation, possibly indicating a relative rise in sea-level during latest Slave Point deposition (Figure 2.8). The top of the Slave Point Formation occurs at higher levels towards the south and east. The overall rise in the top of the Slave Point Formation may coincide with the development of an elevated Slave Point margin bounding the Waterways basin (see Figure 2.6). There is no evidence for structural control of deposition in this section.

Similar to cross-section E-E', the structural cross-section F-F' is dominated by the movement of the Slave Point Formation at the platform margin into a much higher present-day structural elevation (Figure 2.8). The increase in elevation of the Slave Point at the margin with a concomitant decrease in elevation immediately behind this block may be confused with a depositional regime of emergent reef and deeper-water back-reef lagoon.

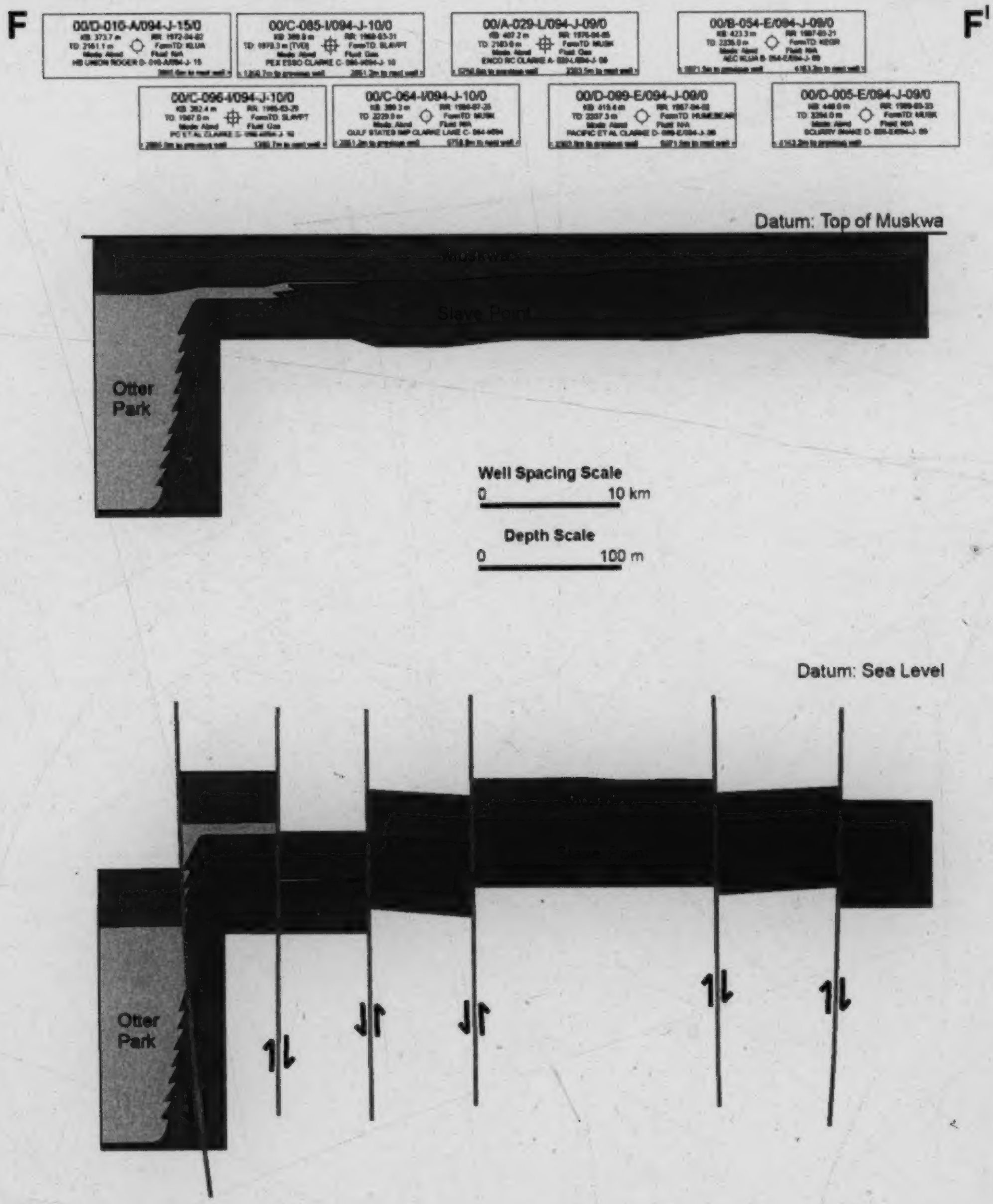
F
00/D-010-A/094-J-15/0
00/C-085-I/094-J-10/0
00/A-029-L/094-J-09/0
00/B-054-E/094-J-09/0
F'
00/C-096-I/094-J-10/0
00/C-064-I/094-J-10/0
00/D-099-E/094-J-09/0
00/D-005-E/094-J-09/0
Datum: Top of Muskwa
Muskwa
Slave Point
Otter Park
Well Spacing Scale
0
10 km
Depth Scale
0
100 m
Datum: Sea Level
Otter Park

Figure 2.8 Stratigraphic (top) and structural (bottom) cross-sections F-F'. The top of the Muskwa Formation was used as a datum in the stratigraphic section, sea level as the datum in the structural section.

Across much of the platform interior though, there appears to have been very little post-depositional movement (Figure 2.8). However, relative to the number of fault-bounded blocks in cross-section E-E', cross-section F-F' is further evidence that the Slave Point Formation was affected by faults with a dominant north-south orientation, which provides a seismic exploration tool.

2.5.4 Cross-section G-G'

Cross-section G-G' roughly parallels the Slave Point platform margin at an equal distance (Figure 2.5). This cross-section is drawn from the far west side of the Clarke Lake field to the edge of the Klua Embayment in the east. The cross-section does not traverse the platform margin anywhere along its length.

Overall, the top of the Slave Point Formation shows a general increase in stratigraphic elevation towards the center of the Clarke Lake field, followed by a similar decrease in elevation towards the east (Figure 2.9). It is difficult to make any judgments regarding this stratigraphic since it is impossible to know if the Slave Point along the entire cross-section was at the same bathymetric position during deposition. However, a few conclusions can be drawn. Firstly, the occurrence of a thin tongue of Otter Park Formation shales across much of the section points to an increase in relative sea-level during the terminal stages of Slave Point deposition (Figure 2.9). Secondly, the absence of Otter Park shale in well c-20-I near the center of the field may indicate either the Slave Point Formation back-stepped to this location, or this position represents a reefal-type buildup somewhat removed from the platform margin (Figure 2.9). Thirdly, a marked increase in the thickness of the overlying Muskwa Formation shale without an intervening layer of Otter Park shale along the east side of the cross-section implies the top of the Slave Point Formation was in a higher position at the end of Slave Point time and rapidly subsided prior to, or concurrent with, deposition of the Muskwa Formation (Figure 2.9). With the exception of the area around well b-70-I, there is little evidence for structural control on deposition. Hence, the increased subsidence of the Slave Point along the east side of the section during relatively late depositional times is probably related to the fact that the Slave Point prograded outward to rest directly on shale that filled the Klua Embayment.

The present-day structural configuration along section G-G' is complex (Figure 2.9). Similar to section D-D', the most obvious elements are numerous horsts and grabens.

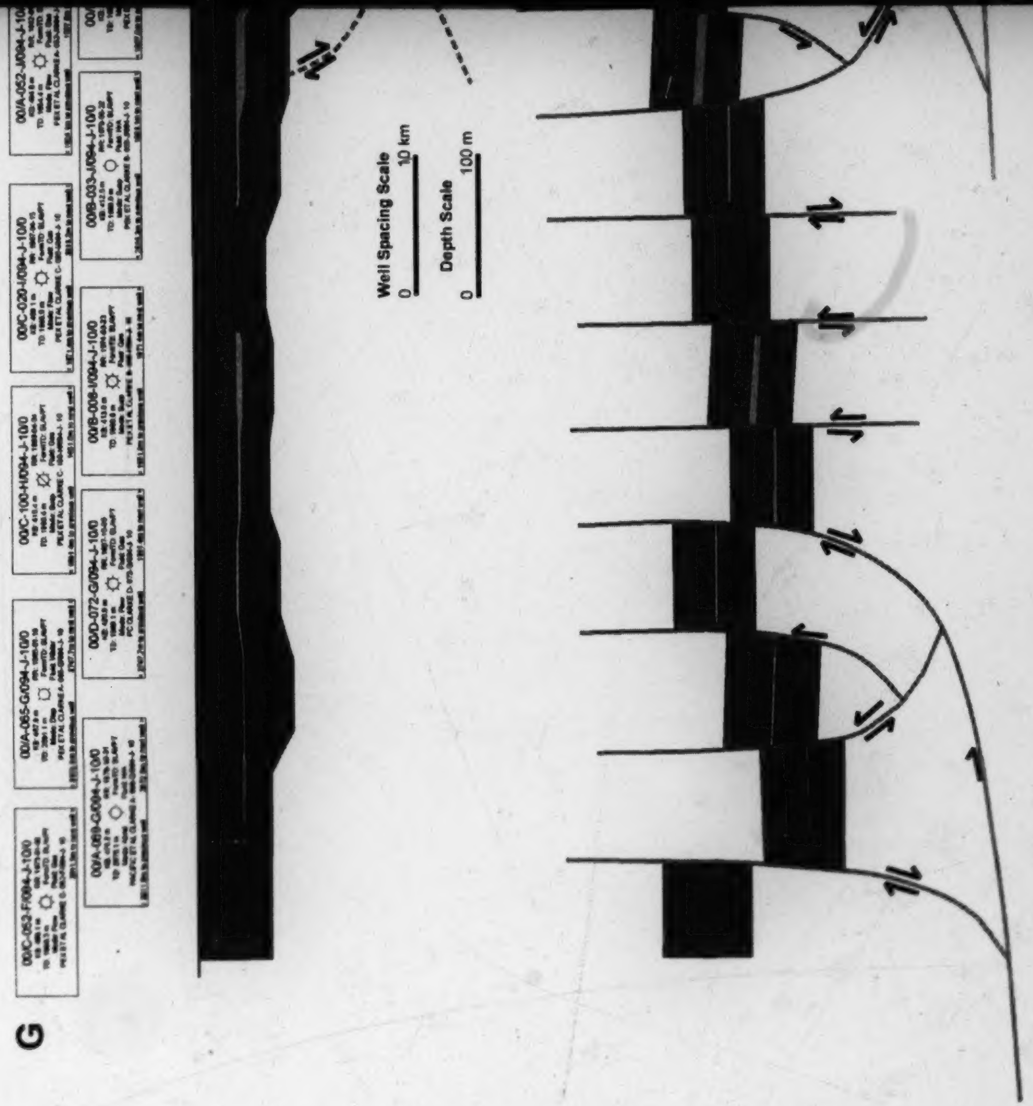
G
00/C-052-F/094-J-10/0
00/A-065-G/094-J-10/0
00/C-100-H/094-J-10/0
00/C-020-I/094-J-10/0
00/A-052-J/094-J-10
00/A-069-G/094-J-10/0
00/D-072-G/094-J-10/0
00/B-008-I/094-J-10/0
00/B-033-J/094-J-10/0
Well Spacing Scale
0
10 km
Depth Scale
0
100 m

Figure 2.9 Stratigraphic (top) and structural (bottom) cross-sections G-G'. The top of the Muskwa Formation was used as a datum in the stratigraphic section, sea level as the datum in the structural section.

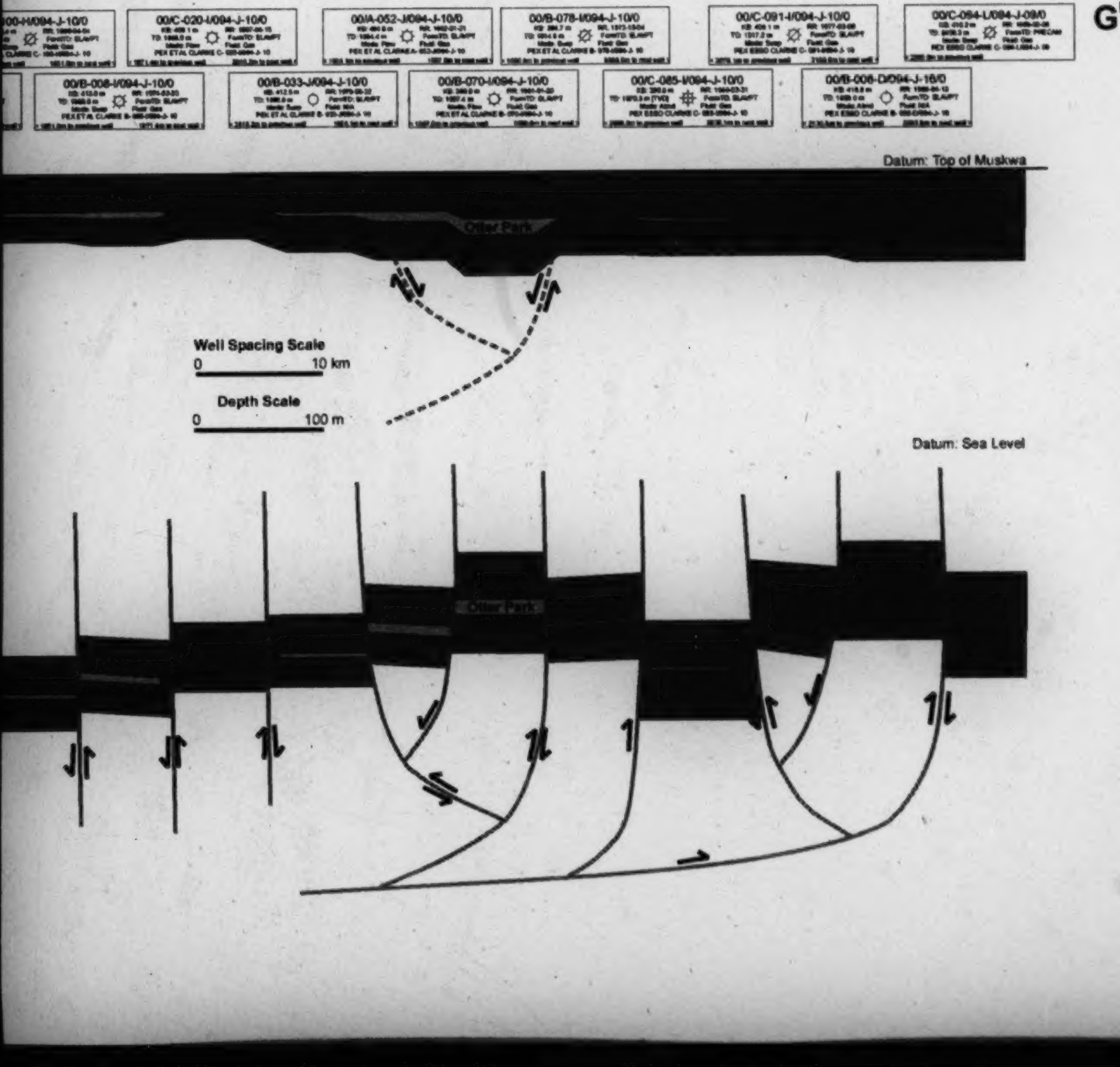
00-H/094-J-10/0
00/C-020-I/094-J-10/0
00/A-052-J/094-J-10/0
00/B-078-I/094-J-10/0
00/C-091-I/094-J-10/0
00/C-094-L/094-J-09/0
G'
00/B-008-I/094-J-10/0
00/B-033-J/094-J-10/0
00/B-070-I/094-J-10/0
00/C-085-I/094-J-10/0
00/B-006-D/094-J-16/0
Datum: Top of Muskwa
Otter Park
Well Spacing Scale
0
10 km
Depth Scale
0
100 m
Datum: Sea Level
Otter Park

There is structural inversion in the Slave Point Formation within the Klua Embayment to the east, which is currently in a structurally high position (Figure 2.9). Conversely, the once elevated top of the Slave Point Formation near well c-20-I in the center of the Clarke Lake field is presently sitting in a structurally low position (Figure 2.9). It is, therefore, obvious that the present structural configuration across the Clarke Lake field bears very little relationship to the original depositional configuration.

CHAPTER 3

DEPOSITIONAL FACIES IN THE SLAVE POINT FORMATION

3.1 Introduction

After having established stratigraphic relationships for the Slave Point Formation based on the cross-sections presented in Chapter 2, the objectives of Chapter 3 are to: 1) provide a comprehensive review of the original carbonate depositional facies and, 2) generate a depositional facies interpretation for the Slave Point Formation at Clarke Lake. These objectives were achieved through the detailed examination of limestone and dolomite samples using subsurface core and thin-section petrographic techniques.

3.2 Methods

During the summer of 2000, twenty-eight (28) subsurface cores from the Slave Point Formation at Clarke Lake were logged and sampled at the British Columbia Ministry of Energy and Mines core warehouse in Charlie Lake, B.C (Appendix I). The cores were examined to identify facies variations and to characterize the distribution of both dolomite and reservoir porosity. The majority of the cores that were sampled are from gas wells that are situated at, or within a few kilometres of, the Slave Point platform margin (Figure 3.1). Cores were classified according to the carbonate classification scheme of Dunham (1962), modified by Embry and Klovan (1971) (Figure 3.2). The cores were investigated at a metre-scale with respect to their gross facies distribution using the carbonate facies model developed by Machel and Hunter (1994) for Middle to Late Devonian shallow-marine carbonates. The Machel and Hunter (1994) model was used for several reasons. Firstly, it integrates data from most of the important studies dealing with Devonian reefs in North America, Europe, and Australia. Secondly, it provides a tool for quick and accurate assessment of carbonate facies in core and outcrop using macroscopic parameters such as sorting, rounding, texture, amount of micrite, porosity types, and fossil assemblage. Thirdly, it contains information on the whole spectrum of carbonate facies from off-reef to intertidal environments.

A total of 383 samples were obtained from the Slave Point cores, from which 195 polished thin sections were made (Appendix III). The thin sections were stained with a mixture of Alizarin Red-S and potassium ferricyanide to determine carbonate mineral

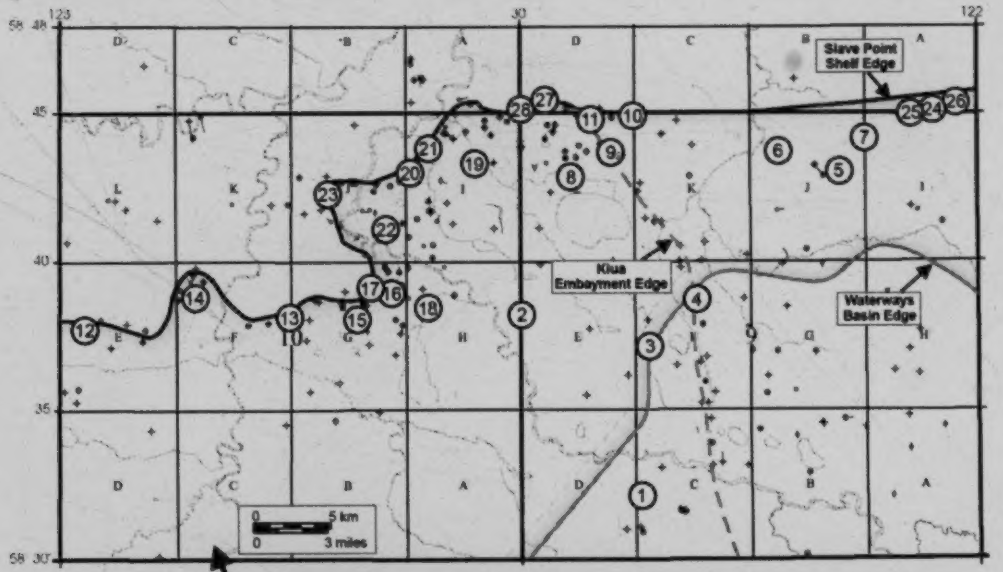
123
30
122
58 45
45
40
35
58 30
D
C
B
A
L
K
J
I
E
F
G
H
Slave Point Shelf Edge
Kiua Embayment Edge
Waterways Basin Edge
0 5 km
0 3 miles
1
2
3
4
5
6
7
8
9
10
11
12
13
14
15
16
17
18
19
20
21
22
23
24
25
26
27
28

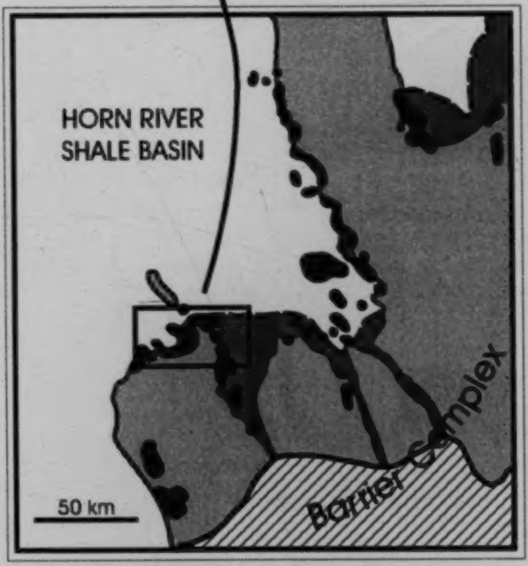
HORN RIVER SHALE BASIN
Barrier Complex
50 km

Figure 3.1 (Left) Location map of the Clarke Lake study area. The inset rectangle represents the area shown above. See Figure 1.1 for further explanation. (Top) Detailed map of the Clarke Lake field showing the location of the wells containing core from the Slave Point Formation. (Right) Table of well locations. Informal abbreviated well locations which occur in the text are also listed.

Number	Well Location	Abbrev.
1	a-50-C/94-J-9	a-50-C
2	c-70-E/94-J-9	c-70-E
3	b-49-F/94-J-9	b-49-F
4	b-75-F/94-J-9	b-75-F
5	a-63-J/94-J-9	a-63-J
6	b-78-J/94-J-9	b-78-J
7	a-81-J/94-J-9	a-81-J
8	c-56-L/94-J-9	c-56-L
9	b-72-L/94-J-9	b-72-L
10	d-91-L/94-J-9	d-91-L
11	c-94-L/94-J-9	c-94-L
12	c-58-E/94-J-10	c-58-E
13	a-61-F/94-J-10	a-61-F
14	d-79-F/94-J-10	d-79-F
15	a-65-G/94-J-10	a-65-G
16	d-72-G/94-J-10	d-72-G
17	a-83-G/94-J-10	a-83-G
18	d-69-H/94-J-10	d-69-H
19	c-64-I/94-J-10	c-64-I
20	b-70-I/94-J-10	b-70-I
21	c-78-I/94-J-10	c-78-I
22	b-22-J/94-J-10	b-22-J
23	c-47-J/94-J-10	c-47-J
24	a-5-A/94-J-16	a-5-A
25	b-6-A/94-J-16	b-6-A
26	b-12-A/94-J-16	b-12-A
27	c-8-D/94-J-16	c-8-D
28	b-10-D/94-J-16	b-10-D

<table>
<tr><td colspan="6">Original components not organically bound during deposition</td><td colspan="3">Original components organically bound during deposition</td></tr>
<tr><td colspan="4">of the allochems, less than 10% > 2 mm</td><td colspan="2">of the allochens more than 10% > 2 mm</td><td colspan="3">boundstone</td></tr>
<tr><td colspan="3">contains carbonate mud (particles less than 0.03 mm diameter)</td><td>mud absent</td><td rowspan="3">matrix supported</td><td rowspan="3">grain supported</td><td rowspan="3">organisms acted as baffles</td><td rowspan="3">organisms encrusting and binding</td><td rowspan="3">organisms building a rigid framework</td></tr>
<tr><td colspan="2">mud-supported</td><td colspan="2" rowspan="2">grain-supported</td></tr>
<tr><td>less than 10% grains</td><td>more than 10% grains</td></tr>
<tr><td>mud-stone</td><td>wacke-stone</td><td>pack-stone</td><td>grain stone</td><td>float-stone</td><td>rud-stone</td><td>baffle-stone</td><td>bind-stone</td><td>frame-stone</td></tr>
</table>

Figure 3.2 Carbonate classification by Dunham (1962), modified by Embry and Klovan (1971).

composition (Dickson, 1965). All thin sections were examined by transmitted light microscopy using a Zeiss Jenapol polarizing microscope, and by cathodoluminescence (CL) microscopy using a cold cathode Premier American Technologies ELM-3R Luminoscope. The operating conditions were maintained at 14-16 kV and 0.5 mA under a vacuum of 30-50 millitorr to provide consistency of results.

3.3 Facies in the Slave Point Formation

3.3.1 General

The sedimentology of the Slave Point Formation is herein characterized using the concepts of facies sequences and facies analysis. These concepts involve consideration of the vertical sequence of facies changes to determine larger-scale depositional processes and environments (Tucker and Wright, 1990).

A facies is a body of rock defined by the association of sedimentary characteristics, such as lithology, texture, composition, sedimentary structures, fossil content, and colour (Tucker and Wright, 1990). Facies boundaries migrate laterally as a result of transgressions and regressions, which suggests that the vertical facies succession in platform carbonates, like the Slave Point Formation, is controlled primarily by changes in sea level. The facies model of Machel and Hunter (1994) for Middle to Late Devonian shallow-marine carbonates distinguishes between fore-reef, reef-core, and back-reef depositional environments (Figure 3.3). As a result, this model can only be applied to reefs that have diversified into distinct facies zones, i.e., reefs that have reached the diversification and domination stages of growth (James, 1983). Reefs that have not undergone diversification, i.e., during the pioneer and colonization stages of growth, do not usually exhibit facies zonation.

All facies types described in Machel and Hunter (1994) were encountered in the Slave Point Formation at Clarke Lake. Using their (ibid.) facies model, the Slave Point carbonates were subdivided into five distinct facies zones based on the degree of wave energy: increasing in energy from I to IV. From this model, the fore-reef zones are narrower than the back-reef zones of comparable wave energy due to the change in the slope. The reef-core represents the highest energy zone, and is subdivided into facies IV/V and V based on the fossil assemblage. In addition to the eight facies zones defined for the Slave Point Formation using the Machel and Hunter (1994) model, a ninth facies zone, the patch reef facies, which is not included in their (ibid.) model, is identified in this study.

3.3.2 Previous studies

There are no previously published facies analyses of the Slave Point Formation at Clarke Lake. There are, however, two earlier proprietary consultant reports that have attempted to provide a depositional facies interpretation at Clarke Lake.

SB Geological Associates (1988), in a core study of the Slave Point Formation, suggested that sediments were deposited on a broad carbonate ramp south of the platform margin. They (ibid.) further subdivided the carbonate ramp into four main facies: basinal, lower ramp, middle ramp, and upper ramp. SB Geological Associates (1988) also demarcated the platform margin of the Slave Point by the presence of well-defined reefal and high-energy grainstone deposits. Their basinal facies consists of crinoids, brachiopods, and pelecypods floating in a matrix of dark brown, silty mudstone (SB Geological Associates, 1988). Their (ibid.) lower ramp facies is characterized by crinoids, cylindrical stromatoporoids, and brachiopods scattered in a dark brown, micrite matrix. The middle ramp facies was further subdivided into lower middle ramp, middle middle ramp, and upper middle ramp; however, characteristic in all of these zones is the presence of *Amphipora*, *Thamnopora*, *Stachyodes*, and minor occurrences of nodular to bulbous stromatoporoids. SB Geological Associates (1988) interpreted these facies zones to represent back-reef depositional environments,

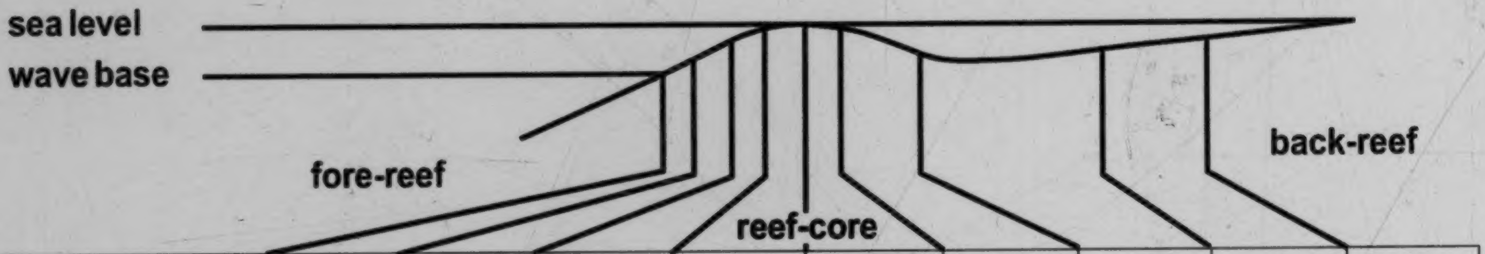

		If	IIf	IIIf	IVf	IV/V	V	IVb	IIIb	IIb	Ib
A	WATER ENERGY	quiet water below wave base negligible turbulence	intermittently agitated water episodic turbulence	slightly agitated water moderate turbulence	moderately agitated water strong turbulence	strongly agitated water strong turbulence		moderately agitated water strong turbulence	slightly agitated water moderate turbulence	intermittently agitated water episodic turbulence	intermittently agitated water episodic turbulence
	ROUNDING	mostly original fossil shapes	poor to good	moderate to good	good to moderate	very good to moderate		good to moderate	moderate to good	poor to good	mostly original fossil shapes
	SORTING	angular fragments if broken	matrix: good fossils: poor to good	matrix: moderate fossils: moderate to good	good to moderate	matrix: moderate fossils: poor		good to moderate	matrix: moderate fossils: moderate to good	matrix: good fossils: poor to good	angular fragments if broken
B	TEXTURE	packstones grainstones mudstones	packstones grainstones rare floatstones	floatstones grainstones rare rudstones	rudstones bafflestones	rudstones bindstones rare grainstones	bindstones framestones rudstones	rudstones bafflestones	floatstones grainstones rare rudstones	packstones grainstones	mudstones wackestones
C	AMOUNT OF MICRITE	primary micrite increasing ←				fibrous calcite, sparite, micrite		→ primary micrite increasing			
D	POROSITY TYPES	intraparticle	intraparticle interparticle	interparticle shelter voids intraparticle	shelter voids growth framework interparticle	shelter voids interparticle	shelter voids growth framework interparticle	shelter voids growth framework interparticle	shelter voids intraparticle interparticle	intraparticle interparticle fenestral	intraparticle fenestral
	SIZE OF PORES		small	medium to small	medium to small	large to medium	medium to small	large to medium	medium to small	small	
	AMOUNT OF POROSITY	below 10%	up to 10% but mostly below 5%	up to 15%	up to 10%	up to 25%	up to 10%	up to 40%	up to 10%	up to 20%	up to 30%
E	FOSSIL ASSEMBLAGE	calcispheres foraminifers	small crinoids	large crinoids	*Thamnopora* *Stachyodes* brachiopods crinoids *Renalcis*	crinoids tabular stromatoporoids	bulbous & massive stromatoporoids micrite envelopes syntaxial rim cements	*Stachyodes* *Renalcis*	*Amphipora* ostracods	algae (fenestral pores)	algae (fenestral laminites)
F	INDICATOR FOSSILS	crinoids / brachiopods				crinoids *Solenopora* *Keega*		*Amphipora*/ calcispheres/ ostracods/ encrusting *Sphaerocodium*			

Figure 3.3 Facies model for Middle to Late Devonian reef carbonates. Modified after Machel and Hunter (1994).

including protected lagoons and patch reefs. The upper ramp facies was distinguished by the occurrence of light coloured mudstones that contain scattered gastropods, ostracodes, and thin-shelled brachiopods (SB Geological Associates, 1988). They (ibid.) interpreted this facies to have formed in an intertidal zone.

A subsequent study by Davies (1999) found that both seismic and petrographic data are more supportive of an overall carbonate rimmed shelf model for deposition of the Slave Point Formation at Clarke Lake. Davies (1999) suggested that south of the rimmed margin, the Slave Point Formation may have taken on a ramp-like character, and progressively deepened in a southward direction. Seven distinct facies were identified in this study, including basinal, deep foreslope, middle to upper foreslope, restricted intertidal, restricted shelf, open shelf, and deep shelf (Davies, 1999). Based on his facies analysis, the most important conclusion drawn by Davies (1999) was that none of the facies zones actually constituted a true reefal facies, i.e., 'ecological' reef of Dunham (1970); rather, the wave-resistant structure at the platform margin was likely a carbonate shoal.

Two studies have been conducted on the Slave Point Formation fringing the Hotchkiss Embayment, located roughly 300 kilometres to the southeast of the Clarke Lake field, and can be used for comparison. In the first of these studies, Clarke (1998), in her examination of the Hamburg field in Alberta, identified seven facies types within the Slave Point Formation. These facies included interbedded mudstone and *Amphipora* rudstone, *Amphipora* rudstone, stromatoporoid floatstone, hemispherical stromatoporoid framestone, stromatoporoid floatstone to rudstone, wackestone, and grainstone. The interbedded mudstone and *Amphipora* rudstone facies is composed of organisms adapted to low energy environments and high rates of sedimentation, and contains thin-shelled brachiopods and crinoids (Clarke, 1998). She (ibid.) suggested that this facies represents deposition in an environment with fluctuating sea levels, such as a shallow shelf or lagoon. The *Amphipora* rudstone facies includes small, bulbous and cylindrical stromatoporoids, with subordinate amounts of gastropods, crinoids, and brachiopods floating in a fine-grained mud matrix, which was interpreted to represent deposition in a back-reef, slightly restricted marine setting (Clarke, 1998). The stromatoporoid floatstone and hemispherical stromatoporoid framestone facies were likely deposited in similar depositional environments, i.e., in the reef-core (Clarke, 1998). The stromatoporoid floatstone to rudstone and wackestone facies are generally dark brown in colour and contain abundant corals, crinoids, and brachiopods, and suggest deposition in a wave-agitated fore-reef environment (Clarke, 1998). Finally, a grainstone facies was found in one core, and contains fragments of stromatoporoids in a matrix consisting principally of corals, crinoids, and brachiopods that were deposited in a high-energy, shallow-marine environment (Clarke, 1998).

Sack (2002), in a study of the Slave Point Formation in the Cranberry field of Alberta, approximately 50 kilometres due east of the Hamburg field, identified ten distinct facies. These facies types include: mudstone, nodular wackestone, coral wackestone, *Stachyodes-Thamnopora* floatstone, tabular stromatoporoid floatstone to rudstone, *Amphipora* rudstone, tidal laminite, hemispherical stromatoporoid rudstone to boundstone, packstone, and bulbous stromatoporoid grainstone. Many of these facies have characteristics that are identical to the facies indentified by Clarke (1998), and have been interpreted as deposits in similar environments.

Farther towards the south, three more studies have been conducted on the Slave Point Formation fringing the Peace River Arch, and can also be used for comparison. These include the study of the Slave field (Dunham et al., 1983), the Golden and Evi fields (Gosselin et al., 1989), and the Dawson field (Keilly, 2005). All of these studies documented similar facies and facies relationships. Dunham et al. (1983) were able to distinguish four distinct facies types, including: carbonate mudstone, stromatoporoid boundstone, *Amphipora* floatstone to rudstone, and dolomite mudstone. The carbonate mudstone consisted of a matrix of dark-brown argillaceous carbonate mud containing scattered crinoids and brachiopods with isolated stromatoporoids. They (ibid.) concluded that this facies is representative of deposition on an open-marine shelf below fair weather wave base. The stromatoporoid boundstone facies consists of small, tabular and bulbous stromatoporoids that were deposited in a high-energy, normal-marine environment characteristic of the shallow fore-reef to reef-core (Dunham et al., 1983). The *Amphipora* floatstone to rudstone facies includes small nodular stromatoporoids, and was interpreted to represent deposition under shallow-water, restricted-marine conditions typical of lagoonal environments (Dunham et al., 1983). Finally, they (ibid.) identified a dolomite mudstone facies that is devoid of macroscopic fossils, has laminations and fenestral pores, and was interpreted to represent restricted-marine carbonate conditions relatively close to the paleoshoreline.

Gosselin et al. (1989) identified three main facies types during the examination of the Slave Point Formation in the Golden and Evi fields. These included open marine facies, platform margin facies, and platform interior facies. The open marine facies consists of off-reef, mud-dominated sediments that contain abundant crinoids and brachiopods (Gosselin et al., 1989), similar to the carbonate mudstone of Dunham et al. (1983). The platform margin facies envelops the entire zone from shallow fore-reef through reef-core to back-reef (Gosselin et al., 1989). In this regard, the facies at Golden and Evi are similar to the facies analysis at Clarke Lake following Davies (1999). Gosselin et al. (1989) further subdivided the platform margin facies into four sub-facies: *Stachyodes-Thamnopora* rudstone to floatstone, tabular stromatoporoid boundstone, hemispherical stromatoporoid boundstone, and stromatoporoid and *Amphipora* rudstone to floatstone. All of these sub-facies types and their environmental interpretations are identical to those discussed by Sack (2002) for the Slave Point Formation in the Cranberry field (see above). The platform interior facies consisted of *Amphipora*-rich floatstones and dark brown, pelletal mudstones, which were interpreted to represent deposition in the restricted-marine environment behind the reef-core (Gosselin et al., 1989).

Finally, Keilly (2005), in a study of the Slave Point Formation in the Dawson field, identified eight distinct facies using the facies model of Machel and Hunter (1994). These include: intertidal mudstone to wackestone, fossiliferous packstone to wackestone, *Amphipora* floatstone to grainstone, stromatoporoid rudstone to bafflestone, reef-core bindstone to rudstone, fore-reef bafflestone to rudstone, crinoid and stromatoporoid floatstone to rudstone, and crinoid floatstone to mudstone. Both the intertidal mudstone to wackestone and the fossiliferous packstone to wackestone facies are equivalent to the platform interior facies of Gosselin et al. (1989). The *Amphipora* floatstone to grainstone facies contains scattered stromatoporoids and gastropods in a dark brown muddy matrix, and was interpreted to have formed in shallow-water, restricted-marine conditions typical of back-reef lagoons (Keilly, 2005). The stromatoporoid rudstone to bafflestone through fore-reef bafflestone to rudstone facies are equivalent to the platform margin facies defined by Gosselin et al. (1989). This facies zone is representative of the narrow zone between the shallow fore-reef and the back-reef environments. The final two facies types identified by Keilly (2005), the crinoid-rich floatstone through mudstone, are similar to the carbonate mudstones of Dunham et al. (1983), which consisted of a matrix of dark-brown argillaceous carbonate mud containing scattered crinoids and brachiopods with isolated stromatoporoids. These facies were likewise interpreted to have been deposited on an open-marine shelf below fair weather wave base (Keilly, 2005).

The facies interpretations forwarded by these previous studies will be used below to aid in the identification of facies in the Slave Point Formation and their distribution within the Clarke Lake study area.

3.3.3 Facies zone If

Facies zone If is a fine-grained fore reef facies that is characterized by dark brown to black mudstones to siltstones with a weakly laminated fabric (Plate 3.1A). Generally, this facies zone is devoid of any macroscopic fossils, although, where present, small, fragmented crinoid ossicles and brachiopod shells comprise maximum 10% of the total rock volume. The matrix consists dominantly of micrite and scattered calcispheres. Primary porosity is not well developed in this facies.

This facies is representative of deposition in a low-energy basinal environment that was below storm wave base, similar to the open-marine facies identified by previous researchers (see above). An estimate for water-depth is hard to determine for this facies, but according to Wendte (1992), from his study of the Devonian Swan Hills reef buildups in northern Alberta, deposition likely occurred in water depths on the order of 10's of metres. This, and subsequent, water depth estimate(s) were based on textural and facies relationships, and on comparisons with Recent analogues.

3.3.4 Facies zone IIf

Facies zone IIf consists of dark brown mudstones to packstones that lack the development of laminations that are characteristic of facies zone If (Plate 3.1B and C). The dominant macrofossils include mm-sized crinoid ossicles, brachiopod shells, and rare cylindrical stromatoporoids that are generally fragmented and poorly to well rounded, indicating they are from higher up on the slope. The matrix consists dominantly of micrite. Primary porosity in this facies is limited to intraparticle pores and concomitant permeability is, therefore, quite low.

This facies indicates deposition in a relatively deep basinal environment at or near fair weather wave base. Additionally, the lack of framework building organisms suggests this facies was deposited far from the site where reef organisms were actively growing.

Plate 3.1 Facies zones If to IIIf

(A) Core photograph of mudstone devoid of macroscopic fossils and displaying syn-sedimentary deformation structures. The upper third of the photo consists of dolomite. Facies zone If. b-70-I/94-J-10; 6263'.

(B) Core photograph showing millimetre-sized crinoid (arrows) and brachiopod wackestone to packstone. Much of the original limestone has been replaced by matrix and replacement saddle dolomite. Facies zone IIf. b-70-I/94-J-10; 6267'6".

(C) Core photograph of crinoid-brachiopod mudstone to packstone. Facies zone IIf. c-70-E/94-J-9; 6383'6".

(D) Core photograph of crinoid-brachipod floatstone. Facies zone IIIf. c-8-D/94-J-16; 6319'9".

Plate 3.1: Facies Zones If to IIIf

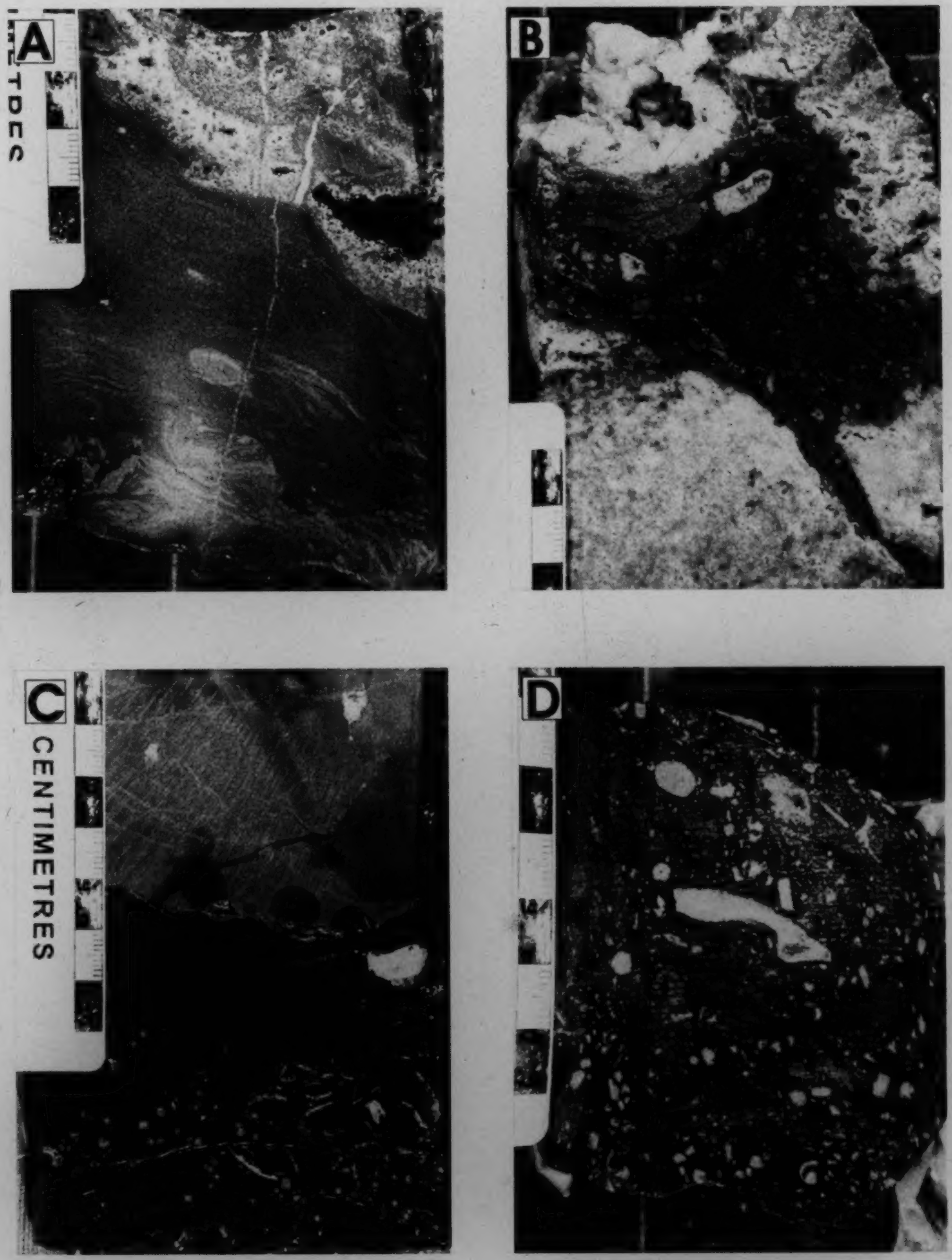
A
B
C
CENTIMETRES
D

Therefore, deposition of facies zone IIf occurred in a paleo-water depth of 10's of metres, similar to facies zone If.

3.3.5 Facies zone IIIf

Facies zone IIIf is characterized by relatively heterogeneous floatstones that consist principally of large crinoids, but also includes fragments of thick-shelled brachiopods, cylindrical stromatoporoids, and corals that are moderately to well rounded, and moderately sorted (Plate 3.1D). The matrix is composed of micrite, peloidal grains, and ostracodes. The primary porosity in this facies is mainly in interparticle pores, and rarely shelter voids.

This facies is interpreted to have been deposited in the lower fore-reef environment around fair-weather wave base. The episodic turbulence in this zone led to the accumulation of crinoid-rich zones in depression and/or channels, while the muddy nature of the matrix suggest deposition in a relatively quiet water environment where lime mud was able to settle out of suspension and would not regularly be winnowed. This facies is still equivalent to the "open-marine" facies of the previous researchers (see above). However, it represents a decreased paleo-water depth compared to either facies zone If or IIf.

3.3.6 Facies zone IVf

Facies zone IVf is characterized by light to dark brown, floatstones to rudstones. Bioclasts include abundant *Stachyodes*, *Thamnopora*, and crinoids in a fine-grained matrix (Plate 3.2). Many of the biochems are well rounded, and the overall fabric of this facies is moderately to well sorted. The matrix consists of micrite, peloidal grains, and other biogenic debris, including fragments of brachiopods and gastropods. The primary porosity is in interparticle pores and shelter voids.

The abundance and types of biochems in this facies suggest both higher energy and oxygen levels relative to the previously discussed facies zones. The diversity in open-marine fauna in this facies zone supports a relatively shallow-water environment that was well above wave base and well circulated, typical of the relatively shallow fore-reef. This facies is similar to the fore-reef platform margin facies identified by Gosselin et al. (1989), the fore-reef bafflestone to rudstone facies of Keilly (2005), or the *Stachyodes-Thamnopora* floatstone facies of Sack (2000). Applying the bathymetric estimates of Wendte (1992), deposition of this facies probably occurred in water depths between 10 and 20 metres.

Plate 3.2 Facies zone IVf

(A) Core photograph of *Thamnopora* floatstone. a-63-J/94-J-9; 1978.0 m.

(B) Core photograph of *Thamnopora* rudstone in a crinoid (arrow) packstone matrix. a-63-J/94-J-9; 1981.7 m.

(C) Core photograph of stromatoporoid-coral floatstone-rudstone in a crinoid (arrows) packstone matrix. Th = *Thamnopora*, St = *Stachyodes*. a-63-J/94-J-9; 1981.3 m.

(D) Core photograph of stromatoporoid-coral floatstone-rudstone. Th = *Thamnopora*, St = *Stachyodes*. b-6-A/94-J-16; 6351'6".

Plate 3.2: Facies Zone IVf

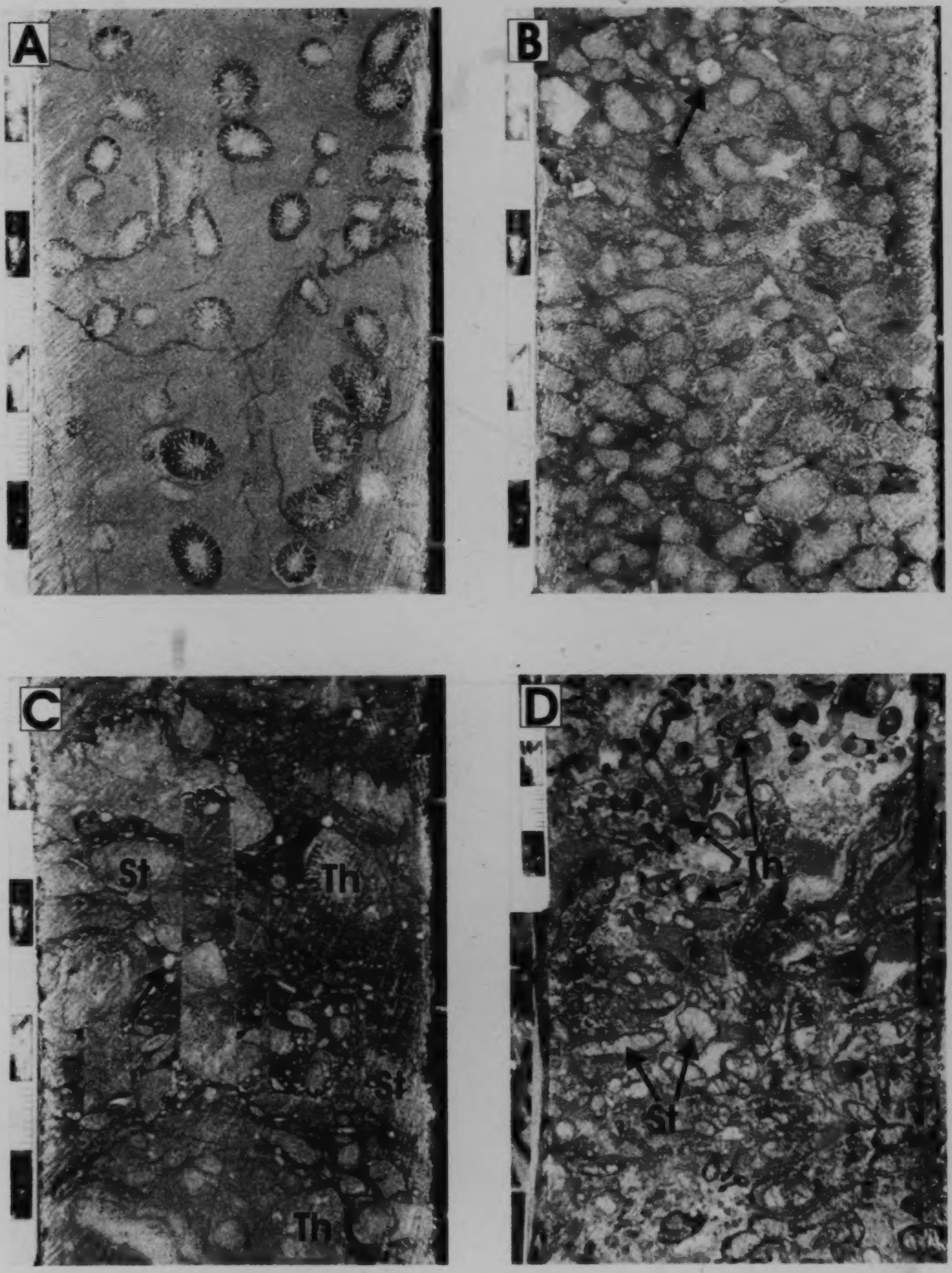
A
B
C
St
Th
St
Th
D
Th
St

3.3.7 Facies zone IV/V

Facies zone IV/V consists of light to dark brown rudstones to bindstones with a skeletal grainstone matrix (Plate 3.3). Bioclasts consist dominantly of massive stromatoporoids, including *in situ* 3-4 cm-thick tabular stromatoporoids and *Stachyodes* that are well rounded but poorly sorted. Accessory fauna include bulbous stromatoporoids, *Thamnopora*, and crinoids. The matrix of this facies consists of peloidal grains, crinoid ossicles, fragments of brachiopods and gastropods, and micrite. Primary porosity is due to both interparticle pores and shelter voids.

This facies zone represents a high-energy, shallow-water environment that is interpreted to represent the basinward side of the reef-core. This facies is similar to the reef margin facies identified by Gosselin et al. (1989), Sack (2000), and Keilly (2005). Deposition of this facies likely occurred between sea level and about 10 metres water depth (Wendte, 1992).

3.3.8 Facies zone V

Facies zone V consists of light brown rudstones to framestones containing a subordinate quantity of crinoid and cylindrical stromatoporoid grainstone matrix (Plate 3.4). Bioclasts consist primarily of decimetre-size, *in situ* massive to bulbous and hemispherical stromatoporoids. Allochems are well rounded and poorly to moderately sorted. The matrix of this facies consists dominantly of peloidal grains, with minor occurrences of crinoid ossicles, fragments of gastropods, and trace quantities of micrite. Primary porosity is due to the presence of interparticle and intraparticle pores, and some shelter voids.

This facies zone represents a high-energy, shallow-water environment similar to facies zone IV/V. The diversity and robust nature of the fauna are characteristic of formation within the shallow reef-core environment. This interpretation is similar to that proposed by Gosselin et al. (1989) for the hemispherical stromatoporoid boundstone. Deposition of this facies likely occurred between sea level and about 10 metres water depth (Wendte, 1992).

3.3.9 Facies zone IVb

Facies zone IVb consists of light brown floatstones to bafflestones with *Stachyodes* as the dominant fossil component (Plate 3.5). Other skeletal fragments include well rounded and good to well sorted *Thamnopora*, as well as a few scattered crinoids, gastropods, and

Plate 3.3 Facies zone IV/V

(A) Core photograph of massive stromatoporoid bindstone. d-91-L/94-J-9; 6460'

(B) Core photograph of stromatoporoid bindstone showing a well developed shelter void (arrow). a-63-J/94-J-9; 1970.4 m.

(C) Core photograph of stromatoporoid bindstone in a crinoid wackestone to packstone matrix. S = stromatoporoid, St = *Stachyodes*, arrows = shelter voids. a-63-J/94-J-9; 1965.1 m.

(D) Core photograph of stromatoporoid rudstone-bindstone in a crinoid-calcisphere-peloid packstone-grainstone matrix. S = stromatoporoid, arrows = shelter voids. a-63-J/94-J-9; 1974.5 m.

Plate 3.3: Facies Zone IV/V

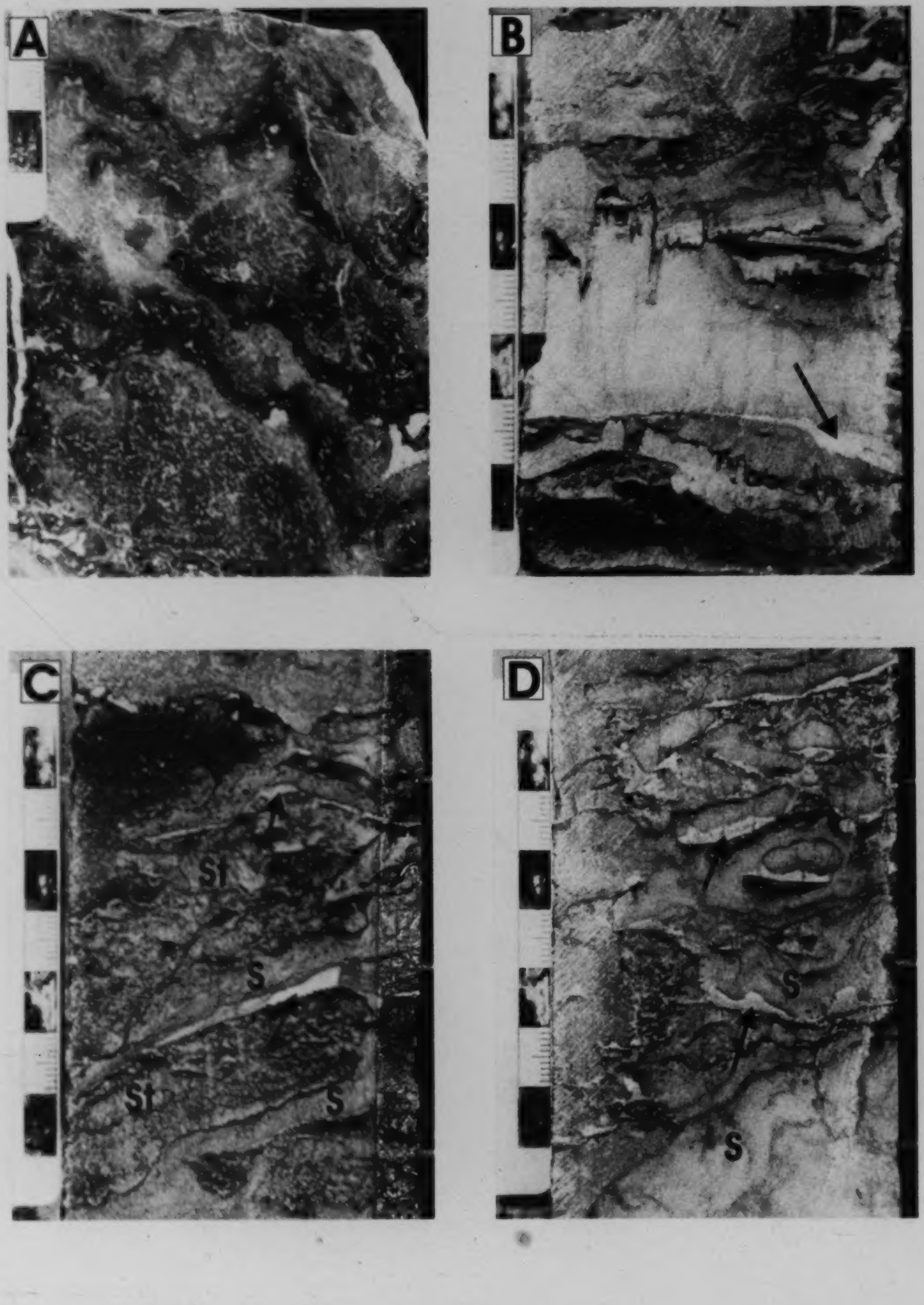
A
B
C
St
S
St
S
D
S
S

Plate 3.4 Facies zone V

(A) Core photograph of wavy stromatoporoid framestone. b-6-A/94-J-16; 6348'.

(B) Core photograph of massive, wavy stromatoporoid framestone. b-6-A/94-J-16; 6396'6".

(C) Core photograph of in situ, massive, wavy stromatoporoid (S) framestone in a well-rounded *Stachyodes* (St) rudstone matrix. b-78-J/94-J-9; 6484'3".

(D) Core photograph of fractured and stylolitized, massive stromatoporoid rudstone-framestone. S = stromatoporoid. b-6-A/94-J-16; 6423'.

Plate 3.4: Facies Zone V

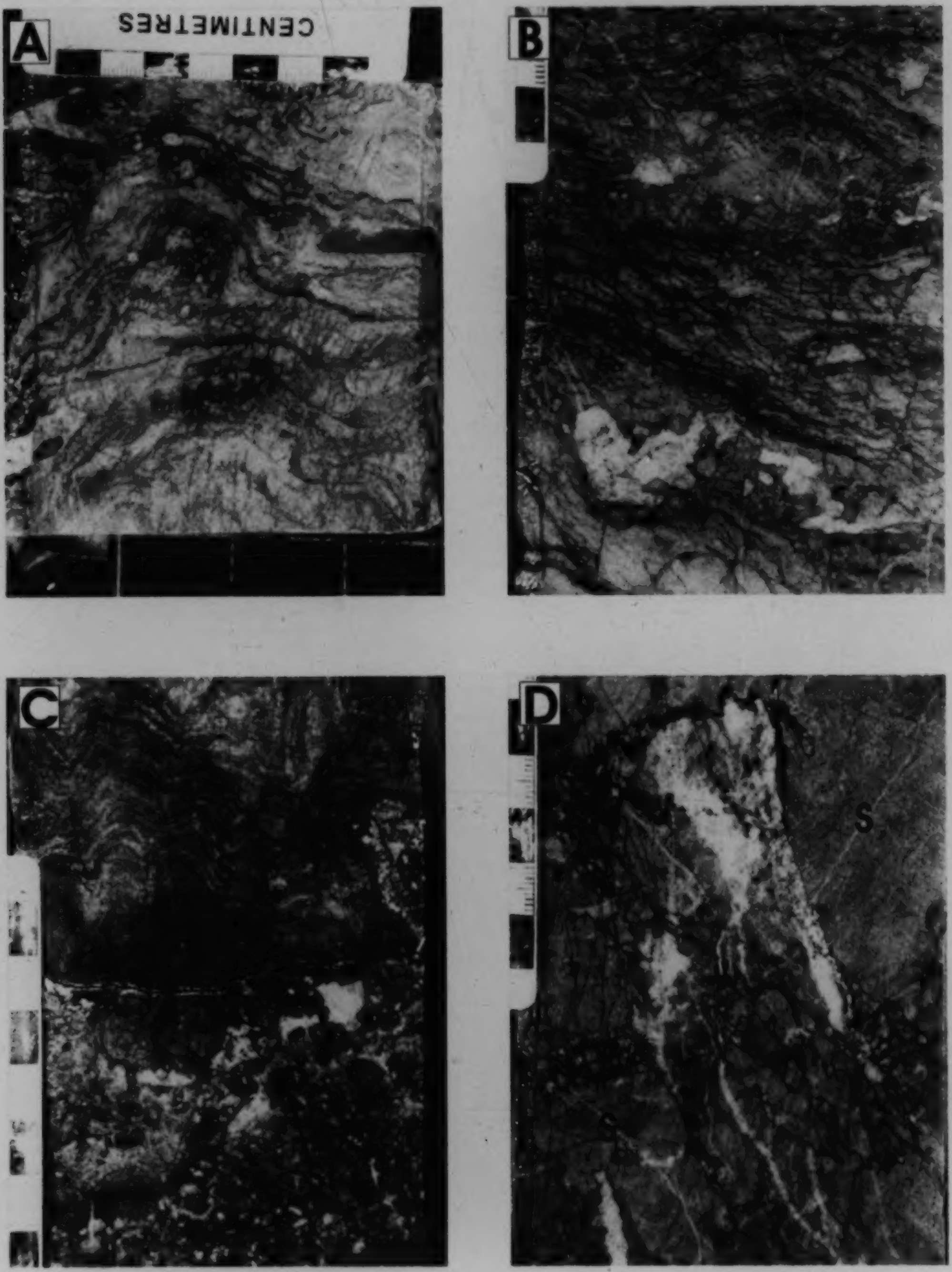
A
CENTIMETRES
B
C
D
S

Plate 3.5 Facies zone IVb

(A) Core photograph of *Stachyodes* bafflestone in a peloidal mudstone-wackestone matrix. St = *Stachyodes*, F = fenestral pores. b-6-A/94-J-16; 6408'6".

(B) Core photograph of *Stachyodes* rudstone with marine, radial fibrous calcite cement (RF) partially infilling interparticle porosity. Remaining primary porosity was filled with drusy calcite cement. b-6-A/94-J-16; 6433'.

(C) Core photograph of *Stachyodes* floatstone-rudstone in a pelletal-calcisphere-ostracod-gastropod grainstone matrix. G = gastropod, H = hydrocarbon residue. b-6-A/94-J-16; 6383'.

(D) Core photograph of stromatoporoid-coral rudstone in a pelletal-ostracod-dasyclad algae grainstone matrix, with some coated grains. St = *Stachyodes*, Th = *Thamnopora*. b-78-J/94-J-9; 6319'6".

Plate 3.5: Facies Zone IVb

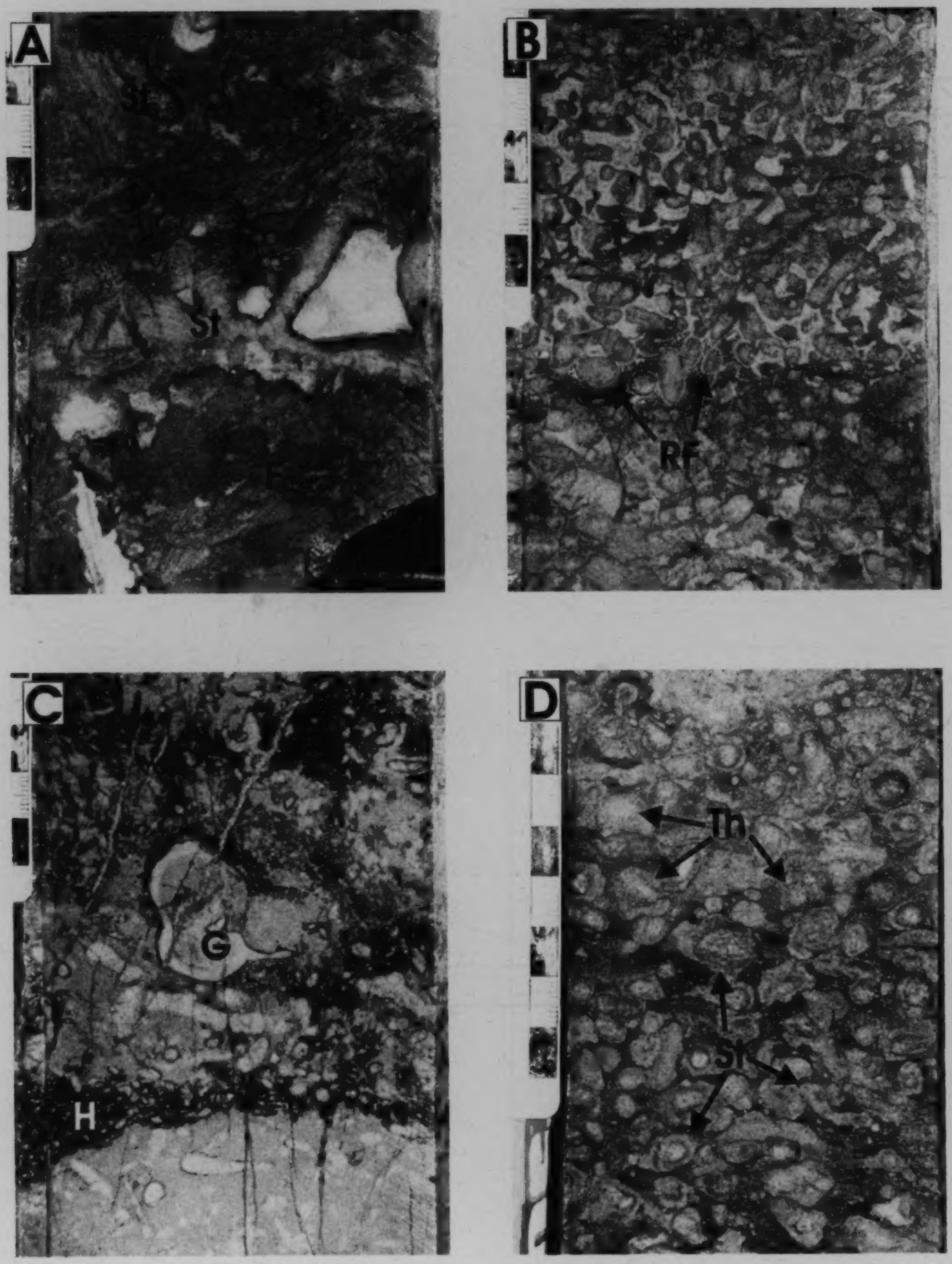
A
St
St
B
RF
C
G
H
D
Th
St

Amphipora. The matrix consists dominantly of micrite and peloidal grains, in addition to small fragments of ostracodes, brachiopods, crinoids, and dasyclad algae. Primary porosity is represented by interparticle and rare fenestral pores and shelter voids, however, much of the original interparticle porosity was cemented by marine calcite.

This facies zone is representative of deposition in a high-energy back-reef environment based on its lateral facies association with facies zone V and IIIb. The occurrence of large, rounded and well-sorted fossil debris is a reflection of episodically turbulent waters in this environment. Additionally, the presence of the indicator fossil *Amphipora* attests to deposition on the backside of the reef proper. This facies zone is equivalent to the near back-reef stromatoporoid rudstones to bafflestones of Keilly (2005). The occurrence of fenestral pores in this zone implies deposition near sea level with maximum water depths of less than 5 metres (Wendte, 1992).

3.3.10 Facies zone IIIb

Facies zone IIIb consists of dark brown packstones to floatstones with a lime mudstone to packstone matrix (Plate 3.6A and B). The dominant bioclast is 0.5 mm to sub-mm-size *Amphipora*, although *Stachyodes* and *Thamnopora* are also present. The bioclasts are usually well rounded and moderate to well sorted. The matrix consists of micrite and peloidal grains with scattered occurrences of calcispheres, ostracodes, and gastropods. Primary porosity is associated with intraparticle pores; however, where the matrix is grainier, interparticle pores are well developed.

The fairly low diversity of fauna, the mudstone to packstone matrix, and the presence of *Amphipora* is diagnostic of a relatively low-energy, lagoonal environment. This facies is equivalent to the *Amphipora* rudstone facies identified by all the previous Slave Point facies studies. Deposition of this facies probably occurred in water depths of less than 5 metres, based on the estimate of Wendte (1992) for similar *Amphipora* lagoon deposits in the Swan Hills Formation.

3.3.11 Facies zone IIb

Facies zone IIb consists of interbedded buff coloured grainstones and laminated mudstones to wackestones (Plate 3.6C). Macroscopic bioclasts are generally absent, with the exception of scattered *Amphipora*. The matrix consists of sand-sized, poor

Plate 3.6 Facies zones IIIb to Ib

(A) Core photograph of *Amphipora* floatstone in a dark brown mudstone-wackestone matrix. Facies zone IIIb. O = ostracod. c-56-L/94-J-9; 6489'.

(B) Core photograph of *Amphipora* packstone-grainstone. Facies zone IIIb. b-49-F/94-J-9; 6556'9".

(C) Core photograph of carbonate grainstone alternating with weakly-laminated mudstone-wackestone. Facies zone IIb. c-64-I/94-J-10; 6425'6".

(D) Core photograph of algal laminite mudstone-wackestone. Facies zone Ib. F = fenestral pores. c-64-I/94-J-10; 6443'3".

Plate 3.6: Facies Zones IIIb to Ib

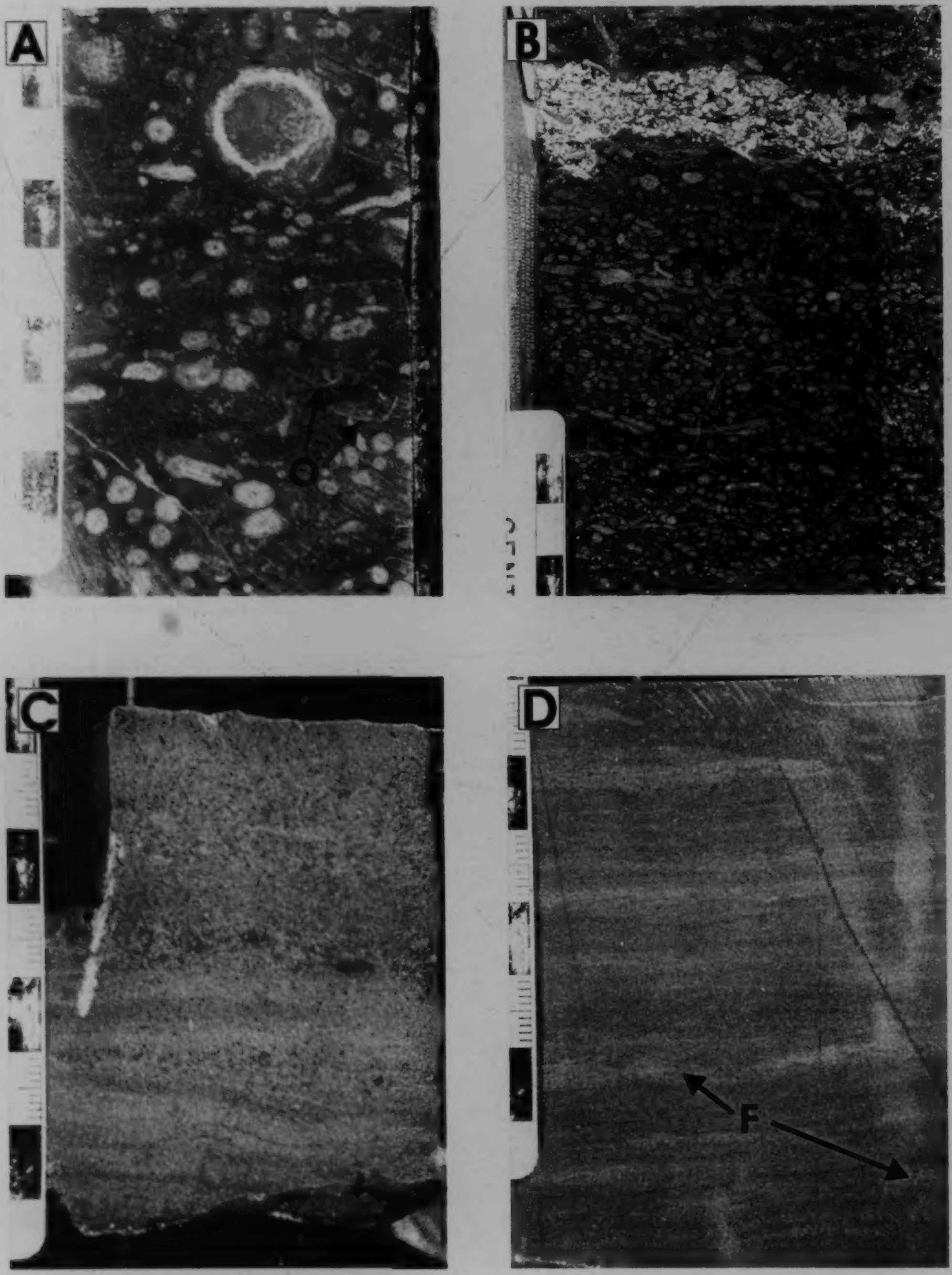

to moderately rounded, and moderately sorted grains, as well as lime mud. Within the mudstone to wackestone, the matrix consists predominantly of micrite, peloidal grains, and calcispheres. Primary pores are mostly interparticle.

The presence of *Amphipora* and the laminated mudstones in this facies support a shallow subtidal depositional environment. This facies is similar to the platform interior facies of Gosselin et al. (1989), and is interpreted to have formed in the shallow-water zones of the back-reef lagoons. Therefore, deposition of this facies likely occurred in water depths of less than 1 metre (Wendte, 1992).

3.3.12 Facies zone Ib

Facies zone Ib consists of poorly laminated mudstones and wackestones (Plate 3.6D). This facies displays cryptalgal laminations and fenestral porosity in some layers. There are few, if any, macrofossils visible in the facies zone. Where present, macrofossils are usually small, angular fragments of *Amphipora*. The matrix consists of micrite, peloidal grains, and calcispheres. Primary porosity in this zone is restricted to fenestral pores.

This facies represents a similar depositional environment to that proposed for facies zone IIb. Deposition of this facies zone would have occurred at slightly shallower water depths, likely on the order of less than 0.5 metres (Wendte, 1992).

3.3.13 Patch reef facies

The patch reef facies is characterized by dark brown, fine-grained floatstones to framestones (Plate 3.7). The dominant bioclasts are centemetre-sized, *in situ* nodular to bulbous stromatoporoids, *Stachyodes*, *Euryamphipora*, and *Thamnopora*. These framework allochems are generally moderately rounded, and poorly to moderately sorted. The matrix is composed of micrite, peloidal grains, *Amphipora*, and *Atrypoid* brachiopods. Primary porosity is limited to intraparticle pores.

This facies represents a variant of facies zone IIIb. The muddy nature of the matrix, and the presence of both *Amphipora* and the wafer stromatoporoid *Euryamphipora*, suggest deposition in a back-reef environment. Machel and Hunter (1994) suggest that stromatoporoid colonies may occur together in small patch reefs within facies zone IIIb. Additionally, Mallamo and Hedinger (1992) found that limestones equivalent to zone IIIb that were deposited below storm wave base, although uncommon, are commonly composed

Plate 3.7 Patch reef facies

(A) Core photograph of stromatoporoid-coral floatstone-rudstone in a muddy, *Amphipora*-rich matrix. The nodular stromatoporoids and *Thamnoporid* corals are not *in-situ*, as evidenced by the coated grains. a-50-C/94-J-9; 6898'.

(B) Core photograph of nodular to bulbous stromatoporoid framestone. b-49-F/94-J-9; 6562.

(C) Core photograph of stromatoporoid-coral floatstone in a dark brown, *Amphipora*-rich wackestone matrix. S = unidentifiable stromatoporoid, St = *Stachyodes*, Th = *Thamnopora*. b-49-F/94-J-9; 6486'3".

(D) Core photograph of coral-stromatoporoid floatstone-rudstone in a dark brown, brachipod-rich wackestone matrix. S = unidentifiable stromatoporoid, Eu = *Euryamphipora*, Th = *Thamnopora*, A = *Atrypoid* brachiopod. b-49-F/94-J-9; 6510'.

Plate 3.7: Patch Reef Facies

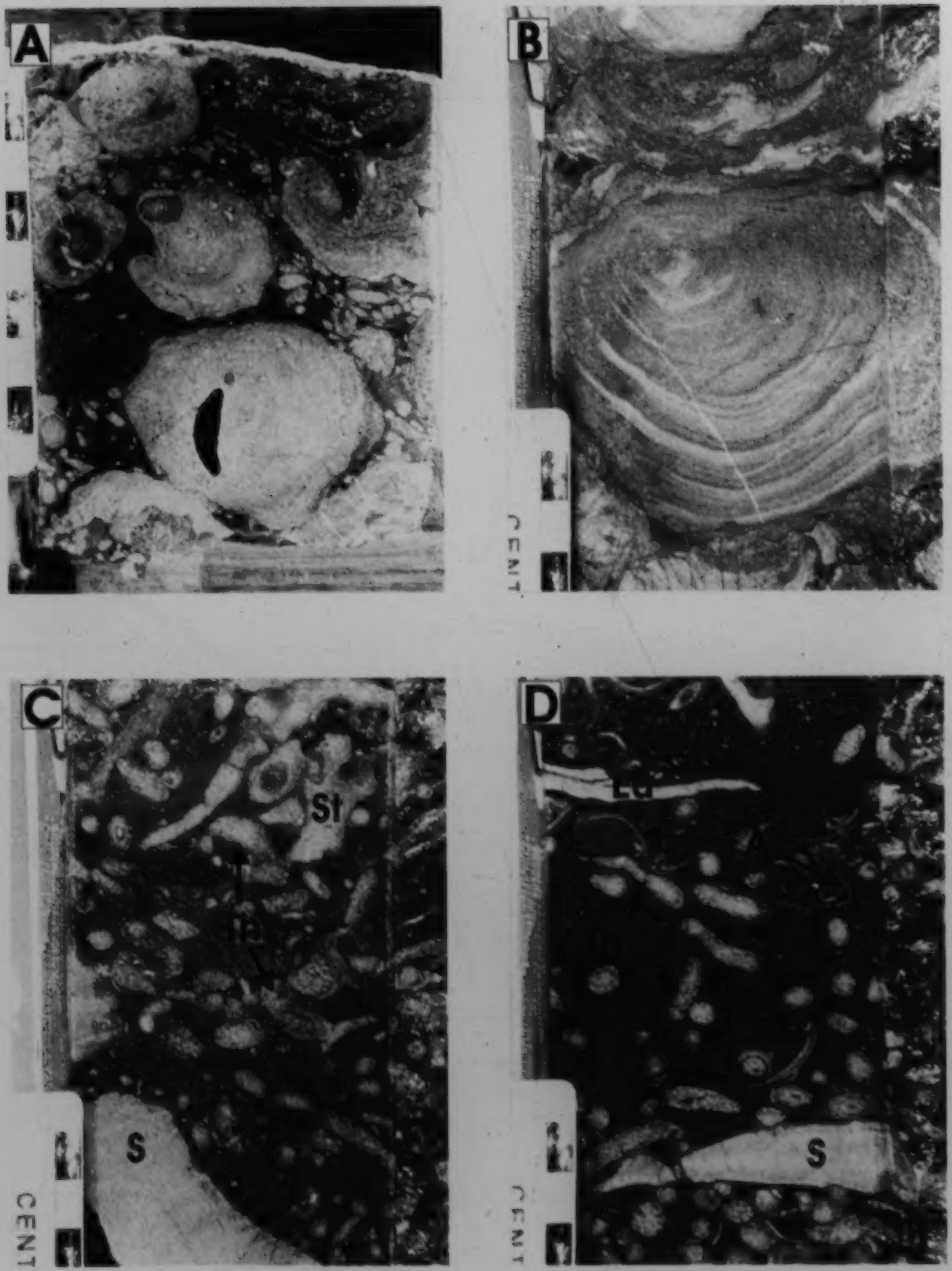
A
B
CENT
C
St
Tb
S
CENT
D
Lu
S
CENT

of abundant coral colonies. Based on this information, and the presence of the deeper-water *Atrypoid* brachiopods, this facies zone was likely deposited in water-depths on the order of 10 to 20 metres.

3.4 Facies distribution at Clarke Lake

The schematic representation of the facies distribution for the Slave Point Formation at Clarke Lake is shown in Figure 3.4. This interpretation is based on the facies identified through core and thin section examination, but is only a "snapshot" of the Slave Point Formation near the closing stages of deposition.

The most notable aspects of the facies distribution is both the lack of a continuous reef-rimmed platform or a ramp-like characteristic to the Slave Point platform interior. As was discussed previously, the former was advocated by Davies (1999), and numerous others, based on both seismic and core data; the latter by SB Geological Associates (1988) to reflect what to them appeared as a progressive increase in paleo-water depth towards the south. This study advocates the formation of true reefal buildups in a series of discontinuous, relatively small and seemingly isolated bioherms that are clustered along the eastern side of the study area, and deposition of both back-reef type facies (*sensu* Machel and Hunter, 1994) traversed by deep-water channels connecting the open-marine environment to the north with deeper-water basinal-type deposits in the platform interior. Importantly, however, the stratigraphic cross-sections (Figures 2.6 to 2.9) show that the platform does have an almost block-shaped paleotopography between the outer and inner platform margins. Hence, the Slave Point Formation exhibits a paleotopography and facies distribution in the Clarke Lake area not unlike parts of the Great Barrier Reef today (Harris and Kowalik, 1994).

To the north of the Slave Point outer platform margin, basinal facies of water depths greater than 30+ metres were deposited, including shales of the Otter Park Formation. Approaching the edge of the platform margin, a laterally extensive band of silty and argillaceous laminated mudstones were deposited. The seismically defined edge of the Slave Point platform is represented by transition between the deep water facies of zone If and the basinal shales of the Otter Park Formation. Over progressively shallow water depths, facies zone If grades into zone IIf followed by zone IIIf. Even at the highest elevation along the fore-reef margin, water depths were on the order of 10's of metres.

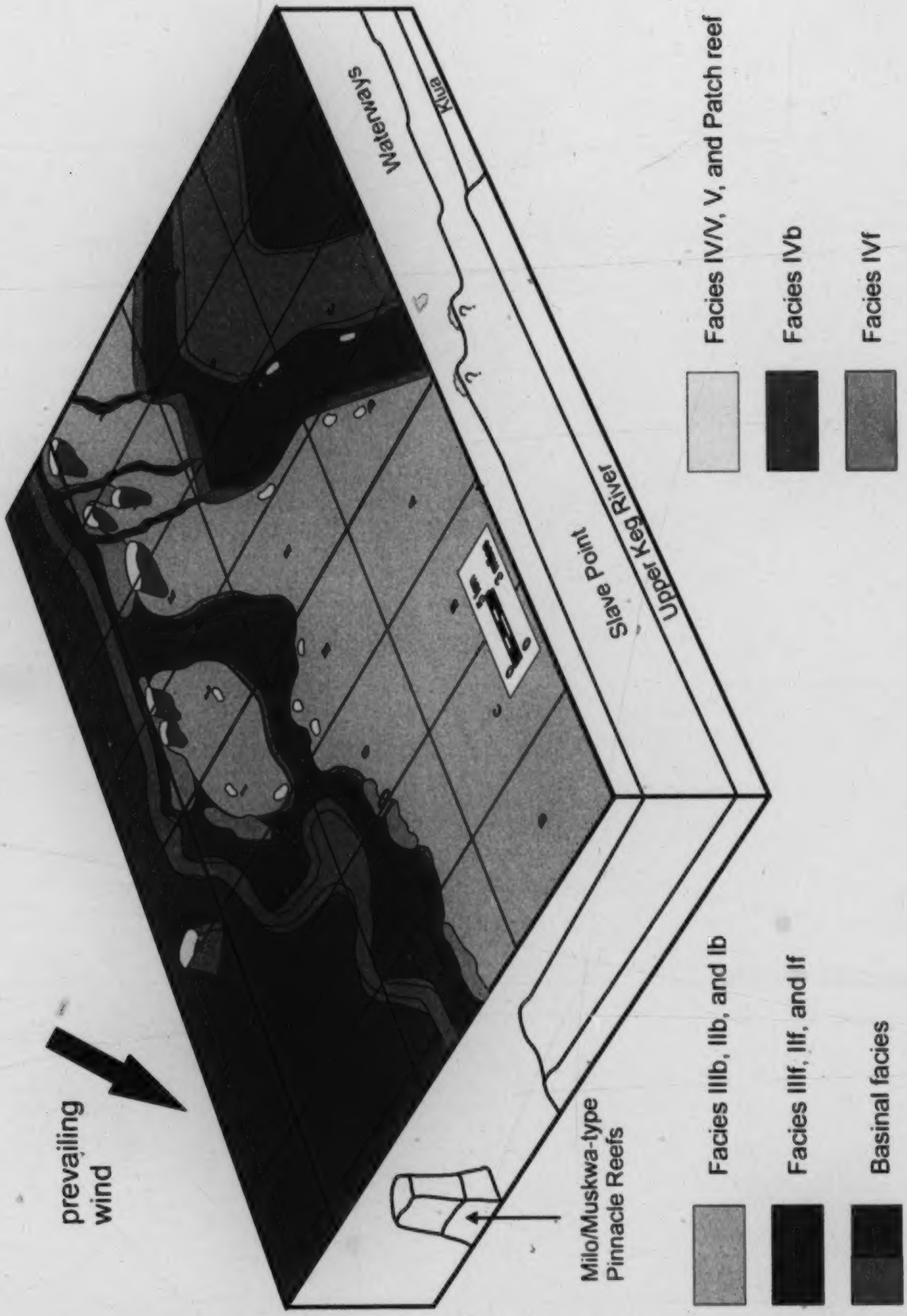
prevailing wind
Milo/Muskwa-type Pinnacle Reefs
Waterways
Klua
?
?
Slave Point
Upper Keg River
Facies IIIb, IIb, and Ib
Facies IIIf, IIf, and If
Basinal facies
Facies IV/V, V, and Patch reef
Facies IVb
Facies IVf

Figure 3.4 Schematic representation of the facies distribution in the Middle Devonian Slave Point Formation at Clarke Lake near the end of the Givetian. The assignment of facies zones follows the facies model from Middle to Late Devonian reef carbonates by Machel and Hunter (1994) (Figure 3.3).

This composite zone, i.e., facies If through IIIf, is present in a broad swath both across the front of the platform margin, and through the platform interior (Figure 3.4 – dark blue). The presence of abundant crinoids on the platform top near the margin point towards a connection with the open-marine environment to the north.

Facies zone IVf developed in patches along the front of the Slave Point platform margin that are in proximity to the identified reef core facies, and both are cut by deeper-water channels. This reef distribution may be attributed to one of two possible mechanisms. Firstly, the lack of wave-resistant reef development along the west side of the study area may be due to the 'shadowing' effect of the platform margin to the east. Gosselin et al. (1989) hypothesized that low fossil diversity in the Slave Point near the Peace River Arch may have been caused by a lesser nutrient supply due to the 'shadowing' effect of a nearby reef complex. If the prevailing wind and ocean currents were from the north and northeast, which is consistent with paleowind and current directions established for the Middle Devonian (Gosselin et al., 1989), the reefs along the eastern edge of the study area, and the movement of the Slave Point platform margin farther to the south along the west side of the study area, may have been nourished by relatively abundant nutrient supply from those directions. Secondly, the top of the Slave Point Formation was in a structurally lower position along the west side of the Clarke Lake study area (Figures 2.6 and 2.9) and it may be that the paleo-water depth was not amenable to the development of framework building reef organisms. Thirdly, the observed clustering of reef and fore reef facies in the eastern parts of the Clarke Lake field may be an artefact, due to a drilling strategy driven by seismic data and interpretive philosophy. In any case, the available data suggest an abundance of 'sweet spots' for exploration, as highlighted in yellow, green, and orange (Figure 3.4), which represent those facies types with relatively high porosities and permeabilities.

Back-reef facies of zone IVf are only found where the platform margin reefal buildups developed. Elsewhere, facies zones IIIb through Ib blanket the remainder of the platform interior. This includes the formation peritidal facies immediately to the rear of the emergent reef bioherms, and the formation of both restricted and open-marine lagoon deposits. Within the platform top, usually adjacent to open-marine channels, the patch reef facies developed. This facies is not representative of the true 'ecological' reef (*sensu* Dunham, 1970); rather, the general lack of a rigid framework advocates for a reef mound structure (*sensu* Kiessling and Flügel, 2002). These patch reefs are not laterally extensive and are probably less than 50 metres in length, similar to the modern patch reefs forming in Bermuda (James, 1983); however, these patch reefs may join together to form a larger structure.

Farther south, deep-water facies are also present in the platform interior landward of the inner platform margin both along the previously mentioned channels, and within the Waterways basin. Based on the stratigraphic evolution discussed in Chapter 2, the formation of the Waterways basin was likely fault-controlled. Additionally, the Slave Point margin shows evidence of backstepping with increasing sea level along the edge of the Waterways basin. As a result, more and hitherto undiscovered patch reefs similar to those discussed above may have developed along the incipient platform margin(s) (see Figure 3.4).

CHAPTER 4

PETROGRAPHIC EVIDENCE FOR THE DIAGENETIC EVOLUTION OF THE SLAVE POINT FORMATION

4.1 Introduction

The objectives of Chapter 4 are to: 1) identify all post-depositional diagenetic phases in the Slave Point Formation; 2) establish the spatial and temporal relationships between the various diagenetic phases; and, 3) establish the controls on dolomite distribution in the Clarke Lake field. These objectives were attained through the detailed macro- and microscopic examination of both limestone and dolomite subsurface cores. The results from this chapter have important implications for the origin and timing of the diagenetic fluids that infiltrated the Slave Point Formation at Clarke Lake, and provide the framework for the geochemical investigations presented in Chapter 5.

4.2 Methods

During the summer of 2000, twenty-eight (28) subsurface cores from the Slave Point Formation at Clarke Lake were logged and sampled at the British Columbia Ministry of Energy and Mines core warehouse in Charlie Lake, B.C (Appendix I). From these cores, a total of 383 samples were obtained, from which 195 polished thin sections were made (see Appendix III for locations). The thin sections were stained with a mixture of Alizarin Red-S and potassium ferricyanide to determine carbonate mineral composition (Dickson, 1965). All thin sections were examined by transmitted light microscopy using a Zeiss Jenapol polarizing microscope, and by cathodoluminescence (CL) microscopy using a cold cathode Premier American Technologies ELM-3R Luminoscope. The operating conditions were maintained at 14-16 kV and 0.5 mA under a vacuum of 30-50 millitorr to provide consistency of results. Photomicrographs were taken with a Minolta SLR camera using Kodak Ektachrome 35mm tungsten slide film.

Porosity and permeability data from nine wells that recovered limestone cores, and sixteen wells that recovered dolostone cores, in the Slave Point Formation were provided courtesy of AccuMap®. Wells containing porosity and permeability data were examined both in core and thin section to identify the original depositional facies, and the type and occurrence of dolomite. See section 3.2 for further information on core examination methods.

4.3 Diagenetic evolution

Diagenesis encompasses all the processes that affect sediments after deposition until the realms of incipient metamorphism at elevated temperatures and pressures (Tucker, 1981). After deposition, carbonate sediments are subjected to a variety of distinctive diagenetic processes that bring about changes in porosity, mineralogy, and overall composition. Diagenetic changes may also destroy or modify original depositional textures. Processes that produce such changes include mechanical and chemical compaction, cementation, dissolution, dolomitization, and recrystallization.

The carbonates of the Slave Point Formation at Clarke Lake have undergone a complex diagenetic history. The paragenetic sequence of these diagenetic events is shown in Figure 4.1. This paragenetic sequence displays both similarities and notable differences compared to previous studies from the both Middle Devonian of northeastern British Columbia (Qing and Mountjoy, 1994a; 1994b; Clarke, 1998; Morrow et al., 2002) and the intensively studied Devonian carbonates of central Alberta (e.g., Machel, 1985; Amthor et al., 1993; Mountjoy and Amthor, 1994; Machel et al., 1996; Wendte et al., 1998; Mountjoy et al., 1999; Machel, 2004). As a result of the petrographic examination of the Slave Point carbonates, 25 distinct diagenetic phases or products were identified. These diagenetic phases were interpreted to span the diagenetic realms from near-surface through deep burial.

Diagenetic settings are commonly divided into 'shallow', 'intermediate', and 'deep' burial (Choquette and James, 1990), yet these terms are ill defined. Machel (1999) combined mineralogic, organic-geochemical (Bustin et al., 1985), and hydrologic (Galloway and Hobday, 1983) criteria from clastics and carbonates, the occurrence of hydrocarbons and fractures, in a comprehensive classification of diagenetic settings. The Machel (1999) classification includes near-surface, shallow burial, intermediate burial, and deep burial settings. Near-surface diagenetic settings are defined as those within the first few metres of burial, where the pore fluids are surface derived and essentially unaltered meteoric, brackish, marine, or evaporitic in origin. Shallow burial diagenetic settings are similar to the near-surface diagenetic settings; however, differences include added physical compaction and certain hydrologic conditions that may vary from place to place. The lower

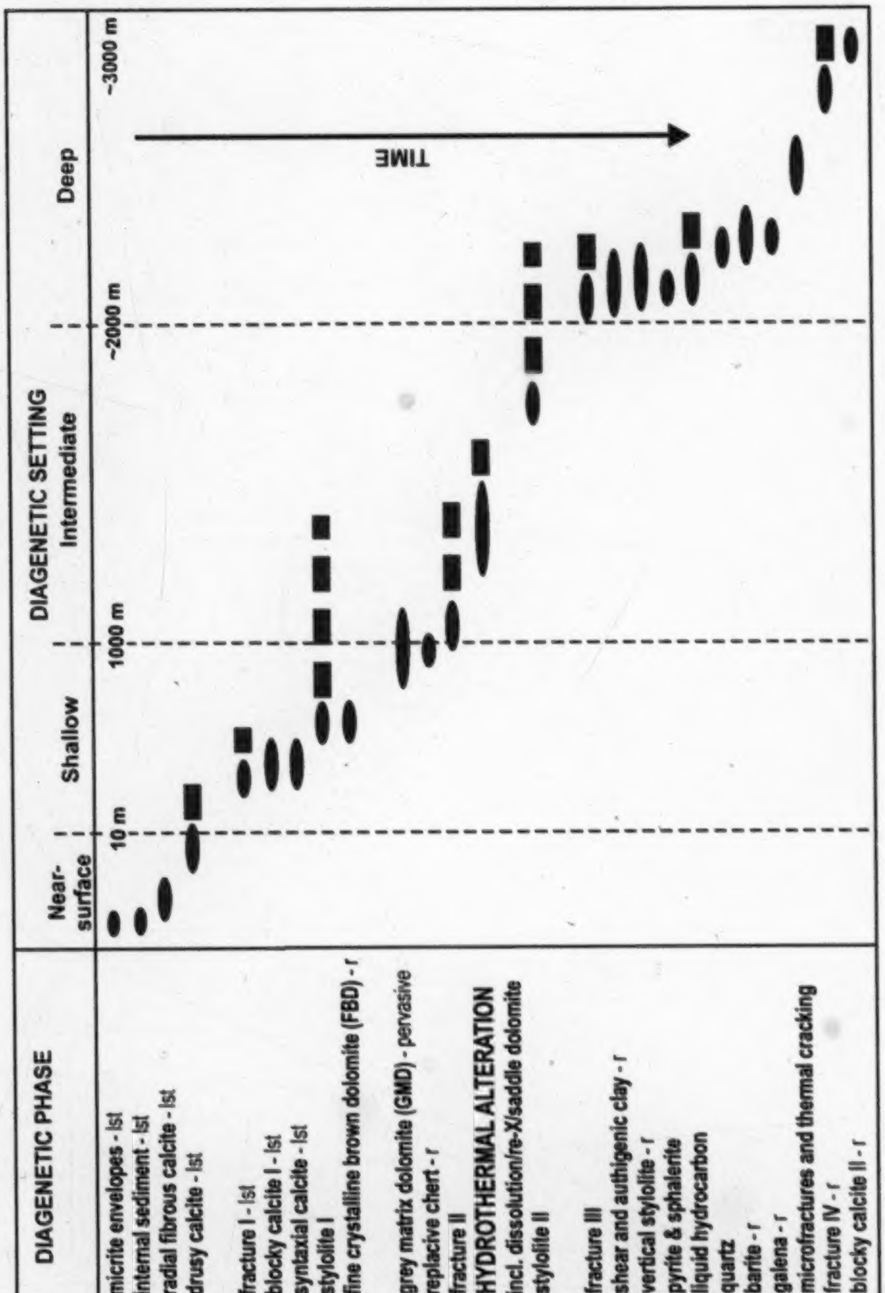

Figure 4.1 Paragenetic sequence for the Middle Devonian Slave Point Formation at Clarke Lake. Hydrothermal alteration includes all phases that resulted from the invasion of hydrothermal fluids into the reservoir. lst = restricted to limestones; r = restricted to rare occurrences. Diagenetic settings and their relative depths after Machel (1999).

boundary of the shallow burial diagenetic setting is placed at roughly 600-1000 metres of burial, and is based on the depth at which chemical compaction generates recognizable stylolites (Machel, 1999). Intermediate and deep burial diagenetic settings represent the zones of intense chemical compaction, cementation, and dissolution (Machel, 1999). The lower limit of the intermediate burial diagenetic setting, and thereby the upper limit of the deep burial diagenetic setting, is defined relative to the top of the liquid oil window in hydrocarbon source rocks (Machel, 1999). In petroleum geology, this depth has been used to define the boundary between "diagenesis" and "catagenesis" (Hunt, 1996). In mineral diagenesis, this boundary is useful since the introduction of oil into pore spaces commonly arrests diagenesis (Machel, 1999). Unfortunately, the depth to the top of the oil window varies widely, depending on kerogen type and geothermal history, but averages about 2000-3000 metres (Hunt, 1996). Therefore, this depth interval is taken as the bottom of the intermediate burial diagenetic setting. Deep burial diagenetic settings merge into the metamorphic realm at temperatures around 200°C and commensurate depths and pressures dependent on the integral geothermal gradient (Machel, 1999).

In the following sections, each distinct diagenetic feature (cement, mineral, fracture, etc.) is called a 'phase'. Each phase is implied to a) last a certain period of time, b) represent a certain process (cementation, dissolution, fracturing, replacement) that was controlled by c) a certain type of fluid in d) a certain pressure and temperature environment. As such, 'phase' has the connotation of a process and time. Where this process formed a mineral phase that is texturally destructive, 'phase' is also used for the diagenetic product. Several phases are then grouped into stages. The most obvious grouping corresponds to depth and water chemistry, e.g., the various phases that form in the intermediate burial setting can be said to form in the intermediate burial stage, and so on.

4.3.1 Near-surface diagenesis (stage)

Near-surface diagenesis occur during both deposition and the initial phases of shallow burial, i.e., to a depth of roughly 10 metres. The products of this stage include: micrite envelopes, internal sediment, radial fibrous calcite, and drusy calcite. These diagenetic phases led to a decrease in primary porosity and lessened the effect of physical compaction.

Micrite envelopes (phase 1)

A dark brown micrite zone that has a maximum thickness of roughly 100 µm surrounds many of the stromatoporoid, *Stachyodes*, and *Thamnopora* allochems from the limestone samples (Plate 4.1A and B). Minor micrite envelopes are also found on fragments of *Amphipora* and crinoids, and grain aggregates or grapestones. The outside margin of the micrite envelopes is always sharp and smooth, while the inner boundary is commonly irregular and continues into the biochem filling previous borings.

Internal sediment (phase 2)

Dark brown micrite and peloidal grains are found as internal sediments within primary intraparticle porosity (Plate 4.1C and D). These internal sediments are relatively common within *Thamnopora*, brachiopod, and gastropod fragments. The internal sediments do not entirely fill the intraparticle pore spaces; rather, they fill the basal half of the pore space, whereas the upper half was subsequently cemented by calcite. This succession resulted in the formation of geopetal fabrics, and, therefore, provides a 'way up' indicator, and estimates of post-depositional dip.

Radial fibrous calcite (phase 3)

Radial fibrous calcite cement is common within primary interparticle porosity developed within facies zone IVb, i.e., *Stachyodes* floatstone to rudstone (Plate 4.2A and B). Radial fibrous calcite is characterized by prismatic crystals up to 500 µm in length, uniform length fast vibration directions, and planar twin-planes (Plate 4.2B). Radial fibrous calcite formed concurrently with deposition of micrite indicating a marine origin for these cements.

Drusy calcite (phase 4)

Drusy calcite cement occurs as clear, non-ferroan crystals that range in size from 10 µm up to approximately 200 µm (Plate 4.2C and D). This cement is common where micrite envelopes are present, and is found partially to completely occluding interparticle porosity within the limestone cores.

Plate 4.1 Near-surface (I) textural and mineralogical changes.

(A) Core photograph of micrite envelopes (phase 1 -arrows) coating stromatoporoid fragments. b-78-J/94-J-9; 6222'9".

(B) Thin section photomicrograph of a dark brown micrite envelope (phase 1 -arrow) coating a *Stachyodes* grain. The interparticle pores were subsequently occluded by drusy calcite cement (phase 4 - dCC). Stained thin section, plane-polarized light. b-6-A/94-J-9; 6433'.

(C) Core photograph of pervasively dolomitized, thick-shelled gastropod-brachiopod rudstone showing geopetal fabrics (G) of internal sediment (phase 2). Matrix dolomite replaced the internal sediment, while dissolution of calcite cement and subsequent formation of saddle dolomite resulted in the generation of secondary vuggy porosity. a-61-F/94-J-10; 6706'6".

(D) Thin section photomicrograph of internal sediment (phase 2 - arrows) in the zooecial tubes of a *Thamnopora*. Remaining intraparticle pores were occluded by blocky calcite cement (phase 6 - bCC). Stained thin section, plane-polarized light. b-78-J/94-J-9; 6272', stratigraphic top is to the left.

Plate 4.1: Near-surface I

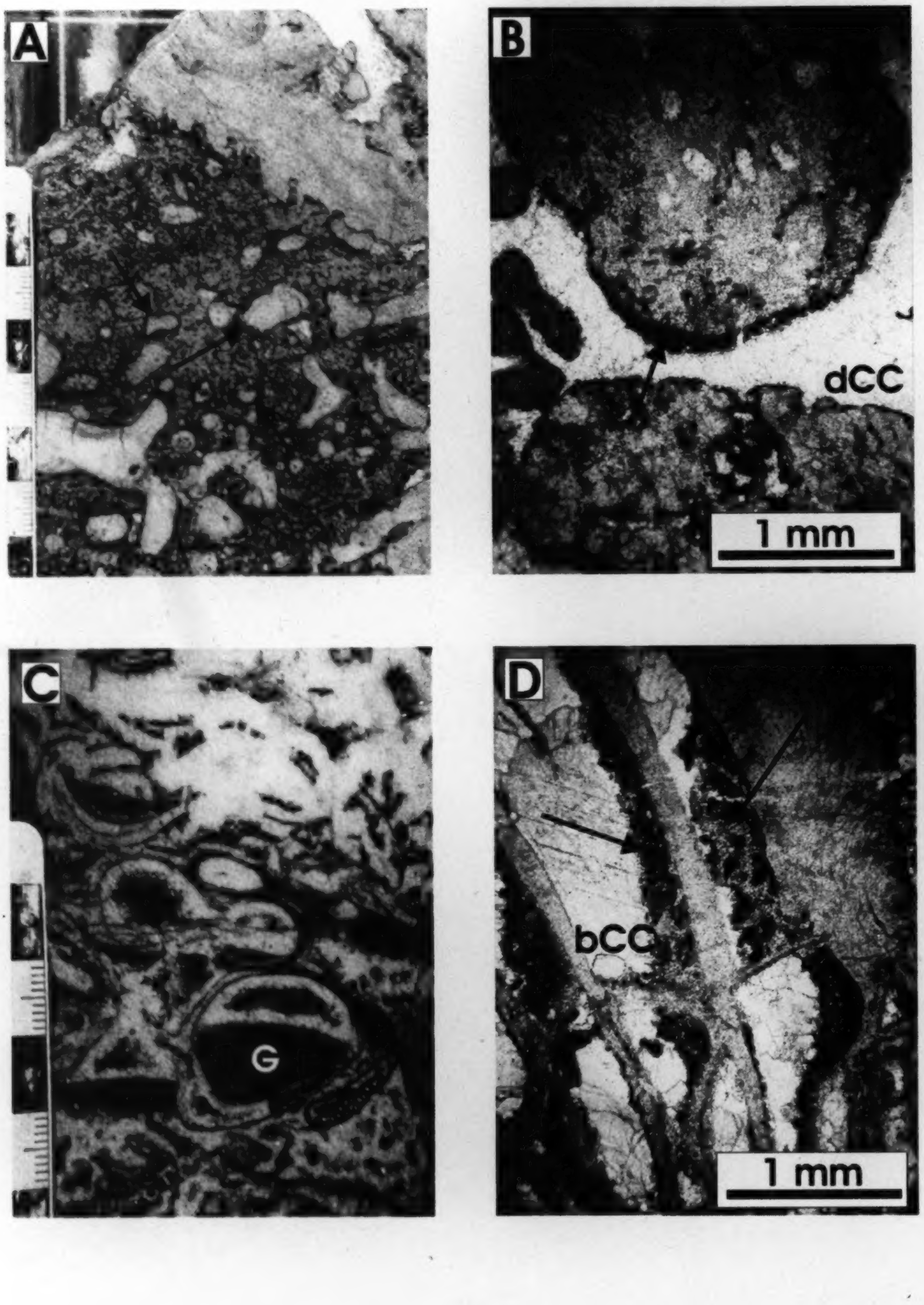
A
B
dCC
1 mm
C
G
D
bCC
1 mm

Plate 4.2 Near-surface (II) textural and mineralogical changes.

(A) Core photograph of radial fibrous calcite cement (phase 3 - arrows) fringing *Stachyodes* grains in a stromatoporoid floatstone-rudstone. Some of the micrite was replaced by fine-crystalline brown dolomite (phase 9 - grey colour). b-6-A/94-J-16; 6433'.

(B) Thin section photomicrograph of sample in A showing radial fibrous calcite cement (phase 3) fringing *Stachyodes* grains. Fine-crystalline brown dolomite that replaced micrite is in the centre of the photo. Stained thin section, cross-polarized light. b-6-A/94-J-16; 6433'.

(C) Core photograph of white drusy calcite cement (phase 4) filling primary interparticle porosity in a *Stachyodes* floatstone-rudstone. b-78-J/94-J-9; 6435'.

(D) Thin section photomicrograph of drusy calcite cement (phase 4) filling primary interparticle porosity between coated allochems. Stained thin section, plane-polarized light. b-6-A/94-J-16; 6433'.

Plate 4.2: Near-surface II

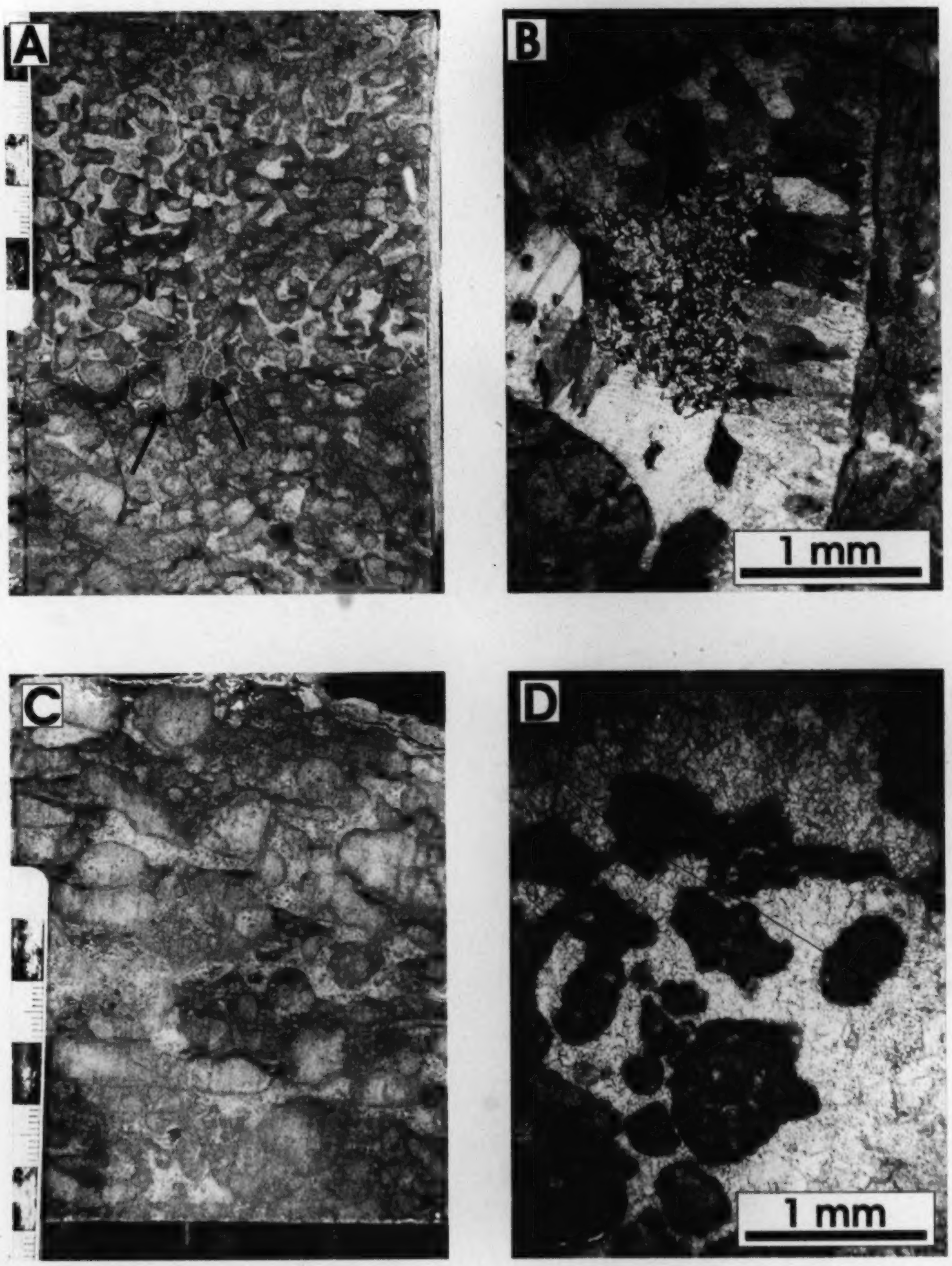
A
B
1 mm
C
D
1 mm

4.3.2 Shallow burial diagenesis (stage)

Shallow burial diagenetic phases form at depths between 10 metres and approximately 1000 metres (Machel, 1999). The products of this stage include: fracture generation I, blocky calcite I, syntaxial calcite, stylolite generation I, and fine crystalline brown dolomite (FBD). Overall, these diagenetic phases further reduced the remaining primary porosity.

Fracture I (phase 5)

Fracture generation I cross-cuts all of the previously discussed diagenetic products. This generation of fractures was found only in limestone cores, and occurs in a vertical to sub-vertical orientation with widths no greater than 5 mm, and lengths up to 5 cm (Plate 4.3A). This fracture generation was subsequently occluded by blocky calcite I (phase 6).

Blocky calcite I (phase 6)

Blocky calcite cement I occurs as clear, non-ferroan, equant, subhedral to euhedral crystals with a maximum long dimension of approximately 600 mm (Plate 4.3B). Blocky calcite fills much of the remaining interparticle porosity and fracture porosity, and cements the upper-half of many marine geopetal structures (Plate 4.1D). This cement is non-luminescent under cathodoluminescence (CL), suggesting low Fe and Mn contents.

Syntaxial calcite (phase 7)

Syntaxial calcite cement is common within the matrix of skeletal grainstones and packstones containing echinoderm fragments (Plate 4.3C and D). This phase occurs as calcite crystals approaching 1 mm in size. Syntaxial calcite cement is inclusion-poor and is non-luminescent under CL. This cement occludes primary porosity suggesting precipitation prior to significant physical compaction.

Stylolite I (phase 8)

Stylolites are common features throughout the study area. They display amplitudes ranging from a few millimeters to 2-3 centimeters in dolomite, and can attain amplitudes of 5-6 centimetres in limestone (Plate 4.4). The stylolites often occur near the boundaries between different diagenetic mineral phases, such as grey matrix dolomite and saddle

Plate 4.3 Shallow burial (I) textural and mineralogical changes.

(A) Core photograph of vertical to sub-vertical fracture set I (phase 5 - arrows) cutting through the micrite matrix of a stromatoporoid floatstone. These fractures were subsequently occluded by blocky calcite cement (phase 6). Much of the micrite matrix (and allochems?) in upper half of the core was later replaced by fine-crystalline dolomite (phase 9 - medium grey colour). b-6-A/94-J-16; 6349'.

(B) Thin section photomicrograph of blocky calcite cement (phase 6 - bCC) occluding primary geopetal porosity. The blocky calcite cement grew out from the radial fibrous calcite cement (phase 3) lining the *Stachyodes* fragment on the right side of the photo, whereas fine-crystalline brown dolomite (phase 9) replaced the geopetal micritic sediment on the left side of the photo. Stained thin section, cross-polarized light. b-6-A/94-J-16; 6249'.

(C) Thin section photomicrograph of syntaxial calcite (phase 7 - arrow) replacing a crinoid ossicle. Stained thin section, plane-polarized light. b-78-J/94-J-9; 6330'.

(D) Thin section photomicrograph of syntaxial calcite (phase 7 - arrows) replacing crinoid fragments in a peloidal grainstone matrix. Stained thin section, plane-polarized light. a-81-J/94-J-9; 1907.4 m.

Plate 4.3: Shallow Burial I

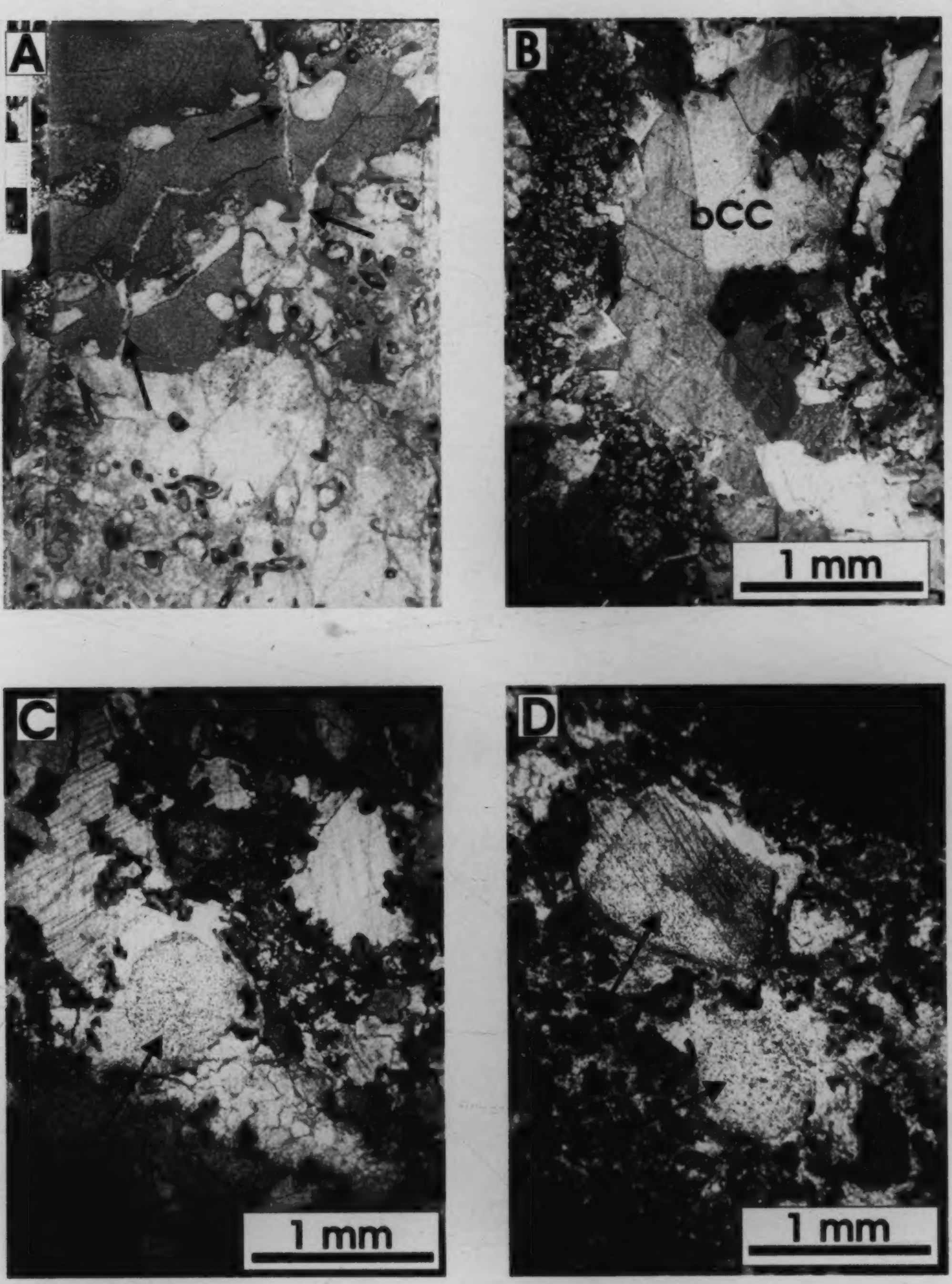
A
B
bCC
1 mm
C
1 mm
D
1 mm

Plate 4.4 Shallow burial (II) textural and mineralogical changes.

(A) Core photograph of low-amplitude stylolite generation I (phase 8 - arrows) in grey matrix dolomite (phase 10 - GMD). Later replacive saddle dolomite (hydrothermal alteration - phase 13 - SD), is only present above the stylolite, i.e., it shows no cross-cutting relationship. b-10-D/94-J-16; 6286'6".

(B) Core photograph of low-amplitude stylolite generation I (phase 8 - arrow) in grey matrix dolomite (phase 10 - GMD) that was cross-cut by fracture set II (phase 12) and subsequently filled with saddle dolomite cement (phase 13 - SD). d-72-G/94-J-10; 6414'6".

(C) Thin section photomicrograph of low-amplitude stylolite generation I (phase 8 - arrows) cutting across a *Stachyodes* grain. Fine-crystalline brown dolomite (phase 9) formed within the stylolite. Stained thin section, plane-polarized light. b-78-J/94-J-9; 6220'3", stratigraphic top to the left.

(D) Thin section photomicrograph of stylolite generation I (phase 8) in grey matrix dolomite (phase 10). The horizontal limbs of the stylolite and the insoluble residue are clearly visible on the right side of the photo. The arrows point to the vertical limbs of the stylolite that were replaced by grey matrix dolomite. Stained thin section, diffuse polarized light. b-10-D/94-J-16; 6291', stratigraphic top to the right.

Plate 4.4: Shallow Burial II

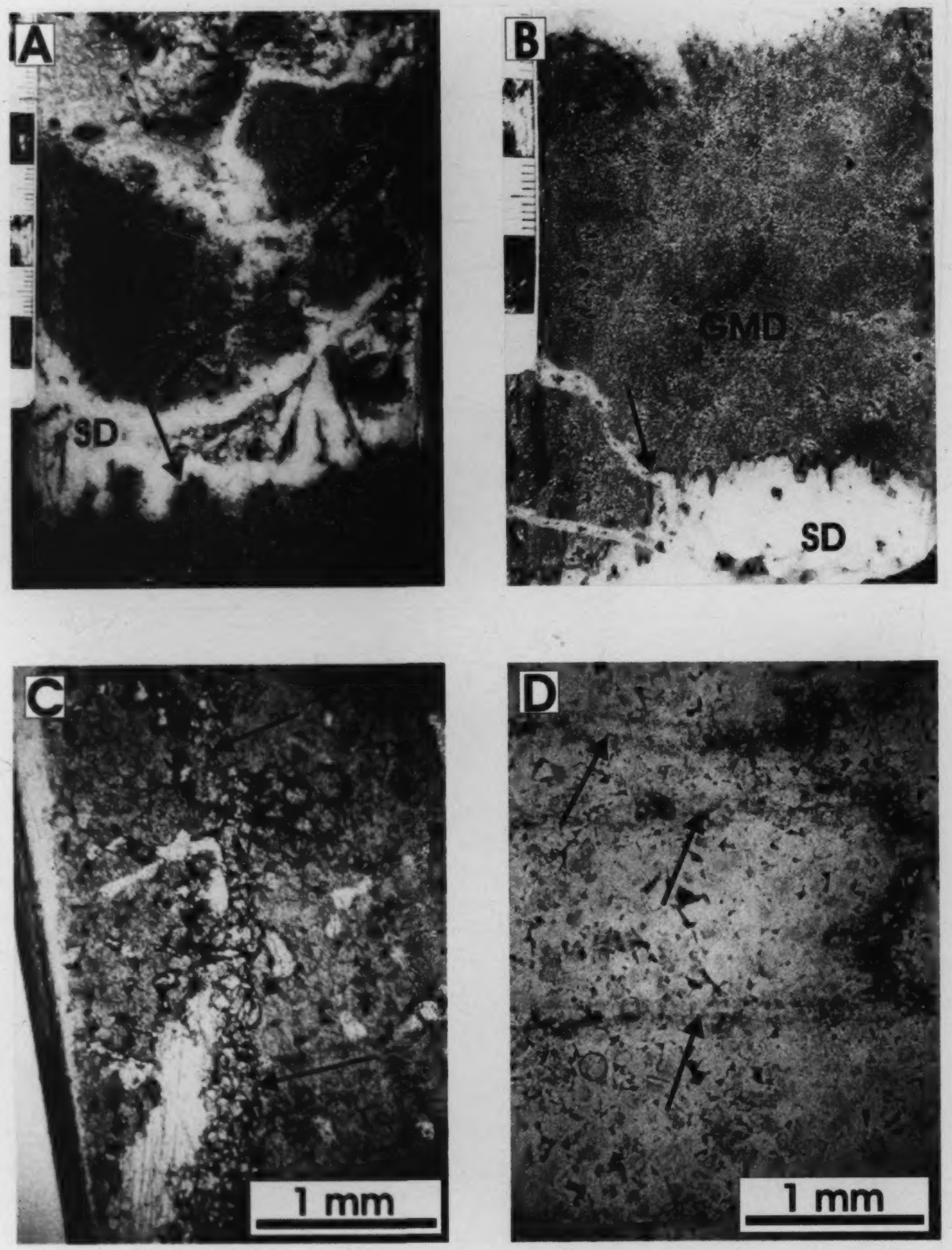
A
SD
B
GMD
SD
C
1 mm
D
1 mm

dolomite (Plate 4.4A and B). This indicates that at least some of the stylolites were formed prior to the latest diagenetic phase, in this case saddle dolomite, and that the stylolites may have acted as vertical permeability barriers to diagenetic fluid flow.

Fine crystalline brown dolomite (phase 9)

Fine crystalline brown dolomite (FBD) is a volumetrically very minor yet destructive component of the Slave Point Formation, generally present in limestone samples as a replacement of interparticle matrix and cement in proximal fore- and back-reef environments (Plate 4.5A and B). Using the classification of Gregg and Sibley (1984) and Sibley and Gregg (1987) shown in Figure 4.2, fine crystalline brown dolomite can be described as a planar-e to planar-s dolomite, with a maximum size of 50 μm. FBD usually displays a cloudy, brown colour in plane-polarized light, with no evidence of zonation (Plate 4.5C and D). Under CL, FBD displays dull red, blotchy luminescence. In limestone samples, FBD is fabric-retentive, replacing near-surface internal sediments while retaining geopetal fabrics. Elsewhere, FBD is found either replacing the fine-grained interparticle micrite in the limestone matrix or occurring as isolated patches associated with stylolite development (see phase 8). This distribution points to preferential replacement of either aragonite or high-Mg calcite muds, and the movement of the dolomite-forming fluid along stylolite generation I.

4.3.3 Intermediate burial diagenesis (stage)

The bulk of the diagenesis in the Slave Point Formation at Clarke Lake occurred during intermediate burial between 1000 and 2000 metres depth. The products of this stage include: continuation of stylolite generation I, grey matrix dolomite, replacive chert, fracture generation II, hydrothermal alteration (including saddle dolomite formation), and stylolite generation II.

Grey matrix dolomite (phase 10)

Grey matrix dolomite (GMD) constitutes the bulk of the dolomites in the Slave Point Formation (Plate 4.6), with about 80% by volume of all dolomite at Clarke Lake; hence, phase 10 is a case of pervasive dolomitization. Individual crystals of GMD range in size from 40μm to 300μm, and exhibit planar-e to nonplanar-a textures (Figure 4.2:

Plate 4.5 Shallow burial (III) textural and mineralogical changes.

(A) Core photograph of fine-crystalline brown dolomite (phase 9 - arrows) replacing geopetal sediment (phase 2) in the shelter cavities of a *Stachyodes* floatstone-rudstone, phase 9 represented by the darkest grey zones. In addition, matrix dolomite (phase 10) replaced calcite cements, represented by the lighter grey zones. a-63-J/94-J-9; 1973.2 m.

(B) Core photograph of fine-crystalline brown dolomite (phase 9) replacing both geopetal sediments and micrite matrix in a stromatoporoid floatstone. The arrows point to sub-vertical microfractures (phase 23), the result of thermal cracking of liquid hydrocarbons (phase 19), that cross-cut the fine-crystalline brown dolomite. b-6-A/94-J-16; 6419'.

(C) Thin section photomicrograph of fine-crystalline brown dolomite (phase 9 - FBD) replacing micrite between *Stachyodes* allochems. The *Stachyodes* grains are fringed by radial fibrous calcite cement (phase 3) and cut by fracture set I (phase 5) cemented by blocky calcite cement (phase 6). Stained thin section, plane-polarized light. b-6-A/94-J-16; 6433'.

(D) Thin section photomicrograph of fine-crystalline brown dolomite (phase 9 - FBD) replacing geopetal sediment. The upper surface of the primary geopetal sediment is represented by the dark seam (arrows). Grey matrix dolomite (phase 10 - GMD) subsequently replaced the primary calcite cements. Stained thin section, cross-polarized light. c-47-J/94-J-10; 6657'3", stratigraphic top to the right. Blue epoxy (top left) represents porosity.

Plate 4.5: Shallow Burial III

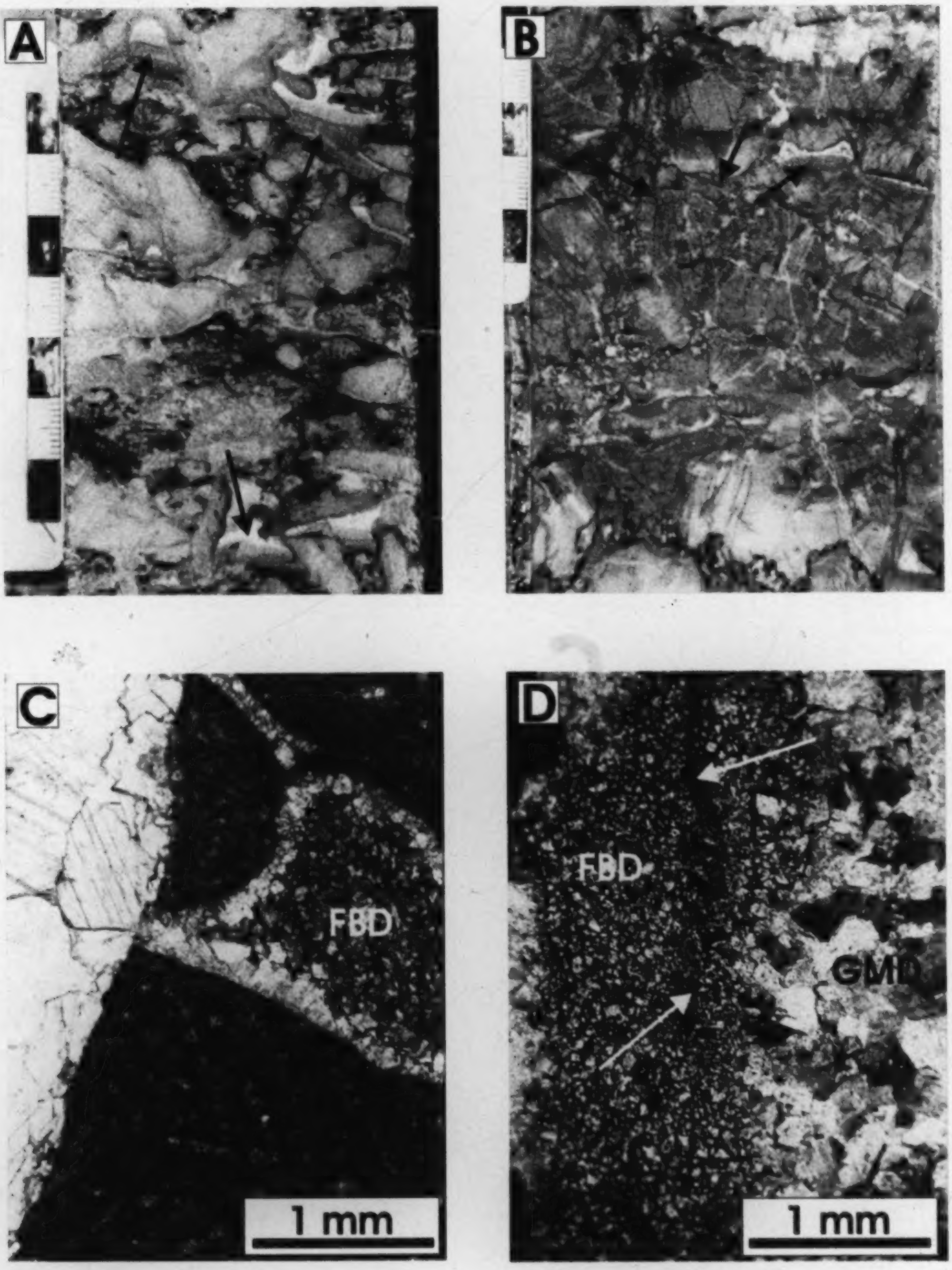
A
B
C
FBD
1 mm
D
FBD
GMD
1 mm

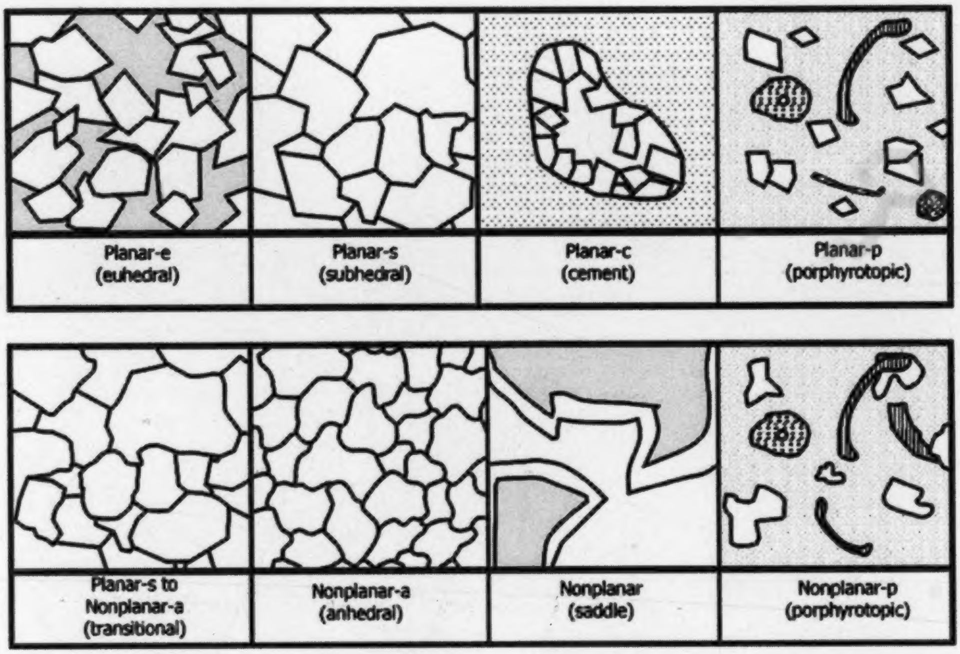
Planar-e
(euhedral)
Planar-s
(subhedral)
Planar-c
(cement)
Planar-p
(porphyrotopic)
Planar-s to
Nonplanar-a
(transitional)
Nonplanar-a
(anhedral)
Nonplanar
(saddle)
Nonplanar-p
(porphyrotopic)

Figure 4.2 Dolomite textural classification combined from Gregg and Sibley (1984), and Sibley and Gregg (1987), supplemented by a 'transitional' form. Reproduced from Wright (2001).

Sibley and Gregg, 1987) (Plate 4.6D). Some crystals display undulose extinction in some locations. Where GMD contains significant intercrystalline porosity, clear overgrowth rims precipitated around cloudy brown cores. GMD displays relatively homogenous dull red CL colours, with spotty occurrences of bright luminescent overgrowth rims. In partially dolomitized rocks GMD preferentially replaces the original micritic matrix and early interparticle calcite cements. Fossils, such as bulbous and tabular stromatoporoids, are not affected by replacement by GMD in such rocks. In completely dolomitized wells, low-Mg brachiopods and crinoids are fully replaced by GMD (Plate 4.6C), and *Amphipora* and *Thamnopora* show evidence of replacement internally, i.e., in their central canals and galleries, and zooecial tubes, respectively. Pervasive dolomitization followed the first generation of stylolites (Plate 4.4D) and was most likely completed during intermediate burial. This conclusion is based on the presence of bitumen in the intercrystal and vuggy pores of the matrix dolomites: reflecting regional kerogen maturation and liquid hydrocarbon migration at the base of the intermediate burial diagenetic setting.

Plate 4.6 Intermediate burial (I) textural and mineralogical changes.

(A) Core photograph of grey matrix dolomite (phase 10) in an *Amphipora* floatstone. Dolomitization of the matrix resulted in the retention of micro-stylolites (phase 8) running sub-horizontally across the width of the core. *Amphipora* were subsequently cemented by saddle dolomite (phase 13) or dissolved to create secondary vuggy/ mouldic porosity. b-72-L/94-J-9; 6249'6".

(B) Thin section photomicrograph of grey matrix dolomite (phase 10) under diffuse light demonstrating the original grainstone texture of the limestone matrix. Stained thin section, diffuse polarized light. a-61-F/94-J-10; 6711'.

(C) Thin section photomicrograph of grey matrix dolomite (phase 10) under diffuse light showing replacement of both brachiopods (B) and crinoids (C). The outline of the biochems is visible due to the increased insoluble residue in the original micrite matrix. Stained thin section, diffuse polarized light. c-47-J/94-J-10; 6550'6".

(D) Thin section photomicrograph of planar-e grey matrix dolomite (phase 10) with pyrobitumen (phase 23) infilling secondary intercrystalline porosity. Stained thin section, plane-polarized light. b-72-L/94-J-9; 6241'.

Plate 4.6: Intermediate Burial I

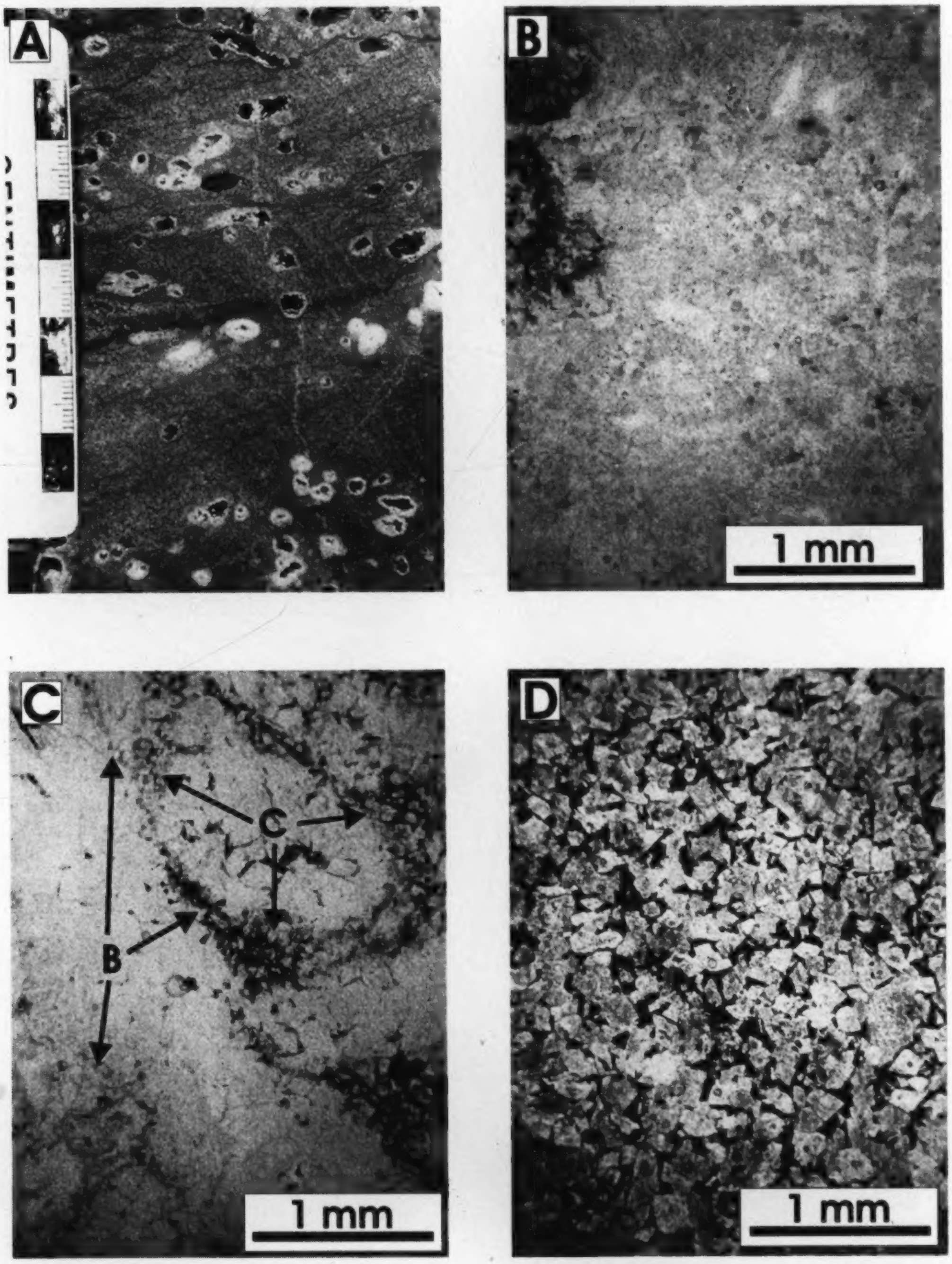
A
B
1 mm
C
C
B
1 mm
D
1 mm

Replacive chert (phase 11)

Chert occurs as a scattered, cryptocrystalline replacement of biochems in both limestones and dolostones in the Slave Point Formation (Plate 4.7). These biochems include previously undissolved calcite skeletons of *Thamnopora* and *Amphipora*. In core, replacive chert appears in a dark yellowish-brown colour (Plate 4.7A). In thin section, it occurs as anhedral masses with banding (Plate 4.7B), and has a white to light brown colour.

Fracture II (phase 12)

Fracture generation II post-dates the main replacement dolomite phase (GMD – phase 10), and is present in all wells that contain saddle dolomite (Plate 4.8). These fractures occur predominantly in a vertical to sub-vertical orientation, with widths ranging from hairline fractures to roughly 1 cm, and core lengths varying up to roughly 50 cm. These fractures clearly post-date stylolite generation I (Plate 4.8A and B), and pre-date later stages of fracturing (phase 15) and shearing (phase 16) (Plate 4.8D). These fractures were partially to completely cemented by both coarse crystalline dolomite and saddle dolomite (hydrothermal alteration - phase 13).

Hydrothermal alteration (phase 13)

The products of the invasion of hydrothermal fluid(s) are here collectively termed *hydrothermal alteration*. These products include: dissolution of matrix dolomite (GMD – phase 10), recrystallization of matrix dolomite, replacement of matrix dolomite by saddle dolomite, and saddle dolomite cement (SD). Petrography suggests that this alteration was from hot fluids, as saddle dolomite forms only at elevated temperatures (Radke and Mathis, 1980; Machel, 1987b; Spötl and Pitman, 1998). Geochemical evidence that this process was also hydrothermal will be presented in Chapter 5.

Initially, hydrothermal alteration created oversized pores through dissolution of GMD (Plate 4.9A through C). The fluid that generated these oversized pores was undoubtedly undersaturated with respect to dolomite at the time it entered the reservoir, for without which there would be no oversized pores in the dolostones. Through dissolution of GMD, the fluid became saturated with respect to dolomite, which initiated recrystallization of GMD in two forms: to recrystallized matrix dolomite (Figure 4.9D) and to saddle dolomite

Plate 4.7 Intermediate burial (II) textural and mineralogical changes.

(A) Core photograph of nodular stomatoporoid-*Amphipora*-coral rudstone. The original micrite matrix was replaced by grey matrix dolomite (phase 10), and the fossils were either replaced by saddle dolomite (phase 13) or dissolved to generate significant mouldic porosity. In some places, the calcite skeletons of *Thamnopora* (Th) and *Amphipora* (A) were replaced by chert (phase 11 - yellowish-brown colour). d-69-H/94-J-10; 6563'.

(B) Thin section photomicrograph of *Amphipora* replaced by chert (phase 11 - C). Stained thin section, plane-polarized light. c-64-I/94-J-10; 6434'.

(C) Thin section photomicrograph of chert (phase 11) and dolomite replacing *Amphipora*. The chert (C) preferentially replaced the original calcite skeleton of the *Amphipora*, while the dolomite (D) - in this case, replacement saddle dolomite (phase 13) - replaced the calcite cemented galleries. Stained thin section, plane-polarized light. c-70-E/94-J-9; 6449'3".

(D) Thin section photomicrograph of *Thamnopora* replaced by saddle dolomite (phase 13 - white) and chert (phase 11 - brown). The dolomite replaced both the calcite cemented zooecial tubes and the outer rim of the coral, while the chert replaced the internal calcite skeleton. Macroscopically, this section would be characteristic of the chertified *Thamnopora* seen in Photo A. Stained thin section, diffuse polarized light. d-69-H/94-J-10; 6538'.

Plate 4.7: Intermediate Burial II

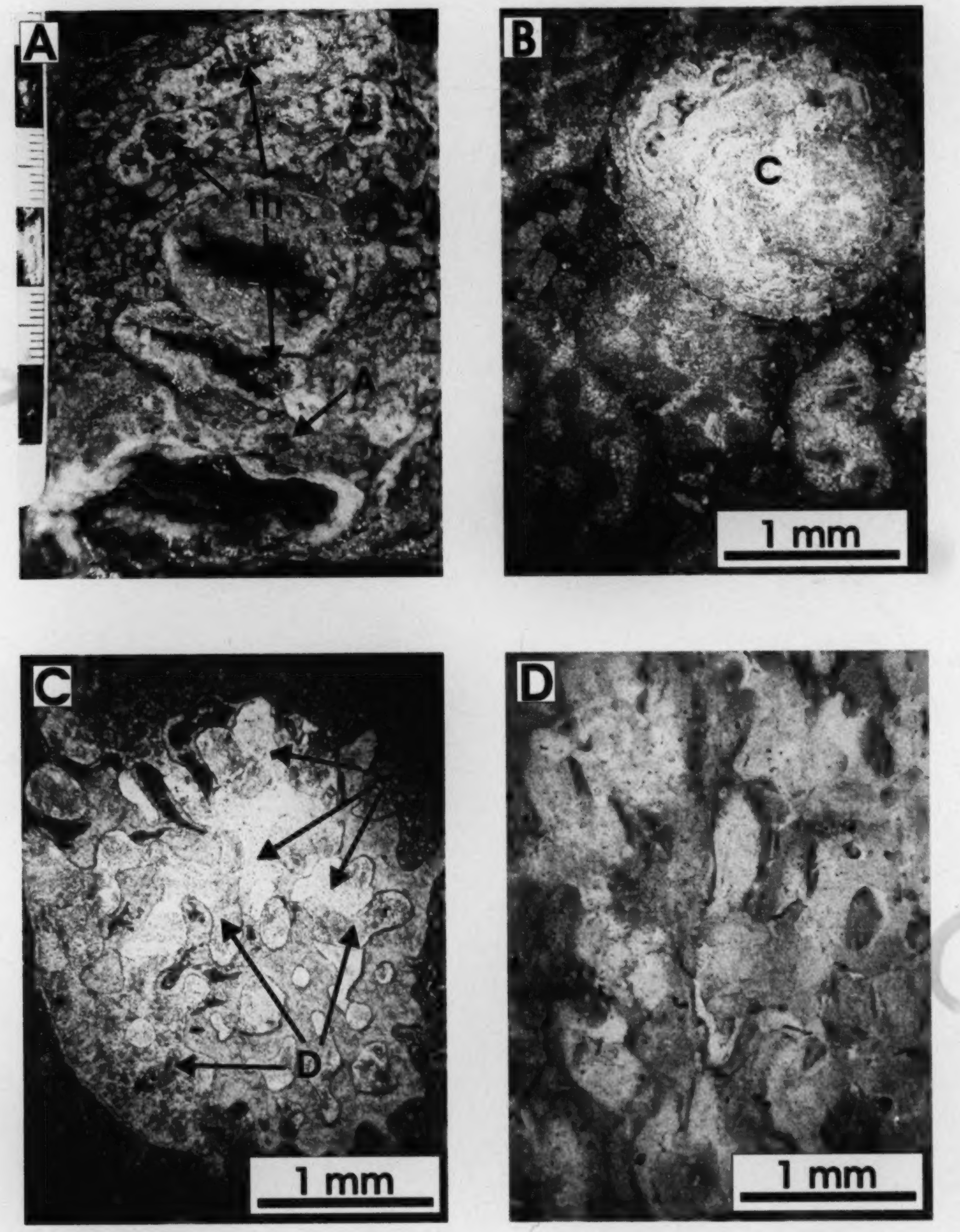
A
m
A
B
C
1 mm
C
D
1 mm
D
1 mm

Plate 4.8 Intermediate burial (III) textural and mineralogical changes.

(A) Core photograph of sub-vertical fracture set II (phase 12) cross-cutting stylolite-bearing grey matrix dolomite (phase 10). The fracture truncates the stylolites (arrows) and was subsequently filled by saddle dolomite cement (phase 13). c-94-L/94-J-9; 6362'.

(B) Core photograph of saddle dolomite cemented (phase 13) sub-horizontal fracture set II (phase 12) cross-cutting a stylolite (arrow), in a pervasively dolomitized *Amphipora* floatstone. c-94-L/94-J-9; 6419'6".

(C) Core photograph of well-developed saddle dolomite crystals (phase 13) partially filling fracture set II (phase 12). c-58-E/94-J-10; 2152.85 m.

(D) Core photograph of saddle dolomite cement (phase 13) in sub-orthogonal fracture set II (phase 12), displaced by a later fracture generation associated with tectonism. d-79-F/94-J-10; 6781'.

Plate 4.8: Intermediate Burial III

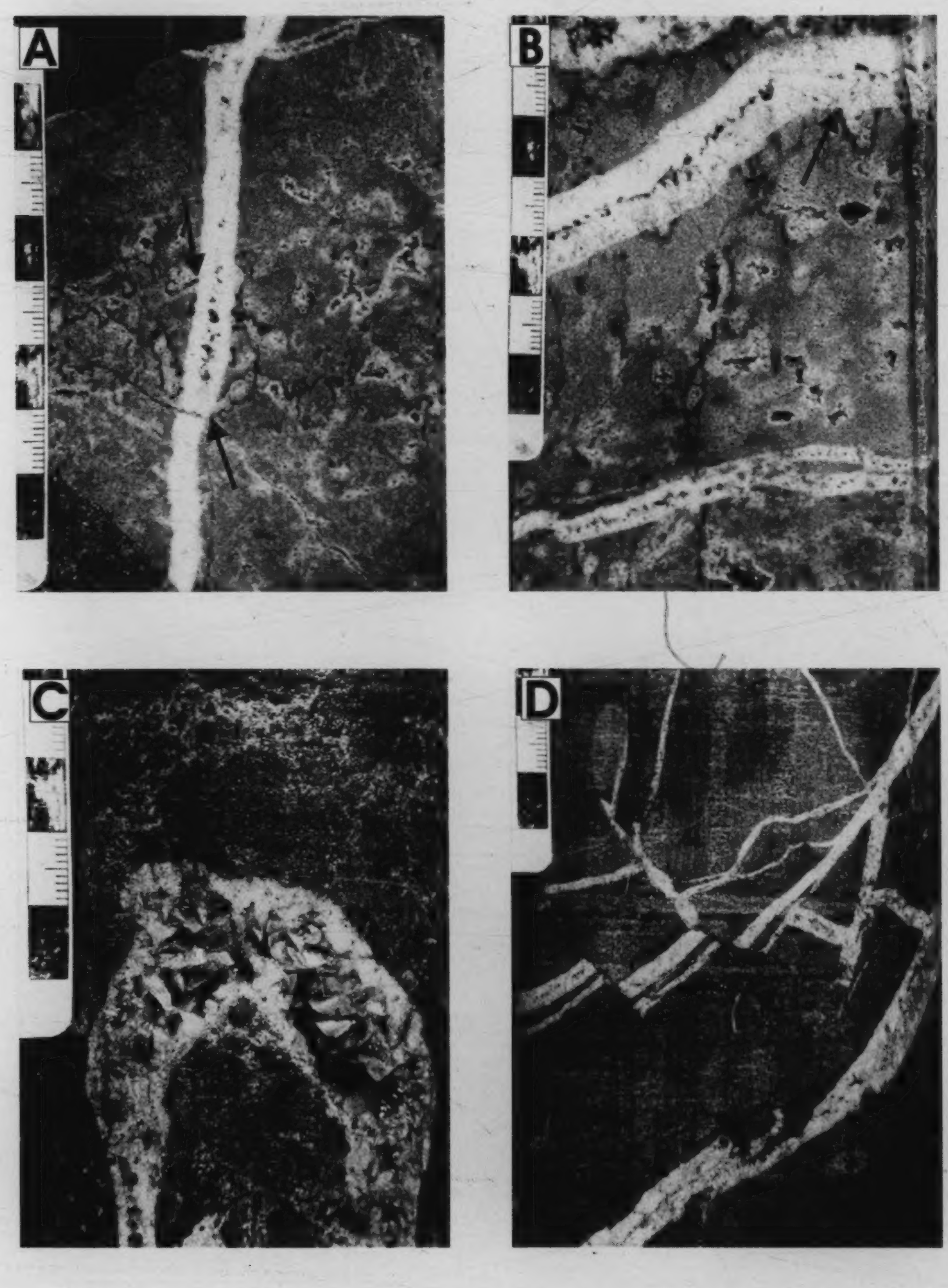

Plate 4.9 Intermediate burial (IV) textural and mineralogical changes.

(A) Core photograph showing dissolution (hydrothermal alteration - phase 13) and generation of oversized vuggy pores in GMD. The pores are lined by either saddle dolomite cement or recrystallized GMD (reX md) adjacent to the pore walls. a-65-G/94-J-10; 6740'.

(B) Core photograph showing dissolution and hydrothermal alteration (phase 13) of grey matrix dolomite (phase 10). The creation of oversized vuggy pores, and the generation of irregular interfaces between GMD and SD and the generation of 'pseudo-breccias' (top left corner) are evidence for alteration. d-72-G/94-J-10; 6429'.

(C) Core photograph showing a horizontal fracture partially cemented by saddle dolomite (phase 13) in a pervasively dolomitized coral-stromatoporoid floatstone-rudstone. The upper half of the photo shows fossil replacement (Rp), while the lower half of the photo shows fossil dissolution (Di). b-10-D/94-J-16; 6292'8".

(D) Thin section photomicrograph showing oversized pore generation through dissolution (phase 13) of grey matrix dolomite (lower left corner). Hydrothermal dissolution and recrystallization of grey matrix dolomite is evident by the appearance of irregular interfaces between GMD and SD, and by non-planar boundaries (arrows). Much of the intercrystalline porosity is filled with pyrobitumen (phase 23 - black). Stained thin section, diffuse polarized light. b-70-I/94-J-10; 6265'. Blue epoxy represents porosity.

Plate 4.9: Intermediate Burial IV

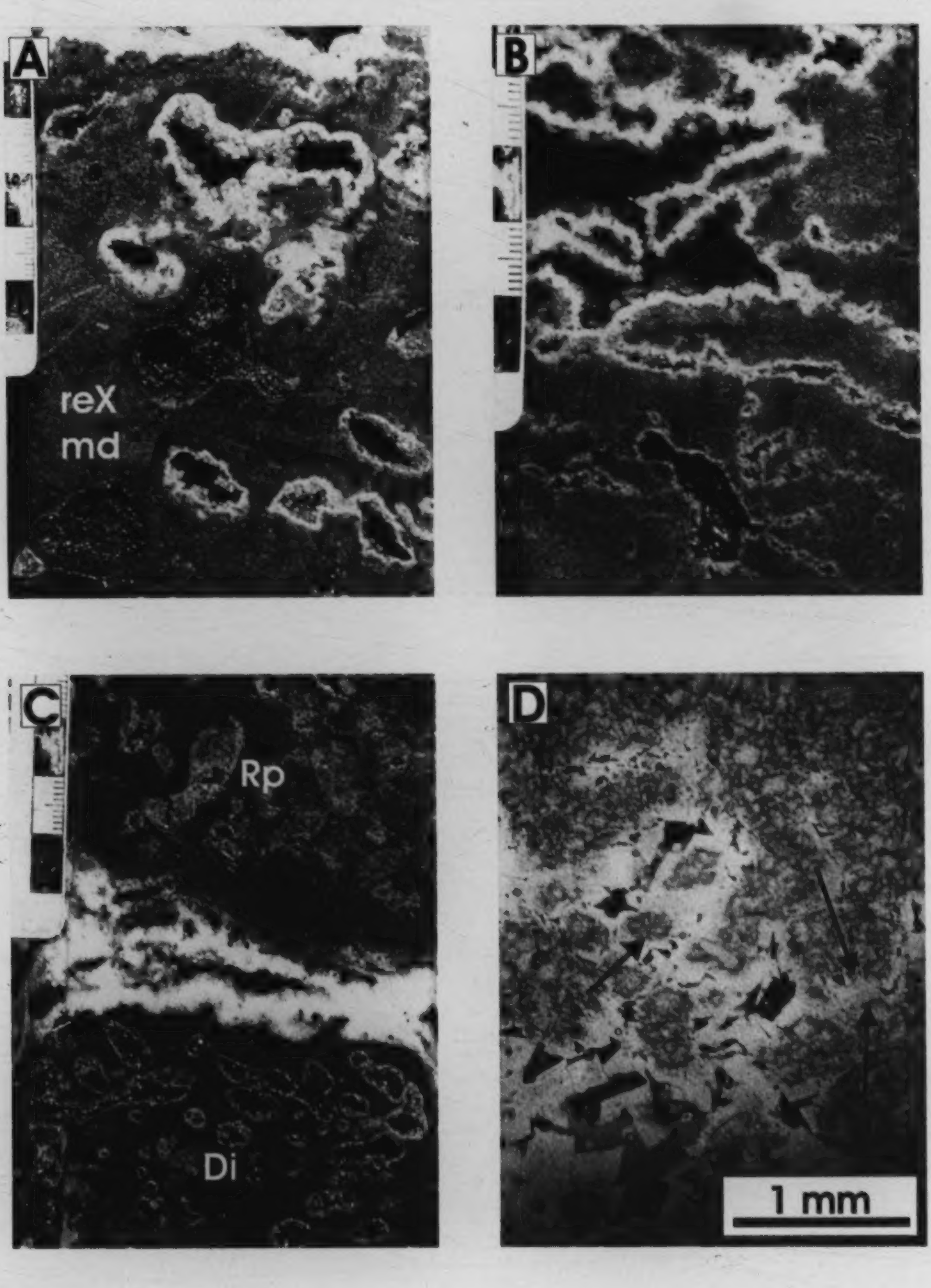
A
reX
md
B
C
Rp
Di
D
1 mm

(Plate 4.9C and D, Plate 4.10A and B). The formation of replacive saddle dolomite may be called a replacement, although it is recrystallization *sensu stricto*.

Evidence for recrystallization of GMD to recrystallized matrix dolomite (reX md) include common non-planar crystal textures, relatively large crystal sizes (up to 2 mm) compared to matrix dolomites elsewhere in the basin (commonly 100-500 µm), formation of clear overgrowth rims, overall spotty to homogenous luminescence, and some crystals exhibiting undulose extinction. In general, these recrystallization textures are found in GMD only in close proximity to fractures, zones of dissolution, and oversized pores containing SD, i.e., as 'alteration halos' (Plate 4.10C and D) immediately next to SD that is also the recrystallization product of matrix dolomite (planar or non-planar GMD). Eventually the fluid became supersaturated with respect to dolomite, leading to cementation with well-developed, coarse crystalline dolomite and saddle dolomite in the remaining vuggy pores (Plate 4.10C and D).

Coarse crystalline dolomite is a volumetrically minor diagenetic phase in the Slave Point Formation, only occurring in 2 wells. Coarse crystalline dolomite is characterized by planar-e crystals that attain a maximum size of about 1 mm (Plate 4.11A). The crystal cores are often turbid, due to an abundance of fluid inclusions, while the crystal rims show alternating turbid and non-turbid crystal growth zones. These crystal zones correspond to alternating bright to dull red luminescent zones under CL. Coarse crystalline dolomite is always found in oversized dissolution vugs in GMD. Due to the limited occurrence of coarse crystalline dolomite in the Slave Point Formation, no conclusions regarding genesis can be made. However, petrographically, coarse crystalline dolomite is linked to the formation of saddle dolomite.

Saddle dolomite in the Slave Point Formation has crystal sizes that range from 500 µm to 2 mm, and display concentric alternating zoning of dull to bright red CL in some samples (Plate 4.11B through D). Saddle dolomite accounts for between 20 and 80% by volume of all dolomite in the Slave Point Formation. Saddle dolomite is a common cement in fracture generation II (phase 12) and oversized vuggy pores, and a replacement of matrix dolomite (hydrothermal alteration). Crystals of saddle dolomite are commonly coated with pyrobitumen (Plate 4.11B and C) implying formation prior to liquid hydrocarbon migration (phase 19) and subsequent thermal cracking (phase 23).

The entire sequence of events from the formation of GMD (phase 10) to hydrothermal

Plate 4.10 Intermediate burial (V) textural and mineralogical changes.

(A) Core photograph of pervasively dolomitized *Thamnopora-Stachyodes*? rudstone. The bulk of the matrix is comprised of grey matrix dolomite (phase 10), while the biochems are mainly comprised of replacement saddle dolomite (phase 13). Large vugs/moulds were subsequently occluded by saddle dolomite cement (bottom right). d-69-H/94-J-10; 6542'.

(B) Thin section photomicrograph showing the replacement of *Amphipora* by saddle dolomite (hydrothermal alteration - phase 13). The original galleries of the *Amphipora* are clearly visible. The arrows point to the 'ghosts' of grey matrix dolomite crystals that were replaced by saddle dolomite during hydrothermal alteration. Stained thin section, diffuse polarized light. b-10-D/94-J-16; 6292'8".

(C) Core photograph demonstrating the various textures related to dissolution and hydrothermal alteration. Knife-edged fractures (phase 12 - F) permitted the invasion of hydrothermal fluids that partially dissolved grey matrix dolomite and created rounded-clast breccias (Di) or 'pseudo-breccias' (PB). Saddle dolomite cement (phase 13) occluded the open fractures, except at the top of the photo, where oversized vuggy porosity remains and saddle dolomite crystals are coated by pyrobitumen (phase 23). a-65-G/94-J-10; 6719'.

(D) Core photograph showing three dolomite types: recrystallized GMD (reX md), petrographically unaltered fine crystalline matrix dolomite (fX md), and saddle dolomite that occurs as a passive cement in the vuggy/fracture porosity. The boundary between fX md and reX md is smooth and highlighted with a white dashed line near the centre of the photo: c-47-J/94-J-10; 6551'9".

Plate 4.10: Intermediate Burial V

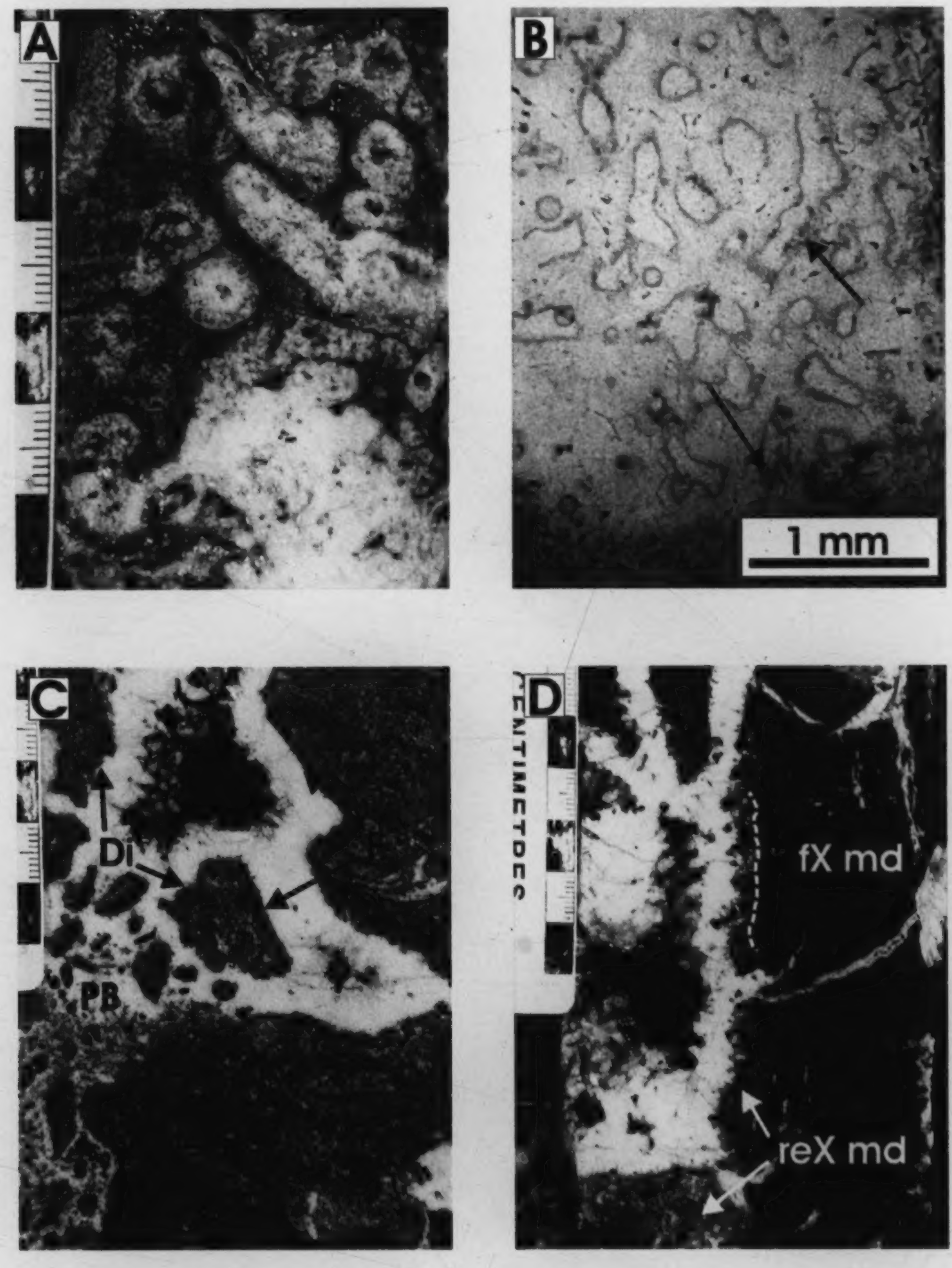
A
B
1 mm
C
Di
PB
D
fX md
reX md

Plate 4.11 Intermediate burial (VI) textural and mineralogical changes.

(A) Thin section photomicrograph of rare, weakly-zoned, coarse crystalline dolomite (hydrothermal alteration - phase 13) surrounded by planar-e to planar-s grey matrix dolomite (GMD - phase 10). The coarse crystalline dolomite is partially filling an oversized vug created by the dissolution of matrix dolomite. Stained thin section, plane-polarized light. b-22-J/94-J-10; 6539'6".

(B) Core photograph of saddle dolomite cement (phase 13) partially filling an oversized vug. The saddle dolomite crystals display curved crystal faces that are partially coated by pyrobitumen (phase 23 - black). a-65-G/94-J-10; 6735'.

(C) Thin section photomicrograph of fracture-lining saddle dolomite cement (phase 13), showing well-developed, dull to bright red, concentric and oscillatory zoning under cathodoluminescence. The remaining fracture porosity was subsequently cemented by non-luminescent blocky calcite (phase 25). Unstained thin section, cathodoluminescence. d-79-F/94-J-10; 6769'.

(D) Similar to Photo C. d-79-F/94-J-10; 6769'.

Plate 4.11: Intermediate Burial VI

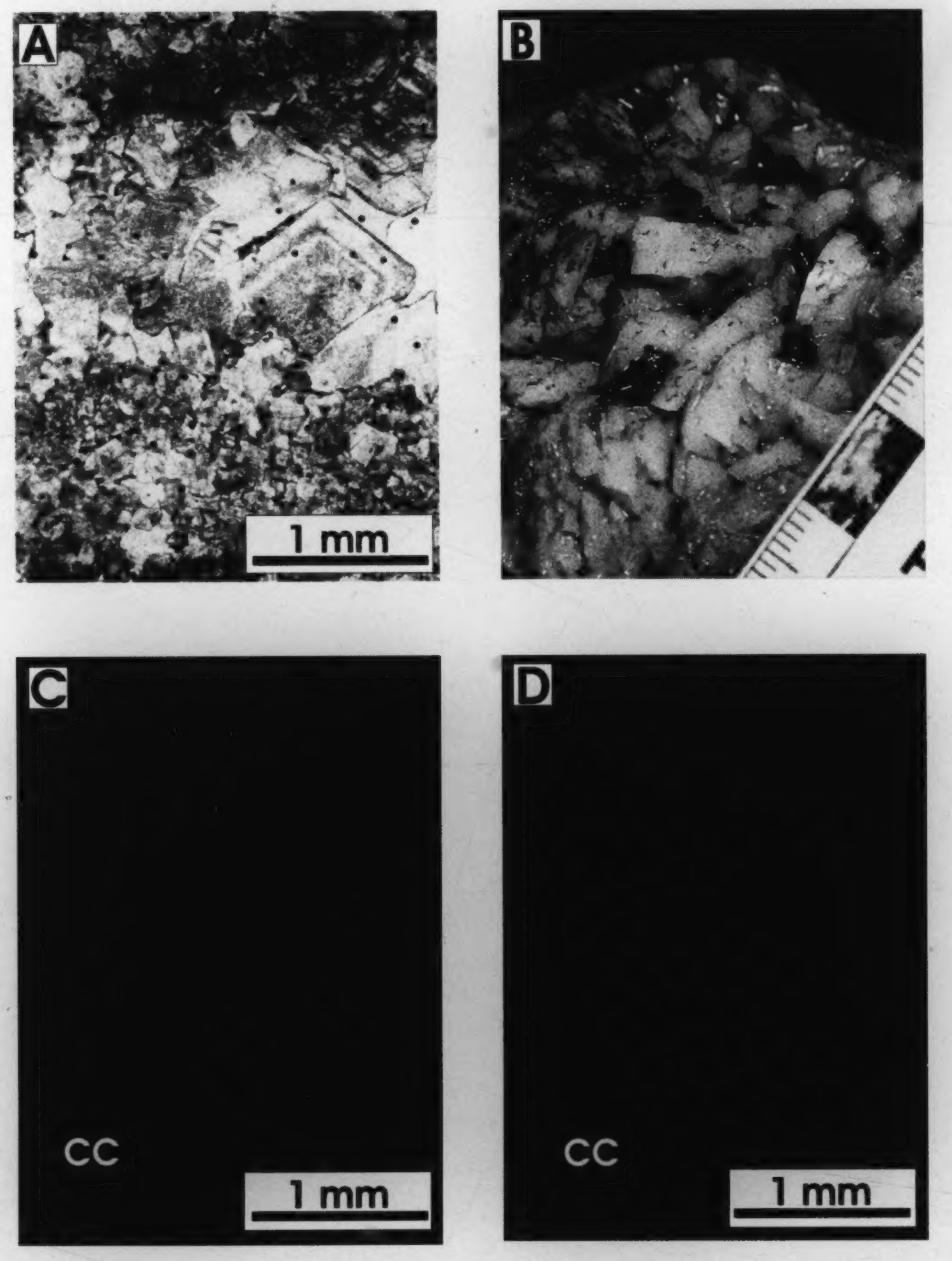
A
1 mm
B
C
CC
1 mm
D
CC
1 mm

alteration (phase 13) in the Slave Point Formation is summarized schematically in Figure 4.3.

Stylolite II (phase 14)

Stylolite generation II display amplitudes ranging from roughly 2 to 10 centimetres, and are most common where the Slave Point Formation is pervasively dolomitized (Plate 4.12). Stylolite generation II cuts across the earlier generation of lower-amplitude stylolites (phase 8), grey matrix dolomite (phase 10), and saddle dolomite (hydrothermal alteration - phase 13) (Plate 4.12B and C). This generation of stylolites clearly pre-dates both pyrite mineralization (phase 18) and liquid hydrocarbon migration (phase 19) (Plate 4.12B, C, and D).

4.3.4 Deep burial diagenesis (stage)

The latest stage of diagenesis in the Slave Point Formation at Clarke Lake occurred during deep burial from 2000 to greater than 3000 metres depth. The products of this stage include: fracture generation III, shearing and authigenic clay mineral formation, vertical stylolite generation, base-metal sulphide mineralization, hydrocarbon migration, quartz and barite, fracture generation IV, and blocky calcite II.

Fracture III (phase 15)

Fracture generation III post-dates both hydrothermal alteration (phase 13), including saddle dolomite formation (Plate 4.13). These fractures occur in a network that show a predominantly vertical to sub-vertical orientation, and extend laterally for 10's of centimetres and vertically up to a few metres. Most of these fractures were subsequently cemented by pyrite, barite (Plate 4.13A), sphalerite (Plate 4.13B and C), galena, and quartz (Plate 4.13C and D)(see below).

Shear and authigenic clay minerals (phase 16)

Very narrow (< 1 cm) zones of breccia formation are found in a few of the pervasively dolomitized wells penetrating the Slave Point Formation at Clarke Lake (Plate 4.14A and B). The clasts within these 'micro'-breccia zones show evidence of rotation, typical of a mosaic texture. As well, many of these clasts have sub-rounded edges, and are floating

Figure 4.3 Schematic representation of dolomitization and subsequent hydrothermal alteration, based on petrographic observations. Scale bar = 1 cm.

(A) Precursor limestone composed principally of micrite (1) and various fossils that have been cemented by early calcite (2) (Drusy calcite - phase 4, Figure 4.1). The limestone also shows evidence of fractures (3) (Fracture I - phase 5, Figure 4.1) subsequently filled with calcite cement (Blocky Calcite I - phase 6, Figure 4.1), and stylolite formation (Stylolite I - phase 8, Figure 4.1).

(B) Micrite (4) and calcite cements - both fracture and intraparticle (5) replaced by grey matrix dolomite (GMD - phase 10, Figure 4.1). The calcite skeleton of the fossil is not replaced by GMD. Both the fracture and stylolite are visible under diffuse plane polarized light.

(C) Vertical to sub-vertical fractures (6) (Fracture II - phase 12, Figure 4.1) cut across all previously formed diagenetic phases. There is some dissolution along the fracture walls, resulting in irregular boundaries, caused by the introduction of a solution undersaturated with respect to dolomite.

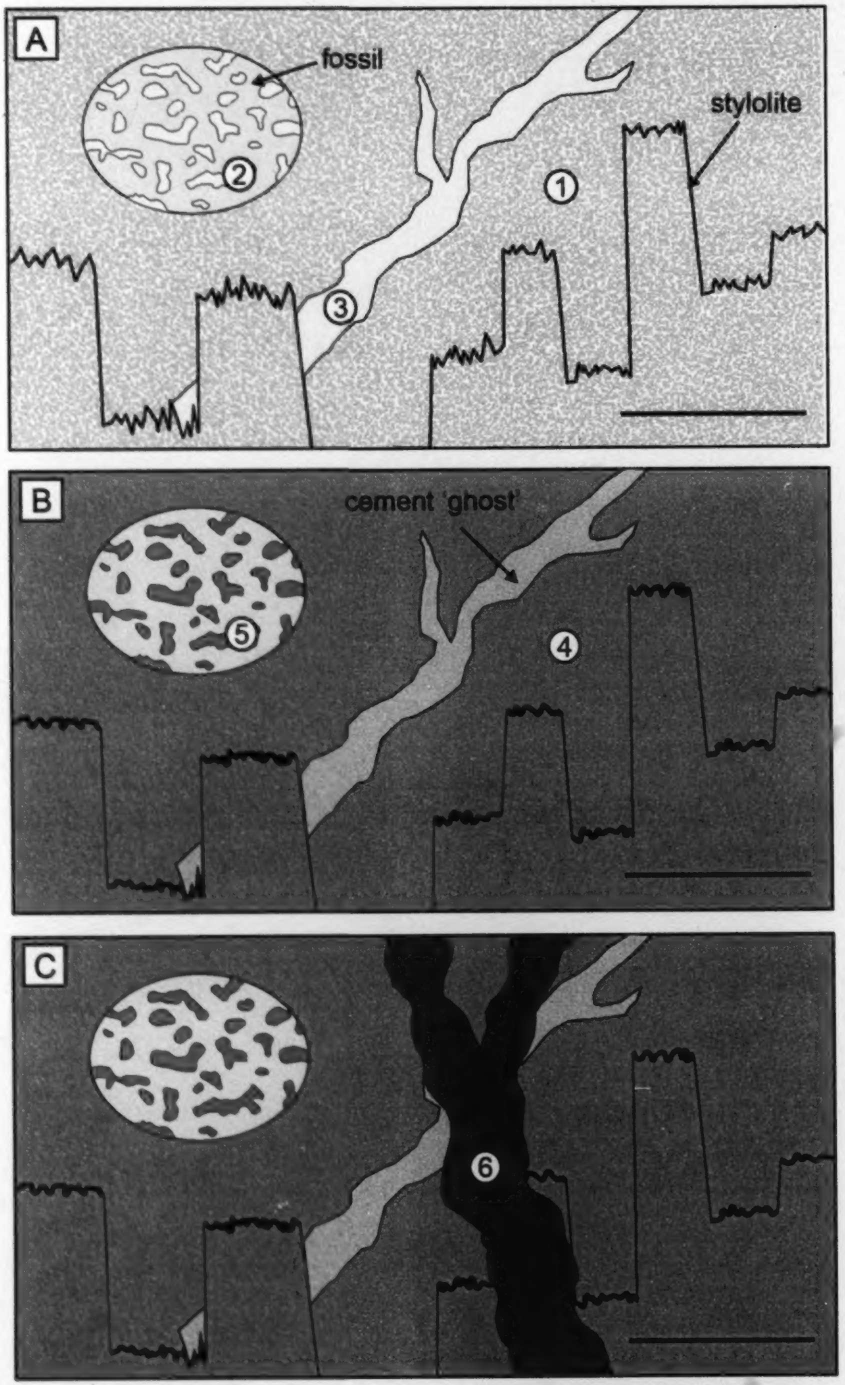
A
fossil
stylolite
①
②
③
B
cement 'ghost'
④
⑤
C
⑥

1 - micrite
2 - intrafossil calcite cement (phase 4)
3 - fracture I cemented with blocky calcite I (phase 6)
4 - grey matrix dolomite (GMD - phase 10)
5 - calcite cement replaced with GMD
6 - open fracture II (phase 12), partially enlarged by dissolution

Figure 4.3 Schematic representation of dolomitization and subsequent hydrothermal alteration, based on petrographic observations (continued).

(D) The hydrothermal fluid undersaturated with respect to dolomite continues to dissolve dolomite adjacent to the walls of the fractures and in adjacent permeable domains. Dissolution (7) by the hydrothermal fluid resulted in an increase in the width of the fractures and the generation of oversized pores (vugs).

(E) Continued dissolution brings the hydrothermal fluid to saturation with respect to dolomite. At this stage, dissolution ceases and immediately adjacent to the fracture walls and oversized vuggy pores, replacive saddle dolomite forms (10), which is characterized by a coarse-crystal size without well defined curved crystal terminations. At greater distances away from the conduits for the hydrothermal fluids, the original grey matrix dolomite shows textural and/or geochemical evidence for recrystallization (9 - reX md). Another product of the recrystallization of grey matrix dolomite is the apparent generation of brecciated dolomite fabrics (11). In domains where the hydrothermal fluids did not enter, there is no textural and/or geochemical evidence for recrystallization of grey matrix dolomite (8).

(F) The latest stage of hydrothermal alteration is represented by the partial cementation of oversized pores and fractures by well-developed crystals of saddle dolomite (12) (SD - phase 13, Figure 4.1). Remaining pore space is represented in blue.

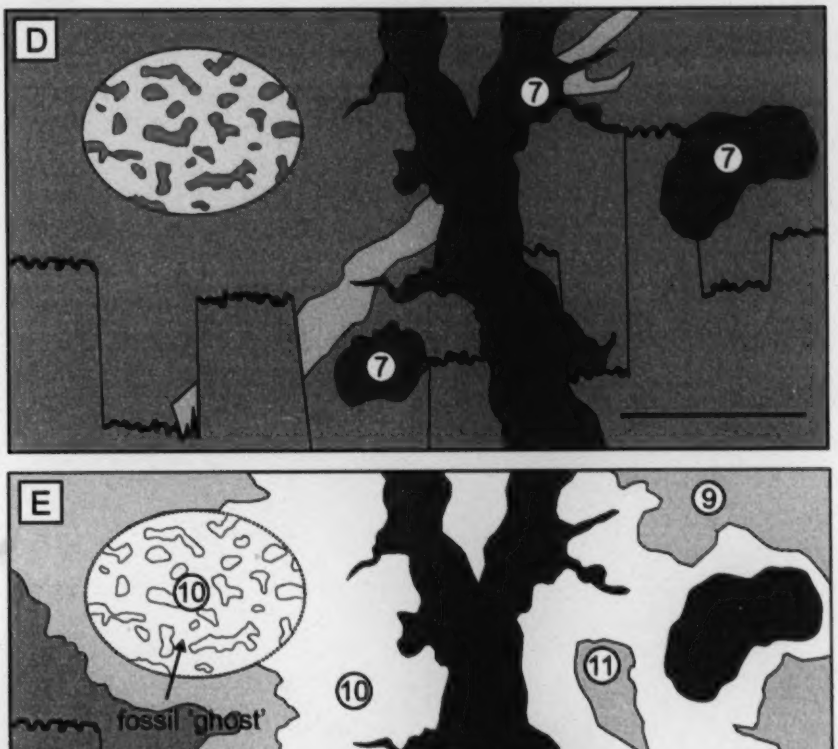
D
7
7
7
7
E
9
10
11
fossil 'ghost'
10
8
9
10
F
12
12
12

7 - dissolution of grey matrix dolomite (phase 13)
8 - 'pristine' grey matrix dolomite (GMD - phase 10)
9 - recrystallized grey matrix dolomite (reX md)

10 - replacement saddle dolomite
11 - 'pseudo'-breccia clast of reX md
12 - saddle dolomite cement
(SD - phase 13)

Plate 4.12 Intermediate burial (VII) textural and mineralogical changes.

(A) Core photograph of high-amplitude stylolite II (phase 14) in a stromatoporoid floatstone. The stylolite post-dates the bitumen-impregnation of the micrite matrix (phase 19 - dark brown). b-78-J/94-J-9; 6274'.

(B) Core photograph of two stylolite generations in dolomite. The earliest generation of stylolites (phase 8 - S1) approximates the boundary between grey matrix dolomite and saddle dolomite. This stylolite generation is truncated by the high-amplitude stylolite (phase 14 - S2). Stylolite II was utilized as a fluid conduit for later pyrite formation (phase 18 - brassy yellow colour) and hydrocarbon migration (phase 19 - black residue). c-47-J/94-J-10; 6554'3".

(C) Core photograph of stylolite generation II (phase 14) cross-cutting both grey matrix dolomite (phase 10) and saddle dolomite (phase 13). The isolated 'pods' (arrows) of both dolomite phases are clear evidence for the timing of stylolite II formation. Subsequent hydrocarbon migration (phase 19) is represented by the black residue along the stylolites. d-79-F/94-J-10; 6789'.

(D) Thin section photomicrograph of stylolite generation II (phase 14) cross-cutting large saddle dolomite crystals (phase 13). Subsequent hydrocarbon migration (phase 19) is represented by the black residue along the stylolite. Stained thin section, plane-polarized light. d-79-F/94-J-10; 6789'.

Plate 4.12: Intermediate Burial VII

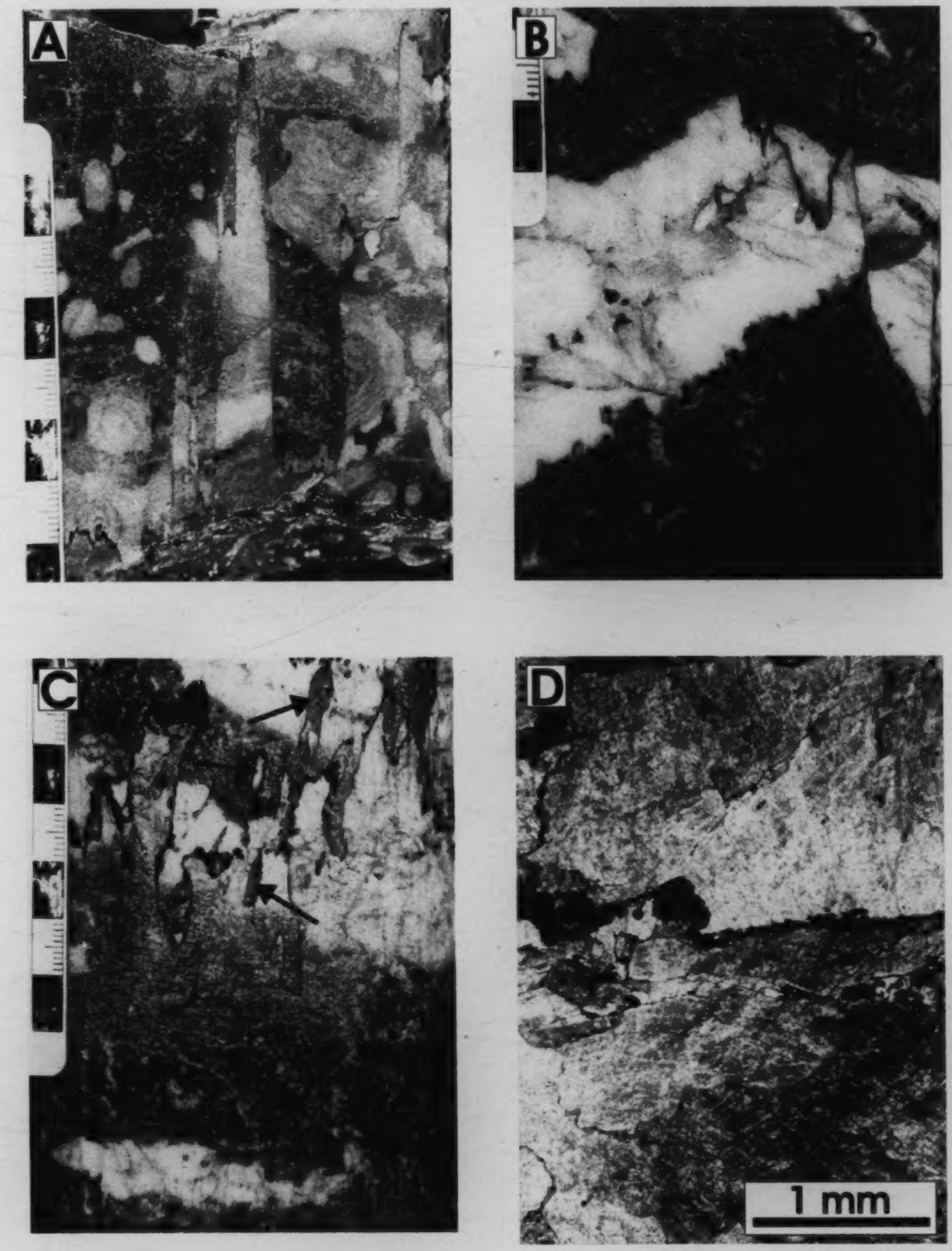

Plate 4.13 Deep burial (I) textural and mineralogical changes.

(A) Core photograph of sub-vertical fracture set III (phase 15) cross-cutting both grey matrix dolomite (phase 10) and saddle dolomite (phase 13 - SD). The fractures were subsequently occluded by sphalerite (phase 18 - orange-brown colour), quartz (phase 20), and barite (phase 21 - Bar). d-79-F/94-J-10; 6785'.

(B) Thin section photomicrograph of fracture set III (phase 15) shown in Photo A. The 'spalling' of saddle dolomite into the fracture is clear evidence that this fracture generation post-dates saddle dolomite cement (phase 13 - SD). The fracture was subsequently occluded by sphalerite (phase 18 - Sph), quartz (phase 20 - Q), and barite (phase 21 - Bar), in that order. Stained thin section, plane-polarized light. d-79-F/94-J-10; 6785'.

(C) Core photograph of fracture set III (phase 15) resulting in the extensive brecciation of grey matrix dolomite (phase 10) and saddle dolomite (phase 13). The breccia matrix is comprised of sphalerite (phase 18 - orange-brown colour), traces of bitumen (phase 23), and quartz (phase 20 - black colour). d-79-F/94-J-10; 6788'.

(D) Thin section photomicrograph of fracture set III (phase 15) shown in Photo C. Breccia clasts of grey matrix dolomite (phase 10 - GMD) and saddle dolomite (phase 13 - SD) float in a matrix of quartz (phase 20 - white) and minor quantities of sphalerite (phase 18) and bitumen (phase 23). Stained thin section, plane-polarized light. d-79-F/94-J-10; 6788'.

Plate 4.13: Deep Burial I

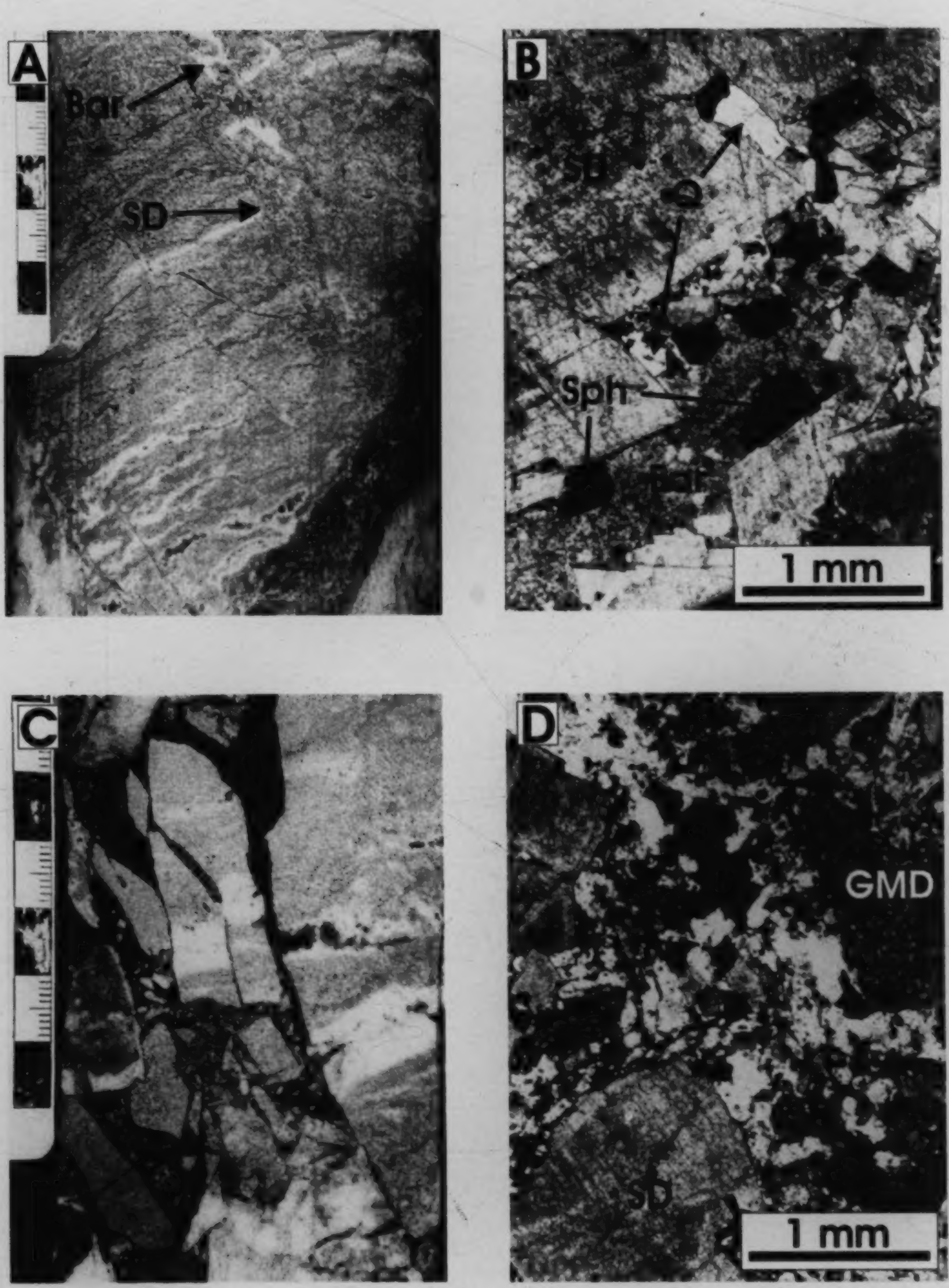
A
Bar
SD
B
SD
Sph
Bar
1 mm
C
D
GMD
SD
1 mm

Plate 4.14 Deep burial (II) textural and mineralogical changes.

(A) Thin section photomicrograph of a saddle dolomite breccia formed as a result of shearing (phase 16). The breccia clasts float in a matrix of fine-grained dolomite and authigenic clay minerals (bright colours). Stained thin section, cross-polarized light. d-72-G/94-J-10; 6443'6".

(B) Similar to Photo A. Stained thin section, plane-polarized light. d-79-F/94-J-10; 6778'.

(C) Core photograph of vertical stylolite (phase 17) cross-cutting grey matrix dolomite (phase 10) and saddle dolomite (phase 13), with a thick pyrobitumen residue (grey-black colour) (phase 23). b-10-D/94-J-16; 6268'6", proper orientation.

(D) Core photograph of vertical stylolite (phase 17 - arrows) cutting saddle dolomite cemented fractures in a stromatoporoid framestone. b-6-A/94-J-16; 6423', proper orientation.

Plate 4.14: Deep Burial II

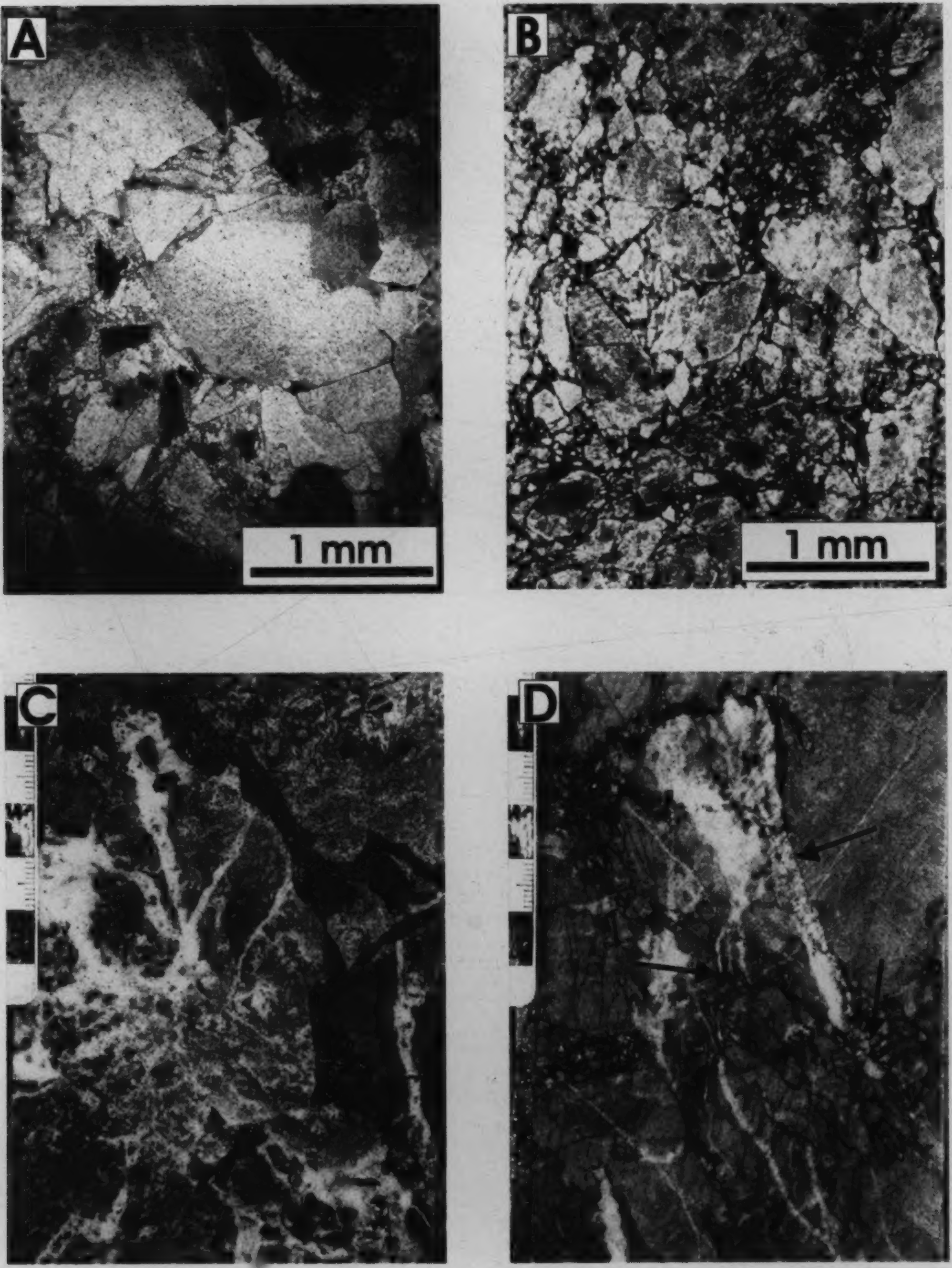
A
1 mm
B
1 mm
C
D

in a matrix of broken up or pulverized dolomite: possibly an indication of shear. Very fine-crystalline, high-birefringence minerals are also found in the breccia matrix, probably authigenic clay minerals.

Vertical stylolite (phase 17)

Vertical stylolites are not especially common features in the Slave Point Formation at Clarke Lake, and, where present, do not show a well defined 'teeth and socket' structure (Plate 4.14C and D). These stylolites are up to a few millimetres in width, but can be traced within individual cores for a distance of a few centimeters to 10's of centimetres. The vertical stylolites cut across all previous diagenetic phases, yet pre-date liquid hydrocarbon migration (phase 19).

Base-metal sulphide minerals (phases 18 and 22)

Within many of the dolomitized intervals, formation of saddle dolomite was followed by very minor, i.e., less than 1% by volume over any core interval, base-metal sulphide precipitation (Plate 4.15). Many individual core segments have visible sulphide mineralization, which partially fills oversized vugs (hydrothermal alteration – phase 13) and fracture generation II (phase 12). Pyrite occurs in the form of small (< 1 mm) cubic crystals either attached to well-developed saddle dolomite crystals in dolostones (Plate 4.15A), scattered throughout the micrite matrix of limestones, or as a replacement of the micrite matrix in limestones (Plate 4.17A). Sphalerite is present as translucent, honey-brown coloured, anhedral to tetrahedral crystals with diameters of less than 1 mm (Plate 4.13B and C, Plate 4.15B). Galena crystals usually exhibit a cubic habit and reach sizes of up to 1 cm (Plate 4.15D). Sphalerite and pyrite always pre-date liquid hydrocarbon migration (phase 19) (Plate 4.13B), and quartz cementation (phase 20) (Plate 4.15C); conversely, galena always post-dates these two diagenetic products. Sphalerite and galena occur only in dolostones.

Liquid Hydrocarbons (phase 19)

A phase of liquid hydrocarbon migration into the Slave Point Formation is recognized by the presence of solid pyrobitumen (Plate 4.17B through D). Pyrobitumen occurs as a hard, glassy, black material that occludes much of the intercrystalline porosity

Plate 4.15 Deep burial (III) textural and mineralogical changes.

(A) Core photograph of a vug fringed by saddle dolomite cement (phase 13 - white) and subsequently partially filled by cubic pyrite (phase 18 - Py) and translucent quartz (phase 20 - Q). c-56-L/94-J-9; 6409'.

(B) Core photograph of sphalerite (phase 18 - arrows) partially filling vuggy pores that are fringed by white saddle dolomite (phase 13). c-58-E/94-J-10; 2153.25 m.

(C) Thin section photomicrograph of sphalerite fragments (phase 18 - arrows) encased in quartz cement (phase 20 - green colour). Stained thin section, cross-polarized light. c-58-E/94-J-10; 2152.25 m.

(D) Core photograph of galena mineralization (phase 22 - arrow) post-dating fracture-lining (generation II - phase 12) saddle dolomite cement (phase 13). b-10-D/94-J-16; 6272'6".

Plate 4.15: Deep Burial III

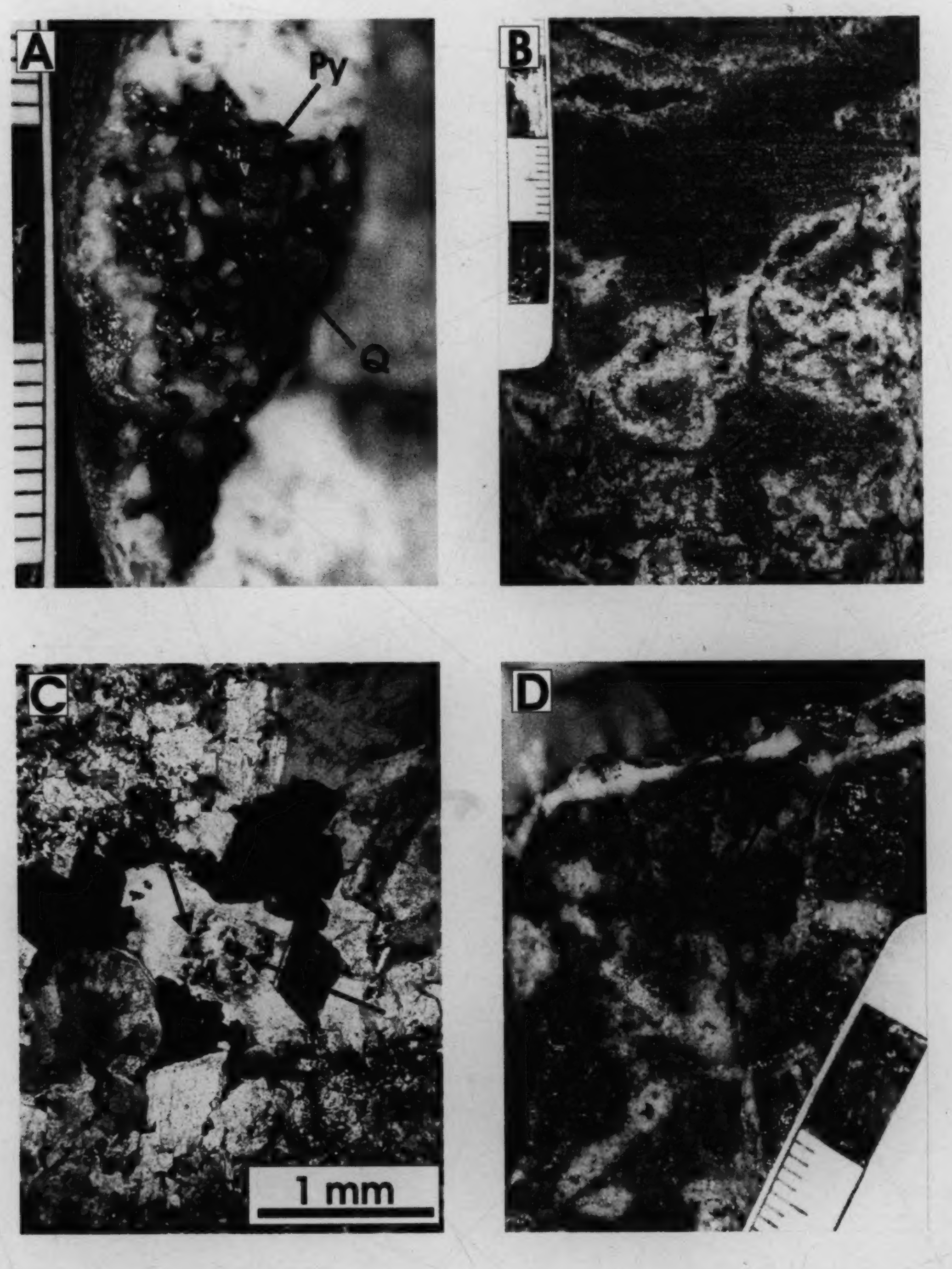
A
Py
Q
B
C
1 mm
D

generated by GMD (Plate 4.9D), coats the well-developed crystal faces of saddle dolomite-lined vugs (Plate 4.11B), and is found along stylolite generation II (Plate 4.12C and D). The presence of solid bitumen inclusions in some quartz crystals suggests that liquid hydrocarbon migration into the Slave Point Formation may have occurred concurrent with quartz precipitation (phase 20). Hydrocarbon migration pre-dates the formation of blocky calcite II (phase 25) (Plate 4.17B through D).

Quartz and barite (phases 20 and 21)

Quartz occurs as clear, euhedral to subhedral, weakly-zoned crystals that vary in diameter from less than 100 μm (Plate 4.13D) to greater than 2 mm (Plate 4.17C and D). The bulk of the quartz in the Slave Point Formation is found partially to completely cementing both fracture generation II (phase 12) and oversized vuggy pores (hydrothermal alteration – phase 13) that are lined with saddle dolomite cement. In these samples, quartz clearly post-dates hydrocarbon migration (phase 19), although, as was previously discussed in the section on base-metal mineralization, solid inclusions of bitumen, i.e., thermally cracked liquid hydrocarbon, are found within a few quartz crystals. Fracture generation III (phase 15) is also cemented by subhedral quartz crystals that appear as a hard, black, microcrystalline material in core (Plate 4.13C and D). Smaller scale fractures (phase 16) in GMD and SD are also cemented by co-genetic phases of quartz and barite, i.e., solid, rounded inclusions of barite within quartz (Plate 4.13A). Where barite occurs without quartz, it occurs as a microcrystalline form that displays sweeping extinction under cross-polarized light (Plate 4.13B).

Microfractures and thermal cracking (phase 23)

Hairline microfractures with widths of less than 1 mm are common in the limestones of the Slave Point Formation, yet entirely absent within the dolomite intervals (Plate 4.15). These microfractures occur predominantly in a vertical, anastamosing orientation, and extend for 10's of centimetres. These microfractures cross-cut matrix, allochems, and all older diagenetic phases (Plate 4.16A). In some cores, the microfractures occur in a random, sub-horizontal, or radial orientation and extend away from intraparticle pores (Plate 4.16B). The microfractures are often lined with solid bitumen or pyrobitumen. As well, the micrite matrix of many of the limestone intervals is impregnated with bitumen (Plate 4.16B and

Plate 4.16 Deep burial (IV) textural and mineralogical changes.

(A) Core photograph of sub-vertical microfractures (phase 23) cutting across a stromatoporoid floatstone. The microfractures are lined with solid bitumen generated from the thermal cracking of liquid hydrocarbons (phase 19). d-91-L/94-J-9; 6300'6".

(B) Core photograph of bitumen impregnated (B) matrix and hemispherical stromatoporoid. b-6-A/94-J-16; 6363'6".

(C) Core photograph of bitumen impregnated matrix (B) in a stromatoporoid-crinoid floatstone-rudstone. a-81-J/94-J-9; 1913.8 m.

(D) Core photograph of vertical microfractures (phase 23) lined with solid bitumen that cut across a tabular stromatoporoid. a-81-J/94-J-9; 1921.2 m.

Plate 4.16: Deep Burial IV

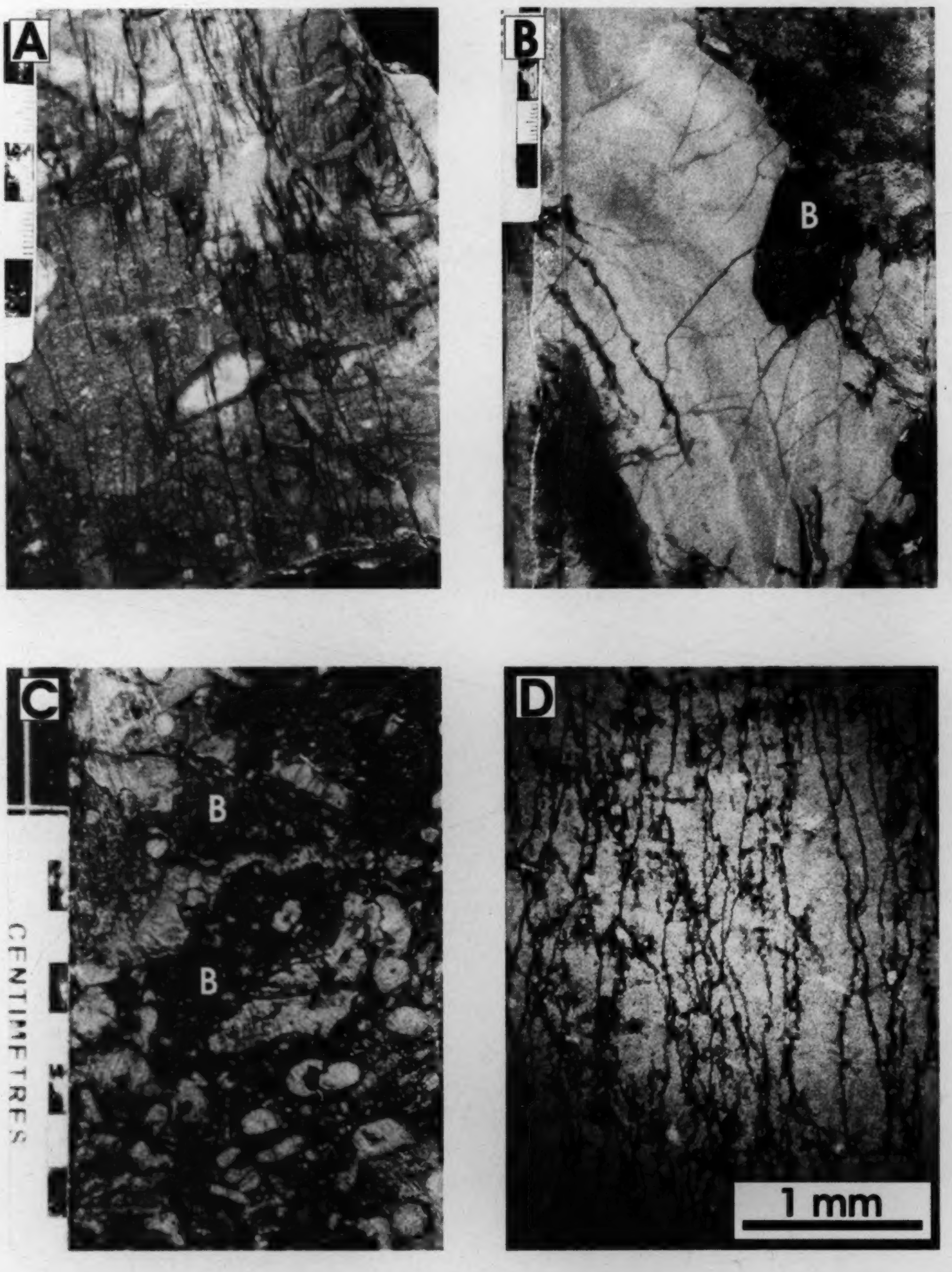
A
B
B
C
B
B
CENTIMETRES
D
1 mm

Plate 4.17 Deep burial (V) textural and mineralogical changes.

(A) Core photograph of coarse crystalline blocky calcite cement (phase 25) partially filling fracture set IV (phase 24). Most of the original micrite matrix of the limestone has been replaced by pyrite (phase 18 - brassy yellow colour). b-6-A/94-J-16; 6339'6".

(B) Core photograph of oversized vug-filling blocky calcite cement (phase 25 - CC). The edge of the vug is lined with well-developed crystals of saddle dolomite cement (phase 13 - SD) coated with pyrobitumen (phase 25 - arrow). c-56-L/94-J-9; 6412'.

(C) Core photograph showing fracture set II (phase 12) occluded by saddle cement (phase 13 - white), bitumen (phase 23 - B), quartz (phase 20 - Q), and blocky calcite (phase 25 - CC), in that order. d-79-F/94-J-10; 6769'.

(D) Thin section photomicrograph of fracture-filling cements shown in Photo C. SD = saddle dolomite, Q = quartz, CC = blocky calcite. Stained thin section, plane-polarized light. d-79-F/94-J-10; 6769'.

Plate 4.17: Deep Burial V

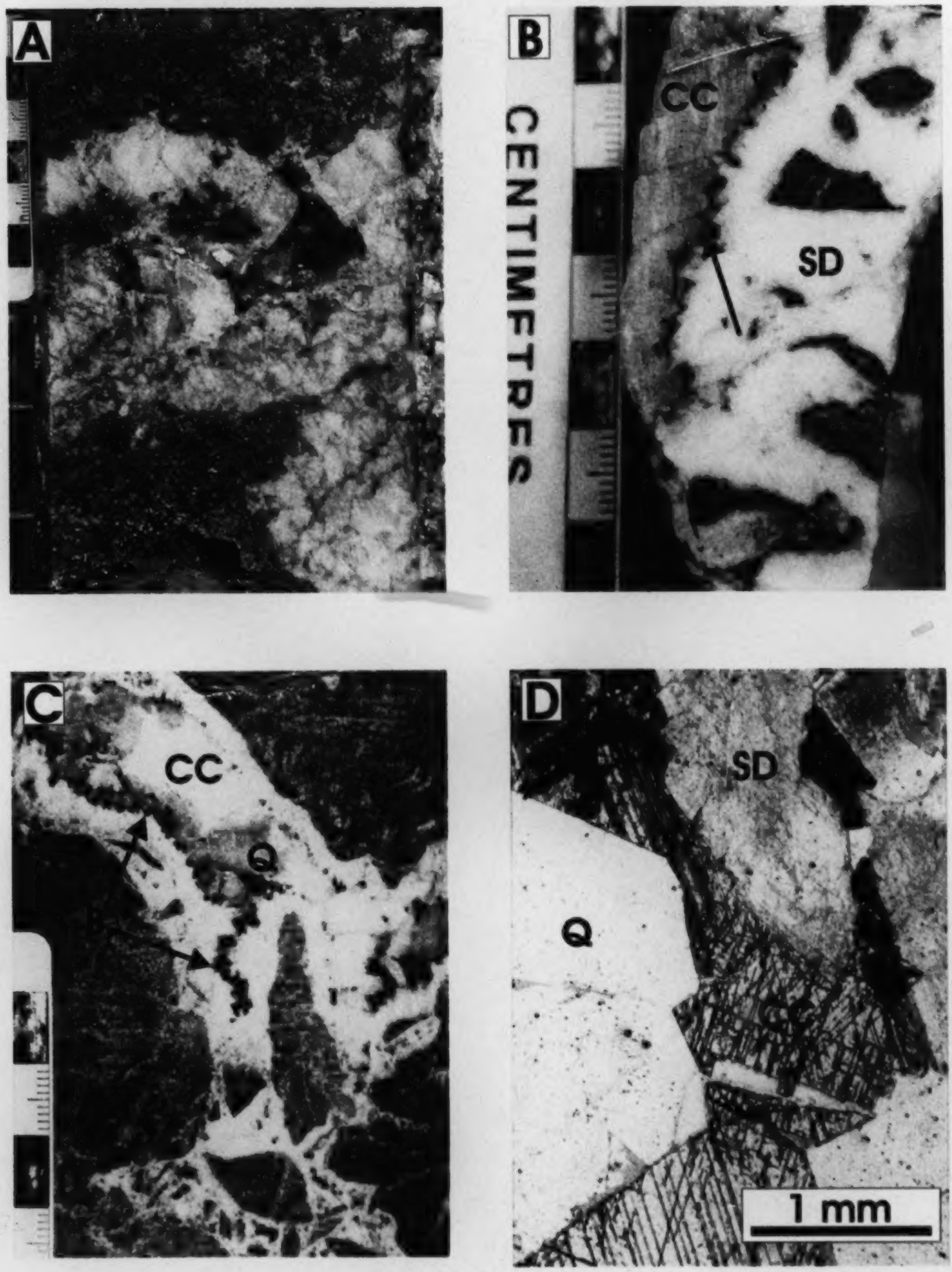
A
B
CENTIMETRES
CC
SD
C
CC
Q
D
SD
Q
1 mm

C).

Fracture IV (phase 24)

Fracture generation IV post-dates all previous diagenetic phases with the exception of blocky calcite II (phase 25). These fractures are rare and occur primarily in the limestone cores. These fractures occur predominantly in a horizontal to sub-vertical orientation, with widths ranging from less than 1 cm up to about 5 cm, and core lengths varying up to roughly 30 cm (Plate 4.17A). These fractures were partially to completely cemented by blocky calcite II.

Blocky calcite II (phase 25)

Blocky calcite generation II occurs as translucent to milky white, euhedral, coarse crystals (up to 3-4 cm) that are non-ferroan and non-luminescent under CL (Plate 4.17). Blocky calcite II is found primarily as a fracture and vug-filling cement in pervasively dolomitized samples of the Slave Point Formation. In fracture generation II (phase 12) and oversized vugs (hydrothermal alteration – phase 13), blocky calcite II always post-dates saddle dolomite, hydrocarbon migration (phase 19), and quartz (phase 20) (Plate 4.17B through D). This calcite cement is rarely found occluding fracture generation III (phase 15), but partially to completely occludes fracture generation IV (phase 24) developed in the limestone intervals (Plate 4.17A).

4.4 Depositional facies control on diagenesis

Depositional facies were identified where possible, so as to characterize their control on textural alteration during diagenesis, including on porosity and permeability development. A key parameter in this context is the porosity and permeability in the limestones prior to pervasive dolomitization (GMD – phase 10) and/or later hydrothermal alteration (phase 13), which controlled access and the fluxes of the invading formation fluids.

The identification of facies zones is based on the criteria outlined by Machel and Hunter (1994) (see Chapter 3). Porosities and permeabilities are plotted in Figure 4.4 of all those facies types for which data are available, grouped according to limestones and dolostones, and using the facies types identified and mapped in Chapter 3. The assumption

Figure 4.4A Crossplot of permeability (Kmax) versus porosity from core analysis data for limestones in the Slave Point Formation. The data is presented according to facies identified through core and thin section petrography. The facies are classified according to the facies model of Machel and Hunter (1994) (Figure 3.2). Data from core analysis provided by AccuMap®. Wells: a-50-C/94-J-9; b-21-E/94-J-9; a-63-J/94-J-9; b-78-J/94-J-9; a-81-J/94-J-9; d-91-L/94-J-9; c-94-L/94-J-9; a-5-A/94-J-16; b-6-A/94-J-16.

Figure 4.4B Crossplot of permeability (Kmax) versus porosity from core analysis data for dolostones in the Slave Point Formation. The data is presented according to facies identified through core and thin section petrography. The facies are classified according to the facies model of Machel and Hunter (1994) (Figure 3.2). Data from core analysis provided by AccuMap®. Wells: a-37-C/94-J-9; b-75-F/94-J-9; c-56-L/94-J-9; b-72-L/94-J-9; d-91-L/94-J-9; c-94-L/94-J-9; c-58-E/94-J-10; a-61-F/94-J-10; c-88-F/94-J-10; a-65-G/94-J-10; d-72-G/94-J-10; a-83-G/94-J-10; b-70-I/94-J-10; c-47-J/94-J-10; c-8-D/94-J-16; b-10-D/94-J-16.

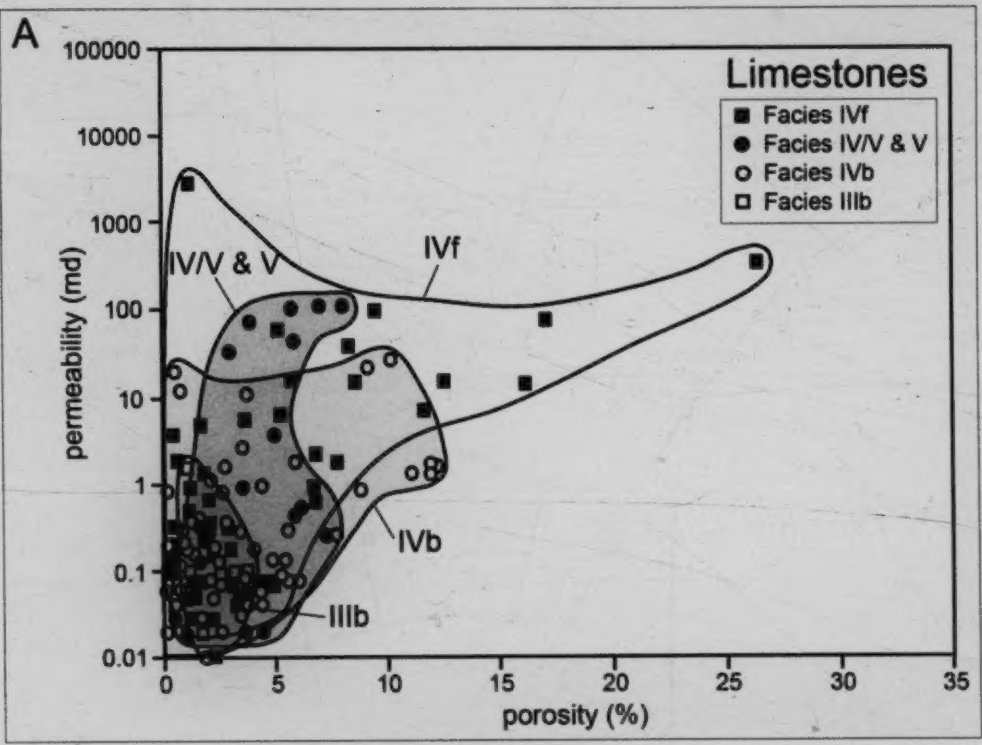
A
Limestones
Facies IVf
Facies IV/V & V
Facies IVb
Facies IIIb
IV/V & V
IVf
IVb
IIIb
permeability (md)
100000
10000
1000
100
10
1
0.1
0.01
porosity (%)
0
5
10
15
20
25
30
35

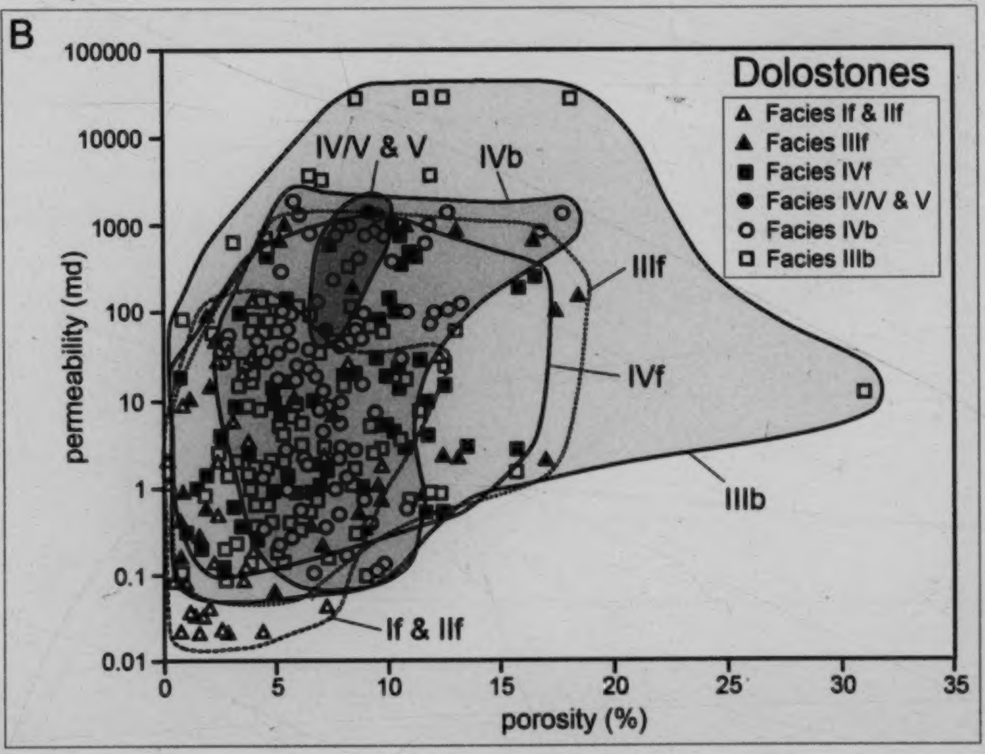
B
Dolostones
Facies If & IIf
Facies IIIf
Facies IVf
Facies IV/V & V
Facies IVb
Facies IIIb
IV/V & V
IVb
IIIf
IVf
IIIb
If & IIf
permeability (md)
100000
10000
1000
100
10
1
0.1
0.01
porosity (%)
0
5
10
15
20
25
30
35

is made herein that the present-day values for porosity and permeability in the limestones are approximately equal to those before dolomitization. Arguments can be made that this assumption is in error in at least some cases, as some limestones were diagenetically altered after dolomitization. For example, a limestone containing calcite cements postdating dolomitization would fall into this category. It is argued here, however, that most such cases are easily recognized and thus can be excluded from the overall analysis of porosity and permeability control on dolomitization. Furthermore, where no porosity and permeability data are available, as in the cases of limestones within facies zones If and IIf, reasonable estimates have been made on the basis of thin section examinations.

4.4.1 Facies zone If

Facies zones If is a fine-grained fore-reef facies that is characterized by dark brown mudstones to siltstones that are usually devoid of any macroscopic fossils (Plate 4.18A). Values for initial porosity and permeability (before burial by more than a few metres to tens of metres) are not available for facies zone If in limestones but are estimated as below 2-3% and 0.1 md, respectively.

Incomplete dolomitization of facies zone If generated patches of matrix dolomite surrounded by dark brown lime muds and/or silts (Plate 4.18B). Matrix dolomite (phase 10) replaced carbonate mud in domains of relatively high primary porosity and permeability. Subsequent dissolution and/or recrystallization (hydrothermal alteration – phase 13) and saddle dolomite formation via hydrothermal fluids affected mainly patches of earlier matrix dolomite and generated small vuggy and intercrystal pores (Plate 4.18B). These pores increased total porosity and permeability to maxima of 5% and 0.1 md, respectively (Figure 4.4B). However, the patchy nature of the dolomite suggests effective porosity and permeability are much lower. Increased porosity and permeability values of up to 8% and 1 md, respectively (Figure 4.4B) may be representative of open fracture networks that developed after dolomite formation.

4.4.2 Facies zone IIf

Facies zone IIf is characterized by dark brown mudstones with mm-sized bioclasts (Plate 4.18C). No data for porosity and permeability are available for limestones of this zone, but are estimated to be similar to those in facies zone If (above).

Plate 4.18 Facies control (I) on diagenesis.

(A) Core photograph of undolomitized mudstone displaying syn-sedimentary deformation structures. The upper third of the photo shows the abrupt contact to dolomite. Facies zone If. b-70-I/94-J-10; 6263'.

(B) Core photograph showing the textural changes associated with dolomite formation in Facies zone If. The dark coloured zones are lime mud. Matrix dolomite (GMD - phase 10) replaced carbonate mud in domains of increased initial porosity and/or permeability. Patches of matrix dolomite (brown) were subsequently hydrothermally altered, generating small vuggy pores (V) that were cemented by saddle dolomite (white - phase 13). b-70-I/94-J-10; 6263'6".

(C) Core photograph showing undolomitized crinoids (arrows) and brachiopods in wackestone to packstone. Larger fragments are *Stachyodes*. About 50% of the original limestone has been replaced by grey matrix dolomite (GMD - phase 10) and replacement saddle dolomite (SD - phase 13). Facies zone IIf. b-70-I/94-J-10; 6267'6".

(D) Core photograph showing the textural changes associated with dolomite formation in Facies zone IIf. Grey matrix dolomite (phase 10) only formed in domains of elevated primary porosity and/or permeability, such as, isolated patches containing a greater abundance of biochems. These fossil-rich patches may also have had a coarser matrix, and thus increased initial permeability. Larger crinoid(?) or *Stachyodes(?)* grains show evidence of dissolution (arrows) and partial to complete replacement by saddle dolomite (SD - phase 13), reducing the porosity generated by the earlier dolomitization event. b-70-I/94-J-10; 6276'6".

Plate 4.18: Facies Control I

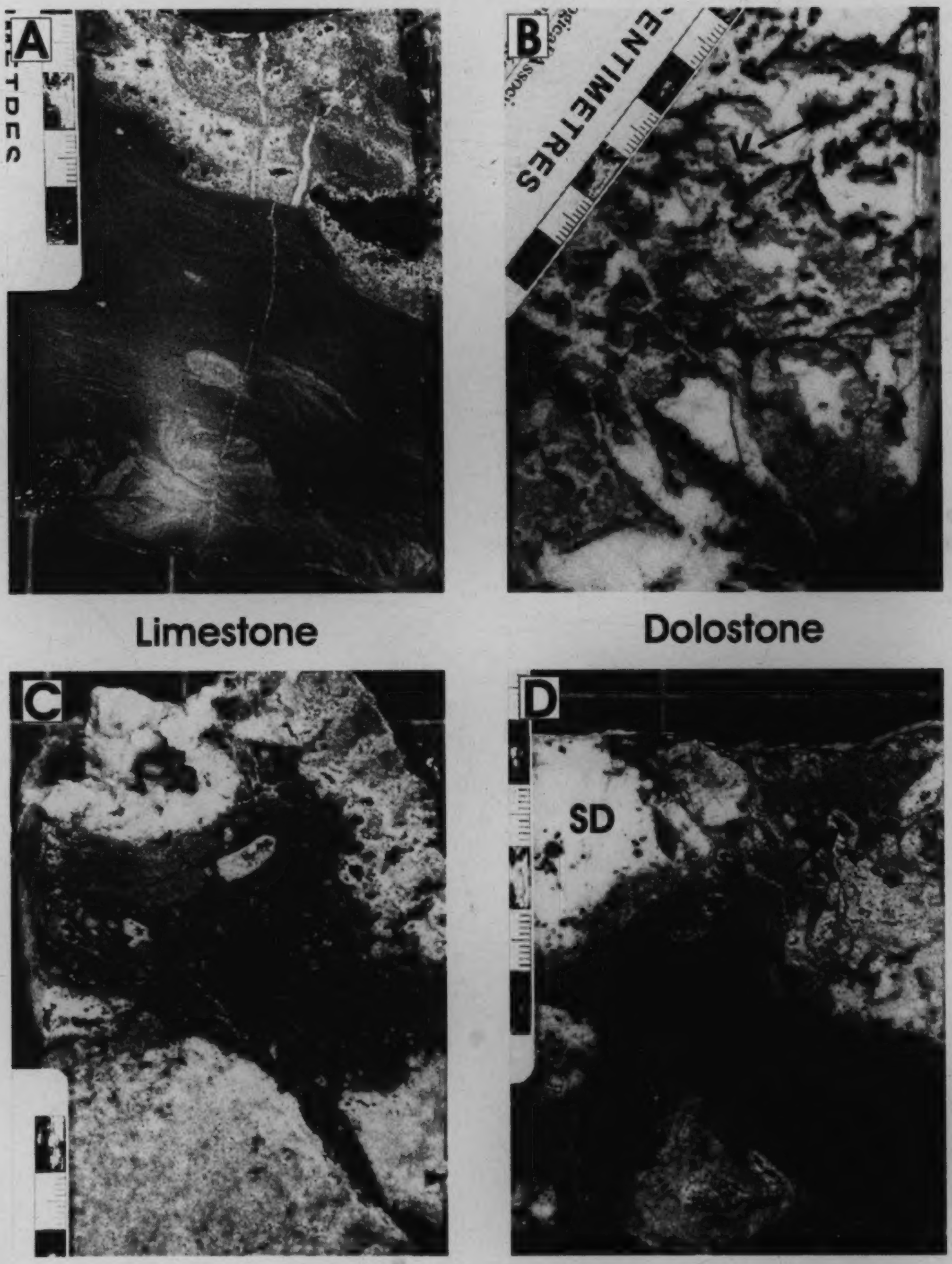
A
B
CENTIMETRES
Limestone
Dolostone
C
D
SD

Pervasive matrix dolomitization (phase 10) preferentially affected domains that contain(ed) more bioclasts and a somewhat coarser matrix (Plate 4.18D), where permeability was higher. Later hydrothermal fluids followed these more permeable and now dolomitized domains, dissolving unreplaced biochems as well as some undolomitized matrix, thereby generating numerous vugs and fossil moulds (Plate 4.18D). In other domains, the matrix dolomite was replaced and/or cemented by saddle dolomite (hydrothermal alteration - phase 13) (Plate 4.18D), reducing previously generated vuggy or intercrystalline porosity. Overall, the porosity and permeability of dolostones in this zone is quite low, approaching 5% and 1 md, respectively (Figure 4.4B). However, where vuggy and mouldic pores remain uncemented, porosity and permeability reaches 13% and 100 md, respectively (Figure 4.4B).

4.4.3 Facies zone IIIf

Facies zone IIIf is characterized by relatively heterogeneous floatstones, with crinoids as the main macrofossils, but also with fragments of brachiopods, cylindrical stromatoporoids, and corals (Plate 4.19A). No data for porosity and permeability are available for limestones in this zone, but estimated values would be below 2-3% and 0.1 md, respectively.

Matrix dolomite (phase 12) preferentially replaces domains of matrix with higher bioclast concentrations due to an overall coarse grain size of the matrix, and, hence, increased permeability (Plate 4.19B). The majority of the biochems were not replaced during matrix dolomitization, probably due to the fact that: 1) the matrix contains or consists of thermodynamically metastable carbonates (aragonite and/or high-Mg calcite), which have higher solubilities than low-Mg calcite; 2) the matrix has a much smaller grain size and therefore a higher surface area per grain than the larger biochems, allochems or cement crystals formed prior to dolomitization; and, 3) the matrix has a higher permeability than the larger, more massive particles or cements (Machel, 2004). Subsequent hydrothermal fluids dissolved any unreplaced fossil allochems and recrystallized much of the earlier matrix dolomite, resulting in the generation of significant mouldic and vuggy porosity (Plate 4.19B). Porosity and permeability values reach as high as 20% and 1000 md, respectively (Figure 4.4B).

Plate 4.19 Facies control (II) on diagenesis.

(A) Core photograph of undolomitized crinoid-brachipod floatstone. Facies zone IIIf. c-8-D/94-J-16; 6320'6".

(B) Core photograph showing the textural changes associated with dolomite formation in Facies zone IIIf. The bulk of the original muddy matrix was replaced by grey matrix dolomite (phase 10), with domains of mud remaining as limestone at the bottom of the photo. The hydrothermal fluid dissolved both unreplaced fossils (mouldic porosity - M) and matrix dolomite (vuggy - V), and replaced previously dolomitized fossils with saddle dolomite (phase 13). c-8-D/94-J-16; 6346'6".

(C) Core photograph of *Thamnopora* rudstone in a crinoid packstone matrix. Facies zone IVf. a-63-J/94-J-9; 1981.7 m.

(D) Core photograph showing the textural changes associated with dolomite formation in Facies zone IVf. The entire remaining micrite matrix, and some of the original fossils are replaced by planar grey matrix dolomite (phase 10). Subsequent hydrothermal alteration (phase 13) resulted in dissolution and partial saddle dolomite cementation to form vuggy porosity (V), and replacement of grey matrix dolomite allowing for the retention of original fossil textures (Th - *Thamnopora*). b-10-D/94-J-16; 6269'6".

Plate 4.19: Facies Control II

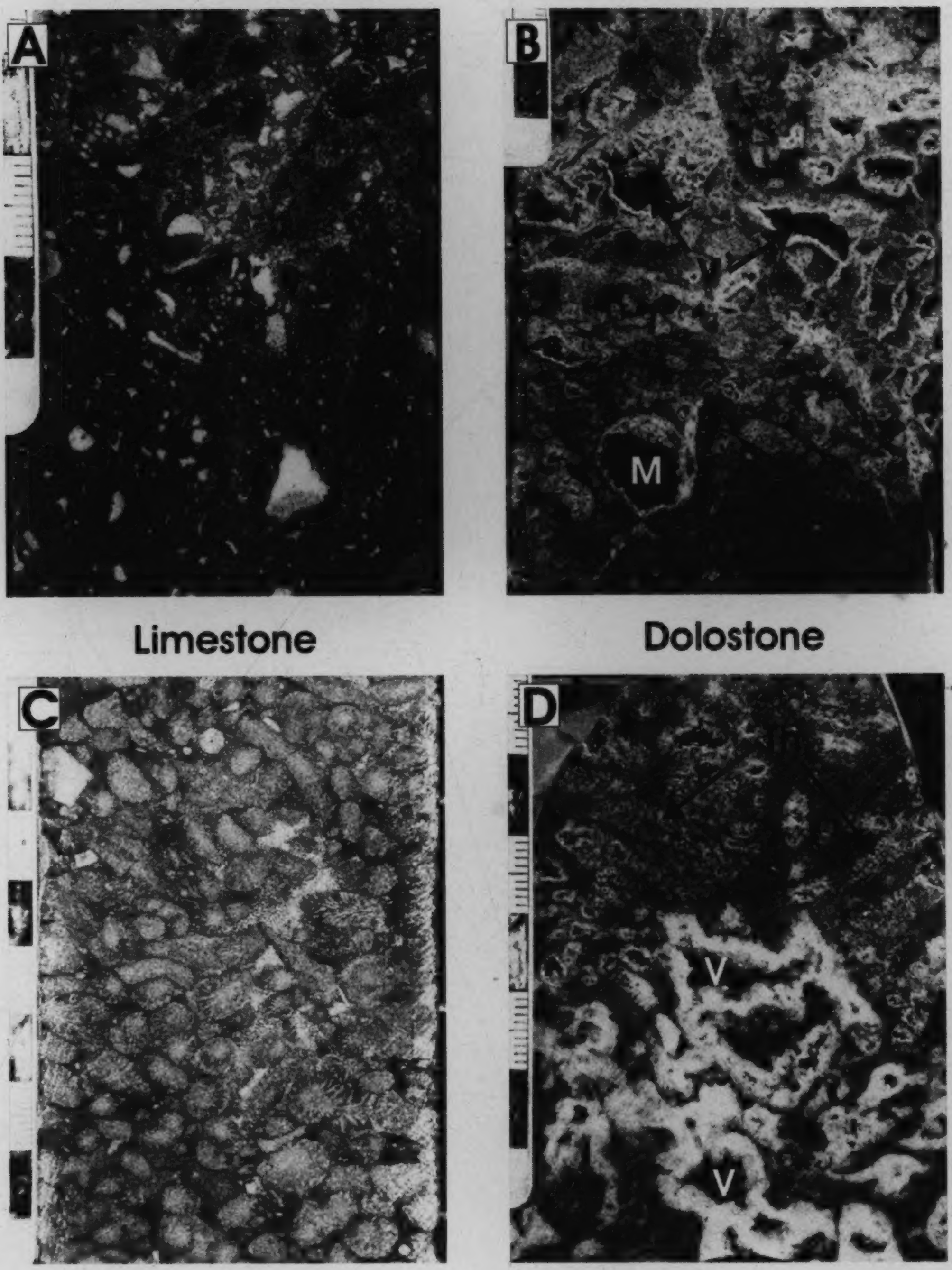
A
B
M
Limestone
Dolostone
C
D
V
V

4.4.4 *Facies zone IVf*

Facies zone IVf is characterized by light to dark brown, floatstones to rudstones that contain large quantities of *Stachyodes*, *Thamnopora*, and crinoids in a fine-grained matrix (Plate 4.19C). Porosity and permeability values from the limestones of this zone average about 7% and 1 md, respectively (Figure 4.4A). However, porosity and permeability values reach as high as 27% and 3000 md, which may reflect the presence of open fracture networks (Figure 4.4A).

Aided by the high original porosity and permeability from the limestones of this zone, the entire micrite matrix and some of the bioclasts were replaced by grey matrix dolomite (phase 10) (Plate 4.19D). Petrographically, significant intercrystalline porosity is developed in this zone, a reflection of the relatively planar crystal forms of the matrix dolomite. Prior to bitumen plugging, the porosity in this zone may have reached 30%. Later hydrothermal fluids dissolved many of the fossils and matrix dolomite, generating vuggy pores, while in other domains, dolomitized fossils were replaced with saddle dolomite (hydrothermal alteration - phase 13) (Plate 4.19D). The average porosity and permeability of dolostones in this zone is around 6-10% and 1-10 md, respectively (Figure 4.4B): little change from the average limestone values.

4.4.5 *Facies zone IV/V*

Facies zone IV/V is a reef-core facies characterized by massive stromatoporoids forming rudstone to bindstone textures (Plate 4.20A). Fine-grained matrix is generally absent in rocks in this zone, but where present contains crinoids floating in lime mud. Due to the limited matrix, and the relative absence of intraparticle pores, original porosity and permeability values from limestones in this zone are on the order of 2-3% and less than 0.1 md, respectively (Figure 4.4A).

Pervasive matrix dolomitization in this zone resulted in the complete replacement of the stromatoporoids by grey matrix dolomite (Plate 4.20B). Very little, if any, porosity was generated as a result of dolomitization. Subsequent hydrothermal fluids both dissolved and replaced (hydrothermal alteration – phase 13) the matrix dolomite. Dissolution of bioclasts in the matrix generated oversized mouldic pores (Plate 4.20B), while intercrystalline porosity was developed along zones of matrix dolomite dissolution. Average porosities and

Plate 4.20 Facies control (III) on diagenesis.

(A) Core photograph of undolomitized massive stromatoporoid bindstone. Facies zone IV/V. d-91-L/94-J-9; 6460'.

(B) Core photograph showing the textural changes associated with dolomite formation in Facies zone IV/V. In this specimen, the entire stromatoporoid was replaced by grey matrix dolomite (phase 10) while preserving much of the original fossil texture. Later diagenesis resulted in partial dissolution and replacement of matrix dolomite by white saddle dolomite (phase 13). Dissolution of nodular stromatoporoids and other bioclasts in the matrix generated oversized mouldic pores (M). Intercrystalline porosity (IX) is developed along zones of dissolution and concomitant saddle dolomite cementation. c-94-L/94-J-9; 6485'.

(C) Core photograph of undolomitized stromatoporoid rudstone-framestone in a crinoid packstone-grainstone matrix. S = stromatoporoid, St = *Stachyodes*. Facies zone V. b-78-J/94-J-9; 6446'.

(D) Core photograph showing the textural changes associated with dolomite formation in Facies zone V. This sample shows the partial dolomitization (arrows) of a stromatoporoid (S) as a result of fluids travelling along small, randomly-oriented fractures. Complete replacement of the limestone matrix generated minor intercrystalline porosity (IX), while dissolution of the limestone matrix created scattered oversized vuggy pores (V). Massive zones of saddle dolomite cement (SD - phase 13) occlude fractures. c-94-L/94-J-9; 6541'

Plate 4.20: Facies Control III

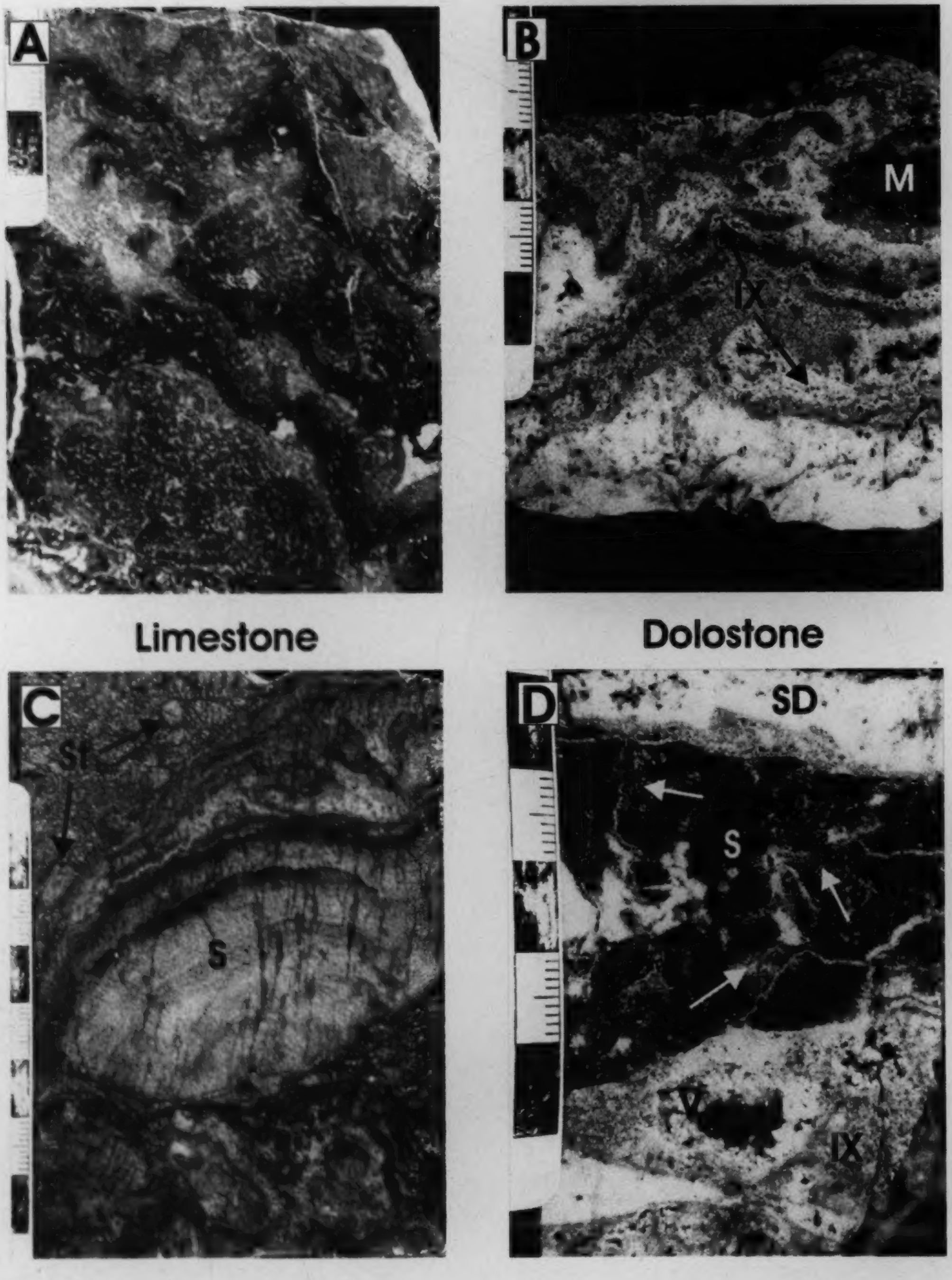
A
B
M
IX
Limestone
Dolostone
C
St
S
D
SD
S
V
IX

permeabilities in dolostones of this facies zone are 8-10% and around 10 md, respectively, which are significantly higher than corresponding samples from limestones (Figure 4.4B).

4.4.6 Facies zone V

Facies zone V is also representative of the reef-core environment, and is characterized by massive to bulbous stromatoporoids forming rudstone to framestone textures (Plate 4.20C). Compared to facies zone IV/V, the percentage of matrix is much higher in facies zone V, and consists of abundant crinoids and cylindrical stromatoporoids (Plate 4.20C). Porosity and permeability in the limestones from this zone reach as high as 8-10% and 100 md, respectively (Figure 4.4A).

Samples from facies zone V rarely show evidence for the formation of grey matrix dolomite (phase 10), but, where present, resulted from the movement of fluids along small, randomly oriented fractures (phase 5) (Plate 4.20D). Dolomitization of the matrix generated minor intercrystal pores. Subsequent hydrothermal fluids dissolved undolomitized fossils generating scattered, oversized vuggy pores (Plate 4.20D). Conversely, saddle dolomite cements (phase 13) reduced secondary fracture porosity. Overall, the porosity and permeability from dolostones in this zone is quite low, averaging less than 5% and 1 md, respectively (Figure 4.4B), which is much lower than corresponding data from the limestones, which may be due to the process of 'overdolomitization' (*sensu* Lucia, 2004).

4.4.7 Facies zone IVb

Facies zone IVb is representative of the proximal back-reef environment, and is characterized by light brown, floatstones to rudstones, with *Stachyodes* as the dominant fossil component (Plate 4.21A). These rocks are usually well-cemented relatively early in their diagenetic history, hence, porosity and permeability values average 4-5% and 0.5 md, respectively (Figure 4.4A). In some samples, porosity reaches 13%, while permeability approaches 30 md (Figure 4.4A).

Dolomitization of this facies zone is represented by the complete replacement of the matrix and cements by grey matrix dolomite (phase 10) (Plate 4.21B). The complete replacement of the limestones was possible as the result of high initial permeability due to the large grain size of the allochems and coarse texture of the matrix. Pervasive matrix dolomitization in this zone generated significant intercrystal pores. Subsequent

Plate 4.21 Facies control (IV) on diagenesis.

(A) Core photograph of undolomitized *Stachyodes* rudstone with radial fibrous calcite cement partially infilling interparticle porosity. Facies zone IVb. b-6-A/94-J-16; 6433'.

(B) Core photograph showing the textural changes associated with dolomite formation in Facies zone IVb. In this specimen, the entire matrix - including any interparticle calcite cements - was replaced by grey matrix dolomite (phase 10). Where the outside edges of the *Stachyodes* (St) are still visible, hydrothermal alteration (phase 13) was in the form of replacement by saddle dolomite. Where there is no discernible fossil outline, alteration was in the form of dissolution of both biochem and any grey matrix dolomite. The zones of dissolution were then cemented with saddle dolomite, with incomplete cementation resulting in the formation of vuggy porosity (V). a-61-F/94-J-10; 6706'.

(C) Core photograph of undolomitized *Amphipora* floatstone in a dark brown mudstone-wackestone matrix. Facies zone IIIb. c-56-L/94-J-9; 6489'.

(D) Core photograph showing the textural changes associated with dolomite formation in Facies zone IIIb. The entire micrite matrix of this sample was replaced by planar grey matrix dolomite (phase 10), producing significant intercrystalline porosity (IX). The majority of the *Amphipora* in this sample were partially to completely dissolved creating mouldic porosity (M). b-72-L/94-J-9; 6249'6".

Plate 4.21: Facies Control IV

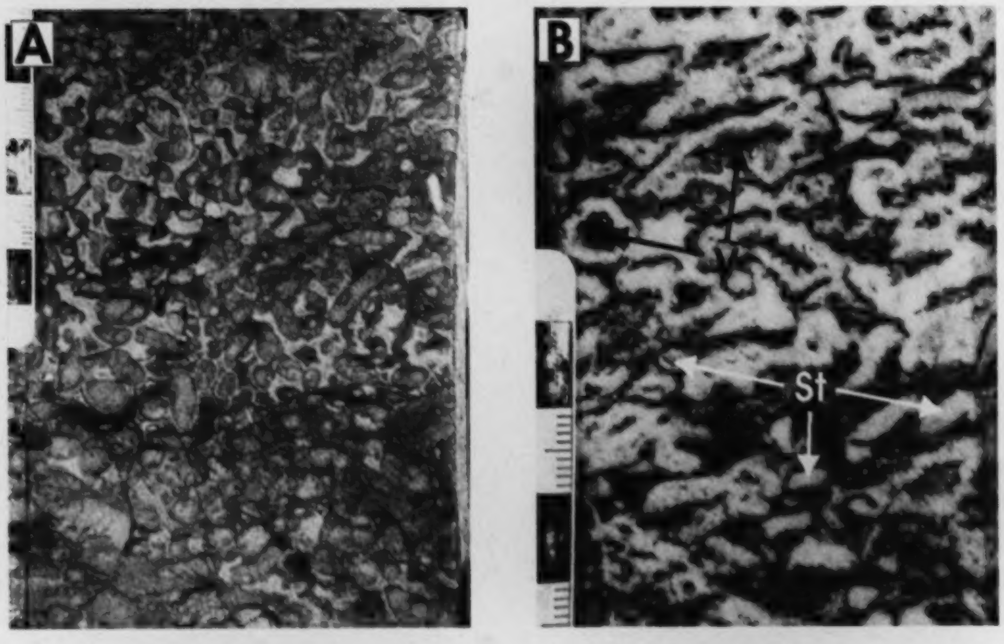

Limestone

Dolostone

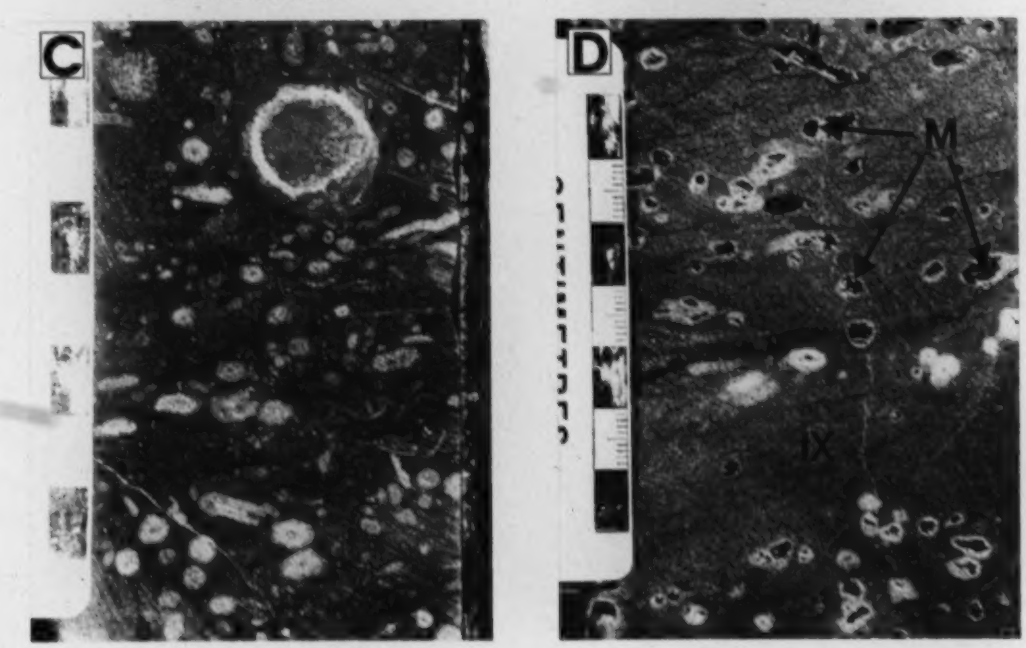

hydrothermal fluids replaced many of the fossil allochems with saddle dolomite (phase 13), while other fossils were completely dissolved, generating vuggy pores (Plate 4.21B – V). Saddle dolomite formation was not strictly confined to the bioclasts as crossing their boundaries to also replace some of the earlier matrix dolomite (Plate 4.21B). Porosity and permeability in dolostones in this zone is highly variable, ranging from 4 to 20% and 0.1 to 3000 md, respectively (Figure 4.4B).

4.4.8 Facies zone IIIb

Facies zone IIIb is characterized by dark brown grainstones containing abundant *Amphipora* and ostracods (Plate 4.21C). The muddy character of the matrix in these rocks result in low primary porosity and permeability values, averaging 3 to 4% and less than 0.1 md, respectively (Figure 4.4A).

Pervasive matrix dolomitization of rocks in this zone resulted in complete replacement of the matrix by grey matrix dolomite (phase 10) (Plate 4.21D). Petrographically, the matrix dolomites have a planar crystal form, and, hence, excellent secondary intercrystalline porosity was developed (Plate 4.21D – IX). Subsequent hydrothermal fluids had little impact on the matrix dolomites in this zone, and instead, dissolved or replaced the bioclasts, e.g., *Amphipora*, generating mouldic pores (Plate 4.21D – M). The highest porosity and permeability values from dolostones in this facies zone are attributed to the intercrystalline porosity in matrix dolomite, reaching 18% and 100 md, respectively (Figure 4.4B). However, bitumen plugging has reduced the average porosity and permeability values in this zone to roughly 6-8% and 5 md (Figure 4.4B). Despite this reduction, the dolostones from this facies zone have porosity and permeability values that are significantly higher than corresponding samples from limestones.

4.4.9 Facies zone IIb

Facies zone IIb is characterized by intercalated, buff coloured grainstones and laminated mudstones to wackestones. Initial porosity and permeability values are not available for facies zone IIb but visual estimates of porosity range from less than 2-3% in the laminated mudstones to as high as 6-10% in the grainstones.

No samples of facies zone IIb containing dolomite were available from the Clarke Lake field, nor is porosity and permeability data available from dolostones of this facies zone. As a result, no statement can be made regarding depositional facies control on diagenesis.

4.4.10 Facies zone Ib

Facies zone Ib is characterized by light brown to tan coloured, weakly laminated mudstones and wackestones (Plate 4.22A). Primary porosity is limited to fenestral pores and fractures. No data is available for porosity and permeability of limestones in zone Ib, but estimated values are below 2-3% and 0.1 md, respectively.

Due to the paucity of rocks from this zone at Clake Lake, it is difficult to evaluate the diagenetic potential of this facies zone. However, the limited data available indicate that the rocks from zone were variably dolomitized. Where the dolomitizing fluids infiltrated this zone, the result was complete replacement of the limestone by grey matrix dolomite (phase 10) (Plate 4.22B). The reasons for the replacement of the micrite matrix are related to its diagenetic potential as outlined in facies zone IIIb. Due to the limited macrofossil content in these rocks, there was limited mouldic pore generation during the invasion of hydrothermal fluids. Rather, reservoir porosity in this facies zone is the result of intercrystal pores in the matrix dolomite (Plate 4.22B – IX). Petrographic estimates of porosity for dolostones in this zone average 5%; no estimates of permeability are available. Similar to facies zone IIIb, porosity in the dolostones is significantly higher than corresponding samples from limestones.

4.4.11 Patch reef facies

The patch reef facies may represent a variant of Facies IIIb, and is characterized by dark brown, fine-grained floatstones to framestones (Plate 4.22C). Porosity and permeability data does not exist for limestones in this facies zone, but visual estimates place porosity at less than 2-3% due to the high mud content of the matrix.

These rocks rarely show evidence of dolomitization, perhaps a reflection of limited drilling activity in the back-reef. Where dolomitizing fluids have entered this zone, the entire matrix was replaced by grey matrix dolomite (phase 10) (Plate 4.22D). However, due to the limited matrix available for replacement, porosity is limited to minor intercrystal pores. Subsequent hydrothermal fluids generated the bulk of the porosity in this zone: either replacing the bioclasts with saddle dolomite (hydrothermal alteration - phase 13),

Plate 4.22 Facies control (V) on diagenesis.

(A) Core photograph of undolomitized algal laminite mudstone-wackestone. Facies zone Ib. c-64-I/94-J-10; 6443'3".

(B) Core photograph showing the textural changes associated with dolomite formation in Facies zone Ib. The entire micrite matrix of this sample was replaced by planar, grey matrix dolomite (phase 10), creating intercrystalline porosity. Oversized vuggy pores are extremely rare. d-72-G/94-J-10; 6449'.

(C) Core photograph of undolomitized stromatoporoid-coral floatstone-rudstone in a muddy, *Amphipora*-rich matrix. Patch reef facies. a-50-C/94-J-9; 6898'.

(D) Core photograph showing the textural changes associated with dolomite formation in the patch reef facies. The entire micrite matrix of this sample was replaced by grey matrix dolomite (phase 10), forming intercrystal pores. The bulk of the large porosity is the result of hydrothermal alteration (phase 13). Most of the bioclasts were replaced by saddle dolomite. However, dissolution of *Amphipora* and nodular stromatoporoids, and incomplete cementation, resulted in significant secondary mouldic (M) porosity. d-69-H/94-J-10; 6563'.

Plate 4.22: Facies Control V

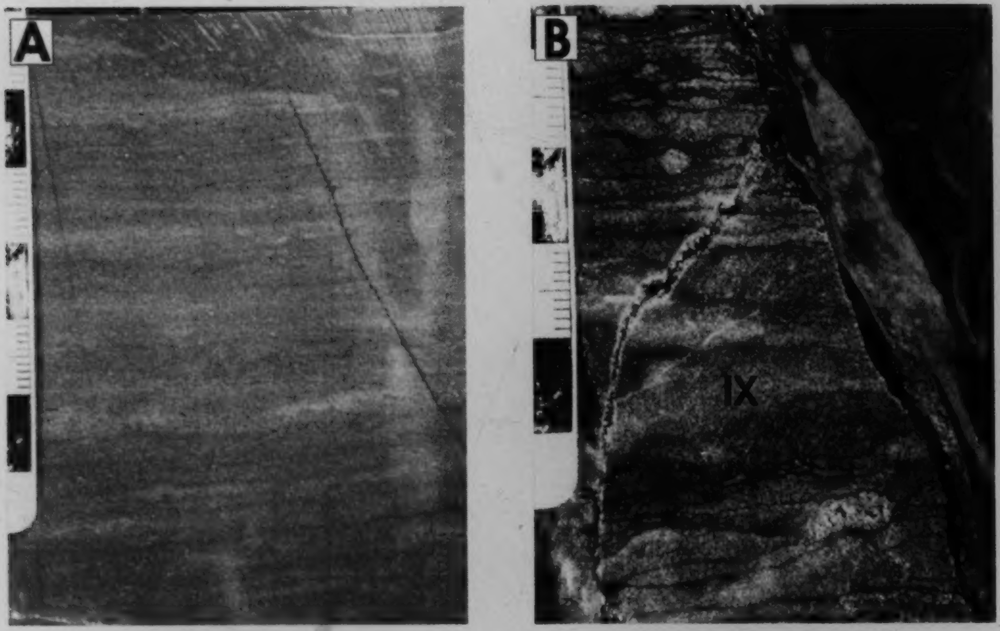

Limestone Dolostone

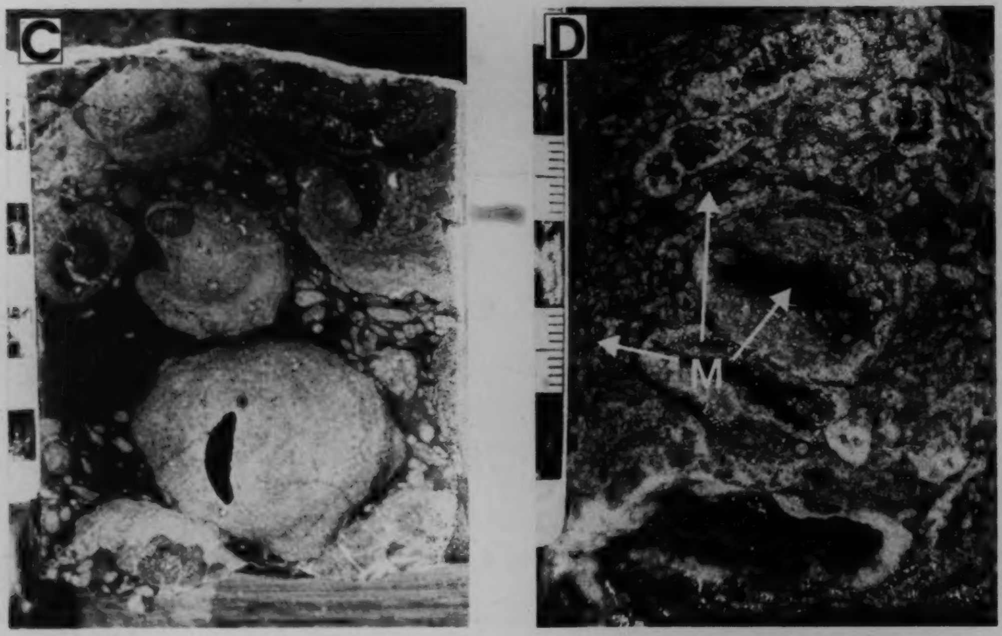

or dissolving the bioclasts resulting in mouldic pore generation (Plate 4.22D – M). No porosity-permeability data was available for dolostones from this facies zone, but visual estimates of porosity range from an average of 8-10% to as high as 30%: all significantly higher than corresponding samples from limestones.

4.5 Spatial distribution of dolomite

The Clarke Lake gas field stretches for about 50 km in a roughly east-west direction, but pervasive matrix dolomitization, and hence, reservoir porosity, is only found in a zone extending about 5 km southward from the platform margin (Figure 4.5). The contour lines in Figure 4.5 represent the depths (in metres) from the top of the Muskwa Formation to the top of the first occurrence of matrix or saddle dolomite in the Slave Point Formation, based on core and cuttings. In wells without core, the first occurrence was accepted as the depth at which the well-site geologist identified as little as a single crystal of grey matrix dolomite (phase 10) or saddle dolomite (phase 13). The line labelled 'Dol-Lst' represents the approximate position of the limestone-dolomite interface toward the platform interior. Limestone makes up the platform carbonates south of this line, and occurs as seemingly isolated patches (shaded in Figure 4.5) within the dolomitized zone. In the limestones of the platform interior, dolomitization is essentially absent.

Two cross-sections that roughly parallel the depositional dip of the Slave Point Formation are shown in Figures 4.6 and 4.7. Stratigraphic sections, using the top of the Muskwa Formation as a datum, generally show complete dolomitization of the Slave Point Formation, i.e., pervasive dolomite from the top of the Slave Point to drilled depth. Core evidence also suggests that the dolomite extends into the overlying Muskwa or Otter Park formations. Figure 4.6 shows the location of a patch of limestone in well b-33-J/94-J-10 that is completely surrounded by dolomite, both to the sides and below. Generally, limited well and core control to the base of the Slave Point make observations regarding the vertical extent of pervasive dolomitization difficult. However, well logs and drill cuttings from the few wells that do penetrate the Slave Point indicate that the dolomite body extends at least down to the top of the underlying Keg River Formation.

Present-day structural cross-sections, shown in Figures 4.6 and 4.7 (bottom), show hypothetical faults that are based solely on the relative movement on the top of the Muskwa Formation (see Chapter 2). The abrupt contact between dolomite and limestone

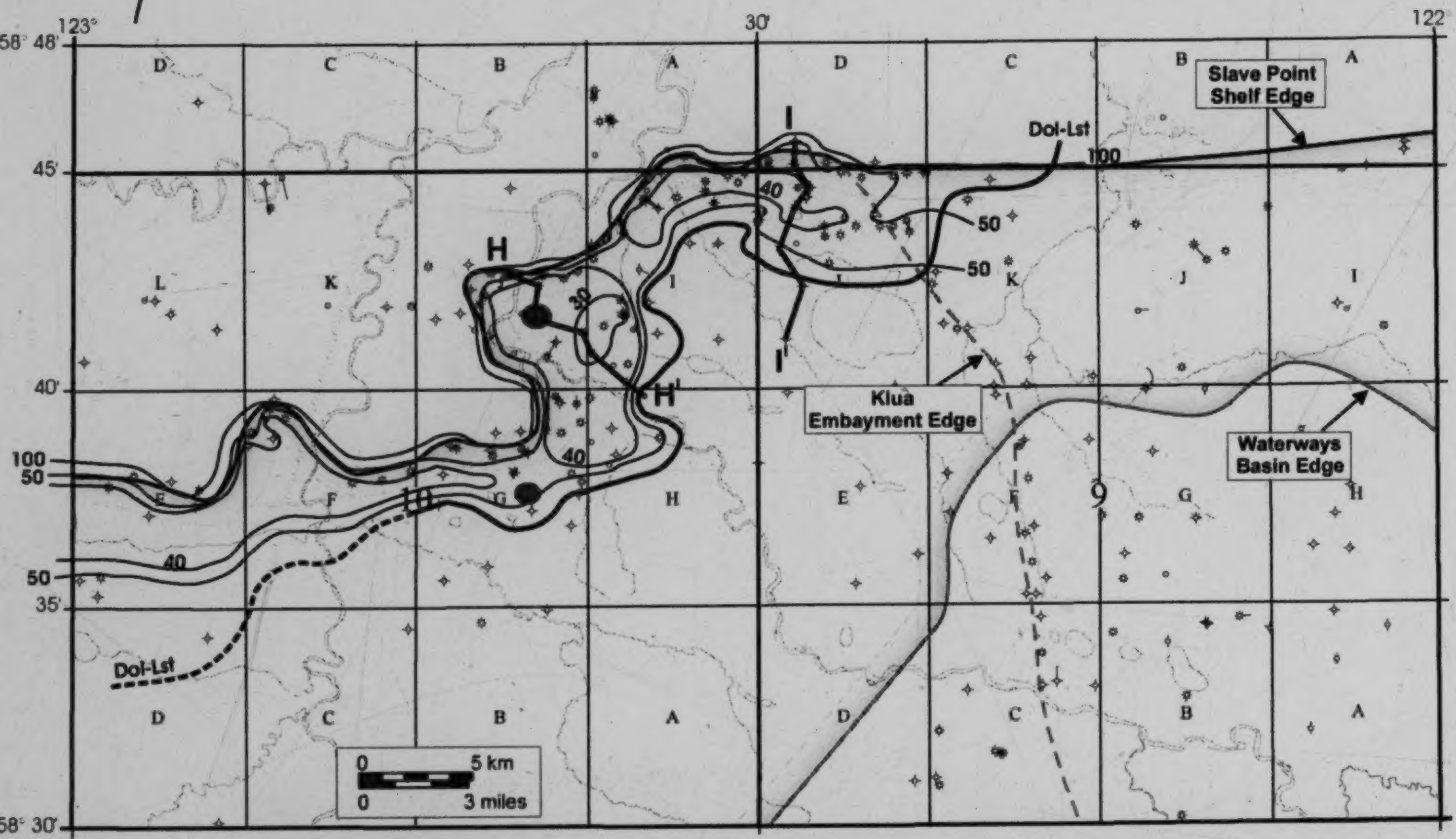
123°
30'
122°
58° 48'
45'
40'
35'
58° 30'
100
50
50
D
C
B
A
L
K
J
I
E
F
G
H
Slave Point Shelf Edge
Dol-Lst
100
50
50
40
40
40
40
30
H
H'
I
I'
10
9
Klua Embayment Edge
Waterways Basin Edge
Dol-Lst
0
5 km
0
3 miles

Figure 4.5 Map of the Clarke Lake field showing the spatial distribution of pervasive matrix dolomitization (GMD - phase 10). Contour lines represent the depth (in metres) from the top of the Muskwa Formation to the first occurrence of dolomite in the Slave Point Formation. Wells to the south of the Dol-Lst line, and the shaded patches within the dolomitized zone, show little to no evidence of dolomite formation. The stratigraphic and structural dolomite distribution is shown along cross-section lines H-H' and I-I' (Figures 4.6 and 4.7).

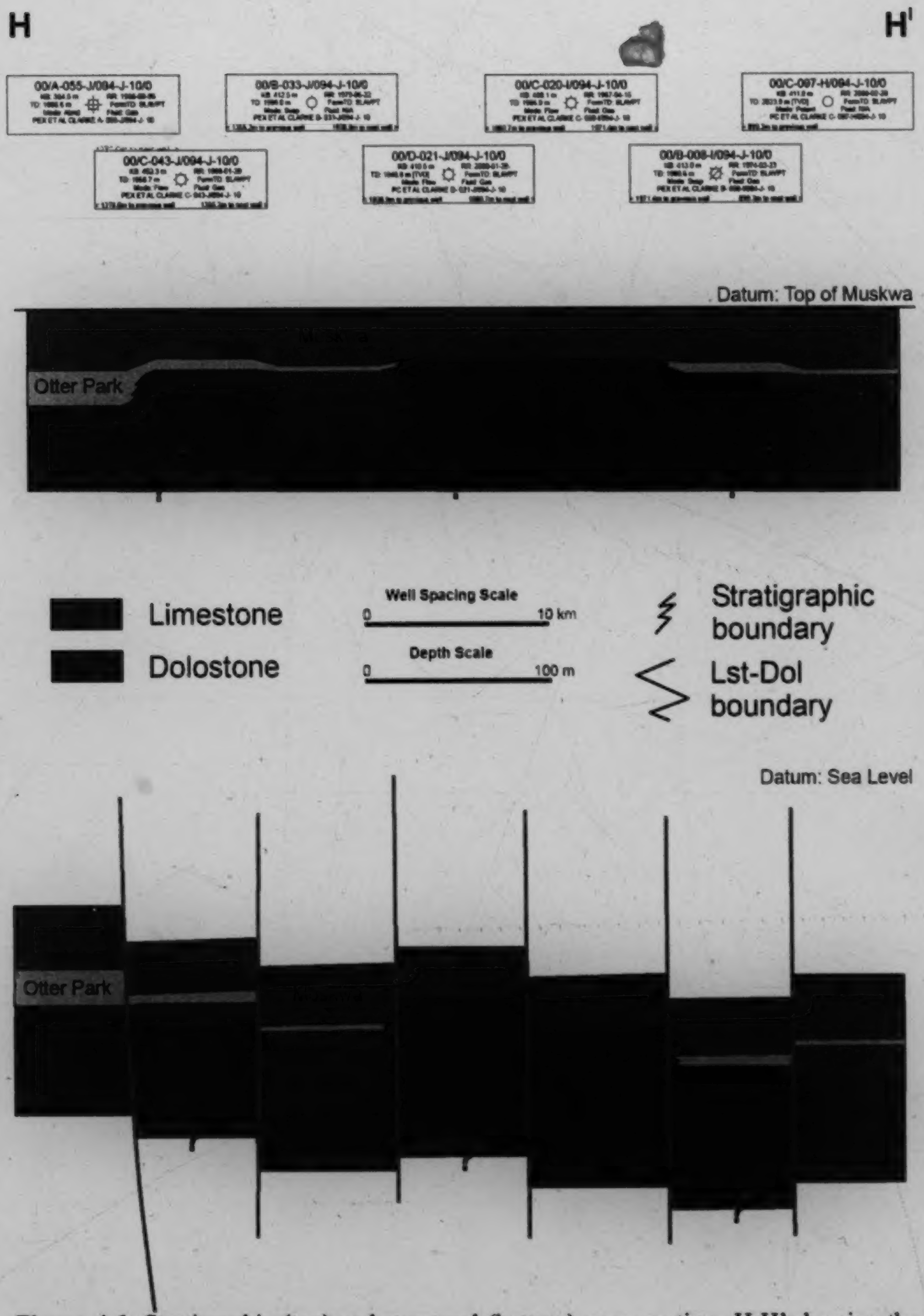
H
H'
00/A-055-J/094-J-10/0
00/B-033-J/094-J-10/0
00/C-020-I/094-J-10/0
00/C-097-H/094-J-10/0
00/C-043-J/094-J-10/0
00/D-021-J/094-J-10/0
00/B-008-I/094-J-10/0
Datum: Top of Muskwa
Otter Park
Limestone
Dolostone
Well Spacing Scale
0
10 km
Depth Scale
0
100 m
Stratigraphic boundary
Lst-Dol boundary
Datum: Sea Level
Otter Park

Figure 4.6 Stratigraphic (top) and structural (bottom) cross-sections H-H' showing the distribution of dolomite in the Clarke Lake field.

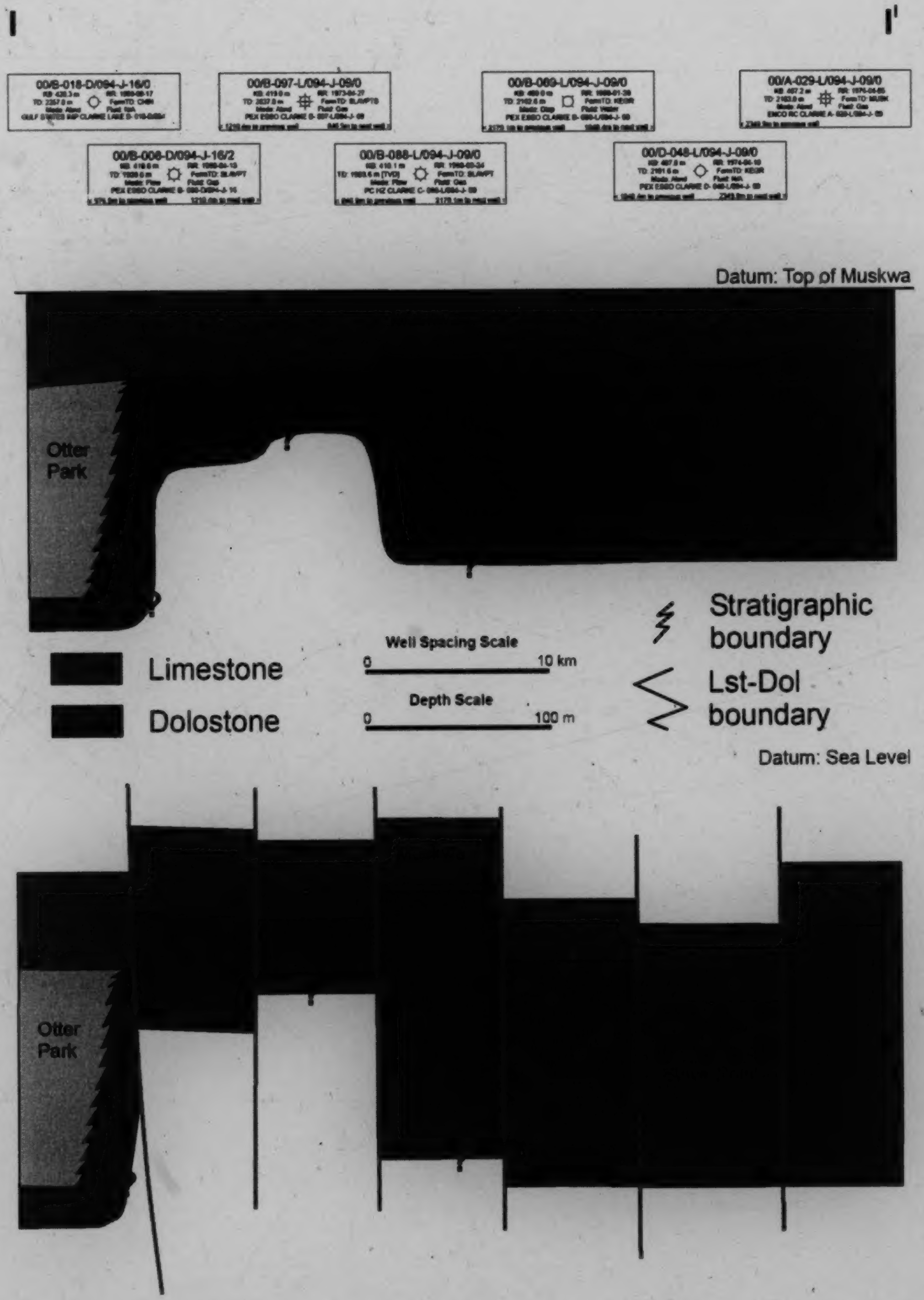
I
I'
00/B-018-D/094-J-16/0
00/B-097-L/094-J-09/0
00/B-069-L/094-J-09/0
00/A-029-L/094-J-09/0
00/B-006-D/094-J-16/2
00/B-088-L/094-J-09/0
00/D-048-L/094-J-09/0
Datum: Top of Muskwa
Otter Park
?
Stratigraphic boundary
Limestone
Dolostone
Well Spacing Scale
0
10 km
Depth Scale
0
100 m
Lst-Dol boundary
Datum: Sea Level
Otter Park

Figure 4.7 Stratigraphic (top) and structural (bottom) cross-sections I-I' showing the distribution of dolomite in the Clarke Lake field.

in Figure 4.7 suggests the geometry of the dolostone body was influenced by faults and/or fractures.

The overall location and geometry of the dolomite body (Figure 4.5) suggest an upward movement of the dolomitizing fluid(s) at the platform margin. The high hydraulic connectivity of, and within, the underlying formations is due to: 1) the absence of aquitards in the underlying Elk Point Group (e.g. Klua, Watt Mountain fms.), and 2) the presence of open faults/fractures (Lonnee and Machel, 2004a; 2004b). Furthermore, the isopach from the top of the overlying Muskwa Formation to the first occurrence of dolomite in the Slave Point (Figure 4.5) shows little variation in the east-west direction. However, abrupt dolomite-limestone contacts, both in the platform interior and within the main dolomite body itself, such as near well locations b-33-J/94-J-10, c-97-H/94-J-10, and b-69-L/94-J-9, suggest faults were the principal conduit for fluid flow into the Slave Point Formation. This suggestion is examined in further detail in Chapter 5.

Overall, on a field scale, facies appear to have little control over the location of dolomite, yet, petrographic observations and extant porosity and permeability data in section 4.4 suggest facies are critical for developing the best reservoir intervals.

4.6 Genetic implications of petrographic observations

As mentioned previously, the diagenetic history of the Slave Point Formation at Clarke Lake is extremely complex. The petrographic characteristics including the spatial and temporal distributions of the 25 diagenetic phases discussed above provide some clues about their formation.

4.6.1 Near-surface diagenesis (stage)

All of the diagenetic products during this stage formed during deposition on the seafloor to burial depths of up to 10 metres. Seafloor processes include micritization and development of internal sediments. Micritization (phase 1) is a process whereby bioclasts are altered by many kinds of microorganisms, such as fungi, bacteria, and algae, through the boring, or sediment-ingesting activities of these organisms (Tucker and Wright, 1990; Boggs, 1992). These microorganisms physically destroy the substrate, thus generating small holes that are subsequently filled with fine-grained aragonite (micrite) or high-magnesian calcite. Internal sediment (phase 2) is fine-grained material that is transported and pumped into the network of cavities near the surface of the reef (Tucker and Wright, 1990). Internal sediments may show multiple generations of deposition, as well as cross-lamination, grading, and bioturbation (James and Ginsburg, 1979).

The earliest cement in the primary pores of the Slave Point Formation at Clarke Lake is radial fibrous calcite (phase 3). The timing of formation of radial fibrous calcite cement is constrained based on the observation that it is coeval with marine internal sediments. Radial fibrous calcite belongs to the group of radiaxial fibrous calcite cements that have been identified as cavity fills in Paleozoic reefs worldwide (Kendall, 1985). Radial fibrous calcite has commonly been interpreted as forming in a marine environment. Based on their well-preserved crystal forms, Kendall (1985) concluded that these cements represent primary high- and low-magnesium calcite that grew in the form of large, sparry crystals within the marine phreatic environment.

Drusy calcite cement (phase 4) formed prior to significant physical compaction, fills most of the intra- and interskeletal pores, and post-dates radial fibrous calcite cement. This type of cement may form in a mixing-zone environment, meteoric-phreatic settings, and also in a deeper burial environment (Foreman, 1989). Drusy calcite cement lacks meniscus or stalactitic fabrics, and has a low iron content; hence, it is not representative of precipitation in a meteoric-phreatic environment (James and Choquette, 1990). Rather, based on its spatial and temporal relationships with previous and subsequent diagenetic phases in the Slave Point Formation, drusy calcite cement likely formed as either a near-surface or shallow-burial product.

4.6.2 Shallow burial diagenesis (stage)

Much of the original primary porosity in the limestones of the Slave Point Formation was reduced during the shallow burial stage to depths of up to 1000 metres. The two main cement phases that formed during this stage, blocky calcite I (phase 6) and syntaxial calcite (phase 7), post-date the early diagenetic features such as radial fibrous calcite and drusy calcite, and occlude the oldest generation of secondary fracture porosity (fracture generation I - phase 5) that formed in response to moderate tension developed during rapid burial following deposition. Chemical compaction of the Slave Point limestones resulted in the extensive development of stylolite generation I (phase 8) and associated fine crystalline brown dolomite (FBD - phase 9).

Blocky calcite cement I (phase 6) has luminescence characteristics that suggest low Fe and Mn contents. The Mn concentration of surface waters is much higher than subsurface waters (Walls and Burrowes, 1985), yet, deep subsurface waters usually contain elevated Fe concentrations (Machel, 1999); hence, this information in conjunction with the paragenetic relationship to fracture generation I (phase 5) suggests blocky calcite I was formed in the shallow burial environment.

Syntaxial calcite cements (phase 7) have been interpreted to be of meteoric origin (Longman, 1980; Tucker, 1985). However, cathodoluminescence data from Walkden and Berry (1984) suggests that syntaxial calcite cements that are highly-zoned, clear, and inclusion-poor were formed in a burial environment. Additionally, there is no petrographic evidence to suggest meteoric water incursion into the Slave Point Formation at Clarke Lake, precluding the possibility that syntaxial calcite was formed via meteoric waters.

Petrographic evidence indicates that some of stylolite generation I (phase 8) predate dolomitization of the matrix. Furthermore, within the limestones, isolated patches of small (< 50 μm), subhedral crystals of dolomite (FBD – phase 9) are associated with stylolite development. Two scenarios exist to explain this spatial relationship. Firstly, Wanless (1979) proposed that dolomites associated with pressure solution features may form through the dissolution of high-Mg calcite that was not stabilized in the near-surface environment. Secondly, the lack of dolomite rhombs in adjacent strata suggests the stylolites acted as conduits for dolomite-forming fluids.

Stylolites are common features in carbonates, and are the result of pressure solution due to increasing overburden pressures. Dolomite is less soluble than limestone, and, therefore, generally is more resistant to pressure solution (Choquette and Steinen, 1980). However, only where two grains of the same mineral are juxtaposed will the pressure solution contact be sutured. Conversely, the contact is smooth where the mineralogy differs, as one mineral effectively dissolves the other (Machel, 2005). Stylolite generation may begin at depths of as little as about 500 metres in limestones (Fabricius, 2000), becoming common below 830 metres (Lind, 1993).

The crystal sizes and shapes, fabric, and temporal relationships with other diagenetic phases place important constraints on the formation of fine crystalline brown dolomite (FBD - phase 9). The planar crystal boundaries exhibited by the FBD in conjunction with the fabric-retentive texture point towards dolomite formation at temperatures of less than about 60°C (Gregg and Sibley, 1984; Saller, 1984; Machel, 2004). In addition, the paragenetic relationship between FBD and stylolite generation I (phase 8) suggest dolomite formation at a minimum depth of 500 metres (Fabricius, 2000). The crystal sizes, which are small relative to most matrix dolomites from the Devonian of western Canada, and the scattered occurrence of FBD, place additional constraints on the dolomite mechanism (discussed in section 5.7). These observations eliminate both seawater and burial dolomitization models as alternatives for the formation of FBD in the Slave Point Formation. Additionally, the temporal relationship between FBD and stylolite generation I eliminates penecontemporaneous and near-surface dolomite models, including the sabkha model. The mixing zone model generally forms scattered lenses of small crystals that dominantly occur as fringing cements and subordinately as replacements (Machel, 2004). However, the dominant diagenetic process in mixing zones is the dissolution of limestone (Machel, 2004), a feature not observed in the Slave Point Formation. The reflux model, first proposed by Adams and Rhodes (1960) to explain the formation of dolomite in the lagoonal sediments of the Permian of west Texas and New Mexico, generally forms dolomites that are fine- to medium crystalline, matrix-selective, and are fabric-retentive, similar to FBD in the Slave Point Formation.

4.6.3 Intermediate burial diagenesis (stage)

Major diagenetic changes occurred during intermediate burial with the continuation of chemical compaction in the form of stylolite generation I (phase 8), and the formation of replacement matrix dolomites (GMD – phase 10) and their subsequent alteration during the invasion of hydrothermal fluid(s).

The petrographic data place some constraints on the formation of GMD (phase 10) through the crystal shapes and paragenesis. In theory, planar crystal boundaries, as exhibited by some of the GMD in the Slave Point, tend to develop at temperatures up to the 'critical roughening temperature', which according to Gregg and Sibley (1984) is around 50 – 60°C for dolomite. However, GMD in the Slave Point Formation also shows the development of non-planar crystal textures, even within a single well. Additionally, there are indications that dolomitization of the Slave Point resulted in both fabric-retentive and fabric-obliterative textures, which are usually (cf. Bullen and Sibley, 1984; Saller, 1984) regarded as distinctive clues resulting from low-temperature and high-temperature dolomitization, respectively (Machel, 2004). Considering these ambiguities, crystal shapes are not sufficient to provide a temperature estimate for GMD formation. However, the paragenetic relationship between GMD and stylolite generation I (phase 8) point towards dolomite formation during intermediate burial at depths in excess of 500 metres (Lind, 1993; Fabricius, 2000), which suggests GMD formation at a temperature similar to the 'critical roughening temperature' by applying a normal geothermal gradient.

The relatively large size of many GMD crystals, in conjunction with the volume of GMD in the Slave Point Formation, place important constraints on the salinity of the dolomitizing fluid and, hence, limits the available models for dolomite formation. The petrographic data from GMD rule out the possibility of dolomitization in shallow-marine to supratidal environments, i.e., penecontemporaneous dolomites, where the bulk of the dolomites are microcrystalline and occur in lenses or thin beds that rarely exceed 5 volume percent (Machel, 2004). This includes sabkha dolomites due to the absence of both microcrystalline dolomite in narrow lenses, and coastal supratidal flat and tidal channel facies in core (see Chapter 3). Formation of GMD in a mixing zone is also excluded as a potential model since mixing zones commonly form dolomite in small amounts as narrow fringing cements and replacements, and recent studies have suggested that massive dolomitization in mixing zones is nearly impossible (Machel, 2004 and references therein). The reflux of hypersaline brines has been proposed to explain the global occurrence of regionally extensive carbonate platforms containing pervasive fine- to medium crystalline matrix dolomites (Shields and Brady, 1995; Potma et al., 2001). However, modelling by Jones et al. (2003) found that reflux of hypersaline brines in the Devonian Grosmont Formation of Alberta could only form dolomite in discrete layers that alternate with limestone. Rather, based on the paragenetic relationships discussed previously, GMD in the Slave Point Formation was likely formed from seawater or a variant thereof. This conclusion is similar to those drawn from studies of the regionally extensive Devonian dolostones south of the Peace River Arch in Alberta. These matrix dolomites were formed at depths of 300 to 1500 metres at temperatures of about 50 to 80°C from chemically slightly modified seawater (Amthor et al., 1993; Machel et al., 1994; Mountjoy and Amthor, 1994; Mountjoy et al., 1999).

Replacive chert (phase 11) is found in association with matrix dolomite (GMD – phase 10) where the latter shows little evidence for dissolution, i.e., curved crystal terminations or pitting. This observation indicates that the $H_4SiO_4^0$-charged fluid was supersaturated with respect to silica, saturated with respect to dolomite, but undersaturated with respect to calcite. Based on modeling studies of brines from Mississippi Valley-type (MVT) deposits, Leach et al. (1991) concluded that mixing of brines with varying saturation states with respect to dolomite and calcite would result in the formation of dolomite and quartz. More importantly, they (ibid.) found that dolomite formation is restricted to the highest temperatures. Conversely, silica should precipitate from solution as the temperature of the fluid decreases, owing to an increase in silica supersaturation (Hesse, 1990).

Fracture generation II (phase 12) post-dates the replacement dolomite phase (GMD – phase 10) and is present in all wells that include the products of hydrothermal alteration (phase 13). This fracture phase occurred in the intermediate burial realm and is likely related to compressional stresses developed during the terminal stages of Antler orogenesis (Nelson et al., 2002).

Dissolution occurred during at least two phases of the diagenetic history of the Slave Point Formation. These two phases include the removal of calcium carbonate associated with the dolomitization process (GMD – phase 10), and the removal of GMD during hydrothermal alteration (phase 13).

The first phase of dissolution and concomitant vuggy porosity generation is a by-product of matrix dolomitization (phase 10), whereby unreplaced fossils and matrix domains are removed during advanced dolomitization when the fluid effectively 'runs out' of Mg^{2+} (Machel, 2004).

The second phase of dissolution and vuggy porosity generation is here interpreted as a result of dissolution of pre-existing GMD by fluids undersaturated with respect to dolomite during hydrothermal alteration (phase 13).

Dissolution and porosity development in carbonates is mainly controlled by the generation of acidic fluids in the burial environment (Mazzullo and Harris, 1992). Several processes can lead to the generation of acidic fluids, including the mixing of two solutions that are both in equilibrium with respect to carbonate minerals but have different pCO_2, temperatures, salinities, and/or pH. Numerous studies in the past have attempted to identify the reasons for the dissolution of carbonates in the subsurface based on the modelling of MVT Pb-Zn deposits (Anderson, 1975; Barnes, 1983; Sverjensky, 1986; Kesler et al., 1994; Plumlee et al., 1994; Hill, 1995; Hitzman and Beaty, 1996; Corbella and Ayora, 2003; Corbella et al., 2004). The simplest reactions to explain porosity generation and sulphide precipitation have several drawbacks when applied to the Clarke Lake field, and to many of the other occurrences worldwide. Firstly, these reactions suggest that for every mole of carbonate dissolved a mole of sulphide mineral is precipitated. However, based on this mass balance, large quantities of sulphide minerals should be present in the Slave Point Formation at Clarke Lake, which is not the case. Evidence of MVT mineralization is restricted to scattered occurrences of sphalerite and galena in a few wells (see deep burial diagenesis, below). Secondly, there is no evidence for sour gas or sulphate reduction in the saddle dolomite that is associated with hydrothermal alteration, precluding the possibility that acids generated during thermochemical sulphate reduction caused dissolution (Machel, 1987a; 1987b). Recent geochemical modelling (Corbella and Ayora , 2003; Corbella et al., 2004) suggests that the simple mixing of two calcite-saturated solutions that only differ in their salinity will create a new solution undersaturated in calcite. This type of modelling has not been confirmed using dolomite, but similar results would be expected. Based on hydrochemical data, the interaction of two fluids of dissimilar salinities has been suggested as the cause of carbonate dissolution and concomitant sulphide mineralization further up-dip along the Presqu'ile Barrier at the Pine Point MVT deposit (Adams et al., 2000). The possibility of fluid mixing causing dissolution of GMD in the Slave Point Formation will be further discussed using geochemical evidence presented in Chapter 5.

Saddle dolomite, the most visible product of hydrothermal alteration (phase 13) at Clarke Lake, can form: 1) from advection, 2) from local redistribution of older dolomite during chemical compaction; and, 3) as a by-product of thermochemical sulphate reduction (TSR) in a closed system (Radke and Mathis, 1980; Machel, 1987a; Machel and Lonnee, 2002). Other authors have suggested that saddle dolomite is only formed from hydrothermal fluids (Davies, 1997; 2002). However, this notion is incorrect: while saddle dolomite formed from rapidly ascending fluids in fracture systems may be hydrothermal, saddle dolomite formed via local redistribution during stylolitization is geothermal: forming in equilibrium with the surrounding strata, and saddle dolomite formed as a by-product of TSR is commonly hydrofrigid (Machel and Lonnee, 2002).

The temperatures of saddle dolomite formation and the temporal relationship to other intermediate burial diagenetic phases limit both the mechanism for the formation of saddle dolomite in the Slave Point Formation, and the composition of the diagenetic fluid. Recalling the fluid responsible for the previously formed GMD, saddle dolomite likely formed at temperatures of at least 60-80°C at burial depths greater than 1000 metres. Previous studies from worldwide occurrences of saddle dolomite demonstrate that saddle dolomite commonly formed from fluids with salinities averaging 6X that of normal seawater (Davies, 1997; Spötl and Pitman, 1998). This information, in conjunction with the other paragenetic evidence, limits the potential dolomite models to those active in the intermediate to deep burial diagenetic realm: compaction flow, thermal convection, topography driven flow, and tectonically driven flow.

Stylolite generation II (phase 14) are most common where the Slave Point Formation is pervasively dolomitized, post-date all phase of dolomite formation, and pre-date sulphide mineralization (phase 18) and liquid hydrocarbon migration (phase 19). As stylolite formation is an ongoing process during continued burial, stylolite generation II is expected to have formed during the latest stages of intermediate burial through the onset of deep burial diagenesis when the Slave Point Formation was rapidly buried due to regional tectonism (evidence for this is discussed in Chapter 5).

4.6.4 Deep burial diagenesis (stage)

Deep burial is characterized by the emplacement of sulphide minerals (phases 18 and 22), liquid hydrocarbon migration (phase 19) and subsequent thermal cracking to natural gas and bitumen (phase 23), and partial cementation of fracture porosity by blocky calcite II (phase 25).

Fracture generation III (phase 15) post-dates hydrothermal alteration (phase 13), including saddle dolomite formation. These fractures are likely related to compressional stresses that developed during the Triassic at the onset of Columbian orogenesis. Also during this time, faulting and fracturing produced the micro-shear zones and related authigenic clay minerals (phase 16) in the pervasively dolomitized rocks of the Slave Point Formation, and the effects of the compressional tectonics are evident by the generation of vertical stylolites (phase 17).

The sphalerite (phase 18) and galena (phase 22) from the Slave Point Formation are petrographically similar to MVT minerals identified in Devonian carbonates across the northern half of the Alberta Basin, from the Rocky Mountains in the west, to Pine Point in the east. Nakai et al. (1993) defined a well-constrained linear Rb-Sr isochron for sphalerite at Pine Point, providing an absolute age of 362 ± 9 Ma. Similarly, Nelson et al. (2002) determined an isochron age of 350 ± 100 Ma for sphalerite in the Robb Lake MVT deposit in northeastern British Columbia (about 200 km downdip to the west from Clarke Lake). Pb-Pb isotope work on galena collected from the Middle Devonian of northeastern British Columbia shows a similar age of mineralization: 350 Ma (Nelson et al., 2002). They (ibid.) suggested that base-metal mineralization occurred during the Late Devonian-Mississippian as a result of regional plate margin tectonics, resulting in thermal convection and fluid flow into the Western Canada Sedimentary Basin.

The main phase of liquid hydrocarbon migration into the Slave Point Formation is recognized by the presence of solid bitumen (phase 19). Spatial relationships indicate that hydrocarbon migration post-dates the formation of saddle dolomite (phase 13) and pre-dates the formation of blocky calcite II (phase 25). Solid bitumen is derived from microbial, oxidative, or thermal alteration of pre-existing bitumen or liquid hydrocarbons (Curiale, 1993). It is frequently encountered in the Devonian gas reservoirs of the Western Canada Sedimentary Basin, and has been interpreted as the insoluble residue of the thermal cracking (phase 23) of oil to gas, i.e., pyrobitumen. Alternatively, bitumen may be the product of thermochemical sulphate reduction processes (Machel, 1987a). However, there is no evidence for sour gas generation in the Slave Point Formation. The conversion of the liquid hydrocarbon to natural gas was the result of either increased burial or a higher geothermal gradient, or a combination of the two. The timing of hydrocarbon maturation and migration will be further discussed with respect to the burial history presented in Chapter 5.

Within the limestones, the bulk of the pyrobitumen is situated within microfractures (phase 23). Marquez and Mountjoy (1996) proposed that microfractures form as a by-product of the cracking of crude oil to gas under increased pore pressures. If this interpretation applied to Clarke Lake, liquid hydrocarbons would have had to been emplaced in the Slave Point Formation prior to thermal cracking. Furthermore, microfractures are not present in pervasively dolomitized rocks. This could mean that a first phase of hydrocarbon migration occurred prior to dolomite formation, and the major dolomite-forming event (phase 10) in the Slave Point Formation occurred at temperatures above 125°C, the approximate temperature at which the bituminous microfractures formed (Marquez and Mountjoy, 1996). Alternatively, it is more likely that hydrocarbons invaded both limestones and dolostones, yet only the limestones responded to the increased pressure from gas generation by brittle failure, whereby the open fractures served as loci for bitumen precipitation. This alternative is consistent with the observation that solid bitumen is present also in intercrystal pore spaces of dolostones that formed as GMD (phase 10).

Fracture generation IV (phase 24) post-dates all diagenetic phases with the exception of blocky calcite II (phase 25). These fractures likely developed during uplift/exhumation in either the Jurassic or the Tertiary following the Columbian and Laramide orogenies.

Blocky calcite II (phase 25) is the latest diagenetic phase to be identified in the Slave Point Formation at Clarke Lake. Similar coarse crystalline calcite cements are usually the latest carbonate phase to precipitate in Devonian formations across the Western Canada Sedimentary Basin. Mountjoy and Amthor (1994), and Mountjoy et al. (1999) suggested that these late-stage calcite cements reflect the chemistry of the basinal fluids at maximum burial or shortly thereafter: Cretaceous through Early Tertiary in most parts of the basin, but as early as Late Triassic in northeastern British Columbia (see burial history presented in Chapter 5). Alternatively, Machel et al. (1996) interpreted the late-stage calcite cements from the Obed field in west-central Alberta to have resulted from the tectonic expulsion of fluids during the Late Cretaceous to Early Tertiary Laramide Orogeny. In the Slave Point Formation, blocky calcite II probably formed as a result of fluid flow following the first phase of deep burial associated with the Late Triassic through Early Jurassic Columbian Orogeny. The distance between the Clarke Lake field and the disturbed belt (~ 50 km) is within the maximum range of 100 – 200 km proposed by Machel et al. (1996) for the lateral migration of fluids during tectonic expulsion. At this point, though, it is unclear whether or not the fluid that precipitated blocky calcite II was the result of tectonic expulsion. This option will be further discussed using geochemical data presented in Chapter 5.

CHAPTER 5

GEOCHEMICAL EVIDENCE FOR THE DIAGENETIC EVOLUTION OF THE SLAVE POINT FORMATION

5.1 Introduction

Using the data presented in the previous chapters, the objectives of Chapter 5 are to: 1) constrain the composition and timing of the various diagenetic fluids; 2) determine whether the dolomite-forming fluids were hydrothermal; and, 3) provide a hydrological interpretation for dolomite formation in the Slave Point Formation. These objectives were fulfilled by applying a variety of geochemical methods to both dolomite and calcite phases in the Slave Point Formation. These methods include: 1) stable isotope analysis; 2) $^{87}Sr/^{86}Sr$ isotope analysis, both bulk and in situ techniques; 3) major and trace element analysis; 4) rare earth element analysis; 5) fluid inclusion analysis, both microthermometric and crush-leach techniques; and, 6) burial and thermal history modeling.

5.2 Methods

Various generations of dolomite and calcite were sampled for oxygen and carbon stable isotope analysis, $^{87}Sr/^{86}Sr$ isotope analysis, and trace element analysis using a low speed dental drill with tungsten carbide and diamond bits. A total of 97 powder samples was obtained, commonly 10-20 mg for stable isotope analyses, about 25 mg for Sr-isotope analyses, and about 250 – 600 mg for trace element analyses.

The samples for stable isotope analysis (n = 91) were reacted in vacuo with 100% pure phosphoric acid (McCrea, 1950) for at least 4 hours at 50°C for dolomite, and at 25°C for calcite. Samples containing both calcite and dolomite were subjected to chemical separation techniques described by Al-Aasm et al. (1990). The evolved CO_2 gas was analysed for isotopic ratios on a Finnigan MAT 252 mass spectrometer at the University of Alberta. Values of O and C isotopes are reported in per mil (‰) relative to the Vienna Peedee belemnite (VPDB) standard. The results were reproducible within ± 0.1‰ for both $\delta^{18}O$ and $\delta^{13}C$. Values for dolomite were not corrected for phosphoric acid fractionation (Land, 1980). Determination of oxygen isotope values for dolomite-forming fluids was conducted using the following dolomite-H_2O equilibrium fractionation equation from Land (1983).

$$1000\ln\alpha = 3.2 \times 10^{6} (T^{-2}) - 3.3$$

Strontium isotopes were analysed for selected dolomite and calcite samples (n = 55). Samples were dissolved in 1N hydrochloric acid, followed by extraction using conventional cation exchange chromatography (Baadsgard, 1987). Strontium isotope ratios were measured on a VG 354 thermal ionization mass spectrometer at the University of Alberta. All analyses were performed in the static multicollector mode using Re filaments. All strontium isotope ratios are presented relative to a value of 0.710245 for the NIST SRM987 standard. The mean standard error was 0.000023 for SRM987. In-run precision was better than 2×10^{-5} (2σ).

Non-carbonate samples (n = 33) were analysed for their extractable $^{87}Sr/^{86}Sr$ values using the method devised by Machel and Cavell (1999). Samples were dissolved in 1N hydrochloric acid at 25°C for a period of roughly 20 hours. Strontium isotope ratios were subsequently obtained using the method outlined above.

In-situ Sr isotope analyses were determined using a Nu Plasma MC-ICP-MS instrument coupled to a 213 nm Nd:YAG laser system (New Wave Research) at the University of Alberta. The analytical protocol adopted in this study is similar to that described in Schmidberger et al. (2003). Dolomite crystals within petrographic thin sections were ablated using a spot size of 160 μm, 20 Hz repetition rate, and laser output at approximately 3 mJ. The ablated particles were flushed out of the ablation cell with He gas (flow rate of 1.0 mL/minute). Argon gas was mixed with the ablated particles and He carrier gas via a 'y-connection' to the 'sample-out' line from a desolvating nebulizing system (DSN-100 from Nu Instruments Inc.). Strontium isotope data were obtained in static multicollection mode using six Faraday collectors. For each analysis, data acquisition consisted of a 30 seconds measurement of the gas blank prior to the start of ablation, which is critical for the correction of the ^{86}Kr and ^{84}Kr isobaric interferences. The isobaric interference of ^{87}Rb was also monitored and corrected for using the ^{85}Rb ion signal; however, the latter is considered negligible for all of the results reported here. The duration of the laser ablation runs were variable (between 20 to 50 seconds), and depended mainly on the time taken to ablate through the grain being analyzed. Accuracy and reproducibility of the Sr isotope values were verified using an internal standard consisting of a modern-day coral yielding an average value of 0.70910 ± 0.00005 (2σ; n>50, Schmidberger et al., 2003).

Trace element and REE concentrations were determined on 40 dolomite and calcite samples using neutron activation analysis (NAA) at the University of Alberta SLOWPOKE II nuclear reactor facility. Aliquots of powdered rock samples, weighing between 250 and 600 mg, were hermetically sealed in polyethylene vials. Samples were individually irradiated for 240 s at a thermal neutron flux of 1×10^{11} $n \cdot cm^{-2}s^{-1}$. Following irradiation, samples were counted twice – after decay periods of 180 s and ~1800 s. Samples were counted using a 41.4% relative efficiency Princeton Gamma-Tech (PGT) hyperpure Ge detector connected to a PC-based APTEC multichannel analyzer (MCA) card. Decay corrections for short-lived radionuclides in the presence of longer-lived radionuclides were applied according to Takeuchi et al. (1980). Following a total decay period of ~ 1 week, samples and standards were re-irradiated in batches for 4 hrs at a thermal neutron flux of 5×10^{11} $n \cdot cm^{-2}s^{-1}$. The individual samples were then counted following decay periods of ~ 24 hrs, 6-7 d, and 3-4 weeks. Element analyses were performed via the semi-absolute method of activation analysis (Bergerioux et al., 1979). For the majority of the elements, the NIST flyash geostandard 1633a was used for elemental calibration, and duplicate aliquots of a Cararran marble standard were analyzed for quality control purposes. Agreement between the measured and recommended concentrations of the elements for the marble standard was generally better than ± 10% (1σ). For the determination of Ca and Mg in the carbonates, calcium carbonate and magnesium fluoride (purity > 99.99%) were used as primary standards.

A single polished thin section was analyzed on a JEOL JXA-8900R electron microprobe at the University of Alberta in order to obtain geochemical information from dolomite crystals that were analysed by in-situ laser ablation MC-ICP-MS. Operating conditions for the microprobe were 15 kV accelerating voltage, 10 nA beam current at the Faraday cup, and 3 μm beam diameter. Individual spots were analyzed for Si, Mg, Ca, Mn, Al, Na, Fe, and Sr. Standard data were obtained from dolomite (Ca, Mg), kaersutite (Si, Al, Na, Fe), willemite (Mn), and strontianite (Sr). Detection limits on the electron microprobe vary depending on the chemistry of the dolomite zones, and are discussed individually in the text.

Fluid inclusion microthermometry analyses were carried out on twelve doubly-polished thin sections using a Linkam THMSG600 heating-freezing stage at the University of Alberta that was calibrated using Syn Flinc synthetic standards. Homogenization temperatures (Th) and melting temperatures (Tm) were measured for each of a total of

143 inclusions using standard microthermometry procedures (Roedder, 1984; Sheperd et al., 1985; Goldstein and Reynolds, 1994). Accuracy was determined to within ± 0.2°C for freezing runs, and ± 2°C for heating to 250°C. Salinities were calculated from final ice melting temperatures using the equation of Bodnar (1993) in terms of the H_2O-NaCl system. Fluid inclusion isochores were constructed using the method described by Zhang and Frantz (1987) for NaCl-KCl-$CaCl_2$-H_2O fluids.

Sixteen samples of dolomite, calcite, and sphalerite were crushed to determine their bulk fluid inclusion chemistry. Each sample is from a specific petrographic phase and was accurately cut from core/hand sample with a trim rock saw. The samples were crushed and sieved to give a 1-2 mm grain size fraction and hand picked under a binocular microscope to obtain 2 g of a clean mineral separate where possible. The samples were then washed in 18.2 mΩ water and heated overnight on a hot plate, then dried in an oven. 1-2 g of sample was ground to a fine powder in an agate mortar and pestle in a clean and controlled environment. Half the powder was transferred to an unreactive vial and 5 ml of clean water was added. These samples were shaken, and filtered through 0.2 micron filters to give a clean leachate. Anions (Cl, Br, F, sulphate, and nitrate) were analysed using a Dionex DX600 ion chromatograph (IC) at the University of Alberta. Sodium and K were analysed on the same leachate using atomic adsorption spectroscopy (AAS). Absolute concentrations of the reported elements were calculated using the method described by Banks et al. (2002).

Vitrinite reflectance values from the Slave Point, Muskwa and Mississippian Exshaw formations from 2 wells in the Clarke Lake area were used in the construction of the burial history. These data were obtained from Stasiuk and Fowler (2002). The reader is referred to their paper for an overview of the analytical procedure.

5.3 Geochemical results and discussion

Extensive geochemical investigations were conducted on the calcites and dolomites of the Slave Point Formation at Clarke Lake. The complete list of data is available in Appendices IV though IX.

5.3.1 Stable isotopes

The stable isotopes of oxygen and carbon are the most commonly used isotopes in the study of carbonate diagenesis. They are used to determine the isotopic differences between fossil remains of organisms and diagenetic phases, i.e., dolomite, calcite, etc., and to make inferences about the physical surroundings of the growth of the organism or crystal phases – especially temperature (Wefer and Berger, 1991). Additionally, if the temperature of crystallization, or a reasonable estimate, is known, the isotopic composition of the diagenetic fluids can be identified.

The following factors control the ratios of oxygen isotopes in carbonates (Brand and Veizer, 1981; Anderson and Arthur, 1983):

1) The isotopic composition of the diagenetic fluids. Meteoric fluids (e.g., rainwater), whose source is evaporated seawater, is typically depleted in ^{18}O relative to coeval marine water. This is due to the preferred incorporation of the lighter ^{16}O isotope in rainwater during evaporation.

2) In the subsurface, under elevated temperature conditions, basinal fluids can exchange oxygen isotopes with carbonate rocks, resulting in the enrichment of ^{18}O in the fluids and commensurate depletion in the carbonates (Clayton et al., 1966).

3) The water-rock ratio or openness of the system. During high water-rock ratios there is a constant supply of isotopes to the fluids, and the rock composition is isotopically dominated by the fluid composition; whereas, low water/rock ratios involve 'recycling' of isotopes between the fluid and the rock, and the rock composition may be little affected by changes in fluid composition.

4) The fractionation factor, determined primarily by the temperature at which the reaction, i.e., precipitation or recrystallization, occurs.

5) Altitude, latitude, and seasonal variations affect the ^{18}O composition of meteoric water. Generally, ^{18}O decreases with increasing altitude and latitude.

6) Secular variations in seawater isotopic composition. In general, the oxygen isotopic compositions of marine carbonates become progressively more depleted in ^{18}O with increasing age of the rocks (Given and Wilkinson, 1987). Though the validity of this data is not disputed, many disagree with the implications. Veizer et al. (1999) listed the implications as one or all of the following:

a) seawater ^{18}O changed during the course of the Phanerozoic;
b) the early oceans were much warmer than today: up to ~700°C; and/or,
c) the early oceans were stratified, with deep waters being generated

by sinking of dense, saline brines from extensive evaporation at low latitudes.

Objections to alternative a) were raised by Muehlenbachs (1998) who claimed that the ^{18}O of ocean water is, and has been, buffered at roughly 0‰ SMOW by water-rock interactions in hydrothermal convection cells at mid-ocean ridges since at least the Proterozoic. For alternative b), the persistence of essentially the same faunal assemblages and the recurrence of ice ages throughout the Phanerozoic are difficult to reconcile with the advocated warm temperatures (Veizer et al. 1999). Finally, for alternative c), the implied permanent saline stratification would be difficult to sustain and, even if sustainable, it could account for no more than ~1.5‰ ^{18}O depletion in the near-surface oceanic layer (Railsback, 1990; Veizer et al., 1999)

7) Biological fractionation or vital effects, as first proposed by Urey et al. (1951). This refers to the 'vital selection' of isotopes during plant or animal metabolism. For example, some organisms, such as crinoids and rugose corals, produce carbonate that is not in isotopic equilibrium with seawater.

With respect to dolomite, the ^{13}C is strongly influenced by that of the precursor $CaCO_3$ as a result of the relative insolubility of CO_2 in water (Land, 1980). Therefore, the ^{13}C value of calcium carbonate being dolomitized is commonly retained by the dolomite (Tucker and Wright, 1990). Additionally, there is little isotopic fractionation between $^{13}C/^{12}C$ with temperature. Hence, the ^{13}C values of dolomite, like those of limestone and calcite, primarily provide information on the source of carbon in the carbonate. However, dolomitization under high water-rock ratios involving fluids of distinct isotopic compositions can potentially alter the original $\delta^{13}C$ composition. As well, depleted $\delta^{13}C$ values are common in near-surface meteoric environments as a result of input from decaying organic matter (James and Choquette, 1984) and during sulphate reduction (Machel, 1987; Hendry, 1993). Conversely, enriched $\delta^{13}C$ values may be obtained through the fermentation of organic matter during methanogenesis (Irwin et al., 1977).

Results

A total of ninety samples of various generations of calcite and dolomite were analyzed for their $\delta^{18}O$ and $\delta^{13}C$ composition. The range of stable isotope values for individual carbonate phases is shown in Table 5.1.

Table 5.1 Carbon and oxygen stable isotope results (in ‰ VPDB) by diagenetic phase. Diagenetic phase numbers from Figure 4.1. The number of analyzed samples is reported in parenthesis. min. = minimum measured value, mean = arithmetic mean of measured values, max. = maximum measured value, Std. Dev. = standard deviation (1σ).

Phase		$\delta^{18}O$	$\delta^{13}C$
Limestone (7)	min.	-13.47	-1.54
	mean	-12.04	+0.34
	max.	-9.47	+2.19
	Std. Dev.	1.76	1.30
Fossils (12)	min.	-12.40	-0.34
	mean	-9.07	+0.95
	max.	-3.67	+3.09
	Std. Dev.	2.55	1.04
Calcite Cement phases 6/25 (10)	min.	-17.00	-3.02
	mean	-13.81	-0.70
	max.	-9.96	+1.65
	Std. Dev.	2.14	1.81
FBD phase 9 (3)	min.	-12.92	+0.93
	mean	-12.47	+1.76
	max.	-12.05	+2.72
	Std. Dev.	0.44	0.91
GMD phase 10 (34)	min.	-16.73	-2.15
	mean	-14.57	-1.04
	max.	-13.00	-0.31
	Std. Dev.	0.88	0.40
SD phase 13 (24)	min.	-16.12	-2.29
	mean	-14.76	-1.02
	max.	-13.59	-0.18
	Std. Dev.	0.70	0.53

Samples of limestone matrix (micrite) have $\delta^{18}O$ values that range from –13.47 to –9.47‰ VPDB (mean = -12.04, 1σ = 1.76), and $\delta^{13}C$ values from –1.54 to +2.19‰ VPDB (mean = +0.34, 1σ = 1.30). The oxygen isotope values from the limestone matrix are significantly depleted with respect to Middle Devonian marine (abiotic) calcite (Figure 5.1A), while half of the carbon isotope values from the limestone matrix are compatible, and vice versa, with values of Middle Devonian marine calcite (Figure 5.1A).

Twelve samples of skeletal calcite from fossil components (i.e., stromatoporoids, *Amphipora*, *Thamnopora*, crinoids, and brachiopods) have $\delta^{18}O$ values that range between –12.40 and –3.67‰ VPDB (mean = -9.07, 1σ = 2.55), and $\delta^{13}C$ values between –0.34 and +3.09‰ VPDB (mean = +0.95, 1σ = 1.04). The stable isotope values from these samples lie along a covariant depletion trend between Middle Devonian marine calcite and the bulk of the subsequent diagenetic phases (Figure 5.1A).

Samples of calcite cements (phases 6 and 25) have $\delta^{18}O$ values ranging from –17.00

Figure 5.1 Crossplots of carbon and oxygen stable isotope results

(A) Plot of $\delta^{18}O$ and $\delta^{13}C$ values from all calcite and dolomite samples. Calcite samples include limestone matrix (micrite) and fossil components (stromatoporoids, *Amphipora*, crinoids, brachiopods). Matrix dolomite includes both fine-crystalline brown dolomite (FBD - phase 9) and grey matrix dolomite (GMD - phase 10). The field for Middle Devonian seawater calcite (SWC) is based on the reference values for Middle Devonian marine calcite (Hurley and Lohmann, 1989). The field for Middle Devonian seawater dolomite (SWD) is based on the reference values for Middle Devonian marine calcite (Hurley and Lohmann, 1989), corrected according to the equilibrium $\Delta^{18}O$ between calcite and dolomite (3 ± 1‰ at 25°C; Land, 1980). The covariant depletion trend exhibited by the fossil components is represented by the solid line.

(B) Plot of $\delta^{18}O$ and $\delta^{13}C$ values of matrix and saddle dolomites enlarged from Figure 5.1A. The position of the west-east separation line is shown in Figure 5.7. The field for Middle Devonian seawater dolomite (SWD) is as in Figure 5.1A. The values from Clarke Lake show a clear separation from the bulk of the matrix dolomites elsewhere in the Devonian of western Canada (Alberta Basin)(Mountjoy et al., 1999; Buschkuehle, 2003).

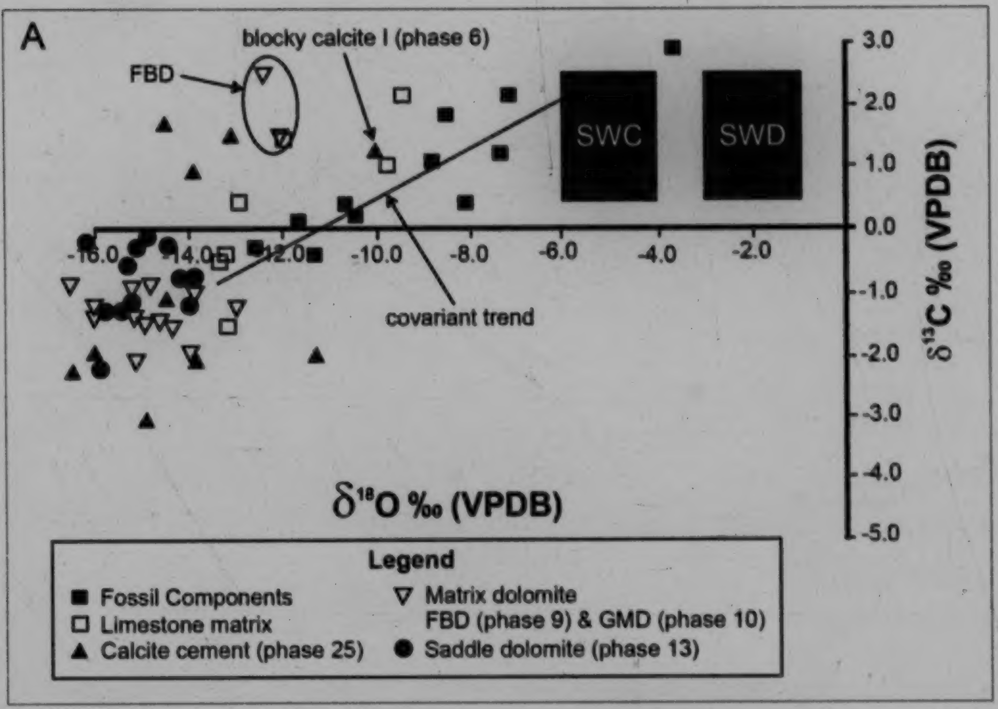
A
blocky calcite I (phase 6)
FBD
SWC
SWD
covariant trend
-16.0
-14.0
-12.0
-10.0
-8.0
-6.0
-4.0
-2.0
3.0
2.0
1.0
0.0
-1.0
-2.0
-3.0
-4.0
-5.0
δ18O ‰ (VPDB)
δ13C ‰ (VPDB)
Legend
■ Fossil Components
☐ Limestone matrix
▲ Calcite cement (phase 25)
▽ Matrix dolomite
FBD (phase 9) & GMD (phase 10)
● Saddle dolomite (phase 13)

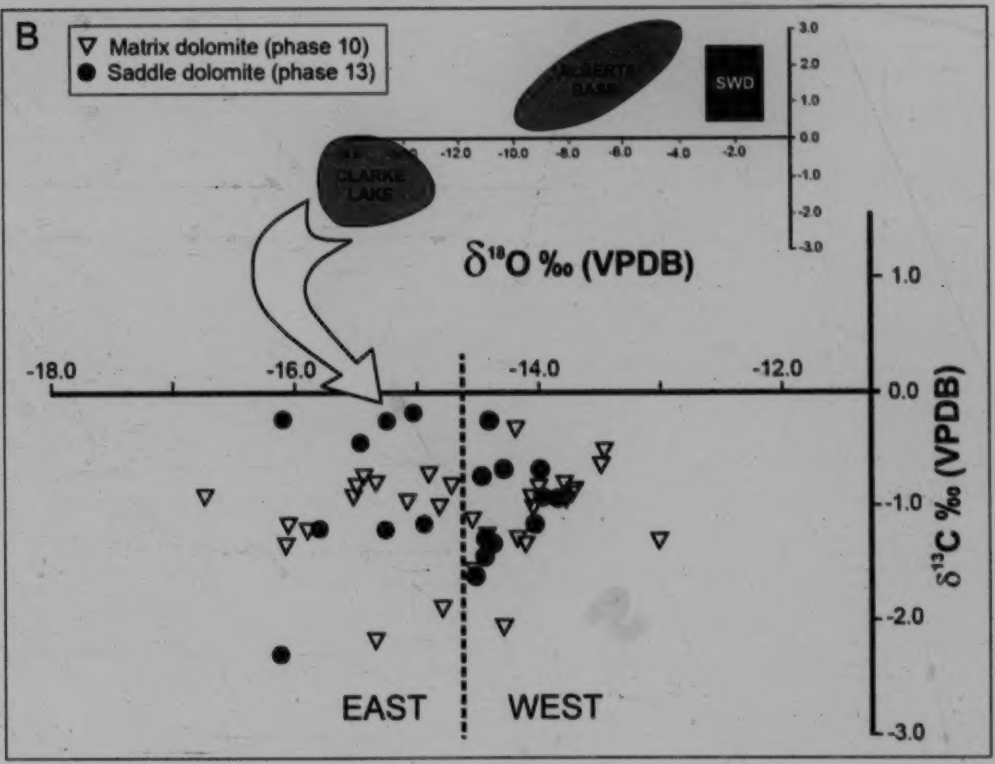
B
▽ Matrix dolomite (phase 10)
● Saddle dolomite (phase 13)
SWD
CLARKE
LAKE
-12.0
-10.0
-8.0
-6.0
-4.0
-2.0
3.0
2.0
1.0
0.0
-1.0
-2.0
-3.0
δ18O ‰ (VPDB)
-18.0
-16.0
-14.0
-12.0
1.0
0.0
-1.0
-2.0
-3.0
δ13C ‰ (VPDB)
EAST
WEST

to –9.96‰ VPDB (mean = -13.91, 1σ = 2.14), and $\delta^{13}C$ values from –3.02 to +1.65‰ VPDB (mean = -0.70, 1σ = 1.81). The oxygen isotope values from the calcite cements are depleted with respect to Middle Devonian marine calcite, while the carbon isotope values display a spread between values characteristic of Middle Devonian marine calcite and values that represent a moderate depletion in ^{13}C (Figure 5.1A).

Three samples of FBD (phase 9) were analysed for their stable isotope values. These samples have $\delta^{18}O$ compositions varying between –12.92 and –12.05‰ VPDB (mean = -12.47, 1σ = 0.44), and $\delta^{13}C$ compositions from +0.93 to +2.72‰ VPDB (mean = +1.75, 1σ = 0.91). All samples of FBD have oxygen isotope values that are significantly depleted with respect to the estimated range of Middle Devonian seawater-derived dolomite, while the observed carbon isotope values show no variation from the calculated composition of Middle Devonian dolomites formed from normal seawater in the near-surface realm (Figure 5.1A).

The GMD (phase 10) samples have $\delta^{18}O$ values that range between –16.73 and –13.00‰ VPDB (mean = -14.57, 1σ = 0.88), and $\delta^{13}C$ values between –2.15 and –0.31‰ VPDB (mean = -1.04, 1σ = 0.40). The SD (phase 13) samples, both cements and recrystallization products of GMD, have stable isotope values in the same range as GMD samples, i.e., the $\delta^{18}O$ values range between –16.12 and –13.59‰ VPDB (mean = -14.76, 1σ = 0.70), and $\delta^{13}C$ values between –2.29 and -0.18‰ VPDB (mean = -1.02, 1σ = 0.53) (Figure 5.1A).

The oxygen isotope values for both GMD and SD show differences with respect to geographic location. Samples from the west side of the Clarke Lake field have $\delta^{18}O$ values that are at or higher than –14.78‰ VPDB, while samples from the east populate the more depleted set of values (Figure 5.1B). Furthermore, all Clarke Lake samples are significantly depleted isotopically (lower $\delta^{18}O$ and $\delta^{13}C$ values) compared to dolomites elsewhere in the Alberta Basin, and to dolomites calculated to have formed from Middle Devonian seawater at near-surface conditions (Figure 5.1B, top).

Discussion

The stable isotope values exhibited by both the limestone matrix (micrite) and the fossil components suggest an original end-member composition within the range of Middle Devonian seawater calcite – as would be expected. The exception is a single sample of skeletal calcite from a *Thamnopora* coral that has $\delta^{18}O$ and $\delta^{13}C$ values of -3.67 and +3.09‰ VPDB, respectively. The oxygen isotope value from this coral is roughly 0.5‰ heavier than the Middle Devonian reference value, and likely reflects local variations in water temperature and/or salinity (James et al., 1997). The carbon isotope value, reflecting enrichment in ^{13}C, is atypical of the Middle Devonian (Hurley and Lohmann, 1989). However, Popp et al. (1986a, 1986b), and Brand and Morrison (1987) both reported higher $\delta^{13}C$ values from Devonian brachiopods. Two scenarios exist to explain this enrichment in ^{13}C. In the marine realm, biological fractionation (or vital effects) in some organisms, including corals, produces carbonate that is not in isotopic equilibrium with seawater (Brand and Veizer, 1981); in the shallow subsurface realm (i.e., down to about 1000 metres), positive $\delta^{13}C$ excursions are likely the result of early-diagenetic fermentation, or methanogenesis (Hudson, 1975; Games and Hayes, 1976; Reitsema, 1980; Lohmann et al., 1985). There is no petrographic evidence to suggest recrystallization, which would be required for the inclusion of methanogenetic carbon; however, textural evidence alone does not preclude the possibility that the skeletal calcite has recrystallized (Machel, 1997). As a result, the exact mechanism for the enrichment of ^{13}C cannot be stated with absolute certainty.

Standard petrography on the limestone matrix and fossil components shows little evidence for recrystallization, however, the covariant depletion trend displayed by these samples suggest either interaction with fluids depleted in ^{18}O (e.g., meteoric water) and/or fluids at elevated temperatures. The possibility of meteoric fluids influencing the stable isotope composition of these phases is highly unlikely, as there is no physical evidence to indicate meteoric waters infiltrating the Slave Point Formation at any time during its diagenetic history. Rather, the covariant trend is indicative of stable isotope resetting, i.e., 'significant' recrystallization (*sensu* Machel, 1997), during throughput of formation fluids at elevated temperatures. Spatially, the isotopically lightest samples, both in $\delta^{18}O$ and $\delta^{13}C$, are associated with wells containing dolomite in the Clarke Lake field. However, isotope values that overlap with dolomite values, i.e., they do not show a fractionation difference of roughly 3‰ VPDB, are not representative of recrystallization during the time, or at the same temperature, as dolomite formation. These observations signify that the covariant isotope trend is a reflection of differences in the water-rock ratio (Taylor, 1979), and that the stable isotope values from these phases were variably reset prior to the formation of dolomite from diagenetic fluids of similar composition but at lower temperatures.

Petrographic evidence indicates that the majority of the samples of calcite cement were precipitated subsequent to dolomite formation (blocky calcite II – phase 25). The only exception is a sample of blocky calcite I (phase 6) precipitated within primary shelter porosity from a limestone core at the extreme eastern edge of the Clarke Lake study area. This sample has the heaviest $\delta^{18}O$ value of all calcite cements, but is still roughly 4‰ lighter than Middle Devonian seawater calcite. The fact that this cement is positioned within a shelter cavity suggests that precipitation occurred prior to significant burial, i.e., greater than 1000 metres, which otherwise may have resulted in the destruction of primary porosity through compaction. Additionally, petrographic evidence show paragenetic relationships between blocky calcite I and both shallow burial fractures (phase 5) and syntaxial calcite (phase 7); which was interpreted to have formed prior to significant physical compaction. With these in mind, there exist only two possibilities to explain the depletion in the oxygen isotope composition of this early calcite cement. Firstly, the stable isotope composition is reflecting either precipitation from fluids at elevated temperatures (i.e., burial), or precipitation in the shallow burial diagenetic realm from slightly modified Middle Devonian seawater. Alternatively, based on evidence for water-rock interaction in micrite and fossil components, this calcite phase may have been recrystallized by later diagenetic fluids that reset its stable isotope composition. In the first case an estimate can be made as to the composition and/or temperature of the precipitating fluid by applying the following calcite-H_2O equilibrium fractionation equation from O'Neil et al. (1969):

$$1000\ln\alpha = 2.78 \times 10^6 (T^2) - 2.89$$

For calcite precipitation from slightly modified Middle Devonian seawater during shallow burial, and a $\delta^{18}O$ composition of seawater from –3 to +1‰ SMOW, in agreement with values published by Carpenter et al. (1991), and Muehlenbachs and Clayton (1976) for seawater, the cement would have been precipitated over a temperature range of 55-85°C. Assuming a near-normal geothermal gradient of 30-35°C/km and an average surface temperature of about 25°C, these temperatures correspond to depths of about 1 - 2 km. This depth range appears to be excessive considering the aforementioned requirement for cementation prior to significant physical compaction. Alternatively, if we input a desired depth of <500 metres, hence a temperature range between 25 and 40°C, the $\delta^{18}O$ composition of the precipitating fluid would fall between -8 and -5‰ SMOW. A fluid with this composition does not appear as a viable alterative either; as such isotopically light fluids are generally an indicator of meteoric water invasion. As discussed previously, there is no physical evidence to indicate meteoric waters infiltrating the Slave Point Formation at any time during its diagenetic history. It therefore appears that the principal control on the $\delta^{18}O$ composition of this calcite cement is significant recrystallization (*sensu* Machel, 1997) through the invasion of later diagenetic fluids.

The remaining samples of calcite cement from the Slave Point Formation are representative of blocky calcite II (phase 25); which was previously interpreted as having precipitated in the deep burial diagenetic realm. The $\delta^{13}C$ values from these cements appear to be controlled by buffering from the host rock. Samples of calcite cement in limestone hosts generally have positive $\delta^{13}C$ values, while those cementing fractures in dolomite have negative $\delta^{13}C$ values. In order for host rock buffering to occur, low water-rock ratios are required, which suggests that the $\delta^{18}O$ composition of the calcite cements is also not representative of the temperature and/or composition of the precipitating fluid, preventing the application of the calcite-H_2O equilibrium fractionation equation.

The few samples of FBD (phase 9) available for stable isotope analysis have $\delta^{18}O$ values that show significant depletion in ^{18}O compared to the Middle Devonian reference values. Similar to the calcite cements, these isotopically light values may be the result of either formation from fluids at elevated temperatures, or formation during near-surface to shallow burial via fluids that had extremely negative $\delta^{18}O$ compositions. This second scenario, which would require meteoric water incursion, is highly unlikely for reasons discussed previously. Additionally, the petrographic/paragenetic evidence (discussed in Chapter 4) favours the formation of FBD from fluids with compositions similar to seawater at temperatures of less than 60°C and at burial depths near 500 metres. Therefore, by applying a $\delta^{18}O$ composition of Middle Devonian seawater between –3 and +1‰ SMOW into the following dolomite-H_2O equilibrium fractionation equation from Land (1983)

$$1000\ln\alpha = 3.2 \times 10^{6} (T^{-2}) - 3.3$$

the result is a potential dolomitizing fluid temperature of roughly 90 to 130°C. These temperatures equate to burial depths of 2 – 3.5 km by assuming a surface temperature of 25°C and a geothermal gradient of 30°C/km. This depth estimate does not conform to range of burial depths estimated from petrographic observations. At depths of 300 to 1000 metres, under the same geothermal gradient, the fluid that formed FBD would have had an oxygen isotope composition that is typical of meteoric water, yet this option has already been eliminated. Therefore, the stable isotope results imply that FBD was recrystallized during the invasion of subsequent diagenetic fluids even though there is no petrographic evidence to substantiate this argument.

As the stable isotope values of both GMD and SD are significantly different from the marine reference values (Figure 5.1B), neither dolomite type formed from marine pore waters under near-surface or shallow burial conditions. Additionally, the oxygen isotope values of both dolomite types from the west half of the Clarke Lake field have slightly higher $\delta^{18}O$ values compared to those in the east half of the field (Figure 5.1B). Assuming that the dolomites formed from the same fluid(s) across the entire field this pattern could represent a temperature differential of about 10-20°C (using the equation by Land, 1983), whereby the lower $\delta^{18}O$ values correspond to the higher temperatures. Assuming a seawater $\delta^{18}O$ value ranging from –3 to +1‰ SMOW, the temperatures of formation of GMD ranges from a minimum of 97°C in the west, to a maximum of 160°C in the east (Figure 5.2A). Similarly, the temperatures of formation of SD range from 105°C in the west to 165°C in the east (Figure 5.2B). These results point to a significant amount of burial and relatively late timing of formation. Assuming a near-normal geothermal gradient of 30-35°C/km and an average surface temperature of about 25°C, these temperatures correspond to depths of about 3 - 4 km.

As a second alternative, the temperature of dolomite formation can be calculated using Devonian meteoric fluids with $\delta^{18}O$ between –7 and -3‰ SMOW, which yields temperatures between 68 and 115°C for GMD (Figure 5.3A), while SD reflects a similar temperature range, 75 to 120°C (Figure 5.3B). Three problems arise by invoking dolomite formation via meteoric fluids. Firstly, petrographic evidence indicates GMD and SD post-date FBD formation. As a result, maximum fluid temperatures from GMD and SD should be significantly higher than fluid temperatures from FBD, which is not the case. Secondly, waters with such highly depleted oxygen isotope composition are not a viable alternative for Clarke Lake. These meteoric waters did not exist in the Clarke Lake region at any time dolomite formation could have taken place (timing is discussed later). Thirdly, meteoric waters do not contain enough Mg to form massive dolostones in the first place (Machel, 2004).

A third alternative fluid, highly evaporated Devonian seawater, must also be examined in light of recent work. Morrow et al. (2002) proposed the convective circulation

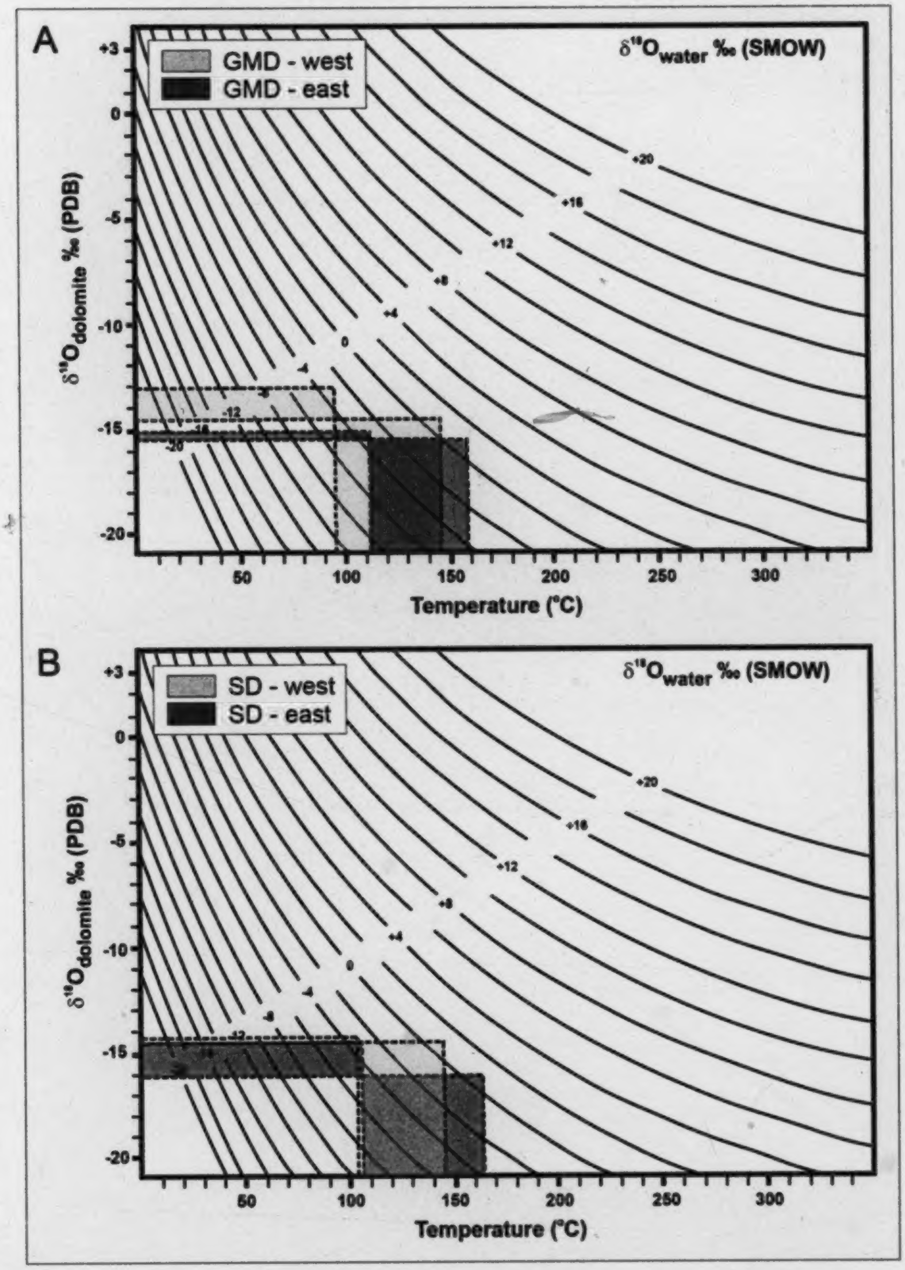

Figure 5.2 Plot of equilibrium isotope fractionation between dolomite and water, after Land (1983). West-east separation is based on the results presented in Figure 5.1B. Fluid composition is representative of Devonian seawater with a composition between -3 and +1‰ SMOW (Carpenter et al., 1991; Muehlenbachs and Clayton, 1976). (A) Grey matrix dolomite (phase 10): west = 97 to 145°C, east = 112 to 160°C. (B) Saddle dolomite (phase 13): west = 105 to 145°C, east = 108 to 165°C.

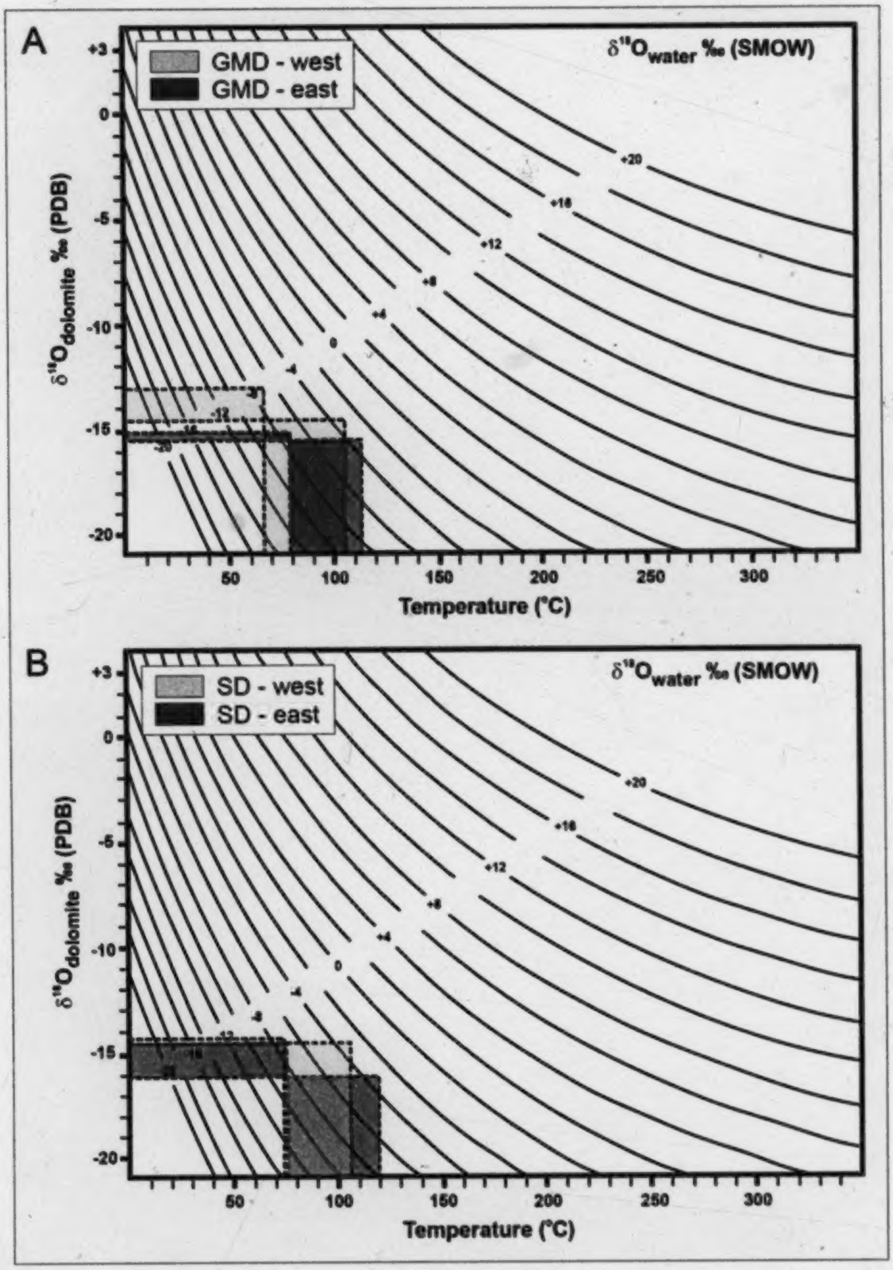

Figure 5.3 Plot of equilibrium isotope fractionation between dolomite and water, after Land (1983). West-east separation is based on the results presented in Figure 5.1B. Fluid composition is representative of Devonian meteoric water with a composition between -7 and -3‰ SMOW (Yurtsever, 1975 - assuming seawater at -1‰ SMOW). (A) Grey matrix dolomite (phase 10): west = 68 to 105°C, east = 80 to 115°C. (B) Saddle dolomite (phase 13): west = 75 to 105°C, east = 75 to 120°C.

of brines pooled in Devonian evaporite formations to the south and east. For this alternative, a $\delta^{18}O$ fluid composition between +2 and +6‰ SMOW can be considered representative of Middle Devonian seawater evaporated past the point of halite saturation (Knauth and Beeunas, 1986). Following the same procedure as for marine and meteoric fluids, GMD would have formed at temperatures ranging from a minimum of 140°C in the west, to a maximum of 235°C in the east (Figure 5.4A). Similarly, SD would have formed in equilibrium with a fluid at temperatures between 155 and 250°C (Figure 5.4B). Applying a surface temperature and geothermal gradient consistent with the models discussed earlier, the minimum dolomite-forming temperature suggests burial at a depth greater than 4 km. As will be discussed later, this depth was never attained by the Slave Point Formation. Therefore, any conclusion that furthers dolomite formation via highly evaporated fluids would be supporting the petrographic interpretation that the dolomites are hydrothermal in origin.

At this stage, two key questions arise: which of the dolomite samples have a chemistry representing the first and volumetrically predominant dolomitization event, i.e., matrix replacement; and, was dolomitization in a one-phase event (one-fluid generating all the observed textures), or a multiple-phase event (more than one fluid generating the observed textures in discrete phases, separated by at least one hiatus)? The first question is answered partially on the basis of the stable isotopes, and is discussed again in the section on fluid inclusions (below). The second question can be answered here.

The fact that the $\delta^{18}O$ values of both dolomite types overlap suggests that GMD and SD are cogenetic. If so, the slightly heavier $\delta^{18}O$ values observed in dolomites from the west half of the Clarke Lake field (and vice versa) would reflect a temperature differential of about 10-20°C, whereby the lower $\delta^{18}O$ values correspond to the higher temperatures. If the tectonically-induced tilting of the basin towards the west occurred prior to formation of the dolomites, an E-W temperature gradient should be expected, but with higher temperatures in the dolomites in the western part of the field. Hence, if the E-W distribution of the oxygen isotope data is indeed due to temperature, burial and/or tectonic tilting was not a factor. Rather, the eastern part of Clarke Lake would have to have been hotter due to a geothermal anomaly that counteracted burial and tectonic tilting.

Another alternative, effectively a variant of the above, arises under the assumption that GMD and SD are not cogenetic, which is suggested by petrography. In this scenario,

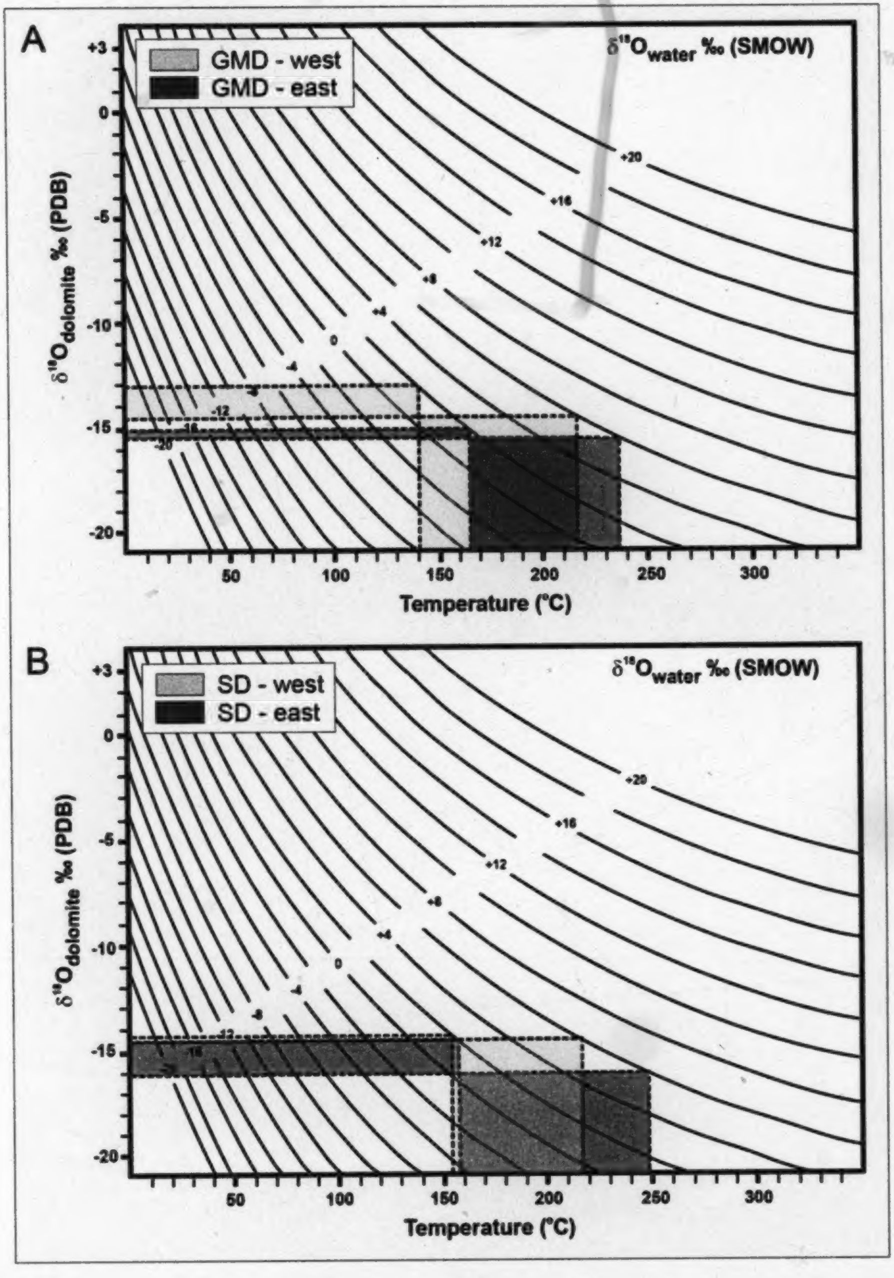

Figure 5.4 Plot of equilibrium isotope fractionation between dolomite and water, after Land (1983). West-east separation is based on the results presented in Figure 5.1B. Fluid composition is representative of highly evaporated Devonian seawater with a composition between +2 and +6‰ SMOW (Knauth and Beeunas, 1986 - assuming seawater at -1‰ SMOW). (A) Grey matrix dolomite (phase 10): west = 140 to 215°C, east = 165 to 235°C. (B) Saddle dolomite (phase 13): west = 155 to 217°C, east = 158 to 250°C.

GMD formed relatively early in the diagenetic history (i.e., before tectonic tilting established a W-E temperature gradient) and later recrystallized to the present fabrics and isotope ranges from a different fluid that also formed replacive saddle dolomite and saddle dolomite cement. Expected changes via recrystallization include crystal coarsening, development of sweeping extinction, destruction of cathodoluminescence zoning, changes in the trace element concentrations, decrease in stable isotope values, increase in strontium isotope values, increase in cation ordering, and an increase in stoichiometry (Mazzullo, 1992; Montanez and Read, 1992; Gao et al, 1992; Smith and Dorobek, 1993; Malone et al., 1994; Machel, 1997). Significant recrystallization (*sensu* Machel, 1997) could generate overlapping isotope values that can be mistaken for cogenesis of both dolomite types, thereby largely or completely eliminating the primary isotope signature of the first replacive dolomitization event.

The carbon isotope values do not help resolve the uncertainty of cogenesis but add another detail. Assuming a marine $\delta^{13}C$ composition of about 0 to +2‰ PDB, it appears that all GMD and SD samples, regardless of $\delta^{18}O$ value, contain a significant amount of organically derived carbon. It is not clear where the organic carbon is derived from, but it is likely the result of the partial oxidation of kerogen in the flow path of the hot fluid(s) that dolomitized Clarke Lake and/or the fluids that led to recrystallization of the matrix dolomites. Thermochemical sulphate reduction (TSR) is not a viable alternative in this case, in contrast to sour gas fields in the deeper parts of the Western Canada Sedimentary Basin (e.g. Machel et al., 1995), because there is no sour gas at Clarke Lake.

5.3.2 Strontium isotopes

^{87}Sr is generated naturally by the radioactive decay of ^{87}Rb (Faure, 1986). In view of the fact that Rb is excluded from the structure of carbonates, their $^{87}Sr/^{86}Sr$ ratio is inherited from the precipitating fluid without fractionation (Veizer, 1983). As a consequence, marine carbonate minerals that have not experienced alteration by diagenetic fluids should record the strontium isotopic composition of seawater at the time of formation. Hence, strontium isotopes can be used as a relative age dating tool under conditions where no external input of strontium was available.

During diagenesis, carbonate minerals acquire their strontium signature from the diagenetic fluids. The composition of these fluids is controlled by prior interaction with different rocks. Enriched or radiogenic ^{87}Sr values are obtained by interaction with Rb-rich minerals such as clays and feldspars, which are abundant in clastic sediments and basement rocks (Mountjoy et al., 1992). Additionally, the ^{87}Sr/^{86}Sr values of the diagenetic carbonates do not change significantly over time due to the fact that they lack Rb. Therefore, it is generally accepted that the diagenetic carbonates retain the ^{87}Sr/^{86}Sr value of the diagenetic fluid from which they were originally formed. Hence, strontium isotopes may provide valuable evidence for the evolution of subsurface fluids and their migration pathways.

Results

A total of fifty-five drilled powder samples of various generations of calcite and dolomite were analyzed for their ^{87}Sr/^{86}Sr composition by traditional bulk analysis. The range of strontium isotope values for individual carbonate phases is shown in Table 5.2.

Limestones (micrite) and fossils have ^{87}Sr/^{86}Sr isotope ratios the range from 0.70795 to 0.71072 (Figure 5.5A). Samples with isotope ratios near the minimum are similar to those expected for calcium carbonate precipitated from Middle Devonian seawater: 0.7078 to 0.7083 (Figure 5.6).

Samples of late calcite cement (blocky calcite II - phase 25) have ^{87}Sr/^{86}Sr ratios between 0.70849 and 0.71871 (mean = 0.71099, $1\sigma = 0.00351$) (Figure 5.5A). All of these samples are slightly to significantly enriched in radiogenic Sr compared to Middle Devonian seawater (Figure 5.6). Additionally, a single sample of calcite cement from well d-79-F/94-J-10 (henceforth labelled d-79-F) has a ^{87}Sr/^{86}Sr result that plots above 0.712 (Figure 5.5A). The value of 0.7120 was previously determined by Machel and Cavell (1999) as the maximum strontium isotope ratio of basinal shales (MASIRBAS) (see following section).

Two powders of FBD (phase 9) yielded ^{87}Sr/^{86}Sr ratios of 0.70899 and 0.70933 (mean = 0.70916, $1\sigma = 0.00024$), which are slightly more radiogenic than the range expected from Middle Devonian seawater-derived dolomite (Figure 5.5A).

GMD (phase 10) yielded bulk ^{87}Sr/^{86}Sr ratios between 0.70886 and 0.71674 (mean = 0.71075, $1\sigma = 0.00220$), while SD (phase 13) yielded bulk ^{87}Sr/^{86}Sr values between 0.70874 and 0.71649 (mean = 0.71084, $1\sigma = 0.00220$) (Figure 5.5A). All these values are enriched in radiogenic Sr compared to Middle Devonian seawater. Similar to the oxygen isotope values, a geographic distribution of ^{87}Sr/^{86}Sr values exists, in that samples from the extreme western part of the Clarke Lake field, specifically from well d-79-F plot above

Phase	$^{87}Sr/^{86}Sr$	
Limestone (2)	min.	0.70827
	mean	0.70864
	max.	0.70900
	Std. Dev.	0.00052
Fossils (3)	min.	0.70795
	mean	0.70889
	max.	0.71072
	Std. Dev.	0.00159
Calcite Cement phase 25 (7)	min.	0.70849
	mean	0.71099
	max.	0.71871
	Std. Dev.	0.00351
FBD phase 9 (2)	min.	0.70899
	mean	0.70916
	max.	0.70933
	Std. Dev.	0.00024
GMD phase 10 (23)	min.	0.70886
	mean	0.71075
	max.	0.71674
	Std. Dev.	0.00220
SD phase 13 (18)	min.	0.70874
	mean	0.71084
	max.	0.71649
	Std. Dev.	0.00220

Table 5.2 $^{87}Sr/^{86}Sr$ isotope results by diagenetic phase. Diagenetic phase numbers from Figure 4.1. The number of analyzed samples is reported in parentheses. min. = minimum measured value, mean = arithmetic mean of measured values, max. = maximum measured value, Std. Dev. = standard deviation (1σ).

0.7120, whereas values in the remainder of Clarke Lake cluster around 0.7110 (Figure 5.7). There is, however, no obvious east-west correlation between the Sr isotope ratios and stable isotope data.

Discussion

The $^{87}Sr/^{86}Sr$ range exhibited by both the limestone matrix and the fossils can be correlated with the stable isotope data discussed previously. As shown in Figure 5.5A, the strontium isotope ratios from these samples progressively increase with a concomitant decrease $\delta^{18}O$ values, and is, therefore, reflecting the variable stages of recrystallization through exchange with later diagenetic fluids. The geochemical signatures of the samples showing evidence for significant recrystallization are also within the range for samples of both GMD and SD. This distribution suggests that the diagenetic fluid(s) that formed GMD and SD was also responsible for the recrystallization of the limestones and fossil

Figure 5.5 $^{87}Sr/^{86}Sr$ results from carbonate phases in the Slave Point Formation.

(A) $^{87}Sr/^{86}Sr$ versus $\delta^{18}O$ for all analyzed calcite and dolomite samples. Encircled data (d-79-F) are from well d-79-F/94-J-10 near the western limit of the field. The similarly shaped but shaded field represents the range in $^{87}Sr/^{86}Sr$ results from mineralized dolomites in the Robb Lake MVT deposit of northeastern British Columbia (Paradis et al., 2005). Estimated $^{87}Sr/^{86}Sr$ of Middle Devonian seawater according to Denison et al. (1997). Oxygen isotope range of Middle Devonian marine calcite (SWC) after Hurley and Lohmann, 1989. The range for Middle Devonian seawater dolomite (SWD) is based on the reference values for Middle Devonian marine calcite corrected according to the equilibrium $\Delta^{18}O$ between calcite and dolomite (3 ± 1‰ at 25°C; Land, 1980). Maximum strontium isotope ratio of basinal shales (MASIRBAS = 0.7120) after Machel and Cavell (1999).

(B) Crossplot of $^{87}Sr/^{86}Sr$ versus Sr concentration. Samples listed as matrix dolomite include only samples of grey matrix dolomite (GMD - phase 10). Encircled data from well d-79-F/94-J-10. A single sample of calcite cement (phase 25) plots off the graph and is represented by the arrow with a posted Sr content of 1141 ppm. Estimated $^{87}Sr/^{86}Sr$ of Middle Devonian seawater according to Denison et al. (1997). Approximate range of strontium concentrations for Devonian abiotic marine calcite (SWC) after Carpenter et al. (1991). Maximum strontium isotope ratio of basinal shales (MASIRBAS = 0.7120) after Machel and Cavell (1999).

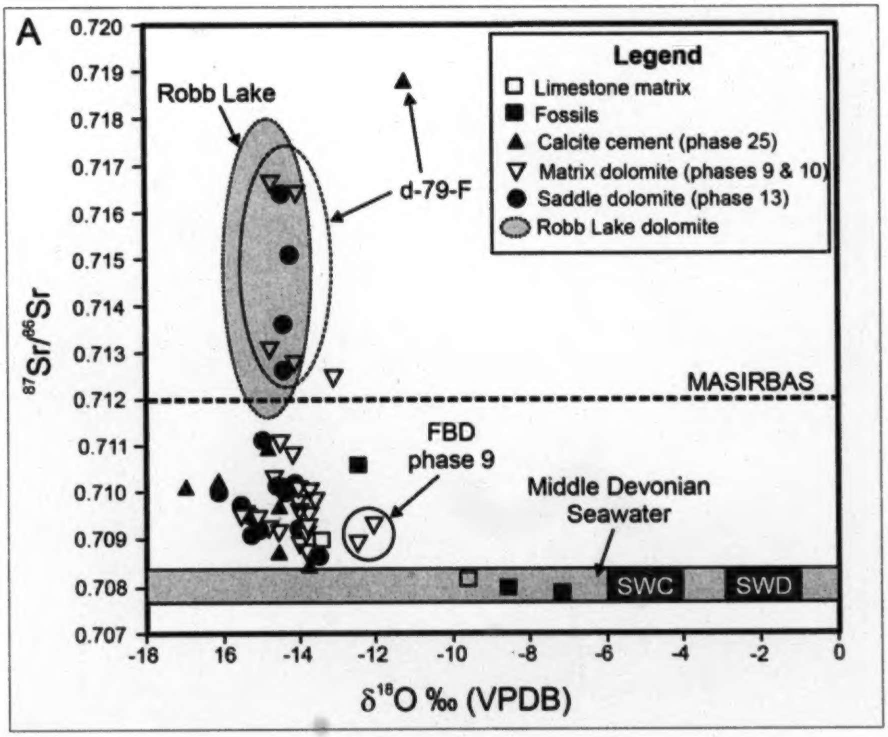
A
Legend
☐ Limestone matrix
■ Fossils
▲ Calcite cement (phase 25)
▽ Matrix dolomite (phases 9 & 10)
● Saddle dolomite (phase 13)
Robb Lake dolomite
Robb Lake
d-79-F
MASIRBAS
FBD
phase 9
Middle Devonian
Seawater
SWC
SWD
^{87}Sr/^{86}Sr
0.720
0.719
0.718
0.717
0.716
0.715
0.714
0.713
0.712
0.711
0.710
0.709
0.708
0.707
-18
16
-14
-12
-10
-8
-6
-4
-2
0
δ^{18}O ‰ (VPDB)

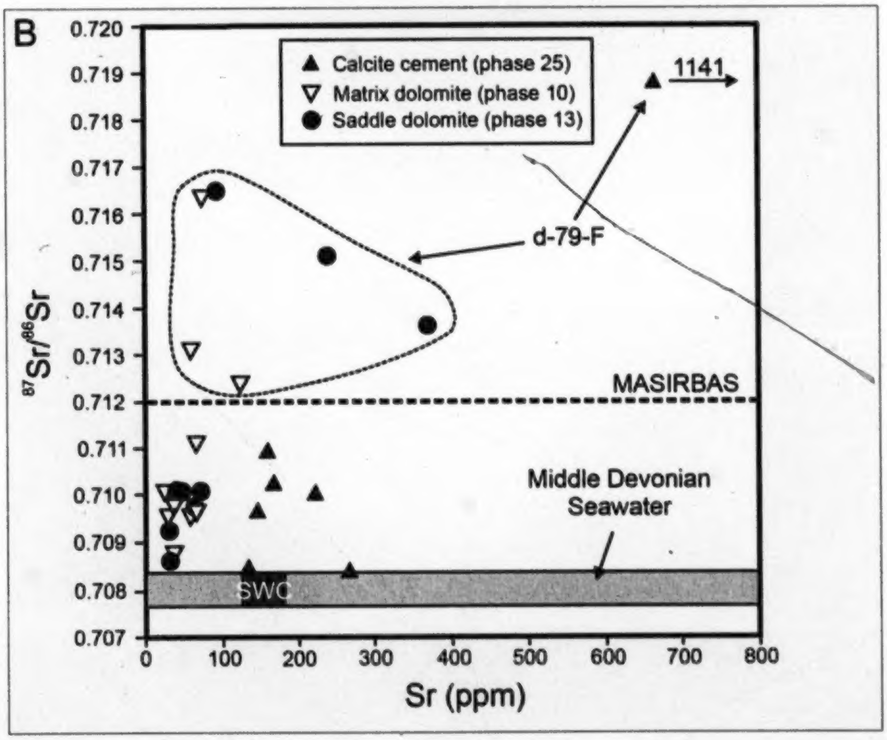
B
▲ Calcite cement (phase 25)
▽ Matrix dolomite (phase 10)
● Saddle dolomite (phase 13)
1141
d-79-F
MASIRBAS
Middle Devonian
Seawater
SWC
^{87}Sr/^{86}Sr
0.720
0.719
0.718
0.717
0.716
0.715
0.714
0.713
0.712
0.711
0.710
0.709
0.708
0.707
0
100
200
300
400
500
600
700
800
Sr (ppm)

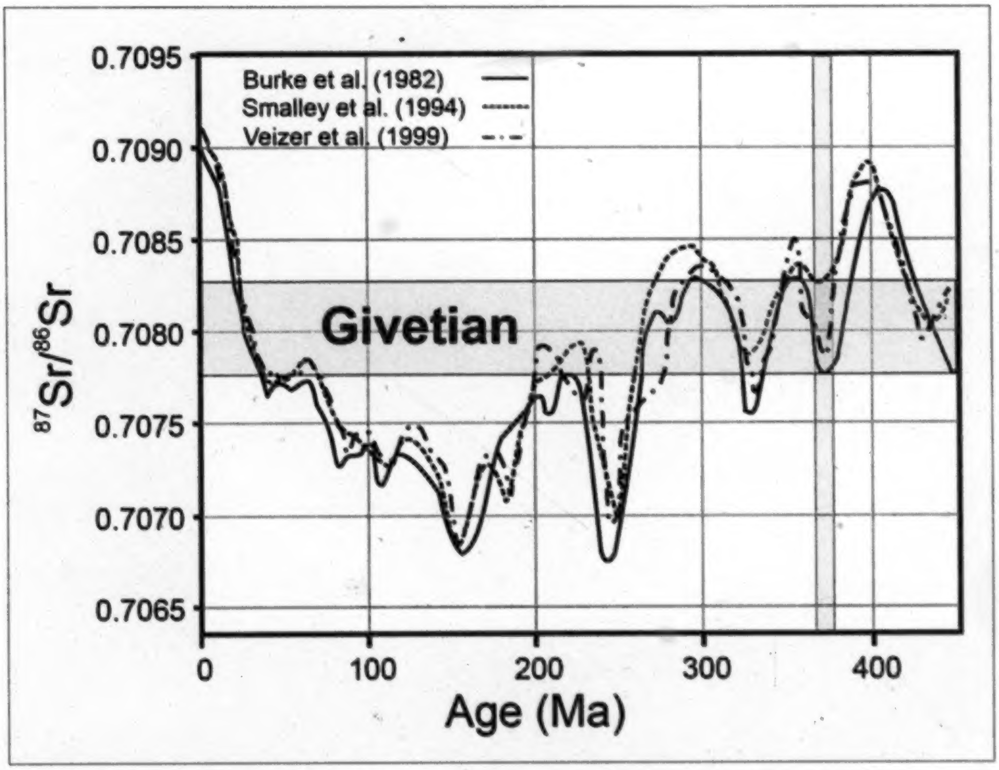

Figure 5.6 Variation of the $^{87}Sr/^{86}Sr$ ratio of marine carbonates during the Phanerozoic. The shaded region represents the approximate $^{87}Sr/^{86}Sr$ ratio of marine carbonates during the Givetian (380-370 Ma). Modified after Burke et al. (1982), Smalley et al. (1994), and Veizer et al. (1999).

components: an interpretation that was previously presented with respect to the stable isotope results with the caveat that recrystallization occurred at temperatures lower than those during the formation of either GMD or SD (Figure 5.1).

All of the samples of late calcite cements (blocky calcite II – phase 25), with one notable exception, have $^{87}Sr/^{86}Sr$ and stable isotope signatures that are nearly identical to both GMD and SD (Figure 5.5A). As discussed previously, the stable isotope results from these cements suggest buffering of the fluid by the host-rock. An alternative method to change the $^{87}Sr/^{86}Sr$ value of the precipitating fluid is end-member fluid mixing. Mixing of two fluid components with variable initial $^{87}Sr/^{86}Sr$ and Sr concentrations would result in a hyperbolic mixing curve when the isotope ratio of the calcite is plotted against the absolute concentration of Sr in the samples. However, as shown in Figure 5.5B, the concentration

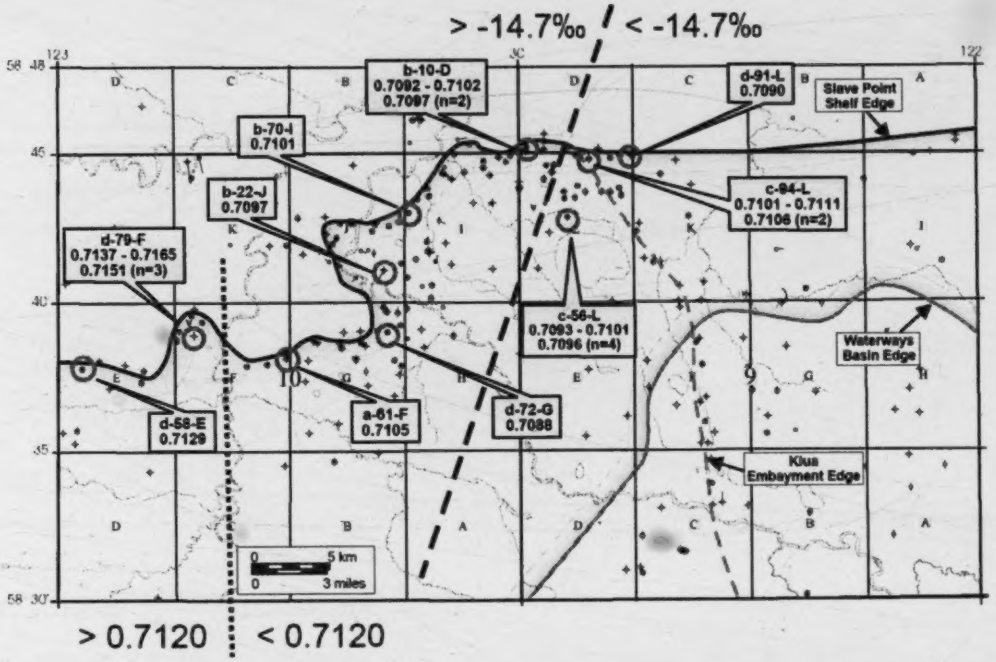

> -14.7‰
< -14.7‰
58 48
123
30
122
45
40
35
58 30
D
C
B
A
K
I
J
E
F
G
H
b-10-D
0.7092 - 0.7102
0.7097 (n=2)
b-70-I
0.7101
b-22-J
0.7097
d-79-F
0.7137 - 0.7165
0.7151 (n=3)
d-58-E
0.7129
a-61-F
0.7105
d-72-G
0.7088
c-56-L
0.7093 - 0.7101
0.7096 (n=4)
d-91-L
0.7090
c-94-L
0.7101 - 0.7111
0.7106 (n=2)
Slave Point
Shelf Edge
Waterways
Basin Edge
Klua
Embayment Edge
10
9
0
5 km
0
3 miles
> 0.7120
< 0.7120

Figure 5.7 Spatial distribution of bulk $^{87}Sr/^{86}Sr$ values from saddle dolomite (phase 13) samples in the Clarke Lake field (average values for each well). The highest values occur in the western part of the study area, whereas, all values in the eastern part bundle tightly around 0.7100. The dashed line separates east from west on the basis of the $\delta^{18}O$ values of both matrix and saddle dolomites, the dotted line separates east from west on the basis of MASIRBAS. See text for further explanation.

of strontium in the calcite samples, with the exception of one from well d-79-F, does not vary significantly, regardless of the strontium isotope ratio. In fact, most of the samples have Sr concentrations that lie within the range expected for abiotic calcite precipitated by Devonian seawater (SWC). Therefore, the fluid that precipitated the late-stage calcite cements was likely derived from Middle Devonian seawater, regardless of initial salinity, that was isotopically-buffered by the host rocks in the Clarke Lake field.

The sample of calcite cement (phase 25) from well d-79-F plots significantly above both the expected value of Middle Devonian seawater and MASIRBAS, and represents precipitation from either a fluid of distinct origin, or a fluid that migrated along a different flow path compared to the other calcite cements discussed above. A distinct origin for the fluid cannot be ruled out due to the fact that the concentration of Sr in this sample is an order of magnitude greater than the bulk of all other calcite samples (Figure 5.5B). A different flow path cannot be ruled out either because: 1) the $^{87}Sr/^{86}Sr$ value is significantly higher than the most radiogenic sample of host dolomite in well d-79-F (Figure 5.5A); and, 2) the $\delta^{18}O$ value (-11.23‰ VPDB: Figure 5.5A) is heavier than the other calcite samples: an indication that host rock buffering did not occur prior to cement precipitation. The suggestion that fluid buffering did not occur points to precipitation under much higher water-rock ratios, as would be expected during episodic fluid pulses along open faults and fractures. This mechanism is similar to that proposed by Buschkuehle (2003) for the formation of coarse crystalline late calcite cements within roughly 100 km from the limit of the Laramide disturbed belt (i.e, subsurface fold and thrust belt) in west-central Alberta. These vug- and fracture-filling calcite cements, much like the calcite cement from well d-79-F, both post-date dolomite formation and have $^{87}Sr/^{86}Sr$ values above MASIRBAS. These observations led Buschkuehle (2003) to suggest that the late calcite cements were formed from diagenetic fluids containing Sr sourced from Precambrian rocks that were expelled during 'squeegee-type' (*sensu* Oliver, 1986) fluid flow. The localized nature of the radiogenic cement in well d-79-F and the similar position of the Clarke Lake field with respect to the disturbed belt, i.e., < 100 km, is circumstantial evidence for the ascension of basement-sourced, extremely radiogenic fluids along open faults/fractures during later stages of diagenesis.

The two samples of FBD (phase 9) have Sr isotope ratios that are slightly enriched with respect to Middle Devonian seawater, but still significantly below the value of MASIRBAS. In conjunction with the stable isotope values, the data suggest that this earliest dolomitization event occurred following shallow burial to depths between 300 and 1000 metres by chemically slightly modified Middle Devonian seawater that may have obtained radiogenic ^{87}Sr during migration through basinal shales.

Samples of GMD (phase 10) and SD (phase 13) show a slight to significant enrichment in radiogenic ^{87}Sr compared to Middle Devonian seawater, paired with highly depleted $\delta^{18}O$ values (Figure 5.5A). The bulk of the dolomite samples have $^{87}Sr/^{86}Sr$ values that plot below 0.710, which is below MASIRBAS = 0.7120 (Machel and Cavell, 1999). This suggests that the dolomite-forming fluid(s) were Devonian seawater or evaporated seawater that had obtained only a very minor amount of radiogenic ^{87}Sr during migration through basinal shales. The geochemical similarities between co-existing samples of GMD and SD indicate that GMD is significantly recrystallized, i.e., stable and radiogenic isotope values were reset by the fluid(s) responsible for the formation of SD. This includes the absolute Sr concentration in GMD and SD. As shown in Figure 5.5B, the data from both dolomite phases overlap, but do not permit identification of fluid end-members. Rather, the Sr concentrations, ranging from roughly 30 to 75 ppm, are approximately 0.5X the concentration of Sr in the late-stage calcite cements. Previously, Behrens and Land (1972), and Jacobson and Usdowski (1976) proposed that the equilibrium concentrations of Sr in dolomite relative to calcite should range between 0.43 and 0.50. As a result, this distribution would be expected from phases formed from a similar, or the same, diagenetic fluid.

Samples from well d-79-F, and from well d-58-E/94-J-10 but with only one sample for Sr-isotopes, have noticeably different $^{87}Sr/^{86}Sr$ values (Figure 5.5A) compared to the results from GMD and SD across the Clarke Lake field (Figure 5.7). The samples from these wells plot above 0.710, and thus contain Sr from another, more radiogenic source. Furthermore, these results are similar to those presented in Paradis et al. (2005) for the mineralized dolomites in the Robb Lake Mississippi Valley-type (MVT) deposit (Figure 5.5A) from the Rocky Mountains of northeastern British Columbia, roughly 200 km downdip to the southwest of the Clarke Lake field. They (ibid.) interpreted these extremely radiogenic dolomites to have formed either from high-temperature fluids that were influenced by siliciclastic sources, i.e., Lower Paleozoic sandstones, or from hydrothermal fluids that were channelled along intrabasinal faults. Paradis et al. (2005) also suggested that the sudden eastward decrease in dolomite $^{87}Sr/^{86}Sr$ results from Robb Lake to Pine Point indicates that the fluids were derived from down-dip clastic sequences or from underlying Precambrian basement.

The possibility of fault control on dolomite formation at Clarke Lake may be represented by the variable Sr chemistry in well d-79-F. Within this particular well, the samples of SD show a roughly 300 ppm difference in Sr concentrations over a similarly variable $^{87}Sr/^{86}Sr$ distribution (Figure 5.5B). This spread in data is the result either of mixing between a low [Sr], extremely radiogenic fluid with a high(er) [Sr], slightly radiogenic fluid, or the result of the introduction of multiple, chemically-distinct fluid pulses. The former alternative is not likely, considering the Sr chemistry of the late-stage calcite cement in d-79-F; this would require a third fluid end-member that was both extremely radiogenic and had a high initial Sr concentration. Alternatively, SD formation as a result of multiple, chemically-distinct fluids may occur during seismic pulses along fault zones, which may explain the limited spatial distribution of high $^{87}Sr/^{86}Sr$ dolomites. A similar conclusion was proposed by Duggan et al. (2001) for the formation of highly radiogenic saddle dolomite cements from the Middle Devonian Swan Hills Formation of west-central Alberta.

Strontium source rocks

A stepwise $^{87}Sr/^{86}Sr$ extraction was performed on potential Sr source rocks in northeastern British Columbia according to the method outlined in Machel and Cavell (1999) (Table 5.3). The analytical values discussed herein are considered representative of acid-soluble Sr, that is, Sr that would be extracted and carried away by permeating formation fluids in the subsurface. Seven (7) samples from the crystalline basement, one (1) from the underlying Cambrian sandstone, nineteen (19) samples of basinal shales spanning the Cretaceous to the Middle Devonian, and six (6) samples from the exposed Proterozoic Muskwa Assemblage of the northern Rocky Mountains were analyzed. The $^{87}Sr/^{86}Sr$ ranges for the various suites are: crystalline basement: 0.7219 - 0.8234; Cambrian sandstone: 0.7198; Phanerozoic basinal shales: 0.7088 – 0.7123; and, Proterozoic Muskwa Assemblage: 0.7090 – 0.8577 (Figure 5.8). All of these values are significantly higher than MASIRBAS.

The ultimate origin of the elevated Sr values in d-79-F and d-58-E, and thus the flow path of the fault-derived injection fluid, can now be approximated. Machel and Cavell (1999) found that basinal fluids in the region south of the Peace River Arch could attain a maximum strontium isotope ratio of 0.7120 (MASIRBAS) by interacting with basinal shales. The results of every shale interval from surface to basement near the Clarke Lake area suggest that the MASIRBAS value of Machel and Cavell (1999) is also valid in the northern part of the basin. The data further show that the Proterozoic rocks and/or the Cambrian sandstone aquifer underlying Clarke Lake qualify as the most likely strontium sources (Figure 5.8). The crystalline basement rocks also are a potential source for radiogenic Sr, although only at very low concentrations, considering the highly elevated $^{87}Sr/^{86}Sr$ ratios (Figure 5.8).

Laser ablation MC-ICP-MS

High resolution, in-situ Sr isotope analyses were conducted on three zoned saddle dolomite (phase 13) crystals from well d-79-F. Samples were selected from this particular

Table 5.3 Stepwise dissolution procedure used to extract strontium from basement rocks and non-carbonate rocks. Samples from this study were analyzed to determine their ^{87}Sr/^{86}Sr ratio following STAGE 2 preparation. After Machel and Cavell (1999).

STAGE 1	solution #1 - 0.01 N HCl 25°C, ~20 hr	dissolves highly soluble salts and traces of carbonate
STAGE 2	solution #2 - 1.0 N HCl 25°C, ~20 hr	dissolves carbonates and traces of exchangeable and absorbed Sr from silicates
STAGE 3	solution #3 - 2.0 N HCl 50°C, ~20 hr	removes more strongly held Sr and frees Sr from silicate lattices
	solution #4 - 8 N HNO_3	
	solution #5 - 16 N HNO_3 +0.03 ml HF, 100°C, ~24 hr	
	solution #6 - total decomposition, HF/HNO_3	

well due to the presence of both extremely radiogenic bulk strontium isotope results and well-developed cathodoluminescence zoning. Results from one of these crystals are shown here. Along a single transect of 11 analyses, the ^{87}Sr/^{86}Sr values range from 0.7111 to 0.7188 ($1\sigma \leq 0.0008$), compared to the bulk ^{87}Sr/^{86}Sr value of 0.7151 of the same sample (Figure 5.9).

The laser ablation transect (Figure 5.9) indicates that saddle dolomite in well d-79-F formed from a fluid that was mixed from two distinct end-members, each with a different ^{87}Sr/^{86}Sr value. One end-member fluid had a ^{87}Sr/^{86}Sr value around 0.7110, which is similar to the upper limit from the bulk of the dolomite samples elsewhere at Clarke Lake, whereas the other end-member fluid had a composition close to 0.7190. The Sr-isotope values in this sample from well d-79-F vary between these two end members, and mimic the CL-zonation as well as the fluid inclusion homogenization temperatures (Th values - Figure 5.9). It appears, therefore, that small amounts of the more radiogenic fluid were episodically injected into a bulk formation fluid with a value close to 0.7110. This finding, together with the fact that wells d-79-F and d-58-E stand alone with elevated Sr isotope values in the westernmost part of the field (Figure 5.7), clearly points to episodic injection of radiogenic Sr via (a) fault(s). The bulk formation fluid at this time, forming the background Sr isotope value, is represented by the dolomites from all the other wells.

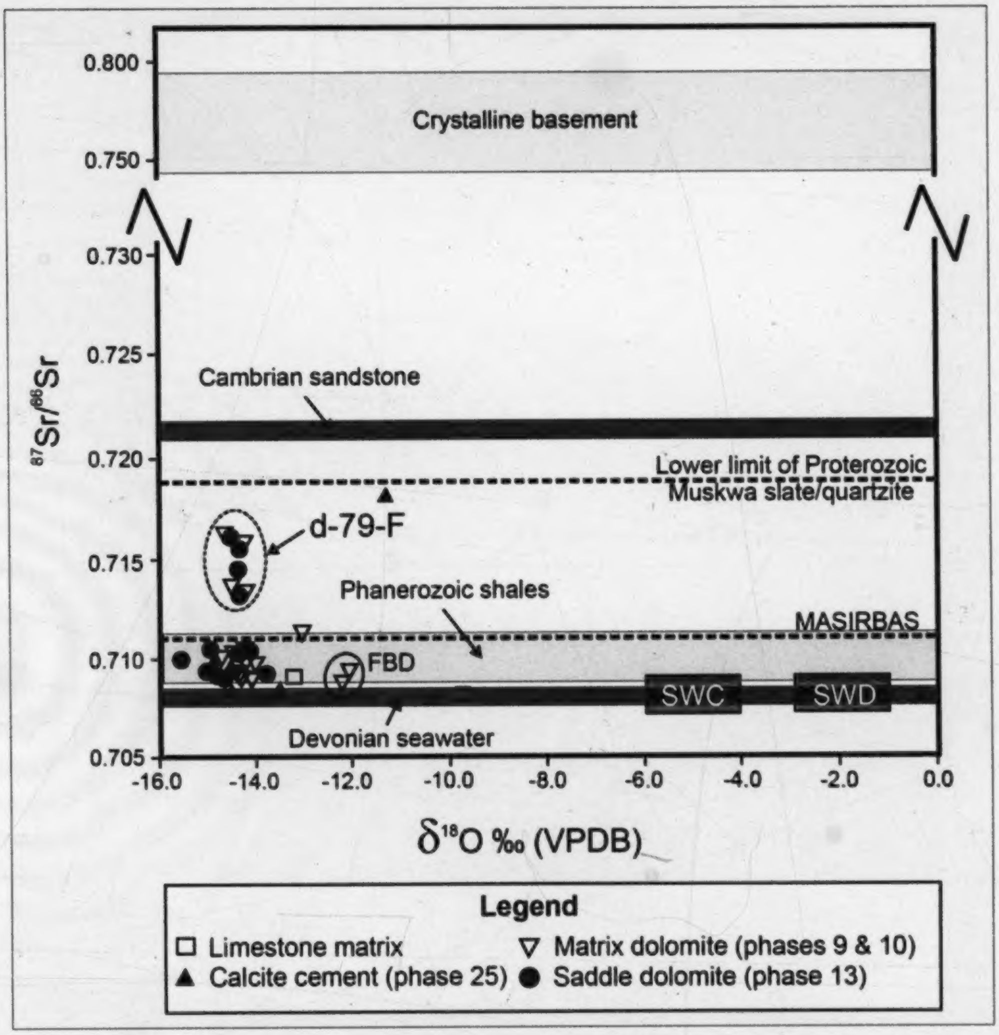

Figure 5.8 $^{87}Sr/^{86}Sr$ versus $\delta^{18}O$ for all analyzed calcite and dolomite samples in the Slave Point Formation. Encircled data (d-79-F) are from well d-79-F/94-J-10 near the western limit of the field. Data encircled with the solid line represent fine crystalline brown dolomite (FBD - phase 9). Estimated $^{87}Sr/^{86}Sr$ of Middle Devonian seawater according to Denison et al. (1997). Oxygen isotope range of Middle Devonian marine calcite (SWC) after Hurley and Lohmann, 1989. The range for Middle Devonian seawater dolomite (SWD) is based on the reference values for Middle Devonian marine calcite corrected according to the equilibrium $\Delta^{18}O$ between calcite and dolomite (3 ± 1‰ at 25°C; Land, 1980). Also included are fields for crystalline basement, Proterozoic Muskwa Assemblage, Cambrian sandstone, and Phanerozoic basinal shales. Maximum strontium isotope ratio of basinal shales (MASIRBAS = 0.7120) after Machel and Cavell (1999).

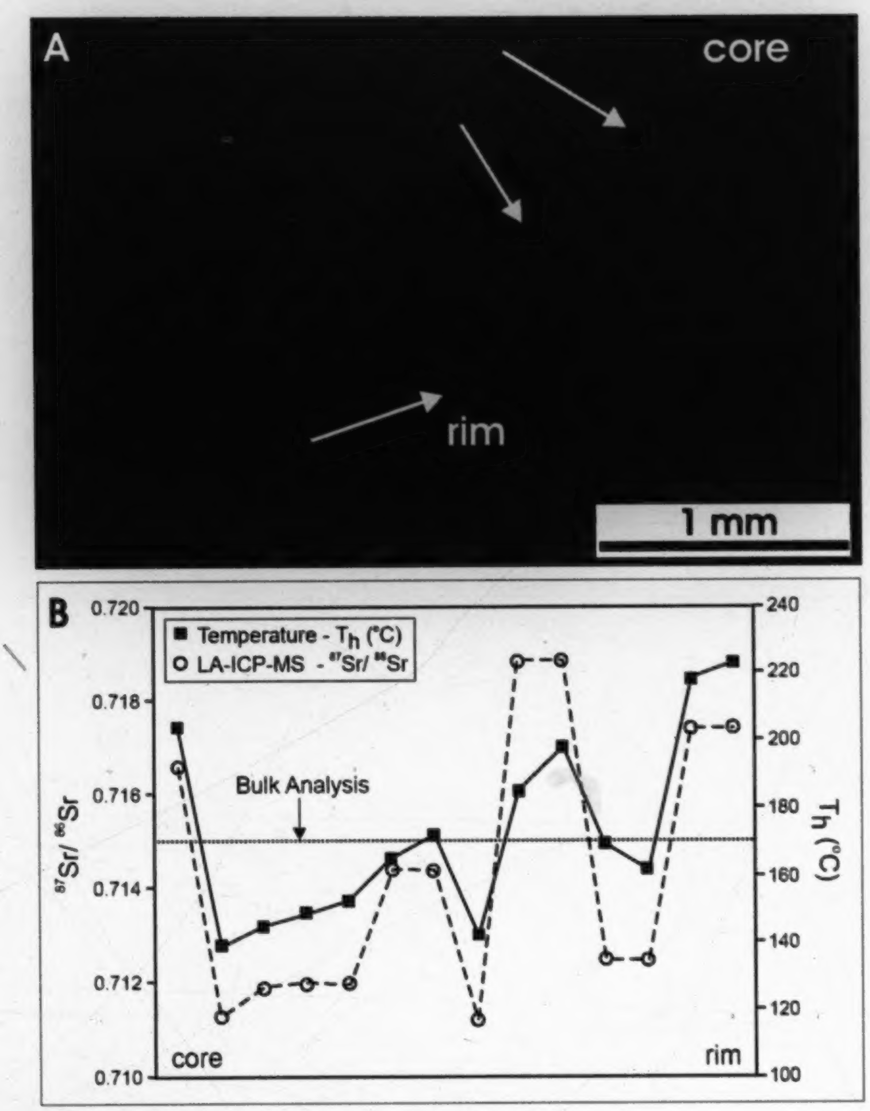

Figure 5.9 Laser ablation ICP-MS strontium isotope results.

(A) Cathodoluminescence photomicrograph showing the concentric zoning developed within a single saddle dolomite crystal: d-79-F/94-J-10; 6769'. The arrows point to the laser ablation ICP-MS Sr-isotope sampling locations.

(B) In-situ $^{87}Sr/^{86}Sr$ results and fluid inclusion homogenization temperatures from a core to rim transect within the single saddle dolomite crystal shown above. Open circles = $^{87}Sr/^{86}Sr$ results by laser ablation ICP-MS; solid squares = fluid inclusion homogenization temperatures. Bulk analysis line represents the value of 0.7151 obtained from a powder that was drilled from the same sample.

5.3.3 Trace elements

Original carbonate phases are stabilized by intervening diagenetic fluids via processes of dissolution and re-precipitation (Bathurst, 1975). During these processes, trace elements from the carbonates are mixed with those from the fluid and are then repartitioned during recrystallization, mineral precipitation and stabilization (Veizer, 1983). Trace elements can be incorporated into carbonate minerals in the following ways (McIntire, 1963; Zemann, 1969; Morse and Mackenzie, 1990):

(1) substitution for Ca in the $CaCO_3$ structure;
(2) interstitial substitution between structural planes;
(3) substitution at defect sites within the structure;
(4) adsorption by remnant ionic charges; and,
(5) present in non-carbonate inclusions.

The most important of these processes is the first process (Veizer, 1983), and diagenetic studies are concerned mainly with this type of trace element substitution. However, in dolomite, trace elements can be incorporated into Ca and/or Mg structural positions.

Incorporation of trace elements into carbonate minerals is controlled by (Tucker and Wright, 1990):

(1) the concentration of trace elements in the fluid;
(2) the water/rock ratio of the diagenetic system; and,
(3) the distribution coefficient (D) of the trace element for a particular mineral-fluid system.

The amount that D deviates from unity determines if a trace element will be concentrated in the fluid or the mineral phase and by what magnitude. When D > 1, the ratio of the trace element to Ca or (Ca + Mg) being incorporated into calcite or dolomite is greater than that of the fluid. When D < 1, the trace element will be partitioned preferentially into the fluid (Veizer, 1983; Tucker and Wright, 1990). The magnitude of the distribution of the trace element is described by:

$$(M_{Me}/M_{Ca})_s = D(M_{Me}/M_{Ca})_w$$

where M is molar concentration, Me is the trace element, Ca is the main element that Me substitutes for and s and w are the solid and liquid phases, respectively. This equation is valid only at complete equilibrium where s and w do not display concentration gradients in Me during precipitation (Veizer, 1983). This is the case for most open diagenetic systems.

For closed systems with low water/rock ratios, the fluid changes its composition and this is reflected in trace element gradients within the solid carbonate phase. For this situation, the previous equation becomes:

$$\log (M^{o}_{Me}/M^{f}_{Me}) = \lambda \log (M^{o}_{Ca}/M^{f}_{Ca})$$

where o and f represent initial and final concentrations, respectively, for the trace and main elements.

Similar to fractionation factors, distribution coefficients for dolomite are poorly constrained because of the inability to experimentally synthesize dolomite at surface temperatures and pressures. Nonetheless, it is suggested that Sr and Na have $D < 1$, whereas Fe and Mn have $D > 1$ (Veizer, 1983; Machel, 1985; Tucker and Wright, 1990). However, Kretz (1982) suggested that there are different distribution coefficients for a single element that is able to substitute into both the Ca and Mg structural sites. For instance, Wildeman (1970) found that Mn substitutes into both positions but it preferred the Mg site, especially at higher temperatures. A general rule is that ions with radii larger than that of Ca (>1.08 Å) are almost completely excluded from Mg sites, while those with radii smaller than Mg (<0.80 Å) are virtually excluded from the Ca sites (Jacobson and Usdowski, 1976; Kretz, 1982).

Results

A total of forty samples of various generations of calcite and dolomite were analyzed for their trace element composition by neutron activation analysis (NAA) of bulk powders. The ranges of $CaCO_3$, Fe, Mn, Sr, and Na for individual carbonate phases are shown in Table 5.4. Information on all other trace elements can be found in Appendix V. Those trace element analyses did not provide any additional information, and are not further discussed.

Calculated stoichiometry from the limestones (micrite) and fossils range from 97.2 to 99.5 (mean = 98.4 mol% $CaCO_3$), and 97.2 to 99.3 (mean = 98.3 mol% $CaCO_3$), respectively (Table 5.4). Similar results were obtained from the late-stage calcite cements (phase 30): 93.5 to 99.6 (mean = 98.3 mol% $CaCO_3$) (Table 5.4).

The four samples of limestone have Fe concentrations that range from 64 to 1297 ppm (mean = 712, $1\sigma = 524$); Mn concentrations that range from 39 to 220 ppm (mean =

Phase		$CaCO_3$ (mol %)	Fe (ppm)	Mn (ppm)	Sr (ppm)	Na (ppm)
Limestone (4)	min.	97.17	64	39	146	9
	mean	98.43	712	117	166	38
	max.	99.45	1297	220	212	103
	Std. Dev.	0.74	524	91	31	44
Fossils (2)	min.	97.28	-	29	-	10
	mean	98.28	141	33	354	28
	max.	99.28	-	36	-	46
	Std. Dev.	1.41	-	5	-	25
Calcite Cement phase 25 (7)	min.	93.51	6	47	139	6
	mean	98.25	100	240	319	27
	max.	99.57	468	621	1141	81
	Std. Dev.	2.12	165	198	365	31
GMD phase 10 (16)	min.	49.54	72	360	37	49
	mean	50.70	1682	919	64	113
	max.	51.80	9369	1322	124	353
	Std. Dev.	0.59	2831	374	28	92
SD phase 13 (11)	min.	49.61	37	377	32	37
	mean	51.23	586	1116	102	126
	max.	52.31	1629	1617	370	361
	Std. Dev.	0.90	607	466	106	117

Table 5.4 Trace element results by diagenetic phase from neutron activation analysis (NAA). Diagenetic phase numbers from Figure 4.1. The number of analyzed samples is reported in parenthesis. min. = minimum measured value, mean = arithmetic mean of measured values, max. = maximum measured value, Std. Dev. = standard deviation (1σ).

117, $1\sigma = 91$); Sr concentrations that vary between 146 and 212 ppm (mean = 166, $1\sigma = 31$); and, Na concentrations that range between 9 and 103 ppm (mean = 38, $1\sigma = 44$) (Table 5.4).

Two samples from fossil components have Mn concentrations that vary between 29 and 36 ppm (mean = 33, $1\sigma = 5$), and Na concentrations between 10 and 46 ppm (mean = 28, $1\sigma = 25$) (Table 5.4). Concentrations of the trace elements Fe and Sr are limited to a single sample, and, therefore, will not be discussed further.

Seven samples of late-stage calcite cements (phase 25) have Fe concentrations that range from 6 to 468 ppm (mean = 100, $1\sigma = 165$); Mn concentrations range from 47 to 621 ppm (mean = 240, $1\sigma = 198$); Sr concentrations range from 139 to 1141 ppm (mean = 319, $1\sigma = 365$); and, Na concentrations range from 6 to 81 ppm (mean = 27, $1\sigma = 31$) (Table

5.4).

In the dolomite samples, the major elements Ca and Mg do not vary significantly (Table 5.4). Calculated stoichiometry ranges from 49.5 to 51.8 mol% $CaCO_3$ (mean = 50.7 mol% $CaCO_3$), and 49.6 to 52.3 mol% $CaCO_3$ (mean = 51.2 mol% $CaCO_3$) for matrix and saddle dolomite, respectively.

Sixteen samples of GMD (phase 10) from five wells have Fe concentrations that range from 72 to 9369 ppm (mean = 1682, 1σ = 2831); Mn concentrations that vary between 360 and 1322 ppm (mean = 919, 1σ = 374); Sr concentrations that range from 37 to 124 ppm (mean = 64, 1σ = 28); and, Na concentrations that range between 49 and 353 ppm (mean = 113, 1σ = 92) (Table 5.4).

Eleven samples of SD (phase 13) from five wells have Fe concentrations that vary between 37 and 1629 ppm (mean = 586, 1σ = 607); Mn concentrations that range from 377 to 1617 ppm (mean = 1116, 1σ = 466); Sr concentrations between 32 and 370 ppm (mean = 102, 1σ = 106); and, corresponding Na concentrations that range from 37 to 361 ppm (mean = 126; 1σ = 117) (Table 5.4).

Discussion

The trace element chemistry from the limestones and fossils is representative of low-Mg calcite that was subsequently recrystallized; a conclusion that has already been drawn based on the isotope results. In particular, the Sr concentrations in these phases are 6 to 7X reduced from the expected value of 1000 ppm in marine limestones (Veizer, 1983). The diagenetic fluid(s) that was responsible for recrystallization must, therefore, have had a very low initial Sr concentration. This restricts the possible fluids to either meteoric water, or seawater. However, the stable and radiogenic isotopes, discussed earlier, preclude the possibility of meteoric water incursion into the Slave Point Formation. Consequently, the fluid of recrystallization was of marine parentage, which Veizer (1983) claims can result in trace element distributions that are similar or identical to those resulting from recrystallization via meteoric waters. Additional information regarding this particular 'fluid of recrystallization' can be garnered from the Fe and Mn results. The relatively high concentrations of both elements in the limestone and fossil samples suggests: 1) significant recrystallization, compared to average concentrations of Fe (< 39 ppm) and Mn (1 ppm) in pristine marine limestones (Veizer, 1983); and, 2) pore waters that were reducing during recrystallization and that a significant source of Fe and/or Mn was present. This second point is critical for two reasons. Firstly, reducing reservoir conditions are generally restricted to intermediate and deep burial settings, i.e., depths greater than 1000 metres (Machel, 1999). Secondly, an allochthonous source for Fe and Mn indicates widespread fluid circulation and water-rock interaction with underlying or adjacent siliciclastic rocks. As a whole, the trace element results from both the limestones and fossils indicate recrystallization by Devonian seawater that interacted with either underlying Cambrian sandstones, or Paleozoic shales, following significant burial.

The Sr content of the late calcite cements (blocky calcite II - phase 25) was discussed previously with respect to the strontium isotope ratios. In that section, it was hypothesized that the fluid that precipitated the calcite cements was a derivative of Devonian seawater. Again, the high concentration of Fe and Mn in the calcite cements suggests formation from reduced diagenetic fluids. This evidence places an upper-limit for the depth of formation at around 1000 metres (Machel, 1999), consistent with the petrographic evidence.

The major and trace element chemistry of GMD (phase 10) and SD (phase 13), unlike the stable and radiogenic isotopes, clearly demonstrate the effects of hydrothermal alteration. Examination of the calculated dolomite stoichiometry in Table 5.4 indicates that spatially related samples of GMD and SD, i.e., samples that co-exist in the core interval, have roughly the same values, with most falling below 51 mol% $CaCO_3$. However, some samples of SD from wells c-56-L/94-J-9 (henceforth labelled c-56-L), d-79-F, and b-10-D/94-J-16 (henceforth labelled b-10-D) have values greater than 51 mol% $CaCO_3$, while the corresponding samples of GMD are significantly lower. Petrographic examination of these samples indicates that most of these SD samples occur as a passive cement in vugs and fractures. Furthermore, in cases where the calculated stoichiometry of the two phases is identical, the petrography points to recrystallization of GMD as the dominant process in those samples, i.e., GMD was hydrothermally altered during the formation of SD. The complete recrystallization of GMD may be taken as evidence of high temperature, i.e., roughly 200°C, (hydrothermal?) fluid invasion into the Slave Point Formation (Malone et al., 1996).

With respect to Sr and Mn concentrations in GMD and SD, several features are conspicuous (Figure 5.10A). First, the data for GMD and SD overlap, with the exception of those from well c-56-L, which shows a marked increase in Mn content between the two

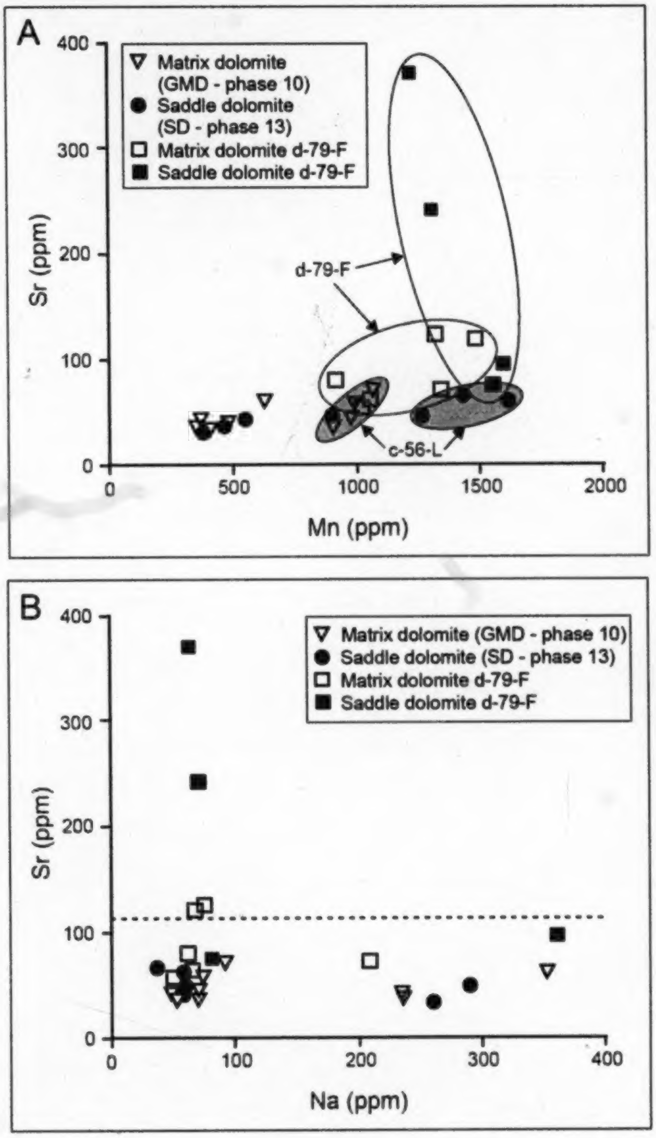

Figure 5.10 Crossplots of trace element results from the Slave Point Formation.

(A) Plot of Sr and Mn concentration for matrix and saddle dolomites from 5 wells. Squares = data from well d-79-F/94-J-10. Samples of GMD and SD from four wells show little variation within each well. However matrix and saddle dolomites from well c-56-L/94-J-9 (shaded fields) show a marked increase in Mn from GMD to corresponding samples of SD.

(B) Plot of Sr and Na concentration for matrix and saddle dolomites from 5 wells. Squares = data from well d-79-F/94-J-10. Dashed line represents maximum Sr concentration in matrix dolomites from the Upper Devonian Nisku Formation of west-central Alberta (Machel, 1985).

phases (shaded loops in Figure 5.10A). Second, data for both GMD and SD from well d-79-F are elevated with respect to Sr and Mn compared to all other wells, with some overlap (unshaded loops in Figure 5.10A). Third, in both wells there is a separation of the GMD and SD data. These data suggest the effect of inheritance or cannibalization of Sr by the fluid(s) responsible for the formation of SD, and therefore, hydrothermal alteration of GMD. Furthermore, samples from well d-79-F generally show an increase in the Sr content between co-existing samples of GMD and SD. The reason for the elevated Sr contents is not clear, however, this may be a reflection of the interaction of "exotic" fluid(s) with radiogenic basement rocks, as discussed in previous sections.

Assuming that the Sr data from GMD and SD in well d-79-F are anomalous, the average Sr concentration from the remaining samples of GMD and SD is 48 ppm; a value similar to the mean Sr content of replacement dolomites from the Devonian of Alberta (Mountjoy and Amthor, 1994; Mountjoy et al., 1999). The likelihood that the Sr distribution in the dolomites of the Slave Point Formation is the result of pure coincidence is doubtful; rather, this distribution is probably a reflection of the recrystallization/alteration of GMD by the hydrothermal fluid(s). However, Malone et al. (1996) suggested that the Sr content of dolomite should decrease as a result of the decrease in the distribution coefficient during an increase in the level of recrystallization. It should be expected then that the GMD have lower Sr concentrations, similar to studies on other ancient dolomites (Montanez and Read, 1992; Kupecz and Land, 1994; Malone et al., 1994). Though, the similarities in the Sr data from both GMD and SD are probably the result of either formation at the same time and from the same fluid, or recrystallization of GMD under low water-rock ratios. The former option is highly unlikely due to both isotopic and petrographic evidence that suggests the two dolomite populations are not co-genetic. However, the alternative option, recrystallization under low water-rock ratios, not only accounts for the similarities in the geochemistry of GMD and SD, it also confirms the hypothesis that the dolomites in well d-79-F formed under higher water-rock ratios which would be expected along fault zones.

The Sr data may also shed light on the origin of the hydrothermal fluid(s). The likelihood that the dolomite-forming fluid was normal seawater is extremely low due to the fact that dolomites that form in equilibrium with seawater should contain between 470 and 550 ppm Sr, and greater than 550 ppm in evaporated seawater (Veizer, 1983). Therefore, if we assume bulk solution equilibrium, the low Sr content of the Slave Point dolomites suggests that: 1) these dolomites were not formed in an evaporitic environment; and, 2) these Clarke Lake dolomites were not formed through the replacement of high-Mg limestones by marine (or less saline) fluids (Machel, 1985). Based on these arguments, Machel (1985), in a study from the Devonian Nisku dolomites from west-central Alberta, suggested that dolomites containing less than 120 ppm Sr (dashed line, Figure 5.10B) cannot be precipitates in equilibrium with marine or hypersaline water. However, a study of Miocene marine dolomites from the Little Bahama Bank indicates that the amount of Sr in dolomite is related to both the Sr content of the dolomite-forming fluid and the stoichiometry of the dolomite crystals (Vahrenkamp and Swart, 1990). As a result, dolomite containing 50 mol% $CaCO_3$ that precipitates in equilibrium with normal marine seawater should contain only about 50 ppm Sr (Vahrenkamp and Swart, 1990). Similarly, Bein and Land (1983) described early-diagenetic dolomite that formed from a halite-saturated brine with as little as 50 ppm Sr. Further, during the course of examining the Bahama dolomites, Vahrenkamp and Swart (1990) were able to establish a relation between the Sr^{2+}/Ca^{2+} ratio of dolomite-forming fluids, the dolomite stoichiometry, and the Sr content of the dolomites, allowing the determination of the Sr^{2+}/Ca^{2+} ratio of fluids involved in the formation of ancient dolomites. Using a range of 49-50 mol% $MgCO_3$ and a Sr content of 50 ppm, this relationship predicts Slave Point dolomite formation from fluids with a Sr^{2+}/Ca^{2+} ratio between roughly 0.040 and 0.058. Based on data for the chemistry of evaporated seawater, these ratios suggest the bulk of the Slave Point dolomites were formed in equilibrium with seawater that was evaporated at least to a point past gypsum saturation (Fontes and Matray, 1993).

The sodium content of GMD and SD, between 37 and 361 ppm (Figure 5.10B), is similar to the range exhibited by many other ancient dolomites (Mattes and Mountjoy, 1980; Machel, 1985; Mountjoy et al., 1999), but significantly lower than values displayed by modern post-depositional dolomites (Rodgers et al., 1982; Humphrey, 1988; Land, 1991; Kimbell, 1993; Budd, 1997). The sodium content in dolomite has been suggested to be a function of the salinity of the precipitating solution (Fritz and Katz, 1972; Land and Hoops, 1973; Veizer et al., 1977; Sass and Bein, 1988), and it seems likely that Na concentrations are also controlled by the number of lattice defects. However, the Na in these defects may occur as fluid or solid (NaCl) inclusions (Bein and Land, 1983), thereby rendering any interpretations regarding salinity as questionable at best. Additionally, Land

(1985) and Kupecz et al. (1992) suspected that Na content decreases with recrystallization, a hypothesis Malone et al. (1996) confirmed experimentally. With this in mind cautious inferences can be made regarding the fluid responsible for SD formation. According to Sass and Bein (1988), dolomite found in association with halite should have a Na content that ranges from 150 to 270 ppm, and be nearly stoichiometric. As discussed earlier, the stoichiometric and Sr-poor dolomites from the Slave Point Formation, i.e., exclusive of dolomite samples from wells d-79-F and c-56-L, were likely formed from seawater that was evaporated to at least gypsum saturation. So, with the dolomites displaying Na contents up to a maximum of 361 ppm (Figure 5.10B), there is another independent line of evidence for dolomite formation by highly evaporated seawater. The slight discrepancy between the maximum Na content in the Slave Point dolomites and those published by Sass and Bein (1988) for dolomites in association with halite may be due to contamination by NaCl inclusions. But, based on data from Staudt et al. (1993), dolomites containing 0.1 wt% fluid inclusions can be expected to contain between 53 and 92 ppm Na if formed from evaporitic brines. Therefore, application of a correction to the Na content of the dolomites brings the maximum value to between 269 and 308 ppm Na, considerably closer to the maximum observed by Sass and Bein (1988).

The incorporation of Fe and Mn into the dolomite lattice is favoured as a result of distribution coefficients that are greater than one (Veizer, 1983). Accordingly, Reeder and Prosky (1986) proposed that Fe and Mn incorporated in the dolomite lattice should not exceed 800 and 500 ppm, respectively. However, some samples of GMD and SD, in particular, those from well d-79-F, plot in excess of these values (Figure 5.11), suggesting another mechanism. Incorporation of both Fe and Mn require that these elements be in a reduced, divalent state. Therefore, the diagenetic fluids that are transporting these elements must be reducing. As a result, Fe and Mn contents less than 300 and 50 ppm, respectively, must reflect either formation from oxidizing fluids, or a lack of either element in the reducing diagenetic fluids (Budd, 1997). At the opposite end of the spectrum, Fe and Mn contents greater than 1000 and 50 ppm, respectively, indicate the diagenetic fluids were reducing and had interacted with a source of Fe and Mn (Budd, 1997). In the previous discussion from the limestone samples, it was expressed that pristine marine limestones should only have Fe and Mn contents of <39 and 1 ppm, respectively (Veizer, 1983). Likewise, dolomites formed in equilibrium with seawater have a similar range of Fe (< 50 ppm) and Mn (1 ppm)

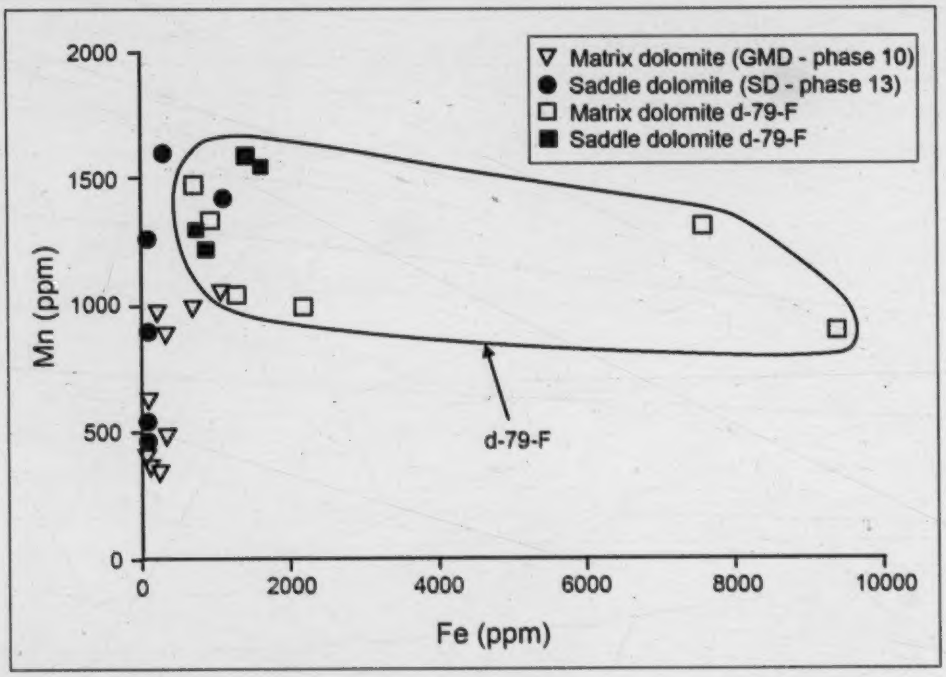

Figure 5.11 Crossplot of Mn versus Fe concentrations for matrix and saddle dolomites. Squares = data from well d-79-F/94-J-10.

contents (Veizer, 1983; Aharon et al., 1987). Therefore, neither GMD nor SD formed from seawater under near-surface conditions.

Similar to the Sr contents discussed previously, the Mn distribution between co-existing phases of GMD and SD is generally identical (Figure 5.10A). Samples from the bulk of the Clarke Lake field have Mn contents of roughly 500 ppm, comparable to the value proposed by Reeder and Prosky (1986) for Mn incorporated in the dolomite lattice. Additionally, the Fe content of these samples is less than 150 ppm (Figure 5.11). These values reflect the low Eh of the original GMD forming fluid; a fluid that must have interacted with underlying or adjacent siliciclastic rocks. Both the Fe and Mn content from the SD phases are then reflecting either recrystallization and cannibalization of Fe and Mn from GMD under low water-rock ratios, or formation from a fluid of identical chemistry and redox conditions. Dolomite samples from well d-79-F have Fe and Mn contents of greater than 500 and 1000 ppm, respectively. In particular, the Fe content of GMD approaches 10 000 ppm in one sample, clearly evidence for the injection of some "exotic" fluid(s) into these wells during matrix dolomitization and/or saddle dolomite formation. Furthermore, the Fe contents from well d-79-F are similar to those presented by Mountjoy et al. (1999) for dolomites of the Devonian Swan Hills Formation of west-central Alberta; dolomites that formed along fault zones, suggesting fault zones were the likely conduit for diagenetic fluids into well d-79-F.

Microprobe analysis

A single sample of saddle dolomite from well d-79-F that was analyzed using laser ablation ICP-MS was subjected to analysis by electron microprobe (EPMA) in order to characterize the compositional controls on cathodoluminescence (CL) zoning. Following analysis, the crystal was subdivided into 3 geochemically distinct zones: iron-poor core, iron-rich rim, and iron-poor rim. The range of $CaCO_3$, Fe, Mn, Sr, and Na results for the three zones is shown in Figure 5.12, along with the backscatter image.

The iron-poor core (A) constitutes the bulk of this SD crystal. It is stoichiometric, and averages 102 ppm Fe, 1440 ppm Mn, and 196 ppm Sr. All trace element data are consistent with results obtained from the bulk analysis of SD from well d-79-F (Figures 5.10 and 5.11). However, under CL, this zone generally exhibits concentric to oscillatory zoning that are not identifiable in the backscatter image (Figure 5.12). Since backscatter electron images are essentially a measure of the mean atomic number of the sample, the lack of compositional variation is likely due to the similar atomic weights of Fe and Mn. This observation precludes the possibility of CL activation due to the incorporation of the much heavier rare earth elements (Machel et al., 1991). Rather, the variable Mn^{2+}/Fe^{2+} ratio is almost certainly the control on CL zoning. An iron-rich zone (B) is slightly less than 100 μm in width. This zone is also stoichiometric, and averages 53 502 ppm Fe, 3574 ppm Mn, and 134 ppm Sr. This zone could be termed ferroan dolomite, as it exceeds the defined value of 10 000 ppm (Morrow, 1990, Tucker and Wright, 1990). Both Fe and Mn contents are significantly higher than bulk trace element results, while the Sr content is equal to the latter (Figures 5.10 and 5.11). Zone B consistently displays non-luminescence when viewed under CL, a result of the critically high concentrations of Fe (Dromgoole and Walter, 1990; Machel et al., 1991). The iron-poor rim (C) is a very thin (< 50μm) zone that represents the terminal growth zone in this SD crystal. This zone is stoichiometric, and averages 586 ppm Fe, 3565 ppm Mn, and 248 ppm Sr. The microprobe data for Fe and Sr

Figure 5.12 Electron microprobe results.

(Top) EPMA back-scatter electron image showing three distinct zones (A through C) from a single saddle dolomite crystal in well d-79-F/94-J-10, depth = 6769'. The approximate location of the back-scatter image is represented by the box on the cathodoluminescence photomicrograph at top right. The core of the saddle dolomite crystal is represented by Zone A. The back-scatter image shows evidence for dissolution in the dolomite crystal either before or coincident with the formation of Zone B. The original crystal boundary prior to the dissolution and formation of Zone B cement is represented by line a'. Following dissolution and/or recrystallization the boundary between zones A and B is represented by line a. The areas where dissolution occured are shown by the arrows and resulted in the formation of 'lumps' of Zone A floating within Zone B. Following the formation of Zone B, a thin layer of Zone C cement terminated crystal growth.

(Bottom) Table of trace element results from electron microprobe analysis. The phases A through C correspond to zones A through C in the back-scatter electron image. The number of spot analyses is reported in parenthesis. min. = minimum measured value, mean = arithmetic mean of measured values, max. = maximum measured value, Std. Dev. = standard deviation (1σ), D.L. = detection limit, BDL = spot analysis below detection limits.

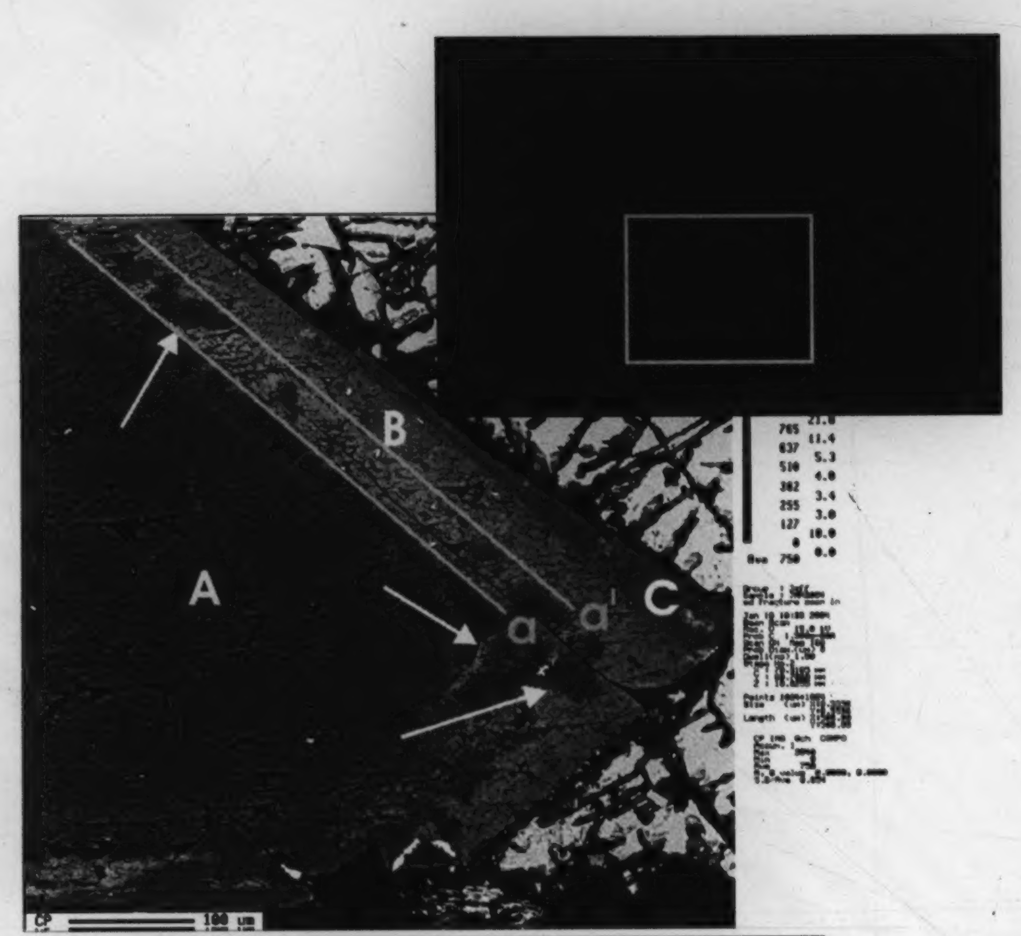
A
B
C
a
a'
765
11.4
637
5.3
510
4.0
382
3.4
255
3.0
127
10.0
0
0.0
Ave 750
Points
Length
CP
100 um

Phase		$CaCO_3$ (mol %)	Fe (ppm)	Mn (ppm)	Sr (ppm)	Na (ppm)
A Fe-poor rim (3)	min.	50.09	567	1990	BDL	BDL
	mean	50.31	586	3565	248	236
	max.	50.71	599	4391	474	709
	Std. Dev.	0.34	16	1364	238	-
	D.L.	-	205	164	413	355
B Fe-rich rim (10)	min.	48.16	34745	2850	BDL	BDL
	mean	49.19	53502	3574	134	131
	max.	49.81	81927	4608	981	360
	Std. Dev.	0.46	15173	480	319	128
	D.L.	-	209	161	438	353
C Fe-poor core (9)	min.	49.95	BDL	496	BDL	BDL
	mean	50.34	102	1440	196	70
	max.	50.99	319	3996	744	204
	Std. Dev.	0.33	114	1017	276	80
	D.L.	-	202	156	410	337

are roughly identical to data from the bulk analysis of SD from well d-79-F (Figures 5.10 and 5.11). However, the Mn content is significantly higher. As well, the Mn^{2+}/Fe^{2+} ratio within this zone, which varies from about 3.5 to 7.3, and the low Fe^{2+} content is reflected in the bright red luminescence that is characteristic of this zone under CL (Figure 5.12).

One of the most striking results to come out of the microprobe analysis is the presence saddle dolomite containing extremely high Fe contents – Zone B. Also of note, is the fact that the Mn contents in zones B and C are relatively constant, while the Fe contents drop significantly (Figure 5.12). These results point towards changes either in the bulk chemistry of the precipitating fluids and/or the physical and redox conditions of the reservoir. The first alternative has its merits in the fact that it has already been proposed that dolomites from well d-79-F were formed from fluids that ascended along fault zones, thereby providing the opportunity for the introduction of fluids of variable chemistry, which was demonstrated for the in-situ Sr isotope analyses. In order to form dolomite with the observed Fe and Mn chemistry, the diagenetic fluid(s) was either a single fluid that interacted with different rocks along its flow path, changing the Fe concentration but maintaining the Mn concentration, or a high-Fe, low-Mn fluid that migrated into the Slave Point Formation and mixed with a previously entrained low-Fe, high-Mn fluid. Both options, although possible, are probably unlikely unless they are integrated with physical and/or redox controls.

Machel and Burton (1991) systematically described the factors that govern cathodoluminescence, with particular emphasis on the controls on Fe and Mn incorporation in dolomite. It is well known that both precipitation rate and temperature control the distribution coefficients of Fe (D_{Fe}^{2+}) and Mn (D_{Mn}^{2+}). As a result, these changes can produce compositional variations in carbonate cements, causing cathodoluminescent zoning (Dromgoole and Walter, 1990; Machel and Burton, 1991). However, Dromgoole and Walter (1990) suggest that such changes are unlikely to be responsible for the major variations commonly observed in natural cements. Similarly, changes in the activity of calcium (a_{Ca}^{2+}) in solution will either increase or decrease the quantity of both Fe and Mn incorporated into carbonate cements resulting in cathodoluminescence zonation due to differences in the distribution coefficients for Fe and Mn (Machel and Burton, 1991). However, this does not appear to be a viable alternative since the Mn content in the dolomite does not change in order of magnitude from Zone B to Zone C, while the Fe content decreases by a factor of about 100. As a result, the constant Mn content accompanied by changing Fe content is best explained through a change in redox conditions (Frank et al., 1982; Dromgoole and Walter, 1990). This assumes that the effect of kinetics is ignored and the solution is reduced instantaneously. Under this scenario, increasingly reducing conditions would mobilize more Fe^{2+} than Mn^{2+} allowing the concentrations of the two species to vary independently. Ultimately, the reasons for the observed compositional variations in well d-79-F are unknown, however, by incorporating other petrographic evidence – particularly the rapid changes in late-stage mineralization from sulphides to sulphates and back to sulphides – it does appear that rapid changes in redox conditions are controlling the chemistry of the dolomites, and may be a reflection of fluid pulses along active faults within the Clarke Lake field.

Another important feature that became evident through electron microprobe analysis is the presence of what appear to be dissolution surfaces in the backscatter electron image (Figure 5.12 – arrows). In this image, 'lumps' of darker grey, Fe-poor Zone A are contained within the brighter, Fe-rich Zone B. These 'lumps' have irregular boundaries, and therefore, are not representing crystal growth surfaces. On closer examination, the bright dolomite occurs as a very narrow seam on top of Zone A, which is then followed by the dark 'lumps' floating in Zone B. The bright seam is a very planar feature across most of the saddle dolomite crystal, and likely represents the crystal margin of Zone A. If this is the case, the dark 'lumps' represent an intermediate metastable dolomite phase between zones A and B. This intermediate dolomite phase was then either partially recrystallized prior to the formation of Zone B or dissolved during the formation of the Zone B dolomite cement. This may then be evidence for continuous hydrothermal alteration in the Slave Point Formation. That is, alteration not only affected matrix dolomite, but also, some phases of saddle dolomite formation.

5.3.4 Fluid inclusions

In order to better characterize the chemistry of the diagenetic fluids, a detailed study of the chemistry of fluid inclusions from various generations of calcite, dolomite, and accessory minerals in the Slave Point Formation was conducted. A summary of the petrographic and microthermometric results is shown in Table 5.5. Complete chemical data from the analysis of fluid inclusions can be found in Appendices VI and VII.

Mineral Phase	Phases	Inclusion size	T_h (°C)		T_{fm} (°C)		Tm_{ice} (°C)	
			range	avg.	range	avg.	range	avg.
Early Calcite phase 6	aqueous liquid	< 5μm	-	-	-	-	-	-
	aqueous liquid + vapour bubble	< 20μm	139 to 145	142 (7)	-45 to -49	-48 (7)	-10.9 to -11.6	-11.1 (7)
Matrix Dolomite phase 10	aqueous liquid + vapour bubble	< 10μm	127 to 212	166 (46)	-50 to -66	-60 (21)	-9.9 to -23.1	-18.2 (40)
Saddle Dolomite phase 13	aqueous liquid + vapour bubble	< 15μm	116 to 228	165 (43)	-36 to -67	-53 (29)	-8.2 to -22.9	-13.0 (41)
Sphalerite phase 18	aqueous liquid	< 5μm	-	-	-	-	-	-
	aqueous liquid + vapour bubble	< 10μm	129 to 140	135 (8)	-40 to -46	-43 (3)	-13.8 to -15.2	-14.5 (8)
Barite phase 21	aqueous liquid + vapour bubble	< 15μm	113 to 238	163 (12)	-40 to -52	-46 (5)	-5.8 to -14.6	-10.1 (12)
Quartz phase 20	aqueous liquid + vapour bubble	< 20μm	109 to 192	145 (17)	-39 to -56	-46 (12)	-8.0 to -17.2	-9.7 (17)
Late Calcite phase 25	aqueous liquid	< 10μm	-	-	-	-	-	-
	aqueous liquid + vapour bubble	< 30μm	139 to 212	170 (20)	-39 to -56	-48 (17)	-7.2 to -11.6	-9.3 (20)

Table 5.5 Fluid inclusion microthermometry results by diagenetic phase. Diagenetic phase numbers from Figure 4.1. T_h = homogenization temperature, T_{fm} = temperature of first melt, Tm_{ice} = ice melting temperature. The number of measurements used to calculated the arithmetic mean (avg.) is shown in parenthesis.

Introduction

Fluid inclusions have been extensively applied in igneous, metamorphic and economic geology studies where the temperature and salinity of precipitating fluids need to be determined. More recently, they have also been used to study the diagenetic history of carbonate sequences, particularly in the Western Canada Sedimentary Basin (e.g., Aulstead and Spencer, 1985; Qing and Mountjoy, 1994a; 1994b; Mountjoy et al., 1999; Lonnee and Al-Aasm, 2000; Morrow et al., 2002).

Crystals often entrap inclusions of the precipitating fluid along structural defects and other crystallographic irregularities. These types of inclusions are called primary inclusions. Inclusions formed after the crystal has stopped growing are called secondary inclusions and typically occur along fracture surfaces and crystal dislocations (Roedder, 1979). To determine if inclusions are primary, it is necessary to compare the volume of liquid versus the volume of gas (i.e., liquid/vapour ratio) of several inclusions. The liquid/ vapour ratio should be relatively constant in primary inclusions. Additionally, primary inclusions are recognized by their isolated occurrences in the interior of a crystal and do not form a "train" of inclusions (Roedder, 1979).

In diagenetic studies there are two common types of inclusions: low temperature (< 50°C) liquid-only inclusions and higher temperature (> 50°C) liquid-vapour inclusions that separate into two phases upon cooling (Roedder, 1979). Minimum trapping temperatures for two-phase inclusions, called homogenization temperatures (Th), can be determined by heating the inclusion until the vapour bubble disappears, i.e., the inclusion homogenizes to one phase. The homogenization temperature represents the minimum crystallization temperature for the mineral that contains the fluid inclusion. By freezing the inclusion in order to produce ice and measuring the temperature at which the last ice crystal melts (Tm_{ice}) upon re-heating, the bulk salinity and major dissolved ions of the precipitating fluids can be estimated. Specifically, the final melting temperature is a measure of the amount the freezing point of inclusion water is depressed below 0°C by the presence of dissolved salts. However, equal concentrations of different ions depress the freezing point by different degrees requiring that assumptions be made regarding the brine composition. For example, the salinity of the fluid inclusion calculated from Tm_{ice} is calculated by assuming the fluid is a pure NaCl brine, hence, salinity is expressed as wt% NaCl equivalent. The composition of the major salts is obtained by measuring the temperature of first melting after supercooling the inclusion to a temperature at which the inclusion contents are entirely frozen, which is known as the eutectic temperature (Te). The eutectic is rarely reported for carbonate minerals since obtaining accurate measurements is extremely difficult due to the small size of the fluid inclusions. Instead, the temperature of first melt (Tfm) is noted.

When examining fluid inclusions, one must be aware of possible changes to the inclusions after burial. Increasing temperatures with increased burial may cause the internal pressure-temperature conditions of the inclusion to change. The pressure within the inclusion increases at a faster rate than the lithostatic and hydrostatic pressures. Therefore, the inclusion is over-pressured, which may cause the inclusion to stretch or fracture. Stretching will result in elevated homogenization temperatures, while fracturing allows for the creation of new Th and Tm_{ice} values (Allan and Wiggins, 1993). The amount of stretching is determined by the size of the inclusion. The smaller the inclusion, the greater the amount of overheating that it can withstand. Th vs. Tm_{ice} plots can aid in identifying whether a set of fluid inclusions were subjected to stretching, leaking, or both. Fluid inclusions that plot in a cluster indicate that they have not undergone any stretching or leaking (Goldstein and Reynolds, 1994), while inclusions that show an increase in Th but little or no change in Tm_{ice} indicate stretching of the inclusions. Inclusions that have leaked and re-equilibrated show a linear trend towards higher Th and Tm_{ice} values. Overall, crossplots of Th and Tm_{ice} data reveal important information regarding the fluid inclusion history and, hence, related information with respect to basin evolution (McLimans, 1987).

Petrography

Coarse-crystalline blocky calcite (phase 25), which occurs as cement in vugs and fractures, contains abundant fluid inclusions. The fluid inclusions are mostly confined to growth-zone boundaries, although, they may occur in isolated clusters. The majority of the inclusions contain both liquid and vapour phases; they attain a maximum diameter of roughly 30μm; and, they are generally spheroidal to oblate in shape. In a few instances, small (< 10 μm) single-phase inclusions were observed along trails, suggesting that they are secondary in origin. Due to the relatively large size of the inclusions, and the relative ease of mineral separation, both microthermometric and crush-leach analysis were conducted on the calcite cements.

Fluid inclusions in matrix dolomite (phase 10) range in size from roughly 10 µm to much less than 1 µm. The turbid nature of the matrix dolomites is attributed to the presence of these abundant, small (< 1 µm), primary fluid inclusions. Due to the dark colour of the crystals and the small size of many of the inclusions, matrix dolomite was generally not suitable for further fluid inclusion analysis. However, the crystals that contained the larger fluid inclusions were used for both microthermometric and crush-leach analysis. These inclusions are distributed in three dimensions, and concentrated in the crystal cores (Plate 5.1A), which according to Goldstein and Reynolds (1994) represent the most common occurrence of primary fluid inclusions in dolomite. The fluid inclusions are two-phase, liquid-rich and display a negative crystal shape.

Saddle dolomite (phase 13) contains abundant, uniformly distributed, two-phase liquid-vapour inclusions. The largest of the crystals have inclusions-rich cores and relatively clear inclusion-free rims. The fluid inclusions attain a maximum size of approximately 15 µm and have an irregular to lobate shape (Plate 5.1B). There is little evidence for secondary fluid inclusion trails within the saddle dolomite crystals, so, both microthermometric and crush-leach analysis should provide a good representation of the bulk fluid chemistry.

Fluid inclusions in sphalerite (phase 18) crystals were extremely difficult to detect due to the colour of the mineral and the small size of the inclusions. In places where fluid inclusions were detectable, they occurred as both small (< 5 µm) liquid inclusions, and larger (< 10 µm) two-phase inclusions. The larger, randomly distributed, fluid inclusion population generally has an irregular shape, and were interpreted to represent primary fluid inclusions. These inclusions were used for further microthermometric analysis, and one sample was used for crush-leach analysis.

Barite (phase 21) and quartz (phase 20) are interpreted to be co-genetic phases, principally based on petrographic evidence. In places, barite inclusions are found within individual quartz crystals (Plate 5.1C). Where barite occurs as a fracture-lining cement it contains abundant, spheroidal, two-phase fluid inclusions that have a maximum diameter of 15 µm (Plate 5.1D). The random distribution of the fluid inclusions is the basis for suggesting that they are primary inclusions; as opposed to negative crystal shaped inclusions or those along cleavage planes in such a soft mineral. The primary fluid inclusions in quartz are slightly larger than those in barite, attaining a maximum diameter of 20 µm. These two-phase inclusions generally have either lobate or irregularly shaped and may

Plate 5.1 Fluid inclusions

(A) Two-phase, liquid-vapour inclusions (arrow) in the core of a planar-e grey matrix dolomite (phase 10) crystal. d-72-G/94-J-10; 6449'.

(B) Lobate, two-phase, liquid-vapour inclusions within a single crystal of saddle dolomite (phase 13) cement. c-8-D/94-J-16; 6437'6".

(C) Single phase inclusions of barite (phase 21 - arrows) encased in euhedral quartz (phase 20 - Q). The quartz partially cements a fracture that cross-cut matrix dolomite (bottom - inclusion-rich) that was subsequently overgrown by saddle dolomite. The wall of the fracture/zone of dissolution is shown by the dashed line. d-79-F/94-J-10; 6785'.

(D) Nearly circular, two-phase, liquid-vapour inclusions in barite (phase 21). d-79-F/94-J-10; 6785'.

(E) Irregular, hydrocarbon-bearing inclusions (phase 19 - arrows) along a growth zone in a quartz (phase 20) crystal. d-79-F/94-J-10; 6785'.

(F) Two-phase, liquid-vapour inclusions and solid bitumen (phase 19 - arrows) inclusions in quartz (phase 20). c-58-E/94-J-10; 2153.25 m.

Plate 5.1: Fluid Inclusions

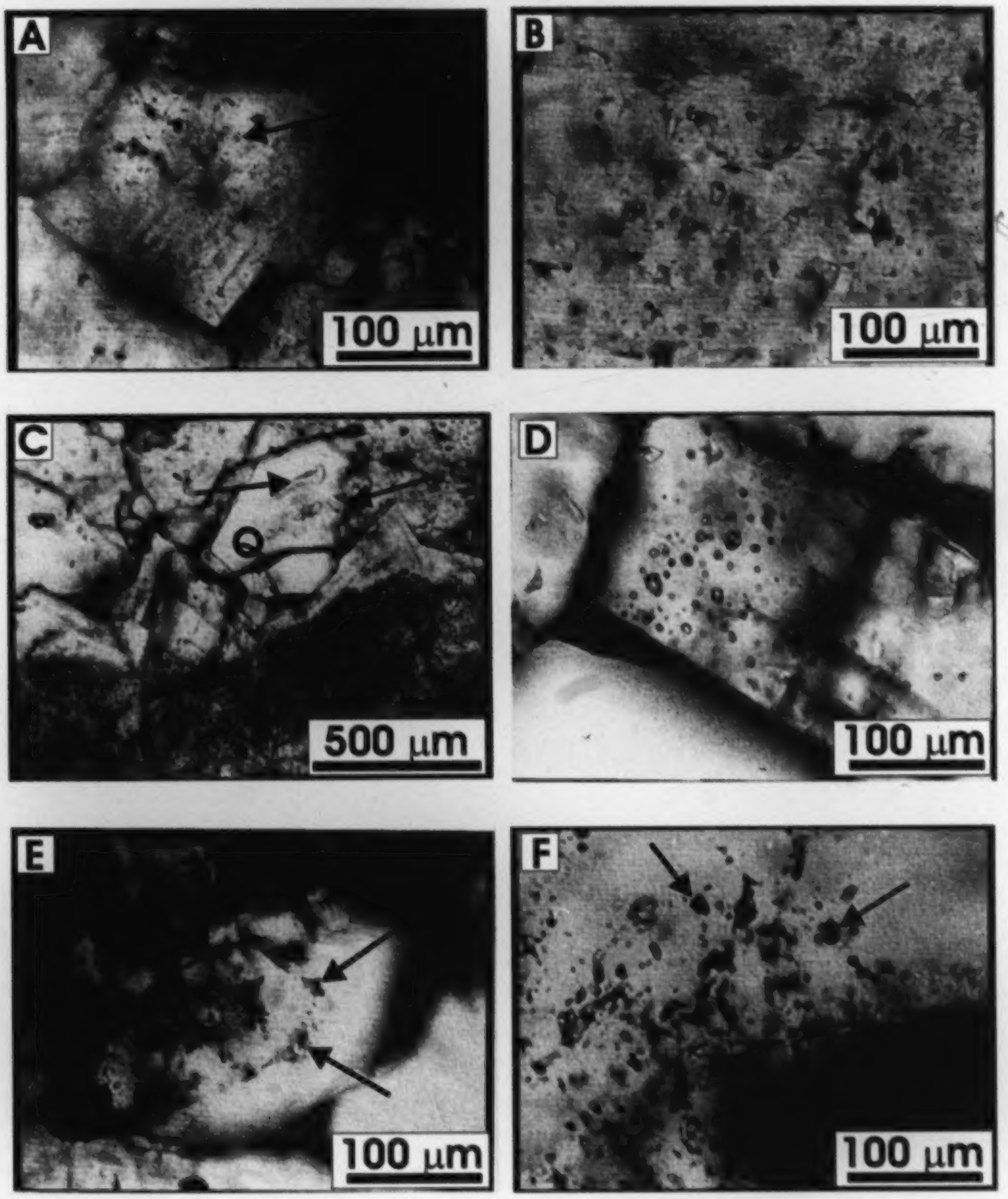
A
100 µm
B
100 µm
C
Q
500 µm
D
100 µm
E
100 µm
F
100 µm

be preferentially distributed along growth zones (Plate 5.1E). Within the same quartz crystals, inclusions of bitumen (phase 19) are also found (Plate 5.1F), which suggests liquid hydrocarbons had migrated into the Slave Point Formation either prior to, or concurrent with, quartz mineralization. As a result of subsequent burial the liquid hydrocarbons were cooked to form solid inclusions of bitumen.

Microthermometry Results

Homogenization temperatures (Th) from forty-six individual fluid inclusions in matrix dolomite (phase 10) range from 127 to 212°C (Figure 5.13A). The large spread in temperatures is based on the position of the inclusions, i.e., core or rim. Where possible, homogenization temperatures were measured in GMD both in the cloudy cores and the clear overgrowth rims under the assumption that the temperatures from the cores represent the original temperature of crystallization. However, as is commonly the case elsewhere in the Alberta Basin, inclusions in the cloudy cores are often too small for microthermometric analysis. The homogenization temperatures in the cores represent a lower temperature regime, averaging about 140 to 150°C, while the rims average between 180 and 200°C. The temperature of first melt (Tfm) from the fluid inclusions, where measurable, range from –50 to –66°C for twenty-one inclusions. This suggests a complex cation composition in the precipitating fluid. With an average Te of –60°C, the dolomite-forming fluid was likely representative of the aqueous system $NaCl-CaCl_2-MgCl_2-H_2O$ (Goldstein and Reynolds, 1994). Temperatures of final ice melt (Tm_{ice}) range from –9.9 to –23.1°C, with an average of –18.2°C for forty individual inclusions. This temperature range corresponds to salinities of 13.8 and 24.4 wt% NaCl equivalent (Bodnar, 1993), or roughly 4 to 7X the salinity of normal seawater (Figure 5.13A). Based on the microthermometric data, GMD generally has a bimodal distribution; one population of high salinity, lower temperature, the other population, representing well d-79-F, high temperature, lower salinity (Figure 5.13A).

Homogenization temperatures (Th) from forty-three individual inclusions in saddle dolomite (phase 13) range from 116 to 228°C, with an average of 165°C (Figure 5.13A). A wide spread in the temperature of first melt also exists – varying from –36 to –67°C. The average value, based on twenty-nine individual inclusions, is –53°C. Based on this temperature data, the cation composition of the dolomite-forming fluid was extremely complex and cannot be represented by one system; rather, the aqueous system appears to

Figure 5.13 Crossplots of fluid inclusion microthermometry results from matrix and saddle dolomites in the Slave Point Formation.

(A) Plot of fluid inclusion homogenization temperatures (Th) versus salinity from matrix (phase 10) and saddle dolomites (phase 13). Squares = samples from well d-79-F/94-J-10. Alteration products are grouped according to their petrographic characteristics: reX GMD = recrystallized GMD; replacement SD = replacement saddle dolomite of GMD; cement SD = open-space filling saddle dolomite.

(B) Fluid evolution trajectories. Large looping arrow represents the inferred evolution of the fluid of hydrothermal alteration during low water-rock ratios. Straight arrow (green) represents the suggested evolution of a similar fluid during high water-rock ratios. See text for further discussion.

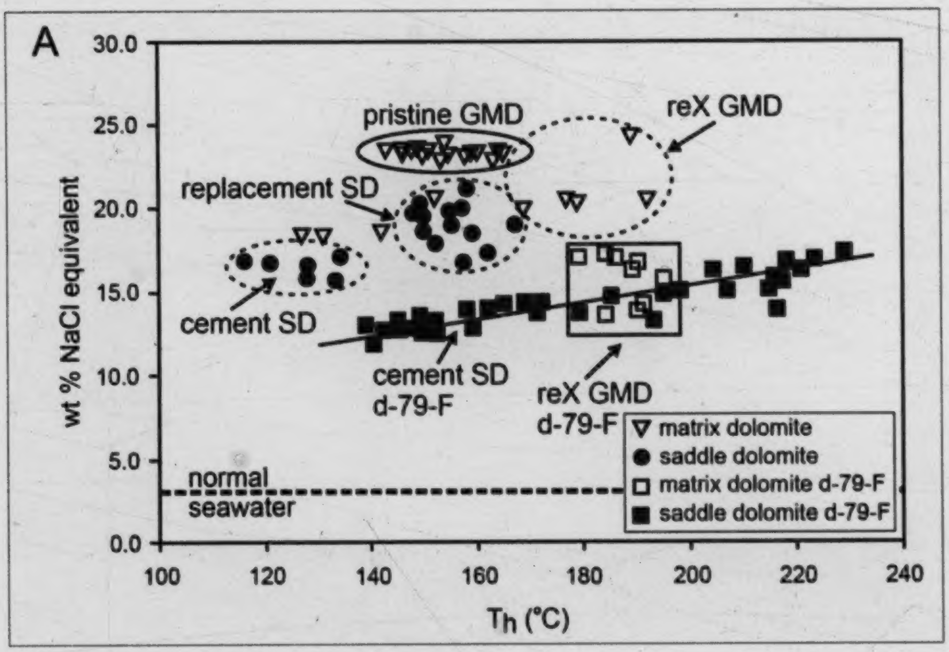
A
30.0
25.0
20.0
15.0
10.0
5.0
0.0
wt % NaCl equivalent
100
120
140
160
180
200
220
240
Th (°C)
pristine GMD
reX GMD
replacement SD
cement SD
cement SD
d-79-F
reX GMD
d-79-F
normal
seawater
▽ matrix dolomite
● saddle dolomite
□ matrix dolomite d-79-F
■ saddle dolomite d-79-F

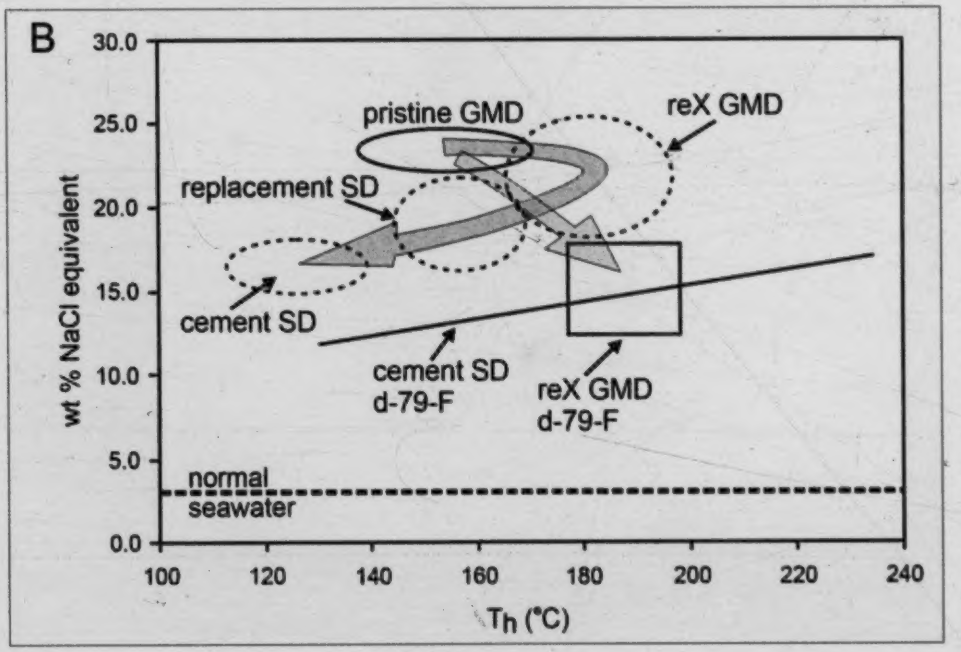
B
30.0
25.0
20.0
15.0
10.0
5.0
0.0
wt % NaCl equivalent
100
120
140
160
180
200
220
240
Th (°C)
pristine GMD
reX GMD
replacement SD
cement SD
cement SD
d-79-F
reX GMD
d-79-F
normal
seawater

have evolved from one dominated by Mg and Ca (similar to GMD), through a NaCl-$MgCl_2$-H_2O system (Goldstein and Reynolds, 1994). Temperatures of final ice melt (Tm_{ice}) range from –8.2 to –22.9°C, with an average of –13.0°C for forty-one individual inclusions. This temperature range corresponds to salinities of 11.9 and 24.3 wt% NaCl equivalent (Bodnar, 1993), or roughly 3.5 to 7X the salinity of normal seawater (Figure 5.13A). Based on the microthermometric data, GMD generally has a bimodal distribution; one population of high salinity, lower temperature, the other population, representing well d-79-F, high temperature, lower salinity (Figure 5.13A). In addition to a similar bi-modal distribution to that exhibited by GMD, the fluid inclusion data show several patterns. Firstly, the Th values in zoned SD crystals from well d-79-F are positively correlated to the $^{87}Sr/^{86}Sr$ values (Figure 5.9B). Secondly, the Th and salinity values of both SD and GMD from well d-79-F are distinct from those of the other wells, i.e., wt% NaCl eq. are lower whereas Th values display a spread toward higher values (Figure 5.13A). Thirdly, SD cement, SD replacement, and recrystallized GMD (reX GMD) display increasing Th values in this order (Figure 5.13A).

A single sample of early blocky calcite cement (phase 6) has homogenization temperatures (Th) from seven individual inclusions that range from 139 to 145°C (mean = 142°C) (Figure 5.14). The corresponding temperatures of first melt range from –45 to –49°C (mean = -48°C), which suggest precipitation from a NaCl-$MgCl_2$-H_2O aqueous system (Goldstein and Reynolds, 1994). Ice melting temperatures are tightly grouped between –10.9 and –11.6°C (mean = -11.1°C). The calculated salinities from these inclusions are between 14.9 and 15.6 wt% NaCl equivalent (Bodnar, 1993), or approximately 4X that or seawater (Figure 5.14).

Homogenization temperatures from sphalerite (phase 18) hosted inclusions range from 129 to 140°C, or an average of 135°C based on eight individual inclusions (Figure 5.14). The temperatures of first melt from three inclusions are similar to those from the early calcite cement: between –40 and –46°C (mean = -43°C). Temperatures of final ice melt (Tm_{ice}) range from –13.8 to –15.2°C, with an average of –14.5°C for the eight inclusions. This temperature range corresponds to salinities of 17.5 and 18.8 wt% NaCl equivalent (Bodnar, 1993), or slightly more than 5X the salinity of normal seawater (Figure 5.14).

Twelve inclusions in barite (phase 21) had homogenization temperatures that ranged from 113 to 238°C (mean = 163°C) (Figure 5.14). First melt temperatures from five

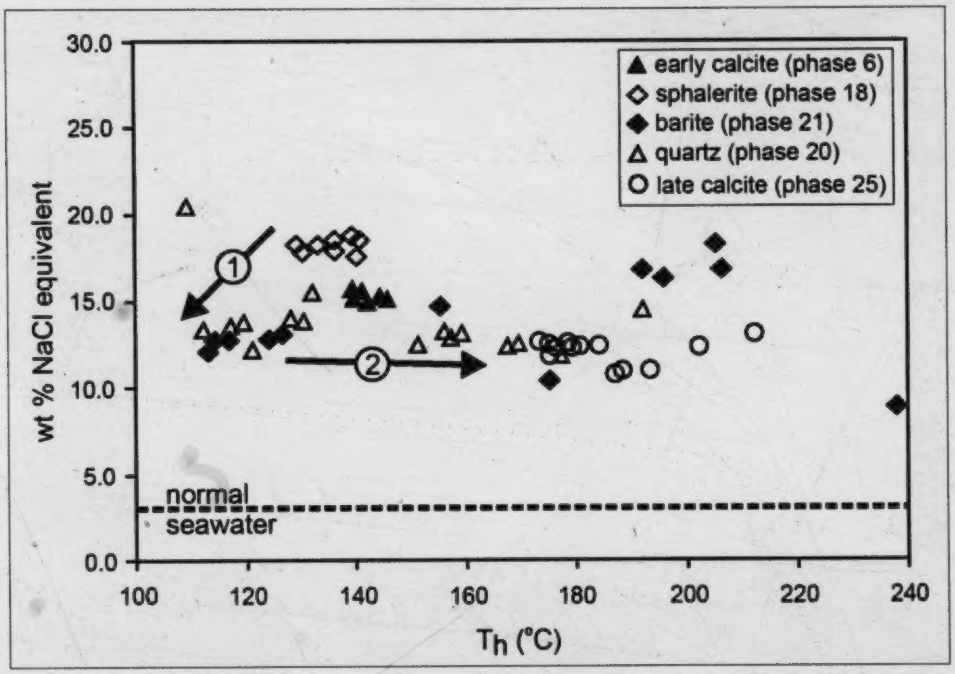

Figure 5.14 Crossplot of fluid inclusion microthermometry results from non-dolomite phases in the Slave Point Formation. Arrows 1 and 2 represent post-dolomite fluid evolution. Arrow 1 shows decreases in both temperature and salinity between the precipitation of sphalerite (phase 18) and the formation of the barite/quartz (phases 20 & 21) vein-filling cements. Arrow 2 shows a marked increase in temperature with very little change in salinity between the barite/quartz event and the formation of later quartz cements and late-stage calcite cements (phase 25).

individual inclusions range from –40 to –52°C (mean = -46°C): similar to the temperatures from both sphalerite and early calcite cement. Ice melting temperatures are widespread, varying from –5.8 to –14.6°C (mean = -10.1°C). The calculated salinities from these twelve inclusions are between 8.9 and 18.3 wt% NaCl equivalent (Bodnar, 1993), or 2.5 to 5X that of seawater (Figure 5.14).

Homogenization temperatures (Th) from seventeen individual inclusions in quartz (phase 20) range from 109 to 192°C, with an average of 145°C (Figure 5.14). A similar spread in the temperature of first melt also exists – varying from –39 to –56°C. The average value, based on twelve individual inclusions, is -46°C. This spread in the temperatures of first melt suggest composition of the precipitating fluid was extremely complex and likely evolved through $NaCl\text{-}CaCl_2\text{-}H_2O$ and $NaCl\text{-}MgCl_2\text{-}H_2O$ systems (Goldstein and

Reynolds, 1994). Temperatures of final ice melt (Tm_{ice}) range from –8.0 to –17.2°C, with an average of –9.7°C for seventeen individual inclusions. This temperature range corresponds to salinities of 11.7 and 20.4 wt% NaCl equivalent (Bodnar, 1993), or roughly 3 to 6X the salinity of normal seawater (Figure 5.14).

Twenty inclusions in late blocky calcite (phase 25) cement have homogenization temperatures that range from 139 to 212°C (mean = 170°C) (Figure 5.14). First melt temperatures from seventeen individual inclusions range from –39 to –56°C (mean = -48°C): nearly identical to temperatures from quartz inclusions. Ice melting temperatures vary from –7.2 to –11.6°C (mean = -9.3°C). The calculated salinities from these twenty inclusions are between 10.7 and 15.6 wt% NaCl equivalent (Bodnar, 1993), or roughly 3 to 4.5X that of normal seawater (Figure 5.14).

Microthermometry Discussion

Results from the fluid inclusion heating-freezing runs indicate that both GMD and SD were formed from hot, saline brines (Figure 5.13). Furthermore, these data can be correlated to the pristine (unrecrystallized) GMD, recrystallized GMD, SD formed from recrystallization of GMD, and SD cement, as recognized in core and thin section. All temperatures of formation (replacement, recrystallization, and cementation) discussed in this section are considered minimum temperatures, as no pressure correction has been applied to the homogenization temperatures. The resulting shift should not be deemed significant considering the uncertainties in the assumptions and calculations made later (regarding temperatures calculated from oxygen isotope values, of thermal maturation and maximum burial).

GMD samples, save those in well d-79-F, suggest formation from fluids with salinities approaching 7X normal seawater ("pristine GMD" in Figure 5.13A, with NaCl-eq. around 23–25 wt% and 140–160°C). These salinity values approach halite-saturation (26.3 wt% NaCl equivalent), which is the first indication in the fluid inclusion data set that the fluid that effected pervasive matrix dolomitization, thus causing the bulk of the diagenesis at Clarke Lake, was seawater evaporated nearly to halite-saturation (henceforth called "halite brine" regarding its salinity, or "connate brine" in comparison to the later invading fluids). This result is in agreement with the previously discussed Sr and Na trace element data in the GMD that suggests formation from a highly evaporated brine near the point of halite saturation.

A second indication that matrix dolomitization was effected by a halite brine arises from combining the fluid inclusion homogenization temperatures with the $\delta^{18}O$ values from the matrix dolomites. Taking the range of homogenization temperatures measured in the matrix dolomites along with their corresponding $\delta^{18}O$ values of –13.00 to –15.35‰ VPDB and applying the dolomite-H_2O equation of Land (1983) an estimate can be made regarding the original $\delta^{18}O$ composition of the dolomite-forming fluid(s). From these calculations, GMD from the west side of the Clarke Lake field would have formed from a fluid with a composition around +0.5 to +6.0‰ SMOW, while GMD from the east side of the field would have formed from a fluid that ranged from –2.0 to +5.0‰ SMOW (Figure 5.15A). These values are consistent with seawater evaporated to halite saturation (Knauth and Beeunas, 1986) allowing for a seawater range from about –3‰ SMOW (Popp et al., 1986; Carpenter et al., 1991) to about 0‰ SMOW (Muehlenbachs and Clayton, 1976). However, the oxygen isotope ratios of halite-saturated brines can vary by as much as about 5‰ as a function of humidity and uncertainties in the original seawater composition.

The hot fluid(s) that later invaded Clarke Lake had to mix with the connate brine, such that hydrothermal alteration was effected by this mixed fluid (henceforth also called hybrid fluid) that evolved along the large looping arrow shown in Figure 5.13B. The invading fluid was considerably hotter yet less saline than the halite brine from which the matrix dolomites had formed, such that the resulting hybrid fluid in which the bulk of GMD recrystallized, apparently with little petrographic change (GMD to reX GMD), was at temperatures up to 190°C with salinities between halite and gypsum saturation (reX GMD in Figure 5.13A). During further recrystallization to saddle dolomite and eventual precipitation of saddle dolomite cement the hybrid fluid cooled to about 120°C, with an apparent decrease in salinity to about gypsum saturation (about 16–17 wt % NaCl-eq. for Cement SD: Figure 5.13A). In other words, as a result of evolving water-rock ratios and with time, the hottest temperatures and lowest salinities shown by this data set come closest to the properties of the invading hot fluid (henceforth called "gypsum brine" or "hydrothermal fluid"). Proof that this fluid was hydrothermal will be provided in subsequent sections. Initially, before cooling and equilibrating with the surrounding rocks, the hybrid fluid was also hydrothermal.

Furthermore, the initial temperature and salinity of the hydrothermal fluid before

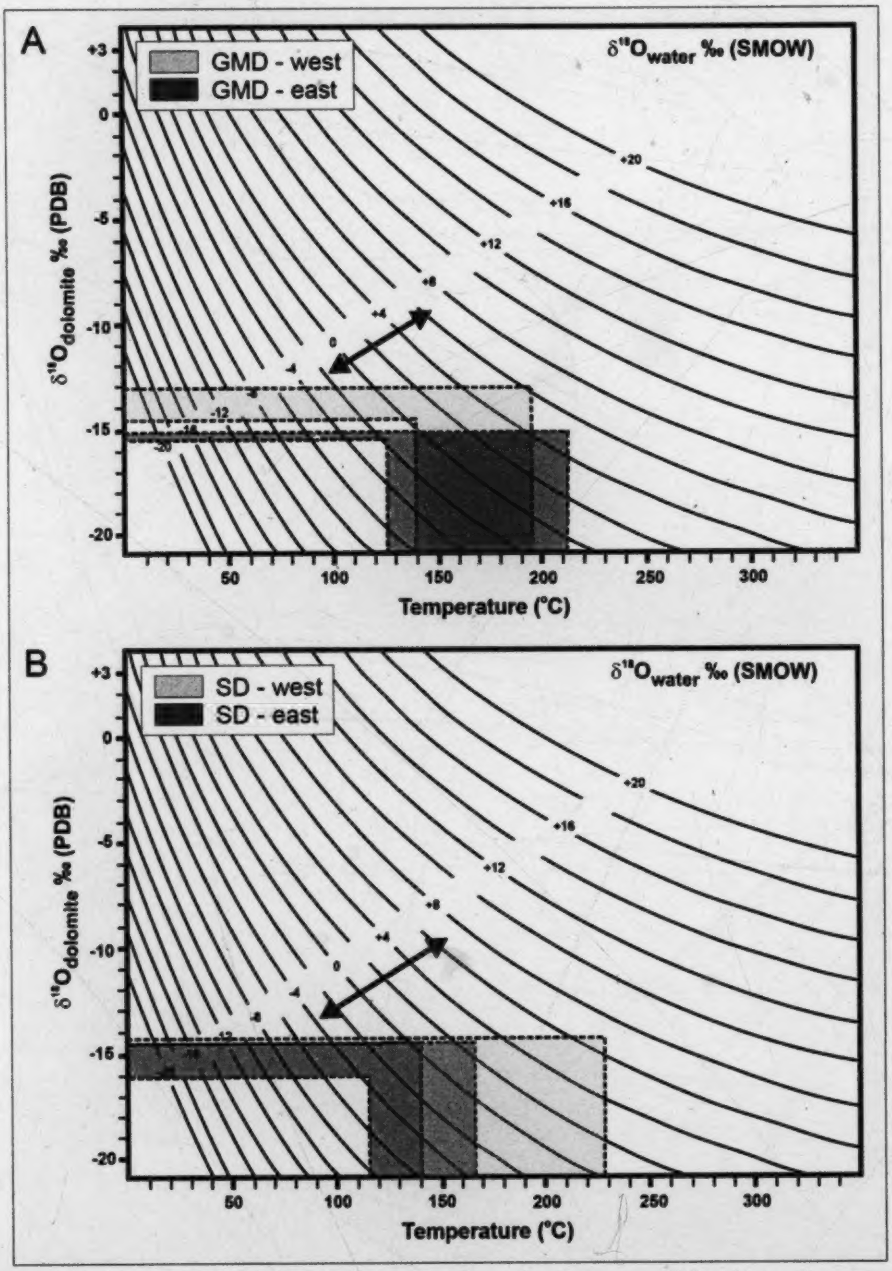

Figure 5.15 Plot of equilibrium isotope fractionation between dolomite and water, after Land (1983). West-east separation is based on the results presented in Figure 5.1B. The values for $\delta^{18}O_{dolomite}$ and temperature (from fluid inclusions) are from Figures 5.1 and 5.13, respectively. (A) Grey matrix dolomite (phase 10): west = +0.5 to +6.0‰ SMOW, east = -2.0 to +5.0‰ SMOW. (B) Saddle dolomite (phase 13): west = +0.5 to +7.0‰ SMOW, east = -3.5 to +3.0‰ SMOW. Arrows represent the range of possible dolomite-forming fluid compositions.

mixing must have been somewhat higher and lower, respectively, than 190°C and 16 wt% NaCl equivalent because both temperature and salinity were buffered by the invaded system, consisting of GMD and the connate halite brine at that time. When the hydrothermal fluid entered the bulk of the rocks in the central and eastern parts of Clarke Lake, the water-rock ratio was rather low, i.e., the mass of connate brine was high relative to the invading hydrothermal fluid. Hence, the bulk salinity of the formation was lowered only slightly, and the temperature rose only by a relatively small amount. Later, when much of the GMD had recrystallized and when saddle dolomite cement formed in the few open voids and fractures, the water rock-ratio in these voids and fractures was high, and the fluid therein was dominated by the invading gypsum brine, albeit significantly cooled.

Following this reasoning, the initial temperature of the invading hydrothermal fluid can only be found in rocks with an initially high water-rock ratio. This happens to be the case in well d-79-F in the westernmost part of the study area. The data from this well once again form a special distribution (Figure 5.13A). All previous data indicate injection of an "exotic" fluid via fault(s) into this well, hence, the water-rock ratio in this well must have been high to begin with, certainly in the vicinity of the fault(s) that carried the invading fluids. Hence, compared to the data from elsewhere in the Clarke Lake field, the fluid inclusion salinities should be lower and the temperatures higher, which is exactly what the data show. The temperatures in well d-79-F range from 140 up to about 230°C, and the salinities range from about 14 to 15 wt % NaCl eq., about 5X the salinity of seawater, a brine near gypsum saturation yet somewhat lower than the lowest salinities calculated for the other wells. Of all the temperature determinations from Clarke Lake samples, the highest values of 230°C (Figure 5.13) is herewith considered to be closest to initial temperature of the hydrothermal fluid. Applying a pressure correction to the homogenization temperatures would raise this temperature estimate somewhat.

The composition of the hydrothermal fluid may be estimated by applying the dolomite-H_2O equation of Land (1983). The $\delta^{18}O$ composition of the saddle dolomites do not vary significantly across the Clarke Lake field, ranging from –14.29 to –16.10‰ VPDB, while the homogenization temperatures range from 116 to 228°C. The resulting calculations indicate that the hydrothermal fluid had a potential $\delta^{18}O$ composition from –3.5 to +3.0, and +0.5 to +7.0‰ SMOW on the east and west sides of the field, respectively (Figure 5.15B). Further, a fluid composition closer to +7.0‰ SMOW is preferred upon consideration of the previous argument that the highest temperatures more than likely represent the pristine hydrothermal fluid. This value is consistent with the hydrothermal fluid being a brine near gypsum saturation (Knauth and Beeunas, 1986).

These data further show that GMD samples in well d-79-F, although petrographically not recognized as recrystallized, clearly contain fluid of recrystallization in their inclusions (box labelled reX GMD d-79-F in Figure 5.13A). The reX GMD samples in this well have compositions different from the petrographically equivalent samples elsewhere in the field presumably because of higher water-rock ratios in the immediate vicinity of the fault that sourced the invading fluid in d-79-F. This suggests that the fluid evolved from pristine GMD to re-X GMD along a different pathway in d-79-F (large straight arrow, Figure 5.13B) compared to the other wells. Moreover, these fluid inclusion microthermometry data are the second indication in the overall geochemical data set, in addition to the Sr and Mn trace element data, that GMD in well d-79-F has been significantly recrystallized, although this is not apparent texturally. This is consistent with the theory that recrystallization may change some properties while leaving others apparently pristine (see discussion in Machel, 1997). Furthermore, at the highest possible resolution of individual growth zones, discrete pulses of injection of heat are apparent (Figure 5.9B), suggesting once again episodic injection of the hot/hydrothermal fluid, probably during multiple faulting events, in well d-79-F. This more than likely also holds true for well d-58-E. The available data for this well, although scant (only a few values for Sr-isotopes), show that fluids of an exotic and roughly similar composition also invaded this well.

All other accessory minerals in the Slave Point Formation have fluid inclusion microthermometry data that support a continually evolving diagenetic fluid chemistry. Petrographically, sphalerite was the first post-saddle dolomite mineral that was formed from these diagenetic fluids. At the time of formation, this fluid had both temperatures and salinities that were similar to the replacement and cement saddle dolomites from the bulk of the Clarke Lake field (Figure 5.14). Sphalerite was followed by co-genetic barite and quartz precipitation. Both of these minerals have temperatures and salinities that are slightly lower than those measured in sphalerite, i.e., following fluid evolution arrow 1 in Figure 5.14. The extremely high temperatures from barite were recorded in the largest inclusions, and may represent fluid inclusions that had stretched as a result of heating and/or burial, and, therefore, are probably not representative of the conditions during formation. Later growth zones in quartz contain fluid inclusions that have much higher temperatures (around 160°C) but little change in salinity (Figure 5.14). Similarly, fluid inclusions in late calcite cement show a slight increase in temperature (around 180°C) but little change in salinity from the fluid that precipitated quartz. Therefore, from the time of barite mineralization, the diagenetic fluid evolved along arrow 2 in Figure 5.14. The insignificant change in salinity of this fluid over this time span may imply no change in the fluid chemistry, either through dilution or fluid flushing. The large increase in temperature between barite and late-stage calcite, between 60 and 80°C over the same time interval may be the result of either an increase in heat flow, which would manifest itself as an increase in the geothermal gradient, or an increase in the ambient temperature of the Slave Point as a result of increased burial. The homogenization temperatures from late calcite cements are similar to those presented by Morrow et al. (1990) in the Manetoe facies of the Northwest and Yukon territories, Morrow et al. (2002) in the Keg River Formation of northeastern British Columbia, and Qing and Mountjoy (1994a; 1994b) in the Presqu'ile facies from the subsurface of British Columbia. Save for Qing and Mountjoy (1994a; 1994b), the calcite cements in these studies were interpreted to have formed by the end of the Paleozoic. However, at that time, the host-rocks would only have been buried to a maximum of a few kilometres, hence, a 60 to 80°C increase in temperature simply as the result of burial seem unrealistic; rather, these temperatures would require a thermal anomaly. Alternatively, Qing and Mountjoy (1994b) concluded that calcite cements in the Presqu'ile facies post-date significant burial, i.e., greater than 3 kilometres, during the Late Cretaceous to early Tertiary. In this option, an increase in burial of only 2 km would account for a temperature increase of at least 60°C, assuming a normal geothermal gradient. At this point though, neither alternative can be discounted. Later discussions on the burial and thermal history of the Slave Point Formation will provide some constraints for the interpretations.

Leachates

Halogen ratios, specifically Cl/Br, are useful as indicators for the source of salinity of a diagenetic fluid. This is a result of the conservative behaviour exhibited by both Cl and Br in solution. In addition, water-rock interactions will not normally affect the Cl and Br concentrations of solutions (Fontes and Matray, 1993), whereas the major cations, i.e., Na and K, may be modified (Yardley and Banks, 1995). As a result, the Cl/Br molar ratio is an important tool for distinguishing the source of diagenetic fluids, i.e., seawater (Cl/Br ~ 655), residual brines (Cl/Br < 655), fluids sourced from the dissolution of evaporite minerals (Cl/Br > 655).

The molar Cl/Br ratios from two samples of calcite cement (blocky calcite II - phase 25) are 514 and 369; from seven samples of matrix dolomite (GMD - phase 10) range from 630 to 333; from six samples of saddle dolomite (phase 13) range from 651 to 407; and, from one sample of sphalerite (phase 18) is 121. All samples are lower than the Cl/Br ratio of normal seawater. Furthermore, data from dolomite samples from well d-79-F are much more similar to the Cl/Br ratios of normal seawater than data from dolomite samples elsewhere in the Clarke Lake field. Data for other cations are listed in Appendix VII.

In order to further evaluate the origin of the diagenetic fluids, plots of the molar ratios Cl/Br, K/Br, and Na/Br were constructed (Figure 5.16). These plots are used in the analysis of fluid inclusion leachates because dilution of the paleofluids will not mask the origin of the solutes (e.g., Kesler et al., 1995; Gleeson and Turner, 2005). Data plotted in K-Cl-Br space are used to assess the possibility of exchange reactions (Figure 5.16A). In this figure, there is clear separation between most samples and the dolomites from well d-79-F. Four samples of GMD from the Clarke Lake field plot slightly above the seawater evaporation trajectory (SET) at a point between halite-saturation (HS) and epsomite-saturation (ES). This indicates that the diagenetic fluid that formed GMD was probably highly evaporated seawater and is the third data set to point towards matrix dolomite formation via halite-saturated brines. Additionally, the slight increase in the K/Br ratio suggests that prior to entering the Slave Point Formation, this fluid had interacted with rocks bearing K-feldspar. These data are similar to data from both matrix and saddle dolomites in the Northwest Territories, which were formed from slightly modified, evaporated seawater (Gleeson and Turner, 2005). The corresponding samples of SD plot along a trajectory back towards the SET close to halite-saturation. The two samples of calcite cement also plot in similar space, between gypsum-saturation (GS) and halite-saturation. This data set suggests that the halite-saturated brine that formed the bulk of the GMD samples was replaced by a later, slightly less-saline diagenetic fluid(s). The samples of GMD from well d-79-F show excessively high K/Br ratios, also indicating an increase in the K concentration of the dolomite-forming fluid. This increase in K has also been noted by Gleeson and Turner

Figure 5.16 Fluid inclusion electrolyte chemistry in the Slave Point Formation

(A) K-Cl-Br systematics of the dolomite and non-dolomite forming fluids. The K/Br ratios from both the matrix (phase 10) and saddle dolomites (phase 13) in well d-79-F/94-J-10 suggest the dolomite-forming fluid was enriched in potassium. Samples of matrix and saddle dolomite from the remainder of the Clarke Lake samples plot close near the seawater evaporation trajectory at a point past halite-saturation. The encircled fields represent data from dolomite hosted by similar age formations in the Northwest Territories (Gleeson and Turner, 2005). Data for the seawater evaporation trajectory (solid line) are from Fontes and Matray (1993). GS = gypsum saturation, HS = halite saturation, ES = epsomite saturation.

(B) Na-Cl-Br systematics of the dolomite and non-dolomite forming fluids. All samples of dolomite and calcite from Clarke Lake plot on or slightly above the seawater evaporation trajectory. Samples lying just above the evaporation trajectory may be the result of sodium depletion through water-rock interaction. Data from well d-79-F/94-J-10 suggests the dolomites were formed from seawater that was evaporated past the point of gypsum saturation. Data from matrix and saddle dolomites in the rest of the Clarke Lake field suggest formation from fluids evaporated past the point of halite saturation. The encircled fields represent data from dolomite hosted by similar age formations in the Northwest Territories (Gleeson and Turner, 2005). Data for the seawater evaporation trajectory (solid line) are from Fontes and Matray (1993). GS = gypsum saturation, HS = halite saturation, ES = epsomite saturation.

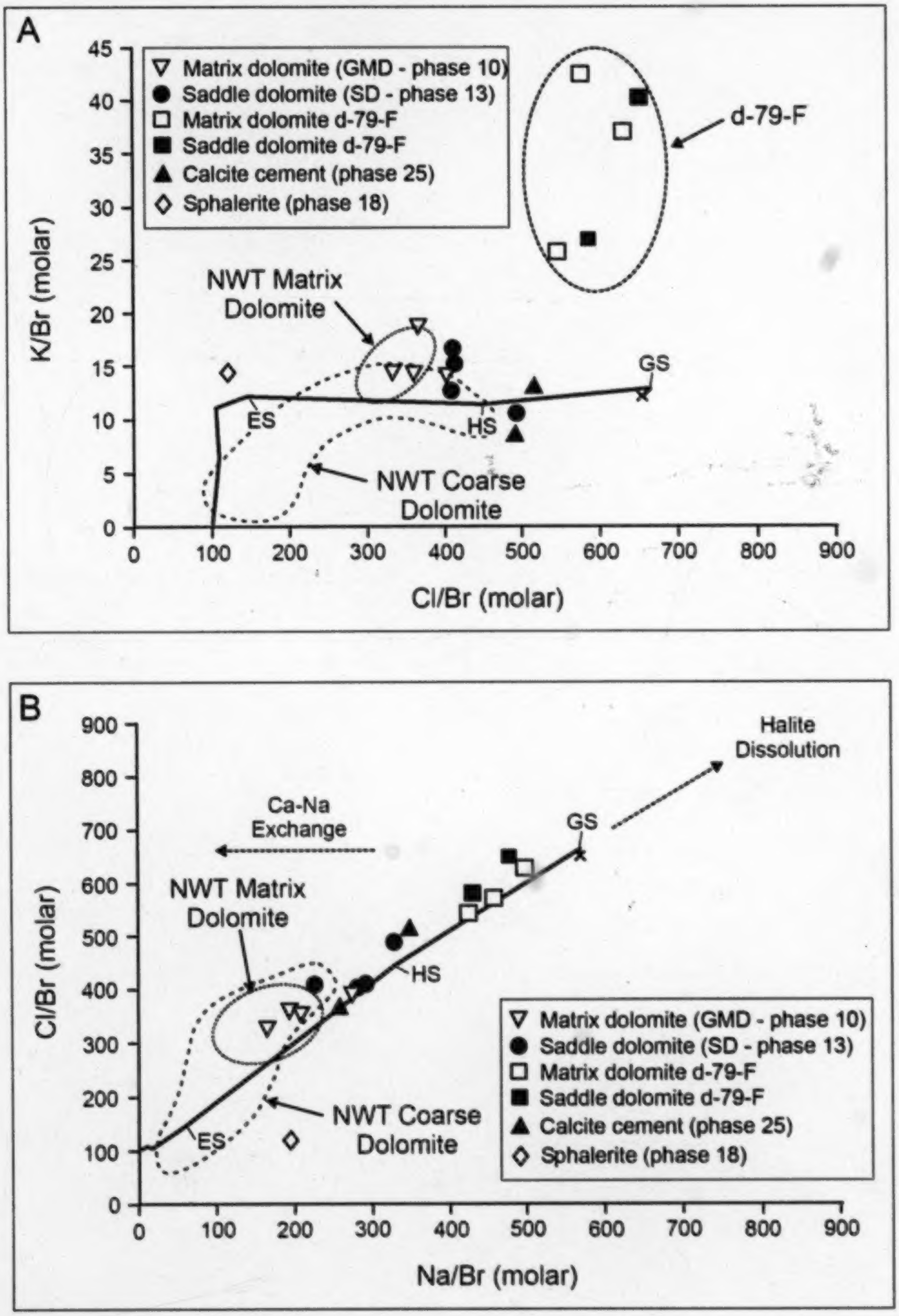
A
K/Br (molar)
Cl/Br (molar)
0
5
10
15
20
25
30
35
40
45
0
100
200
300
400
500
600
700
800
900
▽ Matrix dolomite (GMD - phase 10)
● Saddle dolomite (SD - phase 13)
☐ Matrix dolomite d-79-F
■ Saddle dolomite d-79-F
▲ Calcite cement (phase 25)
◇ Sphalerite (phase 18)
d-79-F
NWT Matrix Dolomite
NWT Coarse Dolomite
ES
HS
GS
B
Cl/Br (molar)
Na/Br (molar)
0
100
200
300
400
500
600
700
800
900
0
100
200
300
400
500
600
700
800
900
Halite Dissolution
Ca-Na Exchange
GS
NWT Matrix Dolomite
NWT Coarse Dolomite
HS
ES
▽ Matrix dolomite (GMD - phase 10)
● Saddle dolomite (SD - phase 13)
☐ Matrix dolomite d-79-F
■ Saddle dolomite d-79-F
▲ Calcite cement (phase 25)
◇ Sphalerite (phase 18)

(2005) from a small population of matrix and saddle dolomites from the Pine Point property in the Northwest Territories. They (ibid.) concluded that this increase was the result of fluid modification through interaction with either clastic or crystalline basement rocks. In Cl/Br space, the data from the d-79-F dolomites would lie along the SET between the points of gypsum-saturation (GS) and halite-saturation. Therefore, in comparison to the majority of the dolomites in the Clarke Lake field, GMD from well d-79-F show evidence for either formation from a fluid of distinct origin, or formation from a fluid of identical origin that migrated into the Slave Point Formation along a different flow path. However, as has already been noted previously, GMD from well d-79-F was interpreted as being recrystallized during the invasion of the hydrothermal fluid, and as such, is reflecting the chemistry of the fluid of recrystallization.

Data plotted in Na-Cl-Br space can also be used to assess the importance of diagenetic exchange reactions, as well as, dilution by meteoric fluids involved in halite dissolution (Figure 5.16B). Similar to what was observed in potassium space, there exists separation between samples from well d-79-F and those from the rest of the Clarke Lake field. Along the Cl/Br axis, there is no change in the position of the samples with respect to the SET; all samples were formed from diagenetic fluids that were highly evaporated. The salinity of these fluids is not the result of mixing with halite dissolution fluids, because otherwise these fluids would have Br concentrations less than seawater. Additionally, many of the samples lie slightly above the SET, which according to Walter et al. (1990), and Kesler et al. (1995) suggests a loss of Na in the diagenetic fluids as a result of interaction with feldspars. This exchange would probably involve the albitization of Ca-feldspars, which may also be reflected in the minimal increase in the K content of the majority of the samples (Figure 5.16A). However, the excess K content in dolomites from well d-79-F exclude Ca-Na exchange reactions, but rather, albitization of K-feldspars. This points towards diagenetic fluid migration along different flow paths. Finally, it should be noted that the single sample of sphalerite shows no relationship to any of the other samples (Figure 5.16B). The fluid that formed sphalerite was enriched in Br compared to evaporated seawater, an enigmatic fluid that has also been found in a few samples of matrix dolomite from the Great Slave Reef property in the Northwest Territories (Gleeson and Turner, 2005).

Cl/Br data from the calcites and dolomites also show a relationship to their bulk $^{87}Sr/^{86}Sr$ ratio (Figure 5.17). The Sr isotope data for each sample is shown in Table 5.6.

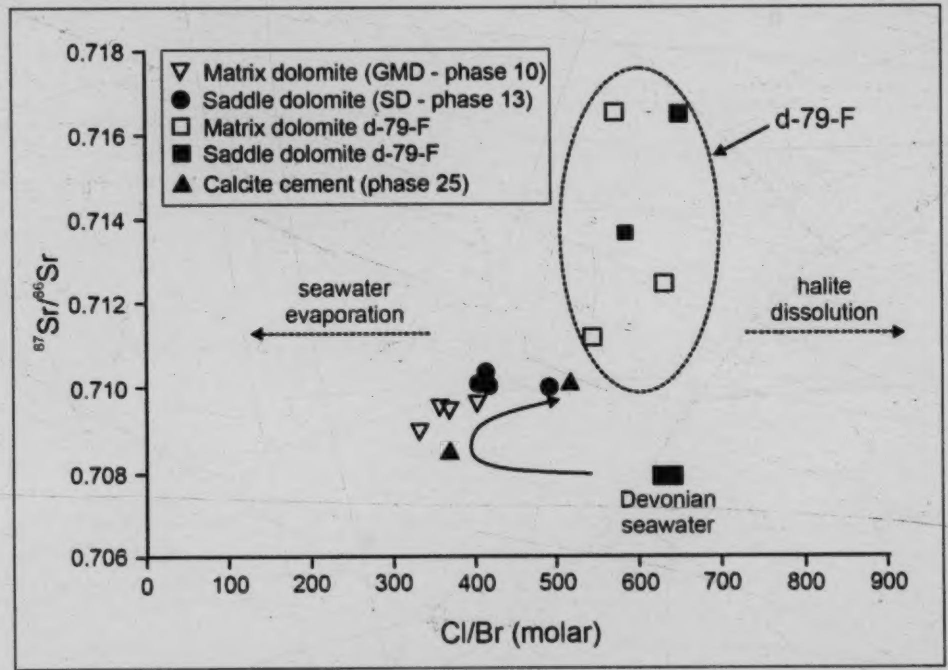

Figure 5.17 Crossplot of $^{87}Sr/^{86}Sr$ and Cl/Br results from dolomites and calcite cements. Squares = data from well d-79-F/94-J-10. Samples from d-79-F indicate the dolomite-forming fluid had a composition similar to seawater, but picked up radiogenic ^{87}Sr along its flow path. Samples from the remainder of the Clarke Lake field indicate the fluid(s) had a composition similar to highly evaporated seawater. The looping arrow demonstrates the chemical evolution of the fluid(s) - increased $^{87}Sr/^{86}Sr$ and lesser degrees of evaporation with increasing time. Values for Devonian seawater after Fontes and Matray (1993), and Denison et al. (1997).

From Figure 5.17, it appears that the diagenetic fluid(s) that entered the Clarke Lake field evolved along a path of increasing $^{87}Sr/^{86}Sr$ with lesser degrees of evaporation (solid arrow). The samples of GMD and SD from well d-79-F, however, do not show any discernible correlation between their Cl/Br ratios and their Sr-isotope ratios. It is clear that the diagenetic fluids were either of distinct origin, or migrated into the Slave Point Formation along different flow paths. However, based on the stable isotope and fluid inclusion microthermometry data, it has already been proposed that the hot fluid(s) that effected hydrothermal alteration of the pre-existing GMD was less saline than the halite brine from which the matrix dolomites had formed, and the chemistry of the dolomites in well d-79-F are a reflection of much higher water-rock ratios. So, the diagenetic fluids that entered most of the Clarke Lake field did not have a distinct origin to those in well d-79-F, but rather, were the result of mixing between the fluid that formed the GMD and the less saline hydrothermal alteration fluid under low water-rock ratios. This would explain both the lesser degrees of evaporation, based on the Cl/Br ratios, and the slight increase in the $^{87}Sr/^{86}Sr$ towards the lower limit displayed by samples from well d-79-F. However, the hydrothermal alteration fluid around well d-79-F must have also migrated along a different flow path to obtain such radiogenic Sr-isotope ratios.

The disadvantage of using the molar ratio plots discussed above is that mixing of fluid end-members can mask the actual source of the solutes (Chi and Savard, 1997). To remedy this problem, it is necessary to calculate the absolute concentrations of Cl and Br in the fluid inclusions. The absolute concentrations were recalculated using the bulk solute data and the salinities determined by microthermometry using the formula published in Banks et al. (2002). The resulting concentrations are listed in Appendix VII. To minimize the error involved in this calculation, the absolute concentrations are generally plotted in logarithmic form. Values of log Cl and log Br for GMD range from 5.07 to 5.16 ppm and 2.87 to 2.99 ppm, respectively, whereas log Cl and log Br for SD samples range from 2.66 to 2.82 ppm and 4.93 to 5.08 ppm, respectively (Table 5.6). Once again, well d-79-F stands out. GMD from well d-79-F has log Cl values that range from 4.94 to 5.02 ppm, while log Br values vary from 2.56 to 2.61 ppm. Corresponding log Cl values from SD range from 4.95 to 4.96 ppm, and log Br values between 2.50 and 2.53 ppm (Table 5.6). All of these values are significantly higher than those for normal seawater calculated by Fontes and Matray (1993), plotting near the seawater evaporation trajectory between gypsum- and halite-saturation (Figure 5.18).

Data from fluid inclusions in GMD from the bulk (eastern) part of the Clarke Lake field form two tight clusters (Figure 5.18). Thereby, the petrographically least altered samples, closest to pristine composition, plot near a halite-saturated brine, thus solidifying the interpretation that a halite brine acted as the principle dolomitizing fluid at Clarke Lake. These data again overlap with similar age dolomites from the Northwest Territories that were interpreted to have formed from comparable brines (Gleeson and Turner, 2005). Further, the recrystallized GMD samples are displaced toward lower salinities; and the SD samples line up with the GMD samples toward yet lower salinities that are consistent with a gypsum-saturated brine, albeit somewhat lower in Cl^- concentration and/or higher in Br^-

Well Location - NTS	Sample	T_h (°C) range	T_m (°C) range	Salinity[1] average	log Cl ppm	log Br ppm	$^{87}Sr/^{86}Sr$[2]	$T_{Na\text{-}K}$[3] (°C)
c-56-L/94-J-9	CC-1	187-193	-7.2 to -7.4	10.9	4.82	2.46	0.71014	181
b-6-A/94-J-16	CC-1	139-145	-10.9 to -11.6	15.1	4.96	2.75	0.70849	174
c-56-L/94-J-9	GMD-1	149-177	-16.8 to -22.1	21.6	5.12	2.87	0.70969	206
c-94-L/94-J-9	GMD-1	155-212	-17.2 to -17.5	19.4	5.07	2.87	0.70953	233
d-79-F/94-J-10	GMD-1	179-190	-12.6 to -13.6	17.1	5.02	2.57	0.71648	260
d-79-F/94-J-10	GMD-2	181-189	-12.6 to -13.4	17.0	5.01	2.81	0.71244	239
d-79-F/94-J-10	GMD-3	184-195	-9.9 to -11.9	14.5	4.94	2.56	0.71119	220
d-72-G/94-J-10	GMD-1	143-163	-21.0 to -22.0	23.5	5.15	2.94	0.70955	266
b-10-D/94-J-16	GMD-1	159-189	-21.6 to -23.1	23.7	5.16	2.99	0.70899	255
c-56-L/94-J-9	SD-1	158	-10.0	13.9	4.93	2.67	0.71008	196
c-94-L/94-J-9	SD-1	116-157	-11.7 to -13.3	16.5	5.00	2.66	0.71005	171
d-79-F/94-J-10	SD-1	150-204	-8.8 to -13.6	15.0	4.96	2.50	0.71649	251
d-79-F/94-J-10	SD-2	140-228	-8.2 to -13.5	14.6	4.95	2.53	0.71365	223
b-70-I/94-J-10	SD-1	155-159	-15.4 to -17.8	19.8	5.08	2.82	0.71008	230
b-10-D/94-J-16	SD-1	139-161	-14.1 to -22.9	22.1	5.13	2.87	0.71034	217
c-8-D/94-J-16	SP-1	133-140	-14.6 to -15.2	18.6	5.04	3.31	-	239

[1] Salinity in wt% NaCl equivalent

[2] Values from carbonate analyses

[3] Calcualated using Na-K geothermometer (Fournier, 1981)

Table 5.6 Fluid inclusion microthermometry and concentrations of the solutes in the fluid inclusion fluids.

concentration compared to the seawater evaporation trend (Figure 5.18). This displacement is to be expected, as the fluid in these samples was the result of mixing of a halite brine with a gypsum brine, with the hybrid brine being altered ionically by the hydrothermal alteration processes itself (the hybrid brine would remain unaltered only if it did not do any diagenetic work, i.e., such as dissolution, recrystallization, and/or cementation). These processes apparently resulted in a slight depletion in Cl^- and/or enrichment in Br^- concentration, and also led to the other subtle ionic changes in the fluid that have already been discussed, i.e., K and Na.

The samples from well d-79-F once again plot as a distinct group and right on the evaporation curve between halite and gypsum saturation (Figure 5.18). This is to be expected considering the higher water-rock ratio in this well, which prohibited or swamped the ionic changes observed in the other wells. Also, the data from well d-79-F plot within the field of brines of similar composition in the Devonian Southesk-Cairn carbonate complex just south of the Peace River Arch (Michael et al., 2003). Although these brines are a fair distance away from Clarke Lake (they are the geographically closest data available), they show that brines with salinities between gypsum and halite saturation do exist at present

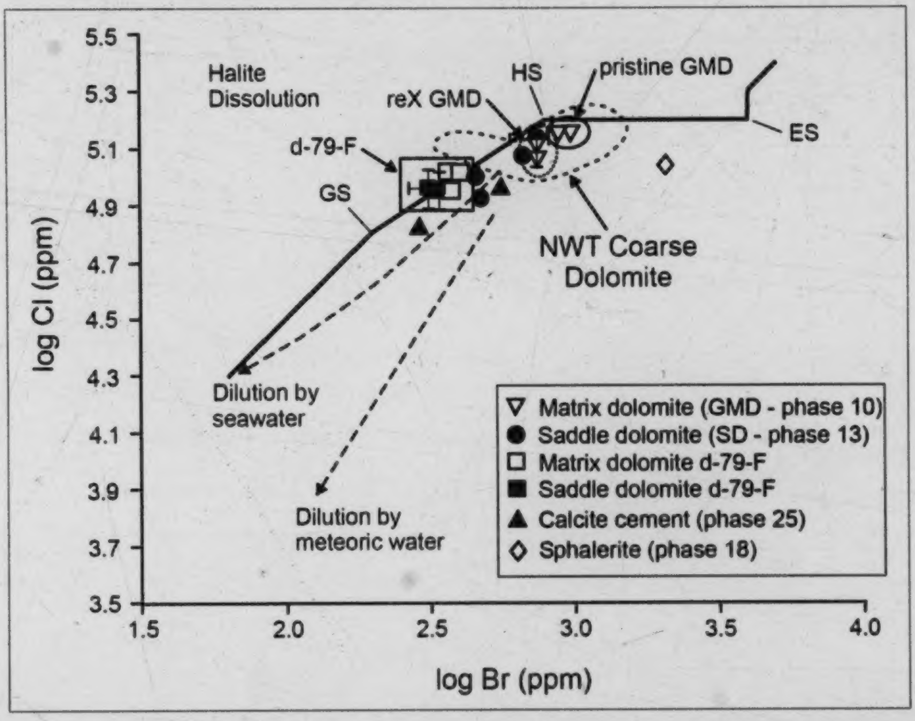

Figure 5.18 Crossplot of Cl and Br concentrations (Carpenter, 1978) with data from Clarke Lake fluid inclusions. Squares = samples from well d-79-F/94-J-10. Data from well d-79-F/94-J-10 suggests the dolomites were formed from seawater that was evaporated past the point of gypsum saturation. Data from matrix dolomites (phase 10) in the rest of the Clarke Lake field suggest formation from fluids evaporated past the point of halite saturation. See Figure 5.13 for an explanation of pristine GMD and reX GMD. Data from corresponding samples of saddle dolomite (phase 13) indicate the fluid evolved along a trajectory towards the field containing samples from d-79-F. The encircled fields represent data from dolomite hosted by similar age formations in the Northwest Territories (Gleeson and Turner, 2005). Solid line = evaporation of seawater (after Fontes and Matray, 1993). GS = gypsum saturation; HS = halite saturation; ES = epsomite saturation.

in parts of the Alberta Basin, thus lending support to the notion that such brines are to be expected as diagenetic agents in the Devonian strata north of the Peace River Arch, past or present.

The absolute concentrations of both K and Na were also calculated using the Banks et al. (2002) method. The data for these cations are listed in Appendix VII. When these data are plotted against the absolute concentrations of Cl, again, it is apparent that dolomites from well d-79-F formed from diagenetic fluids that were dissimilar to those infiltrating the rest of the Clarke Lake field (Figure 5.19). There is also evidence for mixing of fluid end-members based on the somewhat linear correlations between samples. In Figure 5.19A, the matrix and saddle dolomites appear to have formed from mixing of fluids A and C; fluid A representing a highly evaporated brine between halite-saturation and epsomite-saturation, and fluid C representing a fluid between seawater and gypsum-saturation. However, as has been discussed previously, the dolomites from the bulk of the Clarke Lake field have geochemical characteristics that indicate they experienced alteration, i.e., recrystallization, by a later hydrothermal fluid. Therefore, the best estimate for the composition of this hydrothermal fluid is represented by fluid end-member C. Similarly, the dolomites from well d-79-F show a linear array towards another fluid end-member: fluid B. Yet, this trend in all probability does not represent mixing: only exchange reactions with underlying clastics or basement rocks. These trends are also apparent when examining the Na contents (Figure 5.19B): the original dolomite-forming fluid (A) was evaporated past the point of halite-saturation, the later hydrothermal fluid (C) was significantly less saline. The only noteworthy difference between the two figures is the fact that the composition of fluid C is closer to the point of gypsum-saturation in Figure 5.19B.

In summary, the fluid inclusion data indicate pervasive dolomitization by a halite-saturated brine with a temperature of about 150°C (without pressure correction), followed by hydrothermal alteration in a mixed brine that resulted from the invasion of a gypsum brine that had an initial temperature of at least 230°C (without pressure correction). In addition, wells d-79-F, d-58-E (based on Sr-isotopes), and c-56-L (based on trace elements) show a slightly different fluid evolution compared to the rest of the field, presumably as a result of a higher water-rock ratio. A part of the geochemical differences between these two wells and the rest of the field may be due to true geochemical differences in the injected fluids, but they could also be the result of variable water-rock ratios.

Figure 5.19 Crossplots of absolute concentrations of fluid inclusion fluids

(A) Crossplot of K and Cl concentrations from samples subjected to fluid inclusion crush-leach analysis. Squares = data from well d-79-F/94-J-10. Samples of matrix (phase 10) and saddle dolomite (phase 13) from the bulk of the Clarke Lake field plot along a linear path with one end-member fluid composition (labelled A) lying between halite and epsomite saturation, and the other end-member fluid composition (labelled C) lying between normal seawater and gypsum saturation. Samples of matrix and saddle dolomite from well d-79-F also plot along a linear path between end-member C and a fluid of unknown origin (labelled B). This trajectory towards high concentrations of K is likely the result of water-rock interaction along the fluid flow pathway, as is suggested by the K/Br shown in Figure 5.16A. Seawater evaporation trajectory (solid line) after Fontes and Matray (1993). GS = gypsum saturation, HS = halite saturation, ES = epsomite saturation.

(B) Crossplot of Na and Cl concentrations from samples subjected to fluid inclusion crush-leach analysis. Squares = data from well d-79-F/94-J-10. Samples of matrix (phase 10) and saddle dolomite (phase 13) from the bulk of the Clarke Lake field plot along a linear path with one end-member fluid composition (labelled A) lying between halite and epsomite saturation, and the other end-member fluid composition (labelled C) lying near the point of gypsum saturation. Samples of matrix and saddle dolomite from well d-79-F also plot along a linear path between end-member C and a fluid of composition lying between halite and gypsum saturation (labelled B). Seawater evaporation trajectory (solid line) after Fontes and Matray (1993). GS = gypsum saturation, HS = halite saturation, ES = epsomite saturation.

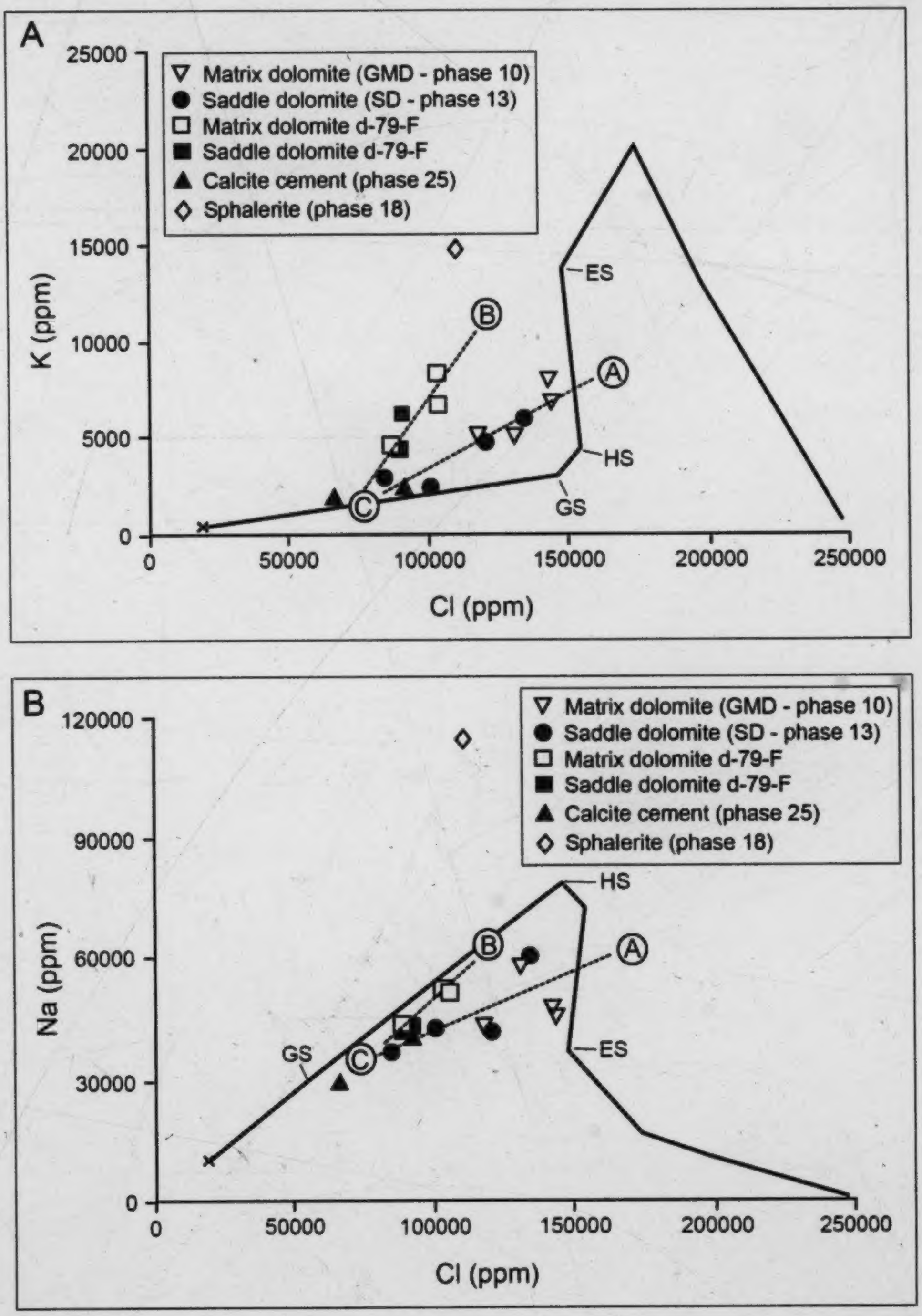
A
K (ppm)
25000
20000
15000
10000
5000
0
Cl (ppm)
0
50000
100000
150000
200000
250000
▽ Matrix dolomite (GMD - phase 10)
● Saddle dolomite (SD - phase 13)
☐ Matrix dolomite d-79-F
■ Saddle dolomite d-79-F
▲ Calcite cement (phase 25)
◇ Sphalerite (phase 18)
Ⓐ
Ⓑ
Ⓒ
ES
HS
GS
B
Na (ppm)
120000
90000
60000
30000
0
Cl (ppm)
0
50000
100000
150000
200000
250000
▽ Matrix dolomite (GMD - phase 10)
● Saddle dolomite (SD - phase 13)
☐ Matrix dolomite d-79-F
■ Saddle dolomite d-79-F
▲ Calcite cement (phase 25)
◇ Sphalerite (phase 18)
Ⓐ
Ⓑ
Ⓒ
HS
ES
GS

5.3.5 Rare earth elements

The same forty samples of various generations of calcite and dolomite that were analyzed for their trace element composition were also analyzed for their rare earth element (REE) composition. The raw data are tabulated in Appendix V.

Introduction

The REEs, Lanthanum to Lutetium (atomic numbers 57-71), have similar chemical and physical properties, which results in predictable geochemical behaviour. Most important of all is the fact that all REEs are found in the 3+ oxidation state with the exceptions of Cerium (Ce) and Europium (Eu), which may occur in 4+ and 2+ states, respectively.

In order to identify trends within the REEs, the absolute concentrations are normalized by dividing the analyzed abundance by the abundance of REE from a standard. All REE concentrations from the Slave Point carbonates are/have been normalized against values for chondritic meteorites (Taylor and McLennan, 1985) (Table 5.7). This eliminates large-scale fluctuations in the absolute concentrations (e.g., ppm to sub-ppb), and results in smoothed plots that allow for recognition of depletion or enrichment of each REE with respect to the standard. Peaks and depressions in the REE distributions are referred to as positive and negative anomalies, respectively. These plots can then be used for comparison against previous studies on dolomite REE chemistry (Graf, 1984; Banner et al., 1988; Dorobek and Filby, 1988; Qing and Mountjoy, 1994c; Qing, 1998).

Anomalies in the REE patterns are usually the result of the partitioning behaviour of Ce and/or Eu. However, since carbonates do not appear to fractionate either Ce or Eu relative to adjacent REEs, the incorporation or exclusion of Ce and/or Eu is likely the result of changes in the redox conditions of the fluids from which the carbonates formed (Henderson, 1984; Fleet, 1984). In most surface to near-surface environments, Eu will occur in the 3+ oxidation state, and will substitute in the carbonate lattice (Dorobek and Filby, 1988). However, under reducing conditions, as would be expected in the subsurface, negative Eu anomalies would be expected since Eu in the 2+ oxidation state does not readily substitute in the carbonate lattice (Dorobek and Filby, 1988). In contrast, negative Ce anomalies from marine carbonates formed in near-surface oxidizing environments are the result of Ce removal by Fe-Mn oxides or scavenging by particulate matter (Elderfield et al., 1981; DeBaar et al., 1985; Dorobek and Filby, 1988).

Phase		La	Ce	Sm	Eu	Tb	Yb	Lu	K (ppm)	Al (ppm)
					*Chondrite Normalized					
Limestone (4)	min.	1.80	0.64	0.25	0.15	0.19	0.09	BDL	26	29
	mean	3.10	1.62	1.00	1.54	0.60	0.31	0.16	274	573
	max.	4.41	2.74	1.84	3.74	1.13	0.54	0.23	644	1383
	Std. Dev.	1.31	1.09	0.82	1.71	0.48	0.23	0.10	295	650
Fossils (2)	min.	1.28	-	0.04	-	-	-	-	37	35
	mean	1.46	1.32	0.21	0.39	0.27	0.18	0.45	42	41
	max.	1.63	1.32	0.39	0.39	0.27	0.18	0.45	46	46
	Std. Dev.	0.25	-	0.25	-	-	-	-	6	8
Calcite Cement phase 25 (7)	min.	0.65	0.29	0.10	0.13	0.08	0.06	-	19	4
	mean	5.35	3.43	2.48	5.91	1.31	0.54	0.34	25	32
	max.	13.90	7.76	6.02	23.32	2.88	1.16	0.55	35	87
	Std. Dev.	4.21	2.73	2.28	8.28	1.12	0.41	0.19	5	34
GMD phase 10 (15)	min.	1.03	0.87	1.20	1.19	0.62	0.20	0.09	40	137
	mean	3.85	2.98	2.19	1.77	1.37	0.88	0.97	455	1141
	max.	8.34	5.22	3.51	2.98	2.08	2.47	2.05	1522	3449
	Std. Dev.	2.41	1.49	0.75	0.54	0.46	0.57	0.81	454	978
SD phase 13 (11)	min.	1.62	1.50	0.84	0.74	0.66	0.41	0.30	22	149
	mean	3.07	2.64	2.62	3.47	2.01	1.13	0.99	61	309
	max.	5.59	6.32	7.19	10.18	5.79	3.04	3.54	101	466
	Std. Dev.	1.36	1.38	1.72	2.74	1.41	0.73	0.95	29	107

Table 5.7 Rare earth element (REE) results and K and Al contents by diagenetic phase from neutron activation analysis (NAA). Diagenetic phase numbers from Figure 4.1. The number of analyzed samples is reported in parenthesis. min. = minimum measured value, mean = arithmetic mean of measured values, max. = maximum measured value, Std. Dev. = standard deviation (1σ). REE results have been normalized against chondrite values (Taylor and McLennan, 1985).

REE abundances in natural waters (e.g., seawater, meteoric water, groundwater) are extremely low, with individual elements ranging from 10^{-6} to 10^{-4} ppm (Qing and Mountjoy, 1994c). Carbonate minerals that are precipitated from these fluids are enriched in REE contents by several orders of magnitude as a result of distribution coefficients on the order of 100 to 1000 (Palmer, 1985; Dorobek and Filby, 1988). The REE patterns in carbonates are sensitive to source material, solution chemistry, and water-rock interaction. They are not influenced by the type of flow system, i.e., open vs. closed, changes in the precipitation rate, or changes that may influence the concentrations of other trace elements or the stable isotope compositions (Graf, 1984). Since the concentrations of REEs in carbonate rocks are roughly 10^2 to 10^6X higher than the concentrations of REEs in natural waters, the resulting REE patterns of diagenetic phases such as dolomite should be similar to their precursors, e.g., limestone, at relatively low water-rock ratios (Dorobek and Filby, 1988; Qing and Mountjoy, 1994c). This is because most of the REE ions are derived from the dissolution of the precursor carbonate (Banner et al., 1988). Under high water-rock ratios, the absolute concentrations of the REEs should be lower than those formed under low water-rock ratios, but the overall REE patterns should be very similar since the REEs are still derived largely from dissolution of the precursor (Dorobek and Filby, 1988). The only time that diagenetic carbonates should record the REE signature of the diagenetic fluids is when water-rock ratios are extremely high ($> 10^4$) (Banner et al, 1988). This has important implications for the study of dolomite formation. As Qing and Mountjoy (1994c) pointed out, the minimum water-rock ratios required for dolomitization are significantly lower than the water-rock ratios required to modify the REE patterns of the precursor limestones. Therefore, examination of the REE patterns in the Slave Point Formation may shed light on the importance of faults with respect to the formation of dolomite.

Results

As discussed in Banner et al. (1988), carbonate samples containing more than 5% siliciclastic material, i.e., insoluble residue, may influence the REE concentrations. Petrographic evidence suggests that only a small number of samples, i.e., limited to well d-79-F, contain any noticeable authigenic clay minerals. This observation is similar to that of Qing and Mountjoy (1994c) for Devonian carbonates from the Presqu'ile Barrier – claiming that the REE contribution by non-carbonates is minor. For this study, a simple plot of the K and Al contents is used to further evaluate the potential for contamination in the Slave Point Formation (Figure 5.20). The majority of samples have K and Al contents below 150 and 600 ppm, respectively. The plot of the samples containing low K and Al contents (Figure 5.20 – inset) shows a very poor correlation, suggesting contamination is minimal. Samples that lie above this threshold are all matrix dolomites. These samples plot in a roughly linear correlation, and are probably reflecting the contribution of interstitial clays or other insoluble residues. However, before culling these samples, it should be noted that other samples of matrix dolomite plot in the low K and Al region (inset) that reflects minimal contamination. Additionally, as will be shown below, the overall REE patterns from all of the matrix dolomite samples are similar, and, therefore, the potential for REE contribution by the insoluble residue appears to be insignificant.

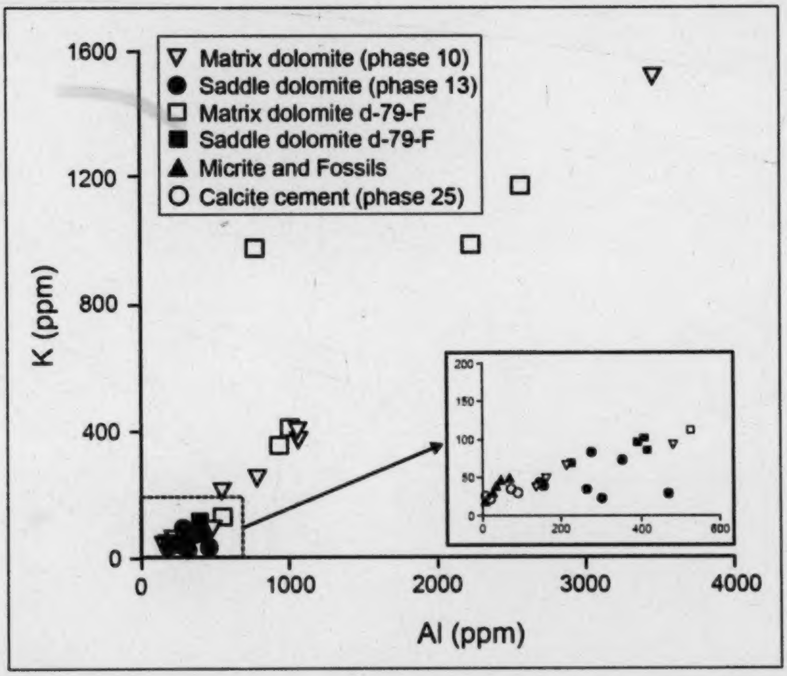

Figure 5.20 Crossplot of K and Al concentrations from all analyzed calcite and dolomite phases. High correlation between the two elements suggest contamination of the carbonate trace/REE results by clay minerals. Samples that display evidence of contamination are limited to matrix dolomites, likely due to the contribution of interstitial clays and/or other insoluble residues.

Four samples from the limestone matrix (micrite), and one sample from a stromatoporoid in well c-56-L were analysed for REE content. All samples display light REE enrichment (Figure 5.21A). The limestone samples from well b-6-A display slight negative Ce and Eu anomalies, while those from well c-56-L have distinct positive Eu anomalies. In contrast, the lone sample of biogenic calcite has a slight positive Ce anomaly, no noticeable Eu anomaly, and a marked positive Lu anomaly.

Seven samples of calcite cements (blocky calcite II – phase 25) that were obtained from four wells have markedly different REE patterns (Figure 5.21B). All samples, with the exception of the lone sample from well d-79-F, display a smoothed trend similar to the limestone samples: light REE enrichment. At least one of the two samples from well b-6-A has a negative Ce anomaly, similar to those seen in samples of limestone from the same well (Figure 5.21A). However, both calcite cements have small positive Eu anomalies,

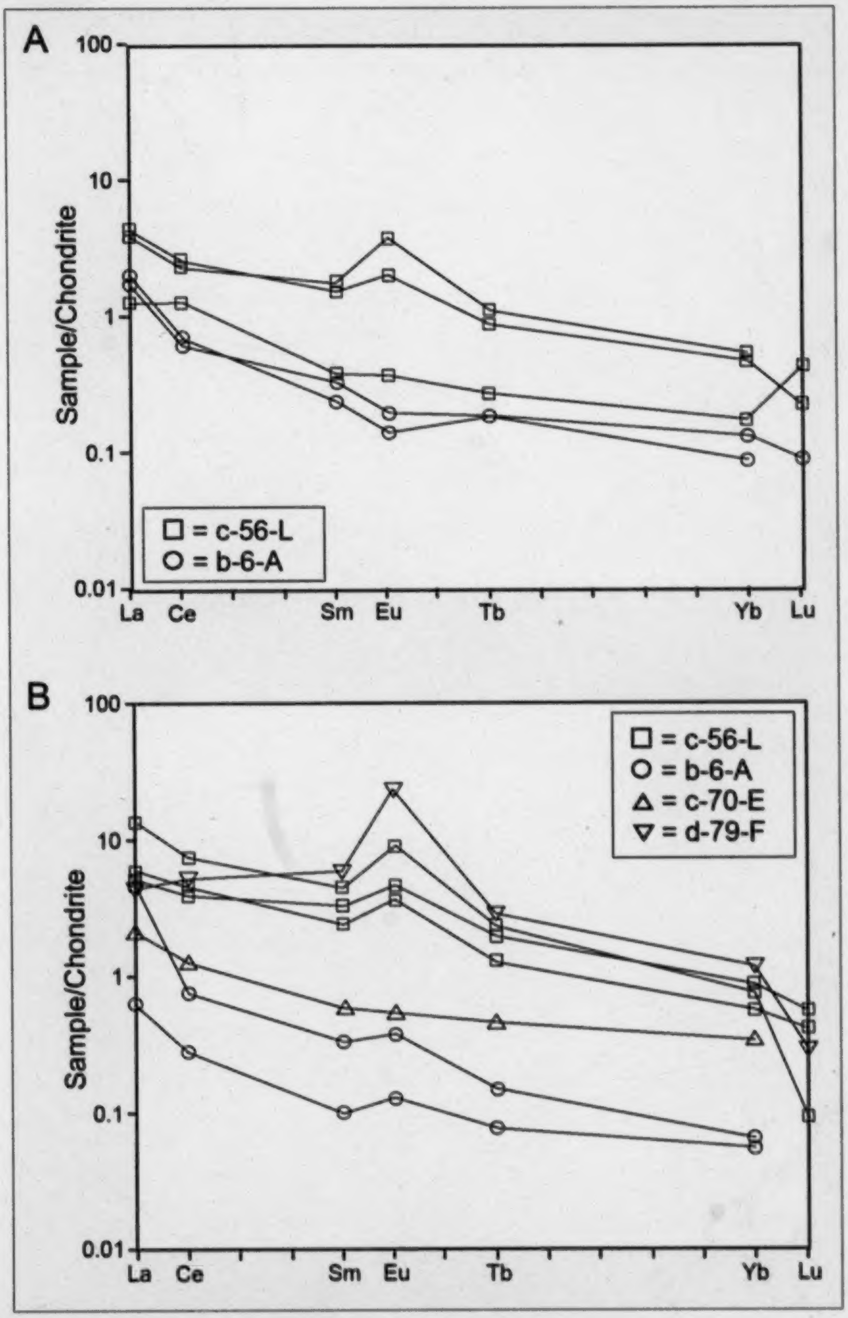

Figure 5.21 Rare earth element plots for calcite components.

(A) REE patterns of five limestone matrix (micrite) samples.

(B) REE patterns of seven calcite cement (blocky calcite II - phase 25) samples.

which were not observed in the limestones. The single sample from well c-70-E, which is located well within the platform interior, has no conspicuous REE anomalies (Figure 5.21B). Three samples from well c-56-L show an almost identical REE pattern to those observed in the corresponding samples of limestone: distinct positive Eu anomalies. The sample of cement from well d-79-F displays an increase from La through Sm, an extremely positive Eu anomaly, followed by a negative Lu anomaly of similar magnitude (Figure 5.21B).

Samples of GMD (phase 10) differ from both the limestones and calcite cements (Figure 5.22). Nine samples of GMD from four wells generally display enrichment in light REEs, show decreasing concentrations from La to Lu, and have no distinct Eu anomalies (Figure 5.22A). In contrast, five samples of GMD from well d-79-F do not show a preference for light REE fractionation over heavy REEs, display slight positive or negative Ce anomalies, increase in Sm contents, slight negative Eu anomalies, nearly constant profiles between Eu and Yb, and rarely display Lu anomalies (Figure 5.22B). The REE profiles from the majority of the GMD samples are similar to those observed in the limestone samples from well c-56-L (Figure 5.21A), while the REE profiles from GMD in well d-79-F do not appear to correlate with either samples of limestone or calcite cement.

The REE profiles exhibited by the saddle dolomite (phase 13) samples are similar to those from the corresponding samples of GMD. Seven samples of SD from four wells display enrichment in the light REEs, variable to absent Eu anomalies, and slight positive or negative Lu anomalies (Figure 5.23A). However, samples from well c-56-L depart significantly, having large positive Eu anomalies and relatively flat profiles (Figure 5.23A). Meanwhile, four samples of SD from well d-79-F display the relatively flat REE profiles that were characteristic of the corresponding GMD, with one obvious difference; the SD samples have slight positive Eu anomalies (Figure 5.23B).

Discussion

The REE profiles from samples of limestone in the Slave Point Formation are very similar to those presented by Qing and Mountjoy (1994c) for the marine limestones on the Pine Point property. In particular, samples from well b-6-A have negative Ce anomalies characteristic of precipitation from oxidizing surface fluids. However, the slight negative Eu anomalies are more than likely representative of recrystallization in the subsurface by

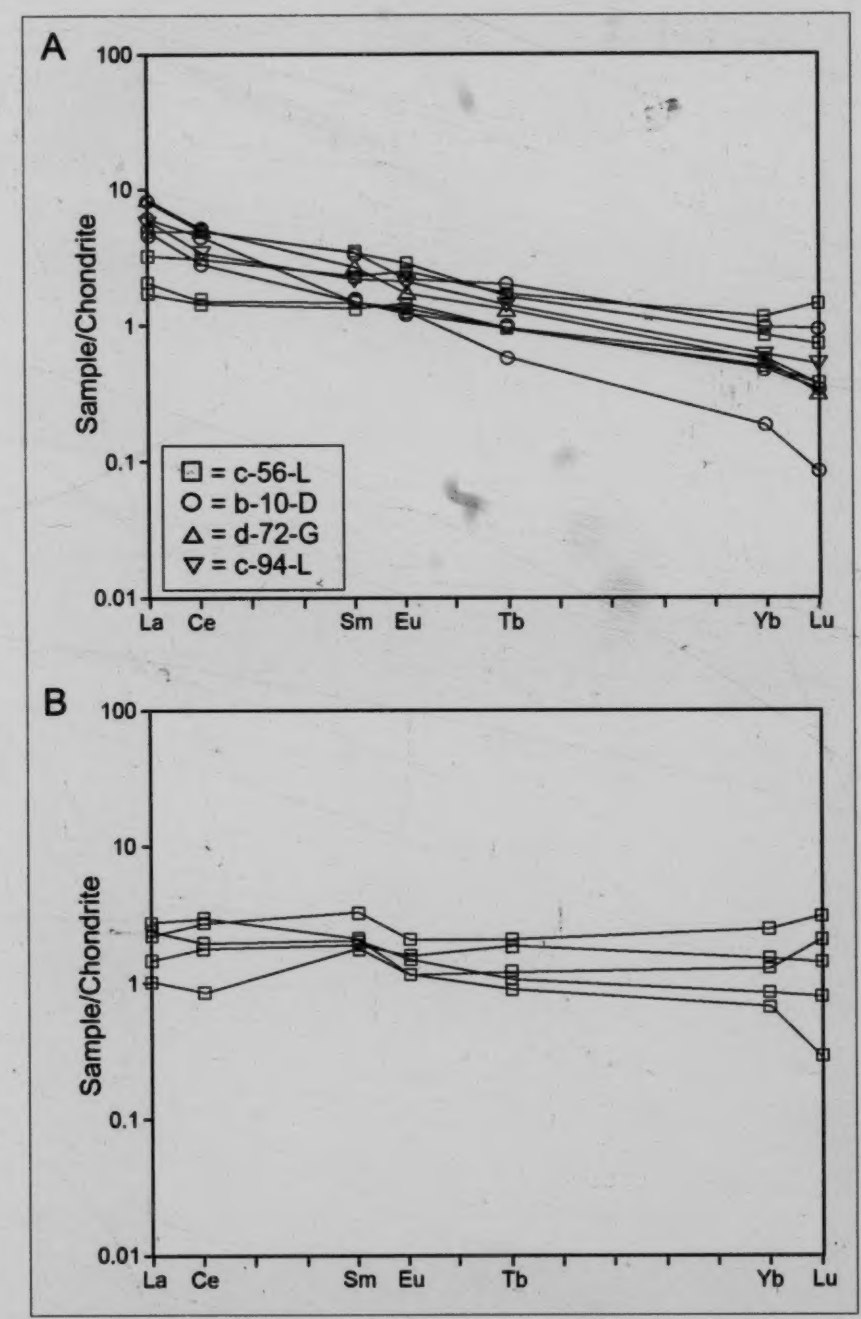

Figure **5.22** Rare earth element plots for matrix dolomites.

(A) REE patterns of nine matrix dolomite (GMD - phase 10) samples.

(B) REE patterns of five matrix dolomite samples from well d-79-F/94-J-10.

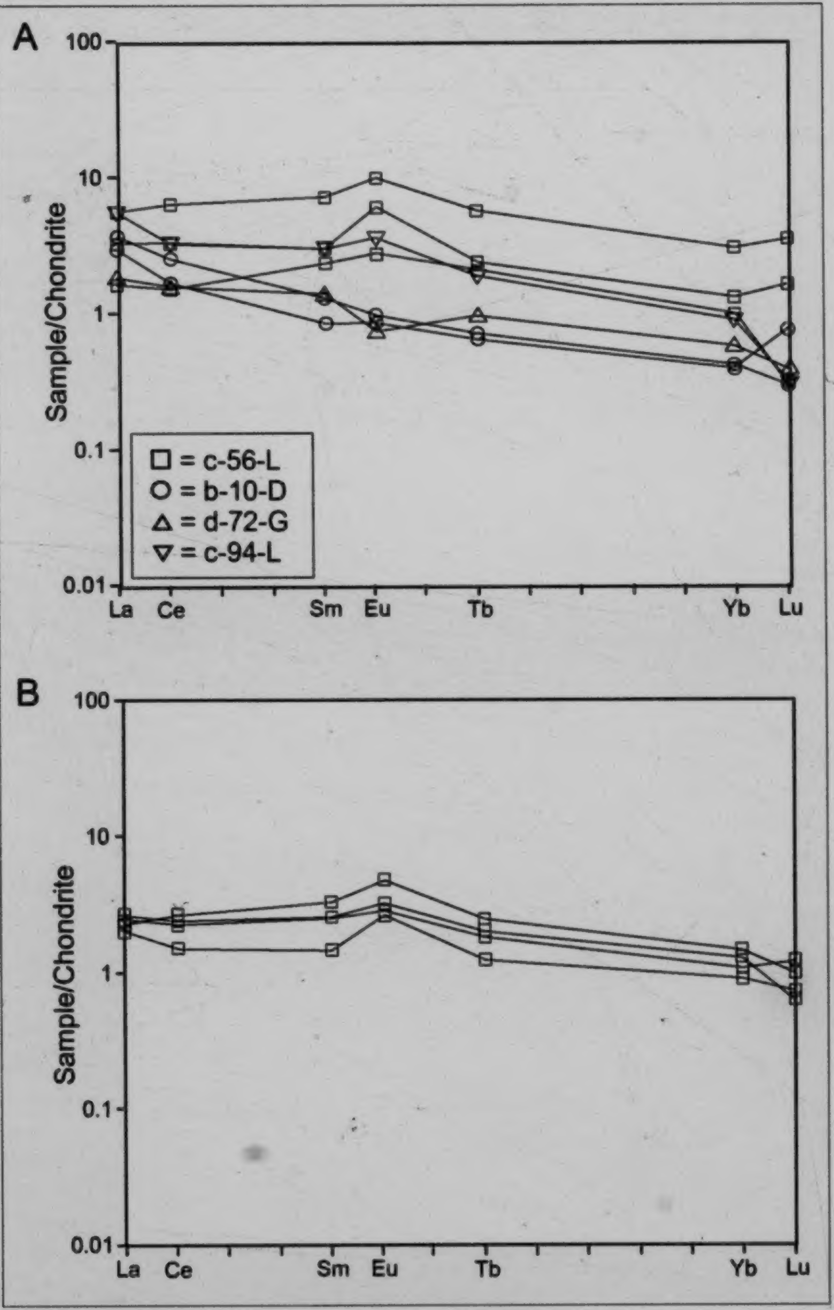

Figure 5.23 Rare earth element plots for saddle dolomites.

(A) REE patterns of seven saddle dolomite (phase 13) samples.

(B) REE patterns of four saddle dolomite samples from well d-79-F/94-J-10.

reducing pore fluids. This had already been suggested through examination of the isotope and trace element results (see sections 5.3.1 and 5.3.3). The sample of biogenic calcite (stromatoporoid) from well c-56-L does not contain an Eu anomaly, but has a slight positive Ce anomaly, which does not reflect precipitation from marine fluids; rather, this REE profile is likely the result of 'vital effects' on REE partitioning (Dorobek and Filby, 1988). The REE profiles exhibited by the limestone samples in well c-56-L, like well b-6-A, are a reflection of post-depositional recrystallization; not an unexpected result, considering much of the core from this well is dolomitized. Of particular note from the limestone samples in well c-56-L are the extremely positive Eu anomalies (Figure 5.21A). Positive Eu anomalies are exceedingly rare from previous studies of carbonate REE geochemistry (Graf, 1984; Banner et al., 1988; Dorobek and Filby, 1988; Qing and Mountjoy, 1994c), but have been documented in metamorphic rocks (Koszela, 2003), and some carbonate-hosted Pb-Zn deposits (Lu et al., 2003). Information presented in the previous section suggests that the only way to change the REE profile is to invoke large-scale fluid flow, i.e., water-rock ratios greater than 10^4 (Banner et al., 1988). This REE distribution is the fourth line of evidence to indicate that both the limestones and fossils were recrystallized. The isotope and trace element results point towards recrystallization by Devonian seawater that interacted with either underlying Cambrian sandstones, or Paleozoic shales, following significant burial, while the high water-rock ratios suggested by the REE results suggest that these diagenetic fluids migrated along open faults and fractures within the Clarke Lake field.

The REE profiles exhibited by the calcite cements (blocky calcite II – phase 25) are nearly identical to their corresponding host-rocks at the time of precipitation. Samples of calcite cement from well b-6-A are almost identical to coexisting limestones, with one noticeable difference, incorporation of a slight positive Eu anomaly (Figure 5.21B). Calcite samples from both wells c-56-L and d-79-F are, for the most part, identical to the host SD cements, including their positive Eu anomalies, suggesting relatively low water-rock ratios at the time of precipitation. Due to the similarities of the REE profiles between the calcite cements and the host dolomites, see the dolomite discussion for an explanation of the conditions during calcite precipitation.

The REE results from both GMD and SD support the interpretations obtained from the isotope, trace element, and fluid inclusion data, and add further detail. Taken together, these data suggest the following alternatives: (i) the pulses of fluid that were injected into the Clarke Lake field varied slightly in space and time; (ii) the observed elemental differences reflect variable water-rock ratios; or (iii) a combination of these two alternatives.

The REE distributions of matrix dolomites (GMD – phase 10) provide the second indication (see section on fluid inclusions) that GMD samples in well d-79-F are recrystallized, despite their petrographic similarity to matrix dolomites elsewhere at Clarke Lake. The remainder of the matrix dolomites have REE profiles that are consistent with corresponding samples of limestone, suggesting they are the product of dolomitization of the limestones. On the other hand, recrystallization, i.e., dissolution and reprecipitation, with extremely high water-rock ratios is the most likely way to change the REE distribution, whereby the injected fluids had a composition enriched in the heavy REEs, generating the overall flat REE distribution for GMD in well d-79-F (Figure 5.24A). The flat slope and slight negative Eu anomaly may be representative of the highly reducing nature of the GMD-forming fluid(s), as would be expected in the subsurface.

The REE profiles exhibited by both replacement and cement saddle dolomites (hydrothermal alteration - phase 13), with the exception of those from wells c-56-L and d-79-F, are nearly identical to the corresponding samples of GMD. Since the profiles are similar to the GMD host-rock, the REE ions were likely derived from the dissolution of the precursor dolomite (Banner et al., 1988), and, therefore, are representative of formation under relatively low water-rock ratios. Samples of SD from well d-79-F have flat slopes similar to corresponding GMD, but a positive Eu anomaly (Figure 5.23B). As mentioned previously, diagenetic carbonates with positive Eu anomalies are generally restricted to either marbles or high-temperature carbonate-hosted mineral deposits, and require large-scale fluid flow. Considering the petrographic evidence for Pb-Zn sulphide mineralization along post-saddle dolomite fractures in well d-79-F, the proposed mechanisms for anomalies in other carbonate-hosted sulphide deposits may apply here. Lu et al. (2003) found that diagenetic carbonates and sulphide minerals that formed almost concurrently in a massive Mississippi Valley-type (MVT) Pb-Zn deposit of China have significant positive Eu anomalies. They (ibid.) concluded that the REE profiles from the diagenetic carbonate minerals were the result of formation from a high temperature, highly reducing, Cl-rich brine. This supports the interpretation of all previous geochemical data that the saddle dolomites from well d-79-F are the product of highly evaporated, i.e., gypsum-

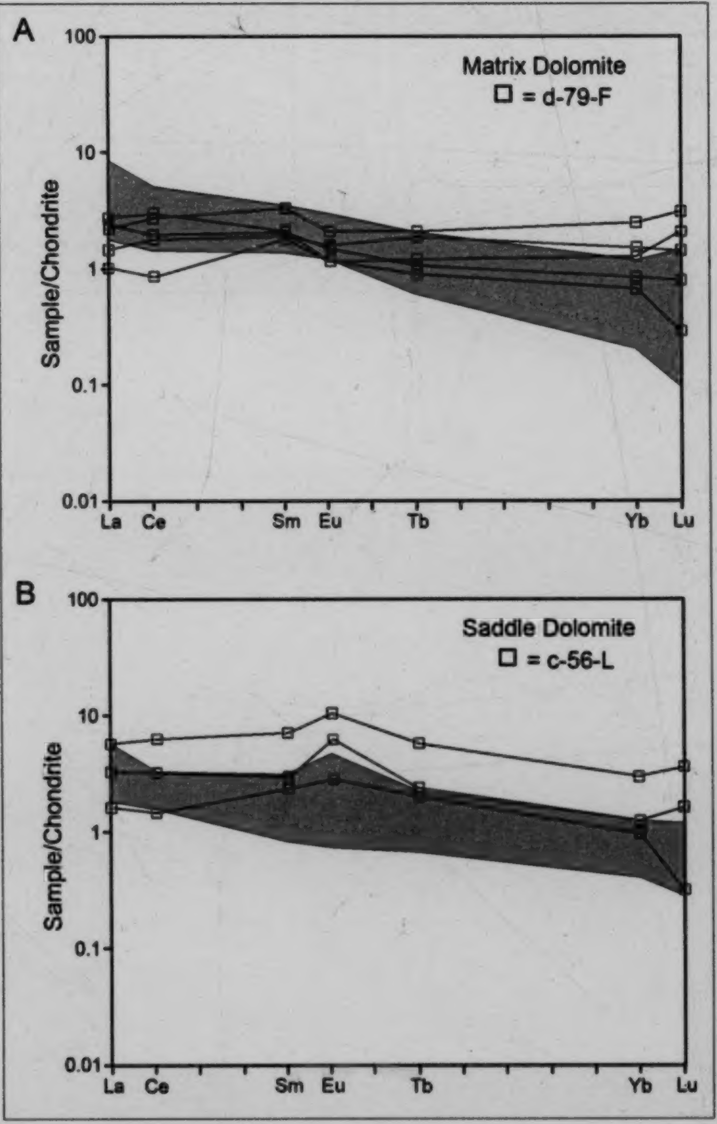

Figure 5.24 Rare earth element patterns resulting from hydrothermal alteration of the Slave Point Formation.

(A) REE patterns of five matrix dolomite (GMD - phase 10) samples from well d-79-F/94-J-10 (lines) and averaged pattern from matrix dolomites from the remainder of the Clarke Lake field (shaded area).

(B) REE patterns of three saddle dolomite (SD - phase 13) samples from well c-56-L/94-J-9 (lines) and averaged pattern from saddle dolomites from the remainder of the Clarke Lake field (shaded area).

saturated, hydrothermal fluids. Similarly, the fluid in well c-56-L during SD formation shows a positive Eu anomaly that is not exhibited by the corresponding samples of GMD. Petrographic evidence from this well indicates that SD occurs principally as an open-space and fracture-filling cement with little evidence of replacement textures (an observation that was confirmed by the stoichiometric differences between co-existing GMD and SD). Where GMD and SD samples from well d-79-F have distinctive trace element and REE distributions that are, for the most part, not matched by the other wells (Figures 5.22B, 5.23B), suggesting that some "exotic" fluid(s) was injected into these wells during matrix dolomitization and/or saddle dolomite formation, samples of SD from well c-56-L may represent an alternative. These samples have profiles that are much more similar to those from vug- and fracture-filling late-stage calcite cements (Figure 5.21B) than profiles of other SD samples from the Slave Point Formation (Figure 5.24B). This suggests that samples of SD from well c-56-L formed principally as passive cements, and, therefore, may be reflecting the much higher water-rock ratios associated with fluid flow within vugs or along fractures. Furthermore, the patterns for both wells are not identical, suggesting a locally variable geochemistry. Regardless of the mechanism for dolomite formation, the fluid composition was buffered by the "connate" bulk fluid already in the reservoir (an interpretation previously noted during the discussion on fluid inclusions), and the injected fluid would be recognizable only once its composition is no longer masked by that of the connate bulk fluid.

5.4 Burial and thermal history

The data and interpretations provided above permit rather far-reaching interpretations regarding the timing and temperatures of dolomitization and later hydrothermal alteration. However, the temperatures, although very hot for diagenetic settings, effectively grading into those typical for the low-grade metamorphic realm, have not yet been demonstrated to be hydrothermal. Proof of hydrothermal activity requires that the temperature of alteration and/or mineralization exceeded that of the wall rocks at the time of formation (Machel and Lonnee, 2002). To this end, a regional and/or local burial curve, including an assessment of the thermal evolution, are necessary. A burial curve provides further constraints on timing.

5.4.1 *Proof of hydrothermal activity*

There is a clear relationship between vitrinite reflectance and the presence of dolomite (both GMD and SD): vitrinite reflectance is highest, i.e., up to 2.45% Ro, where the Slave Point Formation is dolomitized, whereas values are closer to 1.95% Ro (Stasiuk and Fowler, 2002) (Table 5.8). Assuming that the limestone areas are representative of the regional thermal maturation, this finding indicates a hydrothermal anomaly associated with the formation of both dolomites, and thus hydrothermal activity, regardless of when exactly the hot fluids invaded.

The above maturation levels are equivalent to temperatures of about 189°C (regional, limestones) and 267°C (local, dolostones), respectively, using the Ro-T conversions suggested by Barker and Pawlewicz (1994) (Figure 5.25). The difference of 78°C between these two estimates is essentially identical to the difference in the uncorrected fluid inclusion temperatures between GMD and SD, which is 80°C (about 150 versus 230°C). This finding further suggests that pressure correction that has so far not been applied may/should be in the order of 80°C, which, by coincidence, is the difference between the two dolomite phases and the two methods under consideration here. Thus, the temperatures of 189/267°C may be the best approximations of the actual temperatures in Clarke Lake. The highest temperature thus determined for the dolostones is also within the range of temperatures obtained using the Na-K geothermometer on the dolomite leachates (Table 5.6). Taken together, the uncorrected and the corrected temperatures indicate a hydrothermal anomaly.

The question arises whether GMD or SD, or both, are hydrothermal. GMD must be interpreted as hydrothermal if their Th data are pristine, i.e., not reset during further burial and temperature increase during the Triassic and/or Late Cretaceous (see Figure 5.26). On the other hand, if those fluid inclusions are stretched, they represent the maximum burial temperature of the Slave Point Formation. In this case, using only thermal data as constraints, GMD could have formed at any time after limestone stylolitization and maximum burial in the Late Cretaceous, hydrothermally or geothermally (*sensu* Machel and Lonnee, 2002). The saddle dolomite at Clarke Lake is unequivocally hydrothermal, because the corrected regional maximum temperature (189°C) is lower than the uncorrected temperature (230°C) of the hotter saddle dolomites.

The recognition of hydrothermal activity at Clarke Lake is in agreement with

Well Location - NTS	Formation	Depth (m) below KB	% Ro[1] average
c-95-L/94-I-12	Exshaw	1106.4	1.27
a-65-G/94-J-10	Muskwa	2030.58	2.45
c-5-A/94-J-11	Slave Point	2282.95	1.95

[1] Vitrinite reflectance values from Stasiuk and Fowler (2002)

Table 5.8 Vitrinite reflectance values (% Ro) from the Clarke Lake area

conclusions drawn by Davies (2004) for the Devonian Nahanni Formation of British Columbia, and Morrow et al. (1990) for the generation of the Manetoe dolomite in the Yukon and southern Northwest Territories. Davies (2004) demonstrated a 25-40°C difference in thermal maturation between limestone and dolostone intervals only 7.6 m apart. Morrow et al. (1990) presented CAI and TAI thermal data that show a kink in the maturation plot at a level coincident with Late Devonian strata.

5.4.2 *Burial curve and timing of hydrothermal activity*

A burial history of the Slave Point Formation at Clarke Lake was calculated, applying a methodology similar to that of Morrow et al. (2002) in their study on the Slave Point from the Cordova Embayment, roughly 120 km to the northeast of Clarke Lake. The calculations were performed with PetroMod 1D (freeware from Integrated Exploration Systems), and using the stratigraphic data from Moore (1988) and Morrow et al. (2002) for the Devonian, Richards et al. (1994) for the Carboniferous, Henderson et al. (1994) for the Permian, Gibson (1992) for the Triassic, Poulton et al. (1993) for the Jurassic, and Stott (1993a, b) for the Cretaceous and Tertiary. Well c-56-L was used as the reference well for the thickness of the various formations, and was considered representative for the whole Clarke Lake field.

The result is the burial curve shown in Figure 5.26. Burial of the Slave Point was rapid following deposition in the Middle Devonian, and reached a maximum depth of ~1750 m by the end of the Mississippian. Following a period of relative tectonic and sedimentary quiescence, deposition of a thick Triassic succession buried the Slave Point to a depth of ~3000 m. This was followed by a period of uplift and erosion during Columbian Orogeny lasting from the Jurassic to Early Cretaceous. Maximum burial of the Slave Point

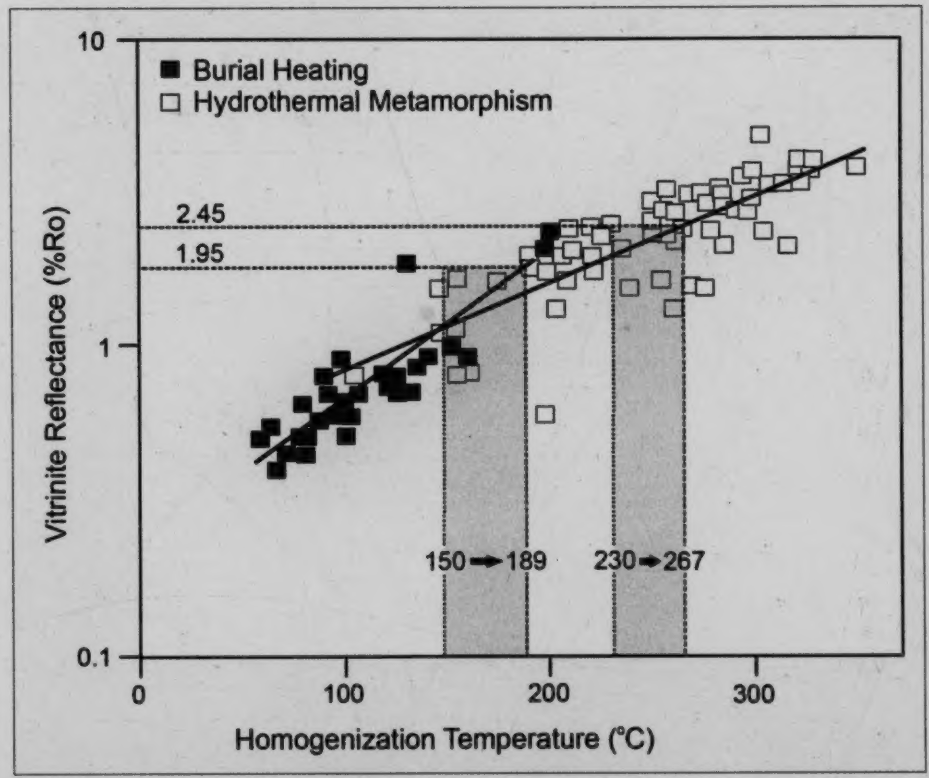

Figure 5.25 Fluid inclusion homogenization temperatures versus mean random vitrinite reflectance for burial heating and hydrothermal metamorphism. Modified after Barker and Pawlewicz (1994). Burial heating includes vitrinite maturation under normal burial geothermal conditions. Hydrothermal metamorphism includes data from hydrothermal ore deposits and active geothermal systems. The vitrinite reflectance values represent the non-dolomitized (geothermal conditions) and dolomitized (hydrothermally-altered conditions) end-members demonstrated in the Slave Point Formation (see Table 5.8). The temperature of 150°C represents the average of the homogenization temperatures from fluid inclusions in grey matrix dolomite (GMD - phase 10). The temperature of 230°C represents the highest homogenization temperature obtained from fluid inclusions in saddle dolomite (SD - phase 13). The temperatures of 189 and 267°C were obtained by applying a correction using the vitrinite reflectance values.

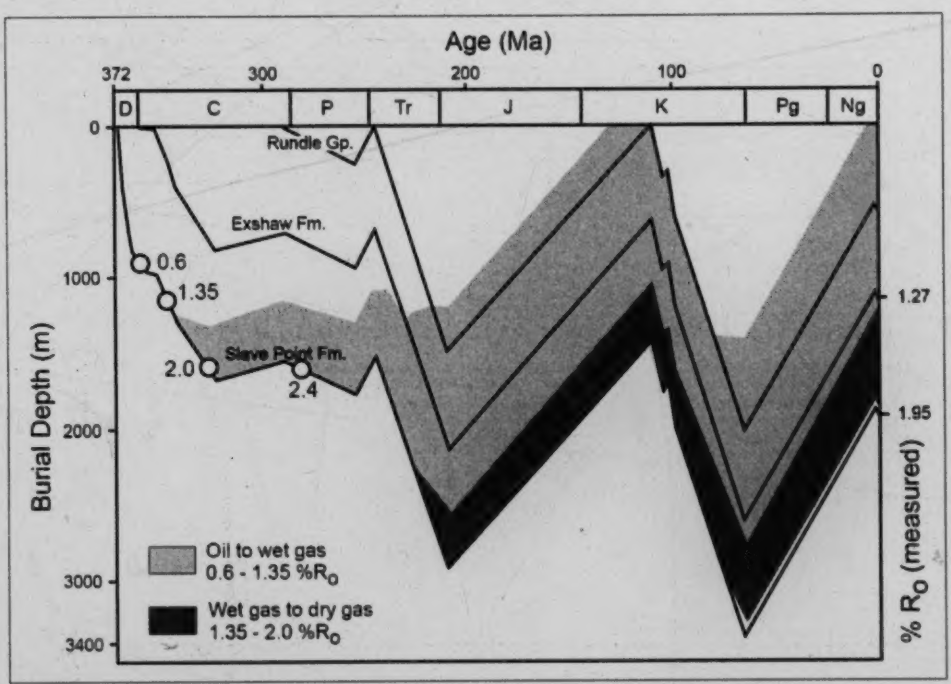

Figure 5.26 Burial and thermal history of the Slave Point Formation based on data from well c-56-L/94-J-9 in the Clarke Lake field. The burial history of the Slave Point and Exshaw formations and the Rundle Group are used to simulate the thermal history based on vitrinite reflectance and present-day formation temperatures. The measured vitrinite reflectance values from Table 5.8 are shown for comparison. Shaded fields = modelled vitrinite reflectance values using a constant geothermal gradient; open circles = modelled vitrinite reflectance values using a high geothermal gradient during the Paleozoic followed by a return to a lower and more constant geothermal gradient by the Triassic.

to a depth of roughly 3500 m occurred during deposition of the Cretaceous succession, which was quickly followed by another episode of uplift and erosion as a result of the Tertiary Laramide Orogeny. At the end point of its burial history the Slave Point has the Ro value of 1.95 % mentioned in the previous section (Figure 5.26).

The thermal history of the Slave Point Formation was determined using the vitrinite reflectance values obtained from organic matter in the Slave Point and overlying Muskwa formations (Table 5.8), as well as from the Mississippian Exshaw Formation. Reflectance values are from primary source rock solid bitumen/pyrobitumen that is generated directly from amorphous marine kerogen, converted into %Ro vitrinite reflectance equivalent (L. Stasiuk, pers. comm. 2005). Maturation was modeled using the Arrhenius-based

EASY%Ro spreadsheet model of Sweeney and Burnham (1990). The vitrinite reflectance values from the non-dolomitized Slave Point and the Exshaw formations were used to construct a thermal history controlled presumably by only the regional burial history and geothermal gradient. To obtain a baseline for comparison with the dolomitized Slave Point, a geothermal gradient of 57°C/km was applied, which is based on the present-day formation temperatures (Figure 5.27).

Modeling through trial-and-error indicates that a relatively constant heat flow of around 95 mW/m^2 from the Devonian to today provides the best overall fit to the vitrinite reflectance data in the non-dolomitized wells (Figure 5.26). This heat flow value is, however, considerably higher than the values of current heat flow value published for the area (82 mW/m^2: Majorowicz et al., 1989; 60 mW/m^2: Bachu and Burwash, 1994). Regardless of which of these studies comes closer to the truth, heat flow probably was higher in the past but decreased in relatively recent times. Further trial-and-error modeling reveals, however, that increased heat flow associated with the Laramide Orogeny results in an over-estimation of the thermal maturity in both the Slave Point and Exshaw formations. On the other hand, modeling with a constant heat flow of 95 mW/m^2 is in agreement with the present-day formation temperatures in both the Slave Point and the Mississippian Debolt Formation (Rundle Group, Figure 5.26).

These considerations are valid for the regional thermal regime. As mentioned earlier, the dolomitized part of the Clarke Lake field represents a local geothermal anomaly. The vitrinite maturation simulations conducted for this study using wells containing dolomite suggest an extremely high geothermal gradient of about 100°C/km during the Late Devonian to Mississippian over a geologically short time interval. This timing is indicated by the fact that the anomalously high vitrinite reflectance values are not seen in the overlying Late Devonian Fort Simpson Formation, which lies roughly 50 metres above the top of the Slave Point (Stasiuk and Fowler, 2002). These data show that the high vitrinite values in the dolomitized Slave Point were almost certainly caused by relatively rapid fluid flow through a relatively small, now hydrothermally-altered rock volume, such that only this rock volume was heated to any significant degree, leaving the surrounding strata relatively cold. This interpretation is the only one in agreement with all available geochemical data and geothermal modeling.

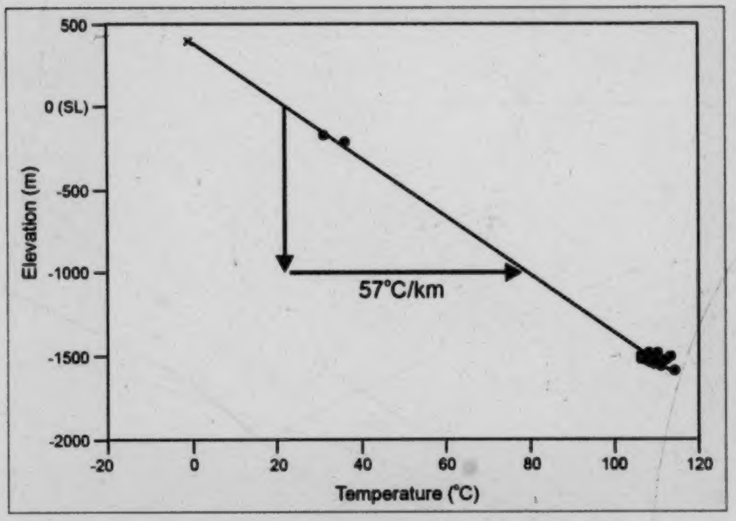

Figure 5.27 Calculated geothermal gradient in the Slave Point Formation at Clarke Lake. The gradient was calculated using a mean annual surface temperature of -1°C and subsurface temperature data from both the Slave Point and Mississippian Debolt formations. Temperature data provided by AccuMap®.

5.4.3 P-T conditions during dolomite formation

Using the temperature difference between the uncorrected and the corrected fluid inclusions (discussed above), it is possible to calculate the pressure at which the fluid inclusions were trapped, thereby enabling an estimate of the burial depth.

At the time of trapping, the fluid inclusions in the dolomites consisted of a single homogenous liquid phase. Through successive periods of uplift and erosion, the vapour phase developed, therefore, the measured homogenization temperatures (Th) represent the minimum temperature of entrapment. The difference between the measured Th and the true trapping temperature (Tt) is referred to as the pressure correction, which depends on the composition and density of the trapped fluids.

The cooling path of a fluid inclusion from trapping conditions (Pt, Tt) to surface conditions (P_{room}, T_{room}) is shown in Figure 5.28. During cooling from Tt (point A) towards Th (point B) the fluid inclusion consists of one homogenous liquid phase. The P-T conditions of the fluid inclusion are constrained by an isochore, or a line of constant volume that originates on the liquid-vapour curve. At point B, the fluid inclusion generates a vapour bubble. Upon further cooling from Th to T_{room} (point C), the vapour fraction increases and the P-T conditions of the fluid inclusions are fixed to the liquid-vapour curve.

As a result of this predictable behaviour, it is possible to estimate the trapping temperature (Tt) of a fluid inclusion by following the isochore from the homogenization temperature (Th) to the presumed trapping pressure (Pt). Unfortunately, in most cases, there is no independent estimate of the trapping pressure. Still, the intersection points of

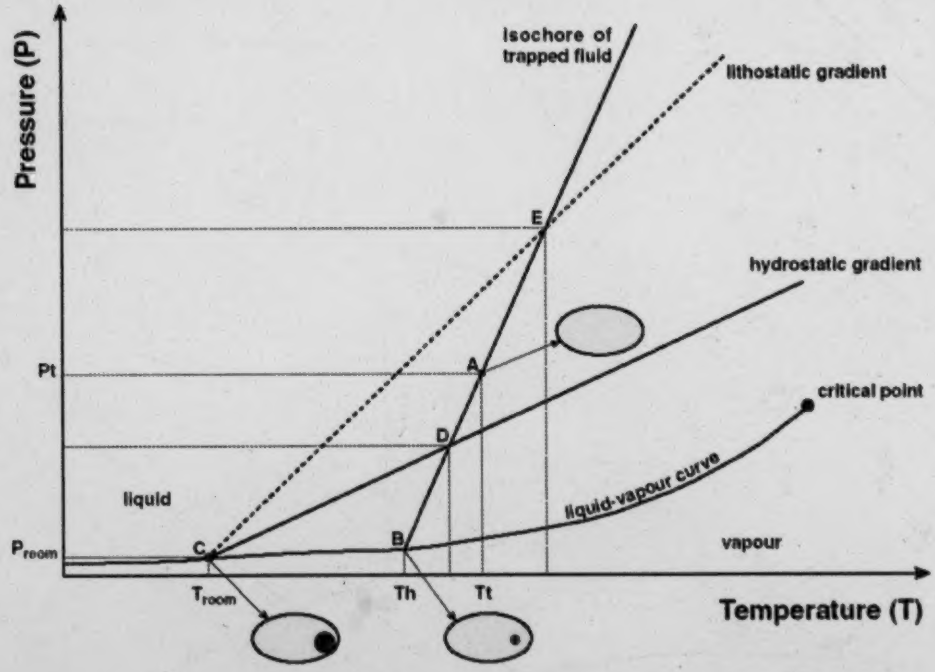
Pressure (P)
Isochore of trapped fluid
lithostatic gradient
E
hydrostatic gradient
Pt
A
critical point
D
liquid
liquid-vapour curve
Proom
C
B
vapour
Troom
Th
Tt
Temperature (T)

Figure 5.28 Pressure-Temperature plot showing the cooling path of an imaginary fluid inclusion from trapping conditions (P_t, T_t) towards surface conditions (P_{room}, T_{room}).

the isochore with the hydrostatic and lithostatic gradients (points D and E, Figure 5.28) will define the possible P-T conditions of the fluid inclusion under hydrostatic and lithostatic regimes. This method may lead to significant error in the trapping temperature as a result of: 1) having to define the gradients that existed at the time of fluid inclusion trapping; and, 2) assuming that the host fluid inclusion formed in equilibrium with either the hydrostatic or lithostatic gradient.

The hydrostatic and lithostatic gradients for the Slave Point Formation were constructed using a geothermal gradient of 57°C/km and geobarometric gradients of 100 and 270 bars/km (10 and 27 MPa/km) for hydrostatic and lithostatic conditions, respectively (Figure 5.29). No correction was applied for surface temperatures. The hydrostatic and lithostatic gradients were calculated assuming linear proportionality between pressure and temperature.

Isochores were constructed for fluid inclusions representing regional geothermal heating, i.e., high-salinity GMD, and local hydrothermal anomalies, i.e., high-temperature

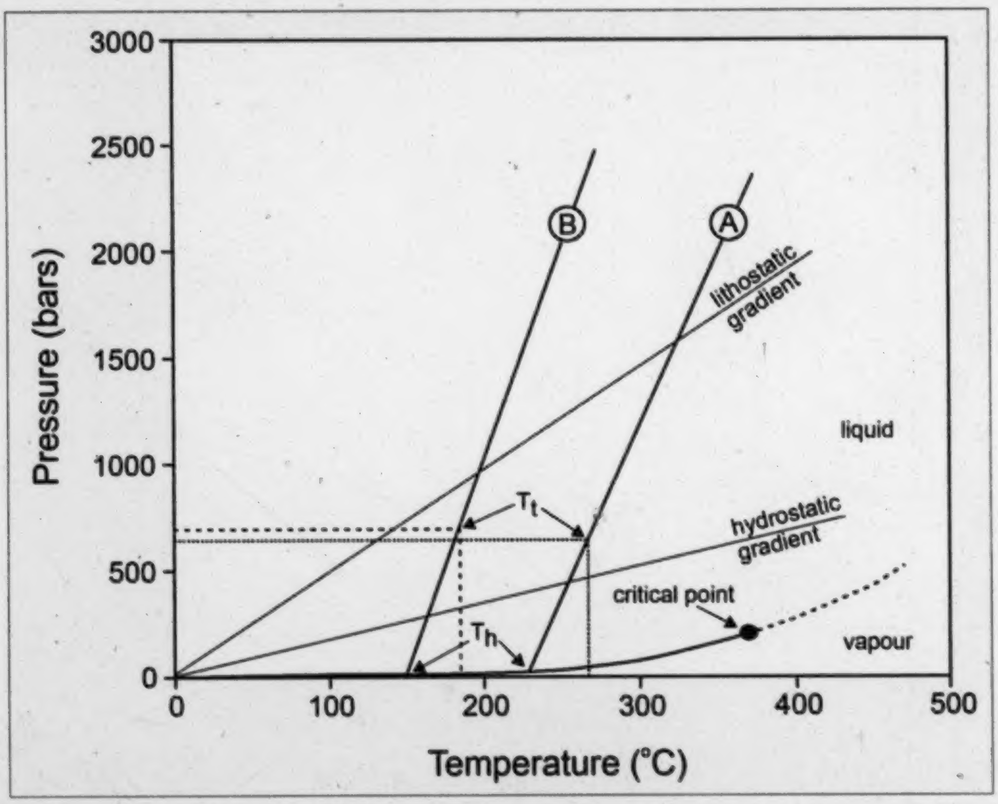

Figure 5.29 Pressure-Temperature plot showing the modelled fluid inclusion isochores for matrix and saddle dolomites in the Slave Point Formation at Clarke Lake. Fluid A represents saddle dolomite (SD - phase 13) with a homogenization temperature (T_h) of 228°C and a molal NaCl composition of 3.58. Fluid B represents grey matrix dolomite (GMD - phase 10) with a homogenization temperature of 150°C and a molal NaCl composition of 5.40. The trapping temperature (T_t) was calculated using the vitrinite reflectance correction shown in Figure 5.25. The hydrostatic and lithostatic gradients were constructed using a geothermal gradient of 57°C/km (Figure 5.27) and geobarometric gradients of 100 and 270 bars/km (10 and 27 MPa/km), respectively.

SD. The bulk density of the fluid inclusions was calculated using the computer program 'BULK' (Bakker, 2003). The slopes of the isochores for GMD and SD were determined using the equations of Zhang and Frantz (1987). The resulting isochores are shown in Figure 5.29: fluid A represents SD (phase 13) with a measured Th of 228°C and a molal NaCl composition of 3.58, fluid B represents GMD (phase 10) with a measured Th of 150°C and a molal NaCl composition of 5.40.

The independent temperature corrections calculated for both GMD and SD using the Ro-T conversion in Figure 5.25, are assumed to represent the true trapping temperature of the fluid inclusions, and, therefore, also provide an estimate for the burial depth during dolomite formation. The trapping pressures determined for GMD and SD are approximately 650 and 700 bars, respectively (Figure 5.29). These pressures equate to depths of roughly 2 to 2.5 km, which indicate dolomite formation between the mid-Triassic and the Tertiary based on the burial curve in Figure 5.26. This relatively late timing is counter to the argument for an earlier timing that was proposed using the thermal history of the Slave Point Formation. Alternatively, assuming that the Ro-T fluid inclusion temperature corrections are inaccurate, it is possible to make both a temperature and pressure estimate using the hydrostatic and lithostatic gradients. Where the GMD isochore intersects the lithostatic gradient, the trapping pressures and temperatures are roughly 1000 bars and 200°C, respectively. A pressure of 1000 bars is equivalent to approximately 3.7 km. However, according to burial curve (Figure 5.26), the Slave Point Formation was never buried to such a depth, indicating GMD did not form under lithostatic conditions. Similarly, the SD isochore intersects the lithostatic gradient at pressures and temperatures around 1600 bars and 330°C. Yet, such conditions were never experienced by the Slave Point Formation, based not only on the geochemical data from the dolomites, but also on the level of thermal maturation in vitrinite from the region. Using the hydrostatic gradient, the isochore for GMD predicts fluid inclusion trapping at pressures and temperatures of roughly 300 bars and 170°C, respectively. This pressure estimate equates to a depth of slightly more than 1 km, which is consistent with the Late Devonian to Mississippian timing proposed in the previous section. Likewise, the SD pressure and temperature estimates, 450 bars and 250°C, point to a burial depth of approximately 1.5 km: a point of maximum hydrothermal activity in the Early Mississippian. Additionally, at hydrostatic conditions, the corrected fluid inclusion temperatures between GMD and SD differ by roughly 80°C, nearly identical to the 78°C difference in temperature predicted using the Ro-T method (Figure 5.25). This relative conformity between independent data sets suggests that the hydrothermal fluid had a temperature that was at least 80°C higher than the fluid(s) that formed earlier GMD. This observation precludes any possibility that the two dolomite populations were co-genetic.

Based on the above results, and in conjunction with data discussed previously in this chapter, it does appear that the dolomites of the Slave Point Formation formed relatively early either when the fluid was in equilibrium with the hydrostatic gradient, or from a fluid that had a pressure slightly above hydrostatic. This latter condition may have developed as a result of a build-up of fluid pressures in cemented fractures that were released in distinct fluid pulses during rupturing: a mechanism that has already been proposed to explain the geochemical variations within individual crystals of SD from well d-79-F.

5.5 Dolomite timing

Within the Slave Point Formation at Clarke Lake, the bulk of the matrix appears to have been dolomitized subsequent to burial of at least 500 m. This depth estimate is based on the recognition that stylolitization of pure limestones, which are more soluble than dolostones, requires a minimum depth of around 500 m (Lind, 1993; Fabricius, 2000). Therefore, a Famennian age is suggested as the earliest age for replacive matrix dolomitization at Clarke Lake, based on the burial history of the Slave Point and the fluid inclusion pressure estimate (Figure 5.26, Figure 5.29). The latest possible timing for matrix dolomitization is provided by the presence of bitumen that is coating GMD, indicating that hydrocarbon maturation and migration followed matrix dolomitization. Using a geothermal gradient comparable to present-day (57°C/km using bottom hole data), the thermal history of the Slave Point Formation predicts the generation of liquid hydrocarbons from potential source rocks (e.g. Klua, Otter Park, Muskwa) around Early Mississippian time (further discussed in the following section). A similar age was obtained by Morrow et al. (2002) in the Cordova embayment region, and has been suggested by Boreen and Davies (2004) in the Ladyfern region, both Slave Point reservoirs in northeastern British Columbia.

Additional evidence regarding the timing of GMD formation is provided by the overall geometry of the dolostone body at Clarke Lake. The notable conformity of the top surface of the dolomite body suggests there was little to no vertical throw along faults (Opalinski, 1984) prior to, or concurrent with, matrix dolomitization. This evidence also advocates a relatively early timing of GMD formation, i.e., prior to significant effects from regional Devonian-Mississippian tectonics (Nelson et al., 2002) (Figure 5.30).

The timing of the hydrothermal alteration of GMD is much harder to determine. One indication for the latest timing is that some SD crystals are cut by high-amplitude stylolites, which could have formed during the two known events of rapid burial in the area, i.e., Triassic-Jurassic and Late Cretaceous-Paleocene. More concise, yet circumstantial evidence is provided from a study of the Robb Lake MVT deposit, located roughly 200 km down-dip to the west in the northern Rocky Mountains. Stable and radiogenic isotope data from saddle dolomites at Clarke Lake have similar characteristics to those exhibited by mineralized dolomites from Robb Lake (Paradis et al., 2005). Based on the results of Pb-Pb isotope analyses from galena, Paradis et al. (2005) interpreted the Robb Lake dolomites to have formed during Devonian-Mississippian plate-margin tectonics on the western margin of North America. During the Famennian, a tectonic regime of subduction and contractional deformation prevailed south of the Peace River Arch, while another regime of slab rollback and back-arc extension prevailed in the north (Figure 5.30B). This crustal extension affected the western margin of North America and resulted in the formation of many sedimentary exhalative and MVT deposits in northeastern British Columbia (MacIntyre, 1992; Paradis et al., 1998). Geothermometers and conodont alteration indices from these deposits suggest temperatures of formation between 250 and 350°C (MacIntyre, 1992; Paradis et al., 1998). Considering the similarly high temperatures from the dolomites in the Slave Point, it is tempting to infer a similar timing for hydrothermal alteration at Clarke Lake. In fact, seismic data from the Clarke Lake field provide another line of evidence for Late Devonian to Early Mississippian hydrothermal alteration. In Figure 5.31, Late Devonian Antler convergence is represented by the formation of syncline-anticline pairs within the Famennian Tetcho Formation (Wabamun equivalent). The structural inversion from compression to extension is then shown by the development of collapse structures, i.e., negative flower structures, from the basement upwards into the lower half of the Banff Formation (Figure 5.31). These Carboniferous faults therefore appear to represent the hydrothermal fluid conduits in the Slave Point Formation. Tangible evidence that the rapid changes in fluid chemistry observed in saddle dolomite samples from well d-79-F (Figure 5.9) in fact could be the result of fluid flow within/adjacent to dilatational jogs in fault systems, as proposed by Sibson (1994). In these zones, the period of earthquake aftershock

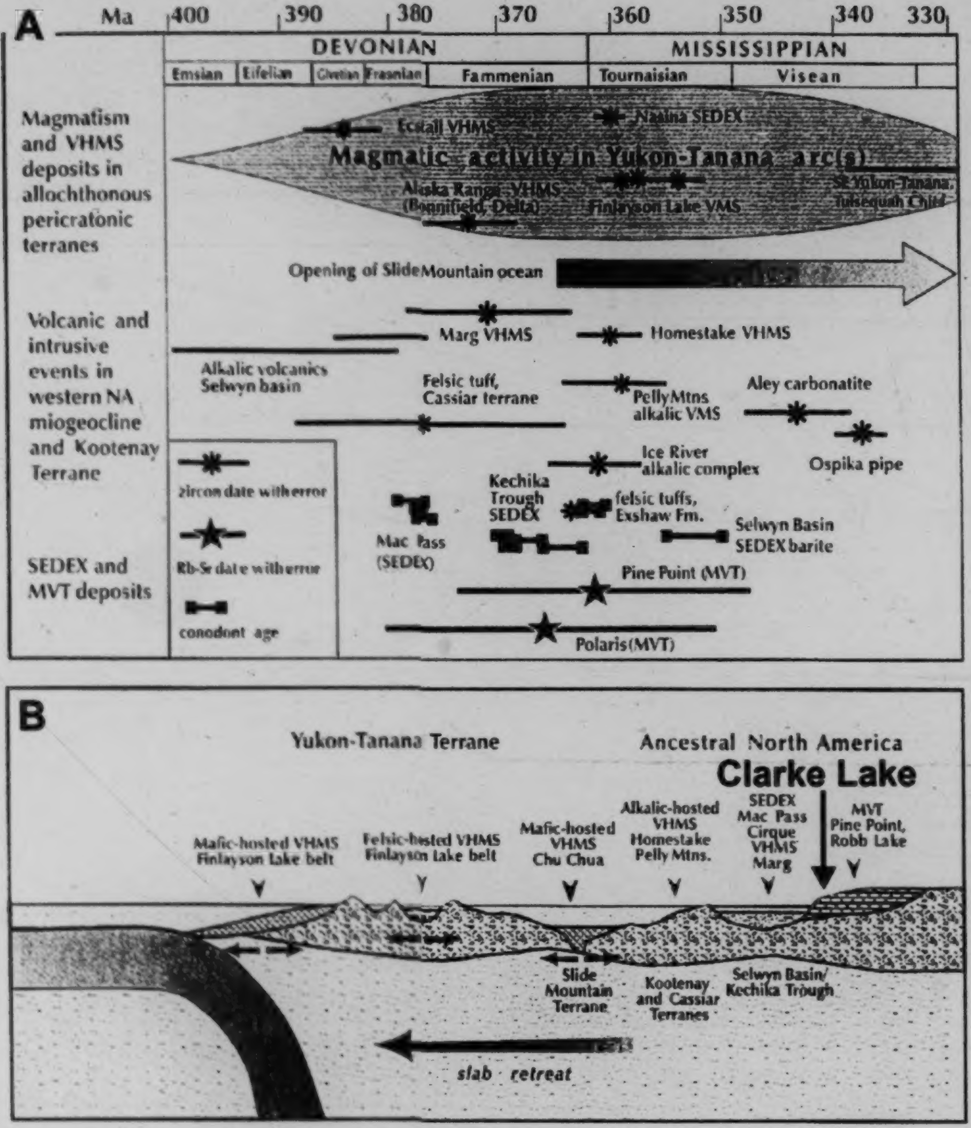
A
Ma
400
390
380
370
360
350
340
330
DEVONIAN
MISSISSIPPIAN
Emsian
Eifelian
Givetian
Frasnian
Fammenian
Tournaisian
Visean
Magmatism and VHMS deposits in allochthonous pericratonic terranes
Ecstall VHMS
Naaina SEDEX
Magmatic activity in Yukon-Tanana arc(s)
Alaska Range VHMS (Bonnifield, Delta)
Finlayson Lake VMS
SE Yukon-Tanana: Tulsequah Chief
Opening of SlideMountain ocean
Volcanic and intrusive events in western NA miogeocline and Kootenay Terrane
Marg VHMS
Homestake VHMS
Alkalic volcanics Selwyn basin
Felsic tuff, Cassiar terrane
PellyMtns alkalic VMS
Aley carbonatite
Ospika pipe
Ice River alkalic complex
zircon date with error
Rb-Sr date with error
conodont age
SEDEX and MVT deposits
Kechika Trough SEDEX
felsic tuffs, Exshaw Fm.
Mac Pass (SEDEX)
Selwyn Basin SEDEX barite
Pine Point (MVT)
Polaris(MVT)
B
Yukon-Tanana Terrane
Ancestral North America
Clarke Lake
Mafic-hosted VHMS Finlayson Lake belt
Felsic-hosted VHMS Finlayson lake belt
Mafic-hosted VHMS Chu Chua
Alkalic-hosted VHMS Homestake Pelly Mtns.
SEDEX Mac Pass Cirque VHMS Marg
MVT Pine Point, Robb Lake
Slide Mountain Terrane
Kootenay and Cassiar Terranes
Selwyn Basin/ Kechika Trough
slab retreat

Figure 5.30 Tectonics and metallogeny during the Devonian-Mississippian. Modified after Nelson et al. (2002). MVT = Mississippi Valley-type, SEDEX = sedimentary exhalative, VHMS = volcanic-hosted massive sulphide, VMS = volcanogenic massive sulphide.

(A) Tectonic and metallogenetic timeline for western Canada. See Nelson et al. (2002) for references to individual events.

(B) Cross-section showing tectonics and metallogeny of the western Canadian continental margin. Slab retreat during the Late Devonian-Mississippian resulted in higher heat flow and convection in the asthenosphere, and a transtensional tectonic regime.

Figure 5.31 2D seismic line across the Slave Point platform margin at Clarke Lake. Line intersects well c-94-L/94-J-9 along the eastern side of the Clarke Lake field. Section shown represents roughly 11 km. Post-stack data. Courtesy of Petro-Canada Oil & Gas.

The position of the underlying Keg River Formation (red line) platform margin is clearly shown between shot points 400 and 450. The Slave Point Formation (yellow line) platform margin progrades out on top of basinal shales of the Klua Formation (green line), and is onlapped by time-equivalent basinal shales of the Otter Park Formation (pink line). The numbers represent interpreted Devonian-Mississippian tectonic events by the author.

Event 1 - Middle Devonian (Eifelian to early Givetian) crustal extension. During this stage, extensional tectonics enabled carbonate precipitation and reef growth within uplifted fault blocks, while argillaceous sediments were deposited within down-dropped or drowned fault blocks.

Event 2 - late Middle Devonian (Givetian) to Late Devonian (early Famennian) crustal convergence. During this stage, Antler orogenic convergence reactivated basement faults, or created new reverse faults, enabling the Slave Point platform margin to prograde out into the previously drowned shale basin. Subtle structural relief continues upward into the Famennian Tetcho Formation (Wabamun equivalent).

Event 3 - Late Devonian crustal convergence. Crustal convergence, the result of the Antler Orogeny, is clearly evident by the syncline-anticline pairs (red arrows) developed in the Tetcho Formation (Wabamun equivalent).

Event 4 - Mississippian (early Tournasian) crustal extension. During this stage, crustal extension, partially along pre-existing faults, resulted in the development of local collapse structures (negative flower structures) in the Devonian succession. Clear evidence of collapse continues upward into the lower-half of the Banff Formation. Within the Slave Point Formation, structural inversion has resulted in previously high areas being changed to structural lows, and *vice versa*.

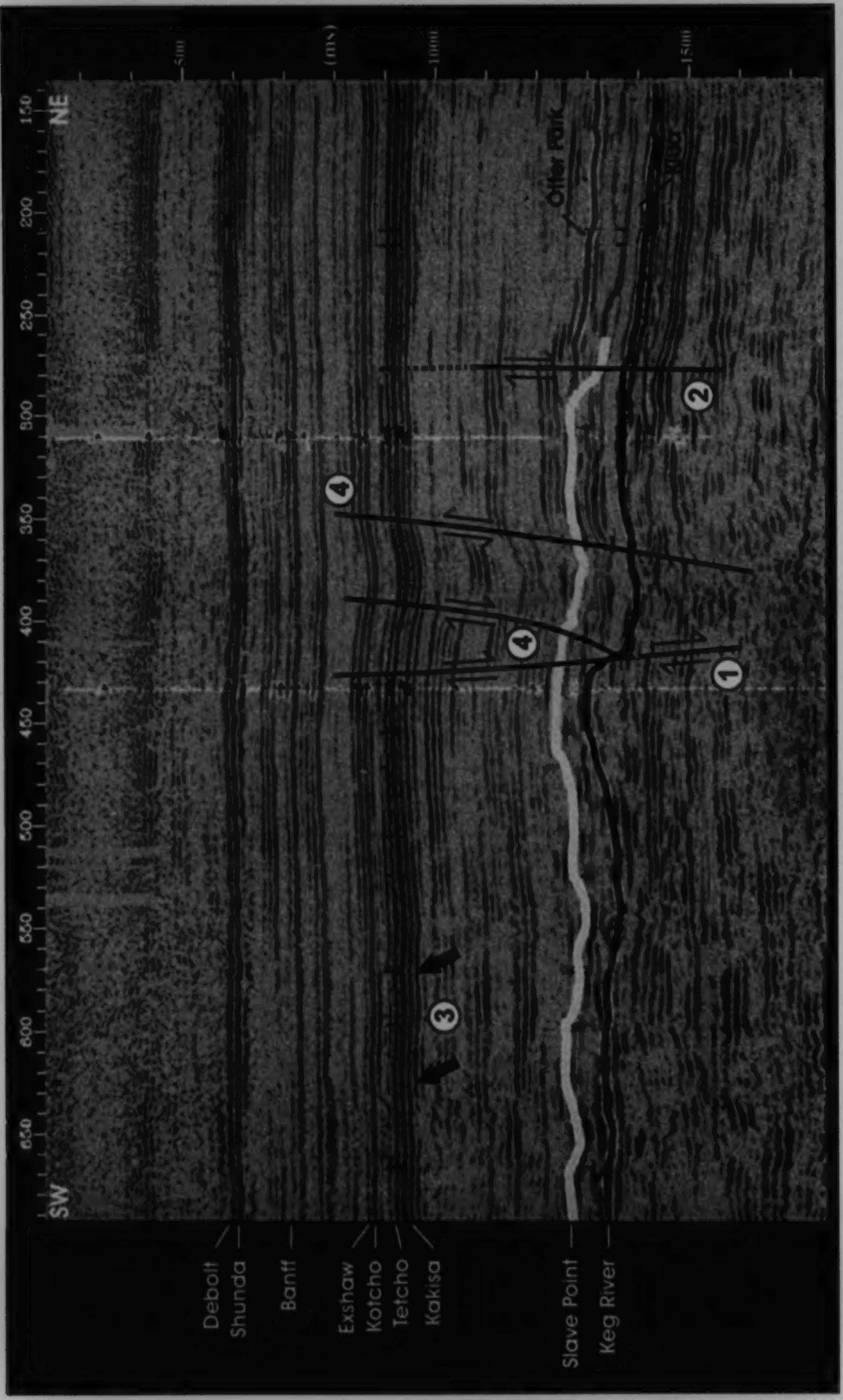

SW
NE
150
200
250
300
350
400
450
500
550
600
650
500
(ms)
1000
1500
Otter Park
Klua
1
2
3
4
4
Debolt
Shunda
Banff
Exshaw
Kotcho
Tetcho
Kakisa
Slave Point
Keg River

activity would likely be enhanced, possibly leading to increased fluid flux (Micklethwaite and Cox, 2004) and precipitation of radiogenic SD due to fluid interaction with underlying basement rocks. Therefore, integration of the evidence suggest hydrothermal alteration at Clarke Lake occurred during the very latest Devonian to Early Mississippian, i.e., very soon after replacive matrix dolomitization.

An overall Late Devonian to Mississippian timing for the various dolomite-forming events is similar to that proposed from other studies of dolomite reservoirs in the northern part of the Western Canada Sedimentary Basin, i.e., north of the Peace River Arch (Aulstead and Spencer, 1985; Morrow et al., 1986; Morrow and Aulstead, 1995; Morrow et al., 2002; Boreen and Davies, 2004). However, different interpretations have been advanced for the formation of saddle dolomite. Qing and Mountjoy (1994a; 1994b) proposed that the main stage of dolomitization and cementation in the Presqu'ile barrier complex was the result of fluid flow associated with tectonic compression, sedimentary loading, and uplift during the Late Cretaceous to early Tertiary Laramide Orogeny. Similarly, Lonnee and Al-Aasm (2000) proposed a Late Cretaceous to Tertiary age for saddle dolomite cements in the Middle Devonian Sulphur Point Formation in northern Alberta. In both of the above-mentioned studies, dolomite formation was accomplished through the movement of residual brines along permeable Devonian carbonates. On the other hand, Al-Aasm and Clarke (2004) proposed that saddle dolomites in the Slave Point Formation from northwestern Alberta formed from high salinity, hydrothermal fluids that were expelled tectonically during the Late Devonian to Mississippian Antler Orogeny. There are, however, two problems with this interpretation; firstly, the geochemical data from their (ibid.) saddle dolomites are nearly identical to GMD at Clarke Lake, suggesting a similar origin (see below), and, secondly, their (ibid.) study area is over 300 km from the disturbed belt, likely precluding the possibility of 'squeegee flow' (*sensu* Oliver, 1986) at such distances (see discussions in Machel and Cavell, 1999; Buschkuehle, 2003). Nevertheless, a Late Devonian to Early Mississippian timing is similar to that suggested by Morrow et al. (2002). In their detailed study from northeastern British Columbia, they (ibid.) proposed that the dolomite-forming brines passed through the Presqu'ile Barrier during and immediately after deposition of the Slave Point Formation.

5.6 Dolomite models

Any model used to explain dolomite formation requires an infinite supply of Mg^{2+} ions as well as a mechanism to deliver the Mg^{2+} and export Ca^{2+} ions (Land, 1985). Expanding on this requirement, Morrow (1990) stated that a number of conditions must be satisfied in order for dolomite formation to take place. These include:

1) the amount of Mg^{2+} available must be sufficient to form dolomite;
2) a mechanism to deliver the Mg^{2+} to the site, plus deliver small amounts of CO_3^{2-} and carry away Ca^{2+} ions; and,
3) the composition of the dolomite-forming fluid must be conducive to dolomite formation.

Based on these three requirements, it should be obvious that all dolomite models are essentially hydrologic models (see below).

Additionally, Machel (2004) suggested that dolomite models must fulfill the following three specific critieria:

1) *thermodynamic* – there must be supersaturation with respect to dolomite, while dolomitization (i.e., replacement of limestone by dolomite) requires undersaturation with respect to calcite. According to Machel and Mountjoy (1986), thermodynamically-favoured fluids have:
   a) low Ca^{2+}/Mg^{2+} ratios;
   b) low Ca^{2+}/CO_3^{2-} (or Ca^{2+}/HCO_3^{-}) ratios; and,
   c) high temperatures;
2) *kinetic* – the rate of dolomite formation must be equal to or greater than the rate of calcite dissolution, otherwise extensive large-scale porosity would result; and,
3) *hydrologic* – there must be long-lasting flow of Mg-bearing fluids

The Mg required to form dolomite can be obtained from:

1) high-Mg calcite;
2) Mg absorbed on clay minerals and organic matter;
3) structure-bound Mg in clays and organic matter;
4) Mg re-mobilized by pressure solution from older dolomites;
5) formation waters;
6) hypersaline seawater; and,

7) fluid injection through fractures and faults (Qing and Mountjoy, 1994a; 1994b).

Several models have been proposed to explain the formation of dolomite (Figure 5.32). Some of the more common models include:

1) hypersaline (reflux/sabkha) model (King, 1947; Adams and Rhodes, 1960; Illing et al., 1965; McKenzie et al., 1980; Patterson and Kinsman, 1981);
2) meteoric-marine mixing zone model (Hanshaw et al., 1971; Badiozamani, 1973);
3) seawater model (Land, 1985; Vahrenkamp and Swart, 1994);
4) burial compaction model (Illing, 1959; Jodry, 1969; Mattes and Mountjoy, 1980; Machel and Anderson, 1989);
5) tectonic (squeegee) model (Oliver, 1986; Dorobek, 1989);
6) topography-driven flow model (Garven and Freeze, 1984);
7) thermal convection model (Kohout et al., 1977); and,
8) hydrothermal model (Aulstead and Spencer 1985; Morrow et al. 1990; Machel and Lonnee, 2002 and references therein).

The successful application of any one of these models requires detailed knowledge of the paleogeography, petrography, geochemistry, facies and dolomite distribution. There is overlap between these models, and several models could apply to one setting. The dolomite precipitated in one model may not be chemically and petrographically distinct from another (Tucker and Wright 1990), and the recrystallization and/or multiple dolomite-forming events in the several different environments must also be considered. For a review and critique of the above-listed dolomite models the reader is referred to Machel and Mountjoy (1986), Hardie (1987), Budd (1997), Warren (2000), and Machel (2004).

5.7 Hydrological interpretation for dolomite formation

The data and interpretations discussed so far in this paper suggest the following hydrogeological scenarios for paleofluid flow. The schematic cross section used to illustrate regional fluid flow is modified from Petrel Robertson (2003).

Considering the chemistry of the dolomitizing fluid and the timing of limestone

Figure 5.32 Summary of current dolomitization models and predicted dolomite distribution patterns (grey shading) in carbonate buildups. Model A through D1 and D4 are kilometre-scale, models D2 and D3 are basin-scale. Arrows denote flow directions. Dashed lines in C1 and C2 represents isotherms. Kv = vertical hydraulic conductivity, KH = horizontal hydraulic conductivity. Models A to D2 modified after Amthor et al. (1993). Hydrological models D3 and D4 modified after Garven (1995). Predicted dolomite pattern in D3 after Morrow (1998). Predicted dolomite pattern in D4 after Braitwaite and Rizzi (1997).

Dolomitization Model	Source of Mg^{2+}	Delivery Mechanism	Hydrologic Model	Predicted Dolomite Patterns
A. Reflux Dolomitization	seawater	storm recharge, evaporative pumping density-driven flow	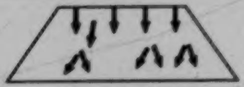	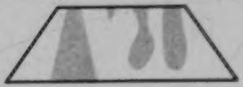
B. Mixing Zone (Dorag) Dolomitization	seawater	tidal pumping	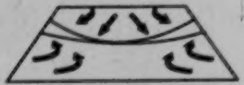	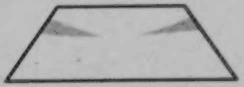
C1. Seawater Dolomitization	normal seawater	slope convection ($K_V > K_H$)	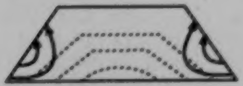	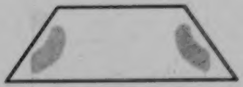
C2. Seawater Dolomitization	normal seawater	slope convection ($K_H > K_V$)	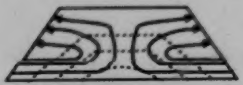	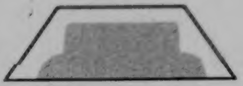
D1. Burial Dolomitization (local scale)	basinal shales	compaction-driven flow	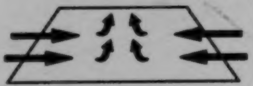	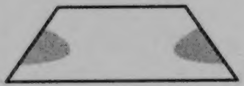
D2. Burial Dolomitization (regional scale)	various subsurface fluids	tectonic expulsion topography-driven flow	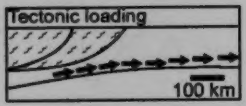	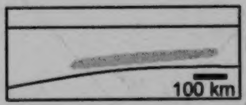
D3. Burial Dolomitization (regional scale)	various subsurface fluids	thermo-density convection	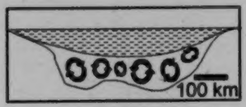	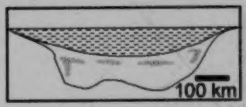
D4. Burial Dolomitization (local and regional scales)	various subsurface fluids	tectonic reactivation of faults (seismic pumping)	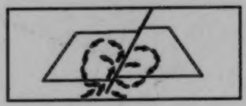	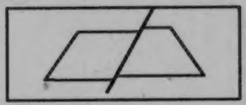

replacement as Late Devonian to Early Mississippian, matrix dolomitization of the Slave Point Formation at Clarke Lake was accomplished by long-distance migration of halite brines that must have come from a southerly or easterly direction, because this is where Middle Devonian halite deposits are located (Meijer Drees, 1994). Using Occam's Razor, we favour a shorter rather than a longer migration route, i.e., about 200 km from the evaporites near the Peace River Arch to the south–southeast, although we have no good reason to exclude brine derivation from the larger Middle Devonian halite deposits due east toward and partially within Saskatchewan. If the halite brine came from the Peace River Arch area, it would have taken a path similar to that illustrated in Figure 5.33A, i.e., regionally down the stratigraphic dip through the Keg River platform aquifer, and then forced upward in the Clarke Lake field by the permeability barrier made up of the shale package Evie-Klua-Otter Park. The halite brine would then have been pushed out of the Clarke Lake area in a transverse direction within the top of the platform (in or out of the field of view of Figure 5.33A). In the process, the brine dolomitized the platform margin complex from the Keg River up to the Slave Point. The hydrologic drive for this overall flow was density, thermal, or a combination of the two. In its area of generation the halite brine had to move downdip because of its weight, thereby flowing toward Clarke Lake and the surrounding part of the platform margin. The energy for the upward movement of the brine at the platform margin was provided by the weight of the brine column between the platform margin and the source of the brine, akin to a locomotive near the Peace River Arch pushing a long series of wagons ahead of itself and even updip at the front, augmented by the upward drive caused by the temperature increase of the brine along the flow path. Perhaps thermal drive was stronger than the density drive at Clarke Lake in facilitating upward brine movement. The relative proportion of density versus thermal drives is unknown and requires numerical modelling for quantification. Either way, the updip movement would stop sometime after the evaporative setting near the Arch stopped generating brine. The brine already in the Keg River aquifer would have kept flowing downdip under its own weight (a process recently termed 'latent reflux" by Jones et al., 2002) until the weight of the brine within the platform margin complex was balanced by the weight of brine remaining in the regional aquifer.

The scenario for hydrothermal alteration in the bulk, central and eastern part of Clarke Lake is illustrated in Figure 5.33B, and the scenario for the far western part (well

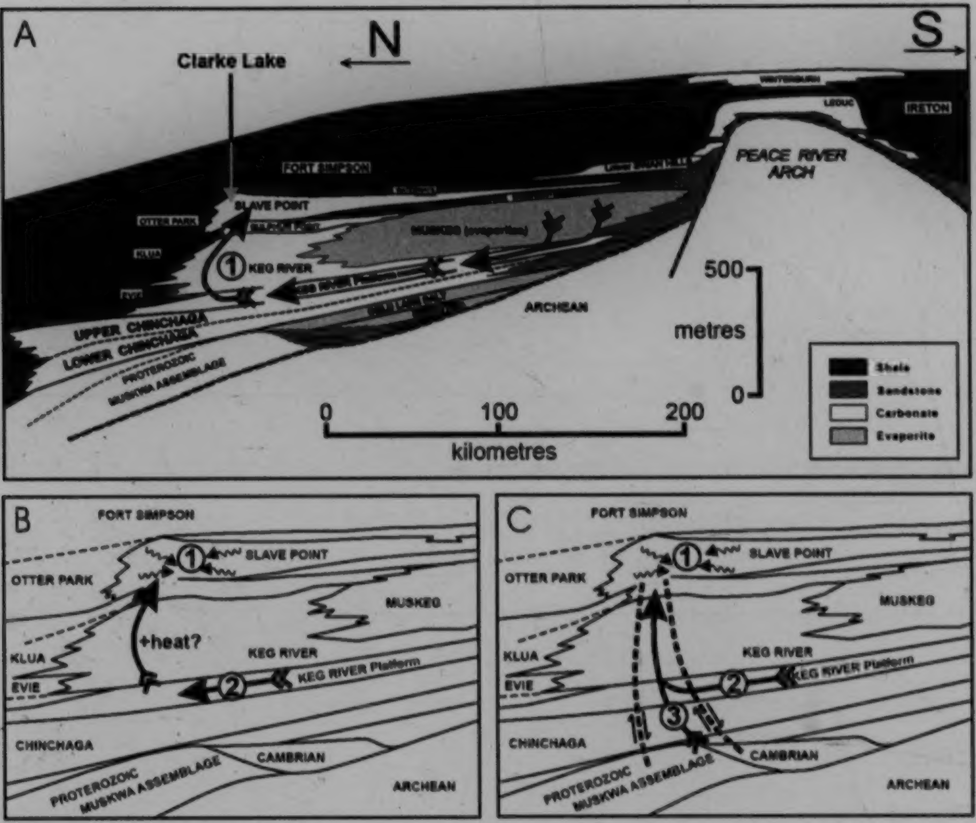

A
N
S
Clarke Lake
FORT SIMPSON
SLAVE POINT
OTTER PARK
KLUA
EVIE
KEG RIVER
MUSKEG (evaporites)
KEG RIVER Platform
UPPER CHINCHAGA
LOWER CHINCHAGA
PROTEROZOIC
MUSKWA ASSEMBLAGE
ARCHEAN
LEDUC
IRETON
PEACE RIVER ARCH
500
metres
0
0
100
200
kilometres
Shale
Sandstone
Carbonate
Evaporite
B
FORT SIMPSON
① SLAVE POINT
OTTER PARK
MUSKEG
+heat?
KLUA
EVIE
KEG RIVER
② KEG RIVER Platform
CHINCHAGA
CAMBRIAN
PROTEROZOIC
MUSKWA ASSEMBLAGE
ARCHEAN
C
FORT SIMPSON
① SLAVE POINT
OTTER PARK
MUSKEG
KLUA
EVIE
KEG RIVER
② KEG RIVER Platform
③
CHINCHAGA
CAMBRIAN
PROTEROZOIC
MUSKWA ASSEMBLAGE
ARCHEAN

Figure 5.33 Hydrological interpretation of dolomite formation at Clarke Lake.

(A) Schematic cross-section of northeastern British Columbia during the Late Devonian (modified after Petrel Robertson, 2003). The arrows represent the suggested flow path of a halite-saturated fluid (fluid 1) causing the main phase of dolomitization (GMD - phase 10) of the Slave Point Formation.

(B) Fluid mixing and hydrothermal alteration across most of the Clarke Lake field. A less saline, gypsum-saturated fluid (fluid 2) following behind the halite-saturated fluid migrated into the Slave Point Formation and mixed with the original dolomitizing fluid (fluid 1). The mixing of fluids 1 and 2 was made possible by the extremely high heat flow values present during hydrothermal alteration. This mixed, hybrid brine promoted the dissolution and recrystallization of matrix dolomite, and saddle dolomite formation (phase 13).

(C) Method for hydrothermal alteration in well d-79-F/94-J-10. Fluid 2 mixed with a small volume of fluid 3, which provided the radiogenic ^{87}Sr to the system through the interaction with rocks of Proterozoic or Cambrian age. This mixed fluid ascended episodically along faults (hatched lines) during rupture. During post-seismic periods, saddle dolomite was precipitated only from the lower temperature, less radiogenic mixture of fluids 1 and 2, similar to scenario B.

d-79-F) is illustrated in Figure 5.33C. It is apparent that the hydrothermal gypsum brine ascended relatively rapidly in both areas, but with one important difference. In the central and eastern parts of Clarke Lake, the ascending brine may not have had any connection to the Cambrian or pre-Cambrian strata, considering that the products of hydrothermal alteration in these parts of the field do not contain anomalously high Sr-isotope values, nor the noted REE anomalies, and considering the overall lower temperatures of formation/ recrystallization. Also, the water-rock ratios with respect to the invading hydrothermal brine were fairly low in this area, probably because of the overall relatively high permeability, which resulted in a thorough mixing and rapid dissipation of the hydrothermal brine within the connate halite brine, also resulting in a dampened temperature anomaly. In contrast, the fluids ascending in the westernmost part of the field seem to have been much more focussed along faults, hence the much higher water-rock ratio within and in the immediate vicinity of these faults, which may very well have penetrated all the way to the basement, thereby acquiring some ionic and isotopic signatures from fluids admixed from the Cambrian and pre-Cambrian rocks. In either case, the source and the hydrologic drive of the gypsum brine to be similar to those of the halite brine. There is no other possible source other than the evaporative depositional areas already mentioned for the halite brine. In these areas, halite is typically associated with and/or overlain by gypsum deposits and then Upper Devonian marine shales as a result of the eustatic sea level rise. Hence, through time the Middle Devonian halite brine evolved into and/or was followed by a Middle to Upper Devonian gypsum brine that used the same flow path. There is an important difference in the energy to drive the halite and gypsum brines up at the platform margin, however. Density alone could not have driven the gypsum brine up into Clarke Lake while the field contained a "slug" of the much heavier halite brine. Rather, the gypsum brine must have obtained additional energy to be able to push up and into the halite brine. This energy was the heat now manifested in the highly elevated homogenization temperatures of saddle dolomites within the field, as well as in the calculated highly elevated geothermal gradients necessary to account for these temperatures. Hence, this interpretation accounts for all data and calculations, i.e., the petrography and chemistry of the rocks; the chemistry of the gypsum brine (and the hybrid brine resulting from its injection into Clarke Lake); the early timing of hydrothermal alteration, here also interpreted as Late(est) Devonian to Mississippian; and the hydrothermal anomaly within the dolomitized parts of Clarke Lake.

CHAPTER 6

ORIGIN AND EVOLUTION OF FORMATION WATERS IN THE SLAVE POINT FORMATION

6.1 Introduction

After having established the diagenetic framework for the Slave Point Formation in the previous chapters, the objectives of Chapter 6 are to: 1) identify the origin and/or evolution of the present-day formation waters in the Slave Point Formation; 2) determine the relationships between present-day formation waters and fluids responsible for the formation of dolomite(s) in the Slave Point Formation; and, 3) provide an interpretation of present-day fluid flow patterns. These objectives were attained through a comprehensive geochemical examination of the present-day formation waters in the Slave Point Formation and comparison with fluid inclusion data in the dolomites. The methods applied include: stable and radiogenic isotope analysis, major and trace element analysis, and computer modeling to determine the extent of fluid-mineral interactions. The results from this chapter have important implications regarding both the diagenetic fluid history in the Slave Point Formation, and the development of hydrocarbon traps along the western edge of the Middle Devonian barrier complex.

6.2 Hydrostratigraphy

Sedimentary strata can be classified as aquifers, aquitards, or aquicludes, depending on their permeability (de Marsily, 1986). A hydrostratigraphic unit is defined as one or more geological units that are in contact with one another and exhibit similar hydraulic properties. The hydrostratigraphy of the Devonian succession in northeastern British Columbia, shown in Figures 6.1 and 6.2, is based on the general lithologies of the stratigraphic units in combination with the results from previous hydrogeological studies of the region (Hitchon, 1984; Bachu, 1997).

The Precambrian crystalline basement represents the lower boundary for the entire stratigraphic succession, and constitutes a basin-wide aquiclude, except where fault zones have acted as conduits for fluid flow (Hitchon et al., 1990; Bachu, 1997). Cambrian strata include sandstones and silty shales, and form the Cambrian aquitard. They are present only in the immediate vicinity of the Clarke Lake field and towards the south and west into the

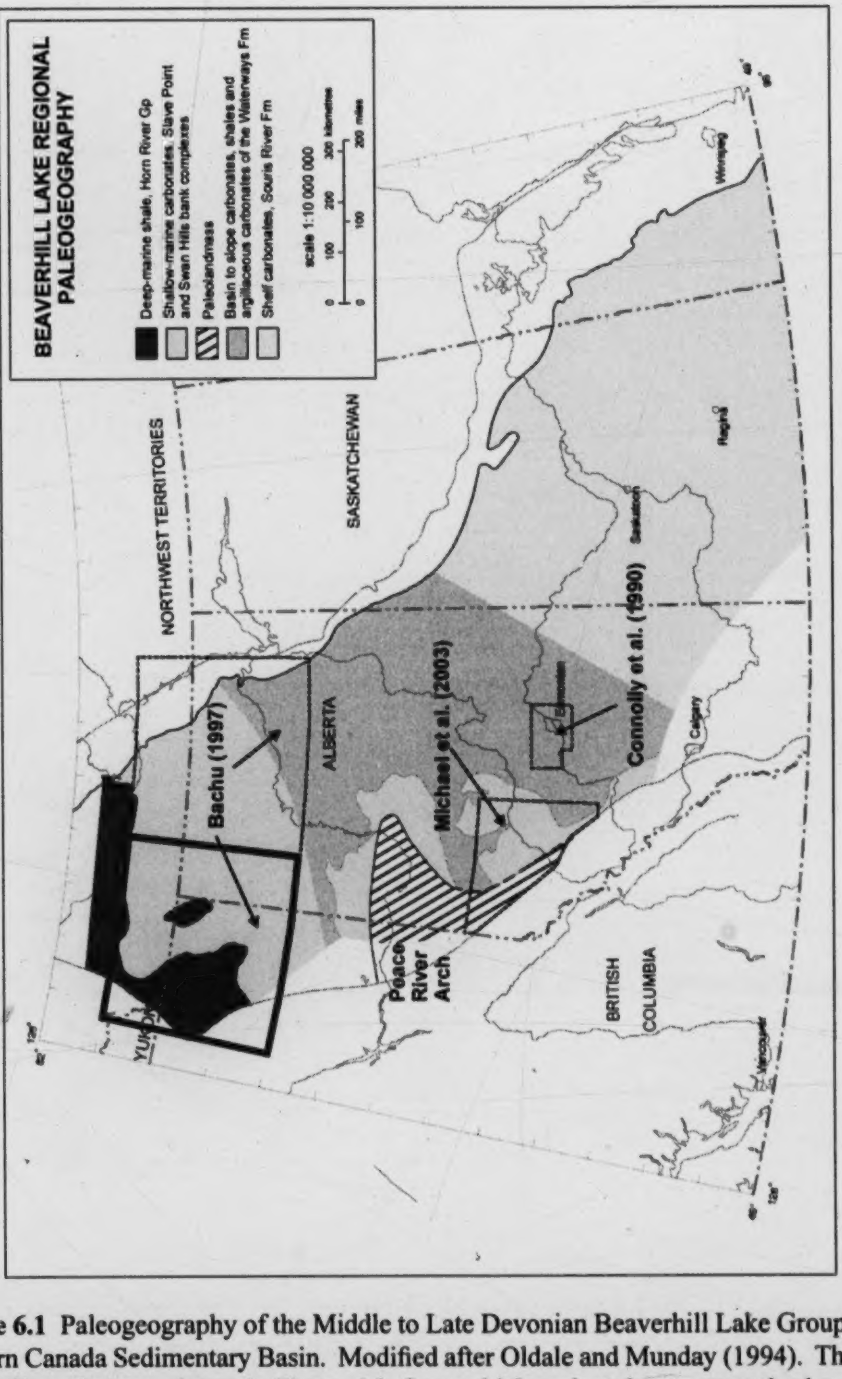
BEAVERHILL LAKE REGIONAL PALEOGEOGRAPHY
Deep-marine shale, Horn River Gp
Shallow-marine carbonates, Slave Point and Swan Hills bank complexes
Paleolandmass
Basin to slope carbonates, shales and argillaceous carbonates of the Waterways Fm
Shelf carbonates, Souris River Fm
scale 1:10 000 000
0 100 200 300 kilometres
0 100 200 miles
NORTHWEST TERRITORIES
SASKATCHEWAN
ALBERTA
BRITISH COLUMBIA
YUKON
Peace River Arch
Bachu (1997)
Michael et al. (2003)
Connolly et al. (1990)
Edmonton
Calgary
Saskatoon
Regina
Winnipeg
Vancouver

Figure 6.1 Paleogeography of the Middle to Late Devonian Beaverhill Lake Group of the Western Canada Sedimentary Basin. Modified after Oldale and Munday (1994). The solid box outlines the area shown in Figure 6.3, from which rock and water samples have been obtained, as well as hydrological data. Study areas of Connolly et al. (1990) and Michael et al. (2003) are referred to in the text.

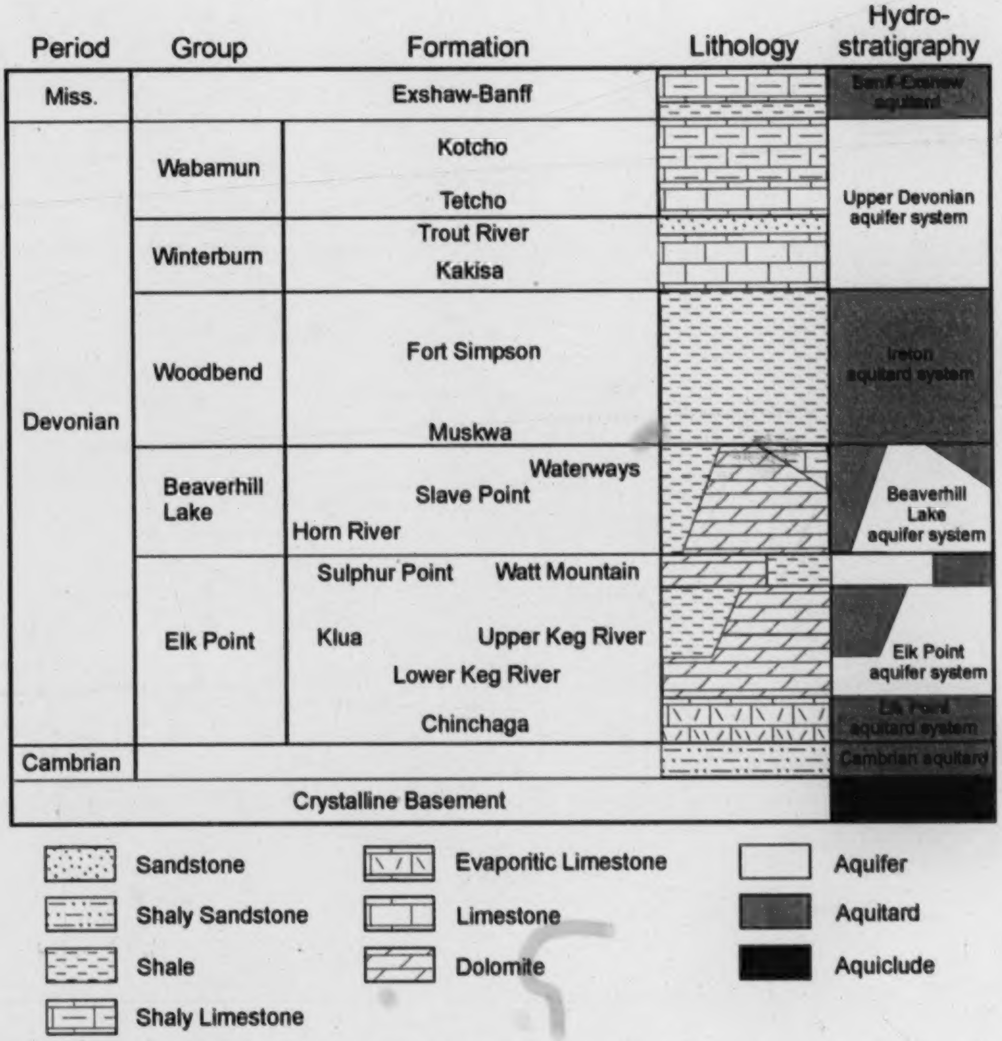
Period
Group
Formation
Lithology
Hydro-stratigraphy
Miss.
Exshaw-Banff
Banff-Exshaw aquitard
Devonian
Wabamun
Kotcho
Tetcho
Winterburn
Trout River
Kakisa
Upper Devonian aquifer system
Woodbend
Fort Simpson
Muskwa
Ireton aquitard system
Beaverhill Lake
Waterways
Slave Point
Horn River
Beaverhill Lake aquifer system
Elk Point
Sulphur Point
Watt Mountain
Klua
Upper Keg River
Lower Keg River
Elk Point aquifer system
Chinchaga
Elk Point aquitard system
Cambrian
Cambrian aquitard
Crystalline Basement
Sandstone
Shaly Sandstone
Shale
Shaly Limestone
Evaporitic Limestone
Limestone
Dolomite
Aquifer
Aquitard
Aquiclude

Figure 6.2 General lithology and hydrostratigraphy of the Paleozoic succession of northeastern British Columbia.

foreland fold and thrust belt (Slind et al., 1994). Towards the north and east of the Clarke Lake field, the Cambrian is absent due to non-deposition or erosion, and the Devonian succession lies unconformably on the crystalline basement.

A mixed succession of low-permeability evaporites and limestones of the Chinchaga Formation overlie the Cambrian unit or the Precambrian crystalline basement. This succession forms the Elk Point aquitard system. The Chinchaga Formation is overlain by the platform carbonates of the Lower Keg River Formation, and the reefal carbonates of the Upper Keg River Formation. This variably dolomitized succession forms the Elk Point aquifer system. North of the Keg River reef margin, in the Horn River shale basin, the Klua shale was deposited. This unit forms a lateral permeability barrier, i.e., an aquitard time-equivalent to/with the Keg River Formation. Continued carbonate platform and reef growth along the Keg River platform margin formed the Sulphur Point Formation, while shales of the Watt Mountain Formation were deposited discontinuously within the platform interior, forming a local aquitard.

The Elk Point Group is overlain by the Beaverhill Lake Group, which is subdivided into the marine platform carbonates of the Slave Point Formation and the argillaceous limestones of the Waterways Formation. The variably dolomitized Slave Point Formation constitutes the Beaverhill Lake aquifer system. Where the Watt Mountain is absent, the Beaverhill Lake Group and the underlying carbonates of the Elk Point Group form a contiguous aquifer system. Basinward of the Slave Point platform margin, shales of the Horn River Formation, i.e., Otter Park equivalent, were deposited.

The Beaverhill Lake Group is overlain by the Woodbend Group, which consists of a thick succession of shale of the Fort Simpson Formation. These shales, and underyling shales of the Horn River Formation and the argillaceous limestones of the Waterways Formation, form both lateral and vertical permeability barriers to fluid flow and have been assigned to the Ireton aquitard system (Bachu, 1997).

The Woodbend Group is overlain by the Winterburn and Wabamun groups, which are dominated by marine carbonates and siliciclastics of the Kakisa, Trout River, Tetcho, and Kotcho formations. This succession forms the Upper Devonian aquifer system. The entire Devonian succession is unconformably overlain by thin shales of the Mississippian Exshaw Formation and a thick package of argillaceous limestones of the Banff Formation. This succession forms the Banff-Exshaw aquitard system.

6.3 Regional Hydrogeology

The regional hydrogeology of the Devonian in northeastern British Columbia and adjacent Alberta has been examined by Bachu (1997). His study evaluated the hydrogeologic characteristics of the entire Phanerozoic sedimentary package from the Rocky Mountains in the west to Great Slave Lake in the east, at latitudes between 58° and 61°N. The relationship between the this study area and the regional paleogeography is shown in Figure 6.1. Hydraulic head and formation water salinity data from Bachu (1997) are shown in Figure 6.3. The only other study from this region of northeastern British Columbia is a report by Underschultz and Bachu (1997) examining the hydrogeology of the Slave Point Formation in, and around, Clarke Lake (Figure 6.3 – dashed box).

Bachu (1997) found that formation waters in the Beaverhill Lake aquifer, i.e., Slave Point Formation, generally flow from southwest to northeast, with a large drop in hydraulic heads over short distances in the southwest (Figure 6.3A). Formation water salinity values range from less than 50 g/L in the northeast and southwest to more than 150 g/L in the central part of the Beaverhill Lake aquifer system (Bachu ,1997) (Figure 6.3B). According to Bachu (1997), the low salinity values in the southwest suggest dilution by meteoric fluids recharging the Beaverhill Lake aquifer within the fold and thrust belt of the northern Rocky Mountains whereby the high hydraulic head gradients imply poor hydraulic connection between the mountains and the subsurface aquifer system. He (ibid.) also found that the flow characteristics in the Beaverhill Lake aquifer are similar to the underlying Elk Point aquifer system, suggesting parts of the Beaverhill Lake aquifer are in direct hydraulic contact with the Elk Point aquifer. Regardless of the prominent eastward-directed flow along the Beaverhill Lake aquifer, the region is not flushed of high-salinity waters. Bachu (1997) suggested that these high-salinity waters are the result of fluid flow from the south, i.e., near the Peace River Arch, where active dissolution of anhydrite and halite is providing continuous solutes to the formation waters. Overall, Bachu (1997) found that the Beaverhill Lake aquifer system has characteristics that support regional-scale steady-state flow driven by topography both from the west and from the south.

Underschultz and Bachu (1997) found that the salinity of formation waters in the Slave Point Formation around the Clarke Lake field varied from 20 g/L to more than 150 g/L, with a characteristic value of approximately 30 g/L in the producing area of the Clarke Lake field. These salinity values are very low but sharply increase to the north of the Slave

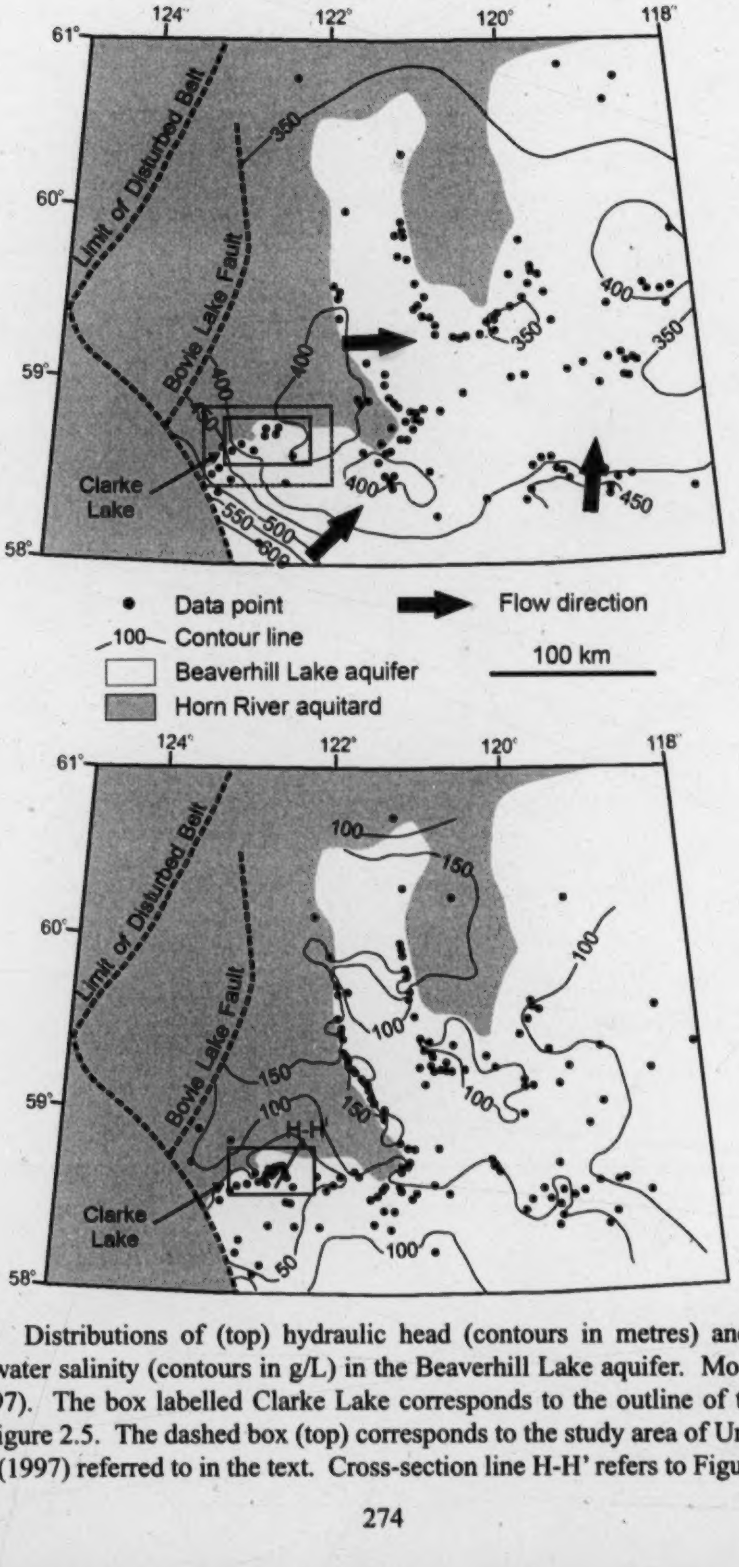
124°
122°
120°
118°
61°
60°
59°
58°
Limit of Disturbed Belt
Bovie Lake Fault
Clarke Lake
350
400
450
500
550
600
Data point
Flow direction
100 Contour line
100 km
Beaverhill Lake aquifer
Horn River aquitard
100
150
50
H-H'

Figure 6.3 Distributions of (top) hydraulic head (contours in metres) and (bottom) formation water salinity (contours in g/L) in the Beaverhill Lake aquifer. Modified after Bachu (1997). The box labelled Clarke Lake corresponds to the outline of the field as shown in Figure 2.5. The dashed box (top) corresponds to the study area of Underschultz and Bachu (1997) referred to in the text. Cross-section line H-H' refers to Figure 6. 18.

Point platform margin, in the Horn River shale basin (Figure 6.3). Hydraulic head values range from more than 600 metres in the southwest to around 400 metres at the platform margin (Underschultz and Bachu, 1997). They (ibid.) suggested that this distribution is the result of the flow of formation waters in a northward direction towards the platform margin. This distribution of hydraulic head values is consistent with the regional-scale topography-driven flow identified by Bachu (1997) (Figure 6.3). North of the platform margin, the hydraulic head values are much lower, and the salinity values are much higher (Underschultz and Bachu, 1997). This likely is the result of a change in the transmissivity of the Beaverhill Lake aquifer system, i.e., a boundary between the carbonates of the Slave Point Formation and the low-permeability shales of the Otter Park Formation. Based on this finding, Underschultz and Bachu (1997) proposed that at the platform margin, formation waters in the Slave Point Formation traveled downward into the underlying Keg River Formation, joining with the regional-scale northeastward-flowing Elk Point aquifer system.

6.4 Methods

Formation water samples were collected from the wellheads of fourteen (14) producing Slave Point Formation gas wells. Wells were selected in an attempt to cover the entire study area, but the ultimate decision on well selection was made by the well operators due to accessibility. Samples were collected in 1L nalgene containers, filled to eliminate any headspace, and sealed with Teflon tape to prevent airborne contamination. Temperature, pH, and alkalinity were not measured during sampling.

The $\delta^{18}O$ composition of the formation water samples was determined using the CO_2-H_2O equilibration method of Epstein and Mayeda (1953). The δD composition of the samples was obtained by converting H_2O to H_2 using Zn at 450°C (Coleman et al., 1982). The evolved gases were analyzed for isotopic ratios on a Finnigan MAT 252 mass spectrometer at the University of Alberta. Values for $\delta^{18}O$ and δD are reported in per mil (‰) relative to the Vienna Standard Mean Ocean Water (VSMOW) standard. The results were reproducible within ± 0.1‰ for both $\delta^{18}O$ and 2‰ for δD.

The $^{87}Sr/^{86}Sr$ values for the formation waters were obtained by evaporating a sample of each fluid and dissolving the residue in 1N hydrochloric acid. Strontium was extracted from the solution using conventional cation exchange chromatography. Strontium isotope ratios were measured on a VG 354 thermal ionization mass spectrometer at the University of Alberta. All analyses were performed in the static multicollector mode using Re filaments. All strontium isotope ratios are presented relative to a value of 0.710245 for the NIST SRM987 standard. The mean standard error was 0.000020 for SRM987. In-run precision was better than 2×10^{-5} (2σ).

The bulk chemistry of the formation waters was analyzed using two methods. Major and minor cations were analyzed using Inductively Coupled Plasma Mass Spectrometry (ICP-MS) at Norwest Laboratories, Edmonton, Canada, following the United States EPA Test Method 200.8. Alkalinity and pH were measured by titration at Norwest Laboratories following APHA Test Method 2320B. Precision of the analyses depends on the technique and sample dilution prior to analysis. Due to difficulties with reproducibility, Na, Cl, and Br were analyzed using Neutron Activation Analysis (NAA) at the University of Alberta SLOWPOKE II nuclear reactor facility. Approximately 250 μL aliquots of each formation water sample were hermetically sealed in polyethylene vials. Samples were individually irradiated for 360 s at a thermal neutron flux of 1×10^{11} $n{\cdot}cm^{-2}s^{-1}$. Following irradiation, samples were counted after a decay period of 10-15 minutes. Samples were counted using a 41.4% relative efficiency Princeton Gamma-Tech (PGT) hyperpure Ge detector connected to a PC-based APTEC multichannel analyzer (MCA) card. Element analyses were performed via the semi-absolute method of activation analysis (Bergerioux et al., 1979). Elemental standards were prepared from pure (> 99.999% purity) salts of KCl, KBr, and NaCl. The detection limits for each element are dependent on the background component and, therefore, varies with sample composition (Currie, 1968).

Gas analyses were obtained from the Geofluids™ database courtesy of IHS Energy. The partial pressure of CO_2, used to calculate the saturation index of CO_2, was obtained by multiplying the mole fraction of carbon dioxide by the reservoir pressure. The pH, saturation indices, and activities of various species in the formation fluids were calculated using the PHREEQC modeling software by setting the saturation index of CO_2 as calculated, and the saturation index of calcite equal to zero assuming equilibrium in the subsurface with respect to calcite.

6.5 Geochemical results and discussion

The complete list of data is available in Appendix X. These results will be interpreted in terms of existing theoretical concepts and by comparison with similar data sets from elsewhere. A guiding principle is the findings of the petrographic and geochemical data discussed in earlier chapters, which place certain constraints on the present-day formation fluids in the Slave Point Formation, i.e.,

a) original formation water of the limestones was seawater (SW),
b) no evidence for incursion of meteoric water (MW) prior to dolomitization,
c) pervasive dolomitization by a (nearly) halite-saturated brine (HB),
d) hydrothermal alteration by 'injection' of a gypsum-saturated brine (GB),
e) localized hydrothermal injection of 'exotic' water (EX), and
f) special wells identified: d-79-F/94-J-10, c-56-L/94-J-9

6.5.1 Stable isotopes

Stable $\delta^{18}O$ and δD data from formation waters in sedimentary basins worldwide are commonly used to answer questions regarding the fluid origin, including meteoric, marine, or evaporative parentage, and to determine the extent of water-rock interactions. Various fluid end members and processes are summarized in Figure 6.4.

Seawater has $\delta^{18}O$ and δD values of approximately 0‰ SMOW (Craig, 1961a) (Figure 6.4 – SMOW). Evaporation of seawater will result in the lighter isotopes of oxygen and hydrogen being preferentially removed (Knauth and Beeunas, 1986), whereby the local climatic conditions control the trajectory, i.e., of the residual evaporitic brines shown as vectors A (high humidity) and B (low humidity) on Figure 6.4. Holser et al. (1979) suggested that enrichment of the heavier isotopes does not continue indefinitely, and the evaporation trajectory abruptly turns at an evaporation ratio of approximately 4X (Figure 6.4 – curve C).

Another source of $\delta^{18}O$ and/or δD-enriched fluids is the water of dehydration of gypsum in the subsurface. With increasing temperatures, i.e., > 50°C, gypsum becomes thermodynamically unstable and recrystallizes to anhydrite (e.g., Hardie, 1967). The expelled water would plot along a trajectory from the point of gypsum saturation (3X) towards progressively heavier isotope values up to about 10X (Figure 6.4 – curve D).

Meteoric water has a large but systematic linear variation in isotopic composition

Figure 6.4 Stable isotope composition of formation waters from the Middle Devonian Slave Point Formation at Clarke Lake. See Figure 6.7 for well locations and Appendix X for data. The majority of the formation water samples plot near seawater $\delta^{18}O$ values of 0‰ SMOW but with strongly depleted δD values. One sample from within the Klua Embayment (a63J) has a value around +10‰ SMOW. Sampled wells include: d-74-C/94-J-9, b-75-F/94-J-9, a-63-J/94-J-9, b-72-L/94-J-9, c-88-L/94-J-9, d-96-L/94-J-9, c-52-F/94-J-10, a-83-G/94-J-10, c-20-I/94-J-10, c-29-I/94-J-10, c-96-I/94-J-10, b-46-J/94-J-10, a-56-J/94-J-10, and a-5-A/94-J-15. The orange field represents Devonian clays (CW) after Longstaffe (1989). The pink field represent thermochemical sulphate reduction (TSR) waters after Machel (1985). The blue field represents metamorphic waters (MetaW) based on the analysis of hydrous minerals after Barnes (1979). The green lines represent Alberta Basin formation waters that have undergone silicate equilibration (vector HFC), after Hitchon and Friedman (1969) and Connolly et al. (1990a). The black and red lines represent the evaporation and dehydration trajectories of Knauth and Beeunas (1986). Vector A represents initial seawater evaporation under relatively humid conditions. Vector B represents initial seawater evaporation under arid conditions. Curve C represents the estimated stable isotope trajectory of evaporating seawater through a concentration of 10X (Holser et al., 1979). The estimated positions of a gypsum-saturated brine (GB) and halite-saturated brine (HB) are shown on Curve C. The isotopic composition of the water of dehydration in gypsum (GDB) precipitated at any point along Curve C is shown by Curve D. Dashed line E parallels vector HFC and represents either simple fluid end-member mixing between or water-rock interaction between meteoric water and metamorphic water (MetaW) or clay dehydration water (CW). Vector SE represents the evolution of present-day meteoric water (MW) through silicate equilibration (water-rock interaction). Vector CE represents the expected isotopic changes in meteoric water due to carbonate equilibration. The δD value for Late Cretaceous meteoric water is obtained from Ayalon and Longstaffe, 1988).

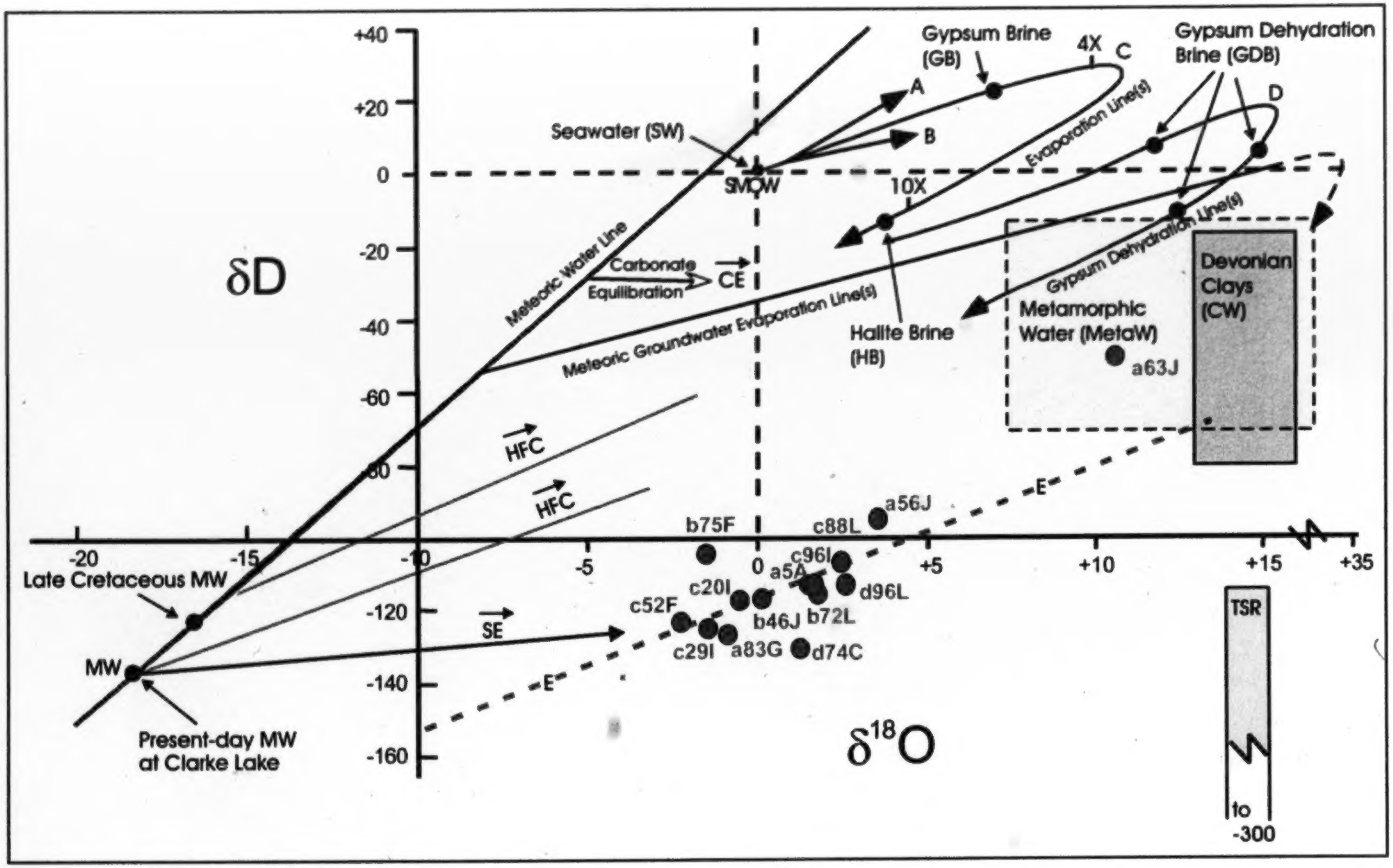

δD
δ18O
+40
+20
0
-20
-40
-60
-80
-120
-140
-160
-20
-15
-10
-5
0
+5
+10
+15
+35
Gypsum Brine (GB)
4X
C
A
B
Seawater (SW)
SMOW
10X
Evaporation Line(s)
Gypsum Dehydration Brine (GDB)
D
Gypsum Dehydration Line(s)
Meteoric Water Line
Carbonate Equilibration
CE
Meteoric Groundwater Evaporation Line(s)
Halite Brine (HB)
Metamorphic Water (MetaW)
a63J
Devonian Clays (CW)
HFC
HFC
SE
E
E
b75F
c88L
a56J
c96I
a5A
c20I
d96L
c52F
b46J
b72L
c29I
a83G
d74C
Late Cretaceous MW
MW
Present-day MW at Clarke Lake
TSR
to -300

($\delta^{18}O$ = -55 to 0‰; δD = -400 to +10‰), which is generally called the global meteoric water line (Craig, 1961b) (Figure 6.4 – meteoric water line). This systematic variation is largely due to the fact that clouds become progressively lighter through successive condensation while travelling across the continents. This produces a geographically controlled distribution of the stable isotope compositions, becoming progressively lighter at higher altitudes and latitudes (Craig, 1961b; Taylor, 1974; Gat, 1980; Yurtsever and Gat, 1981).

Formation waters that have interacted with crystalline basement rocks show enrichment in ^{18}O and depletion in D, whereas interaction with carbonates results only in changes of $\delta^{18}O$, as they do not contain significant hydrogen (Figure 6.4 – carbonate equilibration). From study of the hydrothermal alteration of metamorphic rocks, Barnes (1979) suggested that residual hydrothermal fluids would have a $\delta^{18}O$ composition from +13 to +20‰ SMOW and a δD composition from –65 to -10‰ SMOW (Figure 6.4 – box labelled 'metamorphic water'). Other studies have advocated for the generation of water and CO_2 during prograde metamorphism and devolatilization reactions in the deep burial diagenetic setting, which were then added to the sedimentary basin (Nesbitt and Muehlenbachs, 1989; Land, 1997; Schroyen and Muchez, 2000).

Another possible fluid end-member is the water generated as a by-product of thermochemical sulphate reduction (TSR) reactions. This fluid may result in local dilution of formation waters and show limited variation in $\delta^{18}O$, plotting around +15‰ SMOW, but significant variation in δD, ranging from –300 to –120‰ SMOW (Machel, 1985) (Figure 6.4 – box labelled 'TSR').

The role of isotope exchange between formation water and hydrous clay minerals, likely to have been in the various aquitards of the study area shortly after deposition, has been minimally studied. The extent of isotopic exchange depends on the water-rock ratio, the temperature of the system, and the initial isotopic composition of the clay minerals. Longstaffe (1989) suggested that the interaction of connate fluids with Devonian clay minerals could result in $\delta^{18}O$ range from +13 to +17‰ SMOW and a δD range from –80 to -20‰ SMOW (Figure 6.4 – box labelled 'Devonian clays'). However, the heaviest δD values are only possible in diagenetic systems where all hydrogen fixed in the clay minerals has been derived exclusively from the water (Kharaka et al., 1979; Kharaka and Carothers, 1986). Diagenetic water from the clay minerals must have been added to the formation waters relatively early in the burial history, i.e., depths of 1 to 3 km, where the dominant clay transformations take place, and the volume of water released is relatively small (Osborne and Swarbrick, 1997).

Previous studies from the Western Canada Sedimentary Basin have shown the stable isotopic composition of present-day formation waters to plot to the right of the meteoric water line and significantly below the seawater value (Hitchon and Friedman, 1969; Connolly et al., 1990a). These compositions have been interpreted to have resulted from water-rock interaction, or from mixing of connate fluids with meteoric water, or both (Hitchon and Friedman, 1969; Kharaka and Carothers, 1986; Connolly et al., 1990a). The shift in the $\delta^{18}O$ composition may be significant, but is also ambiguous due to the influence from various water and rock reservoirs. Conversely, formation waters and clay minerals are the basic reservoirs for hydrogen in a sedimentary basin, and the δD values usually show little variation due to the limited volume of exchangeable hydrogen in clay minerals. Hence, the δD values of the present-day formation waters may provide evidence for the mixing of subsurface fluids, while the $\delta^{18}O$ values may be used to indicate the relative proportion of water-rock interaction (Connolly et al., 1990a).

The $\delta^{18}O/\delta D$ diagram (Figure 6.4) can be used to put several constraints on the composition and origin of the Slave Point formation fluids at Clarke Lake. Building on the results from the previous chapters, the following natural waters/fluids could be expected to make up at least a part of the present-day formation waters: 1) seawater (SW); 2) evaporated seawater, gypsum- or halite-saturated brine (GB + HB); 3) either of these modified by water-rock interaction; and, 4) mixing of any of these waters. Additional contributions of waters not recognized in the geochemistry of the solids (Chapter 5) arise from isotope values that do not match any of the above alternatives.

Results

The $\delta^{18}O$ values from the present-day formation waters in the Slave Point Formation range from –2.40 to +10.51‰ SMOW, while δD values vary between –131.2 and –50.7‰ SMOW. These values fall well to the right of the meteoric water line and along a trajectory (E) similar to those proposed by Hitchon and Friedman (1969) and Connolly et al. (1990a) from the Alberta Basin, albeit displaced to lower δD values (Figure 6.4: $\overline{HFC}$)

Discussion

At first glance, of all the waters that are already known to have been involved in the diagenesis of the Slave Point Formation at Clarke Lake, none dominates the present-day formation waters in terms of $\delta^{18}O$ and δD. These possible fluids include: seawater (SW) in the limestones; halite-saturated brine (HB) that effected dolomitization; gypsum-saturated brine (GB) that effected hydrothermal alteration; or, injected 'exotic' water (EX) (Figure 6.4). This suggests that these earlier fluids have been completely flushed from the Slave Point reservoir.

The next most obvious explanation for the distribution of the formation water stable isotope data is through mixing of highly-depleted meteoric water (MW) with either metamorphic water (MetaW) or clay dehydration water (CW) (Figure 6.4 – orange dashed line E). The formation water stable isotope values plot along a trajectory with a slope similar to that proposed by Hitchon and Friedman (1969) and Connolly et al. (1990) (Figure 6.4 - HFC). According to these authors, formation water samples that lie along this trajectory can be interpreted as reflecting either water-rock interaction or mixing between a seawater or modified seawater end-member fluid and a meteoric end-member fluid. The latter alternative can be ruled out in the case of the Clarke Lake formation waters since the upper intercept of this mixing line is atypical of the stable isotopic composition of either seawater or modified seawater (Figure 6.4). Additionally, this mixing line for the Slave Point Formation waters would intercept the global meteoric water line at $\delta^{18}O$ and δD values of roughly –25 and -200‰ SMOW, respectively. However, this projected meteoric water composition has never existed since deposition of the Slave Point Formation in the Middle Devonian. Even with the extremely remote chance that meteoric water did attain such highly depleted stable isotope values, there is no petrographic evidence in the Slave Point Formation for meteoric water incursion in the system in the past. Circumstantial evidence and hydrogeological studies (Bachu, 1997) indicate that meteoric water intrusion was possible since uplift of the Rocky Mountains during the Laramide Orogeny. Present-day rainfall (meteoric waters) in northeastern British Columbia have a weighted annual δD composition of approximately -130‰ SMOW (IAEA, 2005), while data from the Belly River Formation in Alberta suggest meteoric water during the Late Cretaceous had an approximate δD composition of -120‰ SMOW (Ayalon and Longstaffe, 1988) (Figure 6.4). Therefore, meteoric waters since the Late Cretaceous appear to control the δD

composition of the Clarke Lake formation waters.

Further to the possibility that the distribution of stable isotopes in the formation waters at Clarke Lake are the result of mixing between meteoric water and either metamorphic water (MetaW) or clay water (CW), the above interpretation that extremely negative meteoric waters never existed in the Slave Point Formation partially invalidates this alternative. However, under the remote chance that either MetaW or CW are present in the formation fluids, they are discussed further. With respect to metamorphic water, this type of fluid was only generated during the latest stages of the Laramide Orogeny and in only very low fluxes/pore volumes. Similarly, clay waters (CW) were only generated during shallow to intermediate burial in the Late Devonian, and the dehydration of clays is also only likely to generate limited fluid fluxes. Therefore, it is unlikely that either metamorphic waters or clay waters comprise a large percentage of the present formation fluids. Yet, well a-63-J has a stable isotope composition that appears to be dominated by metamorphic water (Figure 6.4). This well is located within relatively impermeable limestones of the Slave Point Formation and is underlain by shales of the Klua Formation, so the possibility exists that the formation fluid in well a-63-J is hydrodynamically isolated from the remainder of the Clarke Lake field.

Compared to present-day meteoric water, the formation waters from the Slave Point Formation show a large ^{18}O enrichment but a comparatively small enrichment in ^{2}H, if any. Assuming a significant contribution of meteoric water since Laramide time, water-rock interaction with carbonates (Figure 6.4: carbonate equilibration - CE) and/or silicates (Figure 6.4: silicate equilibration - SE) alone can account for a shift to the present stable isotope compositions of the Clarke Lake formation waters. Since the δD values of the formation waters plot near, or slightly higher than, -130‰ SMOW - the composition of present-day meteoric water in northeastern British Columbia - it would appear that the meteoric fluid end-member did not isotopically exchange hydrogen in significant quantities along its flow path. This suggests that carbonate equilibration (CE) is the dominant process by which the stable isotope composition of the meteoric waters was reset.

By suggesting that the majority of the Clarke Lake formation fluids have an ultimate origin as meteoric water, this would mean that the previously identified formation waters involved in generating the major mineral phases, including seawater, gypsum-saturated brine, and halite-saturated brine, are all flushed out of the Slave Point reservoir rocks.

Additionally, the minor volumes of either metamorphic water (MetaW) or clay water (CW) have also been flushed from the reservoir rocks. Although, purely on the grounds of the isotope values, any of these fluids could still be present as insignificant admixtures (Figure 6.4). This is evident in well a-63-J, where the stable isotope composition points towards a significant contribution by MetaW. Elsewhere, the presence of earlier formation waters can account for the observed values of total dissolved solids (TDS) in the Clarke Lake formation waters (Figure 6.3), i.e., these fluids are insignificant with respect to the $\delta^{18}O/\delta D$ values, but significant with respect to the present TDS values of >32 000 mg/L.

Other mechanisms could possibly account for the observed stable isotope compositions of the Clarke Lake formation waters. Firstly, if water-rock interaction - either carbonate or silicate equilibration - were minor, mixing meteoric water with large contributions of metamorphic water could account for the observed isotope distribution. However, it was stated previously that the metamorphic water would likely only occur as a one-time pulse, and therefore, results in a limited fluid flux. This caveat makes this alternative unrealistic. Secondly, one could argue for a halite-saturated brine end-member mixing with a meteoric water end-member that had undergone significant silicate equilibration. Though, this alternative would require that the halite-saturated brine be present only in very low concentrations, which also is unrealistic.

Lastly, no thermochemical sulphate reduction (TSR) waters are recognizable in the formation fluids in the Slave Point reservoir. This observation is in concordance with the geochemical data from the Slave Point carbonates in Chapter 5, which do not show any evidence to support being products of TSR reactions.

Therefore, the present stable isotope composition of the formation fluids in the Slave Point Formation is the result of predominantly water-rock interaction. The present-day meteoric fluid that was involved in water-rock interaction, i.e., carbonate equilibration, provides the extremely negative δD values of the formation waters. Circumstantial evidence suggests that this fluid end-member may have mixed in the Slave Point reservoir with previously entrained brines. Finally, a third end-member fluid is identified in well a-63-J, and may represent the contribution of metamorphic water prior to hydrodynamic isolation.

The extent of water-rock interaction can be further evaluated under the assumption that the shift in the $\delta^{18}O$ composition of the meteoric water is the result of exchange with carbonates in the Slave Point Formation. The dolomite-water equilibrium fractionation equation of Land (1983) and the calcite-water equilibrium fractionation equation of O'Neil et al. (1969) were used to calculate the oxygen isotope composition of formation water in equilibrium with both dolomite and calcite as a function of the present-day reservoir temperature (Figure 6.5). In general, Clarke Lake formation waters are not in equilibrium with either the matrix dolomites or the saddle dolomites in the Slave Point reservoir, with the exception of the isotopically lightest formation water samples (Figure 6.5A). Additionally, compared to the range of water $\delta^{18}O$ values modelled for the dolomites, the Clarke Lake formation waters are slightly depleted, likely indicating the effect of the influx of meteoric water subsequent to the Laramide Orogeny (Connolly et al., 1990a). In contrast, the formation waters are, for the most part, in equilibrium with calcite reservoirs (Figure 6.5B). However, the volume of calcite in the Slave Point Formation is extremely restricted, precluding the likelihood that the formation waters equilibrated with calcite but not the volumetrically much greater dolomite. Rather, the results suggest that only the most isotopically depleted formation waters are in equilibrium with the carbonates of the Slave Point Formation. As well, considering that equilibration with carbonate minerals should occur rapidly, i.e., geologically speaking, in the subsurface, the disequilibria exhibited by the Clarke Lake formation fluids with respect to the Slave Point reservoir rocks likely indicates that the formation waters are equilibrating with carbonate rocks farther to the west in the subsurface of northeastern British Columbia.

6.5.2 Strontium isotopes

The strontium isotope composition of formation waters provides a natural tracer for subsurface fluid studies. The $^{87}Sr/^{86}Sr$ ratio of a water sample collected at the wellhead is representative of the subsurface fluid, despite production-related changes in temperature, pressure, or phase that may impact the bulk geochemistry and/or stable isotope composition. Chaudhuri (1978) was the first to propose that strontium isotope data can provide critical information on the chemical history of formation waters. Subsequent studies have used strontium isotopes to assist in the interpretation of regional fluid flow and the evolution of formation waters (Chaudhuri et al., 1987; Stueber et al., 1984; 1987; Posey et al., 1985; Banner et al., 1989; Chaudhuri and Clauer, 1993; Oetting et al., 1996). These studies have provided valuable clues regarding both the chemical evolution of the fluids and a

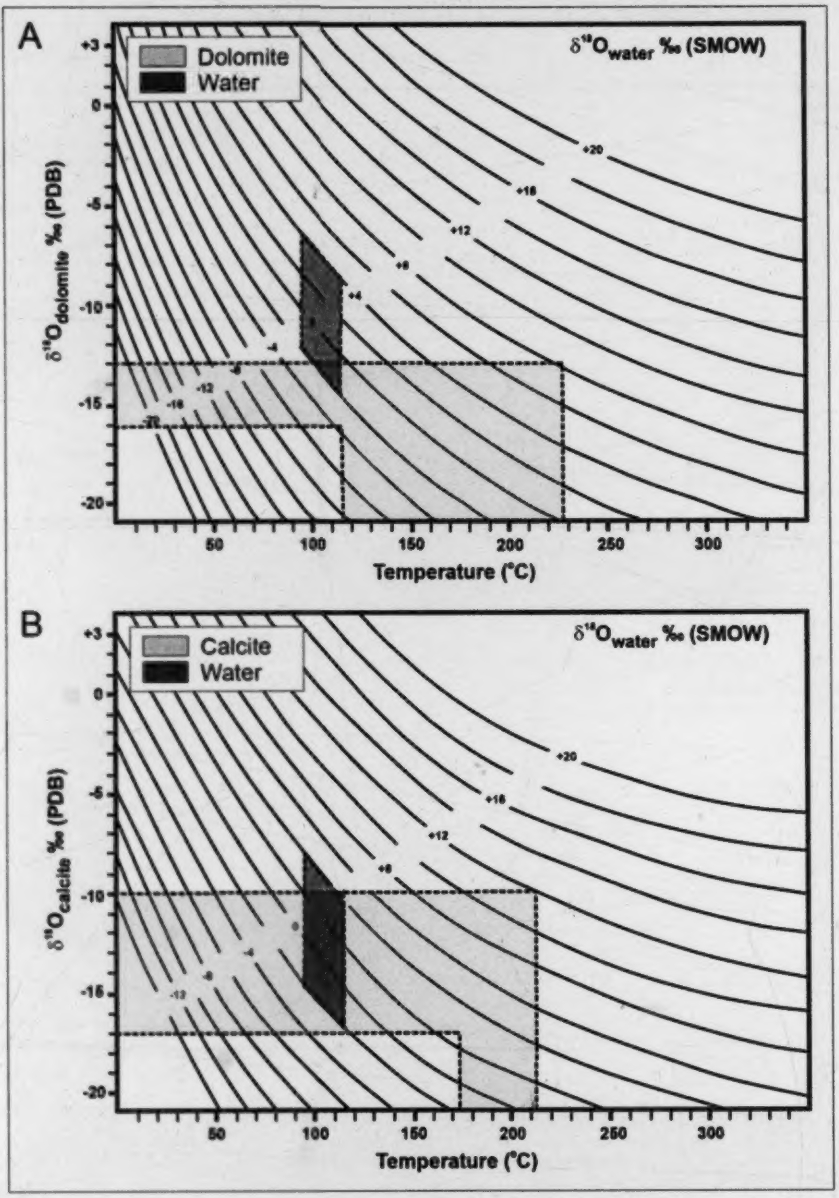

Figure 6.5 Plot of equilibrium isotope fractionation: A) between dolomite and water, after Land (1983); B) between calcite and water, after O'Neil et al. (1969). The dolomite field includes both matrix and saddle dolomite. The calcite field includes late-stage blocky calcite cement. These fields were constructed based on the $\delta^{18}O$ compositions and fluid inclusion temperatures from the phases. The water fields were constructed using bottom hole temperatures and $\delta^{18}O$ compositions, excluding well a63J. Only the isotopically lightest of the formation waters show overlap with the dolomite field, while nearly the entire isotope range of the formation waters are in equilibrium with late-stage calcite cements.

further understanding of the diagenetic history of the reservoir rocks. Unfortunately, few studies have been published on the strontium isotope composition of formation waters in the Western Canada Sedimentary Basin, with the exception of Connolly et al. (1990a), Buschkuehle (2003), and Lonnee and Machel (2003).

Results

The $^{87}Sr/^{86}Sr$ ratios of the formation waters in the Slave Point Formation range from approximately 0.713 to 0.750 (Figure 6.6). Most of these values are significantly enriched in ^{87}Sr compared to the host limestone and dolostones (ranging from 0.708 to 0.718), and are the highest strontium isotope values published from the Western Canada Sedimentary Basin to date. Additionally, these values deviate significantly from the composition of Middle Devonian seawater (around 0.708 - Denison et al., 1997), or seawater at any time during the Phanerozoic (Burke et al., 1982). All formation water samples are also more radiogenic than the entire package of Phanerozoic shales in northeastern British Columbia and the equivalent value of 0.712 (MASIRBAS) (Figure 6.6) from west-central Alberta (Machel and Cavell, 1999). Only one sample, labeled fluid component 1 in Figure 6.6, has a $^{87}Sr/^{86}Sr$ value below either that of Cambrian sandstones or the Proterozoic Muskwa Assemblage, while all other samples are well within the range of $^{87}Sr/^{86}Sr$ values from the Muskwa, significantly above the value from Cambrian sandstone, yet below the range of values from the crystalline basement (Figure 6.6).

Discussion

The extraordinarily high $^{87}Sr/^{86}Sr$ values of the Clarke Lake formation waters preclude a Sr source from seawater of any age, and indicates that highly radiogenic Sr-sources dominate the formation water strontium isotope composition. Additionally, the stable isotopes (Figure 6.4) suggest the present formation waters evolved from values typical of meteoric water by equilibration predominantly with carbonate rocks, and subordinately with siliciclastic rocks. The $^{87}Sr/^{86}Sr$ concentration of these meteoric waters, originally containing no Sr, can only be explained by water-rock interaction. Based on the strontium that is available to the meteoric fluid along its flow path, the only possible sources of radiogenic ^{87}Sr are the Proterozoic Muskwa Formation and the crystalline basement.

Potential mixing relations can be tested by using a plot of $^{87}Sr/^{86}Sr$ versus reciprocal

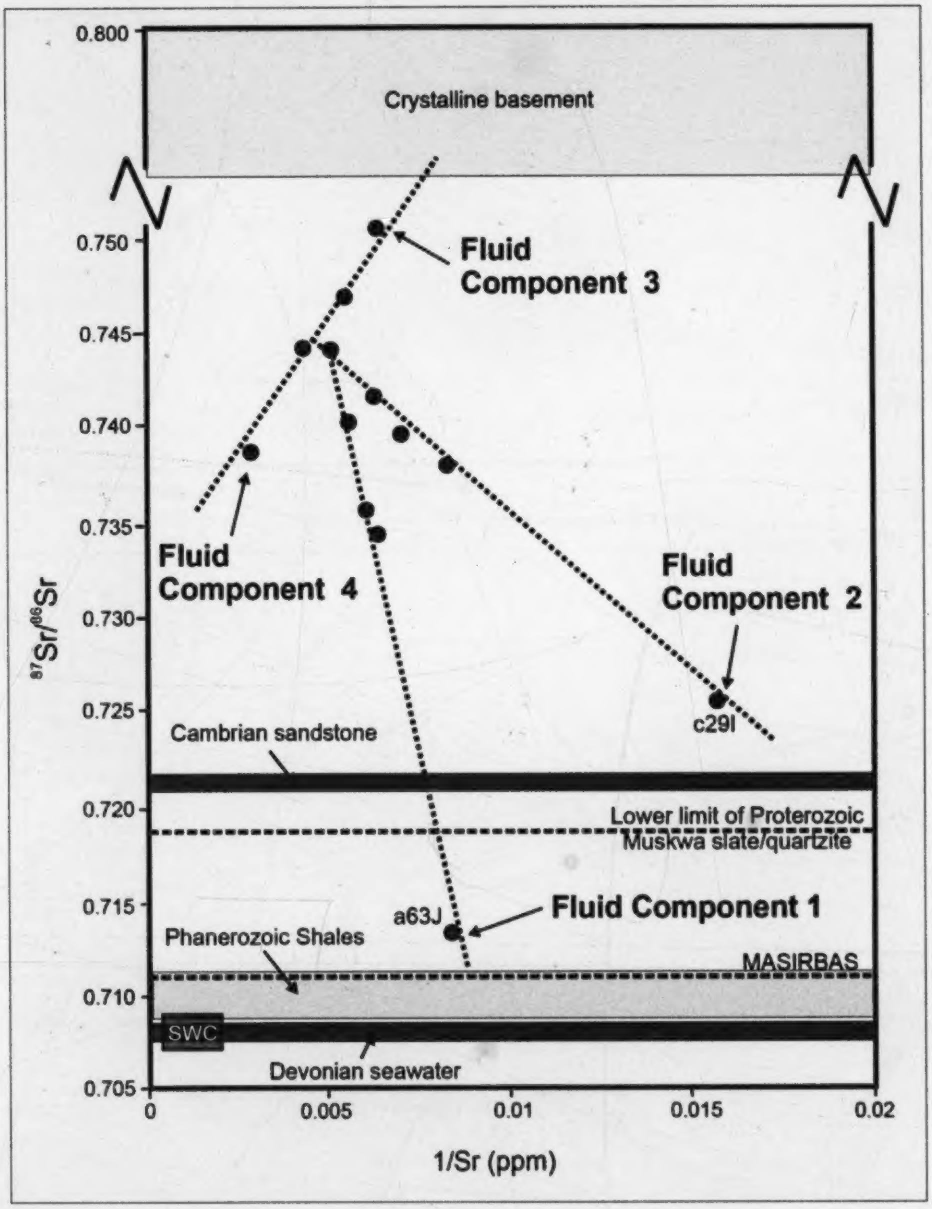

Figure 6.6 Crossplot of formation water $^{87}Sr/^{86}Sr$ versus Sr concentration. Distribution of data indicates possible fluid mixing between 3 or 4 end-member fluid compositions in the Slave Point Formation. Estimated $^{87}Sr/^{86}Sr$ of Middle Devonian seawater according to Denison et al. (1997). Approximate range of strontium concentrations for Devonian abiotic marine calcite (AC) after Carpenter et al. (1991). Maximum strontium isotope ratio of basinal shales (MASIRBAS = 0.7120) after Machel and Cavell (1999). Included are fields for crystalline basement, Proterozoic Muskwa Assemblage, Cambrian sandstone, and Phanerozoic basinal shales (data in Appendix IX).

Sr (Figure 6.6). In this kind of plot, the correlation of data to a straight line suggests end-member fluid mixing under the assumption that the waters were not altered subsequent to mixing (Faure, 1986). The Slave Point Formation data display evidence for the mixing of 3 or 4 fluid end-members around the Clarke Lake field. The first fluid component is the least radiogenic of all formation waters. This sample is from well a-63-J, which was interpreted to represent metamorphic water (MetaW) based on the stable isotopes (Figure 6.4). Due to the relative hydrostatic isolation of this well, it would be expected that the $^{87}Sr/^{86}Sr$ value was unaltered since it entered the reservoir.

The second fluid component is found in the center of the Clarke Lake field in well c-29-I, which is only a few hundred metres away from wells containing significantly more radiogenic formation waters (Figure 6.7). This fluid has a $^{87}Sr/^{86}Sr$ value that is close to that from the Cambrian sandstone (Figure 6.6) and has a relatively low Sr concentration. This may suggest a fluid that followed a different flow path into the Slave Point reservoir, e.g., fluid origin appears to have been from the south (Figure 6.7) and traveled into the reservoir along a fault cutting through the Cambrian.

Fluid components 3 and 4 have Sr-isotope values similar to the Proterozoic Muskwa Assemblage (Figure 6.6), and may in fact represent a single fluid component, since there is no additional evidence to account for the subtle differences in their chemistry. These components are common in the western part of the Clarke Lake field (Figure 6.7), and thus are closer to the recharge location of the meteoric fluids, i.e., in the Rocky Mountains. Therefore, these two fluid components are likely representative of meteoric water that had obtained most of its Sr from the Muskwa Assemblage along its flow path, while other rock units that this water passed through are unrecognizable isotopically. In any case, fluid components 2, 3, and 4 all have a meteoric origin based on the stable isotopes (Figure 6.4).

The formation waters that plot between the line connecting fluid components 3 and 4, and components 1 and 2 may represent mixtures of fluid components 3 and 4 with 1 or with 2, respectively (Figure 6.6). Alternatively, all fluid compositions except for components 1 and 2 may represent variations in water-rock interaction along slightly differing flow paths.

The $^{87}Sr/^{86}Sr$ results from the present-day formation waters provide the first set of data that can be directly compared to the geochemistry of the dolomites in the Clarke

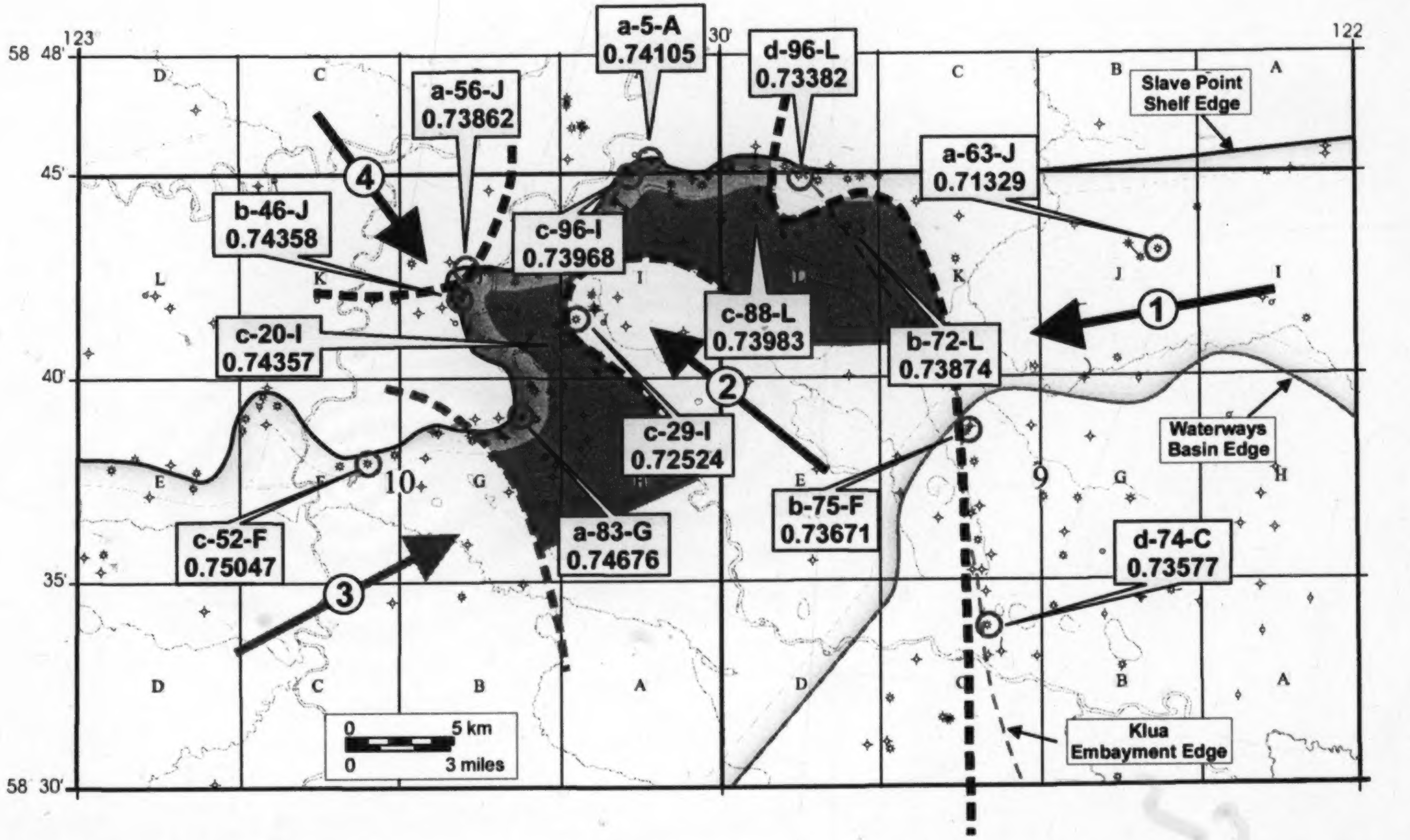
58 48'
45'
40'
35'
58 30'
123
30'
122
a-5-A
0.74105
d-96-L
0.73382
a-56-J
0.73862
b-46-J
0.74358
c-96-I
0.73968
a-63-J
0.71329
c-88-L
0.73983
b-72-L
0.73874
c-20-I
0.74357
c-29-I
0.72524
b-75-F
0.73671
c-52-F
0.75047
a-83-G
0.74676
d-74-C
0.73577
Slave Point Shelf Edge
Waterways Basin Edge
Klua Embayment Edge
①
②
③
④
10
9
0 5 km
0 3 miles

Figure 6.7 Distribution of $^{87}Sr/^{86}Sr$ values in formation water samples from the Slave Point Formation at Clarke Lake. The coloured arrows and dashed lines represent the position and possible direction of flow of the various chemically distinct end-member fluids (see Figure 6.6). The purple shaded region represents the area of maximum end-member fluid mixing.

Lake field. The distribution of Sr-isotope results from the bulk analysis of saddle dolomite crystals across the Clarke Lake field discussed in Chapter 5 (see Figure 5.7) shows little relationship to the present-day formation water $^{87}Sr/^{86}Sr$ results (Figure 6.7). Across much of the Clarke Lake field, saddle dolomites exhibit Sr-isotope ratios of around 0.710, while those from the westernmost parts of the field, in particular, from well d-79-F, have Sr-isotope ratios around 0.715. Yet, the present-day formation waters, with the exception of well a-63-J, have Sr-isotope ratios above 0.725. Only the formation water sample from well a-63-J shows any similarities to the hydrothermal gypsum-saturated brine that was responsible for saddle dolomite formation. However, the likelihood that the formation water in well a-63-J is related to the hydrothermal dolomite-forming fluid is extremely remote given the fact that there is no petrographic evidence for saddle dolomite in this well.

Plots of the $^{87}Sr/^{86}Sr$ results in conjunction with the stable isotope results provide further evidence for the mixing of fluid end-members in the Slave Point Formation. With respect to the $\delta^{18}O$ values, the isotopic trends point towards the mixing of 2, possibly 3, end-members (Figure 6.8A). The first end-member fluid is from well a-63-J, the proposed metamorphic water (MetaW) that has a heavy $\delta^{18}O$ value and is only slightly radiogenic compared to Devonian seawater. A good linear correlation exists between fluid components 1 and 3, with fluid component 3 now including both components 3 and 4 from above. This linear correlation suggests that the bulk of the mixing is between these two fluid end-members. Fluid component 3 is highly radiogenic and has light $\delta^{18}O$ values. This end-member fluid is representative of meteoric water that obtained radiogenic ^{87}Sr from the Proterozoic Muskwa Formation or crystalline basement rocks. Fluid component 2 shows little variation in $\delta^{18}O$ and significant enrichment in ^{87}Sr. This fluid is found around well c-29-I and as suggested earlier, may represent a distinct end-member fluid entering the Clarke Lake field from the south. Furthermore, all water samples from the Slave Point Formation plot in a distinct region compared to samples from the Devonian in west-central Alberta (Figure 6.8: data from Connolly et al., 1990a). The Alberta samples, which were suggested to have formed through the mixing of meteoric water and connate brine, are significantly less radiogenic than samples from this study. According to Connolly et al. (1990a), the formation waters in the Devonian of Alberta have $^{87}Sr/^{86}Sr$ values that reflect water-rock interaction with Devonian and Cambrian shales. A similar interpretation was

Figure 6.8 Crossplots of the isotopic composition of formation waters from the Slave Point Formation at Clarke Lake.

(A) Crossplot of $^{87}Sr/^{86}Sr$ and $\delta^{18}O$. The data from Clarke Lake display two linear trends, indicating the definite mixing between two fluid end-members (1 and 3), and the possible addition of a third fluid end-member (2). Included for reference are formation water data from the Devonian of west-central Alberta after Connolly et al. (1990a). The zones of preorogenic and syn- to postorogenic fluids are based on data presented in Nesbitt and Muehlenbachs (1994) and relate only to the $\delta^{18}O$ composition of the formation fluids.

(B) Crossplot of $^{87}Sr/^{86}Sr$ and δD. The data from Clarke Lake display two weakly correlated linear trends. Similar to the $\delta^{18}O$ composition of the formation waters, the δD data likely shows the effects of fluid mixing between two fluid end-members (1 and 3), and the possible addition of a third fluid end-member (2). Included for reference are formation water data from the Devonian of west-central Alberta after Connolly et al. (1990a). The zones of preorogenic and syn- to postorogenic fluids are based on data presented in Nesbitt and Muehlenbachs (1994) and relate only to the δD composition of the formation fluids.

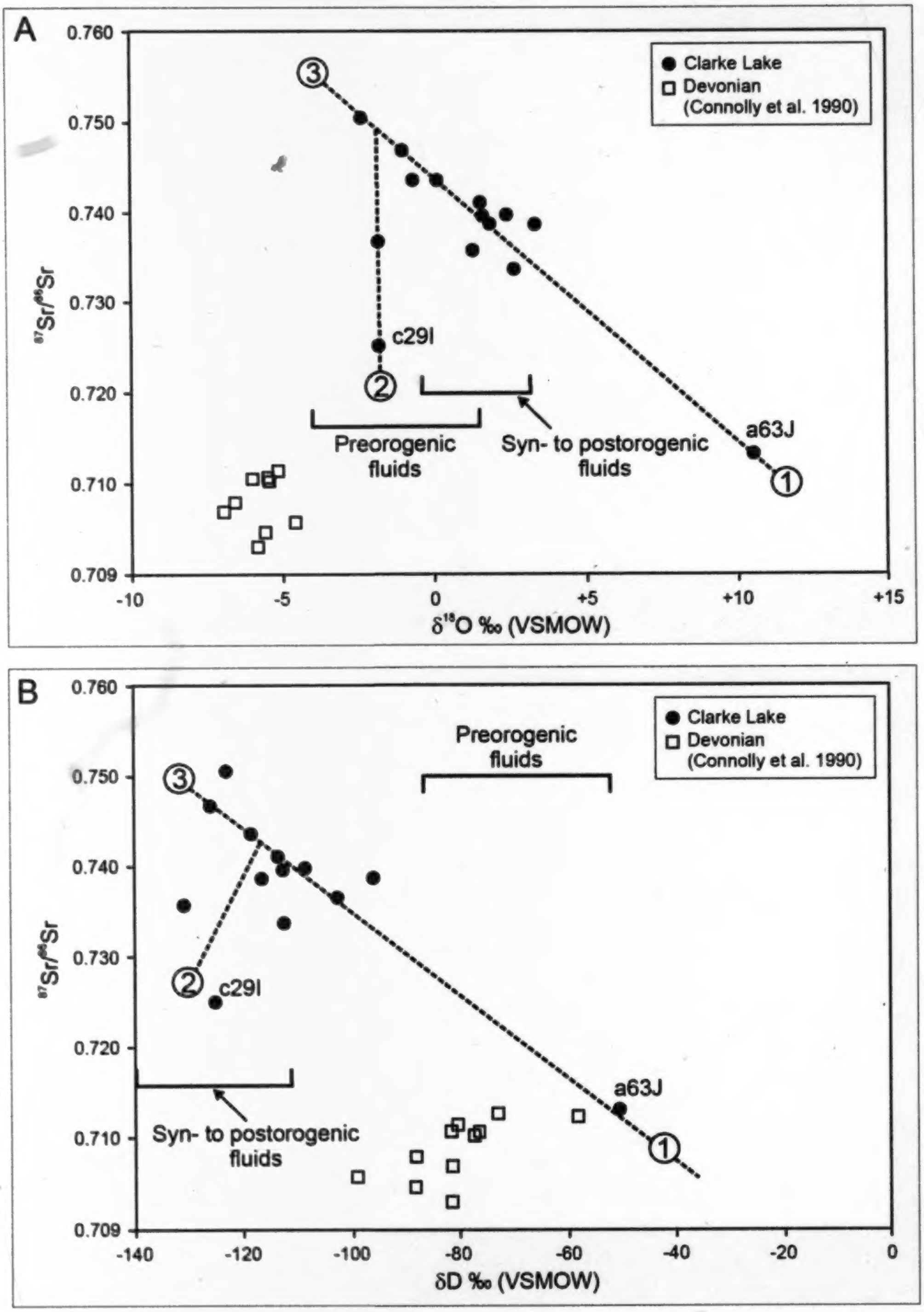
A
0.760
0.750
0.740
0.730
0.720
0.710
0.709
$^{87}Sr/^{86}Sr$
-10
-5
0
+5
+10
+15
δ^{18}O ‰ (VSMOW)
● Clarke Lake
□ Devonian (Connolly et al. 1990)
③
②
①
c29I
a63J
Preorogenic fluids
Syn- to postorogenic fluids
B
0.760
0.750
0.740
0.730
0.720
0.710
0.709
$^{87}Sr/^{86}Sr$
-140
-120
-100
-80
-60
-40
-20
0
δD ‰ (VSMOW)
● Clarke Lake
□ Devonian (Connolly et al. 1990)
Preorogenic fluids
③
②
①
c29I
a63J
Syn- to postorogenic fluids

proposed by Buschkuehle (2003) for formation waters in Frasnian and Famennian-aged carbonates adjacent to the foreland fold and thrust belt in west-central Alberta.

The δD results show similar trends as the $\delta^{18}O$ results (Figure 6.8B). Fluid end-member 1 has a heavier δD value, which is similar to the Devonian samples from Alberta (Connolly et al., 1990a). Additionally, the heaviest δD values were interpreted by Nesbitt and Muehlenbachs (1994) to represent fluids generated prior to the Late Cretaceous to early Tertiary Laramide Orogeny (Figure 6.8B – preorogenic fluids). Fluid component 3 (and 2?), as discussed previously (Figure 6.6), have δD values close to present-day meteoric water in northeastern British Columbia. This range in δD values is similar to the range proposed by Nesbitt and Muehlenbachs (1994) for fluids that were generated concurrent with, or post-date, the Laramide Orogeny (Figure 6.8B – syn- to postorogenic fluids).

6.5.3 Ionic hydrochemistry

The major and trace element composition of subsurface formation fluids is generally dissimilar to present-day fluids, i.e., seawater, evaporated seawater, and meteoric water. However, because the ultimate precursor of most brines in the subsurface was likely seawater, the present-day chemistry of the formation fluids should be compared to seawater, the ratio of components in seawater, or the composition of brines formed by the evaporation of seawater (Hanor, 1987). The average composition of seawater used for comparative purposes is shown in Table 6.1.

In order to characterize the origin and evolution of formation waters, it is commonplace to present the concentrations of dissolved constituents against chloride and bromide concentrations (Figure 6.9). It should be noted, however, that Br^- data are not available for many formation waters, and then only Cl^- data are being used. These two constituents are used due to the conservative behaviour that they exhibit. During the initial evaporation of seawater, both Br^- and Cl^- increase in the residual brine. Past halite saturation, Cl^- is preferentially removed as NaCl, and Br^- remains in the residual brine, a process that proceeds, albeit by differing ratios, during the precipitation of epsomite, sylvite, carnallite, and bishofite. The Cl/Br ratio progressively decreases due to discrimination against Br because the distribution coefficients for each mineral are less than 1. As a result, bromide and chloride concentrations are commonly used as indicators for evaporation in formation waters (Carpenter, 1978).

Table 6.1 Chemical composition of seawater after Drever (1988). Constituents with an asterisk (*) are based on data presented by McCaffrey et al. (1987).

Major Constituents	mg/l	Minor and Trace Constituents	mg/l
Cl	20 500*	Al	0.002
Na	11 300*	Ba	0.01
SO_4	2 880*	Fe	0.002
Mg	1 300*	I	0.06
Ca	390*	Li	0.18
K	427*	Mn	0.0002
HCO_3	142	Ni	0.0005
Br	67	Pb	0.00003
Sr	8	Rb	0.12
B	4.5	Zn	0.002

Subsurface brines that formed by subaerial evaporation of seawater and were not involved in either chemical reactions or mixed with other subsurface fluids will plot along the seawater evaporation trend shown in Figure 6.9. Few subsurface fluids follow this trend, however, so other processes influenced their compositions. One mechanism that has been proposed to alter the Br$^-$ and Cl$^-$ composition of subsurface fluids is via congruent dissolution of halite. Theoretically, the dissolution of halite would remove Br$^-$ and Cl$^-$ in a proportion equal to that in the halite crystals. The resulting brines would have Cl/Br ratios that are higher than seawater because of the relatively low Br$^-$ content of halite (top left corner in Figure 6.9). However, many subsurface brines have lower Cl/Br ratios than expected, and Land and Prezbindowski (1981) and Stoessel and Carpenter (1986) suggested that such lower Cl/Br ratios might be the result of incongruent dissolution of halite. Thereby, any solution depleted in Br$^-$, e.g., meteoric water, and percolating through halite would preferentially dissolve Br. Other mechanisms for changing the Br$^-$ and Cl$^-$ content of subsurface fluids include: membrane filtration, diffusion, and mixing. Kharaka and Berry (1973) showed that Cl$^-$ passes through clay membranes more readily than Br$^-$, lowering the Cl/Br ratios in a brine. The effects of diffusion on the concentration of Cl$^-$ and Br$^-$ are not well understood, since the diffusion coefficients for Br$^-$ in solution at elevated temperatures are not known (Hanor, 1987). Lastly, end-member fluid mixing may produce brines having a wide range of Br$^-$ and Cl$^-$ concentrations.

The few studies that are available from the Alberta Basin are limited to west-central Alberta (Hitchon et al., 1971; Connolly et al., 1990b; Rostron et al., 1997; Michael et al., 2003). In this region, the Devonian formation waters contain two distinct brine types: a

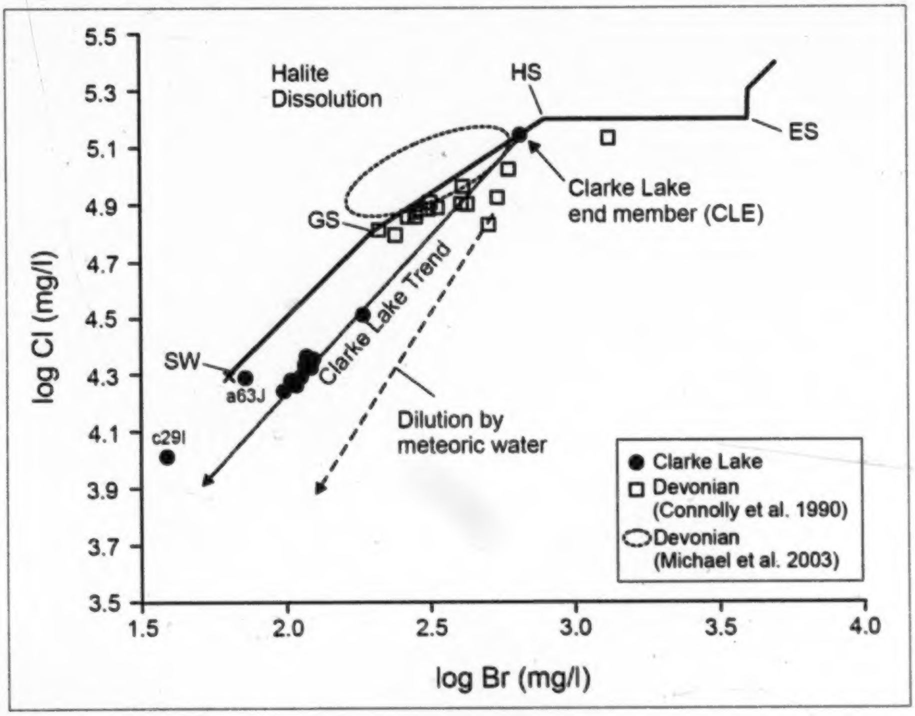

Figure 6.9 Crossplot of Cl and Br concentrations (Carpenter, 1978) with data from Clarke Lake formation waters. Squares represent data from the Devonian of west-central Alberta after Connolly et al. (1990b). The circled field represents the approximate range of Devonian formation waters from west-central Alberta after Michael et al. (2003). Solid line = evaporation of seawater (after Fontes and Matray, 1993). SW = seawater; GS = gypsum saturation; HS = halite saturation; ES = epsomite saturation. Trajectory is shown for the dilution of evaporated seawater by meteoric water. The bulk of the formation water samples from Clarke Lake plot below the seawater evaporation trajectory between normal seawater and gypsum saturation, and plot along a trend (Clarke Lake Trend) between a near halite-saturated brine (Clarke Lake end member - CLE) and chemically slightly modified meteoric water. Wells c29I and a63J are discussed in the text.

'heavy brine', located updip, defined approximately by total dissolved solid (TDS) values greater than 200 g/L, and a 'light brine' with TDS less than 200 g/L (Michael et al., 2003). Based on current hydraulic head distributions, it appears that the 'light brine' is moving updip, thereby pushing the 'heavy brine' ahead (Michael et al., 2003). The ' heavy brine' may be residual Middle Devonian evaporitic brine, or it may have originated from partial dissolution of evaporite deposits to the east of the study area (Michael et al., 2003). The 'light brine' more than likely originated from dilution of the 'heavy brine' by meteoric water following formation of the Rocky Mountains to the west (Connolly et al., 1990b; Michael et al., 2003). No published hydrochemical studies of the formation waters from the Devonian of northeastern British Columbia are available.

Results

The total dissolved solids (TDS) of the formation water samples from the Slave Point Formation in the Clarke Lake region range from 687 to 55 451 mg/L, averaging 32 163 mg/L, which is slightly below the average value for seawater of about 35 000 mg/L (Drever, 1988). Six of the fourteen samples have values greater than seawater, and all values for TDS, with the exception of the sample at 687 mg/L, fall within the category of saline water (TDS = 10 000 to 100 000 mg/L) (Carpenter, 1978).

The formation water samples have Br concentrations that range from 1 to 186 mg/L, and Cl concentrations that vary between 376 and 32 900 mg/L. Sodium concentrations range from 210 to 14 700 mg/L, K concentrations vary between 14 and 2150 mg/L, Ca concentrations range from 35 to 4370 mg/L, and Mg concentrations vary between 4 and 574 mg/L. When plotted against Br, all ions in solution lie off the seawater evaporation trajectory of McCaffrey et al. (1987) (Figures 6.9 to 6.12).

Molar Cl/Br values from the formation waters range from 386 to 855, averaging 465, which is near the point of halite saturation on the seawater evaporation trajectory (Figure 6.11). Molar K/Br values range from 5 to 29, averaging 20, which sits above the seawater evaporation trajectory in space occupied by the dolomites of the Slave Point Formation (Figure 6.11A). Molar Na/Br values vary between 275 and 737, averaging 354, which places most of the data on the seawater evaporation trajectory slightly beyond the point of halite saturation and, also, in the space occupied by the dolomites of the Slave Point Formation (Figure 6.11B).

Discussion

Formation waters from the Slave Point Formation plot below and to the right of the seawater evaporation trajectory in Cl/Br-space (Figure 6.9). The majority of the samples lie along a straight line ('Clarke Lake Trend' in Figure 6.9) that parallels the sloping portion of the seawater evaporation trajectory, which suggests dilution of an evaporitic brine end-member by meteoric water according to Connolly et al. (1990b). Additionally, the intercept of this line with the seawater evaporation trajectory indicates the evaporated end-member fluid originally had a composition similar to seawater evaporated nearly to the point of halite saturation ('Clarke Lake end member' - CLE in Figure 6.9). This intercept is also within the range of values exhibited by formation waters from the Devonian of west-central Alberta (Connolly et al., 1990b; Michael et al., 2003), which these authors interpreted to represent highly evaporated seawater that was variably diluted by meteoric water following the Laramide Orogeny. Two Clarke Lake samples lie off this trend: a-63-J and c-29-I. The sample from well a-63-J lies near the composition of normal seawater. However, considering the previous the previous interpretation of the stable isotope data (Figure 6.4), this sample does not represent entrained seawater, but was suggested to represent a fluid end-member with a composition similar to metamorphic water (MetaW). As a result, the most obvious explanation for the Cl/Br data from well a-63-J, and potentially well c-29-I, is through mixing of a third fluid end-member (MetaW?) that mixed with meteoric water along the flow path. This explanation requires further discussion of the isotope distributions from these two wells, including why neither the stable isotopes (Figure 6.4) nor the Sr-isotope ratios (Figure 6.7) are similar. In these earlier discussions, the formation waters in a-63-J and c-29-I represented fluid components 1 and 2, respectively. The petrographic and geochemical evidence from well a-63-J suggest that there is no fault access at this location. Therefore, this isotopically distinct fluid end-member (MetaW) likely migrated into the Slave Point Formation near well a-63-J during a single pulse. On the other hand, the fluid component in well c-29-I was previously interpreted as meteoric water that migrated along a different flow path into the Slave Point reservoir, e.g., along a fault cutting through the Cambrian. Consequently, the present-day formation water chemistry in well c-29-I is likely a reflection of continuous 'injection' of a third fluid end-member (MetaW?) that mixes with meteoric water in the Slave Point Formation.

None of the Clarke Lake formation water samples plot above the seawater evaporation trajectory (Figure 6.9), suggesting that none of them are derived from the congruent dissolution of halite, which has been proposed by Hitchon et al. (1971) and Michael et al. (2003). They (ibid.) argued that high salinity fluids found in the Devonian of central and eastern Alberta are the result of partial dissolution of evaporite deposits and down-dip flow of these heavy brines from the Williston and Elk Point basins to the south and east, respectively, as also suggested by Spencer (1987).

The Clarke Lake formation waters have Na concentrations that lie below the seawater evaporation trajectory (Figure 6.10A). The bulk of the Clarke Lake formation water data lie along the Clarke Lake Trend in Na/Br-space (Figure 6.10A). The Clarke Lake Trend intercepts the seawater evaporation trajectory at a point near halite saturation. This trend is indicative of mixing between a highly evaporated brine and 'pristine' meteoric water. Similar to the data presentation in Cl/Br-space, both wells a-63-J and c-29-I plot off the Clarke Lake Trend in Figure 6.10A. The distribution of these two data points again suggest injection of a third fluid end-member (MetaW?) in the Slave Point Formation. Compared to well a-63-J, the movement of well c-29-I further away from the Clarke Lake Trend is evidence for injection of increased volumes of MetaW along faults, while a-63-J was isolated both before and after injection of MetaW.

The sodium concentrations from the Clarke Lake formation waters are lower than those in Devonian formation waters from west-central Alberta (Connolly et al., 1990b; Michael et al., 2003) (Figure 6.10A). They (ibid.) concluded that the loss of sodium in the formation waters from the Alberta Basin was the result of ion exchange reactions, which Michael et al. (2003) further characterized as the exchange between Ca and Na during albitization. Based on the data from the formation waters in the Slave Point Formation that have been presented to this point, this interpretation cannot be excluded, however, the distribution of data from the Clarke Lake field are more likely a reflection of dilution by meteoric water.

The K concentrations of the Clarke Lake formation waters are scattered around the seawater evaporation trajectory, suggesting the occurrence of multiple diagenetic reactions involving potassium (Figure 6.10B). The bulk of the formation water samples plot above the seawater evaporation trajectory along a vector (A) that intercepts the curve between gypsum and halite saturation. Three other Clarke Lake water samples, d-74-C, c-96-I, and a-5-A, plot well below the seawater evaporation trajectory along a straight line (B)

Figure 6.10 Crossplots of the Na and K versus Br results from formation waters in the Slave Point Formation at Clarke Lake.

(A) Crossplot of Na and Br concentrations. Squares represent data from the Devonian of west-central Alberta after Connolly et al. (1990b). The circled field represents the approximate range of Devonian formation waters in west-central Alberta after Michael et al. (2003). The solid black line represents the seawater evaporation trajectory after McCaffrey et al. (1987). SW = seawater, GS = gypsum saturation, HS = halite saturation, ES = epsomite saturation. The dashed arrow representing dilution by meteoric water travels from the composition of normal seawater towards the composition of pristine meteoric water. Meteoric water dilution of evaporated seawater would result in a vector array originating near the origin. The bulk of the formation water samples from Clarke Lake lie below the seawater evaporation trajectory between normal seawater and gypsum saturation, and plot along a trend (Clarke Lake Trend) between a near halite-saturated brine (Clarke Lake end member - CLE) and meteoric water. Wells c29I and a63J are discussed in the text.

(B) Crossplot of K and Br concentrations. Squares represent data from the Devonian of west-central Alberta after Connolly et al. (1990b). The circled field represents the approximate range of Devonian formation waters in west-central Alberta after Michael et al. (2003). The solid black line represents the seawater evaporation trajectory after McCaffrey et al. (1987). SW = seawater, GS = gypsum saturation, HS = halite saturation, ES = epsomite saturation. The dashed arrow representing dilution by meteoric water travels from the composition of normal seawater towards the composition of pristine meteoric water. Meteoric water dilution of evaporated seawater would result in a vector array originating near the origin. The formation water samples from Clarke Lake scatter widely, both above and below the seawater evaporation trajectory, between normal seawater and the point of gypsum saturation. Vector A represents dilution of a brine by meteoric fluid with elevated K concentrations. Vector B represents removal of K from the fluid during the formation of authigenic illite.

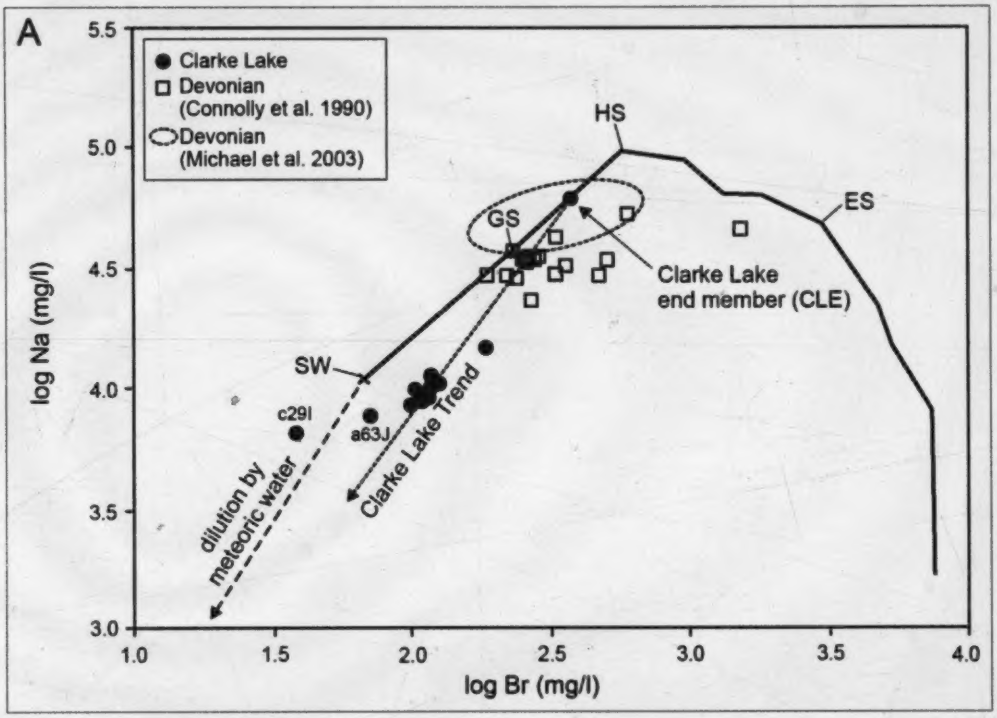
A
Clarke Lake
Devonian
(Connolly et al. 1990)
Devonian
(Michael et al. 2003)
HS
ES
GS
SW
c29I
a63J
Clarke Lake end member (CLE)
Clarke Lake Trend
dilution by meteoric water
log Na (mg/l)
log Br (mg/l)
5.5
5.0
4.5
4.0
3.5
3.0
1.0
1.5
2.0
2.5
3.0
3.5
4.0

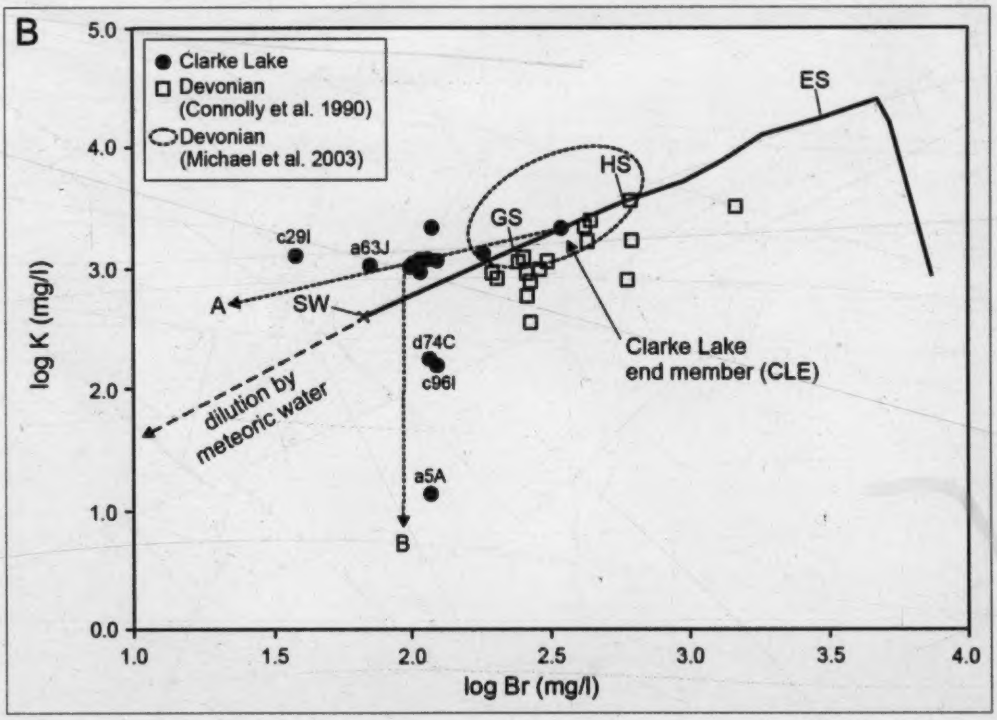
B
Clarke Lake
Devonian
(Connolly et al. 1990)
Devonian
(Michael et al. 2003)
ES
HS
GS
c29I
a63J
A
SW
d74C
c96I
a5A
B
Clarke Lake end member (CLE)
dilution by meteoric water
log K (mg/l)
log Br (mg/l)
5.0
4.0
3.0
2.0
1.0
0.0
1.0
1.5
2.0
2.5
3.0
3.5
4.0

that intercepts the bulk of the formation water data lying above the seawater evaporation trajectory. According to Bjørlykke (1994), meteoric waters in sedimentary basins are capable of dissolving potassium feldspar and forming authigenic kaolinite by the following reaction:

$$2KAlSi_3O_8 + 2H^+ + 9H_2O = Al_2Si_2O_5(OH)_4 + 2K^+ + 4H_4SiO_4$$

This reaction may have occurred, or is presently occurring, along the flow path of the meteoric fluid through water-rock interaction with the clastic-dominated Proterozoic Muskwa Assemblage and/or the Precambrian crystalline basement. The dissolution of feldspar not only accounts for the increase in K concentrations in the formation waters, but also, the high $^{87}Sr/^{86}Sr$ values through the incorporation of radiogenic ^{87}Sr (Figure 6.6). The result of the dilution of the Clarke Lake end member by a meteoric fluid with an elevated K concentration is represented by line A in Figure 6.10B. This high K meteoric fluid end-member would drive the composition of the formation fluids to the left of the seawater evaporation trajectory, away from their original Clarke Lake end-member composition near the point of halite saturation. Conversely, the Clarke Lake formation water data that lie below the seawater evaporation trajectory cannot be explained through feldspar alteration. A similar distribution of data was presented in Connolly et al. (1990b), and was interpreted to represent a single brine of constant composition that was diluted by meteoric water, shifting the data towards the origin. However, the fact that most of the Clarke Lake formation water samples plot above the seawater evaporation trajectory suggests that another, more complex, mechanism is responsible at play. These formation water samples may be reflecting further ion exchange reactions through the formation of illite due to the relative position of these wells with respect to the strata of the Clarke Lake area. These three wells are situated adjacent to, or overlying, basinal shales of the Otter Park and Klua formations, which may have been involved in the diagenetic reactions. According to Bjørlykke (1994), at temperatures of around 130°C, dissolution of any remaining potassium feldspar or the authigenic kaolinite can result in the formation of illite by the following reaction:

$$3Al_2Si_2O_5(OH)_4 + 2K^+ = 2KAl_3Si_3O_{10}(OH)_2 + 2H^+ + 3H_2O$$

This reaction may have occurred through the water-rock interaction between the K-rich meteoric fluid and the shales of the Otter Park and Klua formations. This would result in the removal of K from the meteoric fluid, as represented by line B in Figure 6.10B.

Cl/Br ratios also provide insight into both the origin and evolution of the present-day formation waters. By plotting the water chemistry in ratios with respect to Br, it is possible to remove the effects of dilution by meteoric water, and therefore, reveal the true origins of the brine end-member. The majority of the formation water samples from the Slave Point Formation have Cl/Br ratios that suggest the brine end-member was seawater evaporated slightly past the point of halite saturation (Figure 6.11). Comparison with the fluid inclusion leachate data suggests that the composition of these formation water samples is nearly identical to the composition of the fluids contained in the dolomites in the Slave Point Formation (Figure 6.11). These results may indicate that the current brine end-member in the Slave Point Formation is, in fact, the same fluid that caused hydrothermal alteration during the Late Devonian to Mississippian, which was a gypsum brine that had displaced and/or diluted and older halite brine (see Chapter 5).

Two Clarke Lake formation water samples, c-29-I, and a-63-J, are inconsistent with the remaining data set (Figure 6.11). Both formation water samples were previously interpreted to represent a third fluid end-member that was 'injected' into the Slave Point Formation. According to their distribution in Figure 6.11, both samples had an original composition similar to the bulk of the data set, but were diluted by a fluid that was deficient in K. This distribution may be attributed to the formation of K-feldspar through the dissolution of albite, which liberates Na to solution (Hutcheon, 1989). However, the formation water sample from well a-63-J does not show an increase in Na concentration (Figure 6.11B), rather this sample is likely reflecting dilution by meteoric water that was involved in water-rock interaction, thereby decreasing both the Na and K concentrations. The remainder of the data set from the Slave Point Formation shows evidence of enrichment in K, which was previously attributed to the dissolution of feldspar and the formation of authigenic kaolinite. However, the bulk of the formation water samples show no evidence of exchange reactions involving Na, which was proposed earlier to account for an decrease in the Na content in Figure 6.10A. Therefore, it would appear that albitization reactions had very little impact on the chemistry of the formation fluids, and, the Na depletion observed previously is, in fact, a reflection of dilution by meteoric water devoid of Na.

Ca and Mg concentrations and variations can be used to identify whether formation waters were involved in, or the cause of, dolomitization, arguably the volumetrically most important process that affected the Clarke Lake reservoir rocks. However, considering that

Figure 6.11 Ratio crossplots of formation waters from the Slave Point Formation at Clarke Lake.

(A) K-Cl-Br systematics of the formation fluids. The K/Br ratios from the majority of the formation waters suggest the fluids are enriched in potassium and have Cl/Br ratios that plot near the point of halite saturation. The circled fields represent data from dolomite fluid inclusion fluids (see Figure 5.21A). Data for the seawater evaporation trajectory (solid line) are from Fontes and Matray (1993). GS = gypsum saturation, HS = halite saturation, ES = epsomite saturation.

(B) Na-Cl-Br systematics of the formation fluids. Most of the formation fluid samples lie along the seawater evaporation trajectory, near the point of halite saturation. The circled fields represent data from dolomite fluid inclusion fluids (see Figure 5.21B). Data for the seawater evaporation trajectory (solid line) are from Fontes and Matray (1993). GS = gypsum saturation, HS = halite saturation, ES = epsomite saturation.

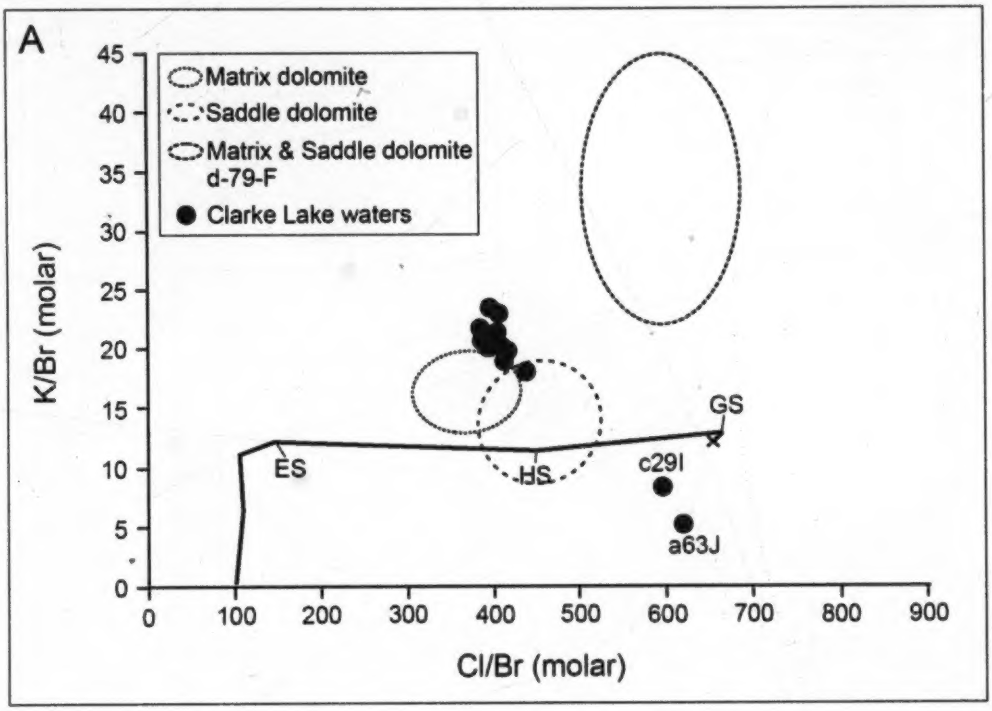
A
Matrix dolomite
Saddle dolomite
Matrix & Saddle dolomite d-79-F
● Clarke Lake waters
K/Br (molar)
Cl/Br (molar)
0
5
10
15
20
25
30
35
40
45
0
100
200
300
400
500
600
700
800
900
ES
HS
GS
c29I
a63J

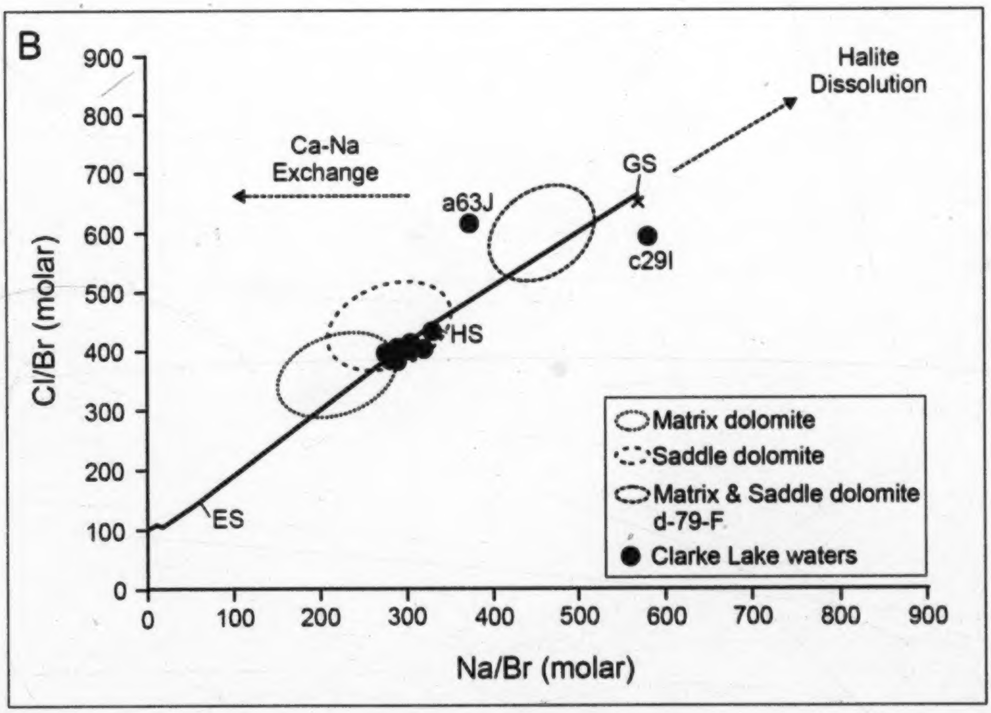
B
Halite Dissolution
Ca-Na Exchange
GS
a63J
c29I
HS
ES
Cl/Br (molar)
Na/Br (molar)
0
100
200
300
400
500
600
700
800
900
Matrix dolomite
Saddle dolomite
Matrix & Saddle dolomite d-79-F
● Clarke Lake waters

there are multiple lines of evidence already for hydrothermal alteration and then incursion of meteoric water, one might expect evidence for dolomitization to have been muted or obliterated.

Plotted against Br, the Slave Point formation water samples have Mg concentrations that are situated below the seawater evaporation trajectory (Figure 6.12A), whereas all but one of the samples have Ca concentrations above the seawater evaporation trajectory (Figure 6.12B) as might be expected from limestone replacement according to:

$$2CaCO_3 + Mg = CaMg(CO_3)^2 + Ca$$

However, the scale of the decrease in Mg concentrations is not matched by the increase in the Ca concentrations, which would be expected if the controlling exchange reaction was the mole per mole replacement of limestone by dolomite. Furthermore, the location of the data relative to the seawater evaporation trend suggests a solution between seawater and a gypsum brine. Considering further that the Clarke Lake data plot roughly parallel to the trend of meteoric water dilution (Clarke Lake Trend), these data – in context – suggest dolomitization by a halite or gypsum brine that was subsequently diluted by meteoric water (Figure 6.12). However, a graph of Mg versus Ca in terms of milliequivalence (Figure 6.13A) shows a strong positive correlation between the two ions (Clarke Lake Trend), which according to Michael et al. (2003) is indicative of reactions in addition to dolomitization. Both Connolly et al. (1990b), and Michael et al. (2003) proposed that the Ca and Mg composition of the formation waters is a reflection of water-rock interactions. The lone sample that does not agree with this interpretation is that from well c-29-I. This sample shows depletions in both Mg and Ca compared to seawater (Figure 6.12), a distribution that is definitely not attributable to dolomitization. It was proposed earlier that the sample from well c-29-I was involved in K-feldspar albitization. Yet, this exchange reaction does not involve the removal of Ca from solution. Rather, this could be accomplished through the albitization of plagioclase feldspar. However, two problems exist if the Ca content of the formation fluid is due to plagioclase alteration. Firstly, the alteration of plagioclase cannot explain the compositional variations in K and Na, and secondly, albitization of plagioclase occurs independently of K-feldspar albitization, and therefore, the removal of Ca from solution must be the result of some other reaction (Davisson and Criss, 1996). Based on these limitations, the likely reactions to account for the depletion in Ca in well c-29-I are the formation of either $CaCO_3$ or $CaSO_4$.

Figure 6.12 Crossplots of the Mg and Ca versus Br results from formation waters in the Slave Point Formation at Clarke Lake.

(A) Crossplot of Mg and Br concentrations. Squares represent data from the Devonian of west-central Alberta after Connolly et al. (1990b). The circled field represents the approximate range of Devonian formation waters in west-central Alberta after Michael et al. (2003). The solid black line represents the seawater evaporation trajectory after McCaffrey et al. (1987). SW = seawater, GS = gypsum saturation, HS = halite saturation, ES = epsomite saturation. The dashed arrow representing dilution by meteoric water travels from the composition of normal seawater towards the composition of pristine meteoric water. Meteoric water dilution of evaporated seawater would result in a vector array originating near the origin. All of the formation water samples from Clarke Lake lie below the seawater evaporation trajectory, with most plotting near the Br composition of normal seawater. The Clarke Lake data plot along a trend (Clarke Lake Trend) between the data presented in Connolly et al. (1990b) and meteoric water. Wells c29I and a63J are discussed in the text.

(B) Crossplot of Ca and Br concentrations. Squares represent data from the Devonian of west-central Alberta after Connolly et al. (1990b). The circled field represents the approximate range of Devonian formation waters in west-central Alberta after Michael et al. (2003). The solid black line represents the seawater evaporation trajectory after McCaffrey et al. (1987). SW = seawater, GS = gypsum saturation, HS = halite saturation, ES = epsomite saturation. The dashed arrow representing dilution by meteoric water travels from the composition of normal seawater towards the composition of pristine meteoric water. Meteoric water dilution of evaporated seawater would result in a vector array originating near the origin. The bulk of the formation water samples from Clarke Lake lie above the seawater evaporation trajectory, with one exception (c29I). The Clarke Lake data plot along a trend (Clarke Lake Trend) between the data presented in Connolly et al. (1990b) and meteoric water. Wells c29I and a63J are discussed in the text.

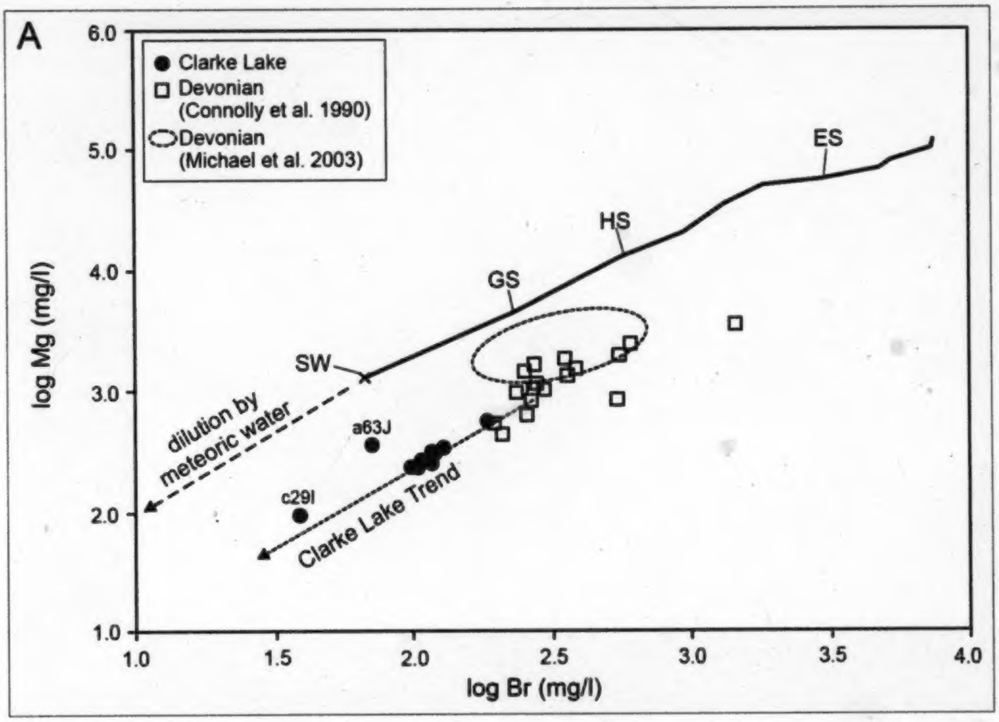
A
● Clarke Lake
☐ Devonian
(Connolly et al. 1990)
Devonian
(Michael et al. 2003)
ES
HS
GS
SW
dilution by
meteoric water
a63J
c29l
Clarke Lake Trend
log Mg (mg/l)
6.0
5.0
4.0
3.0
2.0
1.0
log Br (mg/l)
1.0
1.5
2.0
2.5
3.0
3.5
4.0

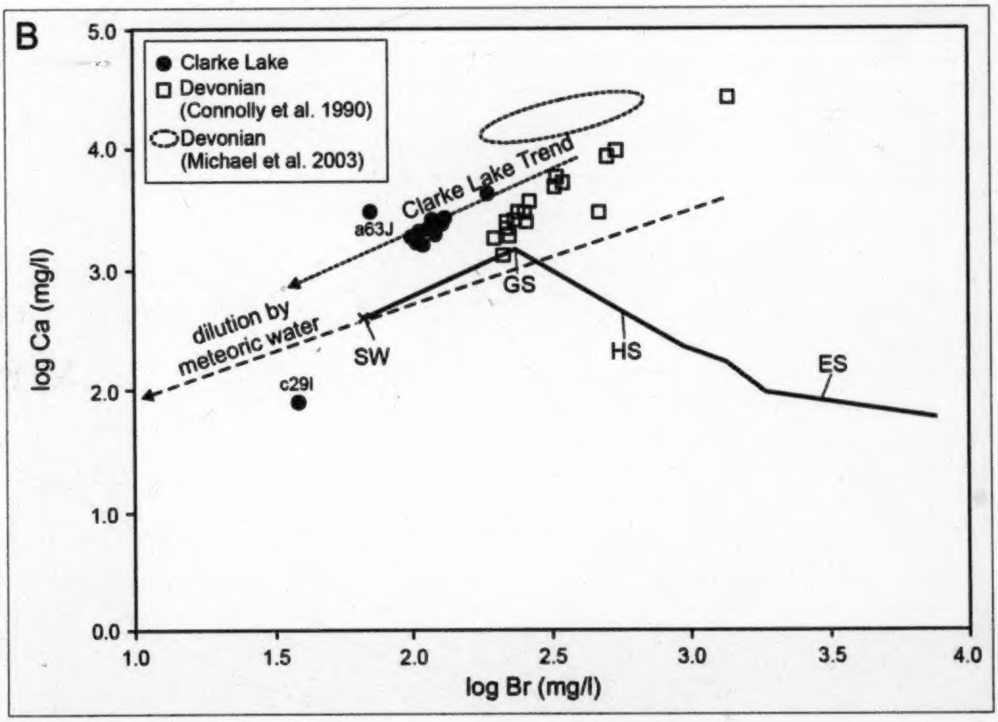
B
● Clarke Lake
☐ Devonian
(Connolly et al. 1990)
Devonian
(Michael et al. 2003)
Clarke Lake Trend
a63J
GS
dilution by
meteoric water
SW
HS
ES
c29l
log Ca (mg/l)
5.0
4.0
3.0
2.0
1.0
0.0
log Br (mg/l)
1.0
1.5
2.0
2.5
3.0
3.5
4.0

Figure 6.13 Crossplots of Ca and Mg in formation waters.

(A) Crossplot of calcium versus magnesium in terms of millequivalence. The value of seawater (SW) is calculated from data presented in Hanor (1987). During dolomitization, Ca replaces Mg in the formation waters in a 1:1 ratio (Hanor, 1987). Formation waters involved in dolomitization should follow the Ca-Mg replacement trend. The evaporation trajectory is based on data from McCaffrey et al. (1987). Data from formation waters in the Slave Point Formation at Clarke Lake (Clarke Lake Trend) display a positive linear correlation that is atypical of formation waters involved in dolomitization reactions. Grey shaded area represents data from formation water analyses from the Mississippian of west-central Alberta after Michael and Bachu (2002). Data from Slave Point equivalent formation waters in west-central Alberta have Ca values greater than 500 meq/l (Michael et al., 2003).

(B) Crossplot of calcium excess versus magnesium deficit in terms of milliequivalence. Formation waters that have only been involved in dolomitization reactions should fall along a 1:1 correlation line assuming mole-by-mole replacement of Ca by Mg. The majority of the formation water samples from Clarke Lake (Clarke Lake Trend) lie below the correlation line, indicating either removal of additional Mg (arrow 1), or removal of additional Ca (arrow 2) - all by non-dolomitization reactions. See text for further explanation.

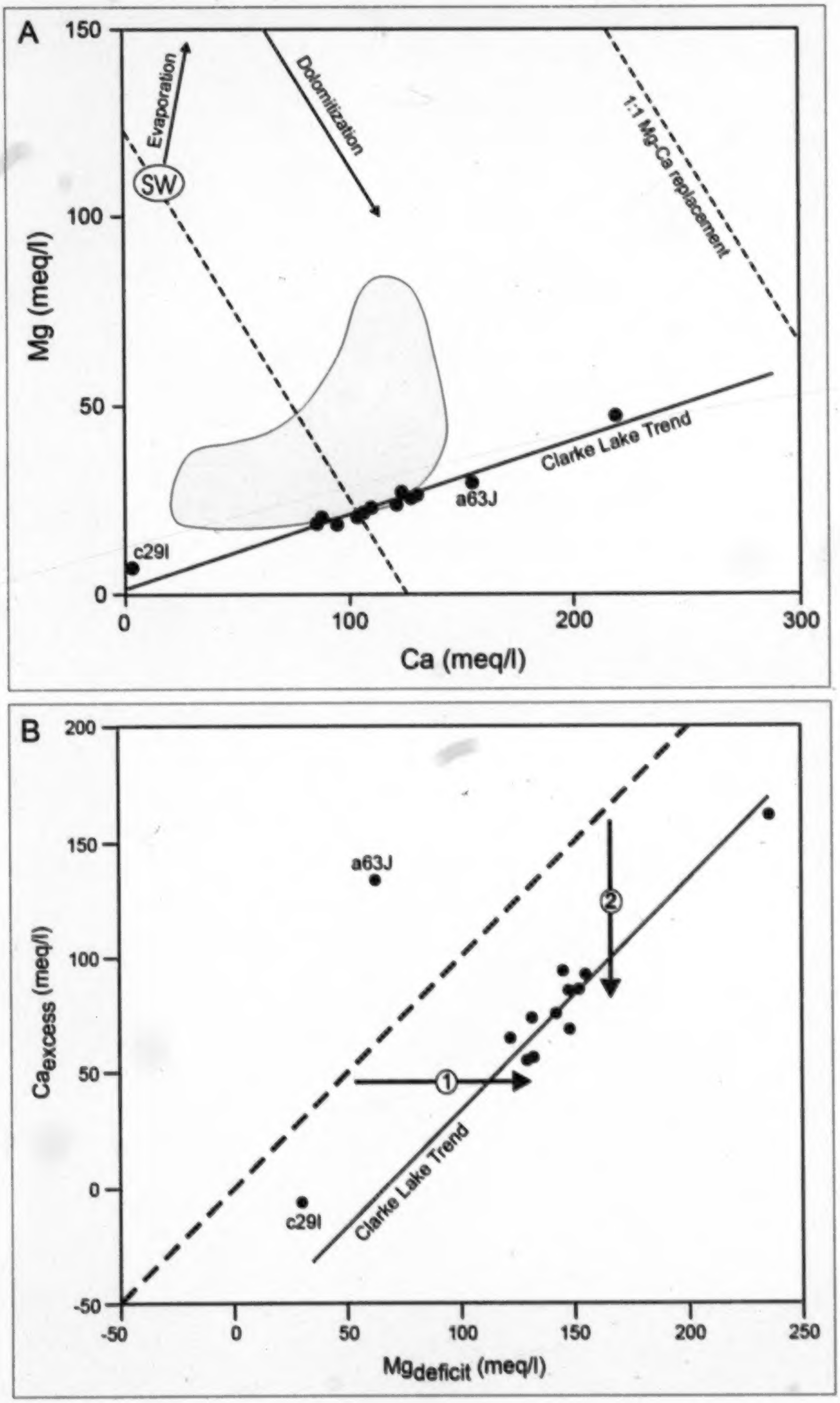
A
Mg (meq/l)
Ca (meq/l)
150
100
50
0
0
100
200
300
Evaporation
Dolomitization
1:1 Mg-Ca replacement
SW
Clarke Lake Trend
a63J
c29I
B
Ca$_{excess}$ (meq/l)
Mg$_{deficit}$ (meq/l)
200
150
100
50
0
-50
-50
0
50
100
150
200
250
a63J
c29I
①
②
Clarke Lake Trend

One method to examine the various exchange reactions affecting the Ca and Mg concentrations in the present-day formation fluids is to estimate their original concentrations using their measured Br values. This method has been used to calculate both the Ca excess and the Mg deficit in highly saline brines from the Williston Basin (Iampen, 2003). A summary of the procedure is discussed herein. Refer to Iampen (2003) for the complete procedure. The first step to calculate the Ca excess is to determine the predicted value based on the measured Br concentration using the following equation:

$$Ca_{predicted}\ (mg/L) = 6.1938 \times Br_{measured}\ (mg/L) - 34.153$$

The predicted Ca value is subtracted from the measured Ca value to obtain the Ca_{excess}, which is also converted to meq/L. The predicted value for Mg based on the measured Br concentration is calculated according to the following equation:

$$Mg_{predicted}\ (mg/L) = 20.296 \times Br_{measured}\ (mg/L) - 333.5$$

In this case, the measured value is subtracted from the predicted value to obtain the $Mg_{deficit}$.

Dolomitization through the mole per mole replacement of Ca by Mg would generate data that lie along a 1:1 correlation line (Figure 6.13B – dashed line), however, the bulk of the formation water samples from the Slave Point Formation are situated below this correlation line (Figure 6.13B – Clarke Lake Trend). The position of this data suggests that these fluids have been involved in exchange reactions that have removed either Mg or Ca. The removal of large concentrations of Mg from formation fluids is generally attributed to the dolomitization reaction. Yet, this alternative has already been eliminated to account for the observed Ca and Mg concentrations. Alternatively, changes in the Ca concentration of formation fluids may be the result of: calcite and/or anhydrite formation, dolomitization, evaporite dissolution, and albitization. The latter three alternatives have already been ruled out based on the previous discussions of the geochemical data from the formation waters in the Slave Point Formation. This leaves calcite or anhydrite formation as the dominant Ca-controlling reactions. However, all Ca data from the Clarke Lake formation waters, with the exception of well c-29-I, sit above the seawater evaporation trajectory (Figure 6.12B). Accordingly, this distribution is not the result of the formation of either calcite or anhydrite, and therefore, no single reaction can account for the observed Ca and Mg compositional variations in the Slave Point Formation waters. Conversely, in well c-29-I, it is possible that the previously discussed 'injected' fluid end-member was involved in the formation of either $CaCO_3$ or $CaSO_4$. These observations suggest a complex interplay between various exchange reactions and the various end-member fluids in the Clarke Lake field.

Davisson and Criss (1996) provided another method for determining the origin of basinal fluids and to evaluate the effect of water-rock interaction on these fluids. They (ibid.) introduced two mathematical relations similar to the Ca excess and Mg deficit described above. These include a different method for calculating Ca excess, and a formula for determining Na deficit. These formulae are shown below:

$$\mathrm{Ca}_{\mathrm{excess}} = [\mathrm{Ca}_{\mathrm{measured}} - (\mathrm{Ca/Cl})_{\mathrm{seawater}} \times \mathrm{Cl}_{\mathrm{measured}}] \times (2/40.08)$$
$$\mathrm{Na}_{\mathrm{deficit}} = [(\mathrm{Na/Cl})_{\mathrm{seawater}} \times \mathrm{Cl}_{\mathrm{measured}} - \mathrm{Na}_{\mathrm{measured}}] \times (1/22.90)$$

By plotting more than 800 formation water samples from various basins worldwide, Davisson and Criss (1996) were able to derive a regression line that they termed the basinal fluid line (BFL) (arrow 1 - Figure 6.14). They interpreted samples that were situated along this line to represent fluid involved in the albitization of plagioclase through the 2 for 1 exchange of Na for Ca. They (ibid.) also suggested that albitization of plagioclase is the predominant process that controls the chemistry of deep formation waters. Additionally, Davisson and Criss (1996) proposed that a $\mathrm{Ca}_{\mathrm{excess}}$ versus $\mathrm{Na}_{\mathrm{deficit}}$ plot could be used to assess the relative importance of evaporation (Figure 6.14 – arrows 2a and 2b), halite dissolution (Figure 6.14 – arrow 3), and dolomitization (Figure 6.14 – arrow 4).

The bulk of the formation water samples from the Slave Point Formation have slight excesses of calcium and concomitant deficits of sodium (Figure 6.14). These data roughly parallel the slope of the basinal fluid line (BFL)(arrow 1), however, they do not plot within the boundaries of the BFL (heavy dashed lines), which suggests that neither dolomitization (arrow 4) nor halite dissolution (arrow 3) have influenced the formation water chemistry. Rather, the data scatter between Cl^- concentration lines of 150 and 180 g/L (Chi and Savard, 1997), both of which parallel the BFL and intersect the lines representing seawater evaporated beyond the point of halite saturation (arrow 2b). This distribution suggests that one end-member fluid had a composition typical of highly evaporated seawater (fluid A). The shift in the data from the seawater evaporation trajectory implies that fluid A was mixed with a second fluid end-member that was involved in the albitization of plagioclase and evolved along the BFL (fluid B). The origin of fluid B cannot be elucidated from this

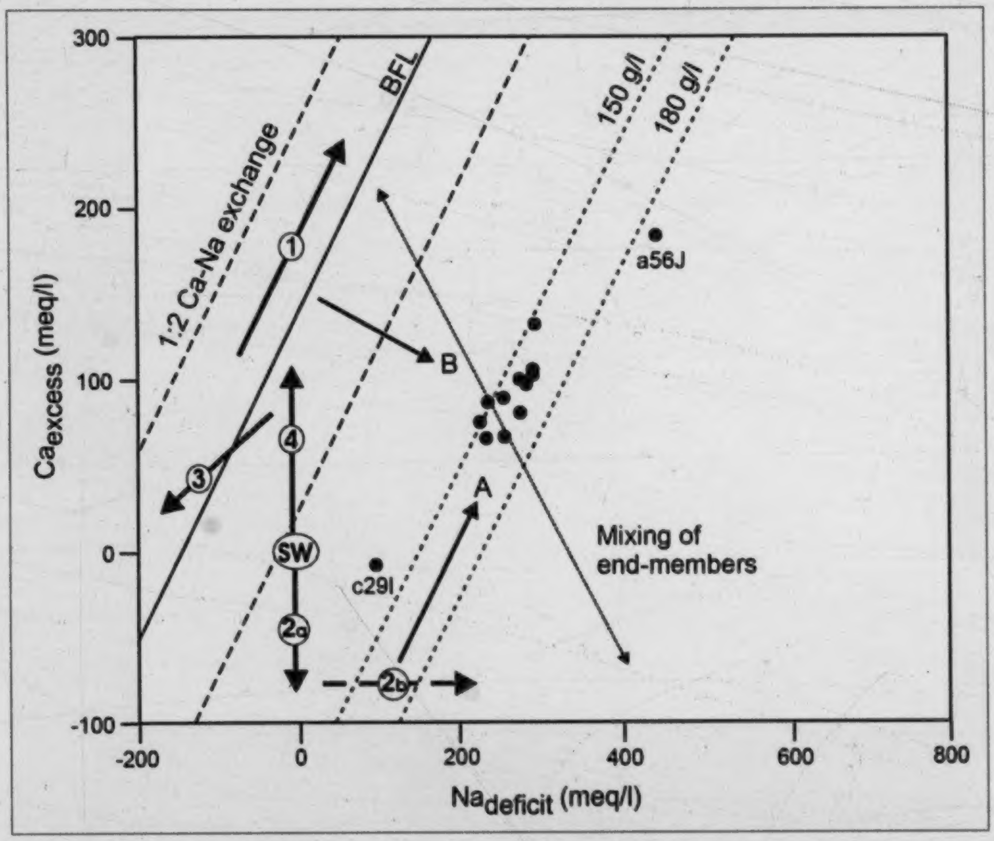

Figure 6.14 Crossplot of calcium excess versus sodium deficit for formation waters in the Slave Point Formation at Clarke Lake. Processes that may have effected the formation water composition include: albitization of plagioclase (arrow 1), evaporation of seawater (arrow 2a) beyond the point of halite saturation (arrow 2b), halite dissolution (arrow 3), and dolomitization and/or gypsum dissolution (arrow 4). The basinal fluid line (BFL) from Davisson and Criss (1996) is shown for reference. The value of seawater (SW) is calculated from data presented by Hanor (1987). Fluid A represents a highly evaporated seawater end-member. Fluid B represents a dilute end-member fluid involved in ion exchange reactions. The bulk of the formation water data from Clarke Lake lie along the predicted position of a halite saturated fluid (Cl^- concentrations between 150 and 180 g/l) that has experienced water-rock interaction (e.g. albitization reactions)(Chi and Savard, 1997).

plot; however, this fluid end-member has a composition typical of deep basinal fluids that have undergone cation exchange reactions (Davisson and Criss, 1996).

6.5.4 Geochemical modeling

Aqueous species distribution and mineral saturation states were calculated in order to investigate the thermodynamic controls on formation water composition and to see if the present formation waters have any relationship to the diagenetic fluid(s) that formed dolomite in the Slave Point Formation.

Phase diagrams constructed from thermodynamic data for the aqueous, gaseous, and mineral species involved in diagenetic reactions are independent of the bulk formation water chemistry. The diagenetic reactions can then be expressed in terms of an equilibrium constant that is a combination of minerals and aqueous and/or gaseous species (Hutcheon, 2000). These reactions can then be plotted on phase diagrams that have the aqueous/ gaseous species as variables on the axes, providing a visual estimate of the equilibrium conditions.

Most subsurface formation water analyses are subject to a variety of errors, including changes in pH due to a large drop in pressure and temperature. A drop in pressure is particularly challenging because CO_2 is lost, causing the pH to increase significantly (Hutcheon, 2000). A change in the pH alters the stability of most silicate and carbonate mineral reactions, leading to inaccurate calculations of both saturation indices and activity coefficients. To account for the change in pH from reservoir conditions to surface conditions, the measured CO_2 content of the gas in the reservoir was multiplied by the reservoir pressure to obtain the partial pressure of CO_2, and thus, the saturation index. By assuming the CO_2 phase and the subsurface fluid were in equilibrium, the pH is calculated from the following reaction:

$$CO_2 + H_2O = HCO_3^- + H^+$$

This reaction requires that the bicarbonate concentration be known, however, assuming equilibrium of the formation waters with respect to calcite satisfies this requirement through the following reaction:

$$Ca^{2+} + HCO_3^- = CaCO_3 + H^+$$

Equilibrium with respect to calcite is a reasonable assumption since carbonate minerals and subsurface fluids rapidly attain equilibrium relative to the residence time of the fluids

(Palciauskas and Domenico, 1976; Plummer et al., 1978; 1979; Busenberg and Plummer, 1982; Connolly et al., 1990b).

Previous studies of the thermodynamic controls on formation water composition in the Western Canada Sedimentary Basin have been limited primarily to Mesozoic clastic units in central and eastern Alberta (Hutcheon, 1989; Hutcheon and Abercrombie, 1990; Hutcheon, 2000). The only study to attempt to characterize mineral equilibria in the Devonian carbonates is that of Connolly et al. (1990b) from formation waters in west-central Alberta.

Results

The results from the calculation of the partial pressure of CO_2 (pCO_2) and the saturation index of CO_2 from subsurface wells that provided formation water samples are shown in Table 6.2.

The calculated saturation indices for dolomite, anhydrite, gypsum, barite, and quartz are shown in Table 6.3. All of the formation fluids have a calculated pH that is less than 5.6, with the majority of the fluids lying near 5.0. At such low values of pH, the formation waters are undersaturated with respect to all of the minerals listed above. The only exceptions are the mineral saturation states calculated for barite, which are slightly positive. However, it should be noted that the formation water samples were collected in two batches roughly one year apart, and all of the samples that show positive saturation indices with respect to barite are from the same batch.

The calculated activities of the aqueous species Ca^{2+}, Mg^{2+}, Na^+, K^+, and $H_4SiO_4^0$ in the formation fluids under reservoir conditions are shown in Table 6.3.

Discussion

Under present-day reservoir conditions, i.e., temperature and pH, all of the potentially predominant minerals that form within subsurface carbonates are in a state of minimal to significant undersaturation in the formation waters. Of particular importance based on the rock and fluid geochemistry discussed to this point is the undersaturation with respect to dolomite. The slight undersaturation for dolomite in the formation waters may imply that the dolomites of the Slave Point Formation are presently being dissolved in the subsurface. However, as discussed in Chapter 4, there is no petrographic evidence to suggest dissolution

Well - NTS	X_{CO_2}	P (kPa)	P (atm)	pCO_2	SI
b-46-J/94-J-10	0.099	14256	140.7	13.90	1.14
c-29-I/94-J-10	0.089	13792	136.1	12.16	1.08
a-5-A/94-J-15	0.112	14185	140.0	15.74	1.20
d-96-L/94-J-9	0.095	14820	146.2	13.89	1.14
b-72-L/94-J-9	0.101	14785	145.9	14.77	1.17
a-63-J/94-J-9	0.123	23376	230.7	28.31	1.45
c-88-L/94-J-10	0.112	13698	135.2	15.11	1.18
a-56-J/94-J-10	0.137	11300	111.5	15.30	1.18
c-96-I/94-J-10	0.120	14258	140.7	16.90	1.23
b-75-F/94-J-9	0.100	16299	160.9	16.09	1.21
c-52-F/94-J-10	0.085	17313	170.9	14.56	1.16
a-83-G/94-J-10	0.089	15575	153.7	13.73	1.14
d-74-C/94-J-9	0.091	17625	173.9	15.79	1.20
c-20-I/94-J-10	0.088	14250	140.6	12.35	1.09

Table 6.2 Partial pressure and saturation index of carbon dioxide from wells providing formation water samples. The mole fraction of carbon dioxide was obtained from Geofluids© gas analyses. The saturation index of carbon dioxide was used to determine the pH of the formation fluids in the subsurface (see Table 6.3).

of dolomites after formation. Consequently, undersaturation with respect to dolomite may be the product of the loss of Mg in the formation waters as a result of dolomite formation. This alternative can be further evaluated by examining the activity coefficients for both Ca^{2+} and Mg^{2+}. Based on previous discussions, the composition of one of the fluid end-members in the present-day formation waters is similar to highly evaporated seawater, i.e., seawater evaporated to near halite-saturation. A brine with this composition is strongly enriched in Mg, and is thus a potential dolomite-forming fluid. By examining the Ca/Mg activity ratios at the current reservoir temperatures compared to those at empirically determined calcite and dolomite stability field boundaries, it is possible to determine whether the present-day formation waters were involved in the formation of dolomite. The Ca/Mg activity ratios of the Slave Point Formation waters plot on, or near, the dolomite-calcite stability boundaries (Figure 6.15A). A pristine halite-saturated brine should plot at much reduced Ca/Mg activity ratios, e.g., around –2.0, hence, this distribution means that the formation waters have lost much of their Mg through the formation of dolomite and no more dolomite can be produced from these fluids, which is reflected in the dolomite undersaturation in the formation waters. This result is corroborated by the theoretical equilibrium activity diagram shown in Figure 6.15B. In this plot, the stability boundaries are calculated for a

Well - NTS	T (°C)	pH	Saturation Index				
			Dol	Anh	Gyp	Bar	Qtz
b-46-J/94-J-10	108	5.04	-0.84	-0.34	-0.94	+0.16	-0.16
c-29-I/94-J-10	107	5.60	-0.25	-2.04	-2.61	+1.38	-0.62
a-5-A/94-J-15	110	5.03	-0.90	-0.05	-0.68	+0.19	-0.11
d-96-L/94-J-9	113	5.09	-0.93	-0.04	-0.62	+0.18	-0.06
b-72-L/94-J-9	110	5.08	-0.89	-0.01	-0.61	+0.16	-0.10
a-63-J/94-J-9	95	4.83	-0.68	-1.10	-1.53	+0.82	-0.04
c-88-L/94-J-10	108	5.00	-0.81	-0.55	-1.14	-0.34	-0.21
a-56-J/94-J-10	112	4.88	-0.85	-0.66	-1.21	-0.32	-0.08
c-96-I/94-J-10	108	4.97	-0.85	-0.46	-1.06	-0.46	-0.27
b-75-F/94-J-9	111	5.30	-1.92	-1.50	-2.12	-1.75	-0.66
c-52-F/94-J-10	106	5.06	-0.84	-1.15	-1.71	-0.49	-0.13
a-83-G/94-J-10	106	5.05	-0.83	-1.04	-1.61	-0.40	-0.08
d-74-C/94-J-9	114	4.98	-0.96	-0.52	-1.20	-0.35	-0.15
c-20-I/94-J-10	109	5.07	-0.85	-1.05	-1.66	-0.48	-0.13

Well - NTS	Activity				
	Ca^{2+}	Mg^{2+}	Na^{+}	K^{+}	$H_4SiO_4^0$
b-46-J/94-J-10	0.01132	0.00252	0.2901	0.01990	6.912e-04
c-29-I/94-J-10	0.00098	0.00081	0.1893	0.00260	2.354e-04
a-5-A/94-J-15	0.01014	0.00213	0.2917	0.01716	8.036e-04
d-96-L/94-J-9	0.00863	0.00194	0.2659	0.01539	9.514e-04
b-72-L/94-J-9	0.00875	0.00188	0.2733	0.01457	8.164e-04
a-63-J/94-J-9	0.01630	0.00326	0.2235	0.00272	6.937e-04
c-88-L/94-J-10	0.01215	0.00287	0.3046	0.01806	6.013e-04
a-56-J/94-J-10	0.02052	0.00529	0.4346	0.03044	8.735e-04
c-96-I/94-J-10	0.01274	0.00277	0.3019	0.01920	5.231e-04
b-75-F/94-J-9	0.00280	0.00006	0.0074	0.00029	2.367e-04
c-52-F/94-J-10	0.00995	0.00203	0.2468	0.01743	7.126e-04
a-83-G/94-J-10	0.01098	0.00230	0.2563	0.01719	7.966e-04
d-74-C/94-J-9	0.01221	0.00264	0.3200	0.01538	7.891e-04
c-20-I/94-J-10	0.01102	0.00246	0.2689	0.01733	7.456e-04

Table 6.3 Formation fluid-mineral equilibria.

(Top) Saturation indices for dolomite (Dol), anhydrite (Anh), gypsum (Gyp), barite (Bar), and quartz (Qtz) calculated with PHREEQC. Temperatures are from bottom-hole data. Subsurface fluid pH calculated using the saturation index of carbon dioxide (see Table 6.2). The calcite saturation index was set at 0 due to the expectation of rapid equilibration with respect to calcite in the subsurface.

(Bottom) Activity of calcium (Ca^{2+}), magnesium (Mg^{2+}), sodium (Na^{+}), potassium (K^{+}), and silicic acid ($H_4SiO_4^0$) in the formation fluids under reservoir conditions.

Figure 6.15 Dolomite stability calculated from formation fluid-mineral equilibria.

(A) Bivariate thermodynamic stability diagram for the system calcite-dolomite-water after Carpenter (1980). The dolomite-calcite stability boundaries were determined from subsurface waters in contact with calcite plus dolomite. Curve 1 from data in Robie et al. (1978). Curve 2 from data in Kharaka and Barnes (1973). Curve 3 from data in Langmuir (1971), and Parizek et al. (1971). The position of normal seawater was calculated using PHREEQC with data from McCaffrey et al. (1987). The majority of the formation waters from the Slave Point at Clarke Lake plot on, or near, the dolomite-calcite stability boundaries.

(B) Theoretical equilibrium activity diagram for the system $HCl-H_2O-CaO-CO_2-MgO$ at 100°C and 1 atm, modified after Helgeson et al. (1969). The majority of the formation waters from the Slave Point at Clarke Lake plot slightly below the phase boundary between dolomite and calcite.

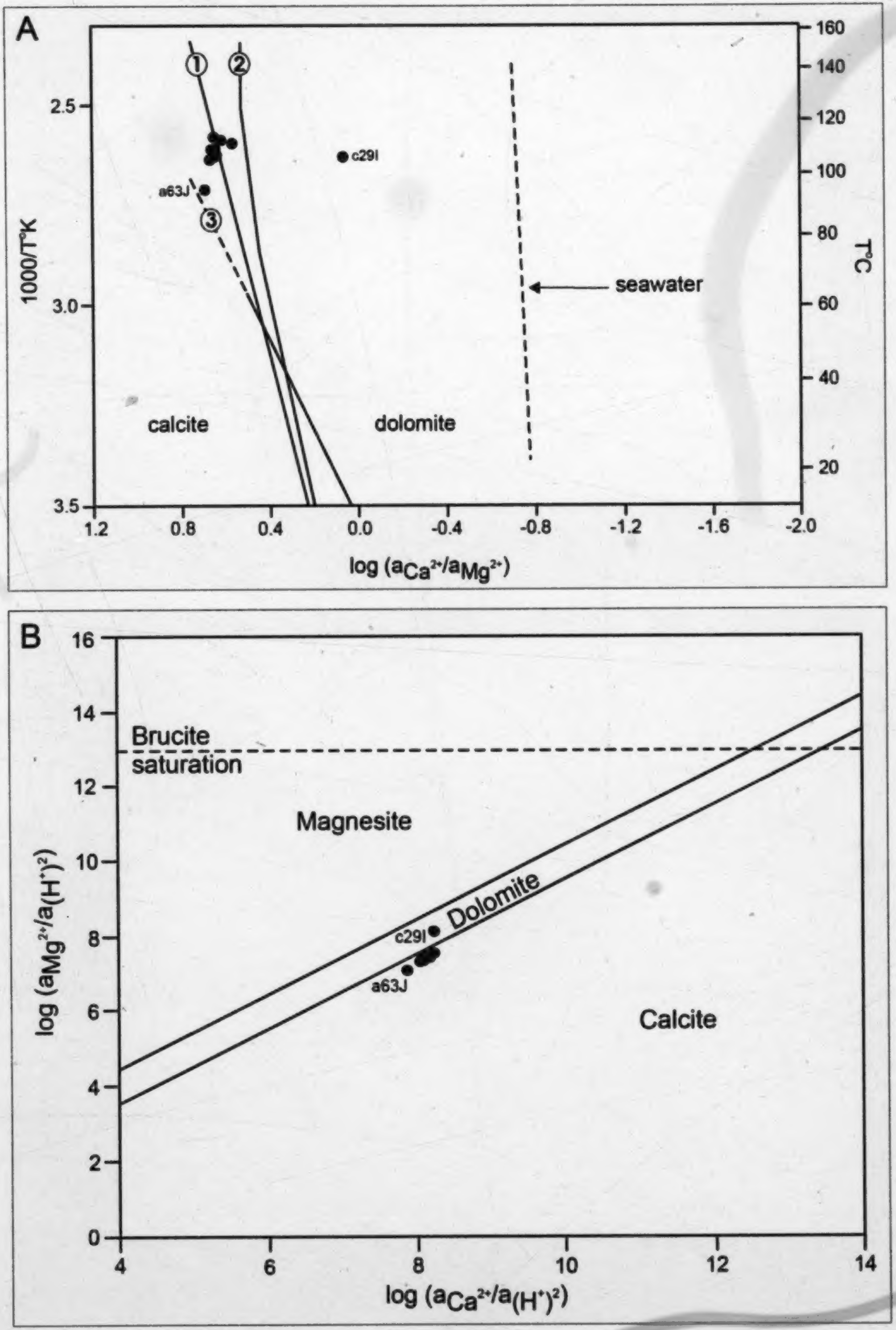
A
①
②
③
a63J
c29I
calcite
dolomite
seawater
1000/T°K
2.5
3.0
3.5
T°C
160
140
120
100
80
60
40
20
1.2
0.8
0.4
0.0
-0.4
-0.8
-1.2
-1.6
-2.0
log ($a_{Ca^{2+}}/a_{Mg^{2+}}$)
B
Brucite saturation
Magnesite
Dolomite
Calcite
c29I
a63J
log ($a_{Mg^{2+}}/a_{(H^+)^2}$)
16
14
12
10
8
6
4
2
0
4
6
8
10
12
14
log ($a_{Ca^{2+}}/a_{(H^+)^2}$)

temperature of 100°C, and the bulk of the formation water samples from Clarke Lake plot on, or slightly below, the dolomite-calcite stability boundary. A few of the formation water samples are dissimilar to the bulk of the samples from the Slave Point Formation. These samples include well c-29-I, which plots within the dolomite stability field suggesting this fluid is presently capable of forming dolomite. However, based on previous discussions in this chapter, the geochemistry of this sample indicates it may have been involved in the formation of $CaCO_3$ and/or $CaSO_4$, or diluted by condensed water vapour during natural gas production. The latter alternative should not change the Ca/Mg activity ratio, however, either of the former alternatives will change the activity of Ca^{2+}. Additionally, the saturation indices for anhydrite and gypsum provide additional evidence that the formation fluid in well c-29-I was involved in the formation of sulphate minerals.

Based on the saturation indices of the sulphate minerals, there is little possibility for the formation of anhydrite and/or gypsum under present reservoir conditions. Both of these minerals have saturation indices that are significantly undersaturated in the formation fluids. There are two implications from these calculations: 1) any sulphate minerals that were in the Slave Point Formation should have been dissolved, although there is no petrographic evidence to suggest that sulphate minerals were ever present; and, 2) the chemistry of the present-day formation waters suggests one end-member fluid was highly evaporated seawater, therefore, these fluids likely precipitated sulphate minerals at some point along their flow paths prior to entering the Slave Point reservoir.

As mentioned previously, the saturation indices calculated for barite range from values of undersaturation to supersaturation in the present-day formation waters. However, due to the variability between the two sample batches, the results from barite will not be discussed further.

The formation waters in the Slave Point Formation are at equilibrium, or minimally undersaturated, with respect to quartz. The calculated saturation indices for quartz may be the result of one of two processes. Firstly, petrographic evidence presented in Chapter 4 advocates for relatively late-stage quartz precipitation within open fractures (fracture generation III – phase 15) and vuggy pores (hydrothermal alteration – phase 13), hence, the saturation indices may be a reflection of prior quartz precipitation from the present formation waters in the Slave Point Formation. Secondly, the near equilibrium exhibited by some of the formation water samples may be further proof that the formation waters interacted with silica-rich rocks in the subsurface. Based on previous discussions, the silica-rich rocks may have been derived from either the Proterozoic Muskwa Assemblage explosed to the west in the Rocky Mountains or the Precambrian crystalline basement that underlies this region. This mechanism can be further evaluated by examining the activities of various aqueous species that are known to be involved in the dominant exchange reactions in the subsurface. The bulk of the formation water samples from the Slave Point Formation plot along, or near, the 250°C equilibrium line for the albitization of plagioclase (Figure 6.16A). This distribution means that the present formation fluids are not in equilibrium with the albitization reaction at the reservoir temperatures of roughly 100°C. However, that distribution of data in Figure 6.16A suggests that albite equilibrium could have been attained at higher temperatures. This result would be in accordance with the interpretations from this study that advocate for the long-distance migration and movement of fluids at great depths in this region. Unfortunately, there is no evidence of temperatures approaching 250°C in either the lowermost parts of the Phanerozoic column or the uppermost parts of the Proterozoic or Precambrian crystalline basement of northeastern British Columbia (Bachu and Burwash, 1994). The distribution of the formation water results in Figure 6.16A also do not correlate with seawater, evaporated seawater, or meteoric water. However, the results from the Slave Point Formation are similar to those from the Paleozoic and Mesozoic of west-central Alberta (Connolly et al., 1990b). They (ibid.) interpreted these results to be the product of the mixing of a residual evaporitic brine with meteoric water. The evaporitic brine was not chemically significantly altered but the meteoric water was involved in feldspar-clay mineral alteration reactions (Connolly et al., 1990b). As a result of this fluid mixing, the present formation waters in the Slave Point Formation would be expected to plot along a tie-line between the two end-member fluids, which may be inferred from the position of the present formation water data in Figure 6.16A. However, the Clarke Lake data is skewed towards the halite-saturated brine end-member suggesting the chemistry of the fluids is predominantly controlled by the composition of the brine. This interpretation is similar to that proposed by Davisson et al. (1994) for the evolution of tectonic fluids in geothermal springs in California. These authors suggested that the geothermal water was diagenetically modified seawater that was involved in albitization and clay-mineral transformations at depth. This saline fluid was mixed with meteoric water and the combined fluid was expelled due to increased fluid pressure in a region of

Figure 6.16 Equilibrium activity diagrams illustrating the effects of water-rock interaction on formation fluids in the Slave Point Formation at Clarke Lake.

(A) Activity diagram of Ca and Na calcuated from the measured ionic concentrations and reservoir conditions. Shown for comparison are the equilibrium lines for the albitization of plagioclase feldspar at temperatures between 150 and 350°C (Davisson and Criss, 1996). The value for seawater (S) was calculated using data presented in McCaffrey et al. (1987). Squares represent data from Paleozoic and Mesozoic formation waters in the Alberta Basin (Connolly et al., 1990b), after Davisson and Criss (1996). Data used to calculated the activities of: meteoric water after Hunt (1996), halite-saturated brine after McCaffrey et al. (1987), and tectonic fluids after Davisson et al. (1994), and Heydari (1997). Data from the Slave Point Formation group around the 250°C fluid-mineral equilibrium line. See text for further discussion

(B) Activity diagram calculated for the system K_2O-Al_2O_3-SiO_2-H_2O at 100°C. The dashed lines represent saturation with respect to quartz and amorphous silica. The majority of the formation waters in the Slave Point plot within the illite stability field under subsurface reservoir conditions. See text for further discussion.

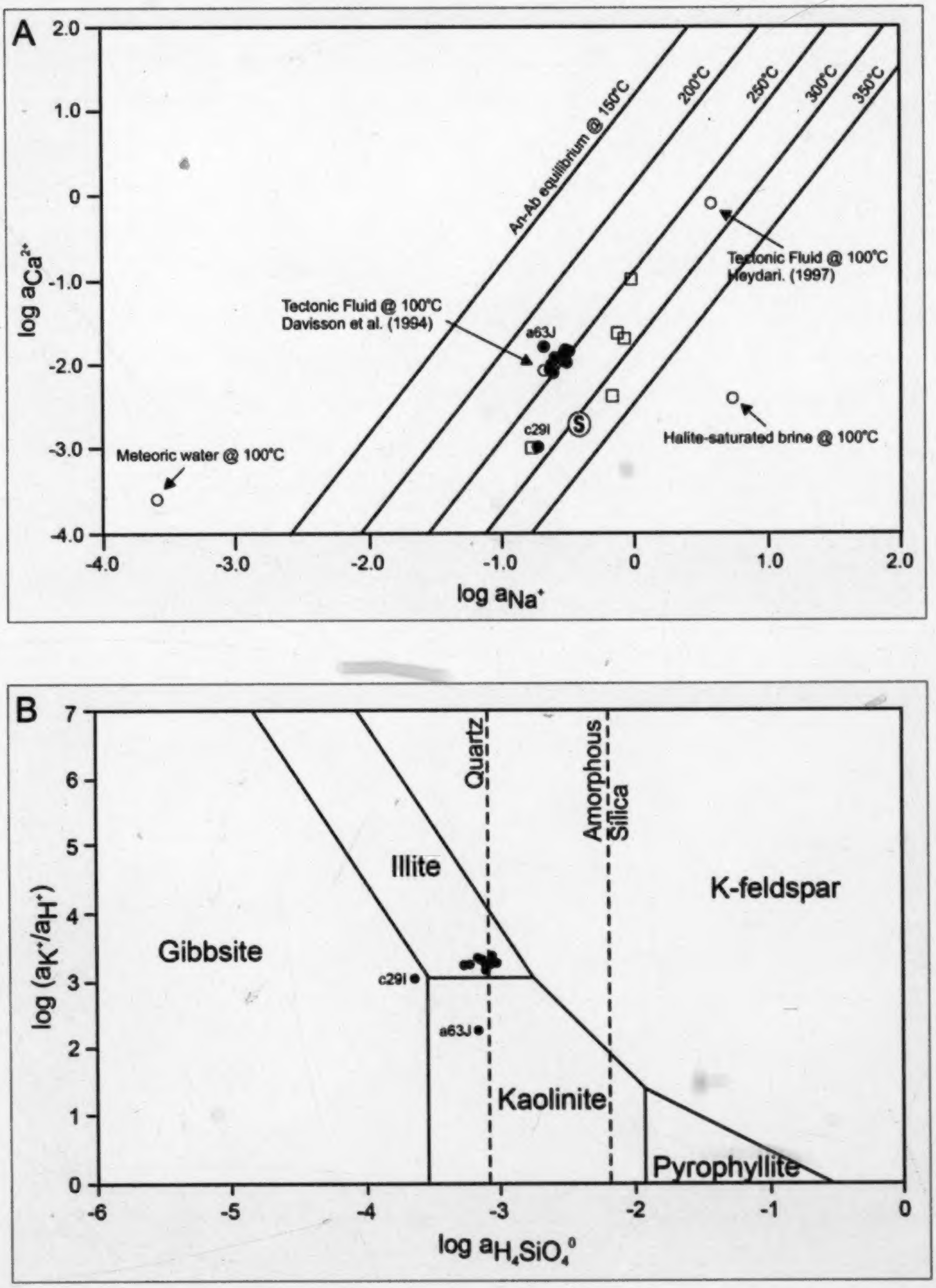
A
2.0
1.0
0
-1.0
-2.0
-3.0
-4.0
log $a_{Ca^{2+}}$
-4.0
-3.0
-2.0
-1.0
0
1.0
2.0
log a_{Na^+}
An-Ab equilibrium @ 150°C
200°C
250°C
300°C
350°C
Tectonic Fluid @ 100°C
Heydari. (1997)
Tectonic Fluid @ 100°C
Davisson et al. (1994)
a63J
c29I
S
Meteoric water @ 100°C
Halite-saturated brine @ 100°C
B
7
6
5
4
3
2
1
0
log (a_{K^+}/a_{H^+})
-6
-5
-4
-3
-2
-1
0
log $a_{H_4SiO_4^0}$
Quartz
Amorphous Silica
Illite
Gibbsite
K-feldspar
Kaolinite
Pyrophyllite
c29I
a63J

ongoing structural deformation.

Further proof for the control that exchange reactions have on the formation water composition at Clarke Lake can be seen in a K_2O-Al_2O_3-SiO_2-H_2O equilibrium activity diagram (Figure 6.16B). The majority of the formation water samples plot within the illite stability field, to the left of the K-feldspar stability field, and slightly above the stability field for kaolinite. Previously, it was proposed that the elevated absolute concentrations of potassium in the formation waters was the result of the transition of K-feldspar to kaolinite, however, the activity diagram suggests that the formation waters are in fact in equilibrium with illite and not kaolinite. Based on evidence presented earlier, it would appear that the formation water chemistry is governed by the following reaction (Thyne et al., 2001):

$$KAlSi_3O_8 + \tfrac{2}{3}H^+ = KAl_3Si_3O_{10}(OH)_2 + \tfrac{2}{3}K^+ + 2SiO_2\ (aq)$$

At temperatures around 130°C the rate of dissolution becomes faster than transport and the K-feldspar dissolves rapidly to form illite. The above reaction produces some illite directly and is the source of dissolved components such as K^+ and SiO_2 (Thyne et al., 2001). Interestingly, the Slave Point formation water data plot near the line of quartz saturation, which was also observed in the saturation indices of quartz. This distribution is likely due to the SiO_2 (aq) produced through the above reaction that can precipitate to form quartz (Thyne et al., 2001). Both of the formation water samples that plot outside of the illite stability field, a-63-J and c-29-I, are considered to represent a distinct water-rock reaction scheme. Based on previously discussed geochemical data from these wells, the chemistry of these formation waters is a reflection of the 'injection' of a third fluid end-member (MetaW) into a mixed fluid made up of halite brine and meteoric water end-members. Additionally, a-63-J was previously interpreted to be isolated from further 'injection' of MetaW due to its position within the relatively low permeability limestones of the Klua Embayment. The position of well a-63-J also prevented further dilution by meteoric waters that were involved in the conversion of K-feldspar to illite.

Overall, the calculated fluid-mineral equilibria from the formation fluids in the Slave Point Formation suggest multiple exchange reactions between the halite brine and meteoric fluid end-members and the rocks in the subsurface of northeastern British Columbia. In particular, the bulk of the formation waters show evidence for being involved in the process of dolomite formation, which controls both their Ca and Mg concentrations. Additionally, there is evidence for the alteration of feldspar, which controls both the K and

Na concentrations in the formation waters. These alteration reactions are further proof that one of the end-member fluids migrated through, and interacted with, feldspar-bearing rocks of either the Proterozoic Muskwa Assemblage or the Precambrian crystalline basement.

6.6 Fluid flow at Clarke Lake

Integration of the formation water geochemical results from this study with the previous hydrogeological studies by Bachu (1997), and Underschultz and Bachu (1997) provide critical evidence for the present-day fluid flow patterns in, and around, the Clarke Lake field. Fluid flow in the Slave Point Formation not only has economic implications in terms of the development and maintenance of the natural gas reservoir at Clarke Lake, but potentially also the position of undiscovered gas pools in the Devonian of northeastern British Columbia.

The regional interpretation of the present-day fluid flow patterns is shown in Figure 6.17. It is assumed that the halite brine (HB) to gypsum brine (GB) end-member that is observed in the ionic hydrochemistry and was interpreted to represent the fluid that effected hydrothermal alteration of the Slave Point dolomites was previously entrained, and mixing of the end-member fluids occurred in the reservoir at Clarke Lake, consequently, the fluid flow patterns are only representative of the meteoric water (MW) end-member. Also displayed on Figure 6.17 are the ranges of the $^{87}Sr/^{86}Sr$ results from the analysis of the Precambrian crystalline basement, Proterozoic Muskwa Assemblage, Cambrian sandstone, and Phanerozoic basinal shales.

Based on the stable isotope results from the formation fluids in the Slave Point Formation, it was proposed earlier that the dilute fluid end-member was, in fact, present-day meteoric water that was involved in water-rock interaction along its migration pathway. As a result, it is proposed that the meteoric water end-member entered the subsurface of northeastern British Columbia through recharge in the uplifted Rocky Mountains to the west of Clarke Lake. The main ranges of the Rocky Mountains in this region of Canada are cored by sub-greenschist facies clastic and carbonate rocks (Ross, 2000) of the Proterozoic Muskwa Assemblage. This package of sediments had an original depositional thickness of at least 6 kilometres in the region underlying the Rocky Mountains, thinning to a thickness of approximately 2 kilometres beneath the Clarke Lake field. The interaction of the meteoric waters with the Muskwa Assemblage, and potentially the Precambrian

Figure 6.17 Cross-section A-A' showing the present-day structural style of the northern Rocky Mountains and the deformed belt of the Western Canada Sedimentary Basin. The location of cross-section A-A' is shown on Figure 1.4. The enlarged area shows the Clarke Lake study area. Modified after Gabrielse and Taylor (1982). The solid black vertical lines on the cross-section indicate the relative stratigraphic position of the various strontium source rocks in northeastern British Columbia. The ranges of $^{87}Sr/^{86}Sr$ values obtained through selective strontium extraction are shown for reference (See Figure 6.6). The cross-section through Clarke Lake shows the decreasing range in $^{87}Sr/^{86}Sr$ of the formation waters from west to east. The dashed lines on the cross-section represent possible fluid flow pathways that would explain the observed $^{87}Sr/^{86}Sr$ values of the present-day formation waters in the Slave Point Formation.

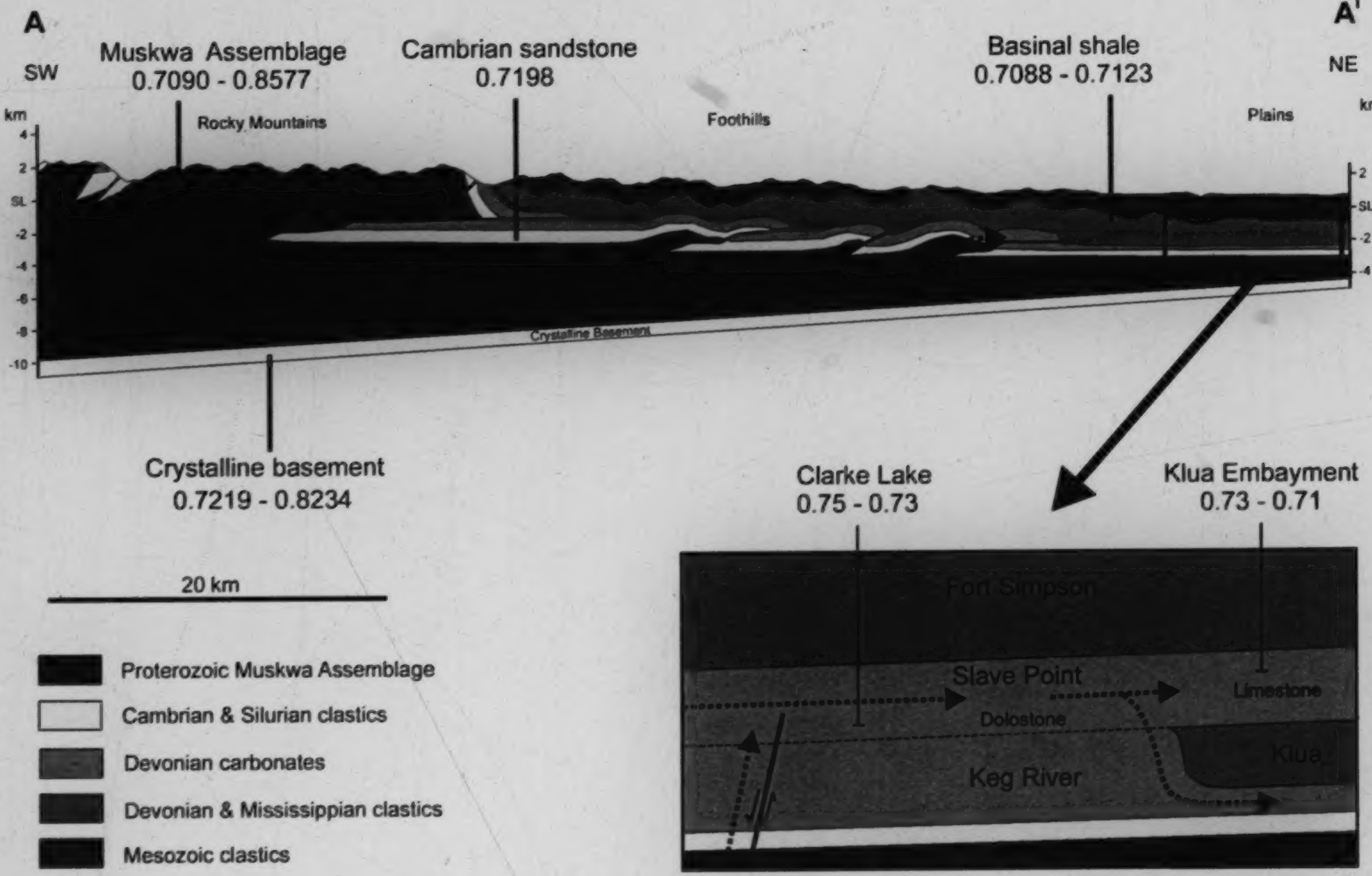
A
SW
Muskwa Assemblage
0.7090 - 0.8577
Cambrian sandstone
0.7198
Basinal shale
0.7088 - 0.7123
A'
NE
km
Rocky Mountains
Foothills
Plains
4
2
SL
-2
-4
-6
-8
-10
Crystalline Basement
Crystalline basement
0.7219 - 0.8234
Clarke Lake
0.75 - 0.73
Klua Embayment
0.73 - 0.71
Fort Simpson
Slave Point
Limestone
Dolostone
Klua
Keg River
20 km
Proterozoic Muskwa Assemblage
Cambrian & Silurian clastics
Devonian carbonates
Devonian & Mississippian clastics
Mesozoic clastics

crystalline basement, is clearly evidenced by the elevated $^{87}Sr/^{86}Sr$ values of the formation waters at Clarke Lake, as these values cannot be the result of interaction with sediments in the Phanerozoic. Additionally, the bulk geochemistry and the results from geochemical modelling of the formation waters suggest the meteoric fluid end-member was involved in the alteration of feldspars, which liberated both K^+ and radiogenic ^{87}Sr. These chemically altered meteoric waters likely entered the Slave Point Formation along faults that propagate down to basement, and migrated into the high permeability Clarke Lake dolostone reservoir. Across most geochemical data sets, both wells a-63-J and c-29-I suggest the 'injection' of a third fluid end-member in addition to the mixed halite/gypsum brine and meteoric water end-members. This 'injected' fluid end-member was emplaced in larger volumes around well c-29-I due to flow along open faults and fractures, while in well a-63-J the stable and radiogenic isotope data suggest that the 'injected' fluid has not mixed in large proportions with the meteoric water end-member. Rather, well a-63-J was isolated from further fluid mixing after initial 'injection' of this third fluid end-member. It is suggested that well a-63-J was isolated due to its position within the Klua Embayment, where relatively low permeability limestones (and shales of the Otter Park Formation) laterally inhibit the movement of the halite/gypsum brine and meteoric water end-members that constitute the mixed formation fluids (Figure 6.18). As a result, these mixed fluids are forced to migrate downward into the underlying Keg River Formation (Figure 6.18) (Underschultz and Bachu, 1997). This interpretation, however, has its pitfalls. Notably, there is very little information available on the chemistry of the formation waters in the Keg River Formation, and if these formation waters have a higher density, i.e., higher TDS, there would be little drive for the mixed and relatively dilute formation waters of the Slave Point Formation to flow downward and mix with the formation fluids in the Keg River Formation. Another alternative calls for the mixed formation waters at Clarke Lake to be relatively static, while, at the same time, being continually diluted by the chemically altered meteoric water end-member. Neither alternative can be discounted entirely at this point in time based on the data available; however, a hydrogeological study of the Keg River formation waters would prove an invaluable asset.

The migration pathways of the chemically altered meteoric water end-member, in combination with the overall geometry of the Slave Point Formation platform margin, are extremely important for both trap development and preventing the previously emplaced

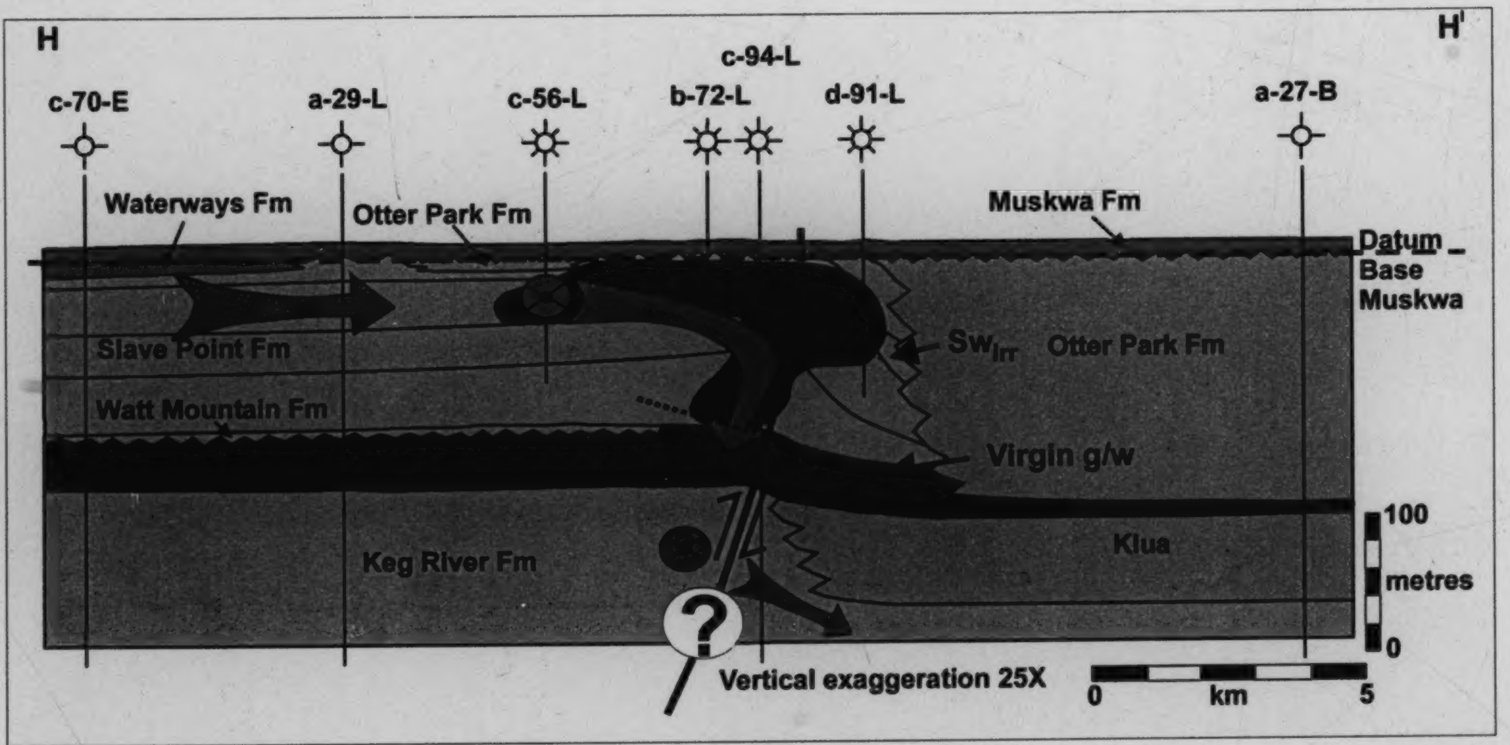
H
H'
c-70-E
a-29-L
c-56-L
b-72-L
c-94-L
d-91-L
a-27-B
Waterways Fm
Otter Park Fm
Muskwa Fm
Datum _ Base Muskwa
Slave Point Fm
Watt Mountain Fm
Sw_{irr}
Otter Park Fm
Virgin g/w
Keg River Fm
Klua
?
100
metres
0
Vertical exaggeration 25X
0
km
5

Figure 6.18 Schematic showing the present-day inferred fluid flow in the Slave Point Formation at Clarke Lake. Location of cross-section is shown in Figure 6.3. The position of the original gas/water contact (virgin g/w) is shown for reference. The present gas/water contact is represented by the position of the line of irreducible water saturation (Sw_{irr}). The movement of present-day formation fluids is updip towards the north and east. Near the Slave Point margin, lateral and vertical permeability barriers force the formation fluids downward into the underlying Keg River Formation.

hydrocarbons from being flushed through the active migration of formation waters in the Devonian. Specifically, with respect to the Clarke Lake Slave Point reservoir, the trapping conditions are controlled mainly by the lateral and vertical permeability barriers of the Slave Point limestone (Figure 6.17), the Otter Park shale, and the Muskwa shale (Figure 6.18). Additionally, from this study and previous hydrogeological studies, it is proposed that the dominant flow direction of the formation waters is from the southwest, in the Rocky Mountains, to the northeast. Based on this geometry and the position of embayments along the Slave Point platform margin, the flow of formation waters towards the northeast would flush all hydrocarbons from the southwest into the Clarke Lake reservoir. As a result, only where the shape of the platform margin is conducive to reservoir closure with respect to the northeastward-directed flow of formation waters is there potential for hydrocarbon trapping. In the Clarke Lake field, it is clear that the main Slave Point hydrocarbon pool is controlled by flow of formation waters (Figure 6.18). During the late 1950's when the Clarke Lake field was discovered, the original gas-water contact at the Slave Point platform margin was at, or close to, the base of the Slave Point Formation (Figure 6.18 – virgin g/w). Following 40 years of gas production, the gas-water contact is now situated at a higher elevation. The position of the present gas-water contact is represented by the line of irreducible water saturation (Sw_{irr}), which is the point where all water is adsorbed onto the pore walls and there is no permeability with respect to water. Below this line, any remaining natural gas is commingling with the formation waters. Based on the position of this line, it is apparent that the flow of formation waters into the Clarke Lake field from the west and southwest is maintaining the position of the hydrocarbon pool adjacent to the Slave Point platform margin (Figure 6.18). This observation may prove critical in the exploration for hydrocarbon accumulations in the Middle Devonian across northeastern British Columbia.

CHAPTER 7

SYNOPSIS

7.1 Restatement of objectives

As stated in Chapter 1, the overall objective of this thesis is to elucidate the spatial distribution, origin, and timing of dolomite formation in the Slave Point Formation at Clarke Lake, British Columbia, using petrographic and geochemical methods. Specifically, the academic (scientific) objectives are to determine:

(1) the primary controls on dolomite distribution;
(2) the controls on primary and secondary porosity distribution;
(3) the temperatures, compositions, and flow directions of the diagenetic fluids;
(4) the relative timing of hydrocarbon migration; and,
(5) the relationship between the present formation fluids and dolomite formation.

The major applied (industrial) objective from this research is to provide a proper reservoir characterization in order to enhance production performance, and to address water production problems in the Clarke Lake field, and in similar dolostone reservoirs elsewhere along the Slave Point platform margin.

The subsequent chapters treated various, but interdependent, aspects of the scientific objectives. In particular, the objectives of Chapter 2 are to: 1) define the local stratrigraphic nomenclature; and, 2) identify the stratigraphic and structural controls on the formation of the Slave Point platform margin. The results from Chapter 2 provided the framework for Chapter 3, the major objectives of which are: 1) to provide a comprehensive review of the original carbonate depositional facies; and, 2) to generate a depositional facies interpretation for the Slave Point Formation at Clarke Lake. The objectives of Chapter 4 are to: 1) identify all post-depositional diagenetic phases in the Slave Point Formation; 2) establish the spatial and temporal relationships between the various diagenetic phases; and, 3) establish the controls on dolomite distribution in the Clarke Lake field. The results from this chapter have important implications for the origin and timing of the diagenetic fluids that infiltrated the Slave Point Formation at Clarke Lake, and provide the framework for the geochemical investigations presented in Chapter 5. The objectives of Chapter 5 are to: 1) constrain the composition and timing of the various diagenetic fluids; 2) identify whether the dolomite-forming fluids were hydrothermal; and, 3) provide a hydrological interpretation for dolomite formation in the Slave Point Formation. Finally, based on the diagenetic framework for the Slave Point Formation, the objectives of Chapter 6 are to: 1) identify the origin and evolution of the present-day formation waters in the Slave Point Formation; 2) determine the relationships between the present-day formation waters and fluids responsible for the formation of the dolomite(s) in the Slave Point Formation; and, 3) provide an interpretation of present-day fluid flow patterns. The objective of this, the final, chapter is to integrate the findings of all previous chapters into a synopsis of the diagenetic evolution of the Slave Point Formation, to highlight the new findings, to evaluate whether the overall objectives of the project have been met, and to point out avenues for future work.

7.2 Diagenetic evolution of the Slave Point Formation

The Slave Point Formation at Clarke Lake underwent a complex diagenetic history, which can be divided into six stages of burial with corresponding stages of pore water evolution. As defined in Chapter 4, a stage generally consists of a grouping of several diagenetic phases based on depth and water chemistry. The burial depth estimates for the first five stages are shown in Figure 7.1, and are based on both the sequence of diagenetic phases and the intrinsically-related evolution of porosity in the Slave Point Formation. An overview of the bulk chemistry of the six main diagenetic fluids affecting the Slave Point Formation is shown in Table 7.1. Schematics showing the diagenetic evolution are shown in Figure 7.2. The north-south schematic is drawn from the outer platform margin at Clarke Lake to a distance approximately 100 km to the southeast. The west-east schematic is drawn from a position within the present-day deformed belt of the Rocky Mountains eastward to the far side of the Klua Embayment – a distance of approximately 100 km.

7.2.1 Stage I – Middle Devonian (phases 1 to 4)

Deposition and shallow burial to approximately 300 metres (Figure 7.2 – Stage I). The Slave Point Formation lies horizontal in the Clarke Lake field. The geometry of the Slave Point platform margin and the distribution of depositional facies within the Slave Point Formation are controlled by the position of faults that originated in the basement. At the time of deposition, i.e., zero depth, the uppermost parts of the Slave Point Formation are predominantly unlithified sediment, while the lowermost parts are partially lithified

Figure 7.1 Paragenetic sequence for the Middle Devonian Slave Point Formation at Clarke Lake. Hydrothermal Alteration includes all phases that resulted from the invasion of hydrothermal fluids into the reservoir. Diagenetic settings and their relative depths after Machel (1999). The estimation of porosity evolution is based on petrographic analysis and comparing samples with measured porosity and permeability. Stages (I though V) relate to distinct fluid flow events and/or fluid chemistry. See Table 7.1 for further explanation.

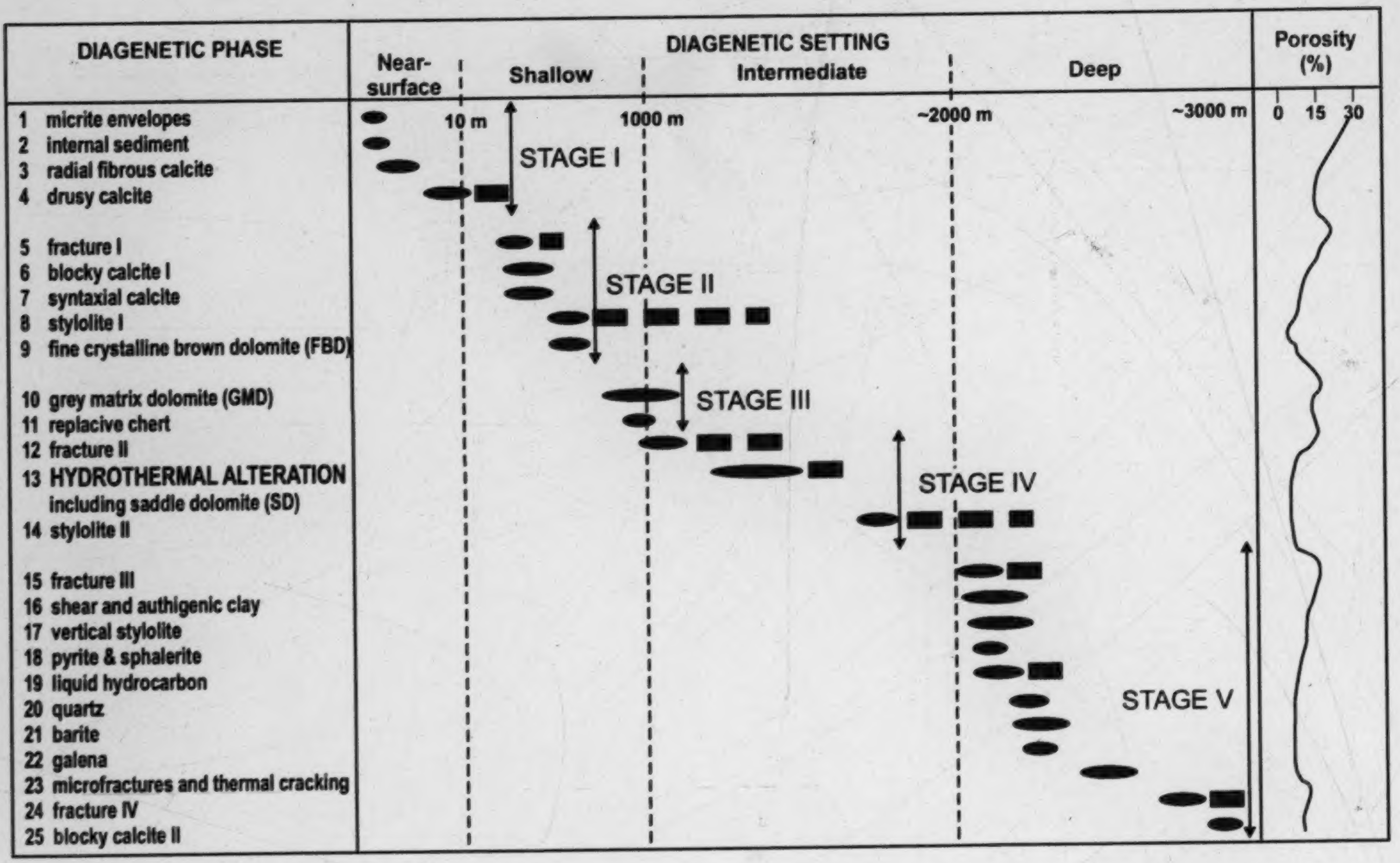
DIAGENETIC PHASE
DIAGENETIC SETTING
Near-surface
Shallow
Intermediate
Deep
Porosity (%)
0
15
30
10 m
1000 m
~2000 m
~3000 m
STAGE I
STAGE II
STAGE III
STAGE IV
STAGE V
1 micrite envelopes
2 internal sediment
3 radial fibrous calcite
4 drusy calcite
5 fracture I
6 blocky calcite I
7 syntaxial calcite
8 stylolite I
9 fine crystalline brown dolomite (FBD)
10 grey matrix dolomite (GMD)
11 replacive chert
12 fracture II
13 HYDROTHERMAL ALTERATION including saddle dolomite (SD)
14 stylolite II
15 fracture III
16 shear and authigenic clay
17 vertical stylolite
18 pyrite & sphalerite
19 liquid hydrocarbon
20 quartz
21 barite
22 galena
23 microfractures and thermal cracking
24 fracture IV
25 blocky calcite II

Stage	Age	Fluid					
		Salinity (wt.% NaCl)	System (based on T_e)	Temp. (°C)	Composition	Source(s)	Flow Mechanism
I	Middle Devonian	~3	Na-Ca-Cl	~25	Seawater	-	-
II	Middle to Late Devonian	-	-	~100	Slightly modified seawater	Middle Devonian seawater	Compaction or convection
III	Late Devonian	~24	Na-Mg-Ca-Cl	~150	Halite-saturated brine	Middle Devonian evaporites	Density-driven flow
IV	Late Devonian to Early Mississippian	~15	Na-Mg-Ca-Cl	~230	- Stage III halite-saturated fluid diluted by gypsum-saturated brine - Variable chemistry and temperature due to water-rock ratio and/or basement interaction	Middle Devonian evaporites	Density-driven flow + heat? Fault action
V	Mississippian to Early Jurassic	~14	Na-Ca-Mg-Cl	~140 to ~185	- Stage IV further diluted and modified by water-rock interaction - Fluctuating salinity, temperature, pH	-	-
VI	Late Cretaceous through Recent	~4	Na-Ca-Cl	~110	- Stage V fluid diluted with meteoric water	Recent meteoric water interacting with basement rocks	Topography-driven flow

Table 7.1 Diagenetic fluid stages in the Middle Devonian Slave Point Formation at Clarke Lake.

Figure 7.2 Schematic representation of the evolution of fluid flow patterns in and around the Clarke Lake field from the Devonian to the present. See text for locations of cross-sections.

STAGE I - Middle Devonian. Fluid 1 represents normal seawater being pumped or convecting through the uppermost layers of the Slave Point Formation. Fluid 2 represents the movement of highly evaporated, halite saturated brines that originated in the region of deposition of the Muskeg Formation, travelling along the relatively permeable Lower Keg River Formation.

STAGE II - Middle to Late Devonian. Fluid 3 represents compaction flow of chemically slightly modified seawater from the lateral and overlying shale sequences into the relatively permeable Slave Point Formation, as well as upward migration. Fluid 4 represents the convection of entrained formation fluids in the Slave Point Formation.

STAGE I - Middle Devonian

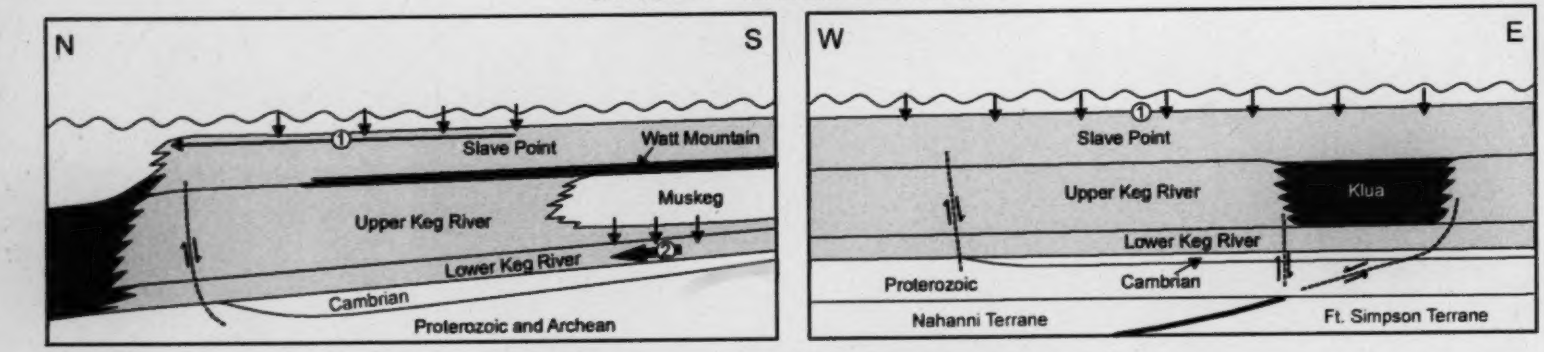
N
S
①
Slave Point
Watt Mountain
Muskeg
Upper Keg River
②
Lower Keg River
Cambrian
Proterozoic and Archean
W
E
①
Slave Point
Upper Keg River
Klua
Lower Keg River
Proterozoic
Cambrian
Nahanni Terrane
Ft. Simpson Terrane

STAGE II - Middle to Late Devonian

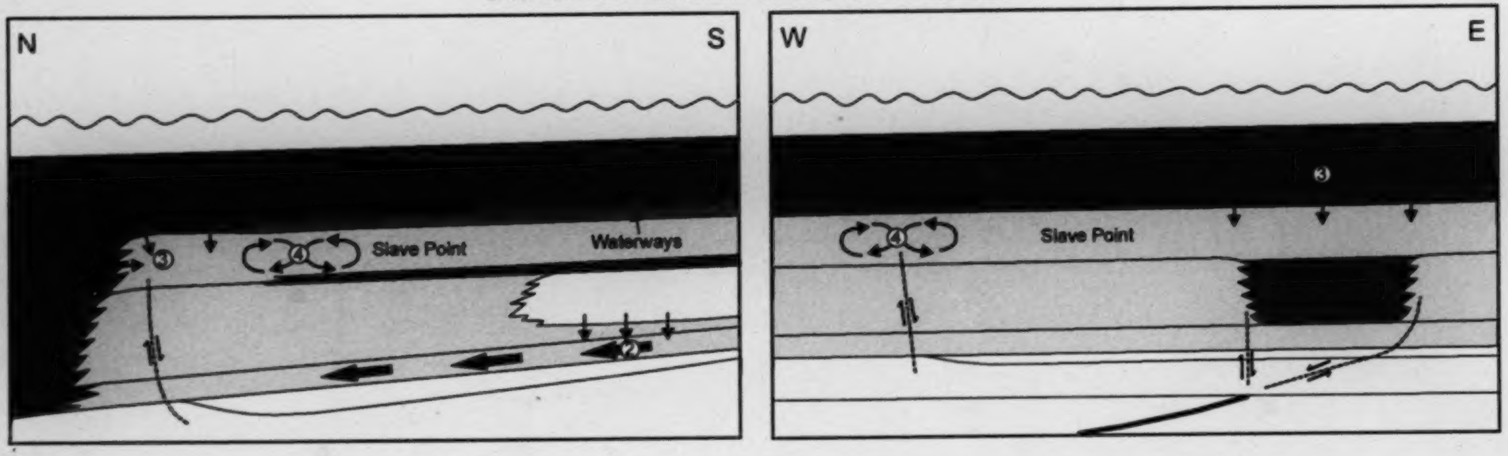
N
S
③
④
Slave Point
Waterways
②
W
E
③
④
Slave Point

limestone. This stage includes all diagenetic processes on or near the seafloor. The results are typical for 'marine diagenesis', i.e., micrite envelopes, internal sediments, and radial fibrous calcite cement (phases 1 to 3). These products are best preserved in the rare, non-dolomitized limestones in the Klua Embayment. As a result of the formation of these diagenetic phases, primary porosity was reduced from about 30-40% to roughly 15%, with a concomitant reduction in both horizontal and vertical permeability. At increased burial depths, much of the remaining primary porosity was further reduced to approximately 10% through the precipitation of drusy calcite cement (phase 4) in both intra- and interparticle pores. By the end of this stage the Slave Point Formation was lithified.

The first fluid that controlled the diagenesis of the Slave Point Formation was Middle Devonian seawater, the chemistry of which has been outlined in previous studies. The driving forces for fluid flow were most likely either free convection through the open marine platform margin and/or tidal pumping (Figure 7.2 – fluid 1). At the same time, a highly evaporated, halite-saturated connate brine that originated in the Muskeg and equivalent formations far to the south of the Slave Point platform margin commenced migration along the relatively permeable Lower Keg River Formation. The driving force for this fluid was density flow (Figure 7.2 – fluid 2), displacing previously entrained fluids ahead of this heavy brine slug.

7.2.2 Stage II – Middle to Late Devonian (phases 5 to 9)

Shallow burial to approximately 700 metres (Figure 7.2 – Stage II). By the end of this stage the entire package of Fort Simpson sediments was deposited. As well, from north to south, the Slave Point strata was still in a predominantly horizontal position, while tectonic and sedimentary loading as a result of the Antler Orogeny initiated tilting of the Slave Point Formation towards the west. The earliest diagenetic products to form during this stage include fracture generation I, blocky calcite cement I, and syntaxial calcite cement (phases 5 to 7). By the time these diagenetic phases formed the remaining primary porosity in the Slave Point limestones was reduced to less than 10%. Near the conclusion of this stage chemical compaction of the limestone had created low-amplitude stylolites (phase 8). Additionally, small quantities of fine crystalline brown dolomite (phase 9) replaced micrite and calcite cement in the matrix of clean, relatively high permeability limestone. This dolomite phase is presently only visible in the back-reef limestones in the

Klua Embayment. Phases 8 and 9 also generated limited volumes of secondary porosity, significantly reducing both the overall porosity to less than 5%, and vertical permeability.

During this stage, the halite-saturated brine generated in the Muskeg Formation to the south migrated by density-driven flow farther downdip towards the Keg River and Slave Point platform margins. Meanwhile, the major fluid facilitating the formation of the diagenetic phases during this stage was still Middle Devonian seawater, as suggested by the isotope data from the calcite cements (blocky calcite I – phase 6). The driving forces for fluid flow were most likely either compaction from adjacent shale horizons, i.e., Otter Park, Muskwa, and Fort Simpson formations (Figure 7.2 – fluid 3), or convection flow (Figure 7.2 – fluid 4). With respect to fine crystalline brown dolomite (phase 9), considering the overall very low quantities and petrographic characteristics, it probably originated from the compaction water movement and/or local liberation of Mg from clays and/or high-Mg calcite allochems and bioclasts.

7.2.3 Stage III – Late Devonian (phases 10 and 11)

Intermediate burial to depths of 700 to 1200 metres (Figure 7.2 – Stage III). This depth range is similar to that for the latter parts of Stage II. The boundary between these two stages is defined by the formation of pervasive matrix dolomite (GMD – phase 10), effected by a dramatic change in formation water chemistry at Clarke Lake.

Continued tectonic loading towards the west, due to the Antler Orogeny, increased the dip on the top of the Slave Point Formation, although there is still little manifestation of basinal tilting along the north-south cross-section. The major diagenetic phase during this stage is the replacement of limestone by grey matrix dolomite (phase 10). This diagenetic event was independent of facies and is rarely found in the limestones in the Klua Embayment that are underlain by the Klua shale, suggesting that the dolomitizing fluid(s) ascended into the Slave Point Formation. Most of the large allochems in the dolomitized domains were preserved as calcite and dissolved at a later stage, but dolomitization of the limestones generated significant secondary intercrystalline porosity in the Slave Point Formation. Limestones that were replaced by grey matrix dolomite and show little evidence for subsequent diagenesis provide the best reservoir rocks in the Clarke Lake field. These rocks increased the total overall porosity to over 15%, while the effective nature of the intercrystal pores increased both horizontal and vertical permeability.

Figure 7.2 Schematic representation of the evolution of fluid flow patterns in and around the Clarke Lake field from the Devonian to the present (cont'd).

STAGE III - Late Devonian. Fluid 2 continues to travel downdip along the Lower Keg River Formation until it reaches the lateral shale permeability barriers at the outer platform margin and is forced upward into the Slave Point Formation. Fluid 5 represents gypsum saturated brines now generated in the region of deposition of the Muskeg Formation. This brine follows behind the earlier-generated halite saturated brines.

STAGE IV - Late Devonian to Early Mississippian. Fluid 5 reaches the Slave Point Formation and mixes and/or displaces Fluid 2.

STAGE III - Late Devonian

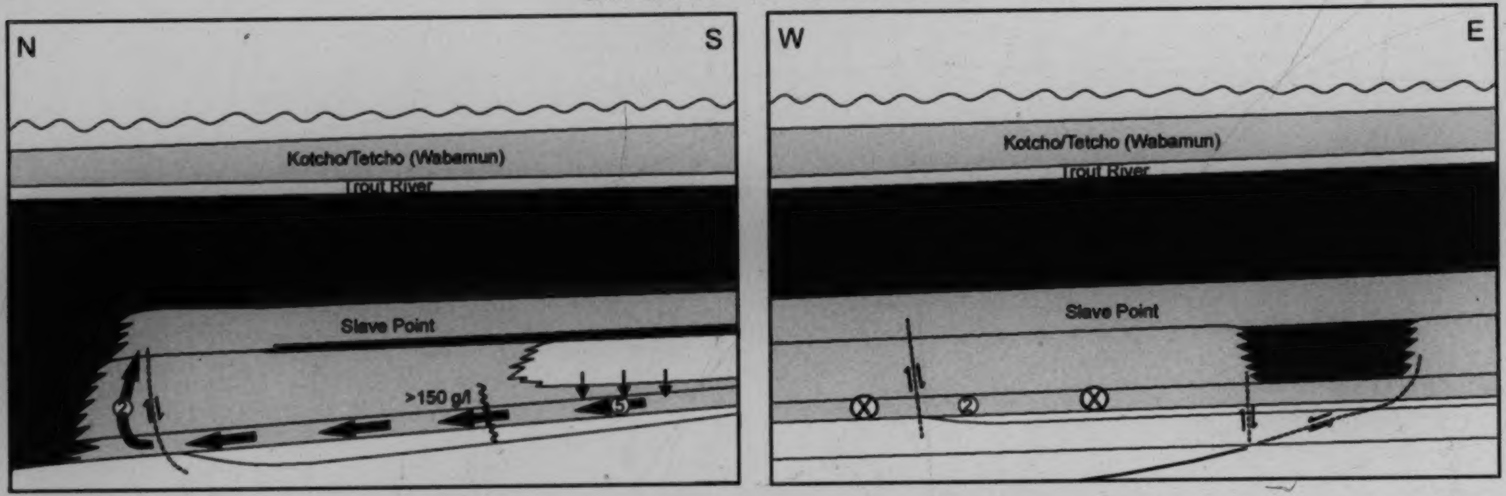
N
S
Kotcho/Tetcho (Wabamun)
Trout River
Slave Point
>150 g/l
②
⑤
W
E
Kotcho/Tetcho (Wabamun)
Trout River
Slave Point
②

STAGE IV - Late Devonian to Early Mississippian

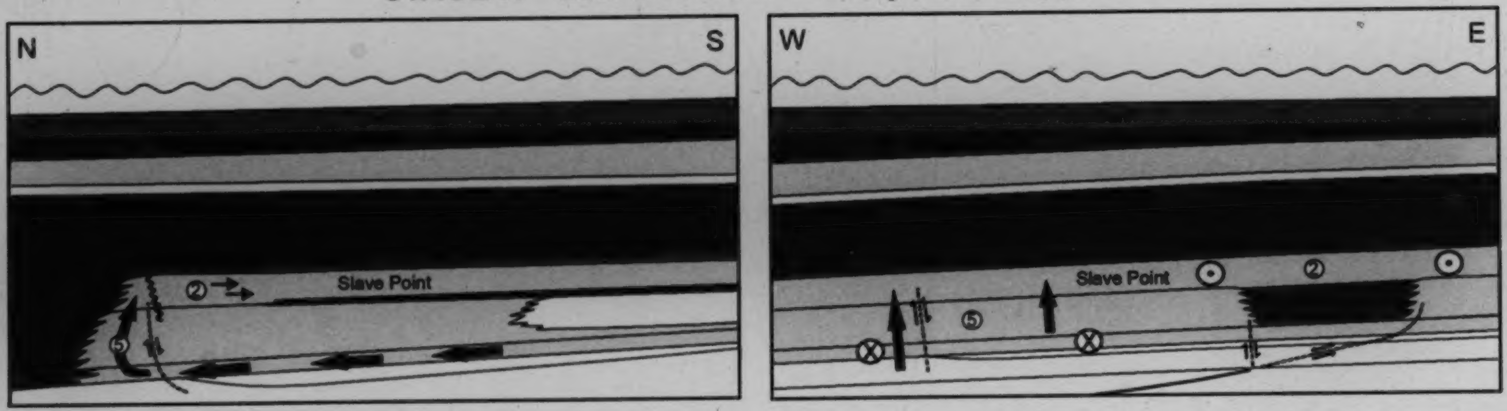
N
S
②
Slave Point
⑤
W
E
Slave Point
②
⑤

Also during this stage, minor volumes of replacive chert formed in the Slave Point Formation, likely the result of mixing of brines with varying saturation states with respect to dolomite and calcite, which precipitated quartz at the lowest fluid temperatures (Leach et al., 1991). This phase had very little impact on the overall porosity in the Slave Point Formation.

Based on isotopic and fluid inclusion evidence, the fluid responsible for the formation of grey matrix dolomite was a halite-saturated brine (Figure 7.2 – fluid 2). By this stage, the halite-saturated brine had migrated to the platform margin of the Keg River Formation from which it was forced upward into the overlying Slave Point Formation because of the lateral permeability barriers at the platform margin, i.e., low permeability basinal shales. The energy to move upward was provided by the weight of the brine 'slug' that extended from the platform margin toward the Muskeg depositional region in the south and southeast, followed by a less dense but still heavy gypsum brine (Figure 7.2 – fluid 5). The interface between the halite- and gypsum-saturated brines is represented by the 150 g/L contour in Figure 7.2. The faults at the platform margin may have provided additional high-permeability conduits for the upward migration of the halite-saturated brine. Based on the distance of brine travel of approximately 200 km, the flow velocity of this halite-saturated brine is estimated at 1-2 cm/year.

7.2.4 Stage IV – Late Devonian to Early Mississippian (phases 12 to 14)

Intermediate burial and deep burial to depths of approximately 2000 to 2200 metres (Figure 7.2 – Stage IV). During this stage, the Slave Point Formation was buried to greater depths with the deposition of the Mississippian Exshaw and Banff formations. The major processes during this stage were fracture generation II, hydrothermal alteration (including saddle dolomite formation), and stylolite generation II (phases 12 to 14). Fracturing could be considered an integral part of the hydrothermal alteration if it could be proven that the hydrothermal fluids could enter the Slave Point Formation dolostones only through faults.

A more important control on the reservoir quality at Clarke Lake is the combined effects of fracture generation II and saddle dolomite formation. Fracture generation II, which probably was a direct result of tectonic movements in this part of northeastern British Columbia during the terminal stages of Antler orogenesis, provided the necessary conduits for the fluid(s) responsible for dissolution, alteration, and saddle dolomite formation, collectively termed hydrothermal alteration in this study.

The geochemical characteristics of the entire spectrum of diagenetic products from pristine grey matrix dolomite through saddle dolomite cement in the Slave Point Formation at Clarke Lake are shown in Table 7.2. Based on these characteristics, it is possible to propose a Slave Point hydrothermal alteration 'model' that incorporates the petrographic characteristics on a larger scale (Figure 7.3). This 'model' is loosely based on the thermochemical sulphate reduction (TSR) – hydrothermal dolomite 'furnace' model for the Slave Point Formation presented by Reimer and Teare (1992). Their model proposed dolomitization of limestones, brecciation and saddle dolomite formation from hydrothermal fluids. This model, as proposed, is untenable, however. Firstly, Reimer and Teare (1992) proposed their model based on the notion that TSR is exothermic, which Simpson et al. (1996), and Simpson (1999) have shown to be incorrect: most TSR sites are endothermic. Secondly, Machel (2001) has suggested that most TSR settings are closed or nearly closed hydrodynamically, whereas dolomitization requires an open system because of the requirement to deliver Mg. Based on these limitations, in conjunction with the petrographic and geochemical evidence from the Slave Point at Clarke Lake, it is proposed that the hydrothermal fluids did not dolomitize limestone but effected alteration of pre-existing dolostones, without in-situ generation of heat. The extent of hydrothermal alteration is thereby controlled by the volume of hydrothermal fluid flowing through a particular volume of dolomite, i.e., the water-rock ratio, and the flow velocity, which controls the heat differential. The fluids responsible for hydrothermal alteration were a mixture of the previously entrained halite-saturated brine (Figure 7.2 – fluid 2) and the gypsum-saturated brine (Figure 7.2 – fluid 5) that had migrated into the Slave Point Formation at the platform margin, in part along faults. The elevated temperatures of these fluids are due to the combined effects of regional tectonics, i.e., subduction and slab rollback, and high heat flow to the west of the Clarke Lake field. The extent of hydrothermal alteration is most pronounced adjacent to the conduits where these hydrothermal fluids entered the Slave Point Formation (Figure 7.3). These zones had the highest water-rock ratios, the result of which was focused fluid flow, fluid chemistry that shows little evidence for dilution by the previously entrained halite-saturated brine, higher dolomite-forming temperatures, and geochemical signatures similar to rocks in the basement, as demonstrated by select wells in the Clarke Lake field (d-79-F/94-J-10, c-56-L/94-J-9). Additionally, these zones

Phase	Hydrothermal Alteration Characteristics				
	Petrography	Stable Isotope	^{87}Sr/^{86}Sr	Elemental	Fluid Inclusion
'Pristine' Matrix Dolomite	colour - grey to brown size - 40 to 300 μm texture - planar-e to planar-s CL - unzoned, dull luminescence porosity - intercrystalline; 15-20%	δ^{18}O = -13 to -15‰ PDB δ^{13}C = -0.3 to -1.0‰ PDB	0.7088 to 0.7095	$CaCO_3$ - 50 to 51 mol% Fe - <500 ppm Mn - <500 ppm Sr - <50 ppm REE - similar to limestone	Temp - 140 to 160°C Sal. - ~24 wt% NaCl Ionic - halite brine
Recrystallized Matrix Dolomite	colour - light grey to white size - 100 to 300 μm texture - planar-s to nonplanar-a CL - unzoned, dull luminescence porosity - intercrystalline; ~ 15%	δ^{18}O = -13 to -17‰ PDB δ^{13}C = -0.5 to -2.1‰ PDB	0.7092 to 0.7110 d-79-F to 0.7165	$CaCO_3$ - 50 to 51.5 mol% Fe - <1000 ppm Mn - 500 to 1000 ppm Sr - 50 ppm REE - similar to pristine MD	Temp - 170 to 190°C Sal. - ~20 wt% NaCl Ionic - halite brine diluted by gypsum brine
Replacement Saddle Dolomite	colour - white size - 300 to 1000 μm texture - nonplanar-a CL - unzoned, dull luminescence porosity - intercrystalline and vuggy; ~10%	δ^{18}O = -15 to -16‰ PDB δ^{13}C = -1.0 to -2.3‰ PDB	0.7095 to 0.7128	$CaCO_3$ - 49.6 to 51.5 mol% Fe - <500 ppm Mn - 500 to 1000 ppm Sr - 50 ppm REE - similar to reX MD	Temp - 150 to 170°C Sal. - 16 to 20 wt% NaCl Ionic - halite brine diluted by gypsum brine
Saddle Dolomite Cement	colour - white size - up to 2000 μm texture - non-planar (saddle) CL - concentric alternating zones dull to bright luminescence porosity - intercrystalline and vuggy; <10%	δ^{18}O = -13.6 to -15‰ PDB δ^{13}C = -0.2 to -1.2‰ PDB	0.7087 to 0.7111 d-79-F to 0.7165	$CaCO_3$ - 51.2 to 52.3 mol% Fe - >1000 ppm Mn - 1200 to 1600 ppm Sr - 50 to 350 ppm REE - may be distinct from replacement SD and reX MD	Temp - 110 to 140°C Sal. - 15 to 17 wt% NaCl Ionic - gypsum brine

Table 7.2 Hydrothermal alteration petrographic and geochemical characteristics exhibited by dolomites from the Slave Point Formation at Clarke Lake.

Figure 7.3 Slave Point hydrothermal alteration 'model' based on petrographic and geochemical evidence from the Clarke Lake field. This diagram is loosely based on a similar one by Reimer and Teare (1992), but differs in several important aspects. The shading of the dolomites in the Slave Point Formation follows the scheme presented in Figure 4.3. This 'model' proposes that the hydrothermal fluid entered the Slave Point Formation from below either along faults or where the Watt Mountain Formation is absent. In zones where the water-rock ratio was high (i.e., adjacent to the faults/fractures), the geochemistry of the dolomites reflects the chemistry of the hydrothermal fluid(s). Away from the highly permeable hydrothermal fluid conduits, the water-rock ratio was lower. In these zones, the hydrothermal fluid was diluted by the entrained connate brine, resulting in dolomite geochemistry similar to the original dolomite host-rock.

SLAVE POINT HYDROTHERMAL ALTERATION 'MODEL'

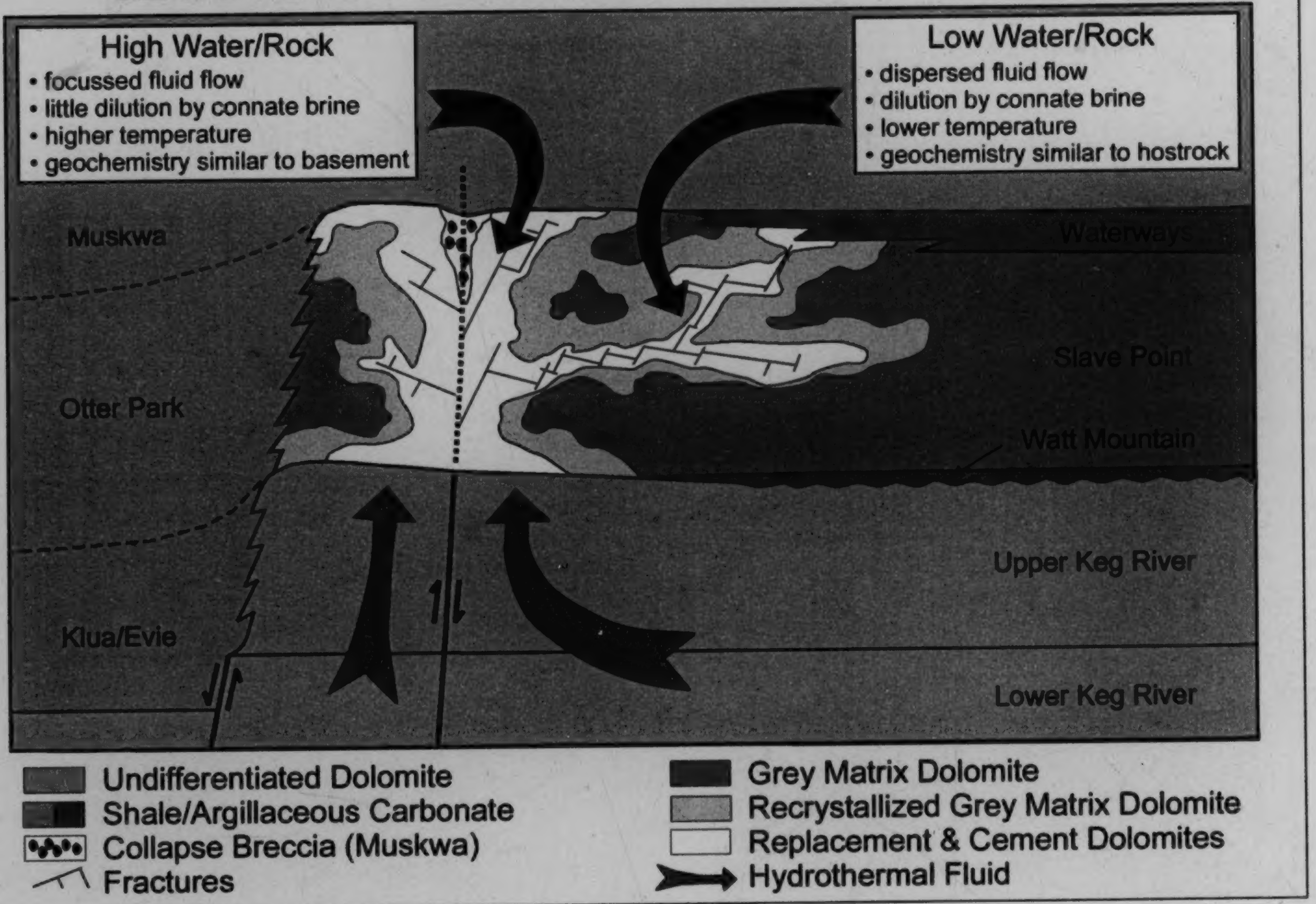

High Water/Rock
- focussed fluid flow
- little dilution by connate brine
- higher temperature
- geochemistry similar to basement

Low Water/Rock
- dispersed fluid flow
- dilution by connate brine
- lower temperature
- geochemistry similar to hostrock

Muskwa
Otter Park
Klua/Evie
Waterways
Slave Point
Watt Mountain
Upper Keg River
Lower Keg River

Undifferentiated Dolomite
Shale/Argillaceous Carbonate
Collapse Breccia (Muskwa)
Fractures
Grey Matrix Dolomite
Recrystallized Grey Matrix Dolomite
Replacement & Cement Dolomites
Hydrothermal Fluid

display evidence for enhanced dissolution, and replacement and saddle dolomite cement formation. The chemistry of the dolomites also suggests that matrix dolomite dissolution was related to the mixing of the halite- and gypsum-saturated brines: two dolomite-saturated fluids that only differ in their salinity. This mechanism has been proposed as the cause of carbonate dissolution and concomitant sulphide mineralization further up-dip along the Presqu'ile Barrier at the Pine Point MVT deposit (Adams et al., 2000). Farther away from the fluid conduits, the water-rock ratios were much lower, resulting in: dispersed fluid flow; significant dilution of the halite-saturated brine by the gypsum-saturated brine; much lower temperatures for dolomite formation; and, geochemical signatures similar to the host rock, i.e., pristine matrix dolomite (Figure 7.3).

Stylolite generation II (phase 14) post-dates hydrothermal alteration. As stylolite formation is an ongoing process during continued burial, stylolite generation II must have formed during the latest stages of intermediate burial through the onset of deep burial diagenesis, when the Slave Point Formation was rapidly buried due to regional tectonism.

7.2.5 Stage V – Mississippian to Early Jurassic (phases 15 to 25)

Deep burial between depths of roughly 2000 and 3000 metres (Figure 7.2 – Stage V). During this stage, deposition exceeded denudation and the Slave Point Formation was buried to even greater depths. The main diagenetic products that formed during this stage include base-metal sulphide minerals (phases 18 and 22), quartz (phase 20), hydrocarbon migration (phase 19), and blocky calcite cement II (phase 25).

The base-metal sulphide minerals, including sphalerite and galena, are genetically similar to sulphide minerals in the Robb Lake MVT deposit roughly 200 km downdip to the west in the northern Rocky Mountains. Isochron ages from these minerals led Nelson et al. (2002) to suggest that base-metal sulphide mineralization at Robb Lake occurred during the Late Devonian-Mississippian as a result of regional plate margin tectonics, resulting in thermal convection and fluid flow into the Western Canada Sedimentary Basin. The absolute ages of the sulphide minerals place the formation of these diagenetic phases at the onset of Stage V at Clarke Lake. The fluid that created these phases was at a lower temperature, but of similar composition than those that entered the Slave Point Formation during the previous stage. The origin of this fluid has not yet been identified. However, the bulk chemistry of the fluid inclusions suggests that this fluid was the previously entrained

Figure 7.2 Schematic representation of the evolution of fluid flow patterns in and around the Clarke Lake field from the Devonian to the present (cont'd).

STAGE V - Mississippian to Early Jurassic. Fluid 6 enters the Slave Point Formation along faults that originate in the basement. Fluid 7 represents the migration of liquid hydrocarbons into the Slave Point Formation.

STAGE VI - Late Cretaceous to Recent. Fluid 8 represents present-day topography-driven fluid flow in the Cretaceous units. Fluid 9 represents the movement of meteoric fluids originating in the Rocky Mountains. This fluid travels down into the Slave Point Formation and mixes with previously entrained formation fluids.

STAGE V - Mississippian to Early Jurassic

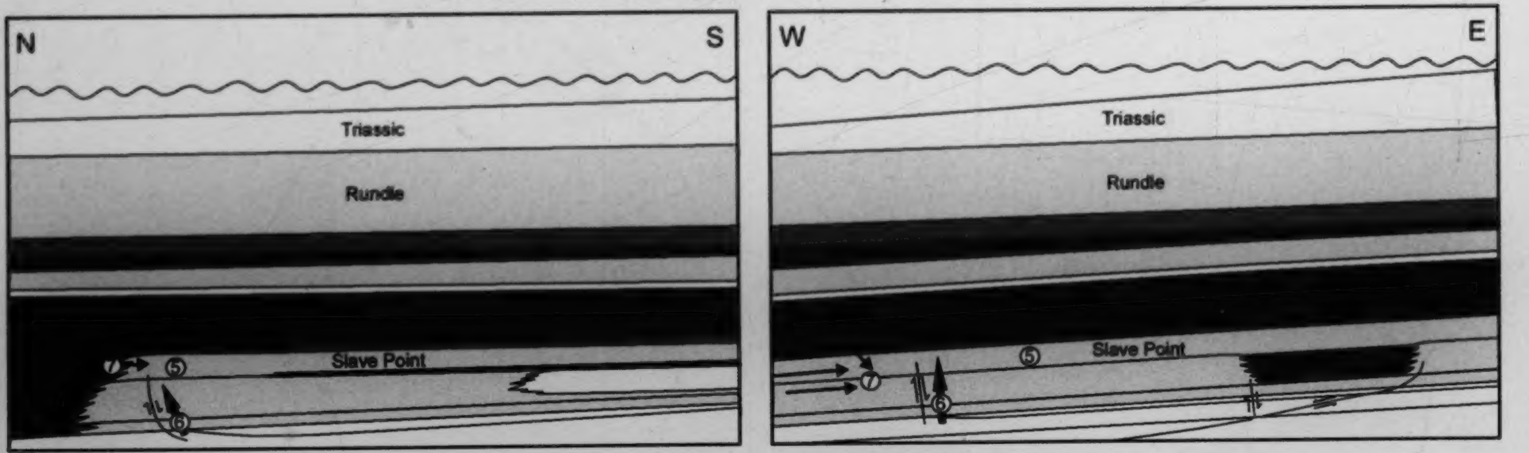
N
S
Triassic
Rundle
Slave Point
7
5
6
W
E
Triassic
Rundle
Slave Point
7
6
5

STAGE VI - Late Cretaceous to Recent

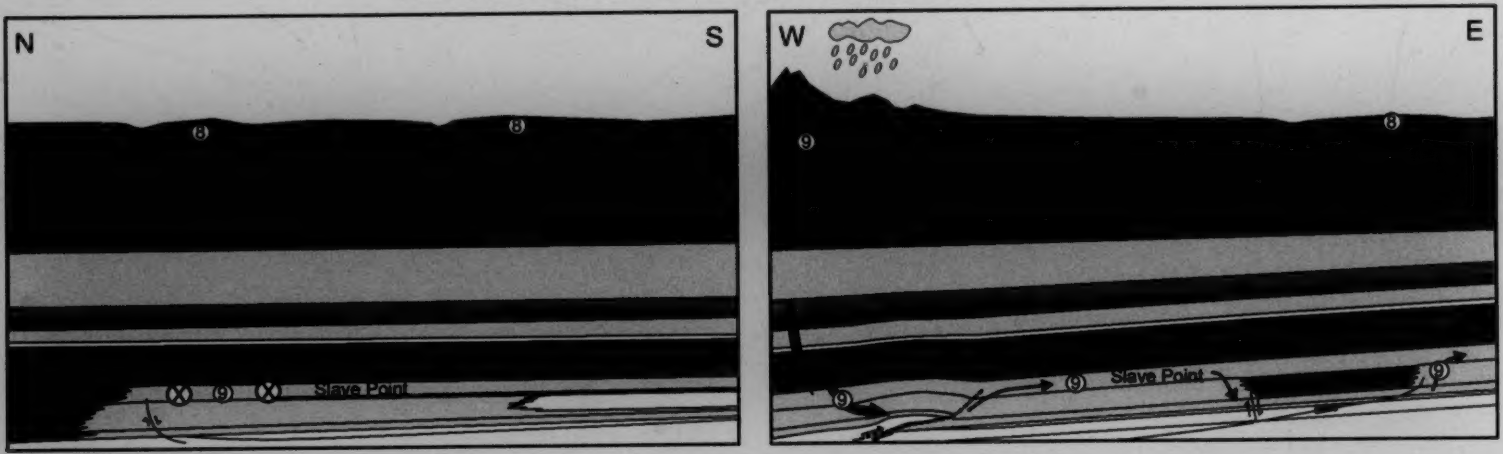
N
S
8
8
9
Slave Point
W
E
9
8
9
9
Slave Point
9

gypsum-saturated brine (Figure 7.2 – fluid 5) that was further diluted but still between gypsum and halite saturation. The limited spatial distribution of the sulphide minerals and their arrangement within fracture generation III (phase 15) suggests that the movement of this dilute fluid end-member into the Slave Point Formation was along faults that originate in the basement (Figure 7.2 – fluid 6). Mineralization during Stage V gradually reduced the overall porosity to less than 5% through the occlusion of open fractures, but these diagenetic phases had very little impact on porosity and permeability of the intergranular/ intercrystalline porosity in the bulk of the rocks.

Hydrocarbon migration is represented in the Slave Point Formation by solid bitumen (phase 19) that coats saddle dolomite (phase 13) crystal faces, is co-genetic with quartz (phase 20), and pre-dates late-stage blocky calcite cement (phase 25). Solid bitumen in the Slave Point Formation is interpreted to be the product of the thermal cracking of liquid hydrocarbons. This requires that the hydrocarbons enter the Slave Point reservoir at an ambient temperature of less than about 125°C (Hunt, 1996). These liquid hydrocarbons were then converted to the currently trapped natural gas as a result of either increased burial or a higher geothermal gradient, or a combination thereof. The source of the liquid hydrocarbons was either the Otter Park or Muskwa formations based on total organic carbon (TOC) and biomarker studies: Fowler et al. (2001) cited TOC contents greater than 2% in northeastern British Columbia. Based on the tilt of the Devonian strata in northeastern British Columbia, the source rocks must have been either adjacent to the Clarke Lake field or downdip to the west where the source rocks would have been in the liquid oil window at a slightly earlier time due to higher temperatures associated with increased burial depths (Figure 7.2 – fluid 7).

The fluid inclusion chemistry of blocky calcite cement II (phase 25) is indicative of formation from a diagnetic fluid that had a composition between gypsum-saturation and halite-saturation at temperatures approaching 200°C. Additionally, the rare earth element chemistry from most of these cements is indicative of formation under relatively low water-rock ratios, which would be expected at distances from the potential fluid conduits. Conversely, the chemistry of these calcite cements from one well (d-79-F/94-J-10) suggests formation at higher water-rock ratios from a fluid that obtained a significant quantity of radiogenic ^{87}Sr. The variable chemistry of the calcite cements across the Clarke Lake field suggests the diagenetic fluid(s) followed preferential pathways. Based on this information, it is proposed that the blocky calcite cements formed in a similar manner to that inferred for the hydrothermal alteration of matrix dolomite (Figure 7.3). The diagenetic fluid entered the Slave Point Formation along faults that propagate down to the basement (Figure 7.2 – fluid 6). This fluid was mixed in variable proportions with the evaporated fluid entrained in the Slave Point Formation at that time, which was a mixture of a halite and gypsum brine, each somewhat modified by water-rock interaction. The ultimate chemistry of the calcite cement (phase 25) was thus determined by the extent of water-rock interactions.

Across much of the Western Canada Sedimentary Basin, similar late-stage calcite cements have been interpreted to reflect the chemistry of the basinal fluids at maximum burial or shortly thereafter, which for the Devonian south of the Peace River Arch is Cretaceous through Early Tertiary (Drivet and Mountjoy, 1997; Mountjoy et al, 1999). However, based on evidence that constrains the timing of liquid hydrocarbon migration into the Slave Point Formation, the blocky calcite cement at Clarke Lake is interpreted to have formed from fluid flow during the first phase of deep burial associated with the Late Triassic through Early Jurassic Columbian Orogeny. Blocky calcite was the concluding diagenetic phase to form in the Slave Point Formation at Clarke Lake, and therefore, was the last phase to impact the reservoir conditions. By the close of this stage, overall porosity in the Slave Point Formation averaged roughly 5-6%.

7.2.6 Stage VI – Late Cretaceous to Recent

Maximum burial of approximately 3500 metres to the present (Figure 7.2 – Stage VI). During this stage, over 1500 metres of Cretaceous sediments were removed in the area around Clarke Lake, exhuming the Slave Point Formation to its present depth of approximately 2000 metres (Stott, 1993a; 1993b). There is no petrographic evidence for the formation of any diagenetic mineral phases during this stage, but there is ample evidence for the incursion of meteoric water.

The present chemistry of the formation waters in the Slave Point Formation is the result of mixing between the previously entrained evaporated fluid and meteoric water. This meteoric water end-member entered the basin through recharge in the Rocky Mountains to the west and was driven by topography (Figure 7.2 – fluid 9). Both the stable and radiogenic isotope results in conjunction with the bulk hydrochemistry suggest the meteoric water end-member was involved in water-rock interaction predominantly with the

Proterozoic Muskwa Formation, but potentially also with the Precambrian basement along its migration pathway. The chemically altered meteoric waters likely entered the Slave Point Formation along faults that propagate down to basement. In the Klua Embayment (well a-63-J/94-J-9), the meteoric waters have not mixed in large proportions with the fluids previously entrained in the limestones of the Slave Point Formation. Instead, the relatively low permeability limestones (and shales of the Otter Park Formation) laterally focussed the movement of the mixed formation fluids through the dolostone reservoir. As a result, these mixed fluids were forced to migrate downward into the underlying Keg River Formation (Figure 7.2) (Underschultz and Bachu, 1997). The migration pathways of the chemically altered meteoric water end-member, in combination with the overall geometry of the Slave Point Formation platform margin, are extremely important for both trap development and preventing the previously emplaced hydrocarbons from being flushed through the active migration of formation waters in the Devonian. The combination of the geometry of the Slave Point platform margin and the flow direction of the meteoric waters from southwest to northeast provides reservoir closure at Clarke Lake. The flow of meteoric waters into the Clarke Lake field maintains the position of the hydrocarbon pool adjacent to the Slave Point platform margin. This observation may prove critical in the exploration for hydrocarbon accumulations in the Middle Devonian across northeastern British Columbia.

7.3 Contributions to original knowledge

When this study commenced in the summer of 2000, there was very little published work detailing either the petrographic or geochemical evolution of the Slave Point Formation in northeastern British Columbia, and next to nothing was published from the Clarke Lake field. Therefore, many aspects of this thesis constitute contributions to original knowledge. The following aspects are considered particularly noteworthy:

1) first comprehensive identification and interpretation of depositional facies in the pervasively dolomitized rocks of the Slave Point Formation at Clarke Lake;
2) first representation of the spatial distribution of dolostone at Clarke Lake;
3) first study to present the entire sequence of diagenetic events affecting the Slave Point Formation at Clarke Lake;
4) first study to investigate the relationships between dolomite, depositional facies, diagenetic phases, and structural features in the Devonian of northeastern B.C.;

5) recognition that the replacive grey matrix dolomite was not co-genetic with coarse crystalline saddle dolomite in the Slave Point Formation;
6) first study worldwide to provide comprehensive evidence for the hydrothermal alteration of pre-existing matrix dolomite to generate oversized pores, to recrystallize matrix dolomite, and to form saddle dolomite cement;
7) first study of the Slave Point Formation in the Western Canada Sedimentary Basin to integrate stable and radiogenic isotope analyses, trace and rare earth element chemistry, and fluid inclusion microthermometry results;
8) first study from northeastern British Columbia to conduct leachate analysis on the fluid inclusions in dolomites and calcites;
9) first study from the Western Canada Sedimentary Basin to identify the composition of the dolomitizing fluid as a halite-saturated brine;
10) first study to identify the similarities in the paleofluids between the Slave Point Formation and the fluids responsible for the formation of the Pine Point MVT deposit;
11) first study from the Western Canada Sedimentary Basin to conduct a laser ablation transect across a single dolomite crystal in order to obtain the $^{87}Sr/^{86}Sr$ values of each crystal zone;
12) first study to analyze the potential strontium source rocks in northeastern British Columbia;
13) first study to identify multiple diagenetic fluid conduits in the Slave Point Formation at Clarke Lake;
14) first study to identify a hydrothermal anomaly in the dolostones of the Slave Point Formation at Clarke Lake;
15) first study to conduct isotopic and hydrochemical investigations of the present-day formation waters in the Slave Point Formation at Clarke Lake;
16) first study to recognize both a highly evaporated fluid end-member and a dilute meteoric fluid end-member in the present-day formation waters in the Slave Point Formation;
17) first study from northeastern British Columbia to suggest that the highly evaporated fluid end-member may have been involved in dolomite formation prior to dilution;
18) first study to clearly identify the origin and evolution of the meteoric fluid end-member in the Slave Point Formation; and,
19) first study to suggest that the flow of meteoric waters is critical in the exploration

for hydrocarbon accumulations in the Middle Devonian across northeastern British Columbia.

7.4 Implications and Future work

The results from this study fully address the original scientific objectives of this project, as well as the original applied (industrial) objective as outlined in Chapter 1. With respect to the first part of the applied objective, this study is the first to provide a comprehensive interpretation of facies distribution in the Slave Point Formation at Clarke Lake. The application of the facies distribution with the present-day structural configuration can provide the necessary information to identify prospective development and/or exploration targets. The second part of the applied objective was to address the water production problems at Clarke Lake. Using pressure-elevation plots, Underschultz and Bachu (1997) suggested that the Clarke Lake field was divided into 8 distinct pools with different gas-water contacts. They (ibid.) suggested that the water production problems are the result of local-scale permeability variations and, therefore, different fluid flow pathways in the Slave Point Formation. Yet, water chemistry data from this study suggests that the formation fluids in the Slave Point Formation at Clarke Lake are well mixed and not hydrodynamically isolated, with the exception of a few wells that show evidence for isolation (a-63-J/94-J-9) or the possible influence of faults (c-29-I/94-J-10). Hence, the observed water production problems are considered time-dependent, in that water will flow and pressures will equalize between the wells, given enough time. Finally, the results from this study have wide-ranging implications for future exploration and development. The general direction of movement of the meteoric water end-member in the Slave Point regional aquifer requires that future successful exploration concentrate on the geometry of the platform margin to identify closure, which, consequently, reduces the effects of hydrocarbon flushing.

This work provides the framework for future research into the geochemistry of dolostone reservoirs across the northern half of the Western Canada Sedimentary Basin, or wherever there is extensive development of saddle dolomites or hydrothermal alteration textures. Within the Clarke Lake field there is very little information that can be further acquired, or that would provide a higher level of resolution with respect to the diagenetic evolution of the Slave Point Formation. That being said, future research in the Clarke Lake field should attempt to: 1) further evaluate the evolution of the dolomite-forming fluids through a dedicated study of the $^{87}Sr/^{86}Sr$ values obtained using laser ablation ICP-MS; 2) provide further evidence for a Late Devonian to Mississippian age for hydrothermal alteration by conducting radiometric age dating of sphalerite and galena in the dolostone intervals using the Rb-Sr or the common Pb isotope systems; 3) further characterize the formation fluid in the non-dolomitized Slave Point Formation by obtaining more samples in the Klua Embayment and other embayments where the Slave Point margin progrades over the underlying Keg River Formation; and, 4) conduct a hydrogeological and hydrochemical investigation of the Keg River Formation around Clarke Lake in an attempt to identify the exact flow path of the formation waters in the Slave Point Formation at the platform margin.

Within certain limits, the results from the Clarke Lake field can be used as a model for Slave Point Formation reservoirs elsewhere in British Columbia. Future studies on the Slave Point Formation should concentrate on: 1) the identification of hydrothermal alteration textures through detailed petrographic examination; 2) the identification of the dolomite-forming fluids using fluid inclusion microthermometric and leachate analyses; 3) the identification of hydrothermal anomalies; 4) the identification of diagenetic fluid flow pathways; and 5) the identification of the present-day formation water chemistry. By focussing efforts on these five points it should be possible to elucidate the spatial distribution, origin, and timing of dolomite formation, and may provide critical information to both improve exploration success and enhance gas recovery.

Finally, the proposed hydrothermal alteration model may be applicable to many coarse-crystalline dolomite reservoirs across North America, and possibly worldwide. In the past, workers have relied principally on petrographic data to promote their various 'models' for the formation of these so-called 'hydrothermal' dolomite reservoirs, with few attempts to relate their observations with either geochemical data or the thermal history of the host-rocks (e.g., Davies, 1997). This, however, is clearly insufficient. Only a detailed analysis and integration of petrographic, structural, and geochemical data can yield satisfactory results, as demonstrated in this study.

CHAPTER 8

REFERENCES

Adams, J. E., and M. L. Rhodes, 1960, Dolomitization by seepage refluxion: American Association of Petroleum Geologists Bulletin, v. 44, p. 1912-1920.

Adams, J. J., B. J. Rostron, and C. A. Mendoza, 2000, Evidence for two fluid mixing at Pine Point, NWT: Journal of Geochemical Exploration, v. 69-70, p. 103-108.

Aharon, P., R. A. Socki, and L. Chan, 1987, Dolomitization of atolls by sea water convection flow: test of a hypothesis at Nieu, South Pacific: Journal of Geology, v. 95, p. 187-204.

Al-Aasm, I. S., and J. D. Clarke, 2004, The effect of hydrothermal fluid flow on early diagenetic dolomitization: an example from the Devonian Slave Point Formation, northwest Alberta, Canada, in R. Swennen, F. Roure, and J. W. Granath, eds., Deformation, fluid flow, and reservoir appraisal in foreland fold and thrust belts: American Association of Petroleum Geologists Hedberg Series, v. 1, p. 297-316.

Al-Aasm, I. S., B. E. Taylor, and B. South, 1990, Stable isotope analysis of multiple carbonate samples using selective acid extraction: Chemical Geology (Isotope Geoscience Section), v. 80, p. 119-125.

Allan, J., and S. Creaney, 1991, Oil families of the Western Canada Basin: Bulletin of Canadian Petroleum Geology, v. 39, p. 107-122.

Allan, J. R., and W. D. Wiggins, 1993, Dolomite reservoirs: geochemical techniques for evaluating origin and distribution: American Association of Petroleum Geologists, Continuing Education Course Notes 36, 129 p.

Amthor, J. E., E. W. Mountjoy, and H. G. Machel, 1993, Subsurface dolomites in Upper Devonian Leduc Formation buildups, central part of Rimbey-Meadowbrook reef trend, Alberta, Canada: Bulletin of Canadian Petroleum Geology, v. 41, p. 164-185.

Anderson, G. M., 1975, Precipitation of Mississippi Valley-type ores: Economic Geology, v. 70, p. 937-942.

Anderson, T. F., and M. A. Arthur, 1983, Stable isotopes of oxygen and carbon and their application to sedimentologic and paleoenvironmental problems, in M. A. Arthur, T. F. Anderson, I. R. Kaplan, J. Veizer, and L. S. Land, eds., Stable isotopes in sedimentary geology: Society of Economic Paleontologists and Mineralogists Short Course 10, p. 1-1 to 1-151.

Aulstead, K. L., and R. J. Spencer, 1985, Diagenesis of the Keg River Formation, northwestern Alberta: fluid inclusion evidence: Bulletin of Canadian Petroleum Geology, v. 33, p. 167-183.

Ayalon, A., and F. J. Longstaffe, 1988, Oxygen-isotope studies of diagenesis and porewater evolution in the western Canada sedimentary basin: evidence from the Upper Cretaceous basal Belly River sandstone, Alberta: Journal of Sedimentary Petrology, v. 58, p. 489-505.

Baadsgard, H., 1987, Rb-Sr and K-Ca isotope systematics in minerals from potassium horizons in the Prairie Evaporite Formation, Saskatchewan, Canada: Chemical Geology (Isotope Geoscience Section), v. 66, p. 1-15.

Bachu, S., 1997, Flow of formation waters, aquifer characteristics, and their relation to hydrocarbon accumulations, northern Alberta Basin: American Association of Petroleum Geologists Bulletin, v. 81, p. 712-733.

Bachu, S., and R. A. Burwash, 1994, Geothermal regime in the Western Canada Sedimentary Basin, in G. D. Mossop, and I. Shetsen, comps., Geological Atlas of the Western Canada Sedimentary Basin: Canadian Society of Petroleum Geologists and Alberta Research Council, p. 447-454.

Badiozamani, K., 1973, The dorag dolomitization model – application to the Middle Ordovician of Wisconsin: Journal of Sedimentary Petrology, v. 43, p. 965-984.

Bakker, R. J., 2003, Package FLUIDS 1. Computer programs for analysis of fluid inclusion data and for modelling bulk fluid properties: Chemical Geology, v. 194, p. 3-23.

Banks, D. A., A. J. Boyce, and I. M. Samson, 2002, Constraints on the origins of fluids forming Irish Zn-Pb-Ba deposits: evidence from the composition of fluid inclusions: Economic Geology, v. 97, p. 471-480.

Banner, J. L., G. N. Hanson, and W. J. Meyers, 1988, Rare earth element and Nd isotopic variations in regionally extensive dolomites from the Burlington-Keokuk Formation (Mississippian): implications for REE mobility during carbonate diagenesis: Journal of Sedimentary Petrology, v. 58, p. 415-432.

Banner, J. L., G. J. Wasserburg, P. F. Dobson, A. B. Carpenter, and C. H. Moore, 1989, Isotopic and trace element constraints on the origin and evolution of saline groundwaters from central Missouri: Geochimica et Cosmochimica Acta, v. 53, p. 383-398.

Barker, C. E., and M. J. Pawlewicz, 1994, Calculation of vitrinite reflectance from thermal histories and peak temperatures: a comparison of methods, in P. K. Mukhopadhyay, and W. G. Dow, eds., Vitrinite reflectance as a maturity parameter: applications and limitations: American Chemical Society Symposium Series 570, p. 230-238.

Barnes, H. L., 1979, Geochemistry of hydrothermal ore deposits: Wiley, New York, 798 p.

Barnes, H. L., 1983, Ore depositing reactions in Mississippi Valley-type deposits, in G. Kisvarsanyi, G. Grant, S. K. Pratt, W. P. Koenig, eds., International Conference on Mississippi Valley-type lead-zinc deposits: Proceedings, p. 77-85.

Bathurst, R. C. G., 1975, Carbonate sediments and their diagenesis: Elsevier, Amsterdam, 658 p.

Behrens, E. W., and L. S. Land, 1972, Subtidal Holocene dolomite, Baffin Bay, Texas: Journal of Sedimentary Petrology, v. 42, p. 155-161.

Bein, A., and L. S. Land, 1983, Carbonate sedimentation and diagenesis associated with Mg-Ca-chloride brines: the Permian San Andres Formation in the Texas Panhandle: Journal of Sedimentary Petrology, v. 53, p. 243-260.

Belyea, H. R., 1971, Middle Devonian tectonic history of the Tathlina Uplift, southern District of Mackenzie and northern Alberta, Canada: Geological Survey of Canada, Paper 70-14.

Belyea, H. R., and A. W. Norris, 1962, Middle Devonian and older Paleozoic formations of southern District of Mackenzie and adjacent areas: Geological Survey of Canada, Paper 62-15.

Bergerioux, C., G. Kennedy, and L. Zikovosky, 1979, Use of the semi-absolute method in neutron activation analysis: Journal of Radioanalytical and Nuclear Chemistry, v. 50, p. 229.

Bjørlykke, K., 1994, Fluid-flow processes and diagenesis in sedimentary basins, in J. Parnell, ed., Geofluids: origin, migration and evolution of fluids in sedimentary basins: Geological Society Special Publication 78, p. 127-140.

Bodnar, R. J., 1993, Revised equation and table for determining the freezing point depression of H_2O-NaCl solutions: Geochimica et Cosmochimica Acta, v. 57, p. 683-684.

Boggs, S., 1992, Principles of sedimentology and stratigraphy: Prentice Hall, New York, 774 p.

Boreen, T., and G. R. Davies, 2004, Hydrothermal dolomite and leached limestones in a Tcf gas play: the Ladyfern Slave Point reservoir, NEBC, in J. J. Packard, and G. R. Davies (eds.) Dolomites: the spectrum – mechanisms, models, reservoir development: Canadian Society of Petroleum Geologists Seminar and Core Conference, C013.

Braithwaite, C. J. R., and G. Rizzi, 1997, The geometry and petrogenesis of hydrothermal dolomite at Navan, Ireland: Sedimentology, v. 44, p. 421-440.

Brand, U., and J. O. Morrison, 1987, Paleoscene #6. Beiogeochemistry of fossil marine invertebrates: Geoscience Canada, v. 14, p. 85-107.

Brand, U., and J. Veizer, 1981, Chemical diagenesis of a multicomponent carbonate system – 2: stable isotopes: Journal of Sedimentary Petrology, v. 51, p. 987-997.

Budd, D. A., 1997, Cenozoic dolomites of carbonate islands: their attributes and origin: Earth-Science Reviews, v. 42, p. 1-47.

Bullen, S. A., and D. F. Sibley, 1984, Dolomite selectivity and mimetic replacement: Geology, v. 12, p. 655-658.

Burke, W. H., R. E. Denison, E. A. Hetherington, R. B. Koepnick, H. F. Nelson, and J. B. Otto, 1982, Variation of seawater $^{87}Sr/^{86}Sr$ throughout Phanerozoic time: Geology, v. 10, p. 516-519.

Burrowes, O. G., and F. F. Krause, 1987, Overview of the Devonian System – subsurface of Western Canada Basin, in F. F. Krause, and O. G. Burrowes, eds., Devonian lithofacies and reservoir styles in Alberta: Canadian Society of Petroleum Geologists Core Conference, p. 1-5.

Buschkuehle, B. E., 2003, Geology, diagenesis and paleofluid flow in the Devonian Southesk-Cairn Carbonate Complex in west-central Alberta, Canada: PhD thesis, University of Alberta, Edmonton, Canada, 320 p.

Busenberg, E., and L. N. Plummer, 1982, The kinetics of dissolution of dolomite in CO_2-H_2O systems at 1.5 to 65°C and 0 to 1 atm P_{CO2}: American Journal of Science, v. 282, p. 45-78.

Bustin, R. M., M. A. Barnes, and W. C. Barnes, 1985, Diagenesis 10. Quantification and modeling of organic diagenesis: Geoscience Canada, v. 12, p. 4-21.

Cameron, A. E., 1918, Explorations in the vicinity of Great Slave Lake: Geological Survey of Canada Summary Report 1917, Part C, p. 22-28.

Cameron, A. E., 1922, Hay and Buffalo Rivers, Great Slave Lake and adjacent country, Northwest Territories: Geological Survey of Canada, Department of Mines Summary Report 1921, Part B, p. 1-44.

Campbell, C. V., 1992, Beaverhill Lake Megasequence, in J. C. Wendte, F. A. Stoakes, and C. V. Campbell, eds., Devonian – Early Mississippian carbonates of the Western Canada Sedimentary Basin: Society of Economic Paleontologists and Mineralogists Short Course 28, p. 163-180.

Campbell, N. L., 1950, The Middle Devonian in the Pine Point area, NWT: Geological Association of Canada Proceedings, v. 3, p. 87-96.

Cant, D. J., 1988, Regional structure and development of the Peace River Arch, Alberta: a Paleozoic failed-rift system?: Bulletin of Canadian Petroleum Geology, v. 36, p. 284-295.

Carpenter, A. B., 1978, Origin and chemical evolution of brines in sedimentary basins: Oklahoma Geological Survey Circular 79, p. 60-77.

Carpenter, A. B., 1980, The chemistry of dolomite formation I: the stability of dolomite, in D. H. Zenger, J. B. Dunham, and R. L. Ethington, eds., Concepts and Models of Dolomitization: Society of Economic Paleontologists and Mineralogists Special Publication 28, p. 111-121.

Carpenter, S. J., K. C. Lohmann, P. Holden, L. M. Walter, T. J. Huston, and A. N. Halliday, 1991, $\delta^{18}O$ values, $^{87}Sr/^{86}Sr$ and Sr/Mg ratios of Late Devonian abiotic marine calcite: implications for the composition of ancient seawater: Geochimica et Cosmochimica Acta, v. 55, p. 1991-2010.

Chaudhuri, S., 1978, Strontium isotopic composition of several oilfield brines from Kansas and Colorado: Geochimica et Cosmochimica Acta, v. 42, p. 329-331.

Chaudhuri, S., V. Broedel, and N. Clauer, 1987, Strontium isotopic evolution of oil-field waters from carbonate reservoir rocks in Bindley field, central Kansas, U.S.A.: Geochimica et Cosmochimica Acta, v. 51, p. 45-53.

Chaudhuri, S., and N. Clauer, 1993, Strontium isotopic compositions and potassium and rubidium contents of formation waters in sedimentary basins: clues to the origin of the solutes: Geochimica et Cosmochimica Acta, v. 57, p. 429-437.

Chi, G., and M. M. Savard, 1997, Sources of basinal fluids and Mississippi Valley-type mineralizing brines: mixing of evaporated seawater and halite-dissolution brine: Chemical Geology, v. 143, p. 121-125.

Choquette, P. W., and N. P. James, 1990, Limestones – the burial diagenetic environment, in I. E. McIlreath, and D. W. Morrow, eds., Diagenesis: Geoscience Canada Reprint Series 4, p. 72-112.

Choquette, P. W., and R. P. Steinen, 1980, Mississippian non-supratidal dolomite, Ste. Genevieve limestone, Illinois Basin: evidence for mixed-water dolomitization, in D. H. Zenger, J. B. Dunham, and R. L. Ethington, eds., Concepts and models of dolomitization: Society of Economic Paleontologists and Mineralogists Special Publication 28, p. 163-196.

✓ Clarke, J. D., 1998, Petrology, geochemistry and diagenesis of the Middle Devonian Slave Point Formation, Hamburg field, northwestern Alberta: MSc thesis, University of Windsor, Windsor, Canada, 126 p.

Clayton, R. N., I. Friedman, D. L. Graf, T. K. Mayeda, W. F. Meents, and N. F. Shimp, 1966, The origin of saline formation waters, I. Isotopic composition: Journal of Geophysical Research, v. 71, p. 3869-3882.

Coleman, M. L., T. J. Sheppard, J. J. Durham, J. E. Rouse, and G. R. Moore, 1982, Reduction of water with zinc for hydrogen isotope analysis: Analytical Chemistry, v. 54, p. 993-995.

Coniglio, M., D. W. Morrow, N. Wilson, and P. Hannigan, 2005, Reassessment of Middle Devonian dolomites, Northwest Territories, in P. Hannigan, ed., Potential for carbonate-hosted lead-zinc Mississippi Valley-type mineralization in northern Alberta and southern Northwest Territories: Geological Survey of Canada Bulletin, in press.

Connolly, C. A., L. M. Walter, H. Baadsgaard, and F. J. Longstaffe, 1990a, Origin and evolution of formation waters, Alberta Basin, Western Canada Sedimentary Basin. 2: Isotope systematics and water mixing: Applied Geochemistry, v. 5, p. 397-413.

Connolly, C. A., L. M. Walter, H. Baadsgaard, and F. J. Longstaffe, 1990b, Origin and evolution of formation waters, Alberta Basin, Western Canada Sedimentary Basin. 1: Chemistry: Applied Geochemistry, v. 5, p. 375-395.

Cook, F. A., A. J. van der Velden, K. W. Hall, and B. J. Roberts, 1999, Frozen subduction in Canada's Northwest Territories: Lithoprobe deep lithospheric reflection profiling of the western Canadian Shield: Tectonophysics, v. 18, p. 1-24.

Corbella, M., and C. Ayora, 2003, Role of fluid mixing in deep dissolution of carbonates: Geologica Acta, v. 1, p. 305-313.

Corbella, M., C. Ayora, and E. Cardellach, 2004, Hydrothermal mixing, carbonate dissolution and sulfide precipitation in Mississippi Valley-type deposits: Mineralium Deposita, v. 39, p. 344-357.

Craig, H., 1961a, Standards for reporting concentrations of deuterium and oxygen-18 in natural waters: Science, v. 133, p. 1833-1834.

Craig, H., 1961b, Isotopic variations in meteoric waters: Science, v. 133, p. 1702-1703.

Crickmay, C. H., 1957, Elucidation of some western Canada Devonian formations: Proprietary report prepared for Imperial Oil Limited, 15 p.

Curiale, J. A., 1993, Occurrence and significance of metals in solid bitumens: an organic geochemical approach, in J. Parnell, H. Kucha, and P. Landais, eds., Bitumens in ore deposits: Society for Geology Applied to Mineral Deposits Special Publication 9, p. 461-474.

Currie, L. A., 1968, Limits for qualitative detection and quantitative determination – application to radiochemistry: Analytical Chemistry, v. 40, p. 586-593.

Davies, G. R., 1997, Hydrothermal dolomite (HTD) reservoir facies: global perspectives on tectonic-structural and temporal linkage between MVT and Sedex Pb-Zn ore bodies, and subsurface HTD reservoir facies: Canadian Society of Petroleum Geologists Short Course Notes, 167 p.

Davies, G. R., 1999, Clarke Lake Slave Point - Keg River reservoir project, northwestern British Columbia: Proprietary report prepared for Petro-Canada Oil & Gas, 70 p.

Davies, G. R., 2002, Thermobaric dolomitization: transient fault-controlled pressure-driven processes and the role of boiling/effervescence: Canadian Society of Petroleum Geologists Annual Meeting Abstracts, p. 105.

Davies, G. R., 2004, Hydrothermal (thermobaric) dolomitization: rock fabric and organic petrology support for emplacement under transient temperature, pressure and shear stress conditions, in J. J. Packard, and G. R. Davies (eds.) Dolomites: the spectrum – mechanisms, models, reservoir development: Canadian Society of Petroleum Geologists Seminar and Core Conference, C032.

Davisson, M. L., and R. E. Criss, 1996, Na-Ca-Cl relations in basinal fluids: Geochimica et Cosmochimica Acta, v. 60, p. 2743-2752.

Davisson, M. L., T. S. Presser, and R. E. Criss, 1994, Geochemistry of tectonically expelled fluids from the northern Coast ranges, Rumsey Hills, California, USA: Geochimica et Cosmochimica Acta, v. 58, p. 1687-1699.

DeBaar, H. J. W., M. P. Bacon, and P. G. Brewer, 1983, Rare earth element distributions with a positive Ce anomaly in the Western North Atlantic Ocean: Nature, v. 301, p. 324-327.

de Marsily, G., 1986, Quantitative hydrogeology: Academic Press, San Diego, 440 p.

Denison, R. E., R. B. Koepnick, W. H. Burke, E. A. Hetherington, and A. Fletcher, 1997, Construction of the Silurian and Devonian seawater $^{87}Sr/^{86}Sr$ curve: Chemical Geology, v. 140, p. 109-121.

Dickson, J. A. D., 1965, A modified staining technique for carbonates in thin section: Nature, v. 205, p. 587.

Dorobek, S., 1989, Migration of orogenic fluids through the Siluro-Devonian Helderberg Group during late Paleozoic deformation: constraints on fluid sources and implications for thermal histories of sedimentary basins: Tectonophysics, v. 159, p. 25-45.

Dorobek, S. L., and R. H. Filby, 1988, Origin of dolomites in a downslope biostrome, Jefferson Formation (Devonian), central Idaho: evidence from REE patterns, stable isotopes, and petrography: Bulletin of Canadian Petroleum Geology, v. 36, p. 202-215.

Drever, J. L., 1988, The geochemistry of natural waters, second edition: Prentice Hall, New Jersey, 437 p.

Drivet, E., and E. W. Mountjoy, 1997, Dolomitization of the Leduc Formation (Upper Devonian), southern Rimbey-Meadowbrook reef trend, Alberta: Journal of Sedimentary Research, v. 67, p. 411-423.

Dromgoole, E. L., and L. M. Walter, 1990, Iron and manganese incorporation into calcite: effects of growth kinetics, temperature and solution chemistry: Chemical Geology, v. 81, p. 311-336.

Duggan, J. P., E. W. Mountjoy, and L. D. Stasiuk, 2001, Fault-controlled dolomitization at Swan Hills Simonette oil field (Devonian), deep basin west-central Alberta, Canada: Sedimentology, v. 48, p. 301-323.

Dunham, J. B., G.A. Crawford, and W. Panasiuk, 1983, Sedimentology of the Slave Point Formation (Devonian) at Slave field, Lubicon Lake, Alberta: Society of Economic Paleontologists and Mineralogists Core Workshop, v. 4, p. 73-111.

Dunham, R. J., 1962, Classification of carbonate rocks according to depositional texture, in W. E. Ham, ed., Classification of carbonate rocks: American Association of Petroleum Geologists Memoir 1, p. 101-121.

Dunham, R. J., 1970, Stratigraphic reefs versus ecologic reefs: American Association of Petroleum Geologists Bulletin, v. 54, p. 1931-1932.

Elderfield, H, C. J. Hawkesworth, M. J. Greaves, and S. E. Calvert, 1981, Rare earth element geochemistry of oceanic ferromanganese nodules and associated sediments: Geochimica et Cosmochimica Acta, v. 45, p. 513-528.

Embry, A. F., and J. E. Klovan, 1971, A Late Devonian reef tract on northeastern Banks Island, NWT: Bulletin of Canadian Petroleum Geology, v. 19, p. 730-781.

Epstein, S., and T. K. Mayeda, 1953, Variations of the $^{18}O/^{16}O$ ratio in natural waters: Geochimica et Cosmochimica Acta, v. 4, p. 213.

Fabricius, I. L., 2000, Interpretation of burial history and rebound from loading experiments and occurrence of microstylolites in mixed sediments of Caribbean Sites 999 and 1001, in R. M. Leckie, H. Sigurdson, G. D. Acton, and G. Draper, eds., Proceedings of the Ocean Drilling Program: Scientific Results, v. 165, p. 177-190.

Faure, G., 1986, Principles of Isotope Geology, second edition: Wiley and Sons, New York, 589 p.

Fleet, A. J., 1984, Aqueous and sedimentary geochemistry of the rare earth elements, in P. Henderson, ed., Rare Earth Element Geochemistry: Elsevier, New York, p. 343-373.

Frank, J. R., A. B. Carpenter, and T. W. Ogelsby, 1982, Cathodoluminescence and composition of calcite cement in the Taum Sauk limestone (Upper Cambrian), southeast Missouri: Journal of Sedimentary Petrology, v. 52, p. 631-638.

Fritz, P., and A. Katz, 1972, The sodium distribution of dolomite crystals: Chemical Geology, v. 10, p. 237-244.

Fontes, J. Ch., and J. M. Matray, 1993, Geochemistry and origin of formation brines from the Paris Basin, France. 1. Brines associated with Triassic salts: Chemical Geology, v. 109, p. 149-175.

Foreman, J. L., 1989, Burial cements, in K. R. Walker, ed., The fabric of cements in Paleozoic limestones: Geological Society of America Short Course 20, p. 66-77.

Fourner, R. O., 1981, Application of water chemistry to geothermal exploration and reservoir engineering, in L. Rybach, and L. J. P. Muffler, eds., Geothermal systems: principles and case histories: Wiley, New York, p. 109-143.

Fowler, M. G., L. D. Stasiuk, M. Hearn, and M. Obermajer, 2001, Devonian hydrocarbon source rocks and their derived oils in the Western Canada Sedimentary Basin: Bulletin of Canadian Petroleum Geology, v. 49, p. 117-148.

Gabrielese, H., J. W. H. Monger, J. O. Wheeler, and C. J. Yorath, 1992, Tectonic framework. Part A: Morphogeological belts, tectonic assemblages, and terranes, in H. Gabrielese, and C. J. Yorath, eds., Geology of the Cordilleran Orogen in Canada: Geological Survey of Canada, Geology of Canada, v. 4, p. 679-705.

Gabrielese, H., and G. C. Taylor, 1982, Geological maps and cross-sections of the Cordillera from near Fort Nelson, British Columbia to Gravina Island, southeastern Alaska: Geological Survey of Canada, Open File Report 864.

Galloway, W. E., and D. K. Hobday, 1983, Terrigenous clastic depositional settings – applications to petroleum, coal, and uranium exploration: Springer-Verlag, Berlin, 423 p.

Games, L. M., and J. M. Hayes, 1976, On the mechanism of CO_2 and CH_4 production in natural anaerobic environments, in J. O. Nriagu, ed., Environmental biogeochemistry, v. I, p. 51-66.

Gao, G., L. S. Land, and R. L. Folk, 1992, Meteoric modification of early dolomite and late dolomitization by basinal fluids, upper Arbuckle Group, Slick Hills, southwestern Oklahoma: American Association of Petroleum Geologists Bulletin, v. 76, p. 1649-1664.

Garven, G, and R. Freeze, 1984, Theoretical analysis of the role of groundwater flow in the genesis of stratabound ore deposits: American Journal of Science, v. 284, p. 1085-1174.

Gat, J. R., 1980, The isotopes of hydrogen and oxygen in precipitation, in A. P. Fritz, and J. Ch. Fontes, eds., Handbook of Environmental Isotope Geochemistry, v. 1: Elsevier, p. 21-47.

Geological Staff, Imperial Oil Limited, 1950, Devonian nomenclature in Edmonton area: American Association of Petroleum Geologists Bulletin, v. 34, p. 1807-1825.

Gibson, D. W., 1992, Triassic strata of the Foreland belt, in H. Gabrielse, and C. J. Yorath, eds., Geology of the Cordilleran orogen in Canada: Geological Survey of Canada, Geology of Canada, no. 4 (The Geology of North America, v. G-2), p. 265-276.

Given, R. K., and B. H. Wilkinson, 1987, Dolomite abundance and stratigraphic age: constraints on rates and mechanisms of Phanerozoic dolostone formation: Journal of Sedimentary Petrology, v. 57, p. 1068-1078.

Gleeson, S. A., and W. A. Turner, 2005, The origin of the Pine Point Pb-Zn mineralizing fluid and coarse and saddle dolomite formation in southern Northwest Territories, in P. Hannigan, ed., Potential for carbonate-hosted lead-zinc Mississippi Valley-type mineralization in northern Alberta and southern Northwest Territories: Geological Survey of Canada Bulletin, in press.

Goldstein, R. H., and T. J. Reynolds, 1994, Systematics of fluid inclusions in diagenetic minerals: Society of Economic Paleontologists and Mineralogists Short Course 31, 199 p.

Gosselin, E. G., L. Smith, and D. J. C. Mundy, 1989, The Golden and Evi reef complexes, Middle Devonian, Slave Point Formation, northwestern Alberta, in H. H. J. Geldsetzer, N. P. James, and G. E. Tebbutt, eds., Reefs – Canada and adjacent areas: Canadian Society of Petroleum Geologists Memoir 13, p. 440-447.

Graf, J. L., 1984, Effects of Mississippi Valley-type mineralization on REE patterns of carbonate rocks and minerals, Viburnum Trend, southeast Missouri: Journal of Geology, v. 92, p. 307-324.

Gray, F. F., and J. R. Kassube, 1963, Geology and stratigraphy of Clarke Lake gas field, British Columbia: AAPG Bulletin, v. 47, p. 467-483.

Gregg, J. M., and D. F. Sibley, 1984, Epigenetic dolomitization and the origin of xenotopic dolomite texture: Journal of Sedimentary Petrology, v. 54, p. 908-931.

Griffin, D. L., 1965, The Devonian Slave Point, Beaverhill Lake and Muskwa formations of northeastern British Columbia and adjacent areas: British Columbia Department of Mines and Petroleum Resources Bulletin 50.

Griffin, D. L., 1967, Devonian of northeastern British Columbia, in D. H. Oswald, ed., International Symposium on the Devonian System: Canadian Society of Petroleum Geologists, p. 803-826.

Hanor, J., 1987, Origin and migration of subsurface sedimentary brines: Society of Economic Paleontologists and Mineralogists Short Course 21, 247 p.

Hanshaw, B. B., W. Back, and R. G. Dieke, 1971, A geochemical hypothesis for dolomitization by groundwater: Economic Geology, v. 66, p. 710-724.

Hardie, L. A., 1967, The gypsum-anhydrite equilibrium at one atmosphere pressure: American Mineralogist,v. 52, p. 171-200.

Hardie, L. A., 1987, Dolomitization: a critical view of some current views: Journal of Sedimentary Petrology, v. 57, p. 166-183.

Harris, P. M., and W. S. Kowalik, 1994, Satellite images of carbonate depositional settings: examples of reservoir- and exploration-scale geologic facies variation: American Association of Petroleum Geologists, Methods in Exploration Series, v. 11, 147 p.

Hay, P. W., 1994, Oil and gas resources of the Western Canada Sedimentary Basin, in G. D. Mossop, and I. Shetsen, comps., Geological Atlas of the Western Canada Sedimentary Basin: Canadian Society of Petroleum Geologists and Alberta Research Council, p. 469-470.

Helgeson, H. C., 1969, Handbook of theoretical activity diagrams depicting chemical equlibria in geologic systems involving an aqueous phase at one atm and 0 to 300°C: Freeman, San Francisco, 253 p.

Henderson, C. M., B. C. Richards, and J. E. Barclay, 1994, Permian strata of the Western Canada Sedimentary Basin, in G. D. Mossop, and I. Shetsen, comps., Geological Atlas of the Western Canada Sedimentary Basin: Canadian Society of Petroleum Geologists and Alberta Research Council, p. 251-258.

Henderson, P., 1984, General geochemical properties and abundances of the rare earth elements, in P. Henderson, ed., Rare Earth Element Geochemistry: Elsevier, New York, p. 1-32.

Hendry, J. P., 1993, Calcite cementation during bacterial manganese, iron and sulphate reduction in Jurassic shallow marine carbonates: Sedimentology, v. 40, p. 87-106.

Hesse, R., 1990, Silica diagenesis: origin of inorganic and replacement cherts, in I. McIlreath, and D. W. Morrow, eds., Diagenesis: Geoscience Canada Reprint Series 4, p. 253-276.

Heydari, E., 1997, Hydrotectonic models of burial diagenesis in platform carbonates based on formation water geochemistry in North American sedimentary basins, in I. P. Montañez, J. M. Greeg, and K. L. Shelton, eds., Basin-wide diagenetic patterns; integrated petrologic, geochemical and hydrologic considerations: Society of Economic Paleontologists and Mineralogists Special Publication 57, p. 53-79.

Hill, C. A., 1995, H_2S-related porosity and sulfuric acid oil-field karst, in D. A. Budd, A. H. Saller, and P. M. Harris, eds., Unconformities and porosity in carbonate strata: AAPG Memoir 63, p. 301-306.

Hitchon, B., 1984, Geothermal gradients, hydrodynamics, and hydrocarbon occurrences, Alberta, Canada: AAPG Bulletin, v. 68, p. 713-743.

Hitchon, B., G. K. Billings, and J. E. Klovan, 1971, Geochemistry and origin of formation waters in the Western Canada Sedimentary Basin. 3: Factors controlling chemical composition: Geochimica et Cosmochimica Acta, v. 35, p. 567-598.

Hitchon, B., and I. Friedman, 1969, Geochemistry and origin of formation waters in the Western Canada Sedimentary Basin. 1: Stable isotopes of hydrogen and oxygen: Geochimica et Cosmochimica Acta, v. 33, p. 1321-1349.

Hitchon, B, S. Bachu, and J. R. Underschultz, 1990, Regional subsurface hydrogeology, Peace River Arch area, Alberta and British Columbia: Bulletin of Canadian Petroleum Geology, v. 38, p. 196-217.

Hitzman, M. W., and D. W. Beaty, 1996, The Irish Zn-Pb-(Ba) orefield, in D. F. Sangster, ed., Carbonate hosted lead-zinc deposits: SEPM Special Publication 4, p. 112-143.

Hoffman, P. F., 1989, Precambrian geology and tectonic history of North America, in A. W. Bally, and A. R. Palmer, eds., The geology of North America – an overview: Geological Society of America, The Geology of North America, v. A, p. 447-512.

Holser, W. T., I. R. Kaplan, H. Sakai, and I. Zak, 1979, Isotope geochemistry of oxygen in the sedimentary sulfate cycle: Chemical Geology, v. 25, p. 1-17.

Hudson, J. D., 1975, Carbon isotopes and limestone cement: Geology, v. 3, p. 19-22.

Humphrey, J. D., 1988, Late Pleistocene mixing zone dolomitization, southeastern Barbados, West Indies: Sedimentology, v. 35, p. 327-348.

Hunt, C. W., 1954, Normal Devonian sequence in southern Mackenzie Basin, western Canada: American Association of Petroleum Geologists Bulletin, v. 38, p. 2290-2301.

Hunt, J. M., 1996, Petroleum geochemistry and geology: W.H. Freeman and Company, New York, 743 p.

Hurley, N. F., and K. C. Lohmann, 1989, Diagenesis of Devonian reefal carbonates in the Oscar Range, Canning Basin, Western Australia: Journal of Sedimentary Petrology, v. 59, p. 127-146.

Hutcheon, I. E., 1989, Application of chemical and isotopic analyses of fluids to problems in sandstone diagenesis, in I. E. Hutcheon, ed., Burial diagenesis: Mineralogical Association of Canada Short Course 15, p. 279-310.

Hutcheon, I. E., 2000, Principles of diagenesis and what drives mineral change, in K. Kyser, ed., Fluid and Basin Evolution: Mineralogical Association of Canada Short Course 28, p. 93-114.

Hutcheon, I., and H. J. Abercrombie, 1990, Fluid rock interactions in thermal recovery of bitumen, Tucker Lake pilot, Cold Lake, Alberta, in I. D. Meshri, and P. J. Ortoleva, eds., Prediction of Reservoir Quality through Chemical Modeling: American Association of Petroleum Geologists Memoir 49, p. 161-170.

Hutton, A. N., 1994, Textural evidence for the origin of dolomization in the Slave Point – Hamburg to Clarke Lake: Canadian Society of Petroleum Geologists – Canadian Society of Exploration Geophysicists Annual Meeting Abstracts, p. 342-343.

Iampen, H. T., 2003, The genesis and evolution of pre-Mississippian brines in the Williston Basin, Canada-U.S.A.: MSc thesis, University of Alberta, Edmonton, Canada, 124 p.

International Atomic Energy Agency (IAEA), 2005, Global network of isotopes in precipitation (GNIP): Isotope Hydrology Section, web access, May 20th, 2005.

Illing, L. V., 1959, Deposition and diagenesis of some upper Paleozoic carbonate sediments in western Canada: Fifth World Petroleum Congress, Preceedings Section 1, p. 23-52.

Illing, L. V., A. J. Wells, and J. C. M. Taylor, 1965, Penecontemporaneous dolomite in the Persian Gulf: Society of Economic Paleontologists and Mineralogists Special Publication 13, p. 89-111.

Irwin, H., C. Curtis, and N. Coleman, 1977, Isotopic evidence for source of diagenetic carbonates formed during burial of organic-rich sediments: Nature, v. 269, p. 209-213.

Jacobsen, R. L., and H. E. Usdowski, 1976, Partitioning of strontium between calcite, dolomite and liquids: Contributions to Mineralogy and Petrology, v. 59, p. 171-185.

James, N. P., 1983, Reef, in P. A. Scholle, D. G. Bebout, and C. H. Moore, eds., Carbonate depositional environments: American Association of Petroleum Geologists Memoir 33, p. 345-462.

James, N. P., Y. Bone, and T. K. Kyser, 1997, Brachiopod $\delta^{18}O$ values do not reflect ambient oceanography: Lacepede Shelf, southern Australia: Geology, v. 25, p. 551-554.

James, N. P., and P. W. Choquette, 1990, Limestones – the sea-floor diagenetic environment, in I. E. McIlreath, and D. W. Morrow, eds., Diagenesis: Geoscience Canada Reprint Series 4, p. 13-34.

James, N. P., and R. N. Ginsburg, 1979, The seaward margin of Belize barrier and atoll reefs: International Association of Sedimentologists Special Publication 3, 191 p.

Jansa, L. F., and N. R. Fischbuch, 1974, Evolution of a Middle and Upper Devonian sequence from a clastic coastal plain – deltaic complex into overlying carbonate reef complexes and banks, Sturgeon – Mitsue area, Alberta: Geological Survey of Canada Bulletin, v. 234, 94 p.

Joachimski, M. M., R. van Geldern, S. Breisig, W. Buggisch, and J. Day, 2004, Oxygen isotope evolution of biogenic calcite and apatite during the Middle and Late Devonian: International Journal of Earth Sciences, v. 93, p. 542-553.

Jodry, R. L., 1969, Growth and dolomitization of Silurian reefs, St. Clair County, Michigan: American Association of Petroleum Geologists Bulletin, v. 53, p. 957-981.

Johnson, J. G., G. Klapper, and C. A. Sandberg, 1985, Devonian eustatic fluctuations in Euramerica: Geological Society of America Bulletin, v. 96, p. 567-587.

Jones, G. D., F. F. Whitaker, P. L. Smart, and W. E. Sanford, 2002, Fate of reflux brines in carbonate platforms: Geology, v. 30, p. 371-374.

Jones, G. D., P. L. Smart, F. F. Whitaker, B. J. Rostron, and H. G. Machel, 2003, Numerical modeling of reflux dolomitization in the Grosmont platform complex (Upper Devonian), Western Canada Sedimentary Basin. AAPG Bulletin, v. 87, p. 1273-1298.

Keilly, R. A., 2005, Depositional facies and reservoir-enhancing dolomitization surrounding monadnocks in the Slave Point Formation, Dawson field, Alberta, Canada: MSc thesis, University of Alberta, Edmonton, Canada, 142 p.

Keith, J. W., 1990, The influence of the Peace River Arch on Beaverhill Lake sedimentation: Bulletin of Canadian Petroleum Geology, v. 38, p. 55-65.

Kendall, A. C., 1985, Radiaxial fibrous calcite: a reappraisal, in N. Schneidermann, and P. M. Harris, eds., Carbonate cements: Society of Economic Paleontologists and Mineralogists Special Publication 36, p. 59-77.

Kesler, S. E., M. S. Appold, A. M. Mertini, L. M. Walter, T. J. Huston, and J. R. Kyle, 1995, Na-Cl-Br systematics of mineralizing brines in Mississippi Valley-type deposits: Geology, v. 23, p. 641-644.

Kesler, S. E., H. D. Jones, F. C. Furman, R. Sassen, W. H. Anderson, and J. R. Kyle, 1994, Role of crude oil in the genesis of Mississippi Valley-type deposits: evidence from the Cincinnati arch: Geology, v. 22, p. 609-612.

Kharaka, Y. K., and I. Barnes, 1973, SOLMENQ: solution-mineral equilibrium computations: United States Geological Survey Computer Contributions, National Technology Information Report PB-215-899, 82 p.

Kharaka, Y. K., and F. A. F. Berry, 1973, Simultaneous flow of water and solutes through geological membranes, 1. experimental investigation: Geochimica et Cosmochimica Acta, v. 37, p. 2577-2603.

Kharaka, Y. K., and W. W. Carothers, 1986, Oxygen and hydrogen isotope geochemistry of deep basin brines, in P. Fritz, and J. Ch. Fontes, eds., Handbook of environmental isotope geochemistry, 2: Elsevier, p. 305-360.

Kharaka, Y. K., M. S. Lico, V. A. Wright, and W. W. Carothers, 1979, Geochemistry of formation waters from Pleasant Bayou No. 2 well and adjacent areas in coastal Texas: Proceedings of the Fourth Geopressured-Geothermal Energy Conference, p. 168-193.

Kiessling, W., and E. Flügel, 2002, PaleoReef – a database on Phanerozoic reefs, in W. Kiessling, E. Flügel, and J. Golonka, eds., Phanerozoic reef patterns: Society of Economic Paleontologists and Mineralogists Special Publication 72, p. 77-92.

Kimbell, T. N., 1993, Sedimentology and diagenesis of Late Pleistocene fore-reef calcarenites, Barbados, West Indies: a geochemical and petrographic investigation of mixing zone diagenesis: PhD thesis, University of Texas, Dallas, 296 p.

King, R. H., 1947, Sedimentation in Permian Castile Sea: American Association of Petroleum Geologists Bulletin, v. 53, p. 830-840.

Knauth, L. P., and M. A. Beeunas, 1986, Isotope geochemistry of fluid inclusions in Permian halite with implications for the history of ocean water and the origin of saline formation waters: Geochimica et Cosmochimica Acta, v. 50, p. 419-433.

Kohout, F. A., H. R. Henry, and J. E. Banks, 1977, Hydrogeology related to geothermal conditions of the Floridan Plateau, in K. L. Smith, and G. M. Griffin, eds., The geothermal nature of the Floridan Plateau: Florida Department of Natural Resources Bureau, Geology Special Publications, v. 21, p. 1-34.

Koszela, S., 2003, Rare earth elements characteristic of carbonate rocks fromthe Klodzko metamorphic units: Mineralogical Society of Poland – Special Papers, v. 23, p. 93-95.

Kramers, J. W., and J. K. Lerbekmo, 1967, Petrology and mineralogy of Watt Mountain Formation: Mitsue – Nippisi area, Alberta: Bulletin of Canadian Petroleum Geology, v. 15, p. 346-378.

Krebs, W., and R. Macqueen, 1984, Sequence of diagenetic and mineralization events: Pine Point lead-zinc property, NWT, Canada: Bulletin of Canadian Petroleum Geology, v. 32, p. 434-464.

Kretz, R., 1982, A model for the distribution of trace elements between calcite and dolomite: Geochimica et Cosmochimica Acta, v. 46, p. 1979-1981.

Kupecz, J. A., and L. S. Land, 1994, Progressive recrystallization and stablilization of early-stage dolomite: Lower Ordovician Ellenburger Group, west Texas, in B. Purser, M. Tucker, and D. Zenger, eds., Dolomites: a volume in honour of Dolomieu: International Association of Sedimentologists Special Publication 21, p. 255-279.

Kupecz, J. A., Montañez, I. P., and G. Gao, 1992, Recrystallization of dolomite with time, in R. Rezack, and D. Lavoie, eds., Carbonate microfabrics: Springer-Verlag, Berlin, p. 187-194.

Land, L. S., 1980, The isotopic and trace element geochemistry of dolomite: the state of the art, in D. H. Zenger, J. B. Dunham, and R. L. Etherington, eds., Concepts and Models of Dolomitization: SEPM Special Publication 28, p. 87-110.

Land, L. S., 1983, The application of stable isotopes to the studies of the origin of dolomite and to problems of diagenesis in clastic sediments, in M. A. Arthur, T. F. Anderson, I. R. Kaplan, J. Veizer, and L. S. Land, eds., Stable isotopes in sedimentary geology: SEPM Short Course 10, p. 4.1-4.22.

Land, L. S., 1985, The origin of massive dolomite: Journal of Geological Education, v. 33, p. 112-125.

Land, L. S., 1991, Dolomitization of the Hope Gate Formation (north Jamaica) by seawater: reassessment of mixing-zone dolomite, in H. P. Taylor, J. R. O'Neil, and I. R. Kaplan, eds., Stable isotope geochemistry: a tribute to Samuel Epstein: Geochemical Society Special Publication 3, p. 121-133.

Land, L. S., 1997, Mass transfer during burial diagenesis in the Gulf of Mexico sedimentary basin; an overview, in I. P. Montañez, J. M. Gregg, and K. L. Shelton, eds., Basin-wide diagenetic patterns; integrated petrologic, geochemical, and hydrologic considerations: Society of Economic Paleontologists and Mineralogists Special Publication 57, p. 29-39.

Land, L. S., and G. K. Hoops, 1973, Sodium in carbonate sediments and rocks: a possible index to the salinity of diagenetic solutions: Journal of Sedimentary Petrology, v. 43, p. 614-617.

Land, L. S., and D. R. Prezbindowski, 1981, The origin and evolution of saline formation water, Lower Cretaceous carbonates, south-central Texas, U.S.A.: Journal of Hydrogeology, v. 54, p. 51-74.

Langmuir, D. L., 1971, The geochemistry of some carbonate ground waters in central Pennsylvania: Geochimica et Cosmochimica Acta, v. 35, p. 1023-1045.

Law, J., 1955, Geology of northwestern Alberta and adjacent areas: American Association of Petroleum Geologists Bulletin, v. 39, p. 1927-1978.

Leach, D. L., G. S. Plumlee, A. H. Hofstra, G. P. Landis, E. L. Rowan, and J. G. Viets, 1991, Origin of late dolomite cement by CO_2-saturated deep basin brines; evidence from the Ozark region, central United States: Geology, v. 19, p. 348-351.

Lind, I. L., 1993, Stylolites in chalk from Leg 130, Ontong Java Plateau, in W. H. Berger, J. W. Kroenke, and L. A. Mayer, eds., Proceedings of the Ocean Drilling Program: Scientific Results, v. 130, p. 445-451.

Lohmann, K. C., K. A. Breining-Afifi, J. M. Budai, and K. R, Cercone, 1985, Enriched carbon-13 compositions in meteoric and shallow burial calcites and dolomites:

evidence of organic fermentation during early diagenesis: Society of Economic Paleontologists and Mineralogists Midyear Meeting Abstracts, p. 55.

Longman, M. W., 1980, Carbonate diagenetic textures from nearshore diagenetic environments: American Association of Petroleum Geologists Bulletin, v. 64, p. 461-487.

Longstaffe, F. J., 1989, Stable isotopes as tracers in clastic diagenesis, in I. E. Hutcheon, ed., Burial Diagenesis: Mineralogical Association of Canada Short Course 15, p. 201-277.

Lonnee, J., 2001, Study of the structure, stratigraphy and dolomite distribution in the Adsett region of northeast British Columbia, NTS 94-J: Report prepared for Petro-Canada Oil & Gas, 27 p.

Lonnee, J. S., and I. S. Al-Aasm, 2000, Dolomitization and fluid evolution in the Middle Devonian Sulphur Point Formation, Rainbow field, Alberta: petrographic and geochemical evidence: Bulletin of Canadian Petroleum Geology, v. 48, p. 262-283.

Lonnee, J., and Machel, H. G., 2003, High-temperature dolomite containing enigmatic formation fluids: Devonian Clarke Lake gas field, British Columbia, Canada: 12th Bathurst Meeting Abstracts, International Conference of Carbonate Sedimentologists, Durham, England, p. 62.

Lonnee, J., and H. G. Machel, 2004a, High-temperature matrix dolomitization by halite-saturated brines in the Slave Point Formation, Clarke Lake gas field, British Columbia, Canada, in J. J. Packard, and G. R. Davies (eds.) Dolomites: the spectrum – mechanisms, models, reservoir development: Canadian Society of Petroleum Geologists Seminar and Core Conference, C012.

Lonnee, J., and H. G. Machel, 2004b, Dolomitization by halite-saturated brine and subsequent hydrothermal alteration in the Devonian Slave Point Formation, Clarke Lake gas field, British Columbia (abs.): Canadian Society of Petroleum Geologists Annual Meeting, S013.

Lu, H., X. Sun, and M. Ma, 2003, REE and C, O and Sr isotopic compositions of hydrothermal carbonate minerals from Fankou superlarge lead zinc deposit, China: Goldschmidt Conference Abstracts, p. A260.

Machel, H. G., 1985, Facies and diagenesis of the Upper Devonian Nisku Formation in the subsurface of central Alberta: PhD thesis, McGill University, Montreal, Canada, 392 p.

Machel, H. G., 1987a, Some aspects of diagenetic sulphate-hydrocarbon redox reactions, in J. D. Marshall, ed., The diagenesis of sedimentary sequences: Geological Society of America Special Publication 36, p. 15-28.

Machel, H. G., 1987b, Saddle dolomite as a by-product of chemical compaction and thermo-chemical sulfate reduction: Geology, v. 15, p. 936-940.

Machel, H. G. 1997, Recrystallization versus neomorphism, and the concept of 'significant recrystallization' in dolomite research: Sedimentary Geology, v. 113, p. 161-168.

Machel, H. G., 1999, Effects of groundwater flow on mineral diagenesis, with emphasis on carbonate reservoirs: Hydrogeology Journal, v. 7, p. 94-107.

Machel, H. G., 2001, Bacterial and thermochemical sulfate reduction in diagenetic settings: Sedimentary Geology, v. 140, p. 143-175.

Machel, H. G., 2004, Concepts and models of dolomitization: a critical reappraisal, in C. J. R. Braithwaite, G. Rizzi, and G. Darke, eds., The geometry and petrogenesis of dolomite hydrocarbon reservoirs: Geological Society Special Publication 235, p.7-63.

Machel, H. G., 2005, Investigations of burial diagenesis with reference to hydrocarbon reservoirs: Geoscience Canada, in press, 57 p.

Machel, H. G., and J. H. Anderson, 1989, Pervasive subsurface dolomitization of the Nisku Formation in central Alberta: Journal of Sedimentary Petrology, v. 59, p. 891-911.

Machel, H. G., and E. A. Burton, 1991, Factors governing cathodoluminescence in calcite and dolomte, and their implications for studies of carbonate diagenesis, in C. E. Barker, and O. C. Kopp, eds., Luminescence microscopy and spectroscopy: qualitative and quantitative applications: Society of Economic Paleontologists and Mineralogists Short Course 25, p. 37-57.

Machel, H. G., P. A. Cavell, and K. S. Patey, 1996, Isotopic evidence for carbonate cementation and recrystallization, and for tectonic expulsion of fluids into the Western Canada Sedimentary Basin: Geological Society of America Bulletin, v. 108, p. 1108-1119.

Machel, H. G., and P. A. Cavell, 1999, Low-flux, tectonically-induced squeegee fluid flow ("hot flash") into the Rocky Mountain Foreland Basin: Bulletin of Canadian Petroleum Geology, v. 47, p. 510-533.

Machel, H. G., and I. G. Hunter, 1994, Facies models for Middle to Late Devonian shallow-marine carbonates, with comparisons to modern reefs: a guid for facies analysis: Facies, v. 30, p. 155-176.

Machel, H. G., H. R. Krouse, and R. Sassen, 1995, Products and distinguishing criteria of bacterial and thermochemical sulfate reduction: Applied Geochemistry, v. 10, p. 373-389.

Machel, H. G., and J. Lonnee, 2002, Hydrothermal dolomite – a product of poor definition and imagination: Sedimentary Geology, v. 152, p. 163-171.

Machel, H. G., R. A. Mason, A. N. Mariano, and A. Mucci, 1991, Causes and emission of luminescence in calcite and dolomite, in C. E. Barker, and O. C. Kopp, eds., Luminescence microscopy and spectroscopy: qualitative and quantitative applications: Society of Economic Paleontologists and Mineralogists Short Course 25, p. 9-25.

Machel, H. G., and E. W. Mountjoy, 1986, Chemistry and environments of dolomitization – a reappraisal: Earth-Science Reviews, v. 23, p. 175-222.

Machel, H. G., E. W. Mountjoy, and J. E. Amthor, 1994, Dolomitisierung von devonischen Riff- und Plattformkarbonaten in West-Kanada: Zentralblatt für Geologie und Paläontologie, Teil I, p. 941-957.

MacIntyre, D. G., 1992, Geological setting and genesis of sedimentary exhalative barite and barite-sulfide deposits, Gataga District, northeastern British Columbia: Exploration and Mining Geology, v. 1, p. 1-20.

Majorowicz, J. A., F. W. Jones, R. W. Macqueen, and M. E. Ertman, 1989, The bearing of heat flow data on the nature of fluid flow in the Keg River Barrier – Pine Point ore field region, Canada: Economic Geology, v. 84, p. 708-714.

Mallamo, M. P., and A. S. Hedinger, 1992, Fairholme (Upper Devonian) carbonate platform-to-basin transition, Kananaskis area, southwestern Alberta: Canadian Society of Petroleum Geologists Field Trip Guidebook, 66 p.

Malone, M. J., P. A. Baker, and S. J. Burns, 1994, Recrystallization of dolomite: evidence from the Monterey Formation (Miocene), California: Sedimentology, v. 41, p. 1223-1239.

Malone, M. J., P. A. Baker, and S. J. Burns, 1996, Recrystallization of dolomite: an experimental study from 50-200°C: Geochimica et Cosmochimica Acta, v. 60, p. 2189-2207.

Marquez, X., and E. W. Mountjoy, 1996, Origin of microfractures in the Upper Devonian Leduc-Strachan reservoir, deep Alberta Basin: American Association of Petroleum Geologists Bulletin, v. 80, p. 570-588.

Mattes, B. W., and E. W. Mountjoy, 1980, Burial dolomitization of the Upper Devonian Miette Buildup, Jasper National Park, Alberta, in D. H. Zenger, J. B. Dunham, and R. L. Ethington, eds., Concepts and models of dolomitization: Society of Economic Paleontologists and Mineralogists Special Publication 28, p. 259-297.

Mazzullo, S. J., 1992, Geochemical and neomorphic alteration of dolomite: a review: Carbonates and Evaporites, v. 6, p. 21-37.

Mazzullo, S. J., and P. M. Harris, 1992, Mesogenetic dissolution; its role in porosity development in carbonate reservoirs: American Association of Petroleum Geologists Bulletin, v. 76, p. 607-620.

McCaffrey, M. A., B. Lazar, and H. D. Holland, 1987, The evaporation path of seawater and the coprecipitation of Br^- and K^+ with halite: Journal of Sedimentary Petrology, v. 57, p. 928-937.

McCrea, J. M., 1950, On the isotopic chemistry of carbonates and a paleothermometer scale: Journal of Chemical Physics, v. 5, p. 48-51.

McIntire, W. L., 1963, Trace element partition coefficients – a review of theory and application to geology: Geochimica et Cosmochimica Acta, v. 27, p. 1209-1264.

McKenzie, J. A., K. J. Hsu, and J. F. Schneider, 1980, Movement of surface waters under the sabkha, Abu Dhabi, UAE, and its relation to evaporative dolomite genesis, in D. H. Zenger, J. B. Dunham, and R. L. Ethington, eds., Concepts and models of dolomitization: Society of Economic Paleontologists and Mineralogists Special Publication 28, p. 11-20.

McLimans, R. K., 1987, The application of fluid inclusions to migration of oil and diagenesis in petroleum reservoirs: Applied Geochemistry, v. 2, p. 585-603.

Meijer Drees, N. C., 1988, The Middle Devonian sub-Watt Mountain unconformity across the Tathlina Uplift; District of Mackenzie and northern Alberta, Canada, in N. J. McMillan, A. F. Embry, and D. J. Glass, eds., Devonian of the World: proceedings of the second symposium on the Devonian System: Canadian Society of Petroleum Geologists Memoir 14, v. II, p. 477-494.

Meijer Drees, N. C., 1994, Devonian Elk Point Group of the Western Canada Sedimentary Basin, in G. D. Mossop, and I. Shetsen, comps., Geological Atlas of the Western Canada Sedimentary Basin: Canadian Society of Petroleum Geologists and Alberta Research Council, p. 129-147.

Michael, K., and S. Bachu, 2002, Origin, chemistry and flow of formation waters in the Mississippian-Jurassic sedimentary succession in the west-central part of the Alberta Basin, Canada: Journal of Marine and Petroleum Geology, v. 19, p. 289-306.

Michael, K., H. G. Machel, and S. Bachu, 2003, New insights into the origin and migration of brines in deep Devonian aquifers, Alberta, Canada: Journal of Geochemical Exploration, v. 80, p. 193-219.

Micklethwaite, S., and S. F. Cox, 2004, Fault-segment rupture, aftershock-zone fluid flow, and mineralization: Geology, v. 32, p. 813-816.

Montañez, I. P., and J. F. Read, 1992, Fluid-rock interaction history during stabilization of early dolomites, Upper Knox Group (Lower Ordovician), U.S. Appalachians: Journal of Sedimentary Petrology, v. 62, p. 753-778.

Moore, P. F., 1988, Devonian geohistory of the western interior of Canada, in N. J. McMillan, A. F. Embry, and D. J. Glass, eds., Devonian of the world: proceedings of the Second International Symposium on the Devonian System: Canadian Society of Petroleum Geologists Memoir 14, v. I, p. 67-83.

Morrow, D. W., 1990, Part 1: the chemistry of dolomitization and dolomite precipitation, in I. A. McIlreath, and D. W. Morrow, eds., Diagenesis: Geoscience Canada Reprint Series 4, p. 112-124.

Morrow, D. W., 1998, Regional subsurface dolomitization: models and constraints: Geoscience Canada, v. 25, p. 57-70.

Morrow, D. W., and K. L. Aulstead, 1995, The Manetoe dolomite – a Cretaceous-Tertiary or a Paleozoic event? Fluid inclusion and isotopic evidence: Bulletin of Canadian Petroleum Geology, v. 43, p. 267-280.

Morrow, D. W., G. L. Cumming, and R. B. Koepnick, 1986, Manetoe facies – a gas-bearing, megacrystalline, Devonian dolomite, Yukon and Northwest Territories, Canada: AAPG Bulletin, v. 70, p. 702-720.

Morrow, D. W., G. L. Cumming, and K. L. Aulstead, 1990, The gas-bearing Devonian Manetoe facies, Yukon and Northwest Territories: Geological Survey of Canada Bulletin 400, 54 p.

Morrow, D. W., M. Zhao, and L. D. Stasiuk, 2002, The gas-bearing Devonian Presqu'ile Dolomite of the Cordova embayment region of British Columbia, Canada: dolomitization and the stratigraphic template: American Association of Petroleum Geologists Bulletin, v. 86, p. 1609-1638.

Morse, J. W., and F. T. Mackenzie, 1990, Geochemistry of sedimentary carbonates: Developments in Sedimentology 48: Elservier, Amsterdam, 707 p.

Mountjoy, E. W., 1980, Some questions about the development of Upper Devonian carbonate build-ups (reefs), western Canada: Bulletin of Canadian Petroleum Geology, v. 28, p. 315-344.

Mountjoy, E. W., and J. E. Amthor, 1994, Has burial dolomitization come of age? Some answers from the Western Canada Sedimentary Basin, in B. Purser, M. Tucker, and D. Zenger, eds., Dolomites: a volume in honour of Dolomieu: International Association of Sedimentologists Special Publication 21, p. 203-229.

Mountjoy, E. W., H. G. Machel, D. Green, J. Duggan, and A. E. Williams-Jones, 1999, Devonian matrix dolomites and deep burial carbonate cements: a comparison between the Rimbey-Meadowbrook reef trend and the deep basin of west-central Alberta: Bulletin of Canadian Petroleum Geology, v. 47, p. 487-509.

Muehlenbachs, K., 1988, The oxygen isotopic composition of the oceans, sediments, and the seafloor: Chemical Geology, v. 145, p. 263-273.

Muehlenbachs, K., and R. N. Clayton, 1976, Oxygen isotope composition of the oceanic crust and its bearing on seawater: Journal of Geophysical Research, v. 81, p. 4365-4369.

Nadjiwon, L., and D. W. Morrow, 2001, Brecciation and hydrothermal dolomitization of the Middle Devonian Dunedin, Keg River, and Slave Point formations of northeastern British Columbia: Canadian Society of Petroleum Geologists Annual Meeting Abstracts, p. 071.

Nakai, S., A. N. Halliday, S. E. Kesler, H. D. Jones, J. R. Kyle, and T. E. Lane, 1993, Rb-Sr dating of sphalerites from Mississippi Valley-type (MVT) ore deposits: Geochimica et Cosmochimica Acta, v. 57, p. 417-427.

Nelson, J., S. Paradis, J. Christensen, and J. Gabites, 2002, Canadian Cordilleran Mississippi Valley-type deposits: a case for Devonian-Mississippian back-arc hydrothermal origin: Economic Geology, v. 97, p. 1013-1036.

Nesbitt, B. E., and K. Muehlenbachs, 1989, Origins and movement of fluids during deformation and metamorphism in the Canadian Cordillera: Science, v. 245, p. 733-736.

Nesbitt, B. E., and K. Muehlenbachs, 1994, Paleohydrology of the Canadian Rockies and origins of brines, Pb-Zn deposits and dolomitization in the Western Canada Sedimentary Basin: Geology, v. 22, p. 243-246.

Norris, A. W., 1963, Devonian stratigraphy of northeastern Alberta and northwestern Saskatchewan: Geological Survey of Canada Memoir 313.

Norris, A. W., 1965, Stratigraphy of Middle Devonian and older Paleozoic rocks of the Great Slave Lake region, Northwest Territories: Geological Survey of Canada Memoir 322, 180 p.

O'Connell, S. C., G. R. Dix, and J. F. Barclay, 1990, The origin, history and regional structural development of the Peace River Arch, western Canada: Bulletin of Canadian Petroleum Geology, v. 38, p. 4-24.

Oetting, G. C., J. L. Banner, and J. M. Sharp, Jr., 1996, Regional controls on the geochemical evolution of saline groundwaters in the Edwards aquifer, central Texas: Journal of Hydrology, v. 181, p. 251-283.

Oldale, H. S., and R. J. Munday, 1994, Devonian Beaverhill Lake Group of the Western Canada Sedimentary Basin, in G. D. Mossop, and I. Shetsen, comps., Geological Atlas of the Western Canada Sedimentary Basin: Canadian Society of Petroleum Geologists and Alberta Research Council, p. 149-163.

Oliver, J., 1986, Fluids expelled tectonically from orogenic belts: their role in hydrocarbon migration and other geologic phenomena: Geology, v. 14, p. 99-102.

O'Neil, J. R., R. N. Clayton, and T. K. Mayeda, 1969, Oxygen isotope fractionation in divalent metal carbonates: Journal of Chemical Physics, v. 51, p. 5547-5558.

Opalinksi, P., 1984, Origin and significance of dolomite reservoirs in the Middle Devonian Slave Point Formation, northeastern British Columbia, in ASEAN Council on Petroleum, The hydrocarbon occurrence in carbonate rocks: ASCOPE Secretariat, Jakarta, Indonesia, p. 179-211.

Osborne, M. J., and R. E. Swarbrick, 1997, Mechanisms for generating overpressure in sedimentary basins; a reevaluation: American Association of Petroleum Geologists Bulletin, v. 81, p. 1023-1041.

Palciauskas, V., and P. A. Domenico, 1976, Solution chemistry, mass transfer, and the approach to chemical equilibrium in porous carbonate rocks and sediments: Geological Society of America Bulletin, v. 87, p. 207-214.

Palmer, M. R., 1985, Rare earth elements in foraminifera tests: Earth and Planetary Science Letters, v. 73, p. 285-298.

Paradis, S., J. L. Nelson, and S. E. B. Irwin, 1998, Age constraints on the Devonian shale-hosted Zn-Pb-Ba deposits, Gataga District, northeastern British Columbia, Canada: Economic Geology, v 93, p. 184-200.

Paradis, S., W. A. Turner, N. Wilson, and M. Coniglio, 2005, Stable and radiogenic isotopic signatures of mineralized Devonian carbonates of the northern Rocky Mountains and the Western Canada Sedimentary Basin, in P. K. Hannigan, ed., Geoscience Contributions, Targeted Geoscience Initiative: Geological Survey of Canada Bulletin, in press.

Parizek, R. R., W. B. White, and D. Langmuir, 1971, Hydrogeology and geochemistry of folded and faulted carbonate rocks of the central Appalachian type and related land use problems: Geological Society of America Field Trip Guidebook, 183 p.

Patterson, R. G., and D. J. J. Kinsman, 1981, Hydrologic framework of a sabkha along the Persian Gulf: American Association of Petroleum Geologists Bulletin, v. 65, p. 1457-1475.

Petrel Robertson Consulting, 2003, Exploration assessment of deep Devonian gas plays, northeastern British Columbia: Report prepared for British Columbia Ministry of Energy and Mines, 24 p.

Phipps, G. G., 1989, Exploring for dolomitized Slave Point carbonates in northeastern British Columbia: Geophysics, v. 54, p. 806-814.

Plumlee, G. S., D. L. Leach, A. H. Hofstra, G. P. Landis, E. L. Rowan, and J. G. Viets, 1994, Chemical reaction path modeling of ore deposition in Mississippi Valley-type Pb-Zn deposits of the Ozark region, U.S. midcontinent: Economic Geology, v. 89, p. 1361-1383.

Plummer, L. N., D. L. Parkhurst, and T. M. Wigley, 1979, Critical review of the kinetics of calcite dissolution and precipitation, in E. A. Jenne, ed., Chemical Modelling in Aqueous Systems: American Chemical Society Symposium Series 93, p. 537-573.

Plummer, L. N., T. M. Wigley, and D. L. Parkhurst, 1978, The kinetics of calcite dissolution in CO_2-water systems at 5 to 60°C and 0.0 to 1.0 atm CO_2: American Journal of Science, v. 278, p. 179-216.

Popp, B. N., T. F. Anderson, and P. A. Sandberg, 1986a, Brachiopods as indicators of original isotopic compositions of Paleozoic limestones: Geological Society of America Bulletin, v. 97, p. 1262-1269.

Popp, B. N., T. F. Anderson, and P. A. Sandberg, 1986b, Textural, elemental, and isotopic variations among constituents in middle Devonian limestones, North America: Journal of Sedimentary Petrology, v. 56, p. 715-727.

Posey, H. H., A. L. Workman, J. S. Hanor, and S. D. Hurst, 1985, Isotopic characteristics of brines from three oil and gas fields, southern Louisiana: Gulf Coast Association of Geological Societies Transactions, v. 35, p. 261-268.

Potma, K., J. A. W. Weissenberger, P. K. Wong, and M. G. Gilhooly, 2001, Toward a sequence stratigraphic framework for the Frasnian of the Western Canada Basin: Bulletin of Canada Petroleum Geology, v. 49, p. 37-85.

Poulton, T. P., W. K. Braun, M. M. Brooke, and E. H. Davies, 1993, Jurassic, in D. F. Stott, and J. D. Aitken, eds., Sedimentary cover of the craton in Canada: Geological Survey of Canada, Geology of Canada, no. 5 (The Geology of North America, v. D-1), p. 321-357.

Price, R. A., 1994, Cordilleran tectonics and the evolution of the Western Canada Sedimentary Basin, in in G. D. Mossop, and I. Shetsen, comps., Geological Atlas of the Western Canada Sedimentary Basin: Canadian Society of Petroleum Geologists and Alberta Research Council, p. 13-24.

Qing, H., 1998, Petrography and geochemistry of early-stage, fine- and medium-crystalline dolomites in the Middle Devonian Presqu'ile Barrier at Pine Point, Canada: Sedimentology, v. 45, p. 433-446.

Qing, H., and E. W. Mountjoy, 1992, Large-scale fluid flow in the Middle Devonian Presqu'ile barrier, Western Canada sedimentary basin: Geology, v. 20, p. 903-906.

Qing, H., and E. W. Mountjoy, 1994a, Origin of dissolution vugs and breccias in the Middle Devonian Presqu'ile barrier, host of the Pine Point MVT deposits: Economic Geology, v. 89, p. 858-876.

Qing, H., and E. W. Mountjoy, 1994b, Formation of coarsely crystalline, hydrothermal dolomite reservoirs in the Presqu'ile barrier, Western Canada Sedimentary Basin: AAPG Bulletin, v. 78, p. 55-77.

Qing, H., and E.W. Mountjoy, 1994c, Rare earth element geochemistry of dolomites in the Middle Devonian Presqu'ile barrier, Western Canada Sedimentary Basin: implications for fluid-rock ratios during dolomitization: Journal of Sedimentary Petrology, v. 41, p. 787-804.

Radke, B. M., and R. L. Mathis, 1980, On the formation and occurrence of saddle dolomite: Journal of Sedimentary Petrology, v. 50, p. 1149-1168.

Railsback, L. B., 1990, Influence of changing deep ocean circulation on the Phanerozoic oxygen isotopic record: Geochimica et Cosmochimica Acta, v. 54, p. 1501-1509.

Reeder, R. J., and J. L. Prosky, 1986, Compositional sector zoning in dolomite: Journal of Sedimentary Petrology, v. 56, p. 237-247.

Reimer, J. D., and M. R. Teare, 1992, Deep burial diagenesis and porosity modification in carbonate rocks by thermalorganic sulphate reduction and hydrothermal dolomitization: TSR-HTD, in Subsurface dissolution porosity in carbonates: recognition, causes and implications: Canadian Society of Petroleum Geologists, Short Course Notes, 26 p.

Reinson, G. E., P. J. Lee, W. Warters, K. G. Osadetz, L. L. Bell, P. R. Price, F. Trollope, R. I. Campbell, and J. E. Barclay, 1993, Devonian gas resources of the Western Canada Sedimentary Basin: Geological Survey of Canada, Bulletin 452, 157 p.

Reitsema, R. H., 1980, Dolomite and nahcolite formation in organic-rich sediments: isotopically heavy carbonates: Geochimica et Cosmochimica Acta, v. 44, p. 2045-2049.

Richards, B. C., J. E. Barclay, D. Bryan, A. Hartling, C. M. Henderson, and R. C. Hinds, 1994, Carboniferous strata of the Western Canada Sedimentary Basin, in G. D. Mossop, and I. Shetsen, comps., Geological Atlas of the Western Canada Sedimentary Basin: Canadian Society of Petroleum Geologists and Alberta Research Council, p. 221-250.

Ricketts, B. D., 1989, Introduction, in B. D. Ricketts, ed., Western Canada Sedimentary Basin – a case history: Canadian Society of Petroleum Geologists, p. 3-8.

Robie, R. A., B. S. Hemingway, and J. R. Fisher, 1978, Thermodynamic properties of minerals and related substances at 298.15K and 1 bar pressure and at higher temperatures: United States Geological Survey Bulletin 1452, 456 p.

Robinson, E. S., P. V. Poland, L. Glover, and J. A. Speer, 1985, Some effects of regional metamorphism and geologic structure on magnetic anomalies over the Carolina slate belt near Roxboro, North Carolina, in W. J. Hinze, ed., The utility of regional gravity and magnetic anomaly maps: Society of Exploration Geophysicists, p. 320-324.

Rodgers, K. A., A. J. Easton, and C. J. Downes, 1982, The chemistry of carbonate rocks of Nieu island, South Pacific: Journal of Geology, v. 90, p. 645-662.

Roedder, E., 1979, Fluid inclusions as samples of ore fluids, in H. L. Barnes, ed., Geochemistry of hydrothermal ore deposits: Wiley, New York, p. 684-737.

Roedder, E., 1984, Fluid inclusions: Mineralogical Society of America Reviews in Mineralogy, v. 12, 644 p.

Ross, G. M., 1990, Deep crust and basement structure of the Peace River Arch region: constraints on mechanisms of formation: Bulletin of Canadian Petroleum Geology, v. 38, p. 25-35.

Ross, G. M., 2000, Proterozoic stratigraphy of western Canada: a short review, in K. Kyser, ed., Fluid and Basin Evolution: Mineralogical Association of Canada Short Course 28, p. 211-224.

Ross, G. M., J. Broome, and W. Miles, 1994, Potential fields and basement structure – Western Canada Sedimentary Basin, in G. D. Mossop, and I. Shetsen, comps., Geological Atlas of the Western Canada Sedimentary Basin: Canadian Society of Petroleum Geologists and Alberta Research Council, p. 41-47.

Rostron, B. J., J. Tóth, and H. G. Machel, 1997, Fluid flow, hydrochemistry and petroleum entrapment in Devonian reef complexes, south-central Alberta, Canada, in I. P. Montañez, J. M. Gregg, and K. L. Shelton, eds., Basin-wide diagenetic patterns; integrated petrologic, geochemical and hydrologic considerations: Society of Economic Paleontologists and Mineralogists Special Publication 57, p. 139-155.

Sack, L. A. M., 2000, Sedimentology and dolomitization of the Middle Devonian (Givetian) Slave Point Formation, Cranberry field, northwestern Alberta, Canada: MSc thesis, University of Manitoba, Winnipeg, Canada, 264 p.

Saller, A. H., 1984, Petrologic and geochemical constraints on the origin of subsurface dolomite, Enewetak Atoll: an example of dolomitization by normal seawater: Geology, v. 12, p. 217-220.

Sass, E., and A. Bein, 1988, Dolomites and salinity: a comparative geochemical study, in V. Shukla, and P. A. Baker, eds., Sedimentology and geochemistry of dolostones: Society of Economic Paleontologists and Mineralogists Special Publication 43, p. 223-233.

SB Geological Associates, 1988, Slave Point and Elk Point facies and stratigraphic study: Fort Nelson area, B.C. NTS 94-J: Proprietary report, 104 p.

Schmidberger, S. S., A. Simonetti, and D. Francis, 2003, Small-scale Sr isotope investigation of clinopyroxenes from peridotite xenoliths by laser ablation MC-ICP-MS – implications for mantle metasomatism: Chemical Geology, v. 199, p. 317-329.

Schroyen, K., and P. Muchez, 2000, Evolution of metamorphic fluids at the Variscan fold-and-thrust belt in eastern Belgium, in P. Muchez, and T. Bechstaedt, eds., Paleofluid flow and diagenesis during basin evolution: Sedimentary Geology, v. 131, p. 163-180.

Sheasby, N. M., 1971, Depositional patterns of the Upper Devonian Waterways Formation, Swan Hills area, Alberta: Bulletin of Canadian Petroleum Geology, v. 19, p. 377-404.

Sheperd, T. J., A. H. Rankin, and D. H. Alderton, 1985, A practical guide to fluid inclusion studies: Blackie and Son, Glasgow, 239 p.

Shields, M. J., and P. V. Brady, 1995, Mass balance and fluid flow constraints on regional scale dolomitization, Late Devonian, Western Canada Sedimentary Basin: Bulletin of Canadian Petroleum Geology, v. 43, p. 371-392.

Sibley, D. F., and J. M. Gregg, 1987, Classification of dolomite rock textures: Journal of Sedimentary Petrology, v. 57, p. 1087-1100.

Sibson, R. H., 1994, Crustal stress, faulting and fluid flow, in J. Parnell, ed., Geofluids: origin, migration and evolution of fluids in sedimentary basins: Geological Society Special Publication 78, p. 69-84.

Simpson, G. P., 1999, Sulphate reduction and fluid chemistry of the Devonian Leduc and Nisku formations in south-central Alberta: PhD thesis, University of Calgary, Calgary, Canada, 228 p.

Simpson, G., C. Yang, and I. Hutcheon, 1996, Thermchemical sulphate reduction: a local process that does not generate thermal anomalies, in G. M. Ross, comp., Alberta Basement Transects Workshop: Lithoprobe Report 51, Lithoprobe Secretariat, University of British Columbia, p. 241-245.

Skall, H., 1975, The paleoenvironment of the Pine Point lead-zinc district: Economic Geology, v. 70, p. 22-45.

Slind, O.L., G. D. Andrews, D. L. Murray, B. S. Norford, D. F. Paterson, C. J. Salas, and E. E. Tawadros, 1994, in G. D. Mossop, and I. Shetsen, comps., Geological Atlas of the Western Canada Sedimentary Basin: Canadian Society of Petroleum Geologists and Alberta Research Council, p. 87-108.

Smalley, P. C., A. C. Higgins, R. J. Howarth, H. Nicholson, C. E. Jones, N. H. M. Swinburne, and J. Bessa, 1994, Seawater Sr isotope variations through time: a procedure for constructing a reference curve to data and correlate marine sedimentary rocks: Geology, v. 22, p. 431-434.

Smith, T. M., and S. L. Dorobek, 1993, Alteration of early-formed dolomite during shallow to deep burial; Mississippian Mission Canyon Formation, central to southwestern Montana: Geological Society of America Bulletin, v. 105, p. 1389-1399.

Spencer, R. J., 1987, Origin of Ca-Cl brines in Devonian formations, western Canada sedimentary basin: Applied Geochemistry, v. 2, p. 373-384.

Spötl, C., and J. K. Pitman, 1998, Saddle (baroque) dolomite in carbonates and sandstones: a re-appraisal of the burial-diagenetic concept, in S. Morad, ed., Carbonate cementation in sandstones: International Association of Sedimentologists Special Publication 26, p. 437-460.

Stasiuk, L. D., and M. G. Fowler, 2002, Thermal maturity evaluation (vitrinite and vitrinite reflectance equivalent) of Middle Devonian, Upper Devonian, and Mississippian strata in the Western Canada Sedimentary Basin: Geological Survey of Canada Open File Report 4341.

Staudt, W. J., E. J. Oswald, and M. A. A. Schoonen, 1993, Determination of sodium, chloride and sulfate in dolomites: a new technique to constrain the composition of dolomitizing fluids: Chemical Geology, v. 107, p. 97-109.

Stoakes, F. A., 1992, Nature and succession of basin fill strata, in J. C. Wendte, F. A. Stoakes, and C. V. Campbell, eds., Devonian – Early Mississippian carbonates of the Western Canada Sedimentary Basin: Society of Economic Paleontologists and Mineralogists Short Course 28, p. 127-144.

Stoessell, R. K., and A. B. Carpenter, 1986, Stoichiometric saturation tests of $NaCl_{1-x}Br_x$ and $KCl_{1-x}Br_x$: Geochimica et Cosmochimica Acta, v. 50, p. 1465-1474.

Stott, D. F., W. G. E. Caldwell, D. J. Cant, J. E. Cristopher, J. Dixon, E. H. Koster, D. H. McNeil, and F. Simpson, 1993a, Cretaceous, in D. F. Stott, and J. D. Aitken, eds., Sedimentary cover of the craton in Canada: Geological Survey of Canada, Geology of Canada, no. 5 (The Geology of North America, v. D-1), p. 358-438.

Stott, D. F., J. Dixon, J. R. Dietrich, D. H. McNeil, L. S. Russell, and A. R. Sweet, 1993b, Tertiary, in D. F. Stott, and J. D. Aitken, eds., Sedimentary cover of the craton in Canada: Geological Survey of Canada, Geology of Canada, no. 5 (The Geology of North America, v. D-1), p. 439-465.

Stueber, A. M., P. Pushkar, and E. A. Hetherington, 1984, A strontium isotopic study of Smackover brines and associated solids, southern Arkansas: Geochimica et Cosmochimica Acta, v. 48, p. 1637-1649.

Stueber, A. M., P. Pushkar, and E. A. Hetherington, 1987, A strontium isotopic study of formation waters from the Illinois basin, U.S.A.: Applied Geochemistry, v. 2, p. 477-494.

Sverjensky, D. A., 1986, Genesis of Mississippi Valley-type lead-zinc deposits: Annual Reviews of Earth and Planetary Sciences, v. 14, p. 177-199.

Sweeney, J. J., and A. K. Burnham, 1990, Evaluation of a simple model of vitrinite reflectance based on chemical kinetics: AAPG Bulletin, v. 74, p. 1559-1570.

Switzer, S. B., W. G. Holland, P. S. Christie, G. C. Graf, A. S. Hedinger, R. J. McAnley, R. A. Wierzbicki, and J. J. Packard, 1994, Devonian Woodbend – Winterburn strata of the Western Canada Sedimentary Basin, in G. D. Mossop, and I. Shetsen, comps., Geological Atlas of the Western Canada Sedimentary Basin: Canadian Society of Petroleum Geologists and Alberta Research Council, p. 165-202.

Symons, D. T. A., H. Pan, D. F. Sangster, and E. C. Jowett, 1993, Paleomagnetism of the Pine Point Zn-Pb deposits: Canadian Journal of Earth Sciences, v. 30, p. 1028-1036.

Takeuchi, T., S. Uehara, and T. Hayashi, 1980, Comparisons of several dead time correction methods in the case of a mixture of short- and long-lived nuclides: Journal of Radioanalytical and Nuclear Chemistry, v. 56, p. 25-35.

Taylor, H. P. Jr., 1974, The application of oxygen and hydrogen isotope studies to problems of hydrothermal alteration and ore deposition: Economic Geology, v. 69, p. 843-883.

Taylor, H. P. Jr., 1979, Oxygen and hydrogen isotope relationships in hydrothermal mineral deposits, in H. L. Barnes, ed., Geochemistry of hydrothermal ore deposits, p. 236-277.

Taylor, S. R., and S. M. McLennan, 1985, The continental crust: its composition and evolution, and examination of the geochemical record preserved in sedimentary rocks: Oxford, Blackwell Scientific, 312 p.

Thyne, G., B. P. Boudreau, M. Ramm, and R. E. Midtbø, 2001, Simulation of potassium feldspar dissolution and illitization in the Statfjord Formation, North Sea: American Association of Petroleum Geologists Bulletin, v. 85, p. 621-635.

Tooth, J. W., and G. R. Davies, 1989, Gift Lake Slave Point reef, Middle Devonian, Alberta, in H. H. J. Geldsetzer, N. P. James, and G. E. Tebbutt, eds., Reefs – Canada and adjacent areas: Canadian Society of Petroleum Geologists Memoir 13, p. 528-534.

Tucker, M. E., 1981, Sedimentary petrology – an introduction: Blackwell Scientific Publications, Oxford, 252 p.

Tucker, M. E., 1985, Shallow-marine carbonate facies and facies models, in P. J. Benchley, and B. P. J. Williams, eds., Sedimentology – recent developments and applied aspects: Geological Society Special Publication 18, p. 139-161.

Tucker, M. E., and V. P. Wright, 1990, Carbonate sedimentology: Blackwell Scientific Publications, Oxford, 482 p.

Underschultz, J., and S. Bachu, 1997, Clarke Lake hydrodynamic evaluation – Slave Point strata: Proprietary report prepared for Petro-Canada Oil & Gas, unpaginated.

Urey, H. C., H. A. Lowenstam, S. Epstein, and C. R. McKinney, 1951, Measurements of paleotemperatures and temperatures of the Upper Cretaceous of England, Denmark, and the southeastern United States: Geological Society of America Bulletin, v. 62, p. 399-416.

Vahrenkamp, V. C., and P. K. Swart, 1990, New distribution coefficient for the incorporation of strontium into dolomite and its implications for the formation of ancient dolomites: Geology, v. 18, p. 387-391.

Vahrenkamp, V. C., and P. K. Swart, 1994, Late Cenozoic dolomites of the Bahamas: metastable analogues for the genesis of ancient platform dolomites, in B. H. Purser, M. E. Tucker, and D. H. Zenger, eds., Dolomites – a volume in honour of Dolomieu: International Association of Sedimentologists Special Publication 21, p. 133-153.

Veizer, J., 1983, Chemical diagenesis of carbonates: theory and application of trace element techniques, in M. A. Arthur, T. F. Anderson, I. R. Kaplan, J. Veizer, and L. S. Land, eds., Stable isotopes in sedimentary geology: Society of Economic Paleontologists and Mineralogists Short Course 10, p. 3-1 to 3-100.

Veizer, J., D. Ala, K. Azmy, P. Bruckschen, D. Buhl, F. Bruhn, G. Carden, A. Diener, S. Ebneth, Y. Godderis, T. Jasper, C. Korte, F Pawellek, O. G. Podlaha, and H. Strauss, 1999, ^{87}Sr/^{86}Sr, δ^{13}C and δ^{18}O evolution of Phanerozoic seawater: Chemical Geology, v. 161, p. 59-88.

Veizer, J., B. Lemieux, B. Jones, M. R. Gibling, and J. Savelle, 1977, Sodium: paleosalinity indicator in ancient carbonate rocks: Geology, v. 5, p. 177-179.

Viau, C. A., 1988, The Devonian Swan Hills Formation at Swan Hills field and adjacent areas, central Alberta, Canada, in A. J. Lomando, and P. M. Harris, comps., Giant oil and gas fields – a core workshop: Society of Economic Paleontologists and Mineralogists Core Workshop 12, p. 803-853.

Walkden, G. M., and J. R. Berry, 1984, Syntaxial overgrowths in muddy crinoidal limestones – cathodoluminescence sheds new light on an old problem: Sedimentology, v. 31, p. 251-267.

Walls, R. A., and G. Burrowes, 1985, The role of cementation in the diagenetic history of Devonian reefs, western Canada, in N. Schneidermann, and P. M. Harris, eds., Carbonate cements: Society of Economic Paleontologists and Mineralogists Special Publication 36, p. 185-220.

Walter, L. M., A. M. Steuber, and T. J. Huston, 1990, Br-Cl-Na systematics in Illinois Basin fluids: constraints on fluid origin and evolution: Geology, v. 18, p. 315-318.

Wanless, H. R., 1979, Limestone response to stress: pressure solution and dolomitization: Journal of Sedimentary Petrology, v. 49, p. 437-462.

Warren, J., 2000, Dolomite: occurrence, evolution and economically important associations: Earth-Science Reviews, v. 52, p. 1-81.

Warren, P. S., 1933, The age of the Devonian limestone at McMurray: Canada Field Naturalist, v. 47, p. 148-149.

Wefer, G., and W. H. Berger, 1991, Isotope paleontology: growth and composition of extant calcareous species: Marine Geology, v. 100, p. 207-248.

Welford, J. K., R. M. Clowes, R. M. Ellis, G. D. Spence, I. Asudeh, and Z. Hajnal, 2001, Lithospheric structure across the craton-Cordilleran transition of northeastern British Columbia: Canadian Journal of Earth Sciences, v. 38, p. 1169-1189.

Wendte, J. C., 1992, Evolution of the Judy Creek Complex: a late Middle Devonian isolate platform-reef complex in west-central Alberta, in J. C. Wendte, F. A. Stoakes, and C. V. Campbell, eds., Devonian – Early Mississippian carbonates of the Western Canada Sedimentary Basin: Society of Economic Paleontologists and Mineralogists Short Course 28, p. 89-125.

Wendte, J., J. J. Dravis, L. D. Stasiuk, H. Qing, S. L. O. Moore, and G. Ward, 1998, High-temperature saline (thermoflux) dolomitization of Devonian Swan Hills platform and bank carbonates, Wild River area, west-central Alberta: Bulletin of Canadian Petroleum Geology, v. 46, p. 210-265.

Wendte, J. C., and F. A. Stoakes, 1982, Evolution and corresponding porosity distribution of the Judy Creek reef complex, Upper Devonian, central Alberta, in W. G. Cutler, ed., Canada's Giant Hydrocarbon Reservoirs: Canadian Society of Petroleum Geologists Core Conference Manual, p. 63-81.

White, D. E., 1965, Saline waters of sedimentary rocks, in A. Young, and G. E. Galley, eds., Fluids in Subsurface Environments: American Association of Petroleum Geologists Memoir 4, p. 342-366.

Wildeman, T. R., 1970, The distribution of Mn^{2+} in some carbonates by electron paramagnetic resonance: Chemical Geology, v. 5, p. 167-177.

Williams, G.K., 1981, Middle Devonian barrier-complex of Western Canada: Geological Survey of Canada, Open File Report 761.

Williams, G. K., 1984, Some musings on the Devonian Elk Point Basin, western Canada: Bulletin of Canadian Petroleum Geology, v. 32, p. 216-232.

Witzke, B. J., and P. H. Heckel, 1988, Paleoclimatic indicators and inferred Devonian paleolatitudes of Euramerica, in N. J. McMillan, A. F. Embry, and D. J. Glass, eds., Devonian of the World: proceedings of the second symposium on the Devonian System: Canadian Society of Petroleum Geologists Memoir 14, v. I, p. 49-68.

Wright, G. N., M. E. McMechan, and D. E. G. Potter, 1994, Structure and architecture of the Western Canada Sedimentary Basin, in G. D. Mossop, and I. Shetsen, comps., Geological Atlas of the Western Canada Sedimentary Basin: Canadian Society of Petroleum Geologists and Alberta Research Council, p. 25-40.

Wright, W. R., 2001, Dolomitization, fluid-flow and mineralization of the Lower Carboniferous rocks of the Irish Midlands and Dublin Basin: PhD thesis, University College Dublin, Belfield, Ireland.

Yardley, B. W. D., and D. A. Banks, 1995, The behaviour of chloride and bromide during the metamorphic cycle, in Y. K. Kharaka, and O. V. Chudaev, eds., Water-rock interaction 8, p. 625-628.

Yurtsever, Y., 1975, Worldwide survey of stable isotopes in precipitation: Reports Section of Isotope Hydrology, International Atomic Energy Agency, p. 567–585.

Yurtsever, Y., and J. R. Gat, 1981, Atmospheric waters, in J. R. Gat, and R. Gonfiantini, eds., Stable Isotope Hydrology: deuterium and oxygen-18 in the water cycle: International Atomic Energy Agency, Technical Report Series 210, p. 103-142.

Zemann, J., 1969, Crystal chemistry, in K. H. Wedepohl, ed., Handbook of geochemistry, v. 1, p. 12-36.

Zhang, Y. G., and J. D. Frantz, 1987, Determination of the homogenization temperatures and densities of supercritical fluids in the system $NaCl$-KCl-$CaCl_2$-H_2O using synthetic fluid inclusions: Chemical Geology, v. 64, p. 335-350.

Ziegler, P. A., 1988, Laurussia – the old red continent, in N. J. McMillan, A. F. Embry, and D. J. Glass, eds., Devonian of the World – second symposium on the Devonian System: Canadian Society of Petroleum Geologists Memoir 14, v. 1, p. 15-48.

APPENDIX I

Table of the 28 core locations examined for this study. Wells are listed according to their National Topographic Series (NTS) location, well name, cored formation(s), and core interval.

Well Location - NTS	Name	Formation	Depth
a-50-C/94-J-9	PC Klua	Slave Point	6882'9" - 6912'1"
c-70-E/94-J-9	BA Shell Klua	Slave Point	6365'8" - 6460'6"
b-49-F/94-J-9	BA Shell Klua	Slave Point	6474'8" - 6584'6"
b-75-F/94-J-9	PC ARC Klua	Slave Point	6600' - 6610'
a-63-J/94-J-9	Advantage PC Hoffard	Slave Point	1964.0 - 1990.0 m
b-78-J/94-J-9	Pex Esso Clarke	Slave Point	6205' - 6331'
a-81-J/94-J-9	Advantage PC Hoffard	Slave Point	1904.0 - 1922.0 m
c-56-L/94-J-9	Pex Esso Clarke	Slave Point	6351' - 6558'
b-72-L/94-J-9	Pex Esso Clarke	Slave Point	6237'9" - 6251'
d-91-L/94-J-9	Pex Esso Clarke	Slave Point	6291' - 6499'
c-94-L/94-J-9	Pex Esso Clarke	Muskwa, Slave Point	6354' - 6565'
c-58-E/94-J-10	PC Gulf Milo	Slave Point	2152.0 - 2156.8 m
a-61-F/94-J-10	Pex et al Clarke	Slave Point	6701' - 6721'
d-79-F/94-J-10	Union HB Milo	Slave Point	6756'6" - 6791'6"
a-65-G/94-J-10	Pex et al Clarke	Muskwa, Otter Park, Slave Point	6659' - 6757'9"
d-72-G/94-J-10	PC Clarke	Slave Point	6413' - 6456'
a-83-G/94-J-10	PC Clarke	Slave Point	1930.2 - 1939.2 m
d-69-H/94-J-10	Pex et al Clarke	Slave Point	6525'6" - 6571'6"
c-64-I/94-J-10	Gulf States Imp Clarke Lake	Slave Point	6423' - 6447'
b-70-I/94-J-10	Pex et al Clarke	Slave Point	6260' - 6284'
c-78-I/94-J-10	Pex et al Clarke	Slave Point	6182'6" - 6199'
b-22-J/94-J-10	PC et al Hz Clarke	Slave Point	6535'9 - 6575'9"
c-47-J/94-J-10	Pex et al Clarke	Slave Point	6549'9" - 6571'9"
a-5-A/94-J-16	Dome et al E Clarke	Slave Point	2081.0 - 2198.8 m
b-6-A/94-J-16	Enermark Hoffard	Slave Point	6319'9" - 6447"
b-12-A/94-J-16	Pengrowth Leader IDE Hoffard	Slave Point	1888.6 - 1905.8 m
c-8-D/94-J-16	Pex Esso Clarke	Slave Point	6307' - 6467'8"
b-10-D/94-J-16	Pex Esso Clarke	Slave Point	6257'9" - 6303'6"

APPENDIX II

List of formation tops picked from electric logs. All tops are listed in metres below Kelly Bushing (KB).

UWI	KB	MUSKWA	WATERWAYS	WATERWAYS D	WATERWAYS C	WATERWAYS B	WATERWAYS A	OTTER PARK	SLAVE POINT	DOLOSTONE	LIMESTONE
00/A-006-B/094-J-09/0	443.1	1984.7	2013.8	2013.8	2018.9	2046.3	2077.3		2087.5		
00/C-055-B/094-J-09/0	430	1962.5	1978	1978	1981.2	2007.3	2041.5		2053.7		
00/D-081-B/094-J-09/0	431.4	1950.9	1971.3	1971.3	1974.7	2000	2038.7		2047.8		
00/D-090-B/094-J-09/0	431	1945.4	1962.1	1962.1	1967.8	1991	2026.8		2038.3		
00/B-092-B/094-J-09/0	431.9	1909	1923.6		1923.6	1946.7	1978.5		1988		
00/B-094-B/094-J-09/0	436.4	1951.7	1970	1970	1971.8	1997	2032.8		2042.7		
00/D-020-C/094-J-09/0	505.5	2001.6	2018.9		2018.9	2040.8	2066.9		2077.8		
00/B-030-C/094-J-09/0	503.2	2027.2	2044.1		2044.1	2066.5	2095		2104.6		
00/A-036-C/094-J-09/0	481.6	1998.2	2014.5		2014.5	2036.4	2064.3		2077		
00/A-037-C/094-J-09/0	480.1	2002.3	2024.3		2024.3	2042.3	2068.3		2077.1		
00/A-050-C/094-J-09/0	474.3	1986.9	2001.6		2001.6	2024.7	2055.6		2065		
00/A-061-C/094-J-09/0	434.4	1953.2	1975	1975	1977.5	2002.9	2037		2050.3		
00/A-064-C/094-J-09/0	421.7	1915.2	1930.9	1930.9	1934.1	1953.9	1986.4		1997.2		
00/B-068-C/094-J-09/0	427.6	1949.3	1967.6		1967.6	1991	2021.4		2029.1		
00/D-074-C/094-J-09/0	431.9	1937.9	1952.1		1952.1	1974.3	2014.7		2022		
00/D-094-C/094-J-09/0	428.4	1896.2	1907.7		1907.7	1926.8	1958.1		1964		
00/B-021-D/094-J-09/0	505.4	2027.3	2044.4		2044.4	2069.5	2098.4		2106.2		
00/D-005-E/094-J-09/0	448	1937.3							1960		
00/B-021-E/094-J-09/0	433	1927.7	1937.6		1937.6				1942		
00/B-054-E/094-J-09/0	423.3	1902.6							1927.9		
00/C-070-E/094-J-09/0	425.8	1898.5							1933		1933
00/D-099-E/094-J-09/0	415.4	1887.1							1915.1		
00/D-099-E/094-J-09/2	415.4	1904.5							1915.1		
00/B-004-F/094-J-09/0	426.1	1933.9	1949.8		1949.8	1977.3	2013		2018.9		
00/A-005-F/094-J-09/0	429.3	1916.4	1931.6		1931.6	1952.4	1985.8		1990.8		
00/A-014-F/094-J-09/0	427.9	1930.3	1946		1946	1974.1	2009.4		2014.4		
00/C-014-F/094-J-09/0	426.4	1907.5	1921.9		1921.9	1943.5	1976.3		1979.1		
00/C-034-F/094-J-09/0	424.5	1895.3	1913.7		1913.7	1932.7	1957.9		1959.7		
00/A-035-F/094-J-09/0	424.6	1890.2	1909.3		1909.3	1928.1			1958.3		
00/A-037-F/094-J-09/0	421.5	1916.7	1932.6		1932.6	1956.8			1981.6		
00/B-049-F/094-J-09/0	421.5	1907.2	1923.8		1923.8				1926.3		
00/D-051-F/094-J-09/0	416.4	1918.3	1936.6		1936.6	1961.8			1992		
00/D-055-F/094-J-09/0	418.6	1888.6	1905		1905	1923.6			1942.8		
00/C-071-F/094-J-09/0	417.8	1931.2	1943.8		1943.8	1968.6			1983		
00/D-097-F/094-J-09/0	415	1873.9							1884.6		
00/B-019-G/094-J-09/0	432.5	1936.5	1956.7	1956.7	1959.5	1983.3	2019.8		2027.5		
00/B-029-G/094-J-09/0	430.9	1914.3	1933.3	1933.3	1933.7	1957.8	1993.1		1999.4		
00/D-035-G/094-J-09/0	422.8	1945.5	1967.2	1967.2	1969.7	1995.4	2032.2		2039.7		
00/C-038-G/094-J-09/0	421.2	1931.2	1950.8	1950.8	1954	1977.9	2014.8		2019.9		
00/C-067-G/094-J-09/0	417.1	1910.5	1929.7	1929.7	1931	1954.2			1980.8		
00/C-094-G/094-J-09/0	423.9	1941.1	1958						1963.2		
00/D-026-H/094-J-09/0	442.4	1959.7	1980.2	1980.2	1986.3	2008.5	2044.5		2056.7		
00/C-028-H/094-J-09/0	440.7	1929	1948.6	1948.6	1954	1973.7	2008.9		2020.3		
00/A-056-H/094-J-09/0	454.2	1976.7	1987.5	1987.5	1992.7	2017.8	2049.8		2055.4		
00/A-089-H/094-J-09/0	444.4	1953.1	1970.9	1970.9	1974.3	2001	2026		2028.6		
00/D-024-I/094-J-09/0	449.6	1942							1967.1		
00/D-036-I/094-J-09/0	447.7	1946.6						1964.7	1967		
00/C-036-I/094-J-09/0	446.5	1943						1963.8	1965.5		
00/D-006-J/094-J-09/0	421.9	1937.8							1959		
00/A-063-J/094-J-09/0	429.1	1921.6							1943.5		
00/A-065-J/094-J-09/0	417.6	1857							1879.8		
00/B-078-J/094-J-09/0	397.8	1870.4							1891.3		
00/A-081-J/094-J-09/0	439.4	1871.8							1890		
00/A-081-J/094-J-09/2	439.4	1871							1890		
00/A-001-K/094-J-09/0	409.1	1913.4							1932		
00/A-005-K/094-J-09/0	410	1907.2							1926.3		
00/A-007-K/094-J-09/0	413.3	1855.3							1878.1		1878.1
00/B-014-K/094-J-09/0	407	1910.4							1929.5		1929.5
00/A-017-K/094-J-09/0	411.5	1901.6							1925.4		1925.4
00/C-028-K/094-J-09/0	412.2	1829.8							1881		1881
00/D-030-K/094-J-09/0	413.9	1855.1							1906.2		1906.2
00/C-050-K/094-J-09/0	413.9	1846.7							1892.1		1892.1
00/D-056-K/094-J-09/0	406	1894.4							1915.1		1915.1
00/B-060-K/094-J-09/0	413	1882.6							1934.6		1934.6

00/C-075-K/094-J-09/0	405.1	1915.7							1932.5		1932.5
00/C-088-K/094-J-09/0	404.8	1895.6							1919		1919
00/D-097-K/094-J-09/0	402.5	1865.6							1889	1923.2	1889
00/B-002-L/094-J-09/0	411.5	1875.1							1921.9		1921.9
00/A-029-L/094-J-09/0	407.2	1877.4							1909.9		1909.9
00/D-048-L/094-J-09/0	407.8	1909.9							1950.2		1950.2
00/C-056-L/094-J-09/0	409.3	1888.8							1930.3	1930.3	1960.5
00/B-069-L/094-J-09/0	409	1897.8							1929.9	2026.1	1929.9
00/B-072-L/094-J-09/0	410.9	1850.3							1897	1897	
00/D-072-L/094-J-09/0	413.6	1848.2							1890.3	1884.7	1890.3
00/B-073-L/094-J-09/0	410.3	1865.3							1911.1	1911.1	
00/D-074-L/094-J-09/0	410.9	1930.2							1984.2	1984.2	
00/A-075-L/094-J-09/0	410.4	1855.2							1894.3	1902.3	1894.3
00/C-075-L/094-J-09/0	414.2	1850.9							1889.8	1889.8	
00/A-076-L/094-J-09/0	410.1	1875.5							1917.7	1917.7	
00/A-077-L/094-J-09/0	413.9	1902.3							1942.2	1942.2	
00/C-080-L/094-J-09/0	413.1	1905.3							1936.6	1936.6	
00/B-088-L/094-J-09/0	418.1	1864							1898	1902	1898
02/D-088-L/094-J-09/0	416.4	1895.1							1937.5	1937.5	1961.1
00/B-090-L/094-J-09/0	413.3	1896.9							1933.2	2037.6	1933.2
00/D-091-L/094-J-09/0	416.4	1863.7							1916.3	1926.3	1916.3
00/C-092-L/094-J-09/0	421.2	1881.4							1939.7	1939.7	
00/D-092-L/094-J-09/0	421.1	1863.9							1919.6	1941.1	1919.6
00/C-094-L/094-J-09/0	418.2	1882.3							1937.9	1937.9	1985.8
00/D-096-L/094-J-09/0	419.4	1881.7							1916.5	1925.5	1916.5
00/B-097-L/094-J-09/0	419	1875.9							1916.6	1916.6	
00/B-097-L/094-J-09/2	419	1885							1925	1925	1990.6
00/B-098-B/094-J-10/0	489.2	1972.2							1990.5		1990.5
00/A-001-C/094-J-10/0	480.4	2004.4							2024.7		2024.7
00/A-002-D/094-J-10/0	481.6	2121.8							2142.2	2222.7	2142.2
00/D-003-D/094-J-10/0	519.4	2075.4							2099.2	2202.1	2099.2
00/D-009-E/094-J-10/0	548.3	2112.1							2143.4	2166	2143.4
00/D-019-E/094-J-10/0	530.4	2107.8							2140.3	2159.9	2140.3
00/B-020-E/094-J-10/0	545.4	2136.6							2168		2168
00/C-043-E/094-J-10/0	503.8	2092						2122.4	2126.7	2126.7	
00/B-046-E/094-J-10/0	520.8	2083.4							2113.5		2113.5
00/D-053-E/094-J-10/0	503.9	2094.2						2086.9	2156.8	2156.8	
00/D-055-E/094-J-10/0	522.7	2083.8						2117	2211.6	2211.6	
00/C-058-E/094-J-10/0	548.5	2113.4							2152	2152	
00/A-067-E/094-J-10/0	575.5	2123.8						2150.5	2179	2179	
00/C-052-F/094-J-10/0	458.1	1944.6							1981.4	1986.5	1981.4
00/C-054-F/094-J-10/0	446.8	1955						1985	1989.6	1969.6	
00/A-061-F/094-J-10/0	461.8	1943.1						1974.5	1980.2	1986.1	1980.2
00/D-079-F/094-J-10/0	458.7	2012.4						2045.2	2050.7	2057.3	2051.7
00/C-080-F/094-J-10/0	470.4	1998.4							2030.7	2034	2030.7
00/C-088-F/094-J-10/0	460.7	1958.5						1996.2	2002.3	2002.3	
00/C-089-F/094-J-10/0	485.9	2021.1						2050	2056.1	2056.1	
00/A-090-F/094-J-10/0	488.1	1994.6						2022.6	2027	2049.5	2027
00/A-099-F/094-J-10/0	469.6	1983.1						2015.1	2020.8	2027.4	2020.8
00/D-099-F/094-J-10/0	477.9	2028.8						2086	2187.9	2187.9	
00/A-019-G/094-J-10/0	493.5	1990							2011.5		2011.5
00/C-031-G/094-J-10/0	455.1	1954.4							1977.6		1977.6
00/A-044-G/094-J-10/0	467.3	1988.8							2019.1	2047	2019.1
00/C-049-G/094-J-10/0	483.5	1992.5						2021.2	2023		2023
00/A-051-G/094-J-10/0	439.9	1944.5							1970.7		1970.7
00/A-054-G/094-J-10/0	463.7	1962.2							1990.3		1990.3
00/D-054-G/094-J-10/2	463.7	1963.1							1982.1	2004.4	1982.1
00/B-061-G/094-J-10/0	439.5	1957.1							1988.7		
00/A-065-G/094-J-10/0	467.9	2002.4						2033.1	2035.6	2035.6	
00/D-066-G/094-J-10/0	466.9	1927.4						1956.5	1962.2	1979.3	1962.2
00/A-069-G/094-J-10/0	475.2	2033.3						2064.2	2065.9	2065.9	
00/D-072-G/094-J-10/0	420.9	1916.5						1944.8	1947.7	1947.7	
00/A-074-G/094-J-10/0	457	2001.8						2028.7	2033.4		
00/B-076-G/094-J-10/0	462.1	1927.9						1957.1	2017.9	2017.9	
00/D-076-G/094-J-10/0	443.8	1996.7						2019.8	2158.5		2158.5
00/B-078-G/094-J-10/0	457.3	1894.4						1933.2	1940.3	1963.8	1940.3

00/A-001-G/094-J-10/0	418.8	1933						1961	1963.7	1963.7	
00/A-083-G/094-J-10/0	429.7	1890.5						1923.5	1928.2	1928.2	
00/B-084-G/094-J-10/0	433.7	1977.2						2000.6	2118.1	2118.1	
00/B-092-G/094-J-10/0	410	1928							1958.3	1958.3	
00/D-060-H/094-J-10/0	429.5	1946.5						1975.3	1978.2	1978.2	
00/C-097-H/094-J-10/0	411.8	1922.1						1955.2	1958.4		1958.4
00/C-100-H/094-J-10/0	415.4	1951.6						1981.4	1985	1985	
00/B-008-I/094-J-10/0	413	1935.2						1964.3	1970.3	1970.3	
00/B-018-I/094-J-10/0	410.8	1923.3						1951.8	1956.2	1956.2	
00/C-020-I/094-J-10/0	408.1	1918.5							1945.8	1945.8	
00/A-023-I/094-J-10/0	409	1891.6							1926.8		1926.8
00/C-026-I/094-J-10/0	411.2	1909.5							1938.9	1988.5	1938.9
00/D-028-I/094-J-10/0	408.8	1924.2							1947.8		
00/C-029-I/094-J-10/0	412.3	1910.9							1933.4	1933.4	
00/D-037-I/094-J-10/0	407.5	1888.5							1910		1910
00/B-038-I/094-J-10/0	408	1939.4							1966	1966	
00/D-063-I/094-J-10/0	401.8	1881.7							1916.6		1916.6
00/C-064-I/094-J-10/0	399.3	1882							1918.1		1918.1
00/C-069-I/094-J-10/0	396.2	1876.3						1910.7	1983	1983	
00/B-070-I/094-J-10/0	399	1855.6						1892	1904.3	1904.3	
00/C-070-I/094-J-10/0	395.3	1923.3						1980.4	2101.7	2101.7	
00/B-078-I/094-J-10/0	394.7	1870.7						1906.3	1908.1	1908.1	
00/C-078-I/094-J-10/0	395	1844.3							1878.2	1878.2	
00/C-085-I/094-J-10/0	389.8	1900.9						1937.1	1939.6	1939.6	
00/B-086-I/094-J-10/0	396.4	1928.4							1964.9	1964.9	
00/C-087-I/094-J-10/0	395.9	1890.8						1890.8	1903	1903	
00/C-091-I/094-J-10/0	408.1	1873.7							1912.9	1912.9	
00/A-092-I/094-J-10/0	407.2	1862.5							1900.8	1900.8	
00/A-094-I/094-J-10/0	395.8	1900.2						1933.9	1938	1938	
00/C-098-I/094-J-10/0	392.4	1856						1895.6	1905.9	1905.9	
00/D-021-J/094-J-10/0	410.5	1906							1932.2	1934.8	1932.2
00/B-022-J/094-J-10/0	409	1954.4						1984.4	1990.2	1990.2	
00/B-026-J/094-J-10/0	388.9	1796.6						1827	1837.3	1837.3	
00/B-033-J/094-J-10/0	412.5	1917						1947.3	1950.7	1986.5	1950.7
00/D-036-J/094-J-10/0	413.8	1949.4						1985.2	2148.4	2148.4	
00/B-039-J/094-J-10/0	420.4	1976.9						2014.5	2193.3		2193.3
00/C-043-J/094-J-10/0	402.3	1893.9						1920.1	1928.3	1928.3	
00/B-046-J/094-J-10/0	312.1	1793.1						1826.6	1833.5	1833.5	
00/C-047-J/094-J-10/0	409.3	1915.8						1940	1965.3	1965.3	
00/A-051-J/094-J-10/0	389.6	1872.9						1899.4	1906.2	1906.2	
00/A-052-J/094-J-10/0	404.8	1887						1917	1925.4	1925.4	
00/B-053-J/094-J-10/0	403.8	1866.4						1892.5	1904.6	1904.6	
00/A-055-J/094-J-10/0	394.5	1778.3						1810.5	1829.5	1829.5	
00/C-057-J/094-J-10/0	409	1940.7						1986.5	2148.8		
00/D-060-J/094-J-10/0	413.6	1952.1						1989.6	2131		
00/C-032-K/094-J-10/0	418	1991.8						2023.9	2221		
00/D-036-K/094-J-10/0	415.2	1972.2						2014	2212.9		
00/A-005-A/094-J-15/0	395.5	1826							1861		
00/D-010-A/094-J-15/0	373.7	1913						1957.5			
00/C-002-A/094-J-16/0	446.2	1907.9							1932.1		
00/A-005-A/094-J-16/0	442.6	1929.8							1955.5		
00/B-006-A/094-J-16/0	440.1	1895.4						1913.4	1920.5		
00/B-012-A/094-J-16/0	448.3	1862.9						1882.5	1885.8		
00/A-027-B/094-J-16/0	386.9	1930.1						1943			
00/A-004-D/094-J-16/0	429.6	1898.7						1957.5	2050.7		
00/B-006-D/094-J-16/0	429.9	1879.5						1921.9	1943.4	1943.4	
00/B-008-D/094-J-16/0	418.8	1868.2							1914		
00/B-008-D/094-J-16/2	416.8	1868.8							1914	1914	
00/C-008-D/094-J-16/4	429.3	1870.1							1915.8	1915.8	
00/A-010-D/094-J-16/2	414.4	1967.5						2010.6	2013.9		
00/B-010-D/094-J-16/0	410	1861.2							1899.1	1899.1	
00/B-018-D/094-J-16/0	420.3	1893.7						1944	2057.5	2057.5	

APPENDIX III

List of samples for petrographic and geochemical analysis.

Abbreviations:

TS = thin section
SI = stable isotope analysis ($\delta^{18}O$ and $\delta^{13}C$)
RI = radiogenic isotope analysis ($^{87}Sr/^{86}Sr$)
TE = trace element analysis
FIM = fluid inclusion microthermometric analysis
FICL = fluid inclusion crush-leach analysis

	Well Location - NTS	Depth	TS	SI	RI	TE	FIM	FICL
1	c-70-E/94-J-9	6367'						
2	c-70-E/94-J-9	6374'6"	X	X				
3	c-70-E/94-J-9	6375'						
4	c-70-E/94-J-9	6379'9"						
5	c-70-E/94-J-9	6384'	X	X				
6	c-70-E/94-J-9	6385'6"						
7	c-70-E/94-J-9	6387'3"						
8	c-70-E/94-J-9	6391'8"						
9	c-70-E/94-J-9	6394'6"						
10	c-70-E/94-J-9	6423'	X	X	X	X		
11	c-70-E/94-J-9	6436'9"	X					
12	c-70-E/94-J-9	6443'						
13	c-70-E/94-J-9	6449'3"	X	X				
14	c-70-E/94-J-9	6454'8"						
15	b-49-F/94-J-9	6475'8"	X	X				
16	b-49-F/94-J-9	6479'	X					
17	b-49-F/94-J-9	6488'						
18	b-49-F/94-J-9	6510'	X					
19	b-49-F/94-J-9	6510'6"						
20	b-49-F/94-J-9	6514'2"						
21	b-49-F/94-J-9	6522'	X					
22	b-49-F/94-J-9	6531'9"						
23	b-49-F/94-J-9	6533'						
24	b-49-F/94-J-9	6541'	X					
25	b-49-F/94-J-9	6547'3"						
26	b-49-F/94-J-9	6548'	X					
27	b-49-F/94-J-9	6556'9"						
28	b-49-F/94-J-9	6561'						
29	b-49-F/94-J-9	6561'9"						
30	b-49-F/94-J-9	6571'3"	X					
31	c-71-F/94-J-9	2218.00 m						
32	b-75-F/94-J-9	6600'						
33	b-75-F/94-J-9	6601'4"						
34	b-75-F/94-J-9	6602'6"						
35	b-75-F/94-J-9	6604'8"						
36	b-75-F/94-J-9	6605'	X					
37	b-75-F/94-J-9	6607'						
38	b-75-F/94-J-9	6610'						
39	a-63-J/94-J-9	1965.50 m						
40	a-63-J/94-J-9	1966.50 m						
41	a-63-J/94-J-9	1968.20 m	X					
42	a-63-J/94-J-9	1969.40 m						
43	a-63-J/94-J-9	1969.80 m	X					
44	a-63-J/94-J-9	1970.55 m						
45	a-63-J/94-J-9	1972.50 m						
46	a-63-J/94-J-9	1973.20 m	X	X	X			
47	a-63-J/94-J-9	1974.50 m						
48	a-63-J/94-J-9	1976.30 m						
49	a-63-J/94-J-9	1976.60 m						
50	a-63-J/94-J-9	1977.40 m						

	Well Location - NTS	Depth	TS	SI	RI	TE	FIM	FICL
51	a-63-J/94-J-9	1978.10 m	X					
52	a-63-J/94-J-9	1981.30 m						
53	a-63-J/94-J-9	1981.70 m	X					
54	a-63-J/94-J-9	1982.10 m						
55	a-63-J/94-J-9	1984.10 m	X					
56	a-63-J/94-J-9	1987.10 m						
57	a-63-J/94-J-9	1988.90 m	X					
58	b-78-J/94-J-9	6207'	X					
59	b-78-J/94-J-9	6220'3"	X					
60	b-78-J/94-J-9	6222'9"						
61	b-78-J/94-J-9	6227'8"						
62	b-78-J/94-J-9	6235'						
63	b-78-J/94-J-9	6235'8"	X					
64	b-78-J/94-J-9	6239'6"						
65	b-78-J/94-J-9	6272'	X					
66	b-78-J/94-J-9	6274'						
67	b-78-J/94-J-9	6276'						
68	b-78-J/94-J-9	6278'						
69	b-78-J/94-J-9	6285'						
70	b-78-J/94-J-9	6294'6"						
71	b-78-J/94-J-9	6298'	X					
72	b-78-J/94-J-9	6304'3"						
73	b-78-J/94-J-9	6309'						
74	b-78-J/94-J-9	6311'6"	X					
75	b-78-J/94-J-9	6314'4"						
76	b-78-J/94-J-9	6319'6"	X					
77	b-78-J/94-J-9	6330'	X					
78	b-78-J/94-J-9	6437'	X					
79	b-78-J/94-J-9	6439'						
80	b-78-J/94-J-9	6439'9"						
81	b-78-J/94-J-9	6440'6"						
82	b-78-J/94-J-9	6446'9"						
83	b-78-J/94-J-9	6452'						
84	b-78-J/94-J-9	6456'8"						
85	b-78-J/94-J-9	6460'						
86	b-78-J/94-J-9	6464'9"	X					
87	b-78-J/94-J-9	6473'8"						
88	b-78-J/94-J-9	6475'6"						
89	b-78-J/94-J-9	6482'						
90	b-78-J/94-J-9	6484'6"						
91	b-78-J/94-J-9	6487'						
92	b-78-J/94-J-9	6489'	X	X				
93	a-81-J/94-J-9	1907.40 m	X					
94	a-81-J/94-J-9	1907.50 m						
95	a-81-J/94-J-9	1908.55 m						
96	a-81-J/94-J-9	1909.30 m						
97	a-81-J/94-J-9	1909.70 m						
98	a-81-J/94-J-9	1910.75 m	X					
99	a-81-J/94-J-9	1911.20 m	X					
100	a-81-J/94-J-9	1913.80 m						

	Well Location - NTS	Depth	TS	SI	RI	TE	FIM	FICL
101	a-81-J/94-J-9	1914.55 m						
102	a-81-J/94-J-9	1916.20 m						
103	a-81-J/94-J-9	1916.50 m						
104	a-81-J/94-J-9	1917.10 m						
105	a-81-J/94-J-9	1917.60 m						
106	a-81-J/94-J-9	1919.10 m	X					
107	a-81-J/94-J-9	1919.85 m	X					
108	a-81-J/94-J-9	1920.80 m	X					
109	a-81-J/94-J-9	1921.20 m	X					
110	c-56-L/94-J-9	6352'						
111	c-56-L/94-J-9	6358'		X	X	X	X	X
112	c-56-L/94-J-9	6369'	X	X		X		
113	c-56-L/94-J-9	6381'6"	X					
114	c-56-L/94-J-9	6386'6"				X		
115	c-56-L/94-J-9	6387'3"	X	X				
116	c-56-L/94-J-9	6392'6"	X	X		X		
117	c-56-L/94-J-9	6408'		X	X	X		
118	c-56-L/94-J-9	6412'	X	X	X	X		
119	c-56-L/94-J-9	6416'	X					
120	c-56-L/94-J-9	6419'9"						
121	c-56-L/94-J-9	6427'	X	X		X		
122	c-56-L/94-J-9	6430'						
123	c-56-L/94-J-9	6433'						
124	c-56-L/94-J-9	6438'						
125	c-56-L/94-J-9	6447'						
126	c-56-L/94-J-9	6452'	X			X		
127	c-56-L/94-J-9	6454'						
128	c-56-L/94-J-9	6471'						
129	c-56-L/94-J-9	6476'						
130	c-56-L/94-J-9	6486'	X	X	X	X		
131	c-56-L/94-J-9	6489'						
132	c-56-L/94-J-9	6498'9"						
133	c-56-L/94-J-9	6504'6"	X	X	X	X	X	X
134	c-56-L/94-J-9	6507'9"	X					
135	c-56-L/94-J-9	6508'						
136	c-56-L/94-J-9	6514'6"						
137	c-56-L/94-J-9	6522'						
138	c-56-L/94-J-9	6524'						
139	c-56-L/94-J-9	6529'						
140	c-56-L/94-J-9	6530'	X					
141	c-56-L/94-J-9	6531'						
142	c-56-L/94-J-9	6535'						
143	c-56-L/94-J-9	6536'6"						
144	c-56-L/94-J-9	6539'6"						
145	c-56-L/94-J-9	6543'						
146	c-56-L/94-J-9	6545'	X	X		X		
147	c-56-L/94-J-9	6547'						
148	c-56-L/94-J-9	6554'6"						
149	c-56-L/94-J-9	6556'9"	X					
150	b-72-L/94-J-9	6241'	X					

	Well Location - NTS	Depth	TS	SI	RI	TE	FIM	FICL
151	b-72-L/94-J-9	6243'						
152	b-72-L/94-J-9	6245'	X					
153	b-72-L/94-J-9	6246'9"						
154	b-72-L/94-J-9	6249'6"	X	X				
155	d-91-L/94-J-9	6291'						
156	d-91-L/94-J-9	6293'6"						
157	d-91-L/94-J-9	6296'		X				
158	d-91-L/94-J-9	6298'						
159	d-91-L/94-J-9	6300'6"						
160	d-91-L/94-J-9	6457'						
161	d-91-L/94-J-9	6460'		X				
162	d-91-L/94-J-9	6461'						
163	d-91-L/94-J-9	6466'	X	X	X			
164	d-91-L/94-J-9	6468'9"						
165	d-91-L/94-J-9	6469'6"						
166	d-91-L/94-J-9	6477'4"						
167	d-91-L/94-J-9	6477'9"						
168	d-91-L/94-J-9	6479'	X					
169	d-91-L/94-J-9	6491'6"						
170	c-94-L/94-J-9	6356'	X					
171	c-94-L/94-J-9	6357'	X	X	X		X	X
172	c-94-L/94-J-9	6361'6"						
173	c-94-L/94-J-9	6362'	X	X				
174	c-94-L/94-J-9	6364'						
175	c-94-L/94-J-9	6372'	X					
176	c-94-L/94-J-9	6402'						
177	c-94-L/94-J-9	6406'	X					
178	c-94-L/94-J-9	6413'		X				
179	c-94-L/94-J-9	6415'	X					
180	c-94-L/94-J-9	6419'6"						
181	c-94-L/94-J-9	6421'	X	X	X			
182	c-94-L/94-J-9	6422'						
183	c-94-L/94-J-9	6426'	X					
184	c-94-L/94-J-9	6444'						
185	c-94-L/94-J-9	6446'						
186	c-94-L/94-J-9	6449'	X					
187	c-94-L/94-J-9	6454'	X	X	X	X	X	X
188	c-94-L/94-J-9	6458'	X					
189	c-94-L/94-J-9	6462'						
190	c-94-L/94-J-9	6466'	X					
191	c-94-L/94-J-9	6470'						
192	c-94-L/94-J-9	6474'						
193	c-94-L/94-J-9	6476'	X					
194	c-94-L/94-J-9	6482'	X	X				
195	c-94-L/94-J-9	6485'						
196	c-94-L/94-J-9	6491'	X					
197	c-94-L/94-J-9	6505'						
198	c-94-L/94-J-9	6525'	X	X	X			
199	c-94-L/94-J-9	6530'						
200	c-94-L/94-J-9	6535'	X	X				

	Well Location - NTS	Depth	TS	SI	RI	TE	FIM	FICL
201	c-94-L/94-J-9	6540'						
202	c-94-L/94-J-9	6541'						
203	c-94-L/94-J-9	6544'						
204	c-58-E/94-J-10	2152.25 m	X				X	
205	c-58-E/94-J-10	2152.40 m	X					
206	c-58-E/94-J-10	2152.85 m	X					
207	c-58-E/94-J-10	2153.00 m						
208	c-58-E/94-J-10	2153.25 m	X	X	X			
209	a-61-F/94-J-10	6702'	X					
210	a-61-F/94-J-10	6705'6"	X					
211	a-61-F/94-J-10	6706'	X	X				
212	a-61-F/94-J-10	6706'6"	X					
213	a-61-F/94-J-10	6711'	X					
214	a-61-F/94-J-10	6713'						
215	a-61-F/94-J-10	6714'	X	X				
216	a-61-F/94-J-10	6716'3"	X					
217	a-61-F/94-J-10	6716'8"						
218	a-61-F/94-J-10	6717'3"	X					
219	a-61-F/94-J-10	6718'	X					
220	a-61-F/94-J-10	6721'3"	X	X	X			
221	d-79-F/94-J-10	6757'						
222	d-79-F/94-J-10	6757'6"	X					
223	d-79-F/94-J-10	6759'	X					
224	d-79-F/94-J-10	6760'	X					
225	d-79-F/94-J-10	6762'	X					
226	d-79-F/94-J-10	6763'						
227	d-79-F/94-J-10	6765'	X	X	X	X		
228	d-79-F/94-J-10	6766'	X					
229	d-79-F/94-J-10	6769'	X	X	X	X	X	X
230	d-79-F/94-J-10	6771'	X	X				
231	d-79-F/94-J-10	6772'						
232	d-79-F/94-J-10	6773'6"	X			X		
233	d-79-F/94-J-10	6776'						
234	d-79-F/94-J-10	6778'3"	X	X	X	X		X
235	d-79-F/94-J-10	6780'	X					
236	d-79-F/94-J-10	6781'						
237	d-79-F/94-J-10	6784'6"	X					
238	d-79-F/94-J-10	6785'	X	X	X	X	X	X
239	d-79-F/94-J-10	6788'	X	X		X		
240	d-79-F/94-J-10	6789'	X					
241	a-63-G/94-J-10	6661'						
242	a-63-G/94-J-10	6672'6"	X					
243	a-63-G/94-J-10	6673'9"	X					
244	a-63-G/94-J-10	6677'	X					
245	a-63-G/94-J-10	6682'	X					
246	a-63-G/94-J-10	6689'	X					
247	a-63-G/94-J-10	6696'6"	X					
248	a-63-G/94-J-10	6711'	X					
249	a-63-G/94-J-10	6723'						
250	a-63-G/94-J-10	6725'6"	X					

	Well Location - NTS	Depth	TS	SI	RI	TE	FIM	FICL
251	a-63-G/94-J-10	6731'	X					
252	a-63-G/94-J-10	6734'						
253	a-63-G/94-J-10	6735'6"						
254	a-63-G/94-J-10	6740'	X					
255	a-63-G/94-J-10	6748'6"	X					
256	a-63-G/94-J-10	6750'	X					
257	a-63-G/94-J-10	6756'	X					
258	d-72-G/94-J-10	6414'	X	X	X	X		
259	d-72-G/94-J-10	6415'						
260	d-72-G/94-J-10	6418'	X					
261	d-72-G/94-J-10	6421'	X					
262	d-72-G/94-J-10	6427'						
263	d-72-G/94-J-10	6429'	X					
264	d-72-G/94-J-10	6433'						
265	d-72-G/94-J-10	6435'	X					
266	d-72-G/94-J-10	6443'6"	X					
267	d-72-G/94-J-10	6448'	X					
268	d-72-G/94-J-10	6449'	X	X	X		X	X
269	d-72-G/94-J-10	6450'	X	X	X			
270	d-72-G/94-J-10	6452'	X					
271	a-83-G/94-J-10	1930.40 m						
272	a-83-G/94-J-10	1931.00 m						
273	a-83-G/94-J-10	1931.50 m	X					
274	d-69-H/94-J-10	6526'6"						
275	d-69-H/94-J-10	6531'	X	X	X			
276	d-69-H/94-J-10	6532'6"						
277	d-69-H/94-J-10	6538'	X					
278	d-69-H/94-J-10	6540'	X					
279	d-69-H/94-J-10	6542'						
280	d-69-H/94-J-10	6544'	X					
281	d-69-H/94-J-10	6557'	X					
282	d-69-H/94-J-10	6560'						
283	d-69-H/94-J-10	6562'	X					
284	d-69-H/94-J-10	6568'	X					
285	c-64-I/94-J-10	6423'	X					
286	c-64-I/94-J-10	6424'8"	X					
287	c-64-I/94-J-10	6425'6"						
288	c-64-I/94-J-10	6426'6"						
289	c-64-I/94-J-10	6427'3"	X					
290	c-64-I/94-J-10	6428'3"	X					
291	c-64-I/94-J-10	6430'	X					
292	c-64-I/94-J-10	6434'	X	X	X			
293	c-64-I/94-J-10	6437'						
294	c-64-I/94-J-10	6439'	X					
295	c-64-I/94-J-10	6440'9"	X					
296	c-64-I/94-J-10	6446'9"	X					
297	b-70-I/94-J-10	6262'	X	X	X			X
298	b-70-I/94-J-10	6263'						
299	b-70-I/94-J-10	6265'	X	X	X			
300	b-70-I/94-J-10	6266'						

	Well Location - NTS	Depth	TS	SI	RI	TE	FIM	FICL
301	b-70-I/94-J-10	6267'6"	X					
302	b-70-I/94-J-10	6272'						
303	b-70-I/94-J-10	6278'	X					
304	b-70-I/94-J-10	6282'						
305	b-70-I/94-J-10	6284'	X					
306	c-78-I/94-J-10	6183'	X					
307	b-22-J/94-J-10	6536'	X	X	X			
308	b-22-J/94-J-10	6538'	X	X	X			
309	b-22-J/94-J-10	6539'6"	X					
310	c-47-J/94-J-10	6550'6"	X					
311	c-47-J/94-J-10	6551'	X					
312	c-47-J/94-J-10	6552'	X					
313	c-47-J/94-J-10	6553'9"						
314	c-47-J/94-J-10	6557'3"	X					
315	c-47-J/94-J-10	6565'	X					
316	a-95-J/94-J-10	7787'	X					
317	a-95-J/94-J-10	7788'						
318	b-6-A/94-J-16	6321'						
319	b-6-A/94-J-16	6327'	X					
320	b-6-A/94-J-16	6337'						
321	b-6-A/94-J-16	6339'6"	X	X	X	X	X	X
322	b-6-A/94-J-16	6346'						
323	b-6-A/94-J-16	6348'						
324	b-6-A/94-J-16	6349'	X	X	X	X		
325	b-6-A/94-J-16	6351'6"	X	X				
326	b-6-A/94-J-16	6363'6"						
327	b-6-A/94-J-16	6370'						
328	b-6-A/94-J-16	6379'6"	X			X		
329	b-6-A/94-J-16	6383'						
330	b-6-A/94-J-16	6387'						
331	b-6-A/94-J-16	6393'						
332	b-6-A/94-J-16	6395'						
333	b-6-A/94-J-16	6396'6"						
334	b-6-A/94-J-16	6405'	X					
335	b-6-A/94-J-16	6408'6"				X		
336	b-6-A/94-J-16	6419'						
337	b-6-A/94-J-16	6425'						
338	b-6-A/94-J-16	6433'	X					
339	b-6-A/94-J-16	6434'6"						
340	b-6-A/94-J-16	6442'						
341	b-6-A/94-J-16	6447'	X	X	X	X		
342	b-12-A/94-J-16	1888.70 m						
343	b-12-A/94-J-16	1889.30 m	X					
344	b-12-A/94-J-16	1889.60 m						
345	b-12-A/94-J-16	1891.40 m						
346	b-12-A/94-J-16	1891.60 m						
347	b-12-A/94-J-16	1892.40 m						
348	b-12-A/94-J-16	1893.00 m	X					
349	b-12-A/94-J-16	1893.50 m						
350	b-12-A/94-J-16	1896.30 m						

	Well Location - NTS	Depth	TS	SI	RI	TE	FIM	FICL
351	b-12-A/94-J-16	1898.90 m						
352	b-12-A/94-J-16	1900.00 m	X					
353	b-12-A/94-J-16	1900.80 m						
354	b-12-A/94-J-16	1902.20 m	X					
355	b-12-A/94-J-16	1904.50 m						
356	c-8-D/94-J-16	6307'	X					
357	c-8-D/94-J-16	6311'	X					
358	c-8-D/94-J-16	6313'6"						
359	c-8-D/94-J-16	6315'	X					
360	c-8-D/94-J-16	6317'	X					
361	c-8-D/94-J-16	6319'	X	X				
362	c-8-D/94-J-16	6319'6"	X					
363	c-8-D/94-J-16	6345'	X					
364	c-8-D/94-J-16	6346'6"	X					
365	c-8-D/94-J-16	6347'6"	X					
366	c-8-D/94-J-16	6437'9"	X				X	X
367	c-8-D/94-J-16	6438'6"	X					
368	b-10-D/94-J-16	6259'	X					
369	b-10-D/94-J-16	6262'	X					
370	b-10-D/94-J-16	6263'						
371	b-10-D/94-J-16	6265'	X					
372	b-10-D/94-J-16	6267'	X					
373	b-10-D/94-J-16	6268'	X	X	X	X	X	X
374	b-10-D/94-J-16	6269'6"	X	X				
375	b-10-D/94-J-16	6271'						
376	b-10-D/94-J-16	6272'6"	X					
377	b-10-D/94-J-16	6286'6"	X					
378	b-10-D/94-J-16	6290'	X	X	X	X		
379	b-10-D/94-J-16	6291'	X	X	X		X	X
380	b-10-D/94-J-16	6292'3"						
381	b-10-D/94-J-16	6292'8"	X					
382	b-10-D/94-J-16	6294'	X	X	X	X		
383	b-10-D/94-J-16	6297'6"	X					

APPENDIX IV

List of stable and radiogenic isotope results.

Well Location - NTS	Depth	Sample ID	Description	$\delta^{18}O$	$\delta^{13}C$	$^{87}Sr/^{86}Sr$
c-70-E/94-J-9	6374'6"	JL-58	limestone - micrite	-11.97	+1.51	
c-70-E/94-J-9	6449'3"	JL-81	limestone - micrite	-9.47	+2.19	
c-56-L/94-J-9	6427'	JL-43	limestone - micrite	-13.47	-0.55	
c-56-L/94-J-9	6545'	JL-82	limestone - micrite	-13.31	-0.45	
c-94-L/94-J-9	6535'	JL-59	limestone - micrite	-12.95	+0.31	
d-69-H/94-J-10	6531'	JL-16	limestone - micrite	-13.43	-1.54	0.70900 +/- 1
b-6-A/94-J-16	6349'	JL-71	limestone - micrite	-9.69	+0.94	0.70827 +/- 2
c-70-E/94-J-9	6384'	JL-83	fossil - brachiopod	-10.69	+0.34	
c-70-E/94-J-9	6384'	JL-84	fossil - crinoid	-7.77	+1.21	
c-70-E/94-J-9	6449'3"	JL-85	fossil - amphipora	-8.78	+1.12	
b-49-F/94-J-9	6475'8"	JL-35	fossil - stromatoporoid	-7.06	1.12	
b-78-J/94-J-9	6489'	JL-36	fossil - stromatoporoid	-11.07	+0.64	
c-56-L/94-J-9	6427'	JL-44	fossil - amphipora	-11.77	+0.08	
c-56-L/94-J-9	6486'	JL-60	fossil - stromatoporoid	-7.26	+2.16	0.70795 +/- 1
d-91-L/94-J-9	6296'	JL-61	fossil - stromatoporoid	-8.11	+0.31	
d-91-L/94-J-9	6460'	JL-86	fossil - stromatoporoid	-11.74	-0.34	
c-94-L/94-J-9	6525'	JL-62	fossil - stromatoporoid	-12.40	-0.30	0.71072 +/- 2
c-64-I/94-J-10	6434'	JL-17	fossil - stromatoporoid	-8.50	+1.91	0.70800 +/- 2
b-6-A/94-J-16	6351'6"	JL-31	fossil - thamnopora	-3.67	+3.09	
c-70-E/94-J-9	6423'	JL-69	sheared calcite cement	-14.51	+1.65	0.70882 +/- 2
b-78-J/94-J-9	6489'	JL-37	calcite vein	-12.72	+1.56	
c-56-L/94-J-9	6408'	JL-70	late calcite cement	-14.83	-3.02	0.71095 +/- 2
c-56-L/94-J-9	6412'	JL-38	late calcite cement	-17.00	-2.18	0.71005 +/- 1
c-56-L/94-J-9	6504'6"	JL-72	late calcite cement	-16.29	-1.91	0.71014 +/- 2
d-79-F/94-J-10	6769'	JL-74	fracture-fill calcite cement	-11.23	-2.04	0.71871 +/- 3
b-22-J/94-J-10	6538'	JL-23	calcite vein	-14.20	-2.09	
b-6-A/94-J-16	6339'6"	JL-73	calcite vein	-13.78	+0.88	0.70849 +/- 1
b-6-A/94-J-16	6351'6"	JL-32	calcite cement - shelter cavity	-9.96	+1.20	
b-6-A/94-J-16	6447'	JL-33	fracture-fill calcite cement	-14.58	-1.05	0.70974 +/- 1
a-63-J/94-J-9	1973.20 m	JL-34	early fine-crystalline dolomite	-12.43	+2.72	0.70899 +/- 1
c-56-L/94-J-9	6358'	JL-51	matrix dolomite	-15.35	-0.79	0.70969 +/- 2
c-56-L/94-J-9	6369'	JL-87	matrix dolomite	-16.73	-0.89	
c-56-L/94-J-9	6392'6"	JL-39	matrix dolomite	-15.43	-0.72	
b-72-L/94-J-9	6249'6"	JL-63	matrix dolomite	-15.50	-0.82	
d-91-L/94-J-9	6466'	JL-64	matrix dolomite	-14.89	-0.72	0.71027 +/- 1
c-94-L/94-J-9	6357'	JL-48	planar-s matrix dolomite	-15.08	-0.95	0.70953 +/- 2
c-94-L/94-J-9	6362'	JL-65	matrix dolomite	-16.05	-1.15	
c-94-L/94-J-9	6413'	JL-88	matrix dolomite	-15.89	-1.20	
c-94-L/94-J-9	6421'	JL-41	matrix dolomite	-14.82	-0.99	0.70932 +/- 1
c-94-L/94-J-9	6454'	JL-47	planar-s matrix dolomite	-15.53	-0.91	0.70963 +/- 2
c-94-L/94-J-9	6482'	JL-89	matrix dolomite	-16.08	-1.32	
c-58-E/94-J-10	2153.25 m	JL-56	matrix dolomite	-14.29	-2.03	0.71098 +/- 1
a-61-F/94-J-10	6714'	JL-2	planar-s to non-planar matrix	-13.46	-0.51	
a-61-F/94-J-10	6721'3"	JL-3	matrix - zebra dolomite	-13.79	-0.79	0.70918 +/- 1
d-79-F/94-J-10	6765'	JL-9	fine-crystalline matrix dolomite	-14.19	-0.31	0.71288 +/- 1
d-79-F/94-J-10	6765'	JL-10	planar-s matrix dolomite	-14.72	-0.81	0.71307 +/- 1
d-79-F/94-J-10	6769'	JL-75	matrix dolomite	-13.00	-1.29	0.71244 +/- 2
d-79-F/94-J-10	6771'	JL-11	planar-e b/w breccia clasts	-14.16	-1.28	
d-79-F/94-J-10	6778'3"	JL-7	planar matrix dolomite	-14.11	-1.33	0.71648 +/- 2
d-79-F/94-J-10	6785'	JL-45	planar-s matrix dolomite	-14.54	-1.10	0.71119 +/- 2
d-79-F/94-J-10	6788'	JL-6	planar-e breccia clast	-14.43	-1.24	
d-72-G/94-J-10	6414'	JL-13	matrix dolomite	-13.78	-0.93	0.70886 +/- 1
d-72-G/94-J-10	6449'	JL-55	matrix dolomite	-13.71	-0.87	0.70955 +/- 1
d-72-G/94-J-10	6450'	JL-14	salt & pepper dolomite	-13.81	-0.87	0.70928 +/- 2
b-70-I/94-J-10	6265'	JL-19	very fine-crystalline matrix	-13.49	-0.63	0.70988 +/- 2
b-70-I/94-J-10	6265'	JL-18	planar-e matrix dolomite	-13.73	-0.90	0.71014 +/- 1
b-22-J/94-J-10	6536'	JL-21	medium-crystalline matrix	-14.53	-1.55	0.70918 +/- 1
b-22-J/94-J-10	6538'	JL-22	fine-crystalline matrix dolomite	-14.78	-1.86	0.71674 +/- 1
b-6-A/94-J-16	6349'	JL-76	early fine-crystalline dolomite	-12.05	+1.59	0.70933 +/- 2
c-8-D/94-J-16	6319'	JL-24	fine-crystalline matrix dolomite	-12.92	+0.93	
c-8-D/94-J-16	6319'	JL-25	medium-crystalline matrix	-15.34	-2.15	

b-10-D/94-J-16	6268'	JL-1	salt & pepper dolomite	-14.05	-0.96	0.71034 +/- 1
b-10-D/94-J-16	6269'6"	JL-28	matrix dolomite	-13.99	-0.87	
b-10-D/94-J-16	6290'	JL-30	planar-s matrix dolomite	-14.00	-0.82	0.70969 +/- 1
b-10-D/94-J-16	6291'	JL-54	matrix dolomite	-14.05	-0.93	0.70899 +/- 1
b-10-D/94-J-16	6294'	JL-77	matrix dolomite	-14.04	-1.01	0.70987 +/- 1
c-56-L/94-J-9	6358'	JL-52	early saddle dolomite	-15.26	-1.21	0.70951 +/- 1
c-56-L/94-J-9	6358'	JL-53	late saddle dolomite	-14.51	-1.61	0.71008 +/- 2
c-56-L/94-J-9	6387'3"	JL-90	saddle dolomite	-16.12	-2.29	
c-56-L/94-J-9	6412'	JL-66	saddle dolomite - vein	-15.47	-0.45	0.70967 +/- 1
c-56-L/94-J-9	6504'6"	JL-78	saddle dolomite - vein	-15.01	-0.18	0.70926 +/- 2
d-91-L/94-J-9	6466'	JL-42	saddle dolomite	-15.25	-0.28	0.70904 +/- 1
c-94-L/94-J-9	6357'	JL-49	saddle dolomite - vein	-14.95	-1.15	0.71111 +/- 2
c-94-L/94-J-9	6362'	JL-40	saddle dolomite - vein	-15.08	-1.42	
c-94-L/94-J-9	6413'	JL-67	saddle dolomite	-15.80	-1.20	
c-94-L/94-J-9	6454'	JL-68	saddle dolomite	-16.10	-0.24	0.71005 +/- 2
c-58-E/94-J-10	2153.25 m	JL-57	saddle dolomite	-14.44	-1.43	0.71284 +/- 2
a-61-F/94-J-10	6706'	JL-5	saddle dolomite	-13.59	-0.74	
a-61-F/94-J-10	6721'3"	JL-4	saddle dolomite - zebra dolomite			0.71050 +/- 2
d-79-F/94-J-10	6769'	JL-50	saddle dolomite - vein	-14.29	-0.66	0.71507 +/- 1
d-79-F/94-J-10	6778'3"	JL-8	saddle dolomite - vein	-14.46	-0.74	0.71649 +/- 1
d-79-F/94-J-10	6785'	JL-46	saddle dolomite - vein	-14.40	-0.26	0.71365 +/- 1
d-72-G/94-J-10	6414'	JL-12	saddle dolomite	-13.81	-0.94	0.70874 +/- 2
d-69-H/94-J-10	6531'	JL-15	saddle dolomite in amphipora	-14.38	-1.32	0.71000 +/- 1
b-70-I/94-J-10	6262'	JL-79	saddle dolomite	-14.03	-1.16	0.71008 +/- 2
b-22-J/94-J-10	6536'	JL-20	saddle dolomite - vein	-15.09	-1.80	0.70969 +/- 1
b-22-J/94-J-10	6538'	JL-23	saddle dolomite - vein in breccia	-13.98	-0.68	
c-8-D/94-J-16	6319'	JL-26	saddle dolomite - vein	-15.21	-1.16	
b-10-D/94-J-16	6269'6"	JL-27	saddle dolomite in strom	-14.61	-1.25	
b-10-D/94-J-16	6290'	JL-29	saddle dolomite	-14.42	-1.29	0.71016 +/- 2
b-10-D/94-J-16	6294'	JL-80	saddle dolomite	-13.99	-0.93	0.70923 +/- 2

APPENDIX V

List of whole rock trace element results.

Well Location		b-10-D/94-J-16	d-79-F/94-J-10	d-79-F/94-J-10	d-79-F/94-J-10	d-79-F/94-J-10	d-72-G/94-J-10
Depth		6268'	6788'	6778'3"	6778'3"	6765'	6414'
Description		matrix dolomite	matrix dolomite	matrix dolomite	saddle dolomite	matrix dolomite	saddle dolomite
Sample ID		JL-1	JL-6	JL-7	JL-8	JL-10	JL-12
Ca	wt %	22.0	20.6	20.2	19.7	20	20.8
Mg	wt %	12.9	11.8	11.6	11.0	11.5	12.4
Al	µg/g	161	523	1010	406	2327	276
As	µg/g	1.23	1.14	2.12	2.49	8.83	0.066
Ba	µg/g	57.7	24.9	17.9	47.9	22.7	57.3
Br	µg/g	1.20	0.63	0.46	0.89	0.39	1.30
Ce	µg/g	2.83	1.31	0.83	2.33	1.9	1.52
Cl	µg/g	420	535	549	677	312	591
Co	ng/g	256	216	555	112	761	213
Cr	µg/g	1.06	1.75	2.21	1.51	2.76	0.45
Eu	ng/g	111	144	104	236	131	64.8
Fe	µg/g	341	730	944	1440	2177	41
Hf	ng/g	39.8	19	59.6	≤ 4	107	9.3
K	µg/g	49	112	404	101	975	83
La	µg/g	1.80	0.71	0.38	0.89	0.865	0.66
Lu	ng/g	13.8	60	11.0	46.8	31	14.7
Mn	µg/g	484	1483	1340	1590	1010	377
Na	µg/g	235	66.7	209	361	51.2	260
Rb	µg/g	0.13	0.45	1.22	0.30	2.36	≤ 0.2
Sb	µg/g	0.148	0.18	0.113	0.020	0.122	0.025
Sc	ng/g	52.0	279	199	388	406	14.8
Sm	µg/g	0.37	0.278	0.43	0.59	0.48	0.31
Sr	µg/g	42	121	72	95	57	32
Ta	ng/g	13	10.3	11.4	≤ 2	24.9	≤ 2
Tb	ng/g	59	ND	51	109	64.9	54
Th	ng/g	49	78	86	173	178	32
U	µg/g	9.14	0.96	1.89	≤ 0.03	3.3	≤ 0.03
V	µg/g	26.4	4.7	10.4	4.33	14.2	0.44
Yb	µg/g	0.126	0.08	0.167	0.273	0.21	0.144
Zn	µg/g	3.18	8149	91.0	1.84	192	1.79
CaCO3	mol-%	50.74	51.16	51.02	51.67	50.78	50.40
MgCO3	mol-%	49.04	48.30	48.30	47.55	48.13	49.41

Well Location		d-72-G/94-J-10	b-10-D/94-J-16	b-10-D/94-J-16	b-6-A/94-J-16	c-56-L/94-J-9	c-56-L/94-J-9
Depth		6414'	6290'	6290'	6447'	6412'	6392'6"
Description		matrix dolomite	saddle dolomite	matrix dolomite	calcite vein	calcite cement	matrix dolomite
Sample ID		JL-13	JL-29	JL-30	JL-33	JL-38	JL-39
Ca	wt %	21.9	21.4	21.5	38.9	38.9	21.3
Mg	wt %	12.9	13	12.8	0.09	0.24	12.6
Al	µg/g	548	149	214	87	5	1053
As	µg/g	0.43	0.17	0.47	1.33	0.11	1.15
Ba	µg/g	24.1	37.2	11.2	698	4.6	9.2
Br	µg/g	1.08	0.85	0.96	0.05	0.04	1.19
Ce	µg/g	4.92	2.44	5	0.28	7.43	1.52
Cl	µg/g	544	502	474	< 80	< 110	1321
Co	ng/g	133	73.8	35	152	46	182
Cr	µg/g	2.03	0.78	0.99	0.76	0.31	1.75
Eu	ng/g	158	85	195	11.2	763	120
Fe	µg/g	191	91	84	55	9	321
Hf	ng/g	88.4	11.3	7	15	69.4	43
K	µg/g	212	41	68	30	19	406
La	µg/g	3.03	1.34	3.06	0.24	5.1	0.771
Lu	ng/g	13.0	11.5	38	< 5	3.5	15
Mn	µg/g	360	550	400	46.8	135	898
Na	µg/g	237	52.1	53	6.5	5.54	69.3
Rb	µg/g	0.69	0.07	0.13	0.06	ND	0.71
Sb	µg/g	0.028	12.6	0.019	15.2	3.4	0.091
Sc	ng/g	89.5	44.1	44	9.9	4.7	214
Sm	µg/g	0.64	0.297	0.8	0.024	1.05	0.35
Sr	µg/g	38	43	37	147	218	37
Ta	ng/g	6.2	ND	ND	3.6	ND	11.8
Tb	ng/g	80	40	120.7	4.4	134.5	58.2
Th	ng/g	58	8.6	25	12.2	5.1	87
U	µg/g	3.09	2.78	1.65	ND	0.29	1.61
V	µg/g	4.13	1.66	6.71	0.59	0.44	6.4
Yb	µg/g	0.144	0.103	0.244	0.014	0.184	0.13
Zn	µg/g	1.64	23.8	2	1.3	12	1
CaCO3	mol-%	50.57	49.89	50.40	99.57	98.94	50.42
MgCO3	mol-%	49.18	49.96	49.46	0.38	1.01	49.16

Well Location		c-56-L/94-J-9	d-79-F/94-J-10	d-79-F/94-J-10	c-94-L/94-J-9	d-79-F/94-J-10	c-56-L/94-J-9
Depth		6427'	6785'	6785'	6454'	6769'	6358'
Description		micrite	matrix dolomite	saddle dolomite	matrix dolomite	saddle dolomite	matrix dolomite
Sample ID		JL-43	JL-45	JL-46	JL-47	JL-50	JL-51
Ca	wt %	35.3	21.7	19.7	22.6	19.9	21.2
Mg	wt %	0.29	12.2	11.1	13.2	11.4	12.5
Al	µg/g	814	932	223	481	393	1046
As	µg/g	2.35	4.63	0.87	0.081	3.77	2.01
Ba	µg/g	11.8	18.2	100500	55.0	15.6	17
Br	µg/g	0.18	0.61	0.5	1.73	0.74	0.83
Ce	µg/g	2.26	1.69	1.47	3.34	2.4	3.03
Cl	µg/g	274	473	468	749	606	583
Co	ng/g	34100	223	53.2	41.7	283	258
Cr	µg/g	0.98	2.09	4.68	0.72	0.52	2.78
Eu	ng/g	325	137	231	189	409	225
Fe	µg/g	916	1298	888	72	767	691
Hf	ng/g	47	35	ND	76.2	ND	356
K	µg/g	377	350	68	95	96	384
La	µg/g	1.48	0.57	0.74	2.18	0.84	1.219
Lu	ng/g	< 14	54	27.8	20.8	39	56
Mn	µg/g	220	1043	1225	630	1310	1001
Na	µg/g	17	64.6	63.9	353	71	73
Rb	µg/g	0.56	0.9	0.34	≤ 0.3	0.22	1.35
Sb	µg/g	0.099	0.064	535.4	0.051	0.045	0.104
Sc	ng/g	104	241	361	61.1	100	581
Sm	µg/g	0.426	0.45	0.34	0.53	0.75	0.54
Sr	µg/g	155	64	370	63	242	59
Ta	ng/g	195	9.1	ND	≤ 2	ND	12.5
Tb	ng/g	65.6	111	73.3	85	145	100
Th	ng/g	83	175	105	69	58	214
U	µg/g	1.22	0.16	11.05	2.55	0.1	0.97
V	µg/g	3.15	4.25	7.37	8.17	2.1	12
Yb	µg/g	0.134	0.379	0.226	0.160	0.367	0.295
Zn	µg/g	3.9	227	195	3.51	3.4	7.3
CaCO3	mol-%	98.23	51.59	51.58	50.76	51.17	50.45
MgCO3	mol-%	1.33	47.80	47.90	48.97	48.31	49.03

Well Location		c-56-L/94-J-9	c-56-L/94-J-9	c-56-L/94-J-9	c-94-L/94-J-9	c-70-E/94-J-9	c-56-L/94-J-9
Depth		6358'	6486'	6412'	6454'	6423'	6408'
Description		saddle dolomite	stromatoporoid	saddle dolomite	saddle dolomite	calcite vein	calcite cement
Sample ID		JL-53	JL-60	JL-66	JL-68	JL-69	JL-70
Ca	wt %	23.4	39.1	22.1	22.5	39.2	37.2
Mg	wt %	12.8	0.64	12.3	12.6	0.21	1.54
Al	µg/g	466	46	301	264	22	31
As	µg/g	1.75	0.25	0.23	0.067	0.36	0.18
Ba	µg/g	8.8	20.3	8.4	18.2	2939	4.5
Br	µg/g	0.39	0.36	0.55	0.84	0.1	0.16
Ce	µg/g	6.05	1.26	3.15	3.10	1.24	3.86
Cl	µg/g	246	145	413	455	117	217
Co	ng/g	121	12000	124	14.6	27.3	40
Cr	µg/g	0.58	2.19	0.25	0.12	0.28	0.55
Eu	ng/g	886	33.5	516	309	47.7	398
Fe	µg/g	1108	141	335	37	18	65
Hf	ng/g	26	ND	42	≤ 4	3.4	7
K	µg/g	28	46	22	34	22	23
La	µg/g	2.05	0.47	1.22	2.00	0.81	1.9
Lu	ng/g	135	17	62	11.9	< 12	21
Mn	µg/g	1430	29.1	1617	901	290	348
Na	µg/g	37.1	45.5	58	290	8.6	19.2
Rb	µg/g	ND	0.03	ND	≤ 0.1	ND	ND
Sb	µg/g	0.054	0.019	0.013	0.012	6.4	0.009
Sc	ng/g	160	45	48	33.0	47.6	32.8
Sm	µg/g	1.66	0.09	0.687	0.71	0.14	0.77
Sr	µg/g	67	354	61	48	262	155
Ta	ng/g	ND	44.6	ND	≤ 2	ND	ND
Tb	ng/g	336	15.8	137	113	27.4	114
Th	ng/g	177	37	68	45	15.2	16
U	µg/g	0.93	0.62	ND	≤ 0.08	0.62	0.16
V	µg/g	3.49	1.34	0.98	0.67	0.34	0.62
Yb	µg/g	0.755	0.045	0.321	0.225	0.085	0.214
Zn	µg/g	3.3	3.1	3	1.73	1.6	3
CaCO3	mol-%	52.31	97.28	51.94	51.86	99.03	93.51
MgCO3	mol-%	47.17	2.62	47.65	47.87	0.87	6.38

Well Location Depth Description Sample ID		b-6-A/94-J-16 6349' micrite JL-71	c-56-L/94-J-9 6504'6" calcite cement JL-72	b-6-A/94-J-16 6339'6" calcite vein JL-73	d-79-F/94-J-10 6769' calcite vein JL-74	d-79-F/94-J-10 6769' matrix dolomite JL-75	b-10-D/94-J-16 6294' matrix dolomite JL-77
Ca	wt %	38.7	38.7	40.1	37.7	25.3	21.8
Mg	wt %	0.23	0.16	0.35	0.16	15.1	13
Al	µg/g	67	4.2	4.3	73	2247	137
As	µg/g	0.44	≤ 0.05	0.093	1.21	28.6	1.11
Ba	µg/g	24.3	≤ 1	4.36	51.3	29	125
Br	µg/g	0.28	0.18	0.47	0.04	0.6	0.81
Ce	µg/g	0.71	4.48	0.77	4.9	2.71	4.53
Cl	µg/g	189	237	215	< 70	440	426
Co	ng/g	113	147	31.9	283	843	115
Cr	µg/g	1.18	0.24	0.12	6.96	5.03	2.15
Eu	ng/g	13.3	316	32.7	2029	183	122
Fe	µg/g	571	6	468	77	7555	161
Hf	ng/g	19.6	≤ 3	≤ 3	9.6	100	51
K	µg/g	47	23	24	35	983	40
La	µg/g	0.80	2.23	1.76	1.71	0.861	2.24
Lu	ng/g	≤ 5	15.9	≤ 5	11.3	117	3.6
Mn	µg/g	39	116	126	621	1322	368
Na	µg/g	103	61.3	80.7	9.3	74	48.7
Rb	µg/g	≤ 0.1	≤ 0.1	≤ 0.1	ND	3.34	0.03
Sb	µg/g	0.070	0.028	0.013	15.5	0.237	41.3
Sc	ng/g	32.3	62.0	2.1	82.1	965	186
Sm	µg/g	0.06	0.57	0.078	1.39	0.76	0.37
Sr	µg/g	146	171	139	1141	124	43
Ta	ng/g	≤ 2	≤ 2	≤ 2	< 2	25.6	8.5
Tb	ng/g	11	77	9	167	120	36.1
Th	ng/g	33	22	≤ 2	10	372	132
U	µg/g	0.27	≤ 0.05	≤ 0.1	ND	2.49	12.6
V	µg/g	1.70	0.72	0.45	< 0.5	20.5	23.1
Yb	µg/g	0.023	0.143	0.016	0.287	0.612	0.05
Zn	µg/g	3.33	1.52	4.37	3.8	48	1.2
CaCO3	mol-%	98.87	99.25	98.44	99.02	49.54	50.37
MgCO3	mol-%	0.96	0.69	1.41	0.69	48.74	49.50

Well Location Depth Description Sample ID		b-10-D/94-J-16 6294' saddle dolomite JL-80	c-56-L/94-J-9 6545' micrite JL-82	c-56-L/94-J-9 6369' matrix dolomite JL-87	d-79-F/94-J-10 6773'6" matrix dolomite JL-91	d-79-F/94-J-10 6773'6" saddle dolomite JL-92	c-56-L/94-J-9 6386'6" matrix dolomite JL-93
Ca	wt %	22.1	38.4	21.3	20.2	20.4	21.9
Mg	wt %	12.8	0.54	12	11.7	12.4	13
Al	µg/g	152	1383	3449	2572	414	777
As	µg/g	0.1	2.67	3.72	36.44	2.59	0.78
Ba	µg/g	5.4	56.2	44.7	33.3	35.8	19.3
Br	µg/g	0.9	0.18	1.33	0.55	0.65	1.27
Ce	µg/g	1.61	2.62	4.84	2.88	2.33	1.44
Cl	µg/g	466	251	1107	434	685	645
Co	ng/g	37	320	878	997	245	153
Cr	µg/g	0.29	2.31	5.72	6.18	0.62	0.94
Eu	ng/g	73.8	180	259	104	275	128
Fe	µg/g	43	1297	1063	9369	1629	232
Hf	ng/g	ND	148	253	149	ND	79
K	µg/g	39	644	1522	1169	86	255
La	µg/g	1.08	1.62	1.83	1.05	0.97	0.65
Lu	ng/g	28	8.7	29	78	24.1	15
Mn	µg/g	465	168	1061	914	1553	973
Na	µg/g	57.1	23	91.1	61.6	81.4	69.3
Rb	µg/g	0.2	2.21	4.34	4.49	ND	0.62
Sb	µg/g	0.011	86.9	0.248	0.601	14.9	36.5
Sc	ng/g	29.9	230	606	1362	343	86.6
Sm	µg/g	0.195	0.36	0.81	0.49	0.585	0.318
Sr	µg/g	39	212	73	80	75	46
Ta	ng/g	1.3	12.8	54.8	31.8	ND	6.7
Tb	ng/g	38.1	51.8	98	69	116	58.5
Th	ng/g	ND	147	314	380	148	67.6
U	µg/g	0.23	0.96	5.99	2.97	ND	0.62
V	µg/g	0.9	2.93	14.3	24.3	4.08	4.83
Yb	µg/g	0.101	0.116	0.22	0.321	0.318	0.147
Zn	µg/g	2	2	3.7	80	2	1.1
CaCO3	mol-%	51.09	97.17	51.31	49.88	49.61	50.37
MgCO3	mol-%	48.78	2.25	47.65	47.62	49.70	49.28

Well Location		c-56-L/94-J-9	c-56-L/94-J-9	b-6-A/94-J-16	b-6-A/94-J-16
Depth		6386'6"	6452'	6379'6"	6408'6"
Description		saddle dolomite	matrix dolomite	micrite	stromatoporoid
Sample ID		JL-94	JL-95	JL-96	JL-97
Ca	wt %	21.2	20.9	38.7	39.3
Mg	wt %	11.8	11.7	0.12	0.17
Al	µg/g	352	779	29	35
As	µg/g	0.08	9.58	0.1	0.09
Ba	µg/g	9.6		41.5	
Br	µg/g	0.91	0.6	0.15	0.17
Ce	µg/g	1.44		0.61	
Cl	µg/g	625	568	< 75	152
Co	ng/g	72.1		1047	
Cr	µg/g	0.23		0.65	
Eu	ng/g	236		17.6	
Fe	µg/g	63		64	
Hf	ng/g	6.2		5.2	
K	µg/g	73	258	26	37
La	µg/g	0.594	1.07	0.661	0.6
Lu	ng/g	12.1		3.5	
Mn	µg/g	1263	1411	41	36.4
Na	µg/g	58.3	54.8	8.5	10
Rb	µg/g	0.12		0.18	
Sb	µg/g	6.6		13.3	
Sc	ng/g	11.4		20.6	
Sm	µg/g	0.54	0.73	0.06	0.009
Sr	µg/g	47		149	
Ta	ng/g	ND		7.5	
Tb	ng/g	121		11.3	
Th	ng/g	34.4		5.5	
U	µg/g	ND	0.71	0.67	0.89
V	µg/g	< 0.4	2	3.54	2.21
Yb	µg/g	0.246		0.033	
Zn	µg/g	1		1.3	
CaCO3	mol-%	51.99	51.80	99.45	99.28
MgCO3	mol-%	47.69	47.79	0.51	0.71

APPENDIX VI

List of fluid inclusion microthermometry results.

Abbreviations:

Position = location of measured inclusion (1 = core, 4 = rim)
T_{fm} = temperature of first melt in inclusion
T_m (ice) = temperature of final melting of inclusion
Salinity = value of T_m (ice) converted to weight percent NaCl equivalent
T_h = homogenization temperature (uncorrected)

Well Location - NTS	Depth	Host	Position	T_{fm}	T_m (ice)	Salinity	T_h
c-56-L/94-J-9	6358'		2	-53	-17.6	20.7	152
			2	< -50	-22.1	23.8	149
			2		-21.0	23.0	153
			3		-16.8	20.1	169
			4				174
			4		-17.5	20.6	177
c-94-L/94-J-9	6357'	brown matrix dolomite					189
							204
							212
		coarse matrix dolomite	1				155
			2				183
			3		-17.2	20.4	179
			4		-17.5	20.6	192
c-94-L/94-J-9	6454'	matrix dolomite		< -57	-15.1	18.7	142
					-14.9	18.6	127
					-14.9	18.6	131
c-58-E/94-J-10	2152.25 m	matrix dolomite		-65	-22.6	24.1	154
					-21.5	23.4	150
					-21.5	23.4	155
d-79-F/94-J-10	6769'	matrix dolomite		< -56	-13.4	17.3	186
				< -56	-13.0	16.9	190
				< -56	-13.6	17.4	184
				< -56	-12.6	16.5	189
				< -56	-13.4	17.3	179
d-79-F/94-J-10	6785'	matrix dolomite adjacent to quartz vein	1	< -56	-9.9	13.8	184
			2	< -56	-10.1	14.0	190
			3	< -56	-10.4	14.4	191
			4	< -56	-11.9	15.9	195
d-72-G/94-J-10	6449'	matrix dolomite	1	-50	-22.0	23.7	143
			1		-21.7	23.5	146
			1	-61	-21.9	23.6	146
			1		-21.8	23.6	148
			1		-21.8	23.6	151
			4	-62	-21.5	23.4	160
			4		-21.0	23.0	163
			4		-21.4	23.3	158
b-10-D/94-J-16	6268'	coarse matrix dolomite	1		-22.8	24.2	161
			2	-66	-21.9	23.6	139
			3		-21.9	23.6	143
			3		-22.9	24.3	139
			4	< -60	-14.1	17.9	152
			4		-15.1	18.7	150
b-10-D/94-J-16	6291'	brown matrix dolomite		-62	-23.1	24.4	189
				-60	-21.6	23.4	159
				-64	-21.8	23.6	164
					-21.6	23.4	165

Well Location - NTS	Depth	Host	Position	T_{fm}	T_m (ice)	Salinity	T_h
c-56-L/94-J-9	6358'	saddle dolomite			-10.0	13.9	158
c-94-L/94-J-9	6357'	saddle dolomite vein	1	-67	-17.1	20.3	149
			1	-64	-16.1	19.5	150
			2	-65	-16.3	19.7	148
			2	-66	-16.8	20.1	157
			3		-16.5	19.8	148
			3		-18.4	21.3	158
			4	-64	-16.6	19.9	155
			4	-62	-15.6	19.1	167
c-94-L/94-J-9	6454'	saddle dolomite cement	1		-11.9	15.9	128
			2	< -54	-13.3	17.2	134
			2		-12.7	16.6	128
			3	-62	-11.7	15.7	133
			4		-12.9	16.8	121
			4	< -50	-13.0	16.9	116
				-42	-12.9	16.8	157
c-58-E/94-J-10	2153.25 m	saddle dolomite cement	1	-61	-22.1	23.8	151
			1	-61	-21.9	23.6	152
			2	-64	-21.7	23.5	158
			2	-67	-22.9	24.3	154
			4	-67			196
d-79-F/94-J-10	6769'	saddle dolomite		-53			168
			1		-9.0	12.8	148
			2	-42	-8.9	12.7	152
			2	-39	-9.9	13.8	179
			3	-46	-11.1	15.1	207
			3	-39	-9.1	13.0	159
			4		-11.9	15.9	216
d-79-F/94-J-10	6785'	saddle dolomite cement	1	-39	-8.2	11.9	140
			1	-36	-8.8	12.6	149
			2		-11.2	15.2	214
			2	-42	-12.4	16.3	221
			2	-44	-13.5	17.3	228
			3	-36	-8.9	12.7	142
			3	-49	-9.2	13.1	145
			3	-46	-9.9	13.8	171
			3		-10.9	14.9	195
			4		-10.1	14.0	216
			4		-11.7	15.7	217
				-49	-12.6	16.5	210
				-48	-9.4	13.3	193
		replacement			-13.6	17.4	162
c-8-D/94-J-16	6437'9"	saddle dolomite		< -50	-15.5	19.0	155
					-14.9	18.6	159
c-58-E/94-J-10	2153.25 m	sphalerite		< -40	-15.2	18.8	139
					-14.9	18.6	136
					-15.0	18.6	140
					-14.6	18.3	133

Well Location - NTS	Depth	Host	Position	T_{fm}	T_m (ice)	Salinity	T_h
d-79-F/94-J-10	6785'	barite			-14.6	18.3	205
					-12.9	16.8	206
				-40	-12.4	16.3	196
		barite in quartz		-44	-8.4	12.2	113
					-9.2	13.1	126
					-8.9	12.7	114
					-9.0	12.8	124
					-9.0	12.8	116
		barite vein		-48	-6.9	10.4	175
				-52	-5.8	8.9	238
				-46	-12.9	16.8	192
					-10.7	14.7	155
c-58-E/94-J-10	2153.25 m	quartz	1	< -50	-8.3	12.0	121
			2	-46	-17.2	20.4	109
			2	-49	-9.5	13.4	117
			3	-48	-9.7	13.6	119
			3	-42	-9.3	13.2	112
			3	-46	-11.3	15.3	132
			4	-56	-10.4	14.4	192
d-79-F/94-J-10	6769'	quartz		-39	-8.0	11.7	176
				-49	-8.9	12.7	157
				-51	-9.1	13.0	156
					-8.5	12.3	151
					-9.0	12.8	159
d-79-F/94-J-10	6785'	quartz		-43	-9.9	13.8	128
					-9.8	13.7	130
				-39	-8.7	12.5	174
					-8.5	12.3	168
					-8.5	12.3	169
c-56-L/94-J-9	6504'6"	calcite cement		-49	-7.4	11.0	193
				-49	-7.2	10.7	187
				-49	-7.4	11.0	188
d-79-F/94-J-10	6769'	calcite cement		-53	-8.6	12.4	179
				-56	-8.7	12.5	175
				-56	-8.6	12.4	184
					-8.7	12.5	178
d-79-F/94-J-10	6785'	calcite cement		-44	-8.1	11.8	175
				-39	-8.8	12.6	173
				-39	-9.2	13.1	212
				-42	-8.5	12.3	202
					-8.4	12.2	176
					-8.6	12.4	180
b-6-A/94-J-16	6339'6"	calcite cement		-45	-11.4	15.4	140
				-49	-11.6	15.6	139
				-49	-10.9	14.9	144
				-49	-11.1	15.1	145
				-47	-11.1	15.1	140
				-49	-11.0	15.0	141
				-49	-10.9	14.9	145

APPENDIX VII

List of fluid inclusion crush-leach results. The upper table lists the molar concentrations. The lower table lists the absolute concentrations of the reported ions and was calculated according to the method described by Banks et al. (2002).

Abbreviations:

avg. = concentration calculated using the mean value for salinity
min. = concentration calculated using the lowest value for salinity
max. = concentration calculated using the highest value for salinity

Sample	Well Location - NTS	Depth	Description	Cl (ppm)	F (ppm)	SO_4 (ppm)	Nitrite (ppm)	Br (ppm)	Na (ppm)	K (ppm)	Cl/Br (molar)	Na/Br (molar)	K/Br (molar)	K/Na (molar)
CL-1	c-94-L/94-J-9	6454'	saddle dolomite	48.34	0.26	1.83	0.25	0.22	20.87	1.16	491	327	11	0.03
CL-2	c-56-L/94-J-9	6504'6"	calcite cement	24.64	0.40	1.44	0.12	0.11	10.74	0.69	514	345	13	0.04
CL-3	c-94-L/94-J-9	6357'	matrix dolomite	24.79	0.38	2.03	0.22	0.16	9.21	1.10	360	206	15	0.07
CL-4	b-6-A/94-J-16	6339'6"	calcite cement	19.80	0.05	8.66	0.11	0.12	8.91	0.51	369	256	9	0.03
CL-5	b-10-D/94-J-16	6291'	matrix dolomite	23.36	0.19	0.52	0.18	0.16	7.48	1.12	333	165	15	0.09
CL-6	b-10-D/94-J-16	6268'	coarse matrix dolomite	19.10	0.15	1.18	0.13	0.11	8.63	0.86	410	285	17	0.06
CL-7	b-70-I/94-J-10	6262'	saddle dolomite	54.87	0.13	1.33	0.21	0.30	19.37	2.24	411	224	15	0.07
CL-8	c-8-D/94-J-16	6437'9"	sphalerite	0.75	0.02	2.43	0.16	0.01	0.78	0.10	121	193	15	0.08
CL-9	c-56-L/94-J-9	6358'	matrix dolomite	22.52	0.25	1.13	0.20	0.13	10.06	0.89	403	277	14	0.05
CL-10	c-56-L/94-J-9	6358'	saddle dolomite	18.79	0.25	4.18	0.12	0.10	8.34	0.65	407	279	13	0.05
CL-11	d-72-G/94-J-10	6449'	matrix dolomite	33.63	0.17	3.05	0.26	0.21	11.42	1.91	366	192	19	0.10
CL-12	d-79-F/94-J-10	6785'	saddle dolomite	28.54	0.16	3.97	0.12	0.11	13.50	1.45	585	426	27	0.06
CL-13	d-79-F/94-J-10	6785'	matrix dolomite	31.74	0.11	2.70	0.23	0.13	15.86	1.64	546	421	26	0.06
CL-14	d-79-F/94-J-10	6769'	matrix dolomite	21.25	0.13	3.11	0.25	0.08	10.78	1.38	630	493	37	0.08
CL-15	d-79-F/94-J-10	6778'3"	matrix dolomite	12.74	0.10	2.39	0.19	0.05	6.52	1.04	574	453	42	0.09
CL-16	d-79-F/94-J-10	6778'3"	saddle dolomite	39.01	0.14	1.43	0.17	0.14	18.40	2.66	651	474	40	0.09

Sample	Cl (ppm) avg.	Cl (ppm) min.	Cl (ppm) max.	Br (ppm) avg.	Br (ppm) min.	Br (ppm) max.	Na (ppm) avg.	Na (ppm) min.	Na (ppm) max.	K (ppm) avg.	K (ppm) min.	K (ppm) max.	Log Cl (ppm)	Log Br (ppm)
CL-1	100121	95267	104369	460	438	479	43229	41133	45063	2398	2282	2500	5.00	2.66
CL-2	66141	64927	66748	290	285	293	28830	28301	29095	1844	1810	1861	4.82	2.46
CL-3	117718	112864	125000	736	706	782	43747	41943	46453	5223	5008	5546	5.07	2.87
CL-4	91626	90413	94660	560	553	579	41260	40713	42626	2365	2333	2443	4.96	2.75
CL-5	143811	141990	148058	973	960	1001	46057	45474	47417	6924	6836	7128	5.16	2.99
CL-6	134102	108617	147451	737	597	811	60589	49074	66620	6021	4877	6621	5.13	2.87
CL-7	120146	115291	124393	659	632	682	42412	40698	43911	4900	4702	5073	5.08	2.82
CL-8	110437	106796	114078	2064	1996	2132	114801	111017	118586	14745	14258	15231	5.04	3.31
CL-9	131068	121966	144417	733	682	808	58538	54473	64501	5158	4800	5683	5.12	2.87
CL-10	84345	84345	84345	467	467	467	37439	37439	37439	2895	2895	2895	4.93	2.67
CL-11	142597	139563	143811	878	859	885	48429	47399	48842	8116	7943	8185	5.15	2.94
CL-12	88592	76456	105583	341	295	407	41890	36151	49923	4495	3879	5356	4.95	2.53
CL-13	87985	83738	96481	363	346	398	43969	41846	48214	4559	4339	4999	4.94	2.56
CL-14	103762	100121	105583	371	358	378	52608	50762	53530	6724	6488	6842	5.02	2.57
CL-15	103155	100121	105583	405	393	414	52769	51217	54011	8388	8141	8585	5.01	2.61
CL-16	91019	76456	105583	315	265	365	42939	36068	49809	6198	5206	7189	4.96	2.50

APPENDIX VIII

List of laser ablation ICP-MS and corresponding fluid inclusion microthermometry results.

Abbreviations:

Spot # = location of the measurement (1 = rim, n = core)
CL char. = observed cathodoluminescence characteristic
$^{87}Sr/^{86}Sr$ = laser ablation $^{87}Sr/^{86}Sr$ isotope value
1σ = statistical variation of the $^{87}Sr/^{86}Sr$ isotope value
T_e = eutectic temperature or temperature of first melt in inclusion
T_m (ice) = temperature of final melting of inclusion
Salinity = value of T_m (ice) converted to weight percent NaCl equivalent
T_h = homogenization temperature (uncorrected)

Well Location - NTS	Depth	Host	Spot #	CL char.	$^{87}Sr/^{86}Sr$	1σ	T_e	T_m (ice)	Salinity	T_h
d-79-F/94-J-10	6769'	saddle dolomite	1	dull	0.72209	0.00070				
			2	bright	0.71834	0.00030				
			3	bright	0.71420	0.00040				
			4	bright	0.71610	0.00030				
d-79-F/94-J-10	6769'	saddle dolomite	1	bright	0.71739	0.00060	-49	-13.1	17.0	223
			1	bright	0.71739	0.00060		-12.9	16.8	218
			2	dull	0.71110	0.00070	-39	-10.2	14.1	162
			3	dull	0.71248	0.00050	-36	-10.4	14.4	169
			4	bright	0.71156	0.00160	-54	-11.1	15.1	198
			5	bright	0.71883	0.00030	-48	-10.8	14.8	185
			6	dull	0.71120	0.00030	-39	-8.9	12.7	142
			7	dull	0.71437	0.00080	-45	-10.4	14.4	172
			7	dull	0.71437	0.00080		-10.3	14.3	165
			8	dull	0.71198	0.00040		-9.4	13.3	152
			8	dull	0.71198	0.00040	-40	-9.7	13.6	149
			9	dull	0.71189	0.00020	-36	-9.4	13.3	145
			10	dull	0.71126	0.00050	-36	-9.1	13.0	139
		matrix dolomite	11	dull	0.71657	0.00040	-49	-12.5	16.4	204
d-79-F/94-J-10	6769'	saddle dolomite	1	dull	0.71401	0.00300				
			2	dull	0.71066	0.00110				
			3	bright	0.71715	0.00060				
			4	dull	0.71158	0.00080				
			5	bright	0.71191	0.00020				
			6	bright	0.71056	0.00070				
			7	dull	0.70984	0.00040				
			8	dull	0.71635	0.00070				
			9	dull	0.71234	0.00070				
			10	dull	0.71234	0.00060				

APPENDIX IX

List of ^{87}Sr/^{86}Sr isotope results from potential strontium source rocks using the selective extraction method described by Machel and Cavell (1999).

Abbreviations:

Collection # = archival collection number: EAS – University of Alberta Department of Earth & Atmospheric Sciences collection number; GSC – Geological Survey of Canada collection number
Location = UWI – universal well identifier (either NTS or DLSS)
Lat/Long – latitude and longitude
Leach #1 = strontium extracted using 0.01N HCl at 25°C for 20 hours
Leach #2 = strontium extracted using 1.0N HCl at 20°C for 20 hours

Sample ID	Collection #	Location UWI or Lat/Long	Depth	Age	Formation	Lithology	^{87}Sr/^{86}Sr Leach #1	^{87}Sr/^{86}Sr Leach #2
JLS-1		d-76-G/94-J-10	4130'	Lower Mississippian	Exshaw	shale		0.70950 +/- 2
JLS-2		b-46-J/94-J-10	1500'	Lower Cretaceous	Wilrich Mb, Spirit River Fm	shale		0.71049 +/- 2
JLS-3		d-76-G/94-J-10	4900'	Upper Devonian	Redknife	shale		0.71146 +/- 2
JLS-4		d-76-G/94-J-10	6850'	Middle Devonian	Otter Park	shale		0.71044 +/- 2
JLS-5		d-76-G/94-J-10	3300'	Lower Mississippian	Banff	shale		0.70190 +/- 1
JLS-6		d-76-G/94-J-10	5700'	Upper Devonian	Fort Simpson	shale		0.71124 +/- 1
JLS-7		d-76-G/94-J-10	1950'	Lower Cretaceous	Wilrich Mb, Spirit River Fm	shale		0.71156 +/- 2
JLS-8		d-76-G/94-J-10	7250'	Middle Devonian	Klua	shale		0.71002 +/- 1
JLS-9		c-94-L/94-J-9	7170'	Middle Devonian	Klua	shale		0.71014 +/- 1
JLS-10		b-72-L/94-J-9	3500'	Lower Mississippian	Banff	shale		0.70878 +/- 1
JLS-11		b-72-L/94-J-9	4600'	Upper Devonian	Redknife	shale		0.70896 +/- 1
JLS-12		b-72-L/94-J-9	1800'	Lower Cretaceous	Wilrich Mb, Spirit River Fm	shale		0.71095 +/- 1
JLS-13		b-72-L/94-J-9	6200'	Upper Devonian	Muskwa	shale		0.71222 +/- 2
JLS-14		b-72-L/94-J-9	5800'	Upper Devonian	Fort Simpson	shale		0.71065 +/- 2
JLS-15		b-46-J/94-J-10	4550'	Upper Devonian	Redknife	shale		0.70954 +/- 1
JLS-16		b-46-J/94-J-10	3730'	Lower Mississippian	Exshaw	shale		0.71123 +/- 1
JLS-17		b-46-J/94-J-10	5750'	Upper Devonian	Fort Simpson	shale		0.71226 +/- 1
JLS-18		b-46-J/94-J-10	3500'	Lower Mississippian	Banff	shale		0.70944 +/- 1
JLS-19		b-46-J/94-J-10	6000'	Upper Devonian	Muskwa	shale		0.71189 +/- 1
JSL-172	EAS M4029	12-31-78-14W6	12038'	Precambrian		blastomylonite	0.79530 +/-2	0.82338 +/- 2
JSL-173	EAS M4025	6-29-81-15W6	11618'	Precambrian		gneiss	0.79452 +/- 2	0.79774 +/- 2
JSL-174	EAS M4030A	1-26-86-16W6	10909'	Precambrian		diabase	0.72105 +/- 2	0.72193 +/- 2
JSL-175	EAS M4027B	a-49-B/94-H-16	10029'	Precambrian		meta-argillite	0.74891 +/- 2	0.77282 +/- 2
JSL-176	EAS M4028A	b-92-D/94-I-4	9925'	Precambrian		diorite	0.74596 +/- 1	0.78393 +/- 2
JSL-177	EAS M4026B	b-29-C/94-I-7	8437'	Precambrian		quartzite	0.75527 +/- 2	0.77723 +/- 2
JSL-178	EAS MB54-8	60°09'29" 121°08'16"	8230'	Precambrian		granodiorite	0.76379 +/- 1	0.78276 +/- 2
JSL-a95J		a-95-J/94-J-10	7787'	Cambrian		quartzite	0.72153 +/- 2	0.71982 +/- 1
M252	GSC C-058027	58°08'15" 124°31'00"	6.10 m	Middle Proterozoic	Muskwa assemblage	slate	1.03075 +/- 1	0.74404 +/- 1
M254	GSC C-057884	57°32'30" 125°04'30"	483.11 m	Middle Proterozoic	Muskwa assemblage	carbonate	0.70979 +/- 1	0.70904 +/- 1
M257	GSC C-057888	57°22'60" 124°34'60"	959.82 m	Middle Proterozoic	Muskwa assemblage	slate & carbonate	0.72383 +/- 1	0.72537 +/- 1
M258	GSC C-057892	57°22'60" 124°34'60"	482.50 m	Middle Proterozoic	Muskwa assemblage	slate	0.71973 +/- 1	
M260	GSC C-058188	58°29'45" 124°35'15"	0.00 m	Middle Proterozoic	Muskwa assemblage	quartzite	0.88375 +/- 1	0.75401 +/- 1
M263	GSC C-033403	58°21'30" 124°30'30"	0.00 m	Middle Proterozoic	Muskwa assemblage	slate & quartzite	0.85758 +/- 4	0.85766 +/- 1

APPENDIX X

List of chemical and isotopic results from formation water samples.

	b-46-J/94-J-10	c-29-I/94-J-10	a-5-A/94-J-15	d-96-L/94-J-9	b-72-L/94-J-9	a-63-J/94-J-9	c-88-L/94-J-9
Ag	<0.005	<0.002	<0.005	<0.005	0.0049	<0.005	<0.02
Al	<0.3	<0.1	<0.3	<0.3	<0.1	<0.3	<1
As	<0.010	<0.004	<0.01	<0.01	<0.005	<0.01	0.056
B	69.73	13.16	64.54	62.4	66.45	34.69	78.8
Ba	3.34	231.8	1.82	1.38	1.23	70.48	1.8
Be	<0.005	<0.002	<0.005	<0.005	<0.003	<0.005	<0.02
Bi	<0.03	<0.01	<0.03	<0.03	<0.01	<0.03	<0.1
Ca	2419.5	82.3	2074.5	1764	1729.75	3079.5	2470
Cd	<0.0005	<0.0002	<0.0005	<0.0005	<0.00025	<0.0005	<0.002
Co	<0.005	<0.002	<0.005	<0.005	<0.003	<0.005	<0.02
Cr	0.043	0.103	<0.03	<0.03	<0.01	0.22	<0.1
Cu	0.07	0.027	<0.05	<0.05	<0.03	<0.05	<0.2
Fe	<0.5	<0.2	<0.5	<0.5	<0.2	0.79	<2
K	1351	162.16	1168	1043.5	983.25	180.55	1230
Li	32.8	9.73	31.07	30.6	28.89	15.28	33.6
Mg	293.6	92.64	258.05	242.45	233.48	358.3	330
Mn	0.5	<0.1	<0.2	<0.2	<0.1	2.79	<1
Mo	<0.05	<0.02	<0.05	<0.05	<0.03	<0.05	<0.2
Na	10015	5178	9465	9500	9035	6915	12800
Ni	0.444	<0.01	0.15	<0.03	0.253	<0.03	<0.1
Pb	<0.005	<0.002	<0.005	<0.005	<0.003	<0.005	<0.02
S	73.45	9.13	139.05	166.45	174.4	15.23	134
Sb	<0.01	<0.004	<0.01	<0.01	0.0053	<0.01	<0.04
Se	<0.01	<0.004	<0.01	<0.01	<0.005	<0.01	<0.04
Si	34.68	13.16	40.52	48.83	41.98	35.41	30
Sn	<0.05	<0.02	<0.05	<0.05	<0.03	<0.05	<0.2
Sr	212.96	63.6	161.44	162.7	121.46	121.21	174
Ti	<0.03	<0.01	<0.03	<0.03	0.014	<0.03	<0.1
Tl	<0.003	<0.001	<0.003	<0.003	<0.001	<0.003	<0.01
U							<0.1
V	<0.005	<0.002	<0.005	<0.005	<0.0025	<0.005	0.076
Zn	<0.05	0.059	<0.05	<0.05	<0.03	<0.05	<0.2
HCO_3	488.79	1340.45	143.62	134.87	70.78	167.84	99
CO_3	6	6	6	6	6	6	<6
OH	<5	<5	<5	<5	<5	<5	<5
SO_4	220.35	27.39	417.15	499.35	523.2	45.68	
Alkalinity	400.92	1099.47	117.8	110.62	58.1	137.67	81
Na	10100	6500	10200	9350	9580	7690	10600
Cl	21600	10300	21400	19700	19100	19700	21800
Br	120	39	118	107	105	71.7	124
I	4.08	6.97	3.94	4.9	4.48	12.6	
TDS	36316	17524	35661	32684	32171	31389	37006
$\delta^{18}O$	+0.10	-1.83	+1.59	+2.69	+1.88	+10.51	+2.41
δD	-118.74	-125.46	-113.51	-112.36	-116.63	-50.65	-108.49
$^{87}Sr/^{86}Sr$	0.74358 +/- 2	0.72524 +/- 2	0.74105 +/- 2	0.73382 +/- 2	0.73874 +/- 1	0.71329 +/- 2	0.73983 +/- 2

	a-56-J/94-J-10	c-96-I/94-J-10	b-75-F/94-J-9	c-52-F/94-J-10	a-83-G/94-J-10	d-74-C/94-J-9	c-20-I/94-J-10
Ag	<0.02	<0.02	0.0003	<0.02	<0.02	<0.02	<0.02
Al	<1	<1	0.021	<1	<1	<1	<1
As	<0.04	<0.04	0.0005	<0.04	<0.04	<0.04	<0.04
B	100	77.7	1.34	68.3	76	70.7	74.5
Ba	4.24	1.2	0.083	3.65	3.92	2.26	3.87
Be	<0.02	<0.02	0.0001	<0.02	<0.02	<0.02	<0.02
Bi	<0.1	<0.1	<0.1	<0.1	<0.1	<0.1	<0.1
Ca	4370	2600	34.7	1900	2120	2580	2210
Cd	<0.002	<0.002	<0.002	<0.002	<0.002	<0.002	<0.002
Co	<0.02	<0.02	<0.02	<0.02	<0.02	<0.02	<0.02
Cr	<0.1	<0.1	<0.1	<0.1	<0.1	<0.1	<0.1
Cu	<0.2	<0.2	<0.2	<0.2	<0.2	<0.2	<0.2
Fe	<2	<2	0.04	<2	<2	<2	<2
K	2150	1310	14	1160	1150	1060	1170
Li	42.4	33.2	0.32	29.3	32.9	28.7	31.9
Mg	574	320	3.6	230	260	310	280
Mn	<1	<1	19	8.1	<1	<1	<1
Mo	<0.2	<0.2	<0.2	<0.2	<0.2	<0.2	<0.2
Na	15900	10900	209	8920	9460	11400	9910
Ni	<0.1	<0.1	<0.1	<0.1	<0.1	<0.1	<0.1
Pb	<0.02	<0.02	<0.02	<0.02	<0.02	<0.02	<0.02
S	92	155	10.8	38	46	110	41
Sb	<0.04	<0.04	<0.04	<0.04	<0.04	<0.04	<0.04
Se	<0.04	<0.04	<0.04	<0.04	<0.04	<0.04	<0.04
Si	39	26	14.4	37	41	39	38
Sn	<0.2	<0.2	<0.2	<0.2	<0.2	<0.2	<0.2
Sr	293	145	1.7	154	177	167	187
Ti	<0.1	<0.1	<0.1	<0.1	<0.1	<0.1	<0.1
Tl	<0.01	<0.01	<0.01	<0.01	0.011	<0.01	<0.01
U	<0.1	<0.1	<0.1	<0.1	<0.1	<0.1	<0.1
V	<0.02	<0.02	<0.02	<0.02	<0.02	<0.02	<0.02
Zn	<0.2	<0.2	<0.2	<0.2	<0.2	<0.2	<0.2
HCO$_3$	105	92	82	82		100	79
CO$_3$	<6	<6	<6	<6		<6	<6
OH	<5	<5	<5	<5		<5	<5
SO$_4$							
Alkalinity	86	75	67	67		82	65
Na	14700	10500	210	8600	8930	11200	9390
Cl	32900	22400	376	17800	18500	23100	19800
Br	186	125	0.99	101	108	119	115
I							
TDS	55451	37693	687	30129	31445	38787	33341
δ^{18}O	+3.35	+1.64	-1.78	-2.40	-1.03	+1.30	-0.71
δD	-95.91	-112.80	-102.68	-123.25	-126.21	-131.18	-118.59
^{87}Sr/^{86}Sr	0.73862 +/- 1	0.73968 +/- 2	0.73671 +/- 1	0.75047 +/- 1	0.74676 +/- 2	0.73577 +/- 2	0.74357 +/- 2

APPENDIX XI

List of refereed publications and abstracts.

REFEREED PUBLICATIONS and/or INVITED EXHIBITIONS

Lonnee, J., and Machel, H.G. 2005. Pervasive dolomitization with subsequent hydrothermal alteration in the Clarke Lake gas field, Middle Devonian Slave Point Formation, British Columbia, Canada. AAPG Bulletin, accepted Aug. 2005

Rice, R.J., and Lonnee, J. 2004. Mississippi Valley-type (MVT) Pb-Zn potential in Middle and Upper Devonian carbonates of northeastern Alberta – implications for future exploration based on sedimentology, diagenesis, and geochemistry. In: P. Hannigan (ed.) Potential for carbonate-hosted lead-zinc Mississippi Valley-type mineralization in northern Alberta and southern Northwest Territories. Geoscience Contributions, Targeted Geoscience Initiative, Geological Survey of Canada Bulletin, in press.

Lonnee, J., and Machel, H.G. 2004. High-temperature matrix dolomitization by halite-saturated brines in the Slave Point Formation, Clarke Lake gas field, British Columbia, Canada. Dolomites: the spectrum – mechanisms, models, reservoir Development. Canadian Society of Petroleum Geologists Conference, CO12.

Lonnee, J. 2002. Mississippi Valley-type (MVT) TGI – Petrography and isotopic interpretation of samples collected from 2002 core examination program. Report prepared for Alberta Energy and Utilities Board, Alberta Geological Survey (AGS), 41 p.

Machel, H.G., and Lonnee, J. 2002. Hydrothermal dolomite – a product of poor definition and imagination. Sedimentary Geology, v. 152, p. 163-171.

Machel, H.G., and Lonnee, J. 2002. Hydrothermal dolomite – a product of poor definition and imagination. Canadian Society of Petroleum Geologists Annual Convention, Invited Talk, p. 212.

Al-Aasm, I.S., Lonnee, J.S., and Clarke, J.D. 2002. Multiple fluid flow events and the formation of saddle dolomite: Examples from the Western Canada Sedimentary Basin. Marine and Petroleum Geology, v. 19, p. 209-217.

Lonnee, J. 2002. Mississippi Valley-type (MVT) TGI - Cathodoluminescence Study. Report prepared for Alberta Energy and Utilities Board, Alberta Geological Survey (AGS), 18 p.

Cioppa, M.T., Lonnee, J.S., Symons, D.T.A., Al-Aasm, I.S., and Gillen, K.P. 2001. Facies and lithological controls on paleomagnetism: an example from the Rainbow South field, Alberta, Canada. Bulletin of Canadian Petroleum Geology, v. 49, p. 393-407.

Lonnee, J.S., and Al-Aasm, I.S., 2000. Dolomitization and fluid evolution in the Middle Devonian Sulphur Point Formation, Rainbow South Field, Alberta: petrographic and geochemical evidence. Bulletin of Canadian Petroleum Geology, v. 48, p. 262-283.

Al-Aasm, I.S., Lonnee, J., and Clarke, J. 2000. Multiple fluid flow events and the formation of saddle dolomite: Examples from Middle Devonian carbonates of the Western Canada Sedimentary Basin. Journal of Geochemical Exploration, v. 69-70, p. 11-15.

NON-REFEREED PUBLICATIONS

Lonnee, J., and Machel, H.G. 2005. Pervasive dolomitization with subsequent hydrothermal alteration in the Clarke Lake gas field, Middle Devonian Slave Point Formation, British Columbia, Canada. Canadian Society of Petroleum Geologists Reservoir, v. 32 (7), p. 13.

Lonnee, J., and Machel, H.G. 2004. Diagenesis by unusual fluid mixing in a Devonian dolostone gas reservoir, Canada. SEPM-Central European Section, Sediment 2004, Aachen, Germany. Schriftenreihe der Deutschen Geologischen Gesellschaft, Kurzfassungen und Exkursionsfuehrer, Heft 33, p. 97.

Lonnee, J., and Machel, H.G. 2004. Dolomitization by halite-saturated brine and subsequent hydrothermal alteration in the Devonian Slave Point Formation, Clarke Lake gas field, British Columbia. CSPG-CHOA-CWLS Joint Conference Abstracts, S013

Lonnee, J., and Machel H.G. 2004. Comparison of Sr-isotope values from bulk analysis and laser ICP-MS with fluid inclusion data: a new level of geochemical resolution. SEPM Carbonate Research Group Meeting, Dallas, TX

Lonnee, J. 2004. Complex fluid evolution in a hydrothermal dolomite reservoir – Devonian Clarke Lake gas field, Canada. American Association of Petroleum Geologists Annual Meeting Abstracts, A87614

Lonnee, J., and Machel, H.G. 2004. Hydrothermal dolomite model – old concept and new challenges. American Association of Petroleum Geologists Annual Meeting Abstracts, A87629

Lonnee, J., and Machel, H.G. 2003. High-temperature dolomite containing enigmatic formation fluids: Devonian Clarke Lake gas field, British Columbia, Canada. 12th Bathurst Meeting Abstracts, International Conference of Carbonate Sedimentologists, Durham, England, p. 62.

Lonnee, J., and Machel, H.G. 2001. Reservoir enhancement in the Clarke Lake Field, British Columbia: facies control on diagenesis in the Middle Devonian Slave Point Formation. American Association of Petroleum Geologists Annual Meeting Abstracts.

Cioppa, M.T., Lonnee, J., Symons, D.T.A., Al-Aasm, I.S., and Gillen, K.P. 2000. Dating dolomitization/recrystallization events using petrologic, geochemical and paleomagnetic techniques. American Association of Petroleum Geologists, Eastern Section Meeting Abstracts. AAPG Bulletin, v. 84, p. 1381.

Lonnee, J.S., and Al-Aasm, I.S. 1999. Deep burial diagenesis in the Middle Devonian Sulphur Point Formation, Alberta Basin. Canadian Society of Petroleum Geologists Annual Meeting Abstracts, p. C99-66.

Lonnee, J.S., and Al-Aasm, I.S. 1999. Fluid flow and dolomitization in the Middle Devonian Sulphur Point Formation, northwestern Alberta. Canadian Society of Petroleum Geologists Annual Meeting, poster presentation.

Lonnee, J.S., and Al-Aasm, I.S. 1999. Fluid flow and dolomitization in the Middle Devonian Sulphur Point Formation, northwestern Alberta. Geological Association of Canada Annual Meeting Abstracts, v. 24, p. 73.

Lonnee, J.S., Cioppa, M.T., Al-Aasm, I.S., Symons, D.T.A., Lewchuk, M.T., and Gillen, K.P. 1998. Correlating paleomagnetic data with the paragenetic sequence in the Middle Devonian Sulphur Point (Bistcho) Formation, northwestern Alberta. Geological Association of Canada Annual Meeting Abstracts, v. 23, p. A-112.